Lecture Notes in Electrical Engineering 91

Giovanni Neri
Nicola Donato
Arnaldo d'Amico
Corrado Di Natale
Editors

Sensors and Microsystems

AISEM 2010 Proceedings

Springer

Lecture Notes in Electrical Engineering

Volume 91

For further volume
http://www.springer.com/series/7818

Giovanni Neri · Nicola Donato
Arnaldo d'Amico · Corrado Di Natale
Editors

Sensors and Microsystems

AISEM 2010 Proceedings

Springer

Giovanni Neri
Department of Industrial Chemistry
and Materials Engineering
University of Messina
Contrada Di Dio
98166 Messina
Italy
e-mail: neri@ingegneria.unime.it

Nicola Donato
Department of Matter Physics
and Electronic Engineering
University of Messina
Contrada Di Dio
98166 Messina
Italy
e-mail: ndonato@unime.it

Prof. Arnaldo d'Amico
Department of Electronic Engineering
University of Rome Tor Vergata
Via del Politecnico 1
00133 Roma
Italy
e-mail: damico@eln.uniroma2.it

Corrado Di Natale
Department of Electronic Engineering
University of Rome Tor Vergata
Via del Politecnico 1
00133 Roma
Italy
e-mail: dinatale@uniroma2.it

ISSN 1876-1100
ISBN 978-94-007-1323-9
DOI 10.1007/978-94-007-1324-6
Springer Dordrecht Heidelberg London New York

e-ISSN 1876-1119
e-ISBN 978-94-007-1324-6

Cover design: eStudio Calamar, Berlin/Figueres

Printed on acid-free paper

Springer is part of Springer Science+Business Media (www.springer.com)

In memory of Giuliano Martinelli.
A colleague, a scientist, a friend

Foreword

This book is the collection of most of the papers presented at the 15th Italian Conference on Sensors and Microsystems, promoted by the Italian Association on Sensors and Microsystems (AISEM). The book includes also three tutorial papers, which address basic concepts in the area of sensors and microsystems. This XV Conference edition, organized by the University of Messina, was held in the Faculty of Engineering, University of Messina, from 8 to 10th February 2010, in conjunction with the SIOF (Italian Society of Optics and Photonics) and GS-CSI (Sensor Group of the Italian Chemical Society).

Aim of AISEM 2010 Conference was to give an update overview of the different aspects (Materials, Processes, Devices, Systems and Applications) in the field of sensors and microsystems. At the Conference, organized in 5 topical sessions, attended about 100 participants, with 3 plenary lectures, 48 oral communications and 52 communications presented in the poster session. Plenary lectures were given by important researchers from University and industrial world. Luigi Campanella (University "La Sapienza", Rome) illustrated the multidisciplinary approach to sensors. Salvatore Coffa (STMicroelectronics, Catania) explained the strategy, both at technical and management level, in the sensors market. Anna Menini (SISSA, Trieste) presented the basic concepts of molecular sensing mechanisms in biological olfactory systems. Nicola Pinna (University of Aveiro) described the recent development in the synthesis of nanostructured metal oxides for sensing applications.

At the end of the Conference, three awards, sponsored by the Conference Organization, were assigned for the best posters. The Best Poster Award, was assigned ex-aequo to the papers "Nonlinear MEMS mechanism for energy harvesting from mechanical vibrations" by B. Andò, S. Baglio, C. Trigona, and "Ultrasensitive detection of non amplified genomic DNA" by L. M. Zanoli, R. D'Agata, G. Spoto, R. Corradini, R. Marchelli, C. Ferretti, M. Gatti and "A research study and development of a hydrogen sensor for fuel cells" by A. Bonavita, G. Micali, G. Neri, N. Donato, M. Latino, S. Licoccia.

This book represents then an exhaustive summary of the excellent scientific work presented at the Conference, with a deep discussion of the many subjects

under study. We hope that it may contribute to a further development of the field of sensors and microsystems in Italy and abroad. The appreciation by the readers will be the best awards for the efforts and time expended.

Special thanks are given to Dr. Mariangela Latino for his effort and dedication in the organization of the Conference and to the guys of LESST Lab. (Dr. A. Bramanti, F. Cincotta, S. Trocino, E. Cardillo, Dr. D. Aloisio, E. Fulco) for their support during the three days of the Conference. The Committee also thanks the sponsors BioAge, Libreria Bonanzinga and FINE Permeation Tubes for their support, and the artists Dr. G. Donato and Dr. V. Saija for their creations and the graphical arrangement of the Conference documents.

P.S. One of us, Prof. Giuliano Martinelli, died this year 24 May!

He was a very good friend, a kind person, an excellent researcher and an outstanding teacher. We will never forget the very sound contribution he gave to the AISEM scientific growth. In our mind we will keep alive also his unique polite and genteel behaviour and in our heart an immense pain.

AISEM Committees

Local Organization Chairman

S. Galvagno
Università degli Studi di Messina

G. Neri
Università degli Studi di Messina

N. Donato
Università degli Studi di Messina

Local Organization Secretary

M. Latino

AISEM Directive Committee

A. D'Amico
Università di Roma "Tor Vergata"
Presidente AISEM

L. Campanella
Università di Roma "La Sapienza"

P. Siciliano
CNR-IMM Lecce

C. Mari
Università di Milano

G. Martinelli
Università di Ferrara

U. Mastromatteo
ST Microelect. Castelletto (MI)

A.G. Mignani
CNR-IFAC Firenze

M. Prudenziati
Università di Modena

G. Sberveglieri
Università di Brescia

G. Soncini
Università di Trento

AISEM Scientific Committee

M.C. Carotta
Università di Ferrara

P. Dario
Scuola Superiore S. Anna
Pisa

F. Davide
Telecom Italia Roma

A. Diligenti
Università di Pisa

C. Di Natale
Università di Roma
"Tor Vergata"

L. Dori
CNR-IMM-LAMEL
Bologna

G. Faglia
Università di Brescia

C. Malvicino
CRFiat Orbassano (To)

G. Martinelli
Università di Ferrara

M. Mascini
Università di Firenze

N. Minnaja
Polo Navacchio SpA
Navacchio-Cascina (PI)

B. Morten
Università di Modena

G. Palleschi
Università di Roma
"Tor Vergata"

F. Villa
ST Microelctr.
Castelletto (Mi)

M. Zen
ITC-IRST Trento

Contents

Part I
Tutorials

Chapter 1
Odorant Detection and Discrimination in the Olfactory System

Simone Pifferi and Anna Menini

Abstract The olfactory system excels in both discrimination and detection of odorants. In mammals, it reliably discriminates more than 3000 structurally diverse odorant molecules and has an amazingly high sensitivity that allows the detection of very low amounts of specific odorant molecules. In addition, the olfactory system has the capability to adapt to ambient odorants, allowing the recognition of a broad range of stimuli. The discrimination among different odorants is achieved by using hundreds of receptors, activated with a combinatorial code. Olfactory transduction uses a canonical second messenger system providing two critical attributes: amplification and high signal-to-noise characteristics, giving the system its remarkable detector capabilities. In this review, we present an introduction to the basic molecular mechanisms of olfactory transduction in olfactory sensory neurons.

1.1 Odorants

The process of chemosensation allows a living organism to detect and discriminate different chemical molecules in the external environment. This task is essential for survival of the individual and of the species, indeed it enables animals to locate nutritious food and suitable mating partners, as well as to smell the presence of predators and to avoid eating toxic substances [56].

The olfactory system is specialized in the detection of odorants, and many mammalian species recognize and discriminate among thousands of odorants with high specificity and sensitivity. For example, the threshold for human detection of

S. Pifferi · A. Menini (✉)
Scuola Internazionale Superiore di Studi Avanzati, SISSA, and Italian Institute of Technology, SISSA Unit, Via Bonomea 265, 34136 Trieste, Italy
e-mail: menini@sissa.it

G. Neri et al. (eds.), *Sensors and Microsystems*,
Lecture Notes in Electrical Engineering 91, DOI: 10.1007/978-94-007-1324-6_1,

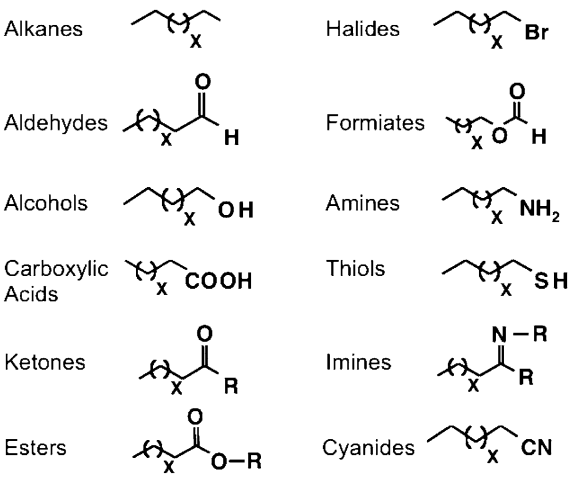

Fig. 1.1 Chemical structures of various functional groups in some odorant molecules

ethyl mercaptan (ethanethiol), commonly added to natural gas as an odorant, is as low as one part in 2.5 billion parts of air [58].

Odorants are mainly organic volatile compounds that bind to odorant receptors (see Sect. 1.6). A common odorant is usually made by a mixture of different types of volatile molecules and the relative concentrations of each component participate to determine the particular perception response. Odorant components include aliphatic and aromatic molecules with varied carbon backbones and diverse functional groups, such as alkanes, aldehydes, alcohols, carboxylic acids, ketones, esters, halides, formiates, amines, thiols, imines, cyanides, and others, as illustrated in Fig. 1.1 (for review see [38]).

1.2 The Olfactory Epithelium

Volatile molecules enter the nose during inspiration and contact the olfactory epithelium, located in the interior of the nasal cavity. The olfactory epithelium is made by three main types of cells: olfactory sensory neurons, which are devoted to the function of transducing chemical information into electrical signals, supporting cells and several types of basal cells (Fig. 1.2a). Olfactory sensory neurons are continuously regenerated by basal cells throughout the life span. Some olfactory glands, named glands of Bowman, produce most of the mucus that normally covers the epithelium surface. It is of interest to note that some odorant-binding proteins (OBPs) are found at high concentrations in the nasal mucus. Although their affinity for odorants suggests a role in olfactory perception, their physiological role in vertebrates is still unclear.

Olfactory sensory neurons have a bipolar morphology with a flask-like shape. Their apical part, located at the surface of the epithelium, is slightly swelled into

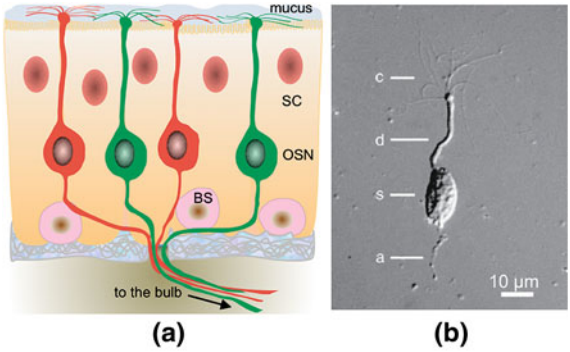

Fig. 1.2 The olfactory epithelium and an isolated olfactory sensory neuron. **a** Schematic diagram showing the various cell types composing the olfactory epithelium (*OSN* olfactory sensory neuron, *SC* supporting cell, *BC* basal cell). **b** Photograph of an isolated frog olfactory sensory neuron under differential interference optic, c cilia; d dendrite; s soma; a axon. Reprinted from Kleene and Gesteland [22], copyright 1981, with permission from Elsevier

an olfactory knob from which several very fine cilia depart (Fig. 1.2b). The cilia are embedded in the mucus covering the epithelium and expose their membrane to odorant molecules arriving from the external environment. Olfactory sensory neurons are primary sensory cells and their axons join in bundles to form the first cranial nerve that reach the olfactory bulbs in the brain.

The diameter of the cell body is about 5–8 μm, while that of the dendrite is about 1–2 μm. In mammals, the cilia are 15–50 μm long, while in some lower vertebrates they can be as long as 200 μm [35, 52]. The diameter of a mammalian cilium tapers from 0.28 μm near the base of the cilium to 0.19 μm in the distal portion [35]. The presence of numerous cilia greatly increases the surface membrane area that can interact with odorant molecules. Some estimations indicated that cilia may increase the cell bare surface some one thousand or more times [15].

The cilia play a fundamental role in olfaction, since they are the site of the sensory transduction apparatus (see Sect. 1.7). Indeed, olfactory sensory neurons deprived of cilia are no longer able to respond to odorants. Furthermore, the damage of the olfactory epithelium can produce a complete loss of the sense of smell, called anosmia.

1.3 Electrical Responses of Olfactory Sensory Neurons to Odorants

Even if olfactory sensory neurons are physiologically devoted to detect odorants, measuring an odorant response in one of these neurons is very challenging. The response to a brief pulse of odorant has been measured with several

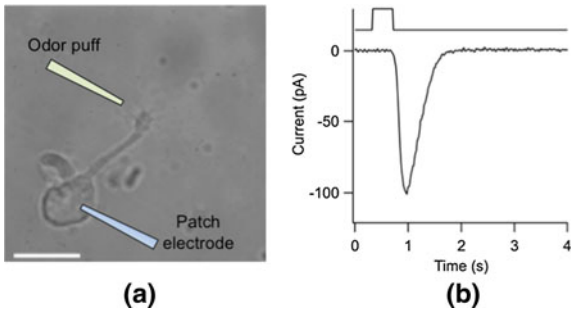

Fig. 1.3 Electrical response to odorants of an isolated olfactory sensory neuron. **a** Experimental method. An isolated olfactory sensory neuron was stimulated with odorants while the electrical response was measured with the patch-clamp technique in the voltage-clamp whole-cell configuration. **b** Current response evoked by the odorant amylacetate at the holding potential of −50 mV. The *top trace* indicates timing and duration of the odorant stimulus. Adapted by permission from Macmillan Publishers Ltd: (Nature) Kurahashi and Menini [25], copyright, 1997

electrophysiological techniques, including the patch-clamp technique (Fig. 1.3a). The percentages of responses to odorants range from 2 to 30%, depending on the choice of odorant. As shown in Fig. 1.3b, when the odorant stimulus causes the excitation of the neuron, a transient inward current is generated that will depolarize the neuron in situ. The response typically lasts 1 s or more. The latency between the arrival of the stimulus and the onset of the current ranges from 150 to 600 ms and, for a strong stimulus, the amplitude of the peak current can reach several hundred pA [21, 36, 52].

The basic electrical properties of olfactory sensory neurons, as well as the ion gradient across the ciliary membrane, play a fundamental role in shaping the properties of the odorant-induced response. In 1989, Lynch and Barry [33] reported that, in rat olfactory sensory neurons, the opening of a single ion channel was sufficient to induce the generation of action potentials. This is due to the very high input resistance, between 3 and 6 GΩ, typical of olfactory sensory neurons, producing a large depolarization also for very small odorant-induced currents [48]. Resting membrane potentials ranges between −90 and −45 mV, with a mean value of −55 mV [21, 28, 48, 52].

The electrical response to odorants is due to ion fluxes across the cell membrane, and therefore ion homeostasis is very important in signal transduction. Since the olfactory cilia are embedded in mucus covering the olfactory epithelium the relevant physiological ion concentrations are those in the mucus and inside the cilia. Data available about the intra- and extra-ciliary concentrations of major physiological ions are summarized in Table 1.1.

Table 1.1 Intracellular and extracellular ion concentrations at the apical side of olfactory sensory neurons

Ion	$[Ion]_{in}$ (mM)	$[Ion]_{out}$ (mM)	E_{Nernst} (mV)
Na^+	53 ± 31	55 ± 12	+1
K^+	172 ± 23	69 ± 10	−24
Free Ca^{2+}	40 ± 9 nM	4.8	+156
Cl^-	54 ± 4	55 ± 11	0

$[Ion]_{in}$ and $[Ion]_{out}$ are respectively the intracellular and extracellular (in the mucus) ion concentrations. E_{Nernst} is the calculated Nernst potential from the reported ion concentrations. Most of the ion concentrations were measured by energy-dispersive X-ray microanalysis in dendritic knobs of rat olfactory sensory neurons [51]. Intracellular Ca^{2+} was from [30]; extracellular Ca^{2+} was evaluated as the midpoint of the range (2.6–7.1 mM) measured by [11]; intracellular Cl^- from [16]

1.4 Dose–Response of Odorant-Induced Currents

Electrophysiological recordings from individual olfactory sensory neurons have shown that they respond to odorants in different ways: some neuron can detect several odorants, and a given odorant can activate neurons with various odorant specificity (Fig. 1.4a).

The relation between odorant dose and peak current is generally well fit by the Hill equation:

$$I = I_{max} \frac{C^n}{C^n + K_{1/2}^n}$$

where I_{max} is the maximal current, C is the concentration of odorant, $K_{1/2}$ is the odorant concentration producing 50% of the maximal current, and n is the Hill coefficient. In the neuron illustrated in Fig. 1.4b, c, $K_{1/2}$ was 53 μM. $K_{1/2}$ values for different odorants ranged between 3 and 100 μM. The Hill coefficient, n, describes the slope of the rising phase of the dose–response relation and its values ranges between 2.7 and 9.7. With such a non-linear amplification, only a slight change in the concentration of odorant molecules produces a large change in the response. As n decreases, the slope also decreases, causing an increase in the range of stimulus strengths over which the neuronal response varies (dynamic range) (for reviews see [21, 36, 52]).

1.5 Adaptation

It is common experience that olfactory sensation gradually decreases during continuous or repeated exposures to odorant stimuli. This phenomenon involves many processes along the entire olfactory pathway, but it begins in the cilia of olfactory sensory neurons. Indeed, during application of a prolonged odorant

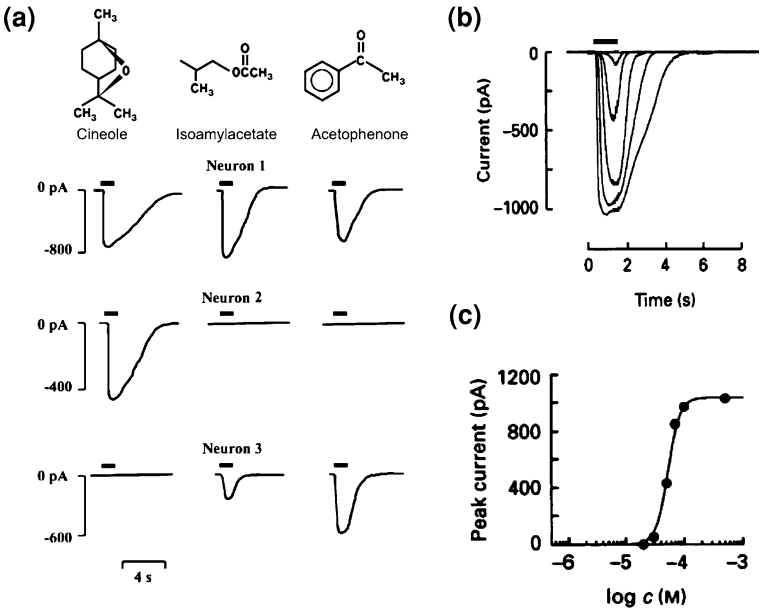

Fig. 1.4 Odorant responses of olfactory sensory neurons. **a** Responses of three different neurons to the odorants indicated at the top were measured with the voltage-clamp whole-cell configuration at −55 mV holding potential. Different neurons respond to a specific subset of odorants. Neuron 1 responded to all three odorants, while neuron 2 responded to only one odorant, and neuron 3 to two of the tested odorants. **b** Response of an olfactory sensory neuron to various concentrations of isoamylacetate. **c** Plot of the peak odorant-induced currents from (**b**) versus the odorant concentration. The *solid line* is the best fit of the Hill equation to the data with $K_{1/2} = 53$ μM and $n = 4.2$. Modified from Firestein et al. [13]

stimulus, the current amplitude decreases with time, despite the continued presence of the stimulus. Figure 1.5a shows that, when two brief odorant pulses are delivered within a short interval, the amplitude of the response to the second pulse is reduced. While the reduction is greater with shorter interstimulus intervals, the current amplitude gradually recovers to the initial value increasing the interval between odorant pulses (Fig. 1.5b).

It is important to note that sensory adaptation is not merely a reduction in response amplitude, but its physiological role involves the adjustment of the response to allow a cell to work over a broad range of stimuli (for review see [57]). Indeed, in odorant adaptation to repetitive stimuli there is a shift of the dynamic range (i.e. the range of stimulus concentrations over which the olfactory sensory neuron is able to respond) toward higher odorant concentrations compared with the control state.

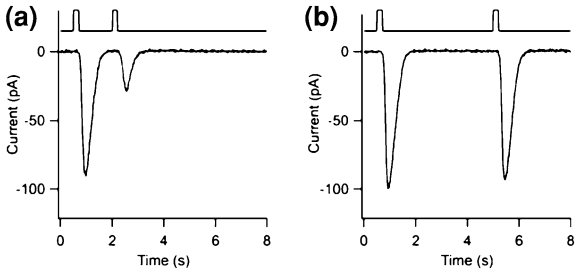

Fig. 1.5 Adaptation to repeated odorant stimuli. In each recording, the *top trace* indicates timing and duration of the odorant stimuli. Two identical pulses of the odorant amylacetate were delivered to an olfactory sensory neuron with different interstimulus intervals. The holding potential was −50 mV. **a** When the interstimulus interval was 1.5 s the response to the second pulse was reduced. **b** With a 4.5 s interval, the response to the second pulse was similar to the initial value. Adapted by permission from Macmillan Publishers Ltd: (Nature) Kurahashi and Menini [25], copyright, 1997

1.6 Odorant Receptors

The identification of the genes encoding for odorant receptors opened a new molecular era in olfactory research. The discovery of odorant receptor genes was first published in 1991 by Buck and Axel [7], who obtained the Nobel Prize in Physiology or Medicine in 2004 "for their discoveries of odorant receptors and the organization of the olfactory system". Odorant receptors belong to the superfamily of G-protein coupled receptors. The mouse repertoire contains about 1,000 potentially functional odorant receptor genes and is by far the largest gene superfamily in a mammalian genome [10, 38, 60]. In humans, about 350 odorant receptor sequences are potentially functional [37].

At the molecular level, odorant receptors share the same general structure of the other G-protein coupled receptors, with seven α-helical membrane-spanning domains connected by intracellular and extracellular loops of variable lengths, and numerous conserved short sequences. The most critical residues involved in odorant binding are hydrophopic and are located in the third, fifth and sixth transmembrane regions, which may form the ligand-binding pocket for odorant molecules [17]. The spatial localization of the binding pocket is similar to that for other members of the family, although the environment is quite different. For example catecholamines have been shown to form multiple electrostatic interactions through ionic bonds with adrenergic receptors. In contrast, in odorant receptors, the interaction of odorants with the binding pocket is based on hydrophobic and van der Waals interactions and therefore is rather weak, producing a low-affinity ligand-binding. Importantly, odorant receptors are still capable of selecting for shape, size and length of the ligand [17].

To understand how olfactory sensory neurons discriminate among odorants it is important to know how many types of odorant receptor genes are expressed in

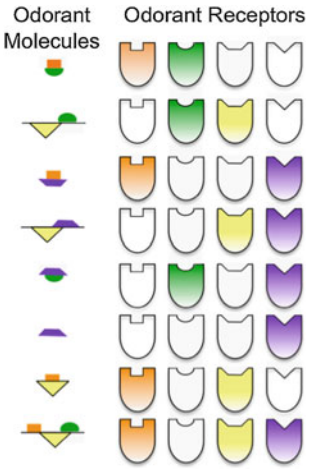

Fig. 1.6 Combinatorial code used by the olfactory system to discriminate between odorant molecules. *Figures on the right* represent odorant receptors activated by the odorants molecules on the *left*. Each type of odorant molecule activates a unique combination of receptors. Viceversa, each activated combination of receptors corresponds to one type of odorant molecule

each olfactory sensory neuron. It has been shown that every olfactory sensory neuron expresses a single odorant receptor gene. Moreover, the choice seems to be a stochastic process, which is likely to remain stable during the entire life of each olfactory sensory neuron, although not all odorant receptors are chosen with the same frequency [37, 38].

Another important information is the knowledge of how many and which odorants bind to each odorant receptor. It has been well established that each odorant receptor can be activated by several types of odorant molecules (Fig. 1.6). On the other hand, one single type of odorant can activate several types of odorant receptors. Thus, the odorant receptor family is used in a combinatorial manner to discriminate odorants and each odorant is recognized by a unique combination of receptors (Fig. 1.6) [34]. This scheme is consistent with previous observations that single olfactory sensory neurons can be stimulated by multiple odorants (Fig. 1.4a). Since each of these neurons expresses only one unknown odorant receptor type, a given neuron responds to a small and unpredictable subset among the many available odorants [13].

The combinatorial receptor coding scheme has the great advantage of allowing the olfactory system to recognize a large number of odorants and also to discriminate between odorants that have very similar but different structures, such as aliphatic odorants with different carbon chain lengths. Unfortunately, the identification of ligands for odorant receptors is still very limited, due to the difficulty to express odorant receptors in heterologous systems suitable for high-throughput screening [37, 38].

1.7 Olfactory Transduction

How is the binding of odorant molecules to odorant receptors converted into an electrical signal? When an odorant molecule binds to an odorant receptor, it

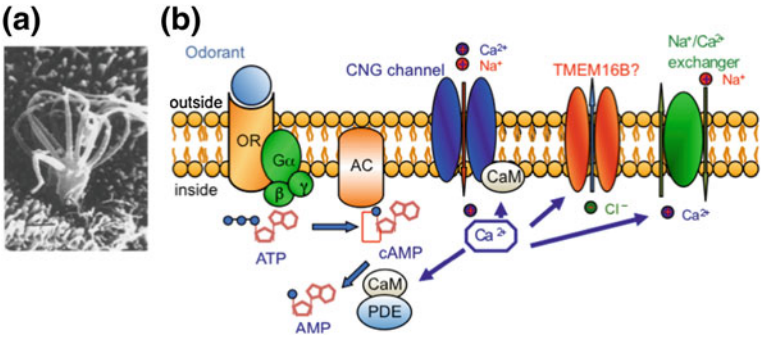

Fig. 1.7 Olfactory transduction in the cilia of olfactory sensory neurons. **a** A scanning electron micrograph of the knob of a human olfactory sensory neuron showing the protrusion of several cilia. Scale bar, 1 μm. Adapted from Morrison and Costanzo [39], with permission. **b** Schematic representation of the olfactory transduction taking place in the cilia. *OR* odorant receptor; *G*, G-protein, *AC* adenylyl cyclase, *CNG channel* cyclic nucleotide-gated channel, *CaM* calmodulin, *PDE* phosphodiesterase. *TMEM16B* indicates the candidate Ca^{2+}-activated Cl^- channel. Modified from Pifferi et al. [43], with permission

initiates a cascade of molecular events that transforms the chemical energy of binding into an electrical signal, as illustrated in Fig. 1.7.

The binding of an odorant molecule to an odorant receptor in the cilia induces a conformational change of the receptor causing the activation of an interacting G-protein. In turn, the G-protein stimulates the enzymatic activity of an adenylyl cyclase (ACIII) generating an increase in the concentration of cyclic AMP (cAMP). Cyclic nucleotide-gated (CNG) channels located in the ciliary membrane are directly activated by cAMP, causing a depolarizing influx of Na^+ and Ca^{2+} ions. The intracellular increase of Ca^{2+} concentration directly gates Ca^{2+}-activated Cl^- channels. As shown in Table 1.1, olfactory sensory neurons maintain an unusually high internal concentration of Cl^-, which is in the same range of the Cl^- concentration present in the mucus at the external side of the ciliary membrane. Therefore, in physiological conditions, the opening of Ca^{2+}-activated Cl^- channels causes an efflux of Cl^- ions from the cilia, corresponding to an inward current that further contributes to the depolarization of olfactory sensory neurons [16, 41, 42, 50–52]. The depolarization spreads passively to the dendrite and soma of the neuron, triggering action potentials that are conducted along the axon to the olfactory bulb.

Several mechanisms contribute to terminate the odorant response and to restore the initial conditions in olfactory sensory neurons. The cilia contain a phosphodiesterase that, after being activated by the complex Ca^{2+}-Calmodulin (CaM), hydrolyzes cAMP [4]; the G-protein is inactivated by its intrinsic GTPase function; the intracellular Ca^{2+} concentration is reduced by Ca^{2+}-extrusion through a Na^+/Ca^{2+} exchanger and Ca^{2+}-ATPase and, finally, the complex Ca^{2+}-CaM decreases the sensitivity of the CNG channel to cAMP, as further discussed in the following section (for reviews see [21, 36, 47, 52]).

1.8 Cyclic Nucleotide-Gated Channels

Cyclic nucleotide-gated (CNG) channels are the mediators of the chemo-electrical energy conversion in olfactory cilia. Indeed, information about odorant molecules is first transmitted as chemical information and then is converted into an electrical signal by ion fluxes through CNG channels activated by the increase in cAMP concentration [24, 31, 40].

The ciliary CNG channels are composed of three types of subunits with a stoichiometry of two CNGA2, one CNGA4, and one CNGB1b (Fig. 1.8a). Transgenic mice lacking CNGA2 are completely anosmic, demonstrating the importance of this channel in olfactory perception [3, 6, 60].

The topology of each CNG subunit consists of six transmembrane spanning domains, a pore region between the fifth and the sixth transmembrane domain, and intracellular N- and C-terminal regions. A cyclic nucleotide-binding site is located near the C-terminal at the cytoplasmic side in each subunit, for a total of four binding sites per each channel. Moreover, Ca^{2+}-calmodulin binding sites are also present at the cytoplasmic side (Fig. 1.8a) (for reviews see [18, 43]).

The relation between concentration of cAMP and CNG current is well fit with a Hill equation. Half-maximal activation ($K_{1/2}$) is in the micromolar range and varies in different species between 2 and 19 μM. The Hill coefficient ranges from 1.3 to 2.3 suggesting that at least two molecules of cAMP must bind before the channel gating (Fig. 1.8b, c).

The unitary conductance of single CNG channels in the presence of Ca^{2+} and Mg^{2+} is very small, with a value of about 1 pS. A small single channel conductance plays a relevant physiological role since, by using a large number of tiny events, the integrated current has a high signal-to-noise ratio.

It is important to note that, once open, CNG channels allow the flow along their electrochemical gradient, not only of monovalent ions, such as Na^+ and K^+, but also of Ca^{2+} [12]. The increase of Ca^{2+} increase in the intraciliary medium plays several important roles in olfactory transduction, mainly in the amplification of the odorant response (see Sect. 1.9) and in the adaptation process [26].

Kurahashi and Menini [25] investigated the localization of the principal molecular mechanism for adaptation in the olfactory transduction process. To determine whether the response reduction in the adapted state (Fig. 1.5a) was attributable to a reduction in the cAMP production or was instead due to other processes occurring after the production of cAMP, CNG channels in intact neurons were directly activated by flash photolysis of caged cAMP. The ciliary cytoplasm was loaded with caged cAMP through diffusion from a patch pipette and application of ultraviolet flashes to the cilia caused the photorelease of various cAMP concentrations. Therefore, cAMP-gated channels could be directly activated, bypassing the early stages of odorant transduction (i.e. receptor activation and G-protein and adenylate cyclase signalling). cAMP and odorant-induced responses were found to have similar adaptation properties, indicating that the entire adaptation process takes place after the production of cAMP. Furthermore, by using a

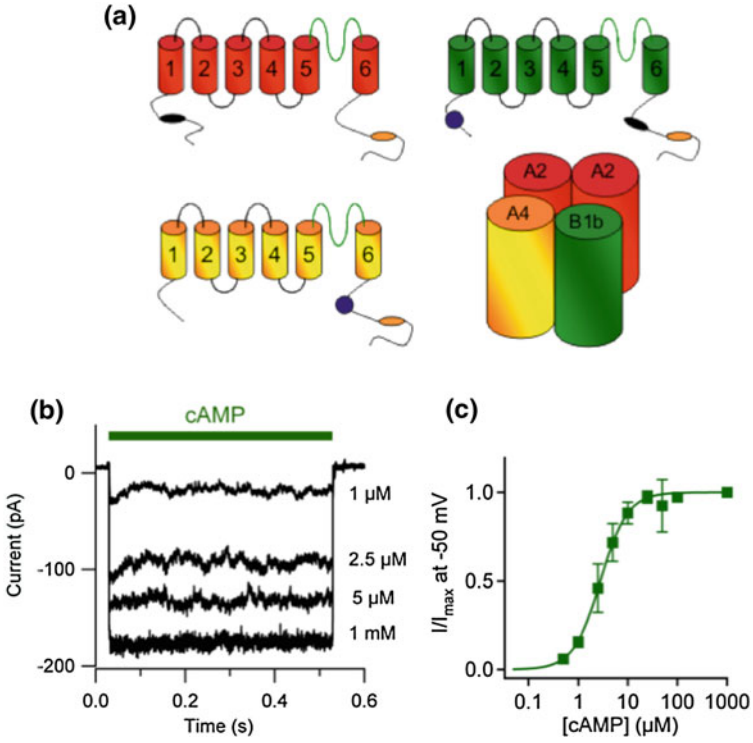

Fig. 1.8 Cyclic nucleotide-gated (CNG) channels. **a** Topological model and assembly of subunits of the olfactory CNG channel. Each transmembrane domain is indicated by a number, the pore loop is located between domains 5 and 6. The cyclic nucleotide-binding site is located in the C-terminal domain. Ca^{2+}-dependent calmodulin binding sites are shown in black. **b** A membrane patch was excised in the inside-out configuration from the knob or ciliary region of an olfactory sensory neuron. CNG channels were activated by the indicated concentrations of cAMP. The holding potential was −50 mV. **c** Normalized currents from experiments as in (**b**). The continuous lines is the best fit of the Hill equation to the data with $K_{1/2} = 2.7$ μM, $n = 1.5$. Modified from Pifferi et al. [43], with permission

hydrolysis resistant caged cAMP analogue, caged 8Br-cAMP, Boccaccio et al. [2] have shown that the hydrolysis of cAMP by PDE is not involved in adaptation. It has also been shown that Ca^{2+}-activated Cl^- channel are unrelated to olfactory adaptation.

All together, the previous experiments indicate that Ca^{2+} is likely to act through a negative feedback on the CNG channel. Indeed, micromolar concentrations of intracellular Ca^{2+} decrease the channel sensitivity to cAMP, probably by activating a Ca^{2+}-responsive endogenous factor already pre-associated with the channel [5, 9]. It has been proposed that the endogenous factor co-assembled with the CNG channel is Ca^{2+}-free calmodulin, called apocalmodulin, although a conclusive demonstration is still lacking [43].

Since Ca^{2+} enters into the olfactory cilia through the CNG channel itself, the pre-associated Ca^{2+} responsive factor provides a very fast feedback modulation at the channel level [54].

1.9 Amplification: Calcium-Activated Chloride Channels

The increase in intracellular Ca^{2+} concentration produced by Ca^{2+} ions entering the cilia through CNG channels plays crucial roles in olfactory transduction: the previously discussed regulation of adaptation, and an amplification of the odorant response by the activation of Ca^{2+}-activated Cl^- channels.

Ca^{2+}-activated Cl^- channels are present in the ciliary membrane and are directly activated by a rise in ciliary Ca^{2+} concentration [19, 23, 27, 32]. In physiological conditions, the opening of Ca^{2+}-activated Cl^- channels in the ciliary membrane causes an efflux of Cl^- ions from the cilia, corresponding to an inward current that contributes further to the depolarization of these neurons [16, 51, 52].

The functional properties of the Ca^{2+}-activated Cl^- current have been investigated under various conditions with a variety of electrophysiological techniques, each revealing important information about the channel properties (for reviews see [14, 21, 47]). The activation of the current by Ca^{2+} has been carefully investigated in inside-out excised membrane patches from the knob and ciliary region. The relation between Ca^{2+} concentration and activated current is well fit by the Hill equation with $K_{1/2}$ between 2.2 and 4.7 μM Ca^{2+}, and the Hill coefficient between 2.0 and 2.8 (Fig. 1.9a).

At present, the molecular identity of Ca^{2+}-activated Cl^- channels is still elusive. In 2008, three groups provided independent evidence that TMEM16/anoctamin family of membrane proteins are Ca^{2+}-activated Cl^- channels [8, 53, 59]. Recent studies [45, 55] found remarkable similarities between the functional properties of the olfactory Ca^{2+}-activated Cl^- channels with those of TMEM16B-induced currents in a heterologous system (Fig. 1.9a–c). However, future studies combining a multidisciplinary approach from genetic, molecular biology and electrophysiology will be necessary to establish the involvement of TMEM16B in the olfactory Ca^{2+}-activated Cl^- channel and its possible interactions with other proteins [46].

The current of a single olfactory Cl^- channel is so small that single-channel studies have not been possible. However, noise analysis of macroscopic currents estimated a unit conductance of about 1.5 pS and a channel's maximum open probability of 0.97 [20, 29, 44, 49]. Similar values were obtained for the TMEM16B-induced currents [45, 55]. The combination of a very small single channel conductance, together with a high maximum open probability, allows a high amplification of the primary current without an increase of noise [20].

For odorant detection, the presence of a pair of cationic (CNG) and anionic currents is likely to be useful because the Cl^- current produces a large amplification of the primary cationic CNG current and the amplified signal has a higher

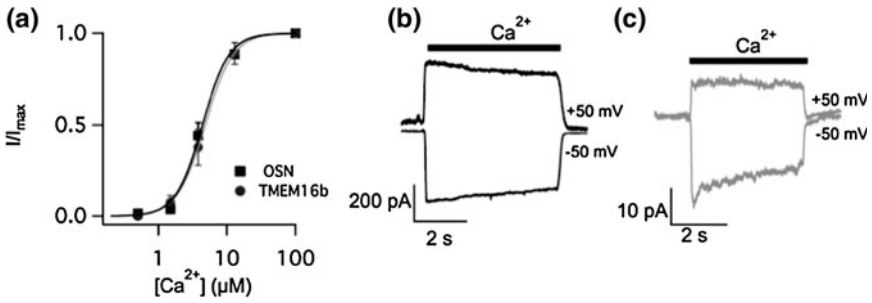

Fig. 1.9 Comparison between the electrophysiological properties of native Ca^{2+} activated Cl^- channels and TMEM16B-induced currents in a heterologous system. **a** Comparison of dose–response relations. $K_{1/2} = 4.7$ μM for native channel and 4.9 μM for TMEM16B. The Hill coefficient was 2.5 both for native and TMEM16B channel. **b**, **c** Currents activated by 100 μM Ca^{2+} at the indicated holding potentials in excised inside-out membrane patches from an olfactory sensory neuron (**b**) or TMEM16B expressing cells (**c**)

signal-to-noise ratio than the primary signal. Therefore, in olfactory transduction, the secondary Ca^{2+}-activated Cl^- channels ensure a high-gain and low-noise amplification of the primary CNG current contributing up to 90% of the total odorant-induced current ([1], for reviews see [21, 36, 47, 52]).

1.10 Conclusions

The understanding of the molecular mechanisms employed by these biological olfactory sensors to achieve their properties of detection and discrimination among odorant molecules is of interest not only for basic research, but it could also provide interesting cues for the development of an artificial nose that operates on the same principles used by living organisms.

References

1. Boccaccio A, Menini A (2007) Temporal development of cyclic nucleotide-gated and Ca^{2+}-activated Cl^- currents in isolated mouse olfactory sensory neurons. J.Neurophysiol 98:153–160
2. Boccaccio A, Lagostena L, Hagen V, Menini A (2006) Fast adaptation in mouse olfactory sensory neurons does not require the activity of phosphodiesterase. J Gen Physiol 128: 171–184
3. Bonigk W, Bradley J, Muller F, Sesti F, Boekhoff I, Ronnett GV, Kaupp UB, Frings S (1999) The native rat olfactory cyclic nucleotide-gated channel is composed of three distinct subunits. J Neurosci 19:5332–5347
4. Borisy FF, Ronnett GV, Cunningham AM, Juilfs D, Beavo J, Snyder SH (1992) Calcium/calmodulin-activated phosphodiesterase expressed in olfactory receptor neurons. J Neurosci 12:915–923

5. Bradley J, Bonigk W, Yau KW, Frings S (2004) Calmodulin permanently associates with rat olfactory CNG channels under native conditions. Nat Neurosci 7:705–710
6. Brunet LJ, Gold GH, Ngai J (1996) General anosmia caused by a targeted disruption of the mouse olfactory cyclic nucleotide-gated cation channel. Neuron 17:681–693
7. Buck L, Axel R (1991) A novel multigene family may encode odorant receptors: a molecular basis for odor recognition. Cell 65(1):175–187
8. Caputo A, Caci E, Ferrera L, Pedemonte N, Barsanti C, Sondo E, Pfeffer U, Ravazzolo R, Zegarra-Moran O, Galietta LJ (2008) TMEM16A, A membrane protein associated with calcium-dependent chloride channel activity. Science 322:590–594
9. Chen TY, Yau KW (1994) Direct modulation by Ca-calmodulin of cyclic nucleotide-activated channel of rat olfactory receptor neurons. Nature 368:545–548
10. Chess A, Simon I, Cedar H, Axel R (1994) Allelic inactivation regulates olfactory receptor gene expression. Cell 78:823–834
11. Crumling MA, Gold GH (1998) Ion concentrations in the mucus covering the olfactory epithelium in rodents. Soc Neurosci Abstr 24:2099
12. Dzeja C, Hagen V, Kaupp UB, Frings S (1999) Ca^{2+} permeation in cyclic nucleotide-gated channels. EMBO J 18:131–144
13. Firestein S, Picco C, Menini A (1993) The relation between stimulus and response in olfactory receptor cells of the tiger salamander. J Physiol 468:1–10
14. Frings S, Reuter D, Kleene SJ (2000) Neuronal Ca^{2+}-activated Cl^- channels–homing in on an elusive channel species. Prog Neurobiol 60:247–289
15. Graziadei P, Bannister LH (1967) Some observations on the fine structure of the olfactory epithelium in the domestic duck. Z Zellforsch Mikrosk Anat 80:220–228
16. Kaneko H, Putzier I, Frings S, Kaupp UB, Gensch T (2004) Chloride accumulation in mammalian olfactory sensory neurons. J Neurosci 24:7931–7938
17. Katada S, Hirokawa T, Oka Y, Suwa M, Touhara K (2005) Structural basis for a broad but selective ligand spectrum of a mouse olfactory receptor: mapping the odorant-binding site. J Neurosci 25:1806–1815
18. Kaupp UB, Seifert R (2002) Cyclic nucleotide-gated ion channels. Physiol Rev 82:769–824
19. Kleene SJ (1993) Origin of the chloride current in olfactory transduction. Neuron 11:123–132
20. Kleene SJ (1997) High-gain, low-noise amplification in olfactory transduction. Biophys J 73:1110–1117
21. Kleene SJ (2008) The electrochemical basis of odor transduction in vertebrate olfactory cilia. Chem Senses 33:839–859
22. Kleene SJ, Gesteland RC (1981) Dissociation of frog olfactory epithelium with N-ethylmaleimide. Brain Res 21:536–540
23. Kleene SJ, Gesteland RC (1991) Calcium-activated chloride conductance in frog olfactory cilia. J Neurosci 11:3624–3629
24. Kurahashi T (1989) Activation by odorants of cation-selective conductance in the olfactory receptor cell isolated from the newt. J Physiol 419:177–192
25. Kurahashi T, Menini A (1997) Mechanism of odorant adaptation in the olfactory receptor cell. Nature 385:725–729
26. Kurahashi T, Shibuya T (1990) Ca2(+)-dependent adaptive properties in the solitary olfactory receptor cell of the newt. Brain Res 515:261–268
27. Kurahashi T, Yau KW (1993) Co-existence of cationic and chloride components in odorant-induced current of vertebrate olfactory receptor cells. Nature 363:71–74
28. Lagostena L, Menini A (2003) Whole-cell recordings and photolysis of caged compounds in olfactory sensory neurons isolated from the mouse. Chem Senses 28:705–716
29. Larsson HP, Kleene SJ, Lecar H (1997) Noise analysis of ion channels in non-space-clamped cables: estimates of channel parameters in olfactory cilia. Biophys J 72:1193–1203
30. Leinders-Zufall T, Rand MN, Shepherd GM, Greer CA, Zufall F (1997) Calcium entry through cyclic nucleotide-gated channels in individual cilia of olfactory receptor cells: spatiotemporal dynamics. J Neurosci 17:4136–4148

31. Lowe G, Gold GH (1993) Contribution of the ciliary cyclic nucleotide-gated conductance to olfactory transduction in the salamander. J Physiol 462:175–196
32. Lowe G, Gold GH (1993) Nonlinear amplification by calcium-dependent chloride channels in olfactory receptor cells. Nature 366:283–286
33. Lynch JW, Barry PH (1989) Action potentials initiated by single channels opening in a small neuron (rat olfactory receptor). Biophys J 55:755–768
34. Malnic B, Hirono J, Sato T, Buck LB (1999) Combinatorial receptor codes for odors. Cell 96:713–723
35. Menco BP (1997) Ultrastructural aspects of olfactory signaling. Chem Senses 22:295–311
36. Menini A, Lagostena L, Boccaccio A (2004) Olfaction: from odorant molecules to the olfactory cortex. News Physiol Sci 19:101–104
37. Mombaerts P (2001) The human repertoire of odorant receptor genes and pseudogenes. Annu Rev Genomics Hum Genet 2:493–510
38. Mombaerts P (2004) Genes and ligands for odorant, vomeronasal and taste receptors. Nat Rev Neurosci 5:263–278
39. Morrison EE, Costanzo RM (1990) Morphology of the human olfactory epithelium. J Comp Neurol 297:1–13
40. Nakamura T, Gold GH (1987) A cyclic nucleotide-gated conductance in olfactory receptor cilia. Nature 325:442–444
41. Nickell WT, Kleene NK, Gesteland RC, Kleene SJ (2006) Neuronal chloride accumulation in olfactory epithelium of mice lacking NKCC1. J Neurophysiol 95:2003–2006
42. Nickell WT, Kleene NK, Kleene SJ (2007) Mechanisms of neuronal chloride accumulation in intact mouse olfactory epithelium. J Physiol 583:1005–1020
43. Pifferi S, Boccaccio A, Menini A (2006) Cyclic nucleotide-gated ion channels in sensory transduction. FEBS Lett 580:2853–2859
44. Pifferi S, Pascarella G, Boccaccio A, Mazzatenta A, Gustincich S, Menini A, Zucchelli S (2006) Bestrophin-2 is a candidate calcium-activated chloride channel involved in olfactory transduction. Proc Natl Acad Sci USA 103:12929–12934
45. Pifferi S, Dibattista M, Menini A (2009) TMEM16B induces chloride currents activated by calcium in mammalian cells. Pflugers Arch 458:1023–1038
46. Pifferi S, Dibattista M, Sagheddu C, Boccaccio A, Al Qteishat A, Ghirardi F, Tirindelli R, Menini A (2009) Calcium-activated chloride currents in olfactory sensory neurons from mice lacking bestrophin-2. J Physiol 587:4265–4279
47. Pifferi S, Menini A, Kurahashi T (2009) Signal transduction in vertebrate olfactory cilia. In: Menini A (ed) The neurobiology of olfaction. CRC Press/Taylor & Francis Group, Boca Raton, pp 203–224
48. Pun RY, Kleene SJ (2004) An estimate of the resting membrane resistance of frog olfactory receptor neurons. J Physiol 559:535–542
49. Reisert J, Bauer PJ, Yau KW, Frings S (2003) The Ca-activated Cl channel and its control in rat olfactory receptor neurons. J Gen Physiol 122:349–363
50. Reisert J, Lai J, Yau KW, Bradley J (2005) Mechanism of the excitatory Cl^- response in mouse olfactory receptor neurons. Neuron 45:553–561
51. Reuter D, Zierold K, Schroder WH, Frings S (1998) A depolarizing chloride current contributes to chemoelectrical transduction in olfactory sensory neurons in situ. J Neurosci 18:6623–6630
52. Schild D, Restrepo D (1998) Transduction mechanisms in vertebrate olfactory receptor cells. Physiol Rev 78:429–466
53. Schroeder BC, Chen T, Jan YN, Jan JY (2008) Expression cloning of TMEM16a as calcium-activated chloride channel subunit. Cell 134:1019–1929
54. Song Y, Cygnar KD, Sagdullaev B, Valley M, Hirsh S, Stephan A, Reisert J, Zhao H (2008) Olfactory CNG channel desensitization by Ca^{2+}/CaM via the B1b subunit affects response termination but not sensitivity to recurring stimulation. Neuron 58:374–386
55. Stephan AB, Shum EY, Hirsh S, Cygnar KD, Reisert J, Zhao H (2009) ANO2 is the cilial calcium-activated chloride channel that may mediate olfactory amplification. Proc Natl Acad Sci USA 106:11776–11781

56. Tirindelli R, Dibattista M, Pifferi S, Menini A (2009) From pheromones to behavior. Physiol Rev 89:921–956
57. Torre V, Ashmore JF, Lamb TD, Menini A (1995) Transduction and adaptation in sensory receptor cells. J Neurosci 15:7757–7768
58. Whisman M, Goetzinger J, Cotton F, Brinkman, D (1978) Odorant evaluation: a study of ethanethiol and tetrahdrothiophene as warning agents in propane. Environ Sci Technol 12:1285–1288
59. Yang YD, Cho H, Koo JY, Tak MH, Cho Y, Shim WS, Park SP, Lee J, Lee B, Kim BM, Raouf R, Shin YK, Oh U (2008) TMEM16A confers receptor-activated calcium-dependent chloride conductance. Nature 455:1210–1215
60. Zheng J, Zagotta WN (2004) Stoichiometry and assembly of olfactory cyclic nucleotide-gated channels. Neuron 42:411–421

Chapter 2
Better Sensors Through Chemistry: Some Selected Examples

G. Neri

Abstract Chemistry play a key role in the design of active materials for sensing applications. Inorganic and polymer chemistry contributed in the past very well to the enhancements in the area of solid state gas sensors. Nowadays, chemistry has also opened a land of opportunities for the development of new sensing materials coming from the field of organic compounds, coordination complexes, hybrid composites, etc., and their synthesis on the nanoscale. In this regard, several examples from our laboratory illustrate how chemical process innovations can result in new materials developments, improving sensor performance. Advances in recent activities concerning novel sensing materials are here reported.

2.1 Introduction

Chemistry is the science of the atomic and molecular constituents of the real world. This fascinating science is one of the most important backgrounds for the materials scientists dealing with the design of new materials for various applications. As molecules are the building blocks of all the materials we use, the synthesis or manipulation of molecules, impacts on virtually every aspect. Chemistry is capable, on the other hand, of selectively modifying existing materials to tailor them for specific applications. Chemical process innovations can therefore result in new materials developments, improving product performance.

G. Neri (✉)
Department of Industrial Chemistry and Materials Engineering,
University of Messina, C/da di Dio Vill. S. Agata, 98166 Messina, Italy
e-mail: neri@ingegneria.unime.it

G. Neri et al. (eds.), *Sensors and Microsystems*,
Lecture Notes in Electrical Engineering 91, DOI: 10.1007/978-94-007-1324-6_2,

Purpose-designed materials, coming from chemical-based synthesis or processes, are essential to power generating and storage systems, computers, mobile phones, etc. Chemical knowledge and expertise can help to provide solution to the challenge of better sensors. Examples can be seen in the materials innovation leading to enhanced gas sensors and instruments based on semiconducting metal oxides developed and patented by Taguchi in the 1960 years, that now form an integral part of today's life.

Ever since, chemical sensors have shown broad advances and various type have been commercialized. To obtain this goal, research on materials and technology of electronics interface are indispensable to their development:

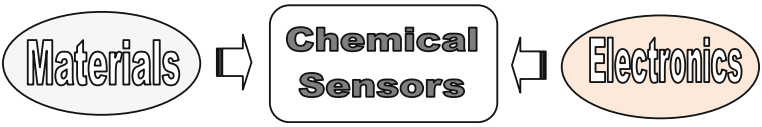

The advantage of chemical approach in the development of material is the possibility of combining the proper constituents of the material on the atomic level. Different areas of chemistry (inorganic, organic, coordination chemistry) open the door to an endless variety of possible materials, having each different sensing properties.

Inorganic semiconducting materials, such as metal oxides, have been studied considerably in the past, and actually are the most used sensing elements in commercial chemoresistive devices. Besides inorganic materials, other sensing element formulations bearing on carbon can be easily synthesized by chemical processes. Deeper understanding of the structure and properties of inorganic, organic, metallorganic or supramolecular sensing elements should lead, in the future, to novel discoveries in the detection and monitoring of gases for environmental and food control, in clinical diagnostics, automotive, and so on.

Today, sensing materials development relies also on opportunities given from new technologies. The past several decades have seen a significant effort worldwide in nanoscience, especially in the synthesis of nanostructures with a desired size, shape, and/or composition. Chemical nanoscience, enabling controllable manipulation of matter at molecular length scale, has becomes fundamental generator for innovations in materials processing. The successful synthesis, modification and assembly of nanobuilding units such as nanoparticles, -wires and -tubes and other shapes of different materials have demonstrated the importance of chemical processes in materials synthesis, and have generated great expectations for the future in many advanced applications [1].

2.2 Chemoresistive Gas Sensors

The need for real-time, compact, and inexpensive chemical gas detectors has become more pressing in recent years. The role of gases and the measurement of their concentration have always received wide spread applications in many fields

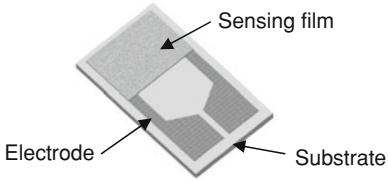

Fig. 2.1 Planar structure of chemoresistive sensor with top side coated thick/thin film

of science and technology. Homeland security and defense applications need effective portal monitoring, chemical weapons sensing, and water quality testing. Devices that can serve as personal exposure monitors, provide advance warning of food spoilage, and enable breath analyzers to uncover pre-symptomatic disease are also in demand. An increasing demand for small scale solid-state sensors for automotive exhaust gas environments are also of great interest because of increasing demands on emission control legislations. These applications pose many challenges because they require high levels of sensitivity and specificity in small, economical packages.

Resistive solid state sensors, relying their functioning on the change of electrical properties, are the most used for gas detection. These sensors in comparison with other ones have excellent sensitivity, very short response time, low cost, and very good suitability for design of portable instruments, and have find great possibilities for applications in alarm systems, portable instruments and electronic nose [2].

The fabrication simplicity of resistive sensors is the main factor contributing to their large use. In the planar configuration, they are constituted of a porous thick/thin film as a gas sensing element, deposited onto a ceramic substrate with interdigited electrodes (Fig. 2.1).

The sensing characteristics of a chemoresistive sensor depend primarily on the nature of the sensing layer. In this respect, most of conventional sensors use films based on metal oxides such as SnO_2, ZnO, or conducting polymers. For the first type of sensors, i.e. metal oxide semiconductor (MOS) sensors, energy is generally required to heat the sensitive layer to an operating temperature of few hundred degree Celsius, typically from 150 to 500°C. Polymer materials operate at lower temperatures, are highly sensitive and selective, but life time of organic film-based sensors is limited. Additionally, some organic materials are not compatible with micro-electronic fabrication technologies and, therefore, not suitable for large scale production. In brief, gas sensors known to date operate at elevated temperatures or suffer from selectivity problem. Improvement regarding these aspects are then essential for the practical use of chemoresistive sensors.

The working principle for gas detection is based on change in the electrical resistance (conductance) due to target gas adsorption [3]. The resultant change in this property is measured to determine the presence and concentration of the gas in

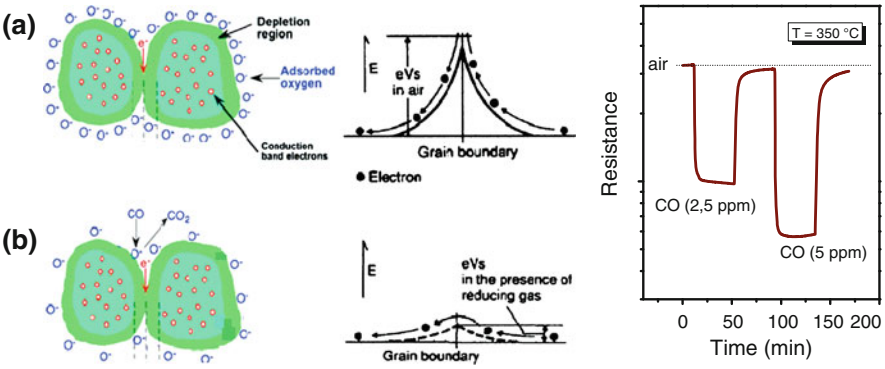

Fig. 2.2 Mechanism of gas sensing operating on *n*-type metal oxide semiconductors with reducing gases

the ambient surrounding the sensor. To investigate the operating sensing mechanism, the responses of resistive gas sensors have been widely explored with respect to surface adsorption, chemical reaction, and resulting conductivity changes. Several sensing mechanisms are possible, on the basis of the different sensing material. With conventional *n*-type metal oxide semiconductors-based sensors (e.g. ZnO, SnO_2) the response to the presence of a target gas relies on the surface reactions which occur between adsorbed oxygen species and the probed gas [4]. In air, point (a), oxygen adsorbed on the surface traps free electrons because of its high electron affinity, forming a potential barrier at the grain boundaries, determine the electrical resistance value. When the sensor is exposed to an atmosphere containing reducing gases, e.g. hydrocarbons, CO, ethanol, etc., point (b), the gas molecules are adsorbed on the surface and react with active oxygen species. Reactions with surface oxygen species will vary depending upon the temperature and the reactivity of the sensing material. This decrease the potential barrier allowing electrons to flow more easily, thereby reducing the electrical resistance, as a function of the concentration of the target gas (Fig. 2.2).

With polymer, organic or metallorganic film as sensing layer, rather than redox chemistry above discussed, weak intermolecular interactions and coordination processes, respectively, can be envisaged as the main pathway of the sensing mechanism. In some cases these interactions require specialized functions of the molecules, making these chemoresistive sensors more selective than those based on metal oxide semiconductors.

This variety of sensing materials and mechanisms, contribute to a practical level to make chemoresistive sensors with different functionality. Some examples from our laboratory are here reported, highlighting how chemistry can influences the microstructure, composition, and properties of sensing materials for chemoresistive gas sensors.

2.3 Chemistry of Sensing Materials

Examples below reported illustrate how chemical processes innovations can result in new materials developments, improving sensor performances. A subdivision of the paragraphs taking into account the chemical nature of the sensing layer has been applied.

2.3.1 Inorganic Materials

Nowadays, metal oxide semiconductors are the most utilized class of inorganic materials for chemical gas sensing. MOS sensors are attracting significant attention due to their simplicity, low cost, small size and ability to be integrated in electronic devices. Despite, many worthy results have been achieved, intensive efforts are still in progress in order to develop new active sensing nanomaterials, with enhanced performance with respect to bulk materials [5, 6].

Sensing materials with nanosized grains have been synthesized using several chemical techniques, such as sol–gel [7]. The success of sol–gel processing routes to nanomaterials is attributed to molecular nature of the precursors, which transform subsequently into solid phases at much lower temperatures than those required for conventional procedures.

In addition, the use of suitable additives simplifies the precursor delivery and/or allows controlling the reaction kinetics, which can be used to influence the particle size and size-dispersion in the final material. In a such way, various simple or mixed metal oxides by sol–gel synthesis, in the presence of starch as an additive, have been synthesized [8]. Starch (**1**) is an organic macromolecule essentially composed of amylose, an unbranched single chain polymer of 500–2,000 units linked through glucosidic bonds (see Fig. 2.3). It behaves in water solutions as a hydrophilic non-ionic stabilizer of nanoparticles, embedding the native metal oxide inside its structure. Starch can be then easily eliminated by enzyme degradation at low temperature. Pure In_2O_3 and mixed In_2O_3-SnO_2 so synthesized have been tested as CO gas sensors [8]. The good performances of the In_2O_3 sensor towards low CO concentrations in the cabin auto-vehicle during a road test, are reported in Fig. 2.3.

Compared to aqueous sol–gel chemistry and additives-assisted routes, simpler approaches were proposed where a solvent acts as a ligand and control the growth of the nanoparticles without the need of additional ligands. Among them, the "benzyl alcohol route" has shown to be powerful alternative for the synthesis of oxide nanoparticles, offering advantages such as high crystallinity of the as synthesized oxides and high reproducibility [9].

Metal oxide nanoparticles that were prepared ranges from simple binary metal oxides to more complex ternary and multi-metal systems such as perovskites. For these latter, e.g. $BaTiO_3$, the preparative involve the dissolution of the alkaline earth metal (Ba) in $C_6H_5CH_2OH$ to form the intermediate (**2**), followed by addition

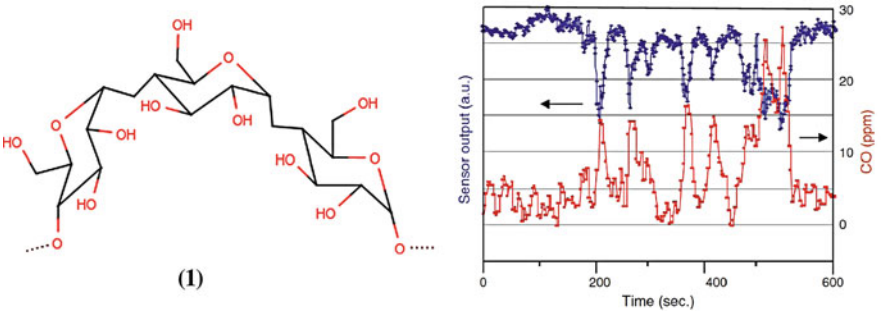

Fig. 2.3 Molecular structure of starch **1**. Sensor response of the In_2O_3 sensor to CO concentration variations during a road test

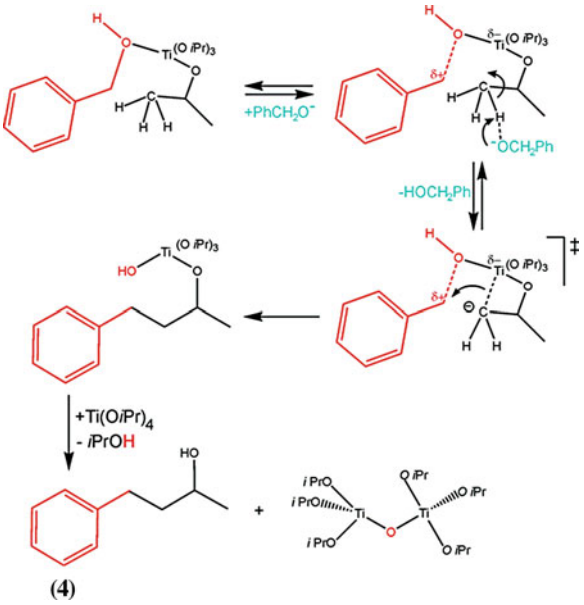

Fig. 2.4 Reaction pathway leading to the formation of Ti–O–Ti bond and 4-phenyl-2-butanol as byproduct. From Ref. [10]

of metal oxide $Ti(OiPr)_4$ (**3**), and heat treatment in autoclave at 200–220°C for 48 h:

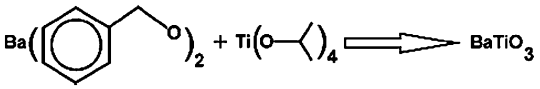

The reaction mechanisms taking place during particles formation is complex. However, precise hypotheses on the chemical pathways involved in the formation of the M–O–M bonds can be formulated [10]. In the specific case above mentioned, the formation of 4-phenyl-2-butanol (**4**) among the by-products, has

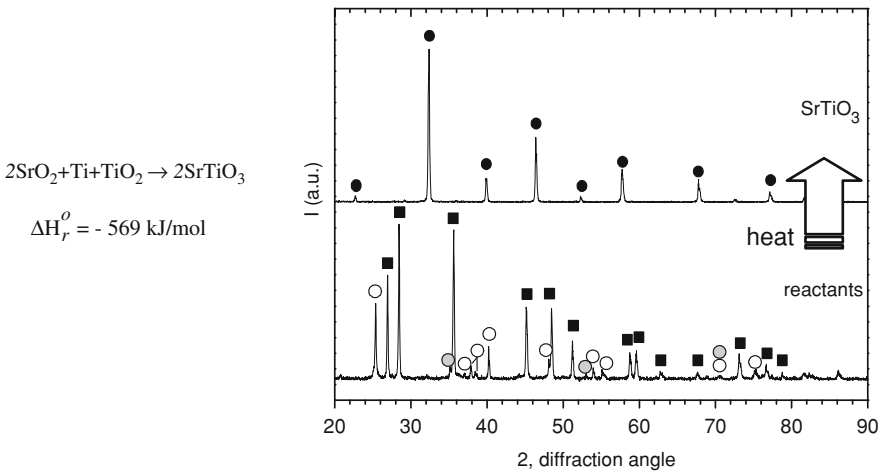

Fig. 2.5 Exothermic reaction for the synthesis of strontium titanate by SHS. XRD analysis evidenced the high purity of the product synthesized

allowed to invoking a C–C bond formation between the isopropoxy ligand and benzyl alcohol as the main reaction pathway (Fig. 2.4).

A further comparison of the reaction mechanism in the case of metal oxides, prepared either with an assisted-microwave route or by conventional heating in autoclave, proved that the same processes are involved for the M–O–M bond formation. This result is of utmost significance, because it gives strong indication that microwave irradiation can be used as a powerful tool, aiding the chemical synthesis to accelerate the formation of metal oxide nanoparticles through directly influencing the organic reaction pathways [11].

Solid-state chemical reactions have been employed successfully in the past to synthesize metal oxide powders. However, a number of limitations in terms of control achieved over stoichiometry, purity, size and homogeneity, have restricted their practical applications to some particular cases. Recently, we proposed some processes typical of the chemical and ceramic industry such as Self-propagating High-temperature Synthesis (SHS) and Ball Milling (BM), in order to synthesize valuable sensing materials [12]. A series of $SrTi_{1-x}Fe_xO_{3-\delta}$ powders, with x ranging from 0 to 0.6, were prepared by SHS starting from SrO_2, Ti, TiO_2 and Fe, by means of highly exothermic reactions (Fig. 2.5).

After ignition, the exothermic reactions generate a propagating high-temperature front at a velocity of about 7–8 mm/s that convert the reactants to products. The syntheses were therefore completed within a few seconds. A ball-milling treatment was subsequently carried out for further structure refinement and size reduction, stabilizing the formation of non-equilibrium structures, increasing surface defects and hence surface reactivity and favoring, in the Fe-doped samples, the substitution of titanium by iron in the $SrTiO_3$ perovskite structure.

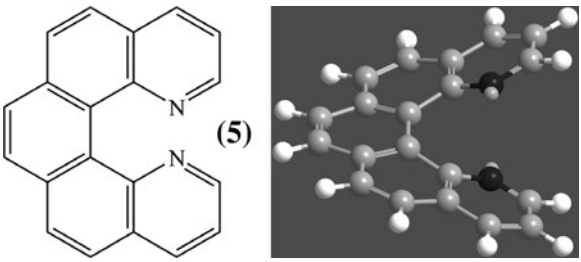

Fig. 2.6 Molecular structure of 1, 14 di-aza[5]helicene

The series of Fe-doped $SrTiO_3$ samples have been investigated in detail, showing promising features for their possible use in high-temperature oxygen sensors for automotive applications [13, 14].

2.3.2 Organic Materials

Organic materials are being extensively studied for the fabrication of electronic and optoelectronic devices and represent a simple and versatile alternative to inorganic materials for built resistive sensors. With respect to current inorganic-based technology, they offer greater substrate compatibility, device processability, flexibility, large area coverage, and reduced cost. Due to these advantages, there is a growing interest in the study of novel organic materials. On the other hand, organic materials suffer of low thermal stability.

In approaching this research area, we starting to investigate novel helical π-electron systems comprising carbocyclic aromatic fused rings in ortho arrangement to one another (Fig. 2.6) and their corresponding perylene structures.

The solubility in many organic solvents and the high fusion temperatures are valuable properties of these compounds for chemoresistor processing and use. One major drawback of the above organic materials is however the low carrier mobility, likely related to the presence of N atoms into the molecule skeleton of the π-electron system which hindered charge transport. Then, to increase their electron carrier mobility, organic/carbon nanotubes (CNTs) composites have been investigated, taking example from the use of CNTs in the development of conductive polymer composites.

Composites based on di-aza[5]helicene (**5**) and its perylene derivate have been investigated as resistive sensors [15]. Due to the presence of nitrogen atoms, they behave as a base manifesting some proton affinity. The resistance variation observed in the presence of humidity or protic organic vapours such as acetic acid, rely on the donation of a proton to the lone pair on the nitrogen atom, giving the protonated form:

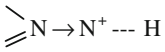

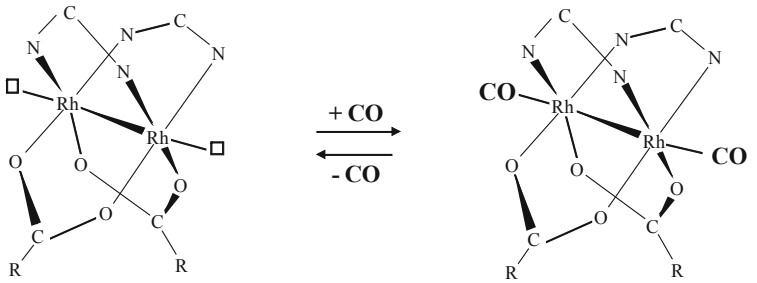

(**6**)

Fig. 2.7 $Rh_2(form)_2(CH_3COO)_2$ complex (**6**) with lantern structure. The reversible reaction occurring in presence of CO is shown

Data obtained have highlighted that the electron transferring (hopping), assisted by the presence of a proton trap (the heterocyclic nitrogen), effectively play a key role in the sensing mechanism.

2.3.3 Metal Complexes

Metal complexes have been used in the past in chemical sensors, but their potentiality have been not still fully exploited. Today, developments are focused on the chemical synthesis of novel coordination compounds with new features for binding selectively specific analytes to the metal center.

Indeed, the metal-analyte coordination primarily govern sensing mechanism on these sensors. This is particularly advantageous as a higher selectivity compared to conventional inorganic materials could be attained. In exploiting selective coordination features for the design of small molecule chemical sensors, we recently reported di-metal complexes as an integral part of a resistive chemical detector, providing both sensitivity and selectivity towards carbon monoxide, an important analyte to be monitored in a variety of industrial and domestic activities [16]. This idea was stimulated by the discovery that some di-rhodium (II,II) complexes exhibit a lantern structure with an open coordination site at the metal (Fig. 2.7).

The selectivity of the coordination reactions suggested a strong potential for adaptation to chemical sensing. A resistive device based on $Rh_2(form)_2(CH_3COO)_2$ complex (**6**), showed a rapid response to gaseous CO, consistent with the expected reversible coordination reaction of carbon monoxide above reported.

Furthermore, these metal complexes can be easily modified to accommodate a range of interesting analytes [17]. In this context, by including different auxiliary functional group in the coordination spheres, it is possible chemically to modify the strength of rhodium binding sites. Thus, one can create a binding site tailored to the appropriate size and chemical functionality of a particular analyte.

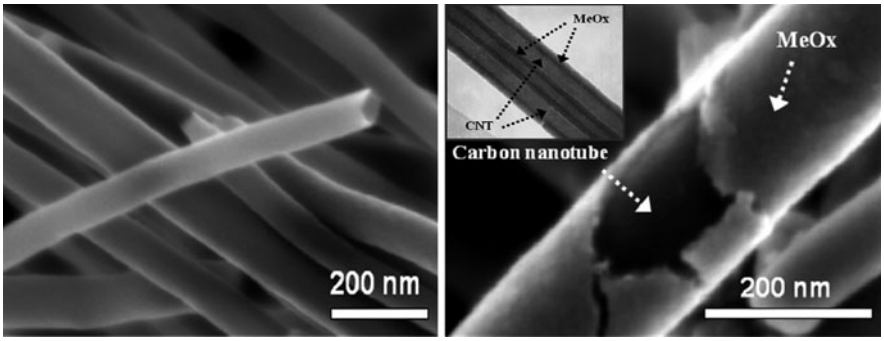

Fig. 2.8 SEM and TEM images of carbon nanotubes coated on the outer and inner surfaces with thin film of metal oxides

2.3.4 Composite Materials

Hybrid composite materials present the paramount advantage to afford a direct connection among the different areas above described. This allows to develop a large variety of structurally well defined inorganic/organic networks into complex architectures. Further, the research of multiscale structured hybrids in the nanometer scale will open a land of opportunities for designing new nano-materials.

Specifically, the combination of the properties of carbon nanotubes with metal oxides is well exploited to develop novel sensors. CNTs have peculiar electrical and mechanical properties and their high surface area and chemical stability, making them suitable for integration in nanoscale conductivity-based devices for gas sensing. In this area, we showed as CNTs can be homogeneously coated on the outer and inner surfaces with thin film of metal oxides (V_2O_5, TiO_2, SnO_2) by applying the non-aqueous sol–gel route combined with Atomic Layer Deposition (ALD) deposition technique, starting from metal isopropoxide and acetic acid as precursors. By using carboxylic acids as oxygen source instead of the more traditionally used ones (e.g. water, ozone, oxygen, etc.), metal oxides coating can be grown from the metal alkoxide precursor even at low temperatures.

The high quality and conformality of the as deposited film is demonstrated by SEM and TEM images reported in Fig. 2.8. These metal oxides-coated carbon nanotubes, as active part of a chemoresistive device, have shown peculiar sensing properties due to the heterojunction formed at the interface between the inorganic film and carbon nanotube [18, 19].

2.4 Conclusion

Through the description of the synthesis and applications of new sensing materials, the key role of chemistry in the relevant technological area of gas sensing has been highlighted. The compositional features at the molecular scale of selected

inorganic, organic and composite materials, has been tuned by different chemical approaches, and their contribution to the fabrication of more sensitive and/or selective chemoresistive devices has been demonstrated.

In conclusion, the success of chemical sensors has been, and will be more in the future, largely built on the strategic concept 'molecules to materials'. The rational design, synthesis, and assembly of novel inorganic/organic/hybrid (nano)materials must take advantage of innovative chemical approaches, providing consequently the design and production of better sensors.

Acknowledgments Special thanks go to my collaborators and colleagues who contributed with their work to the research here presented and helped me with their comments and stimulating discussion.

References

1. Rao R, Müller A, Cheetham AK (2004) The chemistry of nanomaterials. Wiley-VCH, Weinheim
2. Seiyama T (1988) Chemical sensors—current status and future outlook, vol 1. Elsevier, Amsterdam
3. Shimizu Y, Egashira M (1999) Basic aspects and challenges of semiconductor gas sensors. MRS Bull 24:18–24
4. Gurlo A, Bârsan N, Weimar U (2006) Gas sensors based on semiconductiong metal oxides. In: Fierro JLG (ed) Metal oxides: chemistry and applications. CRC Press, Boca Raton, pp 683–738
5. Yamazoe N (1991) New approaches for improving semiconductor gas sensors. Sens Actuators B 5:7–19
6. Bard AJ (1994) Integrated chemical systems: a chemical approach to nanotechnology. Wiley, Chichester
7. Bonavita A, Micali G, Rizzo G, Neri G (2006) Alternative sol–gel routes for synthesizing gas sensing nanostructured materials. ECS Trans 3:221–231
8. Neri G, Bonavita A, Micali G, Rizzo G, Callone E, Carturan G (2008) Resistive CO gas sensors based on In_2O_3 and $InSnO_x$ nanopowders synthesized via starch-aided sol–gel process for automotive applications. Sens Actuators B 132:224–233
9. Niedereberger M, Garnweitner G, Pinna N, Neri G (2005) Nonaqueous routes to crystalline metal oxide nanoparticles: formation mechanisms and applications. Progr Solid State Chem 33:59–70
10. Niederberger M, Garnweitner G, Pinna N, Antonietti M (2004) Nonaqueous and halide-free route to crystalline $BaTiO_3$, $SrTiO_3$, and (Ba, Sr)TiO_3 nanoparticles via a mechanism involving C–C bond formation. J Am Chem Soc 126:9120–9126
11. Bilecka I, Djerdj I, Niederberger M (2008) One-minute synthesis of crystalline binary and ternary metal oxide nanoparticles. Chem Commun 886–887
12. Sanson A, Mercadelli E, Roncari E, Cao G, Licheri R, Orrù R, Marzorati D, Merlone-Borla E, Bonavita A, Micali G, Neri G (2010) Influence of processing parameters on the electrical response of screen printed $SrFe_{0.6}Ti_{0.4}O_{3-\delta}$ thick films. Ceram Int 36:521–527
13. Neri G, Bonavita A, Micali G, Rizzo G, Licheni R, Orrù R, Cao G (2007) Resistive λ-sensors based on ball milled Fe doped-$SrTiO_3$ nanopowders obtained by self-propagating high-temperature synthesis (SHS). Sens Actuators B 126:258–265
14. Neri G, Micali G, Bonavita A, Licheri R, Cao G, Marzorati D, Merlone Borla E, Roncari E, Sanson A (2008) $FeSrTiO_3$-based resistive oxygen sensors for application in diesel engines. Sens Actuators B 134:647–653

15. Caronna T, Fontana F, Donato N, Latino M, Bonavita A, Rizzo G, Neri G (2010) From the photochemical synthesis to the practical application: how to realize sensors with extended π-conjugated systems. In: XIII IUPAC Congress on Photochemistry, Ferrara
16. Lo Schiavo S, Piraino P, Bonavita A, Micali G, Rizzo G, Neri G (2008) A dirhodium(II, II) molecular specie as a candidate material for resistive carbon monoxide gas sensors. Sens Actuators B 129:772–778
17. Lo Schiavo S, Livoti L, Bramanti A, Donato N, Galeano M, Calisto A, Latino M, Neri G (2010) Novel sensing materials for breath analysis devices. In: IEEE EMBC Int. Conference, Buenos Aires 670–673
18. Willinger M-G, Neri G, Rauwel E, Bonavita A, Micali G, Pinna N (2008) Vanadium oxide sensing layer grown on carbon nanotubes by a new atomic layer deposition process. Nano Lett 8:4201–4204
19. Willinger MG, Neri G, Rauwel E, Bonavita A, Micali G, Pinna N (2009) The controlled deposition of metal oxides onto carbon nanotubes by atomic layer deposition: examples and a case study on the application of V_2O_4 coated nanotubes in gas sensing. Phys Chem Chem Phys 11:3615–3622

Part II
Materials and Processes

Chapter 3
Alcohol-Infiltrated One-Dimensional Photonic Crystals

G. Barillaro, A. Diligenti, L. M. Strambini, S. Surdo and S. Merlo

Abstract In this work, experimental results on the optical characterization of alcohol-infiltrated silicon/air one-dimensional photonic crystals (1D-PhCs), fabricated by electrochemical micromachining of silicon, are presented and compared with theoretical predictions. Infiltration of alcohols into 1D-PhCs produces reliable changes (redshift and increase of the bandgap order in the near-infrared region) in the reflectivity spectrum, with respect to air. Such changes, which can be attributed to an increase in the average refractive index of the structure, allow one to discriminate between different alcohols. Experimental data are in good agreement with numerical results calculated by using the characteristic matrix method, modified to take into account surface roughness of silicon walls.

3.1 Introduction

Optofluidics [1] attempt to unify optics and microfluidics, thus providing new paths for optical device integration and tuning. In optofluidic devices, part of the optical structure is in contact with a proper fluid, which is chosen for conditioning the optical properties of the structure itself. Photonic crystals (PhCs) obtained by air-void formation in high-refractive-index materials, such as crystalline silicon, are good candidates for optofluidic device fabrication, as air can be easily replaced by a suitable fluid.

G. Barillaro (✉) · A. Diligenti · L. M. Strambini · S. Surdo
Dipartimento di Ingegneria dell'Informazione: Elettronica, Informatica, Telecomunicazioni, Università di Pisa, Via G. Caruso 16, 56122 Pisa, Italy
e-mail: g.barillaro@iet.unipi.it

S. Merlo
Dipartimento di Elettronica, Università degli Studi di Pavia, Via Ferrata 1, 27100 Pavia, Italy

G. Neri et al. (eds.), *Sensors and Microsystems*,
Lecture Notes in Electrical Engineering 91, DOI: 10.1007/978-94-007-1324-6_3,

PhCs are natural or artificial materials characterized by spatial periodic variation of the refractive index. This materials exhibit photonic bandgaps, i.e. wavelength intervals over which the propagation of the electromagnetic radiation is forbidden. Optical properties of PhCs strongly depend on both geometry and chemical/physical properties of the materials (thickness, dielectric constant) assembling the structure. Consequently, silicon-based PhCs are expected to be very sensitive to air gap liquid infiltration, which is likely to produce significant variation of the transmission/reflection spectrum.

3.2 Design and Fabrication of Vertical 1D-PhCs

Recently, we have demonstrated that electrochemical etching of silicon in HF-based electrolyte (ElectroChemical Micromachining—ECM) [2] can be used for the fabrication of vertical high-aspect-ratio silicon/air 1D-PhCs based on the so-called hybrid quarter-wavelength structure [3, 4]. Hybrid quarter-wavelength 1D-PhCs consist of periodic arrays of vertical silicon layers, with thickness $d_{Si} = k\lambda_0/4n_{Si}$, and air gaps, of width $d_{Air} = h\lambda_0/4$, having spatial period $p = (h + k)\lambda_0/2n_{eff}$, which exploit the $(h + k)/2$ bandgap order at the operation wavelength λ_0, where n_{Si} is the silicon refractive index ($n_{Si} = 3.48$), h and k are odd, integer design parameters, $n_{eff} = D + (1 - D)n_{Si}$, and $D = d_{Air}/p$ is the material porosity [4]. The use of the hybrid structure allows one to design 1D-PhCs with different spatial period and/or exploiting high bandgap orders at the operation wavelength, thus increasing the flexibility of these structures both in terms of fabrication and applications. For instance, depending on the target applications, the possibility of choosing the appropriate period and bandgap order can be extremely important. Optical properties of PhCs for optoelectronic applications must be fairly independent of potential variations occurring as a consequence of chemical/physical changes of the materials assembling the structure. In this case, small period and a low reflectivity order would be preferred, since this choice reduces the structure size and increases the bandgap width. On the other hand, for PhCs used in biosensor or optofluidic applications a more complicated lineshape of the reflectivity spectrum would be better suitable in order to enhance optical changes induced by processes/changes occurring within the structure. In this case, increasing the spatial period of the structure, and, in turn, the thickness of silicon walls, allows (i) exploiting high-order bandgaps with reduced width at the selected wavelength and, in turn, obtaining a more sensitive structure, and (ii) simultaneously fabricating more robust structures able to manage liquid insertion. On the other hand, to efficiently attain the theoretically expected cumulative effects also for high-order bandgaps, PhCs with an improved optical quality (i.e., reduced spreading of the wall thickness, low roughness of surfaces, etc.) need to be fabricated.

Photonic crystals with period up to 8 μm suitable for optofluidic applications were fabricated by ECM technology, as detailed in [3, 4]. As an example, Fig. 3.1 (left) shows the typical Scanning Electron Microscope (SEM) cross-section of a

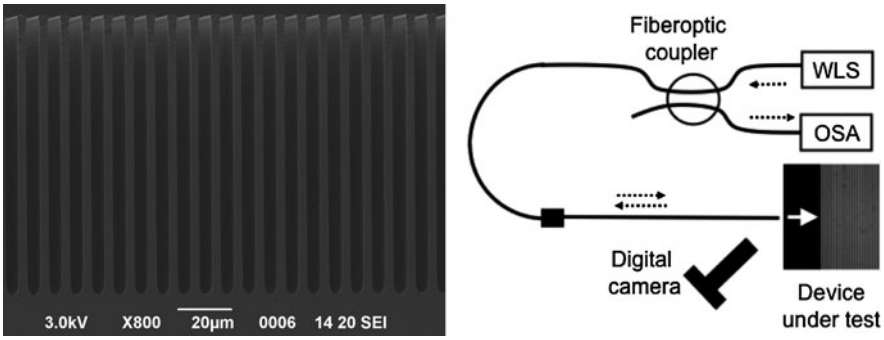

Fig. 3.1 *Left* SEM picture of a 1D-PhC microstructure with spatial period of 8 μm, depth of 100 μm, aspect-ratio of 33, fabricated by silicon ECM; *Right* Fiber-optic setup for reflectivity measurements, and upper view of the measured device taken with an optical microscope (WLS: white light source. OSA: optical spectrum analyzer)

1D-PhC with spatial period of 8 μm, height of 100 μm, and aspect-ratio of 33, exploiting the 20th reflectivity order at $\lambda_0 = 1.55$ μm.

3.3 Liquid Infiltration of Vertical 1D-PhCs

Measurements of spectral reflectivity on 1D-PhCs with period of 8 μm were performed with the optical setup reported in Fig. 3.1 (right), described in detail in [4]. Standard telecommunication single-mode fibers (SMR) were used for back-reflection measurements. The device was exposed to white light radiation in the range 1.1–1.7 μm by means of a single-mode fiber-optic 50% coupler, which also carried the reflected light back to the Optical Spectrum Analyzer (OSA). A ball-lensed fiber was used to simplify optical alignment and to improve input and output coupling between the fiber tip and the PhC device.

The reflected power spectrum of the as-fabricated microstructure (i.e. in air) was collected just before the addition of the liquid and used as a reference spectrum. Then, the power spectra in the presence of liquids as well as after evaporation, which is associated with a rapid return of the bandgap pattern to the reference situation, were recorded. A typical sequence of the reflected power spectra is reported in Fig. 3.2 (left) for two different alcohols, namely ethanol (EtOH) and isopropanol (IPA). In both cases, the power spectrum collected after evaporation is well superposed to the reference, even after a number of experimental insertion/evaporation cycles. Such result demonstrates that vertical 1D-PhCs with period of 8 μm feature a good mechanical stability for biomedical/optofluidic applications. Experimental data were found in good agreement with numerical results (see Fig. 3.2 (right)), calculated by using the characteristic matrix method, modified to take into account both surface roughness of silicon walls and the smoothing effect of a finite resolution bandwidth [4]. As theoretically

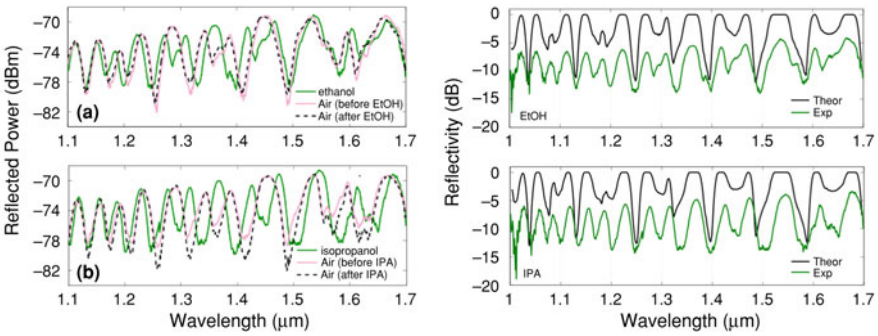

Fig. 3.2 *Left* Experimental reflected power spectra (RB = 10 nm) of a1D-PhC with $p = 8$ μm before and after infiltration of EtOH (*top*) and IPA (*bottom*) in the air gaps, as well as in the presence of the liquid inside the gaps; *Right* Experimental versus theoretical reflectivity spectra of the same 1D-PhC as in Fig. 3.2 (*left*)

predicted, alcohol infiltration produces a reliable redshift of the reflectivity spectrum, together with an increase of the bandgap order characterizing the structure in the near-infrared region under investigation, which allows to discriminate the refractive index difference of $\Delta n = 0.0075$ between the tested alcohols. For instance, the reflectivity spectrum in the presence of EtOH shows a reflectivity peak at 1,604 nm which shifts to 1,612 nm in the presence of IPA. Therefore, high-order 1D-PhCs allow for discriminating the refractive index difference between the tested alcohols by means of a differential shift of about 8 nm, which is of the same order of magnitude of the theoretical value. However, the minimum detectable refractive index variations can be improved, narrowing the RB, which requires a more powerful source to increase the dynamic range of the measurement.

3.4 Conclusions

Vertical silicon/air hybrid 1D-PhCs with period of 8 μm and exploiting high reflectivity orders seem very promising for biochemical and optofluidic applications. In fact, these structures are able to withstand several alcohols insertion/evaporation cycles without mechanical and/or optical damages. Furthermore, they allow discriminating between ethanol and isopropanol by measuring the differential shift of the reflectivity spectrum, according to theoretical predictions. Finally, they feature good high optical properties, such as very low losses and high sensitivity, confirming that the ECM technology is very promising for fabrication of high order 1D-PhCs with improved optical quality.

Acknowledgments This work was partially supported by the Italian Ministry of Research and University (MIUR) under a PRIN-COFIN 2007 and by the CARIPLO Foundation.

References

1. Psaltis D, Quake SR, Yang C (2006) Developing optofluidic technology through the fusion of microfluidics and optic. Nature 442:381–386
2. Lehmann V (1993) The physics of macropore formation in low-doped n-type silicon. J Electrochem Soc 140:2836–2843
3. Barillaro G, Nannini A, Piotto M (2002) Electrochemical etching in HF solution for silicon micromachining. Sens Actuators A102:195–201
4. Barillaro G, Strambini LM, Annovazzi-Lodi V, Merlo S (2009) Optical characterization of high-order 1-D silicon photonic crystals. IEEE J Selected Topics Quantum Electron 15:1359–1367

Chapter 4
Conductance Variation Under UV: A Surface Barrier Modification

C. Malagù, M. C. Carotta, A. Giberti, V. Guidi and G. Martinelli

Abstract We operated WO_3 gas sensor at room temperature under UV illumination. The observed increase in conductance is expected to depend on interband electronic transition, being the bandgap of the material smaller than the incident light. Strong evidence that the main phenomenon is instead surface barrier modulation is given in the present work.

4.1 Introduction

Semiconductor gas sensors using metal oxides have proven to be excellent in important characteristics such as sensitivity, long-term stability, robustness and price. Further progress in basic understanding is required to establish the principles to operate them as gas sensors. Recently, with the aim to improve sensor performances, several investigations on the effect of light (usually UV) have been performed [1]. The basic idea is arising from the fact that some metal oxides, known for their good sensing capabilities, also show photo catalytic behavior. Several materials have been studied versus a specific detecting gas, while there is a lack of experiments devoted to the explanation of such behavior under UV irradiation. In this work, we show experimental results concerning conductance changes of a WO_3-based gas sensor under illumination of the surface through a 397 nm LED, and we try to interpret them.

C. Malagù (✉) · M. C. Carotta · A. Giberti · V. Guidi · G. Martinelli
Department of Physics, University of Ferrara, Via Saragat 1/c, 44124 FE, Ferrara, Italy
e-mail: malagu@fe.infn.it

G. Neri et al. (eds.), *Sensors and Microsystems*,
Lecture Notes in Electrical Engineering 91, DOI: 10.1007/978-94-007-1324-6_4,

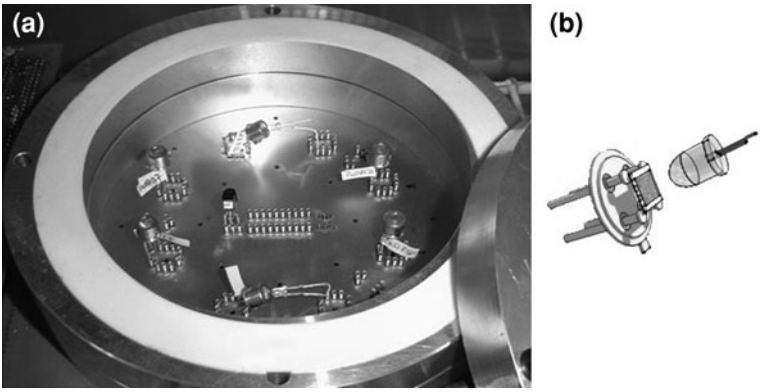

Fig. 4.1 **a** Test chamber with sensor and LED face-to-face, **b** sketch of the LED-sensor relative positions

4.2 Experimental

The set of measurements were performed on a WO_3 thick-film gas sensor. The powder preparation and the sensor's fabrication, together with thermal treatments and structural and morphological characterizations, are described in another work [2]. As a source of light we used a 397 nm LED, which is very cheap and easy to use. With the choice of WO_3 as sensor's material, we are sure that the surface is invested by photons with energy higher than the energy gap. Indeed, the energy gap of WO_3 is 2.56 eV, while a 397 nm light corresponds to photons of an energy of 3.1 eV.

The sensor and the LED were placed in a multi-sensor test chamber, providing the voltage to the LED with a sensor's placement. The supports of both the sensor and the LED were bent in order to illuminate the surface of the sensor with a proper incidence angle (see Fig. 4.1).

The film was kept at room temperature and the flow-through technique was used to probe the sensor. We performed conductance measurements in two kinds of environments: synthetic air and nitrogen. After stabilization of the sensor's signal in dark, the LED were switched on and, after a proper time, switched off, recording the conductance changes instant by instant.

4.3 Results and Discussion

The conductance of WO_3 sensor versus time is shown in Fig. 4.2. The plot begins with the switch on of the LED after stabilization in dark, then the LED is switched off. It can be seen that the signal of the sensor after illumination suffers a very slow change, of the order of tens of hours, and the same happens after the darkening.

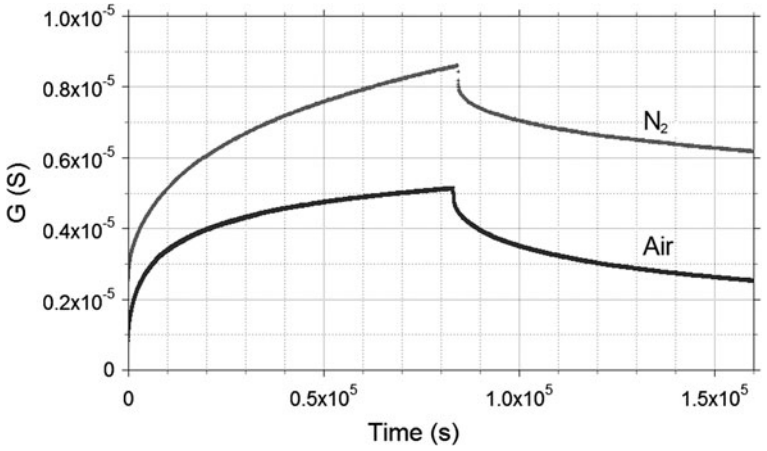

Fig. 4.2 Conductance of the sensor in air and in nitrogen, under illumination and in dark

This behavior was quantified more precisely with a fit of the two curves shown in Fig. 4.2 with a double exponential function, in order to distinguish the time constants of the two cases. The results are very different in the two cases of air and nitrogen. Concerning the behavior after illumination, while the shorter time constant is for both cases less than 1 h, the longer constant is less than 8 h in air and more than 14 h in nitrogen. Similar results were obtained for the behavior after darkening. These results identify the surface effects as the main contribution to the change of conductance under illumination. Indeed, such a slow behavior cannot be attributed to electronic transitions, on the other hand it is compatible with surface reaction kinetics [3–6]. The slower behavior shown in nitrogen, where the surface effects are less important than in air due to the absence of oxygen, together with the strongly reduced response peak, confirm this hypothesis.

4.4 Conclusions

The conductance variation of a WO_3-based thick-film gas sensor under UV illumination has been investigated. From the exceedingly long response time of the signal under illumination, we deduced that the main responsible for the increase in conductance cannot be interband electronic injection from the bulk. It then has to be ascribed to surface phenomena, which are mainly induced by oxygen chemisorbtion. Therefore, we observed the difference of behavior between illumination in air and in nitrogen which confirmed the hypothesis.

References

1. Shukla S, Agrawal R, Cho HJ, Seal S, Ludwig L, Parish C (2005) Effect of ultraviolet radiation exposure on room-temperature hydrogen sensitivity on nanocrystalline doped tin oxide sensor incorporated into microelectro mechanical systems device. J Appl Phys 97:54307
2. Guidi V, Blo M, Butturi MA, Carotta MC, Galliera S, Giberti A, Malagù C, Martinelli G, Piga M, Sacerdoti M, Vendemiati B (2004) Aqueous and alcoholic syntheses of tungsten trioxide powders for NO_2 detection. Sens Actuators B 103:213–218
3. Malagù C, Guidi V, Carotta MC, Martinelli G (2004) Unpinning of Fermi level in nanocrystalline semiconductors. Appl Phys Lett 84:4158–4160
4. Giberti A, Carotta MC, Guidi V, Malagù C, Martinelli G, Piga M, Vendemiati B (2004) Monitoring of ethylene for agro-alimentary applications and compensation of humidity effects. Sens Actuators B 103:272–276
5. Maffe TGG, Owen GT, Malagù C, Martinelli G, Kennedy MK, Kruis FE, Wilks SP (2004) Direct evidence of the dependence of surface state density on the size of SnO_2 nanoparticles observed by scanning tunnelling spectroscopy. Surf Sci 550:21–25
6. Malagù C, Martinelli G, Ponce MA, Aldao CM (2008) Unpinning of the Fermi level and tunneling in metal oxide semiconductors. Appl Phys Lett 92:162104

Chapter 5
Poly[3-(4-Alkoxyphenyl)thiophenes] Based Chemical Sensors

E. Massera, M. L. Miglietta, T. Polichetti, G. Di Francia, F. Borbone, L. Ricciotti, S. Pappalardo and A. Roviello

Abstract Polythiophenes and, in particular, poly(3-alkylthiophenes) have attracted much interest as VOCs sensing materials due to their good environmental stability, easy processability and their particular sensing ability. In this work, the potentiality of a particular class of polythiophenes, the highly regioregular poly [3-(4-alkoxyphenyl)thiophenes], has been investigated as VOCs sensor. This class of polymers showed long term stability under room temperature operation, very high sensitivity towards hydrocarbons and low response time.

5.1 Introduction

Conjugated polymers are intrinsically conductive materials which have been extensively investigated because of their electrical properties. The interest on conductive polymers arises from the suitability of these materials for applications in organic electronics, solar cells, batteries, supercapacitors, biological and chemical sensors [1–5].

Polythiophenes and, in particular, poly(3-alkylthiophenes) have attracted much interest in the sensor field as VOCs sensing materials due to their tunable properties of environmental stability, processability and sensing ability. The mechanism of interaction between an analyte and the polymer can be either physical or chemical: nucleophilic gases (H_2, NH_3, N_2H_4, H_2S, etc.) interact chemically with

E. Massera · M. L. Miglietta (✉) · T. Polichetti · G. Di Francia
ENEA Centro Ricerche Portici, Piazzale E. Fermi 1, 80055 Portici (NA), Italy
e-mail: mara.miglietta@enea.it

F. Borbone · L. Ricciotti · S. Pappalardo · A. Roviello
Dipartimento di Chimica, Università degli Studi di Napoli, Via Cinthia,
80126 Naples, Italy

G. Neri et al. (eds.), *Sensors and Microsystems*,
Lecture Notes in Electrical Engineering 91, DOI: 10.1007/978-94-007-1324-6_5,

the polymeric chain dedoping the polymers and decreasing the conductivity, while electrophilic (NO_x, SO_2, etc.) gases have an opposite effect. Other gases, including VOCs, interact via van der Waals forces with the polymer chain and, upon absorption onto the polymer film, a change in resistance, correlated with the concentration of analyte, can be observed [3]. These features have been mostly exploited in e-nose applications where sensitivities in the low ppm level, good repeatability, reversibility and stable room-temperature operation are required.

In this work, the potentiality of a particular class of polythiophenes, the highly regioregular poly[3-(4-alkoxyphenyl)thiophenes], has been investigated as VOCs sensor. These polymers show several advantages in terms of ease and cost of the synthetic pathway, regioregularity, order and planarity of the polymeric chain.

Moreover, the pronounced electron donor character of the alkoxyphenylic side-chain improves the stability of the doped state conferring a greater stability to the conducting state.

In particular, the potential of poly(3-(4-octyloxyphenyl)thiophene (PO) and of the copolymer poly(4-pentenoxyphenyl-*stat*-4-hexyloxyphenyl)thiophene as VOCs sensor has been probed; polymeric films have been deposited onto a chemiresistor transducers and exposed to toluene, acetone and alcohol vapours. The devices show good responses in terms of sensitivity and response time.

5.2 Results and Discussion

The poly[3-(4-octyloxyphenyl)thiophene] and the copolymer poly[4-pentenoxyphenyl-*stat*-4-hexyloxyphenyl)thiophene] (Fig. 5.1), hereafter indicated as PO and coP5P6 respectively, have been synthesized by an oxidative coupling polymerization reaction that leads to highly regioregular polymers (up to 80%). The polymers have been p-doped with chloroform solution of $FeCl_3$ (2% with respect to polymer) [6].

Chemiresistor devices have been obtained by drop casting 20 μl of a 10 mg/ml chloroform solution of polymers onto a 15 × 5 mm^2 Al_2O_3 substrate with pre-printed gold interdigitated electrodes. The devices, biased at 0,5V DC, have been electrically characterized in a Gas Sensor Characterization System where VOCs vapours, such as toluene, acetone, ethanol and 1-butanol are introduced by means of a bubbler system in controlled amounts [7]. The gas mixture and concentration output were checked by a Thermo Antaris IGS FTIR gas analyzer.

The chemiresistors, exposed to different concentrations of those analytes, show good responses in terms of sensitivity and detection limits in the ppm region (see Fig. 5.2 and Table 5.1). PO has very fast response time – comparable or even lower than the filling time of the test chamber – towards all the selected analytes, with a higher sensitivity to acetone and toluene. The copolymer film shows an overall higher sensitivity but slower response time. In particular, coP5P6 has a very good response to toluene and 1-butanol, with a lowest detection limits as low as 0.2 ppm for toluene (value extrapolated by evaluation of the ratio between

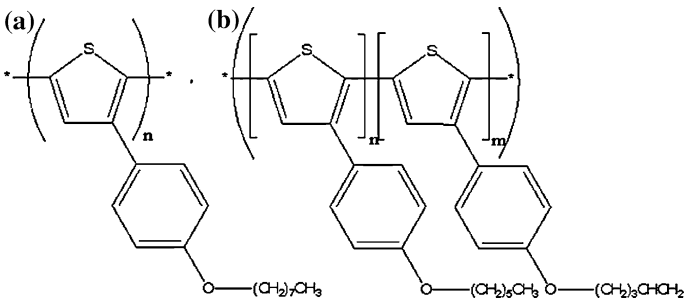

Fig. 5.1 **a** Poly-3 (4-octyloxyphenyl)thiophene and **b** copolymer poly(4-pentenoxyphenyl-stat-4-hexyloxyphenyl)thiophene chemical structures

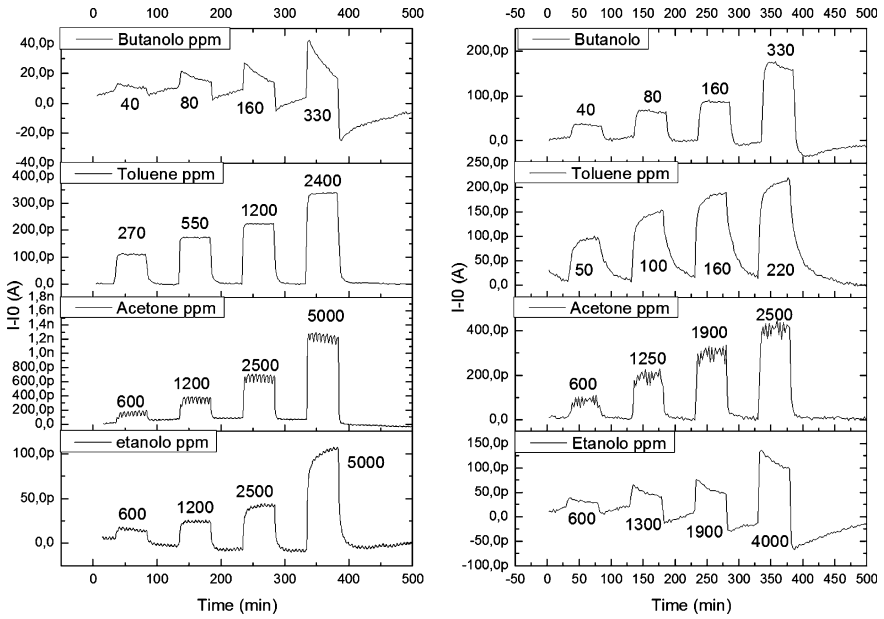

Fig. 5.2 PO and coP5P6 sensors current responses upon exposure to increasing concentration of VOCs

baseline noise and sensitivity). The exposure of coP5P6 to alcohol vapours shows a double effect on the measured current: soon after the inlet of the vapour the conductivity of the film increases but afterwards it seems to reduce with a slower kinetics. The same kind of kinetics can be also observed after the removal of the analyte. In summary, it can be noticed that toluene and 1-butanol are well detected by the copolymer sensing layer while PO shows better responses to more polar compounds, such as acetone and ethanol.

Table 5.1 Responses of PO and coP5P6 chemiresistors to analyte vapours

Analyte	Sensitivity (S/ppm)		Lowest detection limit (ppm)		Response time (10–90% sec)	
	PO	coP5P6	PO	coP5P6	PO	coP5P6
Toluene	7.5×10^{-13}	2.06×10^{-12}	10	<1	<120	595
Acetone	2.3×10^{-13}	1.67×10^{-13}	40	100[a]	<120	240
Ethanol	2.3×10^{-14}	1.6×10^{-11}	250	200[a]	<120	298
1-Butanol	2.5×10^{-13}	1.32×10^{-11}	20	<1	<120	297

[a] measured value

These performances persist even after more than two weeks under ambient conditions; after this period the electrical conductivity of the PO devices is dramatically reduced because of the dedoping process originated from the environmental water humidity [8]. Noteworthy, in the same storage conditions coP5P6 films are stable for more than 1 month.

5.3 Conclusions

Poly[3-(4-alkoxyphenyl)thiophenes] based gas sensors show a good sensitivity towards VOCs combined with a low detection thresholds. In addition, these sensing layers show a good repeatability and reversibility. The two polymers tested, notwithstanding the similar chemical structures, have different sensitivity and response kinetics to the same analytes. In particular, PO sensing layers responds with higher sensitivity to polar compounds whereas coP5P6 exhibits more affinity to apolar analytes. On account of this the sensors based on these layers can be profitably implemented in solid state sensor arrays for VOCs detection.

Acknowledgments The authors gratefully acknowledge the Ministry of Universities and Research (MUR) for financial support as part of Public-Private Laboratory TRIPODE (Technologies and Research for the application of polymers in electronics devices).

References

1. Lange U, Roznyatovskaya NV, Mirsky VM (2008) Conducting polymers in chemical sensors and arrays. Anal Chim Acta 614:1–26
2. Zhan L, Song Z, Shan N, Zhang J, Tang J, Zhan H, Zhou Y, Li Z, Zhan C (2009) Poly(tetrahydrobenzodithiophene): high discharge specific capacity as cathode material for lithium batteries. J Power Sour 193:859–863
3. Guan H, Zhou P, Zeng S, Zhou X, Wang Y, He Z (2009) Detection of deletion mutations in DNA using water-soluble cationic fluorescent thiophene copolymer. Talanta 79:153–158U
4. Dua V, Surwade SP, Ammu S, Zhang X, Jain S, Manohar SK (2009) Chemical vapor detection using parent Polythiophene nanofibers. Macromolecules 42:5414–5415

5. Li B, Santhanam S, Schultz L, Jeffries M, Iovu MC, Sauvè G, Cooper J, Zhang R, Revelli JC, Kusne AG, Snyder JL, Kowalewski T, Weiss LE, McCullough RD, Fedder GK, Lambeth DN (2007) Inkjet printed chemical sensor array based on polythiophene conductive polymers. Sens Actuators B 123:651–660
6. Barra M, Biasucci M, Cassinese A, D'Angelo P, Barone AC, Carella A, Roviello A (2007) Direct current and alternating current electrical transport properties of regioregular poly[3-(4-alkoxyphenyl)-thiophenes]. J Appl Phys 102:093712
7. Quercia L, Cerullo F, La Ferrara V, Di Francia G, Baratto C, Faglia G (2000) Fabrication and characterization of a sensing device based on porous silicon. Phys Status Solidi A 182:473–477
8. Koizumi H, Dougauchi H, Ichikawa T (2005) Mechanism of dedoping processes of conducting poly(3-alkylthiophenes). J Phys Chem B 109:15288–15290

Chapter 6
Electrical Noise Characterization of Epoxy/MWCNT Composites

C. Barone, D. Imparato, S. Pagano, L. Vertuccio, A. Sorrentino and H. C. Neitzert

Abstract We report on electrical transport and noise processes of Epoxy/multi-wall carbon nanotube composites. The dc measurements suggest that the investigated system can be regarded as a random resistor network in which the resistors are located at the junctions between carbon nanotubes and the nodes are the conducting pathways connecting different junctions, namely the nanotubes themselves. The noise-spectral density measurements reveal the existence of a threshold voltage, above which a markedly nonlinear behavior is found and is tentatively related to the specific properties of the Epoxy-mediated contact barrier among the carbon nanotubes.

6.1 Introduction

Carbon nanotubes (CNTs) addition to polymer [1] or Epoxy material [2] strongly enhances the electrical and thermal conduction and also improves the mechanical properties of the organic material. This leads to a variety of new applications for the resulting nanocomposites, namely electromagnetic shielding, electrical heaters, physical and chemical sensoring, and aerospace applications. Regarding the

C. Barone · D. Imparato · S. Pagano
CNR-SPIN Salerno and Dipartimento di Matematica e Informatica, Università degli Studi di Salerno, Via Ponte don Melillo 1, 84084, Fisciano, (SA), Italy

L. Vertuccio · A. Sorrentino
Dipartimento di Ingegneria Chimica e Alimentare, Università degli Studi di Salerno, Via Ponte Don Melillo 1, 84084, Fisciano, (SA), Italy

H. C. Neitzert (✉)
Dipartimento di Ingegneria Elettronica e Ingegneria dell'Informazione (DIEII), Università degli Studi di Salerno, Via Ponte don Melillo 1, 84084, Fisciano, (SA), Italy
e-mail: neitzert@unisa.it

G. Neri et al. (eds.), *Sensors and Microsystems*,
Lecture Notes in Electrical Engineering 91, DOI: 10.1007/978-94-007-1324-6_6,

electrical applications, investigations of the noise properties have been initially aimed at the evaluation of the intrinsic noise level. Recently, the so-called "fluctuation spectroscopy" has been proved to be a very informative method for revealing possible strategies to lower the intrinsic noise response, a mandatory requirement for the realization of high-performance devices based on these compounds. Here we study in detail the electrical transport and noise properties of Epoxy/multi-walled carbon nanotube composites in the temperature range between 10 and 300 K.

6.2 Experimental

The investigated Epoxy/CNT composites have been fabricated in the following way. A diglycidyl ether of bisphenol A-epoxy resin (DGEBA) has been mixed together with ultrasonically dispersed multi-wall carbon nanotubes (MWCNTs) and subsequently hardened with 4,4'diamine-dibenzyl-sulfone (DDS) hardener and cured in a two-step process first at 130°C for 1 h and subsequently at 180°C for 3 h. Because the percolation threshold of this kind of nanocomposites is rather low, CNT concentrations below 0.5wt% are sufficient to create a stable conducting nanotube network.

The electrical transport and noise properties of Epoxy/MWCNT composites have been analyzed using two and four-probe connections to the samples through evaporated gold contact pads. Possible effects of contact noise have been ruled out using appropriate techniques [3]. All the measurements have been carried out in a closed-cycle refrigerator. The temperature was stabilized using a GaAlAs thermometer and a resistance heater controlled in a closed feedback loop, giving a stability better than 0.1 K. The sample temperature has been measured by a Cernox resistance thermometer in contact with the sample holder. Further details of the experimental setup are reported in [3].

6.3 Results and Discussions

The temperature dependence of the resistance is shown in Fig. 6.1. In order to explain the conductivity mechanisms in this class of compounds, several theoretical models can be found in the scientific literature. According to our findings, the one that fits best our data is the fluctuation-induced tunneling (FIT) model, already used for multi-wall carbon nanotube nanocomposites [4].

According to FIT, in disordered materials generally characterized by large conducting regions (in this case the CNTs) separated by small insulating barriers (in this case the Epoxy interstitial matrix) the thermally activated voltage fluctuations across insulating gaps play an important role in the electrical conductivity mechanism [5]. A theoretical expression for the temperature dependence of the resistance can be derived as

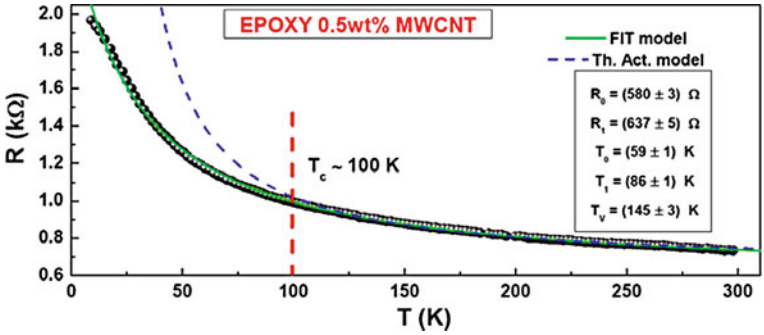

Fig. 6.1 Temperature dependence of the resistance R for a typical investigated Epoxy sample. *Solid* and *dashed lines* represent the best fits to the experimental data using Eqs. 6.1 and 6.2, respectively

$$R(T) = R_0 \exp\left(\frac{T_1}{T + T_0}\right), \tag{6.1}$$

where R_0 is a preexponential factor, and T_0 and T_1 are two characteristic temperatures of the investigated system [5].

The solid line in Fig. 6.1 is the best fit to the experimental data of Eq. 6.1, with the fitting parameter values reported in the inset. The effect of voltage fluctuations on the electric transport can also be understood analyzing the parallel conduction mechanism of thermal activation over the potential barrier. The temperature dependence of the resistance by thermal activation can be expressed as

$$R(T) = R_1 \exp\left[\frac{T_v T_1}{T(T_v + T_1)}(1 - \varepsilon_A)^2\right], \tag{6.2}$$

where T_v is another temperature parameter, and ε_A is the dimensionless applied electric field [5].

The dashed line in Fig. 6.1 is the best fitting curve, using Eq. 6.2 with R_1 and T_V values reported in the inset. As clearly explained in [5], it is possible to define a critical temperature $T_C = T_0 T_V / T_1$ above which thermal activation contribution is indistinguishable from the fluctuation-induced tunneling conductivity. T_C, obtained by fitting our experimental data, is around 100 K and is shown in Fig. 6.1. The small value of T_C, compared with others already reported for different types of MWCNT composites, allows us to consider a distribution of tunnel barriers characterized by small energy levels.

In overall, the dc measurements suggest that our compounds can be regarded as a random resistor network in which the resistors are located at the junctions between carbon nanotubes and the nodes are the conducting pathways connecting different junctions, namely the nanotubes themselves [6].

More sensitive investigations, such as noise measurements, have also been performed to better clarify the aspects related to the electrical transport processes

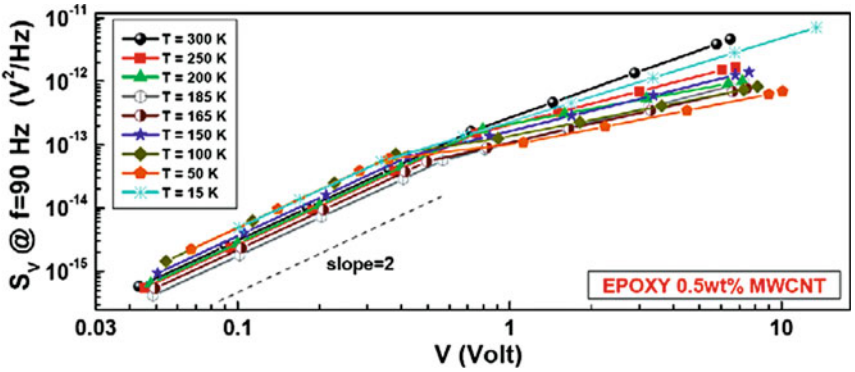

Fig. 6.2 Voltage dependence of the spectral density background at a reference frequency $f = 90$ Hz, in the temperature range from 15 to 300 K

of the analyzed composites. The noise-spectral density S_V shows two main components. One with a $1/f$ dependence and the other with a constant spectrum, corresponding the expected value for Johnson noise $4K_BTR$. The bias voltage dependence of S_V concerns only the $1/f$ part and can be generally expressed as

$$S_V(V) = AV^v + S_0, \tag{6.3}$$

where the factor A is a measure of the noise level expressed in terms of the normalized Hooge parameter [7], v is the voltage slope parameter, and S_0 is the voltage noise background ascribed to measurement electronics.

S_V versus V curves, in the investigated temperature range [15–300] K, are reported in Fig. 6.2, which clearly shows the existence of two different behaviors with a well defined threshold voltage V_T. Below V_T a quadratic voltage dependence of the $1/f$ spectrum is observed, strongly supporting an origin of the electric noise due to "standard" resistance fluctuations [7]. Conversely, a markedly nonlinear dependence of S_V is found above V_T, revealing a significant decrease of the noise level.

This nonlinear behavior is also confirmed by measurements of the differential resistance R_d as a function of the bias voltage V. A step-like decrease of R_d is found in a small region around V_T, for all the investigated temperatures. We speculate that the observed unusual experimental findings, not found in other types of CNT-composites, are strictly related to the specific properties of the Epoxy-mediated contact barrier among the CNTs, and in particular to the low amplitude of the energy barrier between adjacent CNTs, as evidenced by the R versus T analysis.

References

1. Paul DR, Robeson LM (2008) Polymer nanotechnology: nanocomposites. Polymer 49:3187
2. Guadagno L, Naddeo C, Vittoria V, Sorrentino A, Vertuccio L, Raimondo M, Tucci V, De Vivo B, Lamberti P, Iannuzzo G, Calvi E, Russo S (2010) Cure behavior and physical

properties of epoxy resin—filled with multiwalled carbon nanotubes. J Nanoscience Nanotechnology 10:2686
3. Barone C, Galdi A, Pagano S, Quaranta O, Méchin L, Routoure JM, Perna P (2007) Experimental technique for reducing contact and background noise in voltage spectral density measurements. Rev Sci Instrum 78:093905
4. Simsek Y, Ozyuzer L, Seyhan AT, Tanoglu M, Schulte K (2007) Temperature dependence of electrical conductivity in double-wall and multi-wall carbon nanotube/polyester nanocomposites. J Mater Sci 42:9689
5. Sheng P (1980) Fluctuation-induced tunnelling conduction in disordered materials. Phys Rev B 21:2180
6. Wright DC, Bergman DJ, Kantor Y (1986) Resistance fluctuations in random resistor networks above and below the percolation threshold. Phys Rev B 33:396
7. Kogan S (1996) Electronic noise and fluctuations in solids. Cambridge University Press, Cambridge

Chapter 7
Microwave-Assisted Synthesis of Metal Oxide Nanostructures for Sensing Applications

T. Krishnakumar, N. Pinna, A. Bonavita, G. Micali, G. Rizzo and G. Neri

Abstract In this work, microwave-assisted technique was applied in the synthesis of different metal oxide nanostructures for gas sensing applications. Chemoresistive devices consisting of a thick layer of SnO_2, ZnO, $Cd(OH)_2$ and CdO nanostructures on interdigitate alumina substrates were fabricated and their sensing characteristics investigated. Sensor devices based on these metal oxide nanostructures exhibited good performance in the monitoring of low concentrations of toxic gases.

7.1 Introduction

Microwave-assisted synthesis is a promising way to improve the conventional heating process in the preparation of metal oxides, accelerating kinetics of solid state reactions [1]. This technique offers many significant advantages over conventional methods. In addition, compared to solid state materials processing,

T. Krishnakumar (✉)
Department of Physics, VMKV Engineering College, Vinayaka Mission University, Salem, Tamilnadu 636 308, India
e-mail: tkrishnakumar_nano@yahoo.co.in

N. Pinna
Department of Chemistry, CICECO, University of Aveiro, 3810-193 Aveiro, Portugal

N. Pinna
World Class University (WCU) Program of Chemical Convergence for Energy and Environment (C2E2), School of Chemical and Biological Engineering, College of Engineering, Seoul National University (SNU), Seoul 151-744, Korea

A. Bonavita · G. Micali · G. Rizzo · G. Neri
Department of Industrial Chemistry and Materials Engineering, University of Messina, C/da di Dio, Vill. S. Agata, 98166 Messina, Italy

G. Neri et al. (eds.), *Sensors and Microsystems*,
Lecture Notes in Electrical Engineering 91, DOI: 10.1007/978-94-007-1324-6_7,

microwave-assisted wet chemical synthesis is more simple for scaling up. Much effort is however needed to get a more comprehensive understanding of the effects of microwaves on the processing operations and final properties of materials synthesized.

In recent times, microwaves are being widely utilized to synthesize metal oxide nanoparticles and nanostructures by dielectric heating of solution in hydrothermal conditions [2, 3]. Nanostructured metal oxides show peculiar electrical properties making them suitable as active sensing materials in gas sensors, with enhanced performance with respect to bulk materials [4]. From these facts, recently we decided to focus our interest on the preparation of various metal oxides nanostructures by microwave-assisted synthesis. Examples of such efforts are here reported, highlighting the key role of the microwave approach in the synthesis of particular metal oxide nanostructures, and discussing the properties of chemoresistive sensors based on such nanomaterials.

7.2 Experimental

The microwave-assisted synthesis of metal oxide nanostructures was accomplished by dielectric heating in a MW oven (2.45 GHz working frequency, power up to 1 kW) for a few minutes. More details on the synthesis of the various metal oxide nanostructures are reported in previous works [5–7]. Chemoresistive sensors were made depositing by drop coating films (1–10 μm thick) of the synthesized nano-powders dispersed in ethanol on alumina substrates (6×3 mm^2) with Pt interdigitated electrodes and a Pt heater located on the backside. The sensors were then introduced in a stainless-steel test chamber for the sensing tests. Gases coming from certified bottles can be further diluted in air at a given concentration by mass flow controllers.

Electrical and sensing measurements were carried out in the temperature range from 50 to 400°C, with steps of 50°C, under a dry air total stream of 200 sccm, collecting the sensors resistance data in the four point mode. A multimeter data acquisition unit Agilent 34970A was used for this purpose, while a dual-channel power supplier instrument Agilent E3632A was employed to bias the built-in heater of the sensor to perform measurements at super-ambient temperatures. The gas response, S, is defined as $S = [R_{air} - R_{gas}/R_{air}] \times 100$ where R_{gas} is the electrical resistance of the sensor at different concentrations in dry air and R_{air} the baseline resistance in dry air.

7.3 Results and Discussion

7.3.1 Metal Oxide Nanostructures Synthesis

Different SnO_2, ZnO, $Cd(OH)_2$ and CdO nanostructures were synthesized through the microwave-assisted route. Main advantages of this approach were: (i) dramatic reduction of the synthesis time from many hours down to few minutes; (ii) synthesis

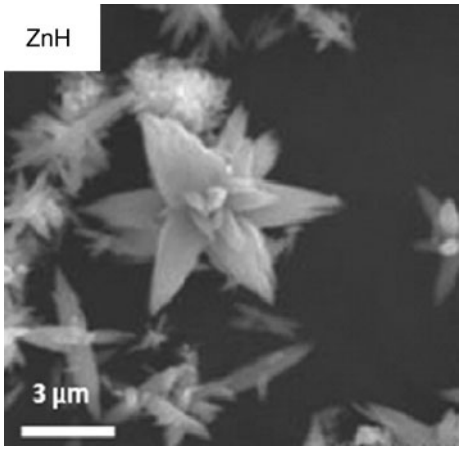

Fig. 7.1 Flower-like ZnO nanostructures prepared by microwave-assisted synthesis

of metal oxide nanoparticles with very different composition and/or morphologies by simply changing the parameters of the process such as the precursor materials, solvent and microwave irradiated time or power.

As an example, crystalline ZnO nanostructures were prepared in 10 m after a suitable microwave treatment [6]. The product obtained in the absence of the microwave treatment led instead, after many hours of reaction, to the formation of zinc hydroxide. This different behavior was due to microwave radiation which induced condensation of the hydroxyl bonds by selectively exciting them, offering in addition a remarkable reduction of the reaction time in comparison to traditional heating. Different ZnO nanostructures (spherical-, flower-, star-like), have been prepared by adapting the experimental conditions. A TEM image of flower-like ZnO nanostructures is shown in Fig. 7.1.

Because of the importance of cadmium hydroxide and oxide for optical and electrical applications, the preparation of cadmium nanostructures was also investigated. Preliminary tests have evidenced that, in the experimental conditions adopted, only $Cd(OH)_2$ can be obtained through the microwave process. Nanowires- or sheet-like cadium hydroxide nanoparticles have been easily synthesized (Fig. 7.2a, b). Efforts are in progress in order to synthesize also CdO nanostructures by the microwave-assisted route.

7.3.2 Sensing Tests

Metal oxide nanostructures synthesized by microwaves have been tested for gas sensing of toxic gases such as CO, NO_2 and NH_3, evaluating the electrical resistance of the deposited layer on interdigitated alumina substrates as a function of operating temperature and gas concentration. Results obtained have demonstrated that the nanostructure assumes a key role in determining the sensing properties of the metal

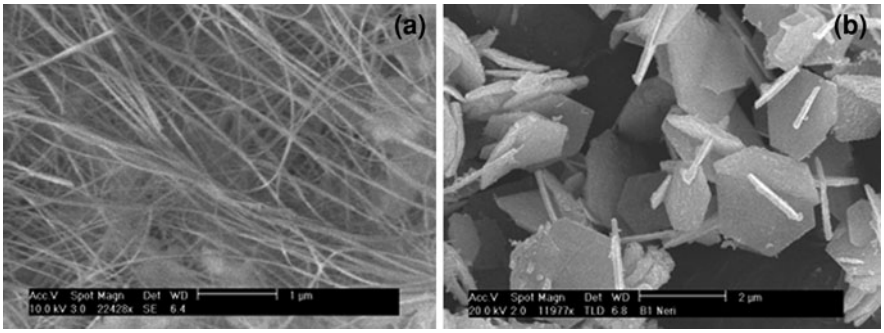

Fig. 7.2 **a** Nanowires and **b** sheet-like $Cd(OH)_2$ nanostructures prepared by microwave-assisted syntheses

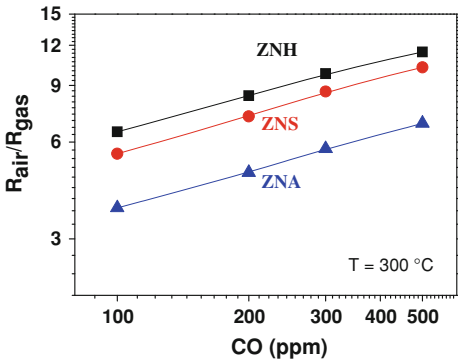

Fig. 7.3 Calibration curves of nanostructured ZnO sensors

oxide, as a result of the smaller grain size and higher surface area compared to bulk counterpart. In addition, also the electronic transport characteristics, strongly modified by the nanostructure, given an important contribute.

As an example Fig. 7.3 shows the response at low concentrations of carbon monoxide in air of resistive sensors based on different ZnO morphologies, obtained through microwave-assisted synthesis routes. On all sensors tested, a high sensitivity to CO was observed, with fast response/recovery times. Making a comparison among them, the flower-like ZnO-based sensor (ZNH) exhibits higher sensitivity to CO with respect to sensors based on other morphologies.

7.4 Conclusion

In summary, this study highlighted that the performance of resistive chemical sensors can be controlled by finely tuning the morphology of the metal oxide sensing layer. Simple and fast wet chemical processes assisted by microwaves, were applied for the synthesis of the nanomaterials.

By changing the main reaction parameters, metal oxide nanostructures with different size, shape and/or morphology have been obtained, providing a easy route to sensing layers for highly sensitive gas sensors. Synergic effects between small crystallite size/high surface area and electron transport properties modification assume the key role for explaining the enhanced sensing properties of some specific nanostructures.

References

1. Rao KJ, Vaidhyanathan B, Ganguli M, Ramakrishnan PA (1999) Synthesis of inorganic solids using microwaves. Chem Mater 11:882–895
2. Lagashetty A, Havanoor V, Basavaraja S, Balaji SD, Venkataraman A (2007) Microwave-assisted route for synthesis of nanosized metal oxides. Sci Technol Adv Mater 6:484–493
3. Bilecka I, Djerdj I, Niederberger M (2008) One-minute synthesis of crystalline binary and ternary metal oxide nanoparticles. Chem Commun 21:886–887
4. Franke ME, Koplin TJ, Simon U (2006) Metal and metal oxide nanoparticles in chemiresistors: does the nanoscale matter? Small 2:36–50
5. Krishnakumar T, Pinna N, Kumari KP, Perumal K, Jayaprakash R (2008) Microwave-assisted synthesis and characterization of tin oxide nanoparticles. Mat Lett 62:3437–3440
6. Krishnakumar T, Jayaprakash R, Pinna N, Donato N, Bonavita A, Micali G, Neri G (2009) CO gas sensing of ZnO nanostructures synthesized by an assisted microwave wet chemical route, Sens. Actuators B 143:198–204
7. Sathiya Raj D, Krishnakumar T, Jayaprakash R, Donato N, Latino M, Neri G (2010) Synthesis and characterization of $Cd(OH)_2$ nanowires obtained by a microwave-assisted chemical route. Sci Adv Mat 2:432–437

Chapter 8
A Novel Organic/MWCNTs Semiconductor Composite for Resistive Gas Sensors

F. Fontana, T. Caronna, N. Donato, M. Latino, A. Bonavita, G. Rizzo and G. Neri

Abstract The synthesis, electrical and sensing properties of 7,8-diazabenzo [*ghi*]perylene (DABP) mixed with multi-walled carbon nanotubes (MWCNTs) have been reported. DABP was synthesized through a photochemical reaction approach and resulted suitable for solution processing, allowing the easy deposition of films on the sensor substrate. Thin films of DABP/MWCNTs composites have shown an electrical behavior depending on the carbon nanotubes loading. Sensing properties of resistive devices fabricated using DABP/MWCNTs semiconducting composites have revealed a high and fast response to relative humidity and vapor of protonated organic solvents.

8.1 Introduction

The preparation of organic materials stable in air, solution-processable and with suitable electrical conductivity, is a fundamental step in organic electronics. Organic materials based on π-conjugated molecules are intensively studied

F. Fontana (✉) · T. Caronna
Department of Industrial Engineering, University of Bergamo, Bergamo, Italy
e-mail: fontana@unibg.it

N. Donato
Department of Matter Physics and Electronics Engineering, University of Messina, Messina, Italy

M. Latino
Department of Chemical Science and Technologies, University of Rome Tor Vergata, Rome, Italy

A. Bonavita · G. Rizzo · G. Neri
Department of Industrial Chemistry and Materials Engineering, University of Messina, Messina, Italy

G. Neri et al. (eds.), *Sensors and Microsystems*,
Lecture Notes in Electrical Engineering 91, DOI: 10.1007/978-94-007-1324-6_8,

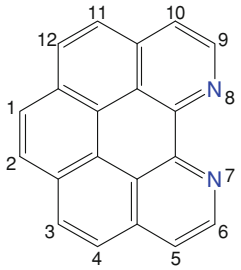

Fig. 8.1 Molecular structure of 7,8-diazabenzo[*ghi*] perylene (DABP)

nowadays in the field of organic semiconductors as a complement to the shortcomings of inorganic semiconductors [1, 2]. Organic semiconductors offer, with respect to current inorganic-based technology, greater substrate compatibility, device processability, flexibility, large area coverage, and reduced cost.

In the framework of our recent interest towards new π-electron organic systems for sensing applications, we have focused the attention on the synthesis of aza-helicenes (with 5 or 6 or even more orthocondensed benzenic or pyridinic rings) and aza-perylenes (with 5 benzenic or pyridinic peripheric rings). These organic molecules appear very promising for gas sensing, due to the presence of a reactive nitrogen functionality on the pyridinic ring, which could be able to interact reversibly with specific gases. Most important, the possible existence of a charge transfer might considerably alter the electronic structure of the conduction channels in the highly conjugated molecule system, modifying as a consequence the transport properties making them very attractive for fabricating resistive chemosensors. In particular, in this study we report data obtained in the investigation of the electrical and sensing properties of 7,8-diazabenzo[*ghi*]perylene (DABP).

8.2 Experimental

The molecular structure of DABP is shown in Fig. 8.1. DABP was synthesized through a photochemical reaction carried out in two steps, as reported elsewhere [3].

DABP is a dark orange solid material with high melting point (226–234°C), and results stable in air. It shows moreover a good solubility in many organic solvents, allowing to prepare processable solutions for thin films deposition. However, notwithstanding the large conjugation, the conductivity of DABP is low, and not suitable for the application in chemoresistive sensors. Therefore the organic material was mixed with a suitable amount of multi-walled carbon nanotubes (MWCNTs), in order to enhance the conductivity of the sensing film.

The composite sensor was fabricated depositing by drop-coating from dichloroethane solution thin films of DABP/MWCNTs on an alumina substrate provided with interdigited electrodes. The sensor was preliminarly conditioned in air for 2 h at room temperature. Electrical tests were carried out at room temperature (25°C). *I*/*V* curves were acquired by means of a Keithley 2400 source meter. The sensing tests were carried out in a home-made apparatus. The relative humidity (RH) and

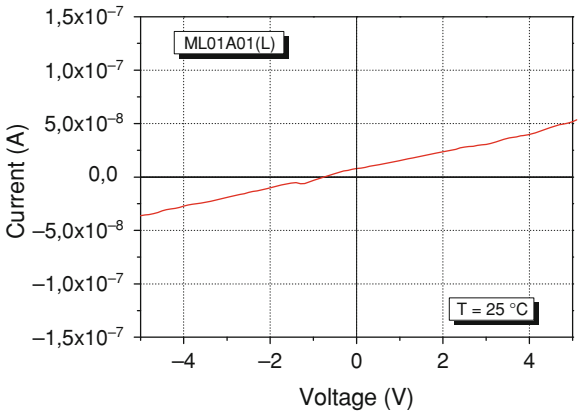

Fig. 8.2 *I/V* characteristics of a DABP/MWCNTs composite film

organic vapours were generated by using a bubbler connected to a mass flow control system, in order to vary their concentration.

8.3 Results and Discussion

8.3.1 Electrical Properties

Electrical properties of the pure DABP film and DABP/MWCNTs composite films with different carbon nanotubes loading, were studied in order to evaluate the effect of the amount of CNTs on the films conductivity.

Figure 8.2 shows the output currents of a DABP/MWCNTs composite film at room temperature as a function of input bias. While the output signal of the pure DABP film is not readable due to its very low conductivity, we noted that the output signal is remarkably amplified with the addition of carbon nanotubes, thus indicating the improvement in conductivity of the active layer. Specifically, current level increases with increasing CNTs loading, likely due to electron transfer from carbon nanotubes to DABP, thus increasing the electron density in the conduction band of the organic molecule. The dependence of conductivity on the CNT content in the composites is in agreement with previously reported results of polymer/CNT composites in which the conductivity exhibits a percolation behavior [4].

8.3.2 Sensing Tests

First, the effect of humidity on the electrical characteristics of the DABP/MWCNTs composite was investigated. A strong variation of current with humidity change was observed, suggesting that the sensor can be used as resistive sensor for

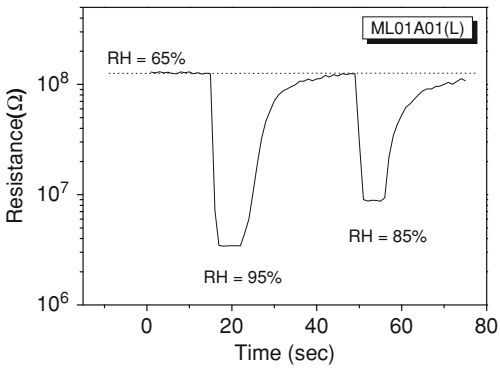

Fig. 8.3 Transient response of the composite sensor to different relative humidity variations

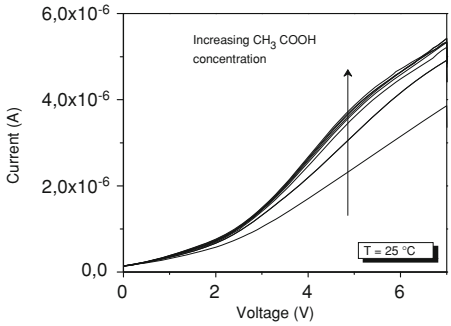

Fig. 8.4 *I/V* characteristics of DABP/MWCNTs composite film-based sensor at different acetic acid concentrations

monitoring relative humidity. Experiments have also shown that no significant variations of currents occurs on devices based only on DABP or MWCNTs, confirming that changes observed on the composite sensor are due to the synergic action between carbon nanotubes and the organic material.

The transient response of the composite sensor to different RH variations is reported in Fig. 8.3. It can be noted a strong decreases of resistance as the relative humidity value increase. Moreover, the response is well reversible, exhibiting a fast response/recovery time.

According to other authors [5], we explained this behaviour assuming that DABP manifests a strong affinity for protons. The electron transferring (hopping) assisted by the presence of a proton trap such as the heterocyclic nitrogen may be considered responsible of the resistance variations observed in humid ambient.

To support the above hypothesis, experiments aimed to investigate the effect of gases of different chemical nature (e.g. cyclohexane and acetic acid) have been carried out. The results of the tests have shown that the DABP/MWCNTs composite film-based sensor displays large variations of the electrical resistance with varying the concentration of acetic acid (Fig. 8.4).

No significant variations were instead observed when cyclohexane vapours contacted the sensor, confirming the formulated hypothesis.

8.4 Conclusion

A novel composite based on a diaza-perylene organic material mixed with MWCNTs has been developed, having the potentiality for selective gas sensing. The sensing mechanism has been investigated and electrical and sensing data acquired have indicated that the proton affinity of the nitrogen functionality of the organic material is the main factor influencing the sensor response. In a more general perspective, the interesting electrical characteristics here reported, in conjunction with the peculiar chemical properties, suggest them as attractive candidates for their investigation in chemo-selective gas sensors.

References

1. Sirringhaus H, Kawase T, Friend RH, Shimoda T, Inbasekaran M, Wu W, Woo EP (2000) High-resolution inkjet printing of all-polymer transistor circuits. Science 290:2123–2126
2. Gamota DR, Brazis P, Kalyanasundaram X, Zhang J (2004) Organic Polymer Field-Effect Transistors. In: Kanicki J and Martin S (eds.) Printed organic and molecular electronics. Kluwer Academic Publishers, New York
3. Caronna T, Fontana F, Longhi G, Mele A, Natali Sora I, Viganò L (2009) 2,13-Diaza[5] helicene: synthesis, theoretical calculations and spectroscopic properties. Arkivoc 8:145–155
4. Coleman JN, Curran S, Dalton AB, Davey AP, McCarthy B, Blau W, Barklie RC (1998) Percolation-dominated conductivity in a conjugated-polymer-carbon-nanotube composite. Physical Review B 58:R7492–R7495
5. Roithová J, Schröder D, Míšek J, Stará IG, Starý I, Mass J (2007) Chiral superbases: the proton affinities of 1- and 2-aza[6]helicene in the gas phase. Spectrom 42:1233–1237

Chapter 9
An Exploratory Study on the Potential of Zeolite P-Based Materials for Sensing Applications

I. Arrigo, M. Caprì, F. Corigliano, A. Bonavita, G. Rizzo, G. Neri and N. Donato

Abstract The synthesis, characterization and electrical properties of zeolite P-based material have been reported. It was verified that thick films can be deposited on ceramic substrates forming a homogeneous and porous structure, making easy the fabrication of thick film-based sensors. The structural properties of these materials revealed moreover an ideal environment for gas or vapor adsorption. Sensing properties of resistive devices fabricated using zeolite-P/MWCNTs composites have shown a rapid response and high sensitivity to relative humidity.

9.1 Introduction

Zeolites are crystalline, microporous hydrated aluminosilicate containing exchangeable alkaline and alkaline earth cations in their structural frameworks. Due to the high absorption properties of micropores, zeolite-based materials have received great attention for sensing applications. Moreover, they can selectively absorb specific chemical species depending on their shape and size, thus enhancing sensor selectivity.

Several chemical sensor device typologies have been reported taking advantage of the zeolite frameworks properties [1–4]. Generally, zeolites exhibit no measurable electronic conductivity since they have a wide electronic band gap of

I. Arrigo · M. Caprì · F. Corigliano · A. Bonavita · G. Rizzo · G. Neri
Department of Industrial Chemistry and Materials Engineering,
University of Messina, Messina, Italy

N. Donato (✉)
Department of Matter Physics and Electronics Engineering,
University of Messina, Messina, Italy
e-mail: ndonato@unime.it

G. Neri et al. (eds.), *Sensors and Microsystems*,
Lecture Notes in Electrical Engineering 91, DOI: 10.1007/978-94-007-1324-6_9,

several eV. On the other hand, since mobile cations are present within the zeolite framework that may hop from one binding site to the next, zeolites exhibit ionic conductivity, allowing their use in impedance sensors. The adsorption of chemical species on zeolite results in a measurable mass change. As a consequence, a great variety of sensor studies investigate the application of zeolite layers onto piezoelectric microbalances (QCM) or surface acoustic wave (SAW) devices. In both cases, the mass change is transformed into a frequency shift of the piezoelectric resonator.

Moving from these facts, we have initiated a study aimed to investigate novel zeolite-based materials as sensing layer for the development of chemical sensors, focusing our interests on zeolite P-based materials. The zeolite P class includes a series of synthetic zeolite phases which may be in cubic configuration (also termed B or Pc) or tetragonal configuration (also termed P1). Recently we prepared a novel zeolite P-based material (Z-PM) by a patented hydrothermal treatment starting from a pumice mine waste [5]. This zeolitized-P material showed a high content of crystalline zeolite P in Na^+ form, Si/Al atomic ratio of about 2.2, surface area of 34 m^2/g and micropore area 3.6 m^2/g. As these structural properties could provide an ideal environment for molecular adsorption, an exploratory study was undertaken on the feasibility of using porous zeolitized-P materials for sensing applications.

9.2 Experimental

Zeolite P-based materials can be obtained by a structural conversion from amorphous natural sources or by chemical synthesis. We recently synthesized a novel zeolite P-based material (Z-PM) by a patented hydrothermal treatment starting from a pumice mine waste, by extracting as much silica as possible by a sodium alkali aqueous solution in hydrothermal conditions and by rinsing the un-extracted residue with water up to neutral pH [5].

Synthetic zeolite P has been prepared according the following procedure. In brief, a solution "A" was prepared dissolving a mixture of sodium aluminate (20% Al_2O_3, 20% Na_2O, 60% water) and NaOH in water under stirring at 348 K. A solution "B" was prepared dissolving sodium silicate (30% SiO_2, 12% Na_2O, 58% water) in water. The solution "A", after a preheating treatment, was poured into a reactor kept at 368 K. When solution "B" was added slowly (about 5 min) to the aluminate solution, a silico-aluminate gel was instantaneously formed. The gel was maintained at 368 K under reflux for 5 h. After this time, it was filtered on a buckner and repeatedly washed with 200 ml of water until a pH of 12.5 was reached. The synthesized zeolite P was finally heated at 383 K in a oven for 8 h.

The characterization of the synthesized Z-PM material was carried out by XRD, SEM-EDX, TEM surface area and porosity measurements. An aqueous suspension of the Z-PM material, in the presence of sodium metasilicate ($Na_2SiO_3 \times 5H_2O$) acting as a binder, was used for the deposition of Z-PM thick films on the

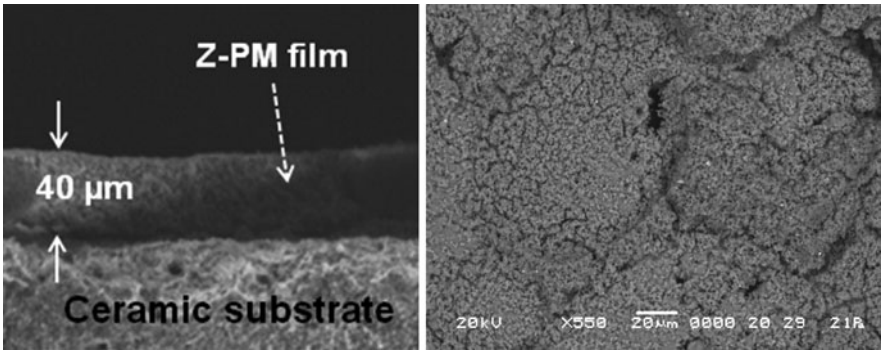

Fig. 9.1 SEM micrographs showing, respectively, the cross-section and the surface of the thick film on the ceramic substrate

interdigitated ceramic substrate of resistive-type sensors. The electronic conductivity of the Z-PM material was modulated by adding to the above aqueous suspension the suitable amount of multiwalled carbon nanotubes (MWCNTs).

9.3 Results and Discussion

Initially, we carried tests aimed to investigate the deposition of thick films of the zeolitized materials on ceramic interdigitated substrates. Practically, the deposition of thick films was accomplished by screen printing from aqueous slurry solutions. In order to exploit better performances, the film must adhere strongly to the substrate, maintaining the same time a relatively high surface area. To improve the adherence of the film on the surface of the ceramic substrate, an aqueous solution of sodium metasilicate has been used as a binder.

SEM micrographs reported in Fig. 9.1 show, respectively, the cross-section and the surface of the Z-PM layer (about 40 µm thick) on the ceramic substrate. It can be noted the good thickness homogeneity and the porous structure of the film.

Humidity sensing tests have been carry out on the fabricated resistive devices. However, as expected, pure Z-PM films were extremely resistive, with resistance values in a range not measurable by our instrumentation.

Then, to decrease the resistance of the sensing layer, Z-PM material was mixed with different loadings of MWCNTs. The excellent electrical conductivity ($>10^5$ S/m for multi-walled carbon nanotubes) should make them suitable candidates in preparing zeolites-CNTs composites, which may offer high electrical performances unattainable by pure zeolites.

Preliminary sensing tests have shown the promising characteristics of the Z-PM material used in combination with MWCNTs for monitoring humidity by resistive sensors. The transient response of the sensor to different relative humidity variations is reported in Fig. 9.2.

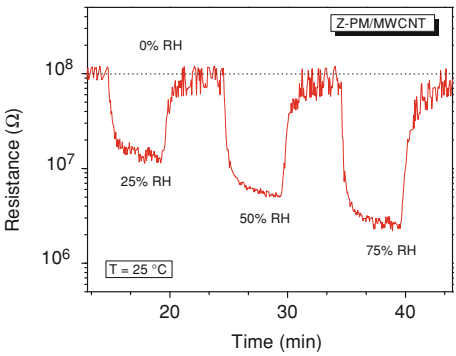

Fig. 9.2 Transient response of the sensor to different relative humidity variations

Starting from an initial conditions of RH = 0, a strong decrease of resistance was observed going towards higher RH. Moreover, the response is well reversible. It was clearly evinced that both the response and the recovery times were fast. Specifically, the response time as humidity changed from 0 to 75% RH, and the recovery time as humidity changed from 75 to 0% RH, was about 90 s.

9.4 Conclusion

A novel resistive humidity sensor has been designed by using a natural zeolitized-P material, showing well characteristics of sensitivity and reversibility. In order to exploit further the potential of these materials, we also will explore the possibility to synthesize zeolite P films directly on the surface of a piezoelectric QCM or SAW devices, to fabricate novel types of humidity and gas sensors. By using cation exchange properties of Z-PM, in a suitable cation form and able to quickly exchange with other cations [6, 7], could open further prospects for the development of selective chemical sensors species also in liquid phase.

References

1. Simon U, Flesch U, Maunz W, Müller R, Plog C (1998) The effect of NH_3 on the ionic conductivity of zeolites Na-beta and H-beta. Microporous Mesoporous Mater 21:111–116
2. Sahner K, Hagen G, Schönauer D, Reiß S, Moos R (2008) Zeolites—versatile materials for gas sensors. Solid State Ionics 179:2416–2423
3. Neumeier S, Echterhof T, Bölling R, Pfeifer H, Simon U (2008) Zeolite based trace humidity sensor for high temperature applications in hydrogen atmosphere. Sens Actuators B Chem 134:171–174
4. Zou J, He HY, Dong JP, Long YC (2004) A guest/host material of LiCl/H-STI (stilbite) zeolite assembly: preparation, characterization and humidity-sensitive properties. J Mater Chem 14:2405–2411

5. Corigliano F, Arrigo I, Catalfamo P, Di Pasquale S, Primerano P (2004) Patent pending no. MI2004A 1766
6. Arrigo I, Catalfamo P, Cavallari L, Di Pasquale S (2007) Use of zeolitized pumice waste as a water softening agent. J Hazardous Mater 147:513–517
7. Catalfamo P, Arrigo I, Primerano P, Corigliano F (2006) Efficiency of a zeolitized pumice waste as a low cost heavy metaladsorbent. J Hazardous Mater 134:140–143

Chapter 10
Thermoelectric Properties of Carbon Nanotubes Layers

M. Penza, R. Rossi, M. Alvisi, D. Valerini, E. Serra, E. Martinelli, C. Di Natale and A. D'amico

Abstract Thermoelectric power (TEP) of the carbon nanotubes (CNTs) films, grown by radiofrequency plasma-enhanced chemical vapor technology onto silicon substrates, has been measured. Two different metal contacts of Cr–Al and Cr–Au have been fabricated for the CNTs-based thermocouples and preliminarily investigated. The CNTs-based thermocouples exhibit large values of TEP due to the Schottky barriers at semiconducting CNTs-metal junctions. The highest TEP of 40.7 μV/K has been achieved for the thermocouple CNTs/Cr–Al. This value is enhanced of about 2 times compared to single-walled CNTs bundles reported in literature (Collins et al. Science 287:1801–1804, 2000), and comparable to isolated suspended single-walled carbon nanotubes with Pt-electrodes reported in literature (Yu et al. Nano Lett 5(9):1842–1846, 2005) as well. The CNTs-thermocouples exhibit linear relationship for the output voltage versus temperature in the range from 20 to 70°C by providing an interesting nanomaterial for energy applications and temperature and/or radiation microsensors.

10.1 Introduction

Carbon nanotubes (CNTs) have been largely studied in the form of networked films for highly-sensitive gas detection applications [1–6]. Due to very high surface-to-volume ratio, hollow nanostructure, high electron mobility, great surface

M. Penza (✉) · R. Rossi · M. Alvisi · D. Valerini · E. Serra
Brindisi Technical Unit for Technologies of Materials, ENEA, PO Box 51,
Postal Office Br4 72100 Brindisi, Italy
e-mail: michele.penza@enea.it

E. Martinelli · C. Di Natale · A. D'amico
Department of Electronic Engineering, University of Rome "Tor Vergata",
Via di Tor Vergata 110, 00133 Rome, Italy

G. Neri et al. (eds.), *Sensors and Microsystems*,
Lecture Notes in Electrical Engineering 91, DOI: 10.1007/978-94-007-1324-6_10,

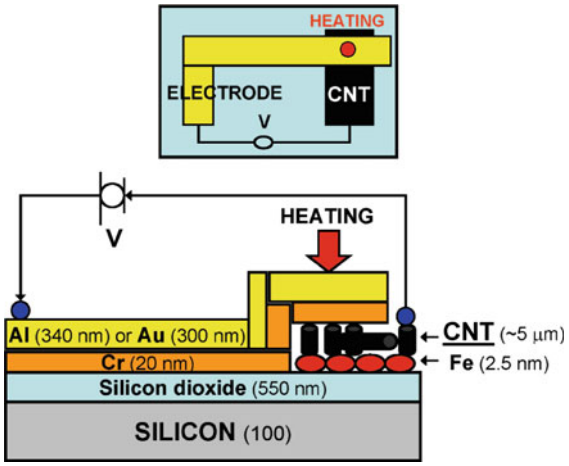

Fig. 10.1 Scheme of the fabricated thermoelectric device

reactivities and high capability of gas adsorption, CNTs have been investigated as building blocks for fabricating novel devices at nanoscale such as high-performance gas sensors and nano-platforms for biosensing.

The thermoelectric properties of the CNTs have been also investigated [7–12]. Thermoelectric experiments have been reported such as the modulation of the thermoelectric power (TEP) in the CNTs bundles by O_2 gas adsorption in vacuum cycles [7]. The thermoelectric transport in the CNTs bundles has been demonstrated to be modulated by doping with gas molecules adsorbed [11]. Doping of the multi-walled CNTs during their growth provides an increase in the Seebeck coefficient [10]. Moreover, at the temperature of 300 K, the observed TEP in the individual single-walled suspended CNT was measured as 42 μ/K, which is one order of magnitude higher than graphite or a typical metal [9].

Low-dimensional thermoelectric materials perform better than bulk materials due to the confinement to low dimensions with sizes comparable to the transport wavelength by producing sharp edges and peaks in the electronic density of states. The enhancement of the density of states near the Fermi energy caused by the reduction of dimensions leads to the enhancement of the Seebeck coefficient [10].

Here, we report on the preliminary experiments devoted to explore the thermoelectric properties of the thermocouples made by Cr–Au/CNT and Cr–Al/CNT thin film structures.

10.2 Experimental Details

The scheme of the fabricated device is shown in Fig. 10.1. CNTs films were grown by RF-PECVD technology onto SiO_2/Si substrates (1.5 × 1.5 cm). Fe (2.5 nm thick) catalyst was sputtered onto silicon substrates at a working pressure of

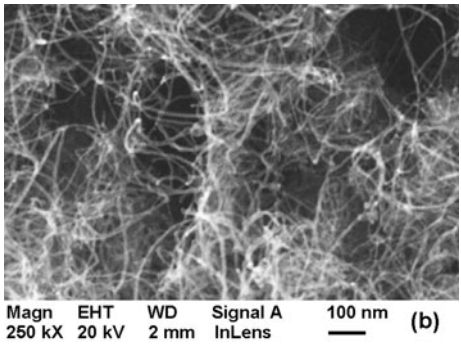

Fig. 10.2 FE-SEM image of the RF-PECVD Fe-grown CNTs layers

1.2×10^{-1} mbar, at room temperature and a supplied RF power of 150 W. Then, the Fe-coated substrates were placed in the RF-PECVD processing chamber to grow CNTs. The chamber was evacuated up to 1×10^{-2} Torr, then the substrates were heated at 600°C upon H_2 flow (100 sccm) at a pressure of 1.5 Torr. A RF discharge at 100 W for 5 min was supplied at the heated substrates (600°C) to promote the Fe clustering for CNTs growth. Finally, a carbon gaseous precursor of acetylene (C_2H_2) with a flow rate of 20 sccm was added to H_2 gas-plasma with a flow rate of 80 sccm. The working pressure was fixed at 1.5 Torr and RF power at 100 W with a deposition time of the CNTs layers for 20 min. After CNTs growth, the samples were equipped by vacuum thermally evaporated Cr–Au (20 nm/300 nm) or Cr–Al (20 nm/340 nm) contacts to serve for the electrical measurements.

The morphology and structure of the fabricated CNTs networks has been characterized by scanning electron microscopy (SEM), as shown in Fig. 10.2. A dense network of bundles of multiple tubes consisting of multi-walled carbon nanostructures appears with a maximum length up to 10 μm and single-tube diameter in the range of 5–35 nm.

The fabricated CNTs-based thermocouples have been located in an experimental setup for the thermoelectric measurements. The scheme of the experimental setup has been reported in Fig. 10.3. A thermo-controlled water-bath was used to generate a temperature gradient. The water was heated by a commercial heater by Joule-effect. The water temperature was measured by a commercial Pt100 thermocouple. The temperature range was from 18 to 70°C. The CNTs-based thermocouple to be characterized was held in air as cold junction ($T_{hot} = T_{cold}$) and immersed in water for the measurement as hot junction ($T_{hot} > T_{cold}$). Measurement time (~ 3 s) was as shorter as possible to maintain constant the cold junction temperature. The output voltage of the CNTs-based thermocouple under test was measured by a multimeter (Agilent, 34401A).

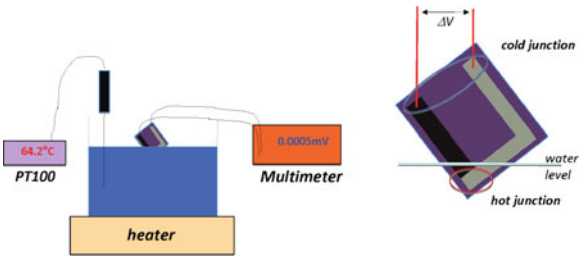

Fig. 10.3 Scheme of the experimental setup for measuring the CNTs-based thermocouples

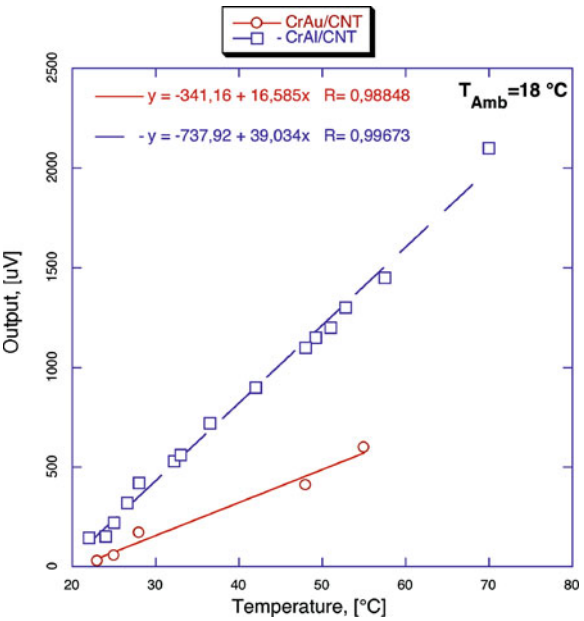

Fig. 10.4 Thermoelectric voltage value versus temperature for two types of thin film thermocouples

10.3 Results and Discussion

Two kinds of devices namely Cr–Au/CNT and Cr–Al/CNT thin film structures have been characterized as thermocouples that could be used as both temperature and radiation sensors. To this purpose this work aims at estimating, in a controlled experimental condition, their thermoelectric power. The hot junction was, for each measurement and for a short time (about 3 s), immersed into water whose temperature was controlled by a reference thermocouple and the other junction was left in air (about 18°C). This procedure was adopted in order to avoid the thermal diffusion effect from the hot to the cold junction that could have a negative effect on the measurement accuracy.

Figure 10.4 shows preliminary data relative to the two thermocouples thermal behaviours. A linear temperature-dependent thermoelectric power has been observed on CNTs-networks for both structures Cr–Al/CNT and Cr–Au/CNT in the measured range of temperature from 20 to 70°C. A voltage output for the Cr–Al/CNT thermocouple has been measured in the range from 50 to 2,200 μV with a related increasing temperature gradient. The two thermoelectric powers, expressed as slope of the voltage-versus-temperature relationships, are estimated to be as high as about 39 and 16.6 μV/°C respectively for Cr–Al/CNT and Cr–Au/CNT structures. The resistance of the two thermocouples are in the range of about 500 Ω, which does represent a negligible noise source.

The studied thermocouple is formed by three materials: CNT, Cr, Al or Au. According to the *homogeneous conductors* law, the active junction is based on top-layer of Al or Au and down-layer of CNT. Generally, the thermocouple voltage is given by the relationship:

$$V = \int_{T_1}^{T_2} (S_A - S_B)\, dT$$

where S_A and S_B are the Absolute Thermoelectric Power (ATP) of the thermoelements; ATP is temperature-dependent. In our case of maximum measured TEP for Al/CNT structure, the ATP of the Al, S_{Al}, has been reported in literature by Huebener et al. [13] as indicated as follows:

$$S_{\mathrm{Al}} = (-1.41 - 0.001 \cdot T)\, \frac{\mu\mathrm{V}}{\mathrm{K}}$$

By using this value of S_{Al}, the ATP of the CNT, S_{CNT}, has been calculated as follows as:

$$S_{\mathrm{CNT}} = (145.7 - 0.35 \cdot T)\, \frac{\mu\mathrm{V}}{\mathrm{K}}$$

At $T = 300$ K, $S_{\mathrm{CNT}} = 145.7 - 0.35.300 = 40.7$ μV/K.

Figure 10.5 shows temperature-dependent thermoelectric power calculated from data of Fig. 10.4 on CNTs-networks for Cr–Al/CNT structure in the measured range of temperature from 298 to 335 K. Table 10.1 reports the comparison of the TEP of the fabricated CNTs-based thermocouple with other thermocouples reported in literature. A high TEP of 40.7 μV/K has been achieved for the thermocouple CNTs/Cr–Al. This value is enhanced of about 2 times compared to single-walled CNTs bundles [7] and multi-walled CNTs bundles [10], and comparable to isolated suspended single-walled carbon nanotubes with Pt-electrodes [9] as well.

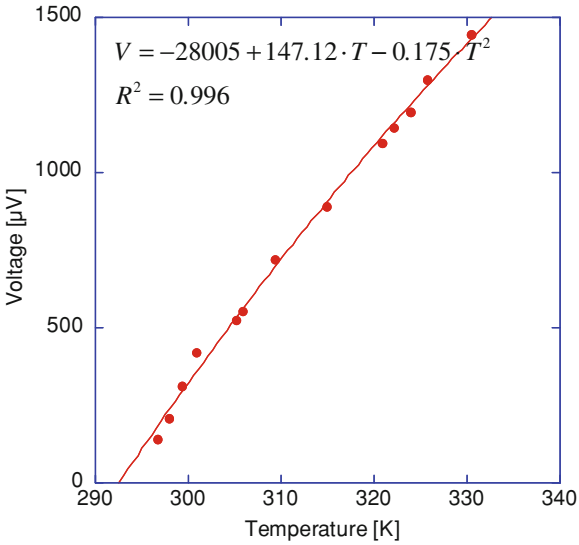

Fig. 10.5 Thermoelectric voltage versus temperature for Cr–Al/CNT thin film thermocouple

Table 10.1 Comparison of the thermoelectric power (TEP) for the CNT-based thermocouples

Thermocouple type	TEP (μV/K) at T (K)	Reference
SWCNTs bundles	24 μV/K (at 350 K)	Ref. [7]
Isolated suspended SWCNTs with Pt-electrodes	42 μV/K (at 300 K)	Ref. [9]
Doped MWCNTs bundles with metal contacts	22 μV/K (at 300 K)	Ref. [10]
CNTs bundles with Cr–Al electrodes	40.7 μV/K (at 300 K)	This work

10.4 Conclusions

The CNTs-based thermocouples are very promising sensors for measuring temperature and future applications (e.g., radiation). RF-PECVD technology has been used to grow networked layers of multi-walled CNTs. Metal contacts (Cr–Al, Cr–Au) have been used to fabricate the junction in the CNTs-based thermoelectric cells. High thermoelectric power of 39 and 16.6 μV/°C has been measured for Cr–Al/CNT and Cr–Au/CNT thermocouples, respectively. In particular, the high value of 40.7 μV/K measured for the fabricated Cr–Al/CNTs thermocouple is comparable to the suspended individual single-walled CNT with Pt-electrodes. Finally, CNTs-based thermocouples are very interesting for advanced nanosensors and energy harvesting applications.

References

1. Kong J, Franklin NR, Zhou C, Chapline MG, Peng S, Cho K, Dai H (2000) Nanotube molecular wires as chemical sensors. Science 287:622–625
2. Someya T, Small J, Kim P, Nuckolls C, Yardley JT (2003) Alcohol vapor sensors based on single-walled carbon nanotube field effect transistors. Nano Lett 3(7):877–881

3. Penza M, Cassano G, Rossi R, Alvisi M, Rizzo A, Signore MA, Dikonimos Th, Serra E, Giorgi R (2007) Enhancement of sensitivity in gas chemiresistors based on carbon nanotube surface functionalized with noble metal (Au, Pt) nanoclusters. Appl Phys Lett 90:173123
4. Penza M, Rossi R, Alvisi M, Cassano G, Serra E (2009) Functional characterization of carbon nanotube networked films functionalized with tuned loading of Au nanoclusters for gas sensing applications. Sens Actuators B 140:176–184
5. Penza M, Rossi R, Alvisi M, Cassano G, Signore MA, Serra E, Giorgi R (2008) Pt- and Pd-nanoclusters functionalized carbon nanotubes networked films for sub-ppm gas sensors. Sens Actuators B 135:289–297
6. Penza M, Rossi R, Alvisi M, Valerini D, Serra E, Paolesse R, Martinelli E, D'Amico A, Di Natale C (2009) Metalloporphyrins-functionalized carbon nanotube networked films for room-temperature VOCs sensing applications. Procedia Chem 1:975–978
7. Collins PG, Bradley K, Ishigami M, Zettl A (2000) Extreme oxygen sensitivity of electronic properties of carbon nanotubes. Science 287:1801–1804
8. Small JP, Perez KM, Kim Philip (2003) Modulation of thermoelectric power of individual carbon nanotubes. Phys Rev Lett 91(25):256801
9. Yu C, Shi L, Li ZYD, Majumdar A (2005) Thermal conductance and thermopower of an individual single-wall carbon nanotube. Nano Lett 5(9):1842–1846
10. Kunadian I, Andrews R, Pinar Menguc M, Qian D (2009) Thermoelectric power generation using doped MWCNTs. Carbon 47:589–601
11. Adu CKW, Sumanasekera GU, Pradhan BK, Romero HE, Eklund PC (2001) Carbon nanotubes: a thermoelectric nano-nose. Chem Phys Lett 337:31–35
12. Bradley K, Jhi S-H, Collins PG, Hone J, Cohen ML, Louie SG, Zettl A (2000) Is the intrinsic thermoelectric power of carbon nanotubes positive? Phys Rev Lett 85(20):4361–4364
13. Huebener RP (1968) Thermoelectric power of aluminum and dilute aluminum alloys. Phys Rev 171(3):634–641

Chapter 11
Bis-Pyrazole Based Thin Films for Optical Gas Detection

R. Touzani, S. El Kadiri, A. Zerrouki, S. Scorrano, G. Vasapollo, M. G. Manera and R. Rella

Abstract We propose a novel optical gas recognition thin film layer of 4-[*bis*[(3,5-dimethyl-1H-pyrazol-1-yl)methyl]-amino]phenol on quartz substrates. The gas optical response to the following analytes have been investigated as air pollutants (SO_2, NO_2, CO, CH_4 and NH_3). The spin-coated pyrazole layer appears to have reversible sensitivity towards SO_2 and very low and irreversible sensitivity for NO_2.

11.1 Introduction

To meet the demand of gas detection devices, considerable research into new sensors is underway. Recently, there is an increasing technological interest in the synthesis of organic nanomaterials in the perspective of fabrication of devices showing specific molecular properties. Several organic materials are exploited as new materials to enhance the performance of traditional devices. Different examples can be found in the literature about the use of pyrazole-based thin films for the realization of specific devices: for instance they have been applied in

R. Touzani · S. El Kadiri · A. Zerrouki
Department de Chimie, Université Mohamed Premier, BP 524, 60000 Oujda, Morocco

S. Scorrano · G. Vasapollo
Dipartimento di Ingegneria dell'Innovazione, Università del Salento, Via per Arnesano, 73100 Lecce, Italy

M. G. Manera · R. Rella (✉)
Istituto per la Microelettronica e Microsistemi del CNR – IMM Lecce, Via Monteroni, 73100 Lecce, Italy
e-mail: roberto.rella@le.imm.cnr.it

G. Neri et al. (eds.), *Sensors and Microsystems*,
Lecture Notes in Electrical Engineering 91, DOI: 10.1007/978-94-007-1324-6_11,

Fig. 11.1

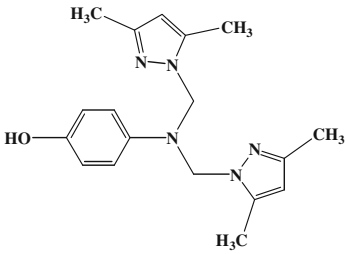

OLEDs as hole transporting materials due to their good hole-transporting and film-forming abilities [1]. Pyrazole-based ligands have been also used in the preparation of new ion selective membrane sensors for transition metal ions and various anions [2] in ion-selective membrane sensors. A field still unexplored for this kind of molecules is gas sensing for environment monitoring. In this work, a first attempts to use pyrazole-based material as sensing layers in chemical gas sensors is reported. An optical detection method, based on the change of optical UV–Vis absorption curves, following to the interaction with the investigated gases, has been experimented.

11.2 Experimental Setup

*11.2.1 Synthesis of 4-[***Bis***[(3,5-dimethyl-1H-pyrazol-1-yl) methyl]amino]phenol*

A mixture of hydroxymethyl-3,5-dimethylpyrazole (Fig. 11.1) (5.84 g, 0.046 mol), primary amine (2.5 g, 0.022 mol) in acetonitrile (20 mL) was put in flask sealed under room temperature and stirring for 24 h. The reaction mixture solid product was filtrated then the residue was recrystallized in chloroform. The solid was obtained with good yields.

11.2.2 Thin Films Deposition

All the sensing layers were prepared in thin film form by spin coating the prepared solution on suitably cleaned quartz substrates.

The thin film was prepared by spinning the solution at 2,000 rpm for 30 s onto the quartz substrates by using chloroform as solvent.

Different thickness of the thin films were obtained by using different concentrations of the starting solution.

Fig. 11.2

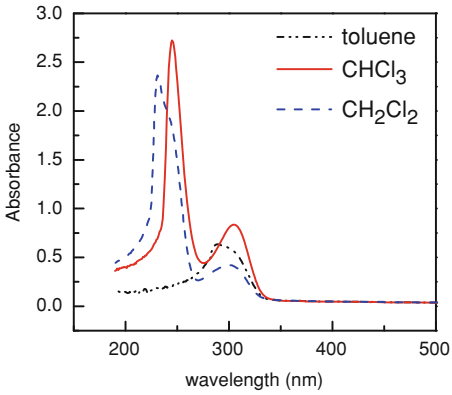

11.2.3 Optical Measurements

A Cary 100 Scan UV–Vis spectrophotometer was used to perform absorption spectra of a solution containing 4-[*bis*[(3,5-dimethyl-1H-pyrazol-1-yl)methyl]-amino]phenol and of spin-coated thin films deposited onto quartz substrates.

All the optical measurements in the UV–Visible spectral range were performed in controlled atmosphere, at room temperature and at normal incidence of the light beam by using a filtered light source from AVANTES tungsten–halogen lamp guided into an optical fiber and the absorption spectra were registered and analyzed using a multichannel commercial spectrophotometer AVANTES mod MC 2000. The optical responses of the thin film versus different gases (i.e. SO_2, NO_2, NH_3, CO and CH_4) were measured by allowing the flow of each gas into the pipeline of the experimental apparatus.

The dynamic response was measured by recording the integral area (A) of the absorption spectrum in the selected wavelength region versus time.

11.3 Results and Discussion

11.3.1 Optical Characterization of Solutions

In Fig. 11.2 UV–Vis spectra of the sample in three different solvents are reported. The UV–Vis solution spectrum of the sample prepared in dichloromethane is characterized by two absorption bands centered at 294 and 297 nm; in chloroform solution as well, two main bands, centered at 254 and 283 nm, are evidenced. It is to note that the UV–Vis spectrum in toluene solution is characterized just by one absorption band at 285 nm. This effect is due to the difference of solvent polarities.

Fig. 11.3

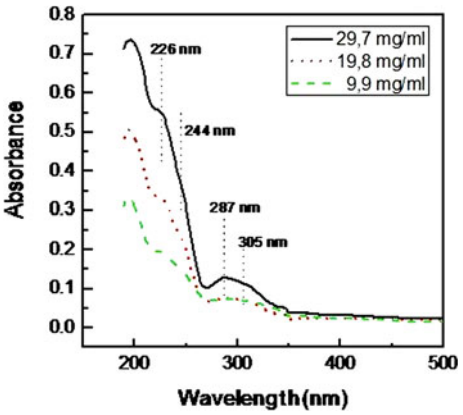

11.3.2 Optical Characterization of Thin Films

The deposited films were optically characterized in the UV–Vis region. The optical absorption of the thin film deposited starting from a chloroform solution with concentrations of 9.9, 19.8 and 29.7 mg/ml respectively, were reported in Fig. 11.3. All the absorption curves are characterized by absorption bands centered at about 244 and 305 nm. The blue shift of the absorption bands at about at 226 and 287 nm can due to the formation of complexes during the formation of thin film by spin coating.

11.3.3 AFM Characterization

Figure 11.4 reports a 20 μm × 20 μm image of the thin film obtained form a starting chloroform solution having a concentration of 29.7 mg/ml. The whole glass substrate coverage is obtained a smooth surface with different aggregates randomly distributed on the surface, which size distribution is inhomogeneous over the whole film surface ranging between 20 nm and few mm. The measured thickness is (26 ± 8) nm.

11.3.4 Optical Sensing Proprieties

The optical measurements in the UV–Visible spectral range were performed in controlled atmosphere, at room temperature and at normal incidence of the light beam. The optical responses of the thin film versus different gases (i.e. SO_2, NO_2,

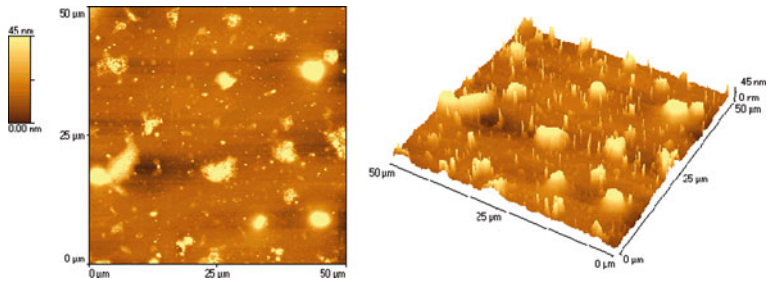

Fig. 11.4

Fig. 11.5

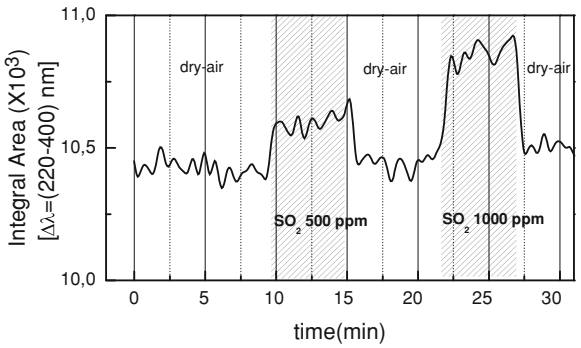

Fig. 11.6

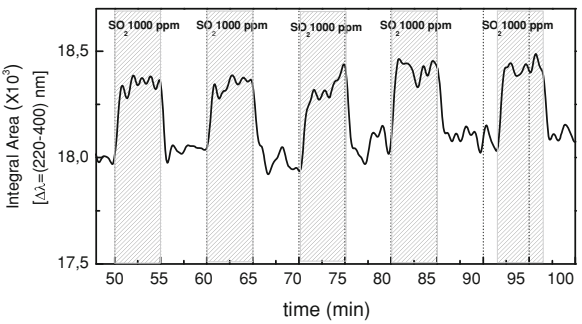

NH_3, CO and CH_4) were measured by allowing the flow of each gas into the pipeline of the experimental apparatus. The dynamic response was measured by recording the integral area (A) of the absorption spectrum in the selected wavelength region versus time.

Figure 11.5 shows the response of the thin film in presence of dry air, and a mixture containing 500 and 1,000 ppm SO_2 in dry air. An interesting but small variation in the sensor signal is observed when the sensing layer is exposed to SO_2 gas.

In Fig. 11.6 it is possible to observe the response of the thin film in presence of dry air and SO_2 at the highest concentration; the restoring at the initial value of the absorbance spectrum confirms the reversibility of the interaction during the cycles of the measurement.

11.4 Conclusions

The investigated pyrazole-based thin film shows an interesting sensitivity signal and selectivity to SO_2 gas with a good reversible response which opens us further innovative issues in gas sensing.

References

1. Wu F, Tian W, Zhang Z et al (2000) Electroluminescent device based on balanced carriers injection and transportation. Thin Solid Films 363:214–217
2. Singh AK, Mehtab S, Singh UP, Aggarwal V (2007) Thiocyanate selective sensor based on tripodal zinc complex for direct determination of thiocyanate in biological samples.Sens Actuators B 125:453–461

Chapter 12
Room Temperature Hydrogen Sensor Based on Pt/TiO_2/MWCNT Composites

L. De Luca, A. Donato, G. Apa, S. Santangelo, G. Faggio, G. Messina, N. Donato, A. Bonavita and G. Neri

Abstract Pt-doped TiO_2/MWCNT composites have been prepared by the sol–gel route and tested in resistive devices for the low temperature monitoring of hydrogen. A morphological and microstructural investigation by SEM, TEM, XRD and micro-Raman spectroscopy of the composites was carried out. Results indicated that, regardless the nominal C/Ti molar ratio, only the anatase phase of titania is formed. Thin films of the Pt-doped composites, deposited on interdigitated ceramic substrates, showed promising hydrogen sensing at low temperatures. On the basis of the results obtained, some hypotheses on the sensing mechanisms operating on these nanostructured hybrid materials have been formulated.

12.1 Introduction

Hydrogen-based systems truly promise a futuristic energy scenario, where hydrogen fuel will be used in fuel cells for civil transportation and in rockets for space vehicles. All these applications necessitate the development of hydrogen sensor devices, which allow its safe and controlled use [1].

L. De Luca · A. Donato · G. Apa · S. Santangelo · G. Faggio · G. Messina
Department of Mechanics and Materials, University "Mediterranea" of Reggio Calabria, Reggio Calabria, Italy

N. Donato (✉)
Department of Matter Physics and Electronic Engineering, University of Messina, Messina, Italy
e-mail: ndonato@unime.it

A. Bonavita · G. Neri
Department of Industrial Chemistry and Materials Engineering, University of Messina, Messina, Italy

G. Neri et al. (eds.), *Sensors and Microsystems*,
Lecture Notes in Electrical Engineering 91, DOI: 10.1007/978-94-007-1324-6_12,

Numerous metal oxide thin films work at high temperature in air as effective resistive hydrogen sensors, allowing detection of this gas down to very low concentration. However, many of these devices need ambient oxygen to operate, and moreover they fail to detect hydrogen at high concentrations due to saturation effects.

Then, there is also great interest in detecting high concentrations of hydrogen in reducing or inert atmosphere, by means of devices operating at temperature as low as possible, preferably room temperature. In this paper, preliminary data are reported obtained employing a Pt/TiO_2/MWCNT composite as sensing layer for monitoring high concentrations of hydrogen in inert atmosphere at near room temperature.

12.2 Experimental

Pt/TiO_2/MWCNT composites were prepared as follows. First, TiO_2/MWCNT was synthesized by a sol–gel method starting from a mixture of MWCNTs, previously functionalised by a nitric acid treatment at 110°C for 18 h, dispersed in a solution of titanium isopropoxide in isopropanol. A detailed characterization by XRD, SEM, TEM and micro-Raman spectroscopy was carried out. Sensing tests were carried out in an apparatus, interfaced with a PC, composed by a stainless steel box, where is allocated the sensor, and connected to gas supply (He and H_2) and a power supply that allows fixing and controlling the working temperature (in the range 25–100°C), and measuring the resistance values of the sensor when it is maintained under H_2/He mixtures flow (100 ml/min) by means of a resistance meter. The sensor response is defined as $[(R–R_0)/R_0] \cdot 100$, where R_0 is the resistance recorded under He and R the resistance recorded under H_2/He mixture. Before carrying out the sensing measurements, sensors were pre-treated "in situ" upon different experimental conditions.

12.3 Results and Discussion

12.3.1 Microstructural Investigation

TiO_2/MWCNT composite samples with nominal C/Ti molar ratio ranging from 3.6 to 17.0 were first synthesized. The typical morphology of the resulting composite materials is reported in the SEM and TEM micrographs of Fig. 12.1, showing the titania particles dispersed in the mats of carbon nanotubes.

XRD analysis showed only the presence of the diffraction peaks of crystalline anatase. This agrees with micro-Raman analysis carried out on the same samples. Indeed, regardless the C/Ti molar ratio, four main spectral features are clearly

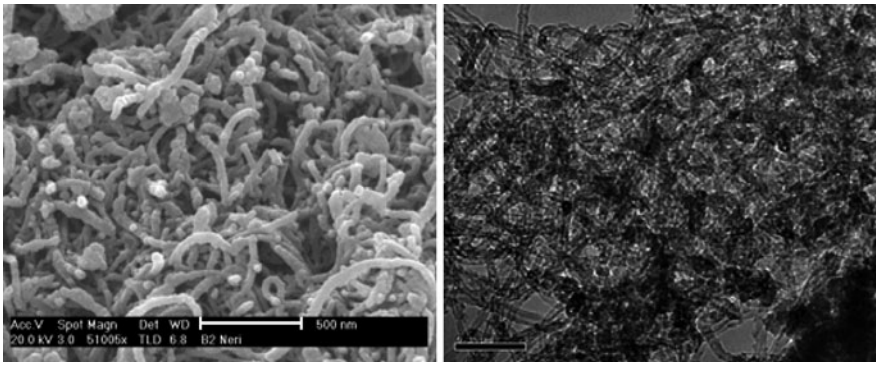

Fig. 12.1 SEM and TEM micrographs showing the morphology of the TiO_2/MWCNT composite materials

visible in the spectra of TiO_2/MWCNTs, centred approximately at 150, 395, 515 and 635 cm^{-1}. The comparison with frequency positions and relative intensities of titania reference-spectra evidences a marked similarity with the spectrum of anatase [2]. Therefore, it is concluded that, even if the presence of smaller amounts of rutile and/or brookite cannot in principle ruled out, anatase is the phase mainly present in the titania nano-clusters of the TiO_2/MWCNT hybrid composites.

Subsequently, 2 wt% of Pt was introduced by the wetness impregnation method, using a solution of platinum acetylacetonate in acetone. The resulting Pt/TiO_2/MWCNT composites were treated at 200°C for 2 h in a mixture of 5% H_2 in argon. Micro-Raman spectra of the ternary composites do not differ from those reported for the corresponding TiO_2/MWCNT composites.

12.3.2 Hydrogen Sensing Tests

Preliminary data have shown that the behaviour of the composite sensors is, as expected, strongly related to Pt presence, working temperature and "in situ" pre-treatment under reducing conditions.

Moreover, the sensor response is strongly affected by the C/Ti ratio; preliminary tests indicated that the best sensing performance is obtained for C/Ti = 3.6.

Figure 12.2 shows the resistance variations registered for the Pt/TiO_2/MWCNT (C/Ti = 3.6) composite-based sensor, after different "in situ" reducing treatments. It can be seen that the reducing treatment has a positive effect on the sensor performance. Specifically, the "in situ" pre-treatment is useful to obtain a better stability of the baseline. Moreover, a decrease of the baseline resistance and an enhancement of the sensor response were registered.

The comparison of the response of the Pt/TiO_2/MWCNT sensor, with that of binary sensors, is reported in Fig. 12.3. It can be clearly seen that hydrogen

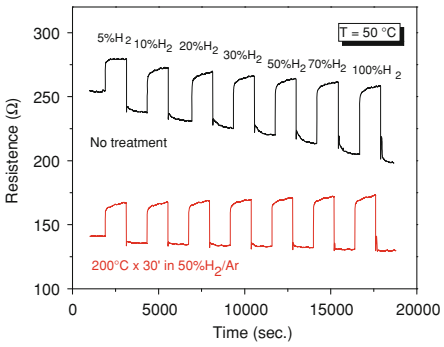

Fig. 12.2 Response to different H_2 concentrations of the Pt/TiO_2/MWCNT sensor (C/Ti = 3.6) after various "in situ" reducing treatments

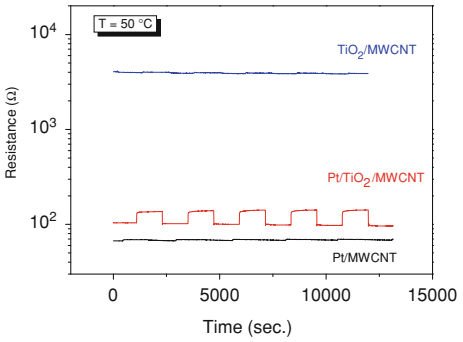

Fig. 12.3 Response to hydrogen of sensors investigated based on different compositions

monitoring takes place only with the Pt/TiO_2/MWCNT ternary sensor, suggesting a synergic action among metal oxide, noble metal and carbon nanotubes.

12.3.3 Hydrogen Sensing Mechanism

A detailed investigation of these materials to better understand the hydrogen sensing mechanism is actually in progress. However, on the basis of the preliminary data so far obtained, some hypotheses can be formulated. Starting from the observation that the sensor measurements were conducted in inert atmosphere without oxygen, the usual mechanism involving the removal of chemisorbed oxygen by hydrogen cannot be invoked. It is likely that the hydrogen molecules get adsorbed at the defects on the titania surface. Then, the sensor response can be attributed to a "spill-over" mechanism, in which chemisorbed hydrogen molecules, are dissociated by platinum, and finally spill out of the Pt, diffusing into the TiO_2 surface layer. This agrees with the fact that both platinum and TiO_2 are necessary to obtain the sensor response. MWCNTs act providing a preferential pathway to the current flow and a larger specific surface area for the adsorption of

hydrogen molecules. According to current view, once the active hydrogen atom is chemically adsorbed at the interstitial positions in the oxide lattice structure, partial electron charge transfer occurs to the *n*-type TiO_2 and the conductance should increases [3]. Vice versa, we observed that the sensor resistance increases in hydrogen. In literature this has been explained suggesting a *p*-type behavior of the metal oxide [4], or a H → TiO_2/MWCNT charge transfer which reduces the hole concentration in the carbon nanotube structure, increasing the resistivity in the system [5]. In order to get a deeper insight into the sensing mechanism a more systematic investigation was planned, aimed at clarifying the role of MWCNTs-TiO_2 interaction. Further investigations are also planned aiming to optimise the formulation of the sensing layer devoted to the development of a prototypal device.

12.4 Conclusion

Pt-doped TiO_2/MWCNT composites have been synthesized by a sol–gel approach, characterized and tested as sensing layer in resistive devices. Results of characterization studies have revealed that, regardless the nominal C/Ti molar ratio, only the anatase phase of titania is formed. Their sensing behaviour towards near room temperature monitoring of hydrogen was strongly related to C/Ti ratio, working temperature and "in situ" pre-treatment under reducing conditions. The results reported seem to be promising in view of obtaining inexpensive high concentration hydrogen-sensors.

References

1. Aroutiounian VM (2005) Hydrogen detectors. ISJAEE 23:21–31
2. Hu Y, Tsai HL, Huang CL, (2003) Effect of brookite phase on the anatase-rutile transition in titania nanoparticles. J Eur Ceram Soc 23:691–696
3. Varghese OK, Gong D, Paulose M, Ong KG, Grimes CA (2003) Hydrogen sensing using titania nanotubes. Sens Actuators B 93:338–344
4. Hossein-Babaei F, Keshmiri M, Kakavand M, Troczynski T (2005) A resistive gas sensor based on undoped p-type gas sensor. Sens Actuators B 110:28–35
5. Guirado-Lopez RA, Sanchez M, Rincon ME (2007) Interaction of acetone molecules with carbon-nanotube-supported TiO_2 nanoparticles: possible applications as room temperature molecular sensitive coatings. J Phys Chem C 111:57–65

Chapter 13
Gas Influence on Photocurrent Generation in Metal Oxide Nanowires

S. Todros, C. Baratto, E. Comini, G. Faglia, M. Ferroni and G. Sberveglieri

Abstract Quasi-1D nanostructures of metal-oxide semiconductors, in particular ZnO and SnO_2 nanowires, have been extensively investigated for their novel physical properties and are used in many applications such as gas sensors, transparent conducting electrodes, catalysts, solar cells and many other opto-electronic devices. They are *n*-type semiconductor with a wide band gap, showing a broad visible photoluminescence (PL) emission at room-temperature, depending on gas atmosphere. Moreover, when irradiated with UV-visible radiation (at energy higher than or equal to their band gap), metal oxide nanowires show a great increase of conductance and photocurrent (PC) is generated, if a constant potential is applied. PL emission and PC generation are strongly dependent on surface states and can thus be tuned depending on the surrounding atmosphere. In this work, we studied PC generation in SnO_2 nanowires synthesized via evaporation-condensation (EC) process and its dependence on surrounding gas atmosphere, targeting NO_2 sensing application.

13.1 Introduction

ZnO and SnO_2 nanowires are *n*-type semiconductor with a wide band gap, showing a broad visible photoluminescence (PL) emission at room-temperature, depending on gas atmosphere, and can thus be employed as optical gas sensors.

Moreover, when metal oxide nanowires are irradiated by light of energy higher than or equal to their band gap, electron-hole pairs are generated.

S. Todros (✉) · C. Baratto · E. Comini · G. Faglia · M. Ferroni · G. Sberveglieri
Sensor Laboratory, CNR-IDASC & Dipartimento di Chimica e Fisica,
University of Brescia, Via Valotti 9, 25133, Brescia, Italy
e-mail: silvia.todros@ing.unibs.it

G. Neri et al. (eds.), *Sensors and Microsystems*,
Lecture Notes in Electrical Engineering 91, DOI: 10.1007/978-94-007-1324-6_13,

The electron promoted into the conduction band enhances the conductance, giving rise to photoconductivity (PC) phenomenon [1].

PC generation in metal oxide nanowires has been found to be strongly dependent on gas species in the surrounding environment.

13.2 Experimental

13.2.1 Synthesis of Metal Oxide Nanowires

SnO_2 nanowires with highly crystalline structure were prepared by evaporation-condensation technique, in a horizontal tube furnace, starting from the oxide powder, on an alumina substrate in presence of Au catalyst, previously deposited by DC magnetron sputtering. The source material is evaporated and transported by an inert gas carrier towards the substrates, kept at a lower temperature, and it condenses on them. The deposition conditions have been tailored to promote the growth of one-dimensional (1D) nanostructures, by changing the evaporation temperature and the carrier gas composition and flux.

13.2.2 Characterization Via Scanning Electron Microscopy

Scanning Electron Microscopy (SEM) was used to analyse the morphology of the nanowires. SEM analysis was carried out by field-emission LEO 1525 microscope, equipped with In-Lens detector for secondary-electrons imaging. The SEM was operated at 5 kV accelerating voltage to prevent the insulating substrate from electrostatic charging.

13.2.3 Experimental Set-Up for Photocurrent Measurements

An experimental set-up was implemented for PC measurements. The beam produced by an UV-visible lamp (Hamamatsu Lightnincure 200) is focused in a monochromator, remotely controlled in order to scan a range of wavelengths. The out-coming radiation hits the sample, mounted in a closed chamber, with a controlled atmosphere. The photocurrent generation can be also studied under high power incident light, using as excitation source He-Cd laser lines at 325 and 442 nm. PC measurements require the application of electrical contacts and an electric field to measure the photogenerated carriers in the sample under investigation. When a bias voltage and a load resistor are used in series with the semiconductor, a voltage drop across the load resistors can be measured when the

change in electrical conductivity varies the current flowing through the circuit. In preliminary characterization, electric signals can be monitored in continuous mode, through an electrometer (Keithley 6514). However, the PC signal can be very small: to resolve the weak photoconductivity signal, the incident light on the sample is then modulated using a chopper and the induced AC signal is acquired through a lock-in phase sensitive amplifier (Stanford Research Systems SR850 PSD).

13.3 Results and Discussion

13.3.1 SEM Images of SnO_2 Nanowires

As shown in Fig. 13.1, SnO_2 nanowires, grown by evaporation-condensation method, are homogeneously deposited over large area substrates; their lateral dimensions depend on the deposition parameters and their length depends on deposition time. The length of the wires is up to several microns while the width is in the nanometer range. The high crystalline degree of the nanowires has been proved by Transmission Electron Microscopy [2].

13.3.2 SnO_2 Photocurrent Generation in Dry Air

SnO_2 nanowires were tested in order to evaluate their response to different excitation conditions (wavelength, incident light power, time of excitation/de-excitation).

When SnO_2 nanowires are illuminated with light of energy above their energy gap, a great increase of conductance takes place, while photo-conductance decreases when irradiation ceases, as can be seen in Fig. 13.2. This measurement is of primary importance to evaluate the time constants of the reactions taking place when rise and decay of photocurrent occur. It allows setting the best parameters, such as chopper frequency and lock-in integration time constants.

13.3.3 SnO_2 Photocurrent Response to NO_2

SnO_2 nanowire samples were tested in different gas atmosphere, under continuous excitation by UV-visible lamp. The signal acquisition was carried out both by an electrometer and by chopper/lock-in amplifier.

The photo-response to NO_2 can be seen in Fig. 13.3. The photo-response to NO_2 is marked by an increase in photo-conducibility. The percentage current

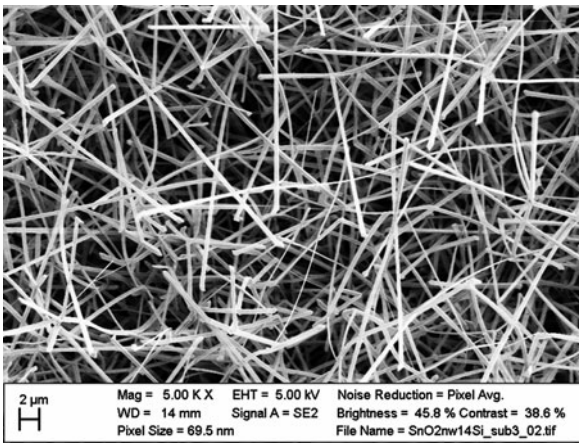

Fig. 13.1 SEM image of SnO_2 nanowires

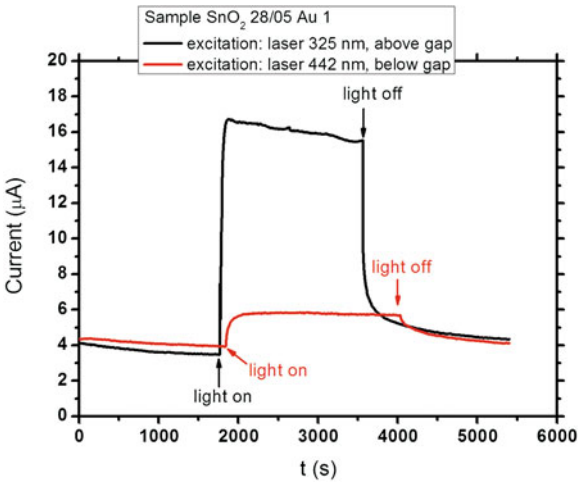

Fig. 13.2 Photoresponse of SnO_2 nanowires under continuous illumination with 325 and 442 nm laser beam, in dry air at RT, at a bias voltage of 0.5 V

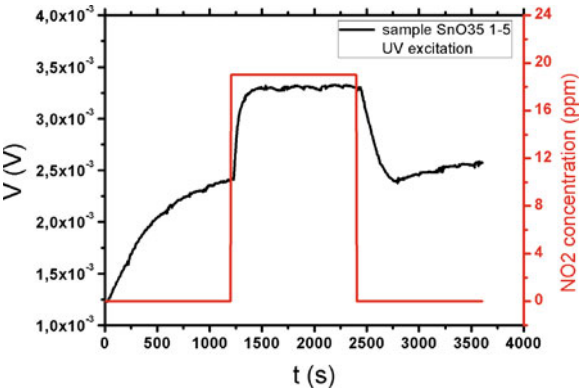

Fig. 13.3 Photocurrent measurement on SnO_2 nanowires in NO_2 (19 ppm)

variation is generally higher when measured via lock-in amplifier, due to its ability to get rid of dark currents and spurious signals and to achieve a more precise measurement. The surface processes taking place are probably slower and are normally hindered by the much faster low frequency (DC) response. Given that the lock in signal is almost unaffected in the frequency range 10–200 Hz, the observed processes time constants are shorter than 0.5 ms.

13.4 Conclusions

PC measurements, via a lock-in amplifier, have the potential to develop new gas sensors with improved sensitivity. Indeed, further measurements are scheduled in order to fully understand the origin of the photocurrent generation processes and its dependence on surrounding gas atmosphere.

Acknowledgments This work was supported, within the EU FP6, by the ERANET project "NanoSci-ERA: NanoScience in the European Research Area".

References

1. Keem K, Kim H, Kim GT, Lee JS, Min B, Cho K, Sung MY, Kim S (2004) Photocurrent in ZnO nanowires grown from Au electrodes. Appl Phys Lett 84:4376
2. Comini E, Baratto C, Faglia G, Ferroni M, Sberveglieri G (2007) Single crystal ZnO nanowires as optical and conductometric chemical sensor. J Phys D: Appl Phys 40:7255–7259

Chapter 14
Transition Metal Complexes as Ammonia Responsive Materials for SAW Chemical Sensors

S. Lo Schiavo, P. Cardiano, N. Donato, M. Latino and G. Neri

Abstract In the present paper we describe the development of a surface acoustic wave (SAW) ammonia sensor which utilizes the $Rh_2(form)_4$ complex as responding material. It has observed that the SAW resonance frequency shifted reversibly upwards upon NH_3 exposures at room temperature. Moreover, the greater affinity of the $Rh_2(form)_4$ film coating for the N-Lewis bases guaranteed a selective binding capability towards NH_3 in the presence of water vapour, allowing to monitor the concentration of ammonia gas in the head-space of aqueous solutions.

14.1 Introduction

Ammonia is the major basic gas in a variety of important sample matrixes, for example, the ambient atmosphere, indoor air, human breath and in liquid phase solutions. Although many analytical instruments are available for monitoring

S. Lo Schiavo · P. Cardiano
Department of Inorganic Chemistry, Analytical Chemistry and Physical Chemistry, University of Messina, Messina, Italy

N. Donato (✉)
Department of Matter Physics and Electronics Engineering, University of Messina, Messina, Italy
e-mail: ndonato@unime.it

M. Latino
Department of Chemical Science and Technologies, University of Rome Tor Vergata, Rome, Italy

G. Neri
Department of Industrial Chemistry and Materials Engineering, University of Messina, Messina, Italy

G. Neri et al. (eds.), *Sensors and Microsystems*,
Lecture Notes in Electrical Engineering 91, DOI: 10.1007/978-94-007-1324-6_14,

ammonia at sub-ppm level, the development of ammonia solid state chemical sensors still represents a challenge for the scientific world. For example, resistive sensors based on metal oxide semiconducting layers, which exhibit the characteristics required to an analytical system for a large diffusion (miniaturizing, easy handling, real time response, low costs), lack of selectivity and sensibility at ambient conditions. Hence, a significant improvement, in this context, may derive from finding out novel materials sensitive at room temperature, whose sensors response is based on different mechanism with respect to traditional ones.

Transitions metal complexes (TMCs), exhibiting any physico-chemical change (conductivity, optical, etc.) as a consequence of site specific interactions with gaseous species, at molecular level, are now recognized as a promising source of sensor materials. TMCs are well known for their binding capability towards small molecules (CO, NO_x, etc.) and a variety of ligands. Such a property, if properly modulated by an appropriate choice of the metal and the surrounding ligands, leads to responsive materials with the required characteristics of binding reversibility, sensibility and selectivity.

Recently, we focused our attention on the responsive properties of dirhodium (II,II) complexes having the general formula Rh_2(X–C–Y)n where X–C–Y is a bridging ligand [1, 2]. In the present paper we report on a surface acoustic wave (SAW) ammonia sensor based on the Rh_2(form)4 complex as a novel ammonia responding material.

14.2 Experimental

The synthesis of [$Rh_2(form)_4$] has been carried out as previously reported [3]. A mixture of [$Rh_2(form)_2(CF3COO)_2(H_2O)_2$] and N,N-di-p-tolylformamidine was heated at 135°C for 30 min. The green molten mixture obtained was cooled to room temperature and washed repeatedly with diethyl-ether to remove the unreacted formamidine. Crystallization of the remaining greenish solid from benzene-heptane gave analytically pure material as green plates (83% yield).

Commercially available SAW two-port resonators, covered by a thin Rh2(form)4 overlayer deposited by drop-coating from a chloroform solution and operating at a nominal resonance frequency of 235 MHz have been here used as passive acoustic elements. The frequency response of the SAW device to NH_3 vapour in the headspace of ammonia solution of different concentrations has been measured by a vector network analyser (VNA).

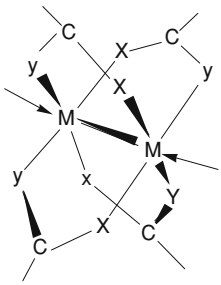

M = Rh
arrows = axial binding sites
Y-C-X = bridging equatorial ligand: formamidinate

Fig. 14.1 Dirhodium (II,II) complex, $Rh_2(form)_4$, with lantern structure

14.3 Results and Discussion

14.3.1 Dirhodium (II,II) Complex Properties

Di-metallic complexes, featured by the classic lantern structure as shown in Fig. 14.1, are a class of transition metal complexes which have shown to have a large potential as sensing materials.

These species, exhibit a peculiar axial reactivity and are capable to coordinate (reversibly or not) at the axial sites (see arrows in Fig. 14.1) a variety of small molecules (CO, NO_x, etc.) as well as O- and N-Lewis bases with formation of labile axial adducts, which makes them ideal candidates as gas-responding materials. On the other hand, their equatorial activity allows, by established synthetic procedures, to modulate the electron density (hence, the axial activity) at the dimetal centre by simply varying the nature of the bridging ligands.

In this regard, recently, a mixed acetate/formamidinate dirhodium complex properly functionalized, was utilized for the realization of a selective CO optical sensor [1]. Otherwise, the peculiar electrical properties of dirhodium square molecular (box) assemblies have been exploited for the fabrication of CO-chemoresistive sensor [2]. Azotate ligands usually bind to dirhodium(II,II) centre strongly than CO, affording stable bis axial adducts, at ambient conditions. It is well established that the presence in the lantern structure of formamidinates, better electron-donor ligands than carboxylates, modifies significantly the axial activity at the dimetal centre. As a consequence, not only more labile azotate-dirhodium links may be obtained, but also reversible linking processes may be favoured.

14.3.2 $[Rh_2(form)_4]$ SAW Sensor

To exploit the ammonia coordination characteristics of $[Rh_2(form)_4]$ in the development of NH_3 vapour sensors, the surface acoustic wave platform was here

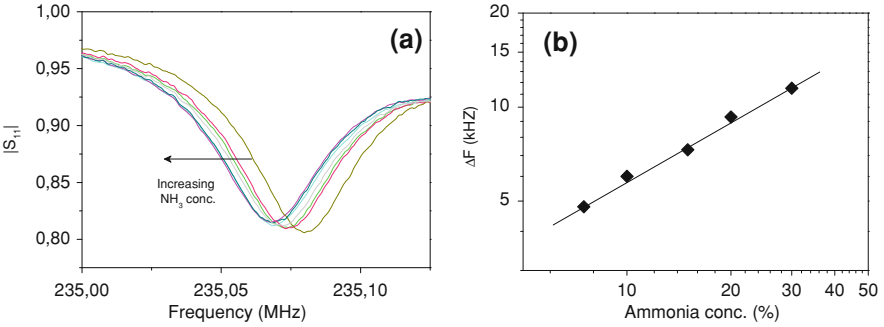

Fig. 14.2 **a** Resonance frequency shift of the SAW resonator in different ammonia ambient; **b** Calibration curve of the SAW resonator

considered. Through the vector network analyzer, the parameters of the acoustic wave sensor (resonance frequency, phase velocity, attenuation) have been acquired during exposure of the device to different ammonia concentrations. Data regarding the S_{11} module are shown in Fig. 14.2a.

The investigations have shown that the SAW resonance frequency shift upwards upon NH_3 exposures. The decrease in resonant frequency of the sensor is caused by the perturbations in propagation velocity due to mass loading of gas molecules adsorbed onto the sensing material surface.

Moreover, the frequency shift is proportional to the concentration of ammonia in the aqueous solution (Fig. 14.2b). The SAW resonance frequency is only slightly influenced by water vapour, indicating a high selectivity of the sensor towards ammonia vapours coming from aqueous solutions. This behaviour arises from the stronger affinity of the $Rh_2(form)_4$ film towards N-Lewis bases, compared to O-Lewis bases such as water.

14.4 Conclusion

In summary, a room temperature ammonia SAW sensor based on a $Rh_2(form)_4$ has been developed. The sensor showed low affinity for water vapour, resulting very selective towards ammonia, and thus avoiding the problem of cross sensitivity in the monitoring of ammonia gas in the head-space of aqueous solutions. Further experiments are planned to optimize the sensor performance for monitoring lower ammonia concentrations.

Acknowledgments The work was funded by the University of Messina under the framework of the project “PRA Interdisciplinare 2007”.

References

1. Gulino A, Gupta T, Altman M, Lo Schiavo S, Mineo PG, Fragala'IL, Evmenenko G, Dutta P, van der Boom ME (2008) Selective monitoring of parts per million levels of CO by covalently immobilized metal complexes on glass. Chem Comm 2900–2902
2. Lo Schiavo S, Piraino P, Bonavita A, Micali G, Rizzo G, Neri G (2008) A dirhodium(II,II) molecular species as a candidate material for resistive carbon monoxide gas sensors. Sens Actuators B 129:772–778
3. Piraino P, Bruno G, Tresoldi G, Lo Schiavo S, Zanello P (1987) New adducts of dirhodium(II) formamidinate complexes with polycyano acceptor molecules. X-ray crystal structure of the tricyanomethanide complex $Rh_2(form)_4[C(CN)_3]$ (form = N,N′-Di-p-tolylformamidinate). Inorg Chem 26:91–96

Chapter 15
Gas Microsensors with Metalloporphyrin-Functionalized Carbon Nanotube Networked Layers

M. Penza, R. Rossi, M. Alvisi, D. Valerini, G. Cassano, E. Serra, R. Paolesse, E. Martinelli, C. Di Natale and A. D'Amico

Abstract Networked carbon nanotubes (CNTs) films have been grown by chemical vapor deposition (CVD) technology onto miniaturized Co-coated alumina substrates for NO_2 and NH_3 gas sensing applications, at a sensor temperature of 150°C. The sidewalls of the CNTs films have been modified by spray-coating with two different metalloporphyrins (MPPs) consisting of a TetraPhenylPorphyrin coordinated by a central metal of zinc (Zn-TPP) and manganese (Mn-TPP) for enhanced sensitivity and tailored specificity. It was demonstrated that the gas sensitivity of the MPPs-modified CNTs-sensors significantly improved by a factor up to four-times through a catalytic effect of the MPPs. The gas sensing properties of CNTs-sensors, including MPPs-modified CNTs, are characterized by a change of the electrical conductivity in a model of charge transfer with a semiconducting *p-type* character. A response of the CNTs-sensor functionalized with 2 spray-layers of Mn-TPP has been measured as 0.43% to 0.5 ppm NO_2, and as 0.09% to 10 ppm NH_3, at 150°C. The MPPs-functionalized CNTs-sensors exhibit high sensitivity, fast response, reversibility, good repeatability, sub-ppm range detection limit.

M. Penza (✉) · R. Rossi · M. Alvisi · D. Valerini · G. Cassano · E. Serra
ENEA, Brindisi Technical Unit for Technologies of Materials,
PO Box 51, Postal Office Br4, 72100 Brindisi, Italy
e-mail: michele.penza@enea.it

R. Paolesse
Department of Electronic Engineering, University of Rome "Tor Vergata",
Via della Ricerca Scientifica, 00133 Rome, Italy

E. Martinelli · C. Di Natale · A. D'Amico
Department of Electronic Engineering, University of Rome "Tor Vergata",
Via di Tor Vergata 110, 00133 Rome, Italy

G. Neri et al. (eds.), *Sensors and Microsystems*,
Lecture Notes in Electrical Engineering 91, DOI: 10.1007/978-94-007-1324-6_15,

15.1 Introduction

Gas sensors based on carbon nanotubes (CNTs) have been largely studied in the form of networked films for highly-sensitive gas detection applications [1–3]. Due to very high surface-to-volume ratio, hollow nanostructure, high electron mobility, great surface reactivities and high capability of gas adsorption, CNTs have been investigated as building blocks for fabricating novel devices at nanoscale such as high-performance gas sensors and nano-platforms for biosensing.

Networked films of carbon nanotubes (CNTs) have been grown by CVD technology onto low-cost miniaturized alumina substrates. The sidewalls of the CNTs films have been modified by spray-coating with two different metalloporphyrins (MPPs) consisting of a TetraPhenylPorphyrin coordinated by a central metal of zinc (Zn-TPP) and manganese (Mn-TPP) for enhanced sensitivity and tailored specificity. Hazardous gases such as NO_2 and NH_3 have been detected with various responsiveness in the range of concentration from 0.1 to 1,000 ppm. The response of the chemiresistors in terms of p-type electrical conductance has been investigated as a function of the thickness of the functionalizing MPPs, at the sensor temperature of 150°C.

Carbon nanotubes (CNTs) are 1D-nanometre hollow structures rolled as single-walled or concentric multi-walled cylinders with high capability of gas molecules adsorption for enhanced gas sensitivity even at low sensor temperature. Various gas sensor nanomaterials include semiconducting metal oxides, conducting polymers, metal nanostructures and nanocomposites with nanofillers. However, it has been demonstrated that single-walled CNTs are functional nanostructures for detecting very low gas concentrations of NO_2 and NH_3 under ambient conditions [1]. Various principles of transduction using CNTs have been implemented for chemical sensing including field effect transistors (FET), surface acoustic waves (SAW), quartz crystal microbalance (QCM), optical fibers, electrochemical devices, chemiresistors. Here a two-pole chemiresistor has been integrated.

Surface modifications of the CNTs with different functionalizing materials have been employed to improve gas sensitivity and to tailor specificity. In fact, nanoclusters of noble metals (Au, Pt, Pd, Ag) have been used to enhance gas sensitivity of CNTs networked films, operating at a sensor temperature from room temperature to 200°C [4–7]. Moreover, metalloporphyrins consisting of TetraPhenylPorphyrins (TPP) coordinated by a central metal of zinc and manganese, are functional materials that have been prepared as highly-sensitive receptors for artificial olfaction [8] and volatile organic compounds (VOCs) detection at room temperature [9, 10].

In this study, MPP-modified CNTs networked films have been investigated for sub-ppm gas sensing of NO_2, including NH_3 at ppm-level, working at a temperature of 150°C.

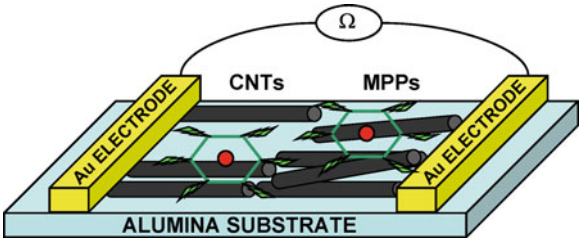

Fig. 15.1 Scheme of the fabricated MPPs-modified CNTs-chemiresistor device

15.2 Experimental Details

The scheme of the fabricated device is shown in Fig. 15.1. CNTs films were grown by CVD technology onto miniaturized alumina substrates (5 mm width × 5 mm length × 0.6 mm thickness). Co (6 nm thick) catalyst was sputtered onto alumina substrates at a working pressure of 6×10^{-2} mbar, at room temperature and a supplied RF power of 150 Watts. Then, the Co-coated substrates were placed in a quartz boat and inserted at the center of a 1-in. diameter quartz tube reactor housed in a furnace of the CVD processing chamber to grow CNTs. The chamber was evacuated up to 5×10^{-3} Torr, then the substrates were heated at 550°C upon H_2 flow (100 sccm) at a working pressure of 100 Torr. Then, a carbon gaseous precursor of acetylene (C_2H_2) with a flow rate of 20 sccm was added to H_2 gas with a flow rate of 80 sccm. The working pressure was fixed at 100 Torr with a deposition time of the CNTs layers for 30 min. After CNTs growth, the samples were equipped by vacuum thermally evaporated Cr–Au (20/300 nm) contacts to serve for the electrical measurements of the two-pole chemiresistor. The Cr/Au electrode sizes were 1 mm width × 5 mm length. The gap between two electrodes was 3 mm. The CNTs films have been modified with a metalloporphyrins layer: (5,10,15,20-tetraphenylporphyrin)zinc [ZnTPP] and (5,10,15,20-tetraphenylporphyrin)manganese chloride [MnTPPCl] have been synthesized according to literature methods [11, 12]. A layer of two distinct M-TPPs with different thickness corresponding to 1 and 2 spray-layers was deposited by spray-coating onto the surface of the CNTs networks previously grown. The M-TPPs were dispersed in solvent of chloroform for spray-coating. Metalloporphyrins were not modified to be covalently anchored onto the surface of the nanotubes, nonetheless even non-covalent interactions between metalloporphyrins and carbon nanotubes are strong enough to ensure the adhesion of the M-TPPs film.

The electrical resistance, at room temperature and upon inert atmosphere, of the un-modified, 1 spray-layer and 2 spray-layers ZnTPP, 1 spray-layer and 2 spray-layers MnTPPCl functionalized CNTs-sensors was measured as 4.51, 4.68 and 7.20, 4.65 and 6.69 kΩ, respectively. The presence of a given MPPs layer at increasing thickness onto the surface of the CNTs film increases the electrical resistance in the chemiresistor proportionally to the thickness of the deposited MPPs. The sheet resistance of the CNTs films was estimated in the range of 1–2 kΩ/square.

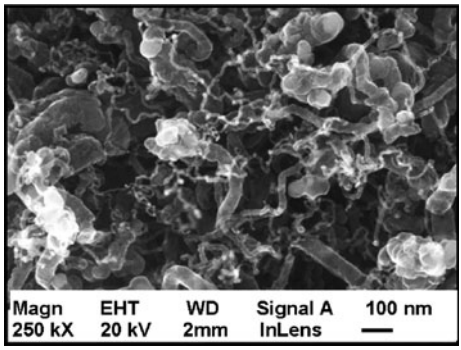

Fig. 15.2 FE-SEM image of the CVD Co-grown CNTs layers

The fabricated CNTs sensors have been located in a test cell (500 ml volume) for gas exposure measurements. The cell case is able to host up to four chemiresistive sensors. Dry air was used as reference gas and diluting gas to air-conditioning the sensors. The gas flow rate was controlled by mass flowmeters. The total flow rate per exposure was kept constant at 1,500 ml/min. The gas sensing experiments have been performed by measuring the electrical conductance of CNTs thin films in the two-pole format upon controlled ambient of individual NH_3 reducing gas and NO_2 oxidizing gas in the range of 10–1,000 ppm, and 0.1–10 ppm, respectively, at sensor temperature of 150°C.

The temperature was measured with a J-type thermocouple by means of a multimeter (Agilent, 34401A). The dc electrical conductance of the CNTs-sensors has been measured by the volt-amperometric technique in the two-pole format by a multimeter (Agilent, 34401A). The sensors were scanned by a switch system (Keithley, 7001) equipped by a low-current scanner card (Keithley, 7158) with a multiplexed read-out.

15.3 Results and Discussion

The morphology and structure of the fabricated CNTs networks has been characterized by scanning electron microscopy (SEM), as shown in Fig. 15.2. A dense network of bundles of multiple tubes consisting of multi-walled carbon nanostructures appears with a maximum length up to 5 μm and single-tube diameter in the range of 5–40 nm. Amorphous carbon, non-nanotube material, metal impurities are present in the grown nanomaterial as well. Figure 15.3 shows the atomic force microscopy (AFM) image of the CNTs layers coated with MPPs. This demonstrates a good local coverage of the carbon nanotubes with the sprayed metalloporphyrins to enhance gas adsorption.

The measured electrical conductance of the functionalized CNTs upon exposure of a given oxidizing (NO_2) or reducing (NH_3) gas is modulated by a charge transfer model with *p-type* semiconducting characteristics. Figure 15.4 shows the

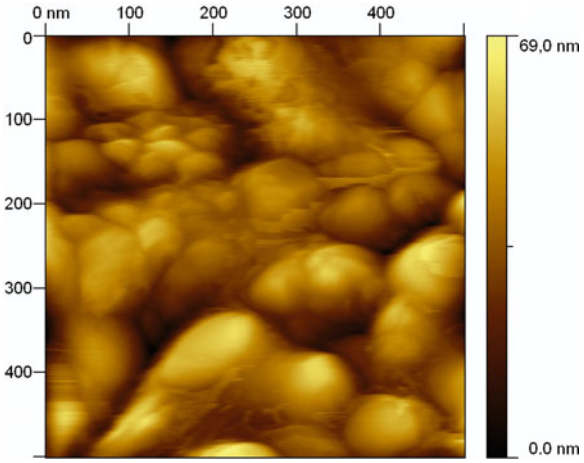

Fig. 15.3 AFM image of the Metalloporphyrins-modified CNTs layers

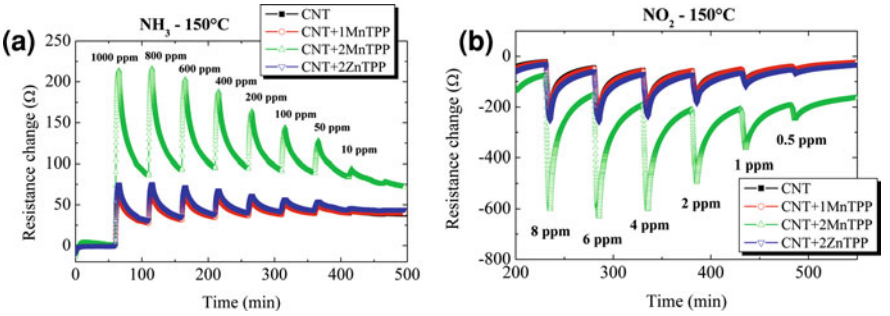

Fig. 15.4 Time responses towards 5-min pulses of **a** NH_3 and **b** NO_2 of the four chemiresistors based on CNTs, un-functionalized and functionalized with 1 and 2 sprayed-layers of Mn-TPP and 2 sprayed-layers of Zn-TPP, at 150°C

typical time response in terms of electrical resistance change for four chemiresistors based on unmodified CNTs, MnTPP-modified CNTs (CNT + 1MnTPP, CNT + 2MnTPP), and ZnTPP-modified CNTs (CNT + 2ZnTPP), exposed to NH_3 and NO_2 gas, at 150°C. The electrical resistance of all CNTs-sensors increases (decreases) upon a single gas exposure of the NH_3 reducing (NO_2 oxidizing) gas due to molecules adsorption. These results demonstrate that MPPs-modified CNTs-chemiresistors are able to detect a wide range of gas concentrations of NH_3 (10–1,000 ppm) and NO_2 (0.5–10 ppm) with a very low limit of detection in the range of sub-ppm for NO_2 and a few ppm level for NH_3, at 150°C. These minimal detection limits are very interesting for environmental NO_2 air-monitoring and industrial processes control NH_3 detection applications.

Figure 15.5 shows the calibration curves of the resistance change of the four CNTs-chemiresistors operating at 150°C for ammonia and nitrogen dioxide. The MnTPP-modified CNTs sensor with two spray-layers exhibits the maximum

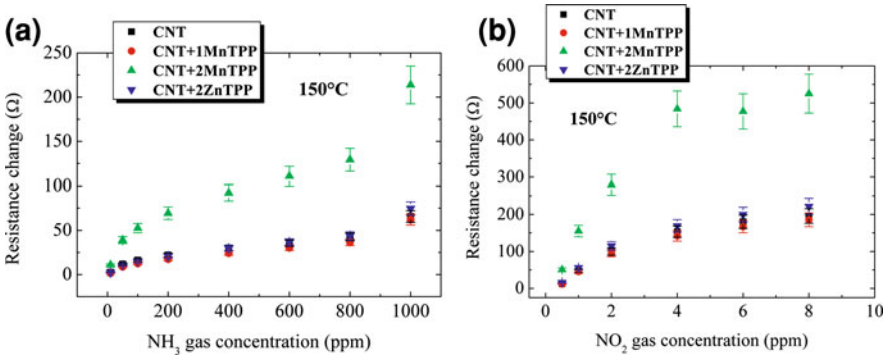

Fig. 15.5 Calibration curves towards **a** NH_3 and **b** NO_2 of the four chemiresistors based on CNTs, un-functionalized and functionalized with 1 and 2 sprayed-layers of Mn-TPP and 2 sprayed-layers of Zn-TPP, at 150°C. The exposure time per any gas concentration under test is 5 min

response for both gases considered. This could be attributed to catalytic effects of the metalloporphyrin for enhancing gas adsorption.

15.4 Conclusions

CVD technology has been used to grow networked layers of multi-walled CNTs onto cost-effective miniaturized alumina substrates. CNTs-chemiresistors have been fabricated for NO_2 and NH_3 gas sensing applications, at a sensor temperature of 150°C. The sidewalls of the CNTs films have been modified by spray-coating with two different metalloporphyrins (MPPs) consisting of a TetraPhenylPorphyrin coordinated by a central metal of zinc (Zn-TPP) and manganese (Mn-TPP) for enhanced sensitivity compared to un-functionalized CNTs networked layers. Detection limit of 0.5 ppm NO_2 and 10 ppm NH_3 has been measured. Finally, MPPs-modified CNTs-sensors are very interesting for advanced nanosensors operating at moderate temperatures with low power consumption. These micro-sensors could be used for environmental air-monitoring applications (NO_2) and industrial processes control (NH_3).

References

1. Kong J, Franklin NR, Zhou C, Chapline MG, Peng S, Cho K, Dai H (2000) Nanotube molecular wires as chemical sensors. Science 287:622–625
2. Someya T, Small J, Kim P, Nuckolls C, YardleyJT (2003) Alcohol vapor sensors based on single-walled carbon nanotube field effect transistors. Nano Lett 3(7):877–881
3. Penza M, Cassano G, Rossi R, Alvisi M, Rizzo A, Signore MA, DikonimosTh, Serra E, Giorgi R (2007) Enhancement of sensitivity in gas chemiresistors based on carbon nanotube surface functionalized with noble metal (Au, Pt) nanoclusters. ApplPhys Lett 90:173123

4. Penza M, Rossi R, Alvisi M, Cassano G, Serra E (2009) Functional characterization of carbon nanotube networked films functionalized with tuned loading of Au nanoclusters for gas sensing applications. Sens Actuators B 140:176–184
5. Penza M, Rossi R, Alvisi M, Cassano G, Signore MA, Serra E, Giorgi R (2008) Pt- and Pd-nanoclusters functionalized carbon nanotubes networked films for sub-ppm gas sensors. Sens Actuators B 135:289–297
6. Penza M, Rossi R, Alvisi M, Serra E (2010). Metal-modified and vertically aligned carbon nanotube sensors array for landfill gas monitoring applications. Nanotechnology 21:105501
7. Kong J, Chapline MG, Dai H (2001) Functionalized carbon nanotubes for molecular hydrogen sensors. Adv Mater 13:1384–1386
8. Di Natale C, Paolesse R, D'Amico A (2007) Metalloporphyrins based artificial olfactory receptors. Sens Actuators B 121:238–246
9. Penza M, Rossi R, Alvisi M, Valerini D, Serra E, Paolesse R, Martinelli E, D'Amico A, Di Natale C (2009) Metalloporphyrins-functionalized carbon nanotube networked films for room-temperature VOCs sensing applications. Procedia Chemistry 1:975–978
10. Penza M, Rossi R, Alvisi M, Signore MA, Serra E, Paolesse R, D'Amico A, Di Natale C (2010) Metalloporphyrins-modified carbon nanotubes networked films-based chemical sensors for enhanced gas sensitivity. Sens Actuators B 144:387–394
11. Paolesse R, Mandoj F, Marini A, Di Natale C (2004) Porphyrin based chemical sensors. Encyclopedia of nanoscience and nanotechnology, Vol. 9. American Science Publishers, Stevenson Ranch, CA, USA, pp 21–35
12. Monti D, Nardis S, Stefanelli M, Paolesse R, Di Natale C,D'Amico A (2009) Porphyrin-based nanostructures for sensing applications. J. Sens 856053

Chapter 16
Gas Sensing Properties of Indium Oxide Nanoparticles Prepared by Laser Ablation in Water

F. Barreca, S. Spadaro, G. Currò, N. Acacia, F. Neri, N. Donato, M. Latino and G. Neri

Abstract Water colloids of indium oxide were synthesized by laser ablation in liquids (LAL). TEM measurements have shown the formation of indium oxide nanoparticles with a bimodal distribution, consisting mainly of particles of small diameters (2–5 nm) accompanied by larger nanoparticles (about 10–20 nm in diameter).These colloidal solutions have been used to deposit films on interdigitated substrates in order to fabricate carbon monoxide resistive sensors. In_2O_3(LAL) films-based sensors have shown good performances, indicating that LAL is a very promising technique for the synthesis of metal oxide nanoparticles for gas sensing.

16.1 Introduction

Indium oxide (In_2O_3) is an important material because of its unique properties such as high electrical conductivity and optical transparency in the visible region. It is successfully used, for example, for the conductive top layers in solar cells, flat

F. Barreca (✉) · S. Spadaro · G. Currò
Advanced and Nano Materials Research s.r.l, Messina, Italy
e-mail: process@anmresearch.it

N. Acacia · F. Neri · N. Donato
Department of Matter Physics and Electronic Engineering, University of Messina, Messina, Italy

M. Latino
Department of Chemical Science and Technologies, University of Rome Tor Vergata, Rome, Italy

G. Neri
Department of Industrial Chemistry and Materials Engineering, University of Messina, Messina, Italy

G. Neri et al. (eds.), *Sensors and Microsystems*,
Lecture Notes in Electrical Engineering 91, DOI: 10.1007/978-94-007-1324-6_16,

panel displays, low-emissivity windows. Moreover, the wide band gap of such material and the possibility of its tuning due to quantum confinement effects in very small nanoparticles boosted its application in UV detectors or as an active layer in chemo-resistive sensing of gases like O_3 and NO_2 [1].

Metal oxide semiconducting (MOS) gas sensors are small devices, used for the transduction of a chemical information about concentration into electrical signal. They are low cost mass-production devices that offer the possibility to build in wireless nets and are suitable for tong-term operations. Moreover, they are more appreciate for the ability to detect combustible, environmental and toxic gases like NH_3 and H_2S, and CH_4, for applications in homeland security, industry and agriculture. Nanosized metal-oxides are promising candidates for MOS gas sensors, due to small size, low power consumption and large surface to bulk area ratio to increase sensitivity.

Laser ablation in liquids (LAL) provides a new technique for the synthesis of size controlled metallic and metallic oxide nanoparticles in colloidal as well as powdered phases [2, 3]. A large number of available parameters to control size, shape, and morphology of nanostructured materials is one of the advantages of this very fast and very cheap approach not requiring costly vacuum chambers.

In the presented work, we studied the gas sensing properties of nanostrucured indium oxide films obtained from water colloids of indium oxide nanoparticles prepared by LAL.

16.2 Experimental Section

Indium oxide nanoparticles in water colloids were prepared by irradiating a metallic indium target immersed in distilled water with a pulsed laser beam.

The target was pure indium (99.7%) with a thickness of 1 mm, obtained by Koch-Light Laboratories LTD. The target was positioned on an off-axially rotating target holder and immersed in the ablation vessel filled with 10 mm of distilled water. The ablation was performed focusing the beam of a second harmonic (532 nm) of a Nd:YAG laser operating at 10 Hz repetition rate, with a pulse width of about 5 ns. Experiments with a duration of 30 min were carried out at 1 J cm^{-2} fluence.

The size and shape of the indium oxide nanoparticles were examined by TEM analysis, using a JEOL JEM 2000 FX microscope operating at 200 kV.

A SEM equipped with EDX was used to measure the presence of large oxide nanoparticles and to evaluate the bulk chemical composition of the nanoparticle films obtained by dropping the colloidal solutions on a clean Silicon substrate and allowing them to dry at room temperature and at atmospheric pressure.

The chemical composition was investigated by means of XPS spectroscopy using a K-Alpha system of Thermo Scientific and the binding energy shifts were calibrated keeping the C1s position fixed at 285 eV.

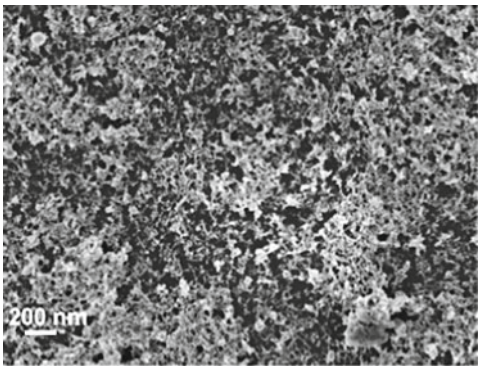

Spectral lines	*Atomic %*
C K	7
N K	6
O K	51
Si K	19
In L	17

Fig. 16.1 SEM image (*on the left*) and EDX derived chemical composition (atomic%, *on the right*) of the indium oxide film after deposition on a silicon substrate

Indium oxide nanostructured sensors were prepared by depositing In_2O_3 on alumina substrates by drop coating from the LAL colloidal solutions. The sensor devices were mounted onto a suitable holder and hosted in the test chamber for gas sensing measurements, performed by recording the changes of the resistance caused by the exposition to different gases concentrations.

16.3 Results and Discussion

A clear evidence about the effective formation of the nanoparticles in the colloidal samples, concerning their sizes and shapes, was obtained from a TEM analysis. Generally, the presence of sizeable nanoparticles aggregates was detected, which suggests a relatively poor stability of the colloid during the deposition. The coexistence of about two chief nanoparticles diameters is evident from TEM images (not reported here). Both an high density of spherical nanoparticles of about 2–5 nm in diameter ($\approx$85%) and a limited number of 10–20 nm nanoparticles (12%) are found while larger ones were uncommon (about 0.1%).

TEM results, by themselves, do not give information about the overall qualitative structure and the compositional nature of the observed nanoparticles. Therefore a SEM analysis with EDX probe was carried out after the deposition of the colloids on silicon substrates and a natural drying process at room temperature. As shown for example in Fig. 16.1, a nanoporous film is observed (on the left), and the results of the EDX analysis performed on it are reported (on the right). The presence of oxygen concentrations exceeding the 3:2 ratio, with respect to In (i.e. In_2O_3) together with significant amounts of carbon and nitrogen is typical of these nanostructured films and may be due to a getter ability of indium oxide nanoparticles against volatile species in the atmospheric ambient.

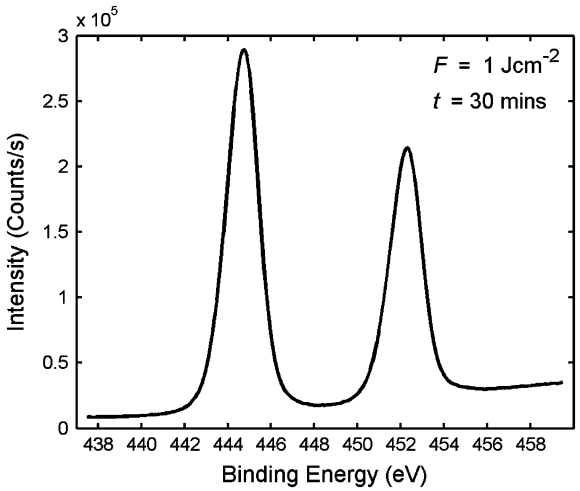

Fig. 16.2 In $3d_{5/2}$ and $3d_{3/2}$ core levels X-ray photoelectron spectra of indium oxide nanoparticles

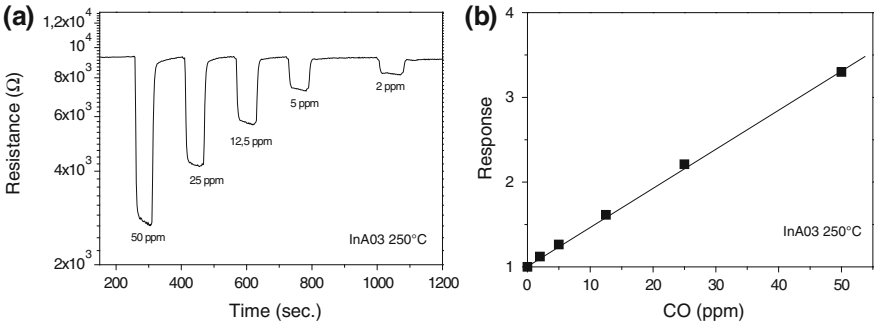

Fig. 16.3 **a** Transient responses of the sensorto different CO conc.; **b** calibration curve

An evaluation of the deposited nanoparticles composition was obtained from XPS analysis. The In 3d photoelectron peak, showed in Fig. 16.2, is characterized by the presence of a spin–orbit doublet, namely In $3d_{5/2}$ and $3d_{3/2}$ core levels. The doublet peaks positions are located at 444.7 and 452.3 eV, respectively, which correspond to In_2O_3 compared with the reported In $3d_{5/2}$ peak of metallic indium which appeared under 444 eV [4]. The ratio O/In = 1.7, calculated using the area under respective peaks and sensitivity factors for In and O, is quite close to the stoichiometric value of In_2O_3 (O/In = 1.5) if an chemisorbed oxygen at the nanoparticles surface is considered according to the EDX results.

The sensing properties of the LAL water colloids of indium oxide nanoparticles were tested in the monitoring of low concentrations of carbon monoxide.

Fig. 16.3a–b summarizes the results obtained. The operating temperature of the sensor was set to 250°C, which represents a good compromise between high sensitivity and fast response/recovery time. Fig. 16.3a shows the transient

responses of the sensor to different CO concentrations. The sensor response is high, allowing the determination of very low CO concentrations, down to 1 ppm, and display a linear trend, when plotted in a log–log scale, as a function of the gas target concentration (Fig. 16.3b).

16.4 Conclusions

LAL provides a new technique for the synthesis of size controlled metal oxide nanoparticles in colloidal phase. Results here presented, specifically regarding In_2O_3 nanoparticles, underline the potential of this technique which constitutes an interesting alternative to the current preparation of metal oxide nanoparticles for gas sensor applications. However, more investigations will be necessary in order to optimize and standardize metal oxide colloidal solutions preparation as well as the long term stability against nanoparticles coalescence.

References

1. Pinna N, Neri G, Antonietti M, Niederberger M (2004) Nonaqueous synthesis of nanocrystalline semi-conducting metal oxides for gas sensing. Angew Chem Int Ed 43:2–5
2. Sasaki T, Shimizu Y, Koshizaki N (2006) Preparation of metal oxide-based nanomaterials using nanosecond pulsed laser ablation in liquids. J Photochem Photobiol A Chem 182:335–341
3. Barreca F, Acacia N, Barletta E, Spadaro D, Currò G, Neri F (2010) Small size TiO_2 nanoparticles prepared by laser ablation in water. Appl Surf Sci 256:6408–6412
4. Moulder JF, Stickle WF, Sobol PE, Bomben KD (1992) Handbook of X-ray photoelectron spectroscopy. Perkin-Elmer, Eden Prairie p 125

Chapter 17
Chemical Sensors for Indoor Atmosphere Monitoring

R. Paolesse, L. Tortora, C. Di Natale, F. Dini and A. D'amico

Abstract For an accurate indoor air composition analysis the most useful tool is represented by the combination of a manual SPME collection of samples and the subsequent gas chromatography/mass spectrometry characterization. This method is lengthy, expensive and moreover it cannot allow a prompt danger signal. In this paper, different classes of indoor air pollutants have been evaluated, focusing the attention on acid and basic compounds and comparing the efficiency of a commercial pH indicator to corrole response. The reactions induced by acids or bases onto the dye embedded membranes led to absorption spectra considerable changes. The computer screen photoassisted technique has been able to discriminate among the tested analytes, showing also low detection limits in the case of trimethylamine.

17.1 Introduction

In the last few years the need of environmental control of indoor ambients has been more and more stringent, for both safety and security reasons. Chemical sensors are the devices most promising for the satisfaction of such a requirement, but for residential ambient they should be integrated in the design architecture.

R. Paolesse · L. Tortora (✉)
Dipartimento di Scienze e Tecnologie Chimiche, Università degli Studi di Roma "Tor Vergata", Via della Ricerca Scientifica 1, 00133 Rome, Italy
e-mail: luca.tortora@uniroma2.it

C. Di Natale · F. Dini · A. D'amico
Dipartimento di Ingegneria Elettronica, Università degli Studi di Roma "Tor Vergata", via del Politecnico, 00133 Rome, Italy

G. Neri et al. (eds.), *Sensors and Microsystems*,
Lecture Notes in Electrical Engineering 91, DOI: 10.1007/978-94-007-1324-6_17,

Different gas sensing technologies have been applied to indoor atmosphere monitoring, such as electrochemical sensors, metal-oxide semiconductor gas sensors and quartz crystal microbalances, but all these devices must be installed de novo. The computer screen photoassisted technique (CSPT) [1] apparatus exploits the capillary diffusion of a webcams and polychromatic light sources. Their integration with chemically sensitive dyes transforms these electronic devices in a gas sensing system. Starting from this concept of colorimetric sensor array, to confirm the proof of concept our initial choice regarded indoor volatile analytes having an acid or base character that could interact with pH indicators.

The CSPT analyses have been performed on gaseous products which arise from food spoilage processes such as trimethylamine (TMA) [2] and acetic acid or from furniture industrial processings [3] such as formaldehyde. In addition to these compounds also carbon dioxide was detected.

17.2 Experimental

The measuring setup involved a transparent cell placed between a web cam and a computer screen, which provides a sequence of 50 colours (from red to violet). To develop the sensing platform, a glass surface has been coated by a polymeric membrane [based on poly(4-styrenesulfonate) sodium salt, PSS], where the dyes have been dispersed. The stage circular shape has been divided in three quadrants, and in one of them the pH indicator [Bromocresol Purple (BP)] has been dispersed, in the second a functionalized corrole [5,10,15-tris (4-phosphonatophenyl)corrole] and in the last quadrant a background reference has been deposited.

The sensors were placed in a 10 mL TEFLON® measurement cell; the detector was represented by a Logitech Quickcam pro 4000 operating at resolution of 320 × 240 pixels. The software to acquire the video and to extract the information (fingerprints) from manually selected region of interests (ROIs), written in MATLAB®. We decided to start testing the performances of the developed sensing system using TMA as a case study. We used Bromocresol purple as indicator, because it has been used in the past for TMA detection [4]. The system was exposed to TMA, acetic acid, carbon dioxide and formaldehyde for 45 min. TMA and CO_2 were flowed into the measurement chamber at different concentrations by a computer-assisted 4-channel mass-flow controller (MKS), diluting certified TMA/nitrogen (500 ppm) and carbon dioxide tanks with nitrogen, used as gas carrier. Acetic acid and formaldehyde saturated vapours were obtained by nitrogen bubbling into liquid samples. All the measurements were performed at constant temperature (298 K), relative humidity (50%) and flow rate (200 mL/min).

The sensor array responses have been interrogated before, during and after the analyte fluxing by the webcam, providing a typical adsorption spectrum for each dye at starting and ending point.

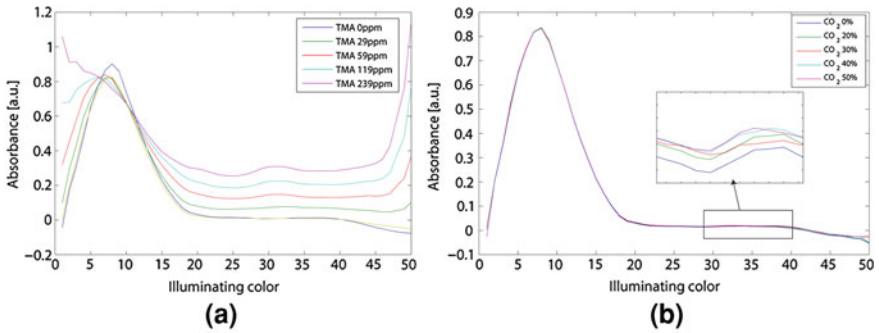

Fig. 17.1 Bromocresol Purple absorption spectrum variations during exposure to TMA (**a**) and CO_2 (**b**)

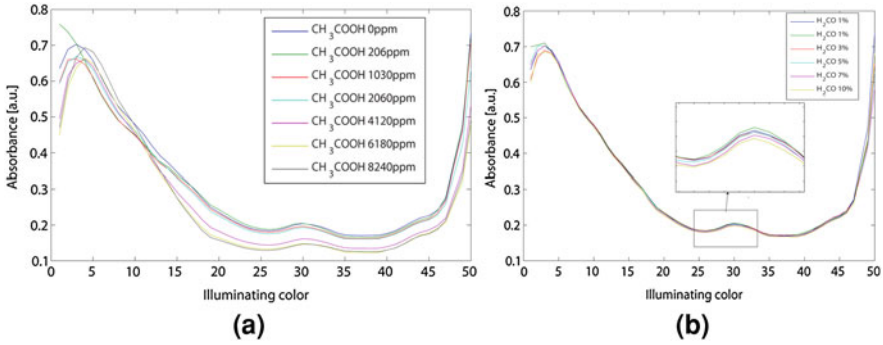

Fig. 17.2 5, 10, 15 tris (4-phosphonatophenyl) corrole absorption spectrum variations during exposure to acetic acid (**a**) and formaldehyde (**b**)

17.3 Results and Conclusions

The chromophores exploited for CSPT analyses are usually dispersed in PVC membranes. In our case, we had to use a different polymer, because the dyes used are water soluble and cannot be dispersed in a hydrophobic matrix, such as PVC. For this reason we used a PSS polymeric matrix, where Bromocresol Purple showed a good response to TMA vapors (Fig. 17.1a). The observed detection limit (29 ppm), supported its potentiality for an application as solid state sensors. On the other hand, the effect of carbon dioxide on the BP optical features was less evident but still appreciable (Fig. 17.1b).

Supported by these encouraging results, we decided to use a different dye, in order to wide the detection potentialities of the system. For this reason we dispersed in the PSS matrix a water soluble corrole, where other kind of interaction could be operating, so allowing also the detection of molecules, such as formaldehyde, not having an acid or base character. The acetic acid concentration

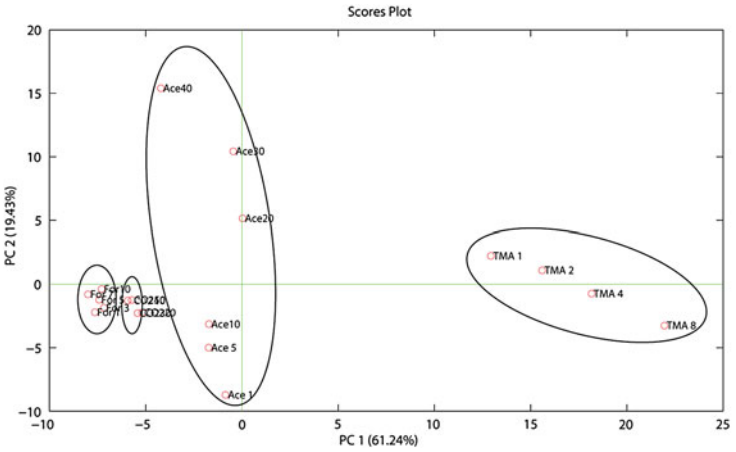

Fig. 17.3 Scores plot of the first two components showing the relationship between the strength of acid/base compounds and the responses obtained

changes were revealed by corrole with a good rate (Fig. 17.2a). The formaldehyde vapours were also detected, although if this analyte induced less variations (Fig. 17.2b) than acetic acid.

The PCA (Fig. 17.3) revealed that the system was able to detect analytes concentration in the ppm range. In particular, the discrimination on the first two components among the TMA and the acetic acid was evident. This phenomenon could be related to the relative acid or base strength higher for these VOCs than to carbon dioxide. The exploitation of corrole other than a pH indicator could allow the detection of a wider range of analytes, as demonstrated by formaldhyde, although with a lower sensitivity.

In conclusion, the BP/PSS membrane can be useful to monitor some important indoor parameters, such as for example TMA and CO_2 concentrations, while corrole proved to be useful for acetic acid and formaldehyde detection. It is also worth mentioning that, by optimization of the chromophores dispersed in the polymeric membranes, it is possible to create a sensor array able to monitor a wide range of analytes. Further work is in progress in such a direction and the results will be reported in due course.

References

1. Filippini D, Di Natale C, Paolesse R, D'Amico A, Lundström I (2007) Computer screen photoassisted techniques for global monitoring of environmental and sanitary parameters. Sens Actuators B 121:93–102
2. Alimelli A, Pennazza G, Santonico M, Paolesse R, Filippini D, D'Amico A, Lundström I, Di Natale C (2007) Fish freshness detection by a computer screen photoassisted based gas sensor array. Anal Chim Acta 582:320–328

3. Gibson LT, Cooksey BG, Littlejohn D, Tennent NH (1997) A diffusion tube sampler for the determination of acetic and formic acid vapours in museum cabinets. Anal Chim Acta 341:11–19
4. Pacquit A, Tong Lau K, Mc Laughlin H, Frisby J, Quilty B, Diamond D (2006) Development of a volatile amine sensor for the monitoring of fish spoilage. Talanta 69:515–520

Chapter 18
Electrochemical and Morphological Investigation on Gold Bio-Nano-Electrodes. Preliminary Results

Livia Della Seta, Maria Rita Montereali, Chiara Patriarca, Antonella Marone and Walter Vastarella

Abstract Gold nano-electrode ensembles were synthesized within nanoporous polycarbonate membranes and coupled with screen printed substrates. A disposable and versatile electrochemical system for biosensing and bio analytical applications has been obtained. Scanning Electron Microscopy and Scanning Probe Microscopy techniques were used to characterize the membrane surface, the nanostructured surfaces and the resulting biosensing devices. Efficiency and response of nano-probes were tested with several enzymatic immobilizations on the sensitive surface. Herein, the model case of a glucose oxidase biosensor based on nanoelectrodes is taken into account, for further evaluations on the accuracy of the biosensor system.

18.1 Introduction

Gold electrodes are used because of their window of potential, which enables to work with low interferences and offer the possibility of easily functionalizing their surface by self assembled monolayers (SAMs) or electrochemically deposited

L. Della Seta · M. R. Montereali · C. Patriarca · A. Marone · W. Vastarella (✉)
ENEA, C.R. Casaccia, Via Anguillarese 301, 00123, S. Maria di Galeria, Rome, Italy
e-mail: walter.vastarella@enea.it

L. Della Seta
e-mail: livia.dellaseta@enea.it

M. R. Montereali
e-mail: mariarita.montereali@enea.it

C. Patriarca
e-mail: chiara.patriarca@enea.it

A. Marone
e-mail: antonella.marone@enea.it

G. Neri et al. (eds.), *Sensors and Microsystems*,
Lecture Notes in Electrical Engineering 91, DOI: 10.1007/978-94-007-1324-6_18,

multilayers (EDM) through thio- or amino-coordinate derivatives [1–3]. Nanoelectrode ensembles (NEEs) fabricated by growing metal nanowires/fibres into the pores of a template have already found application in a variety of fields ranging from electro-analysis to sensors and electronics. By using specific nanoporous membranes as templates for such NEEs, it is possible to obtain an assembly of very small gold ultra-microelectrodes confined in a rather small space, which can be either used such as, or for biomolecules immobilization.

In this work gold NEEs were synthesized within track-etched polycarbonate (PC) membranes with controlled pore size using an electroless deposition method based on the pioneering work of Martin's group [4], recently modified in order to optimize the resulting product and obtain a well defined nanostructure for specific applications [5–10]. As already reported [7], PC membranes are preferred over alumina membranes because of their minor pore densities and fragility.

Gold NEEs were coupled with a screen printed substrate to give a disposable and versatile electrochemical device for biosensing and bio-analytical applications named nano electrode ensembles on screen printed substrate (NEEs/SPS) [7, 11]. The specific response to glucose, used as a model substrate, immobilizing glucose-oxidase (GOx) by different techniques on the sensing probe, was evaluated. NEEs/SPS-based biosensors were tested under flow conditions and their analytical performances were compared to unmodified carbon or conventional gold electrodes with equal enzymatic loading [11].

The parallel immobilization of an enzyme on the polymeric part of the membrane, and of a polyelectrolyte on the gold nanostructures, has been used for the development of mediatorless third generation biosensors. Experiments are going on, to further study the direct electron transfer between redox proteins and modified gold nanoelectrodes, through the conducting polymer cables. The accuracy of analytical performance in glucose detection is here evaluated by comparing this biosensor with a classical liquid chromatographic method (HPLC).

18.2 Experimental

18.2.1 Chemicals, Reagents and Materials

Glucose oxidase (GOx) from *Aspergillus niger* (EC 1.1.3.4), with specific activity of 198 units per mg of solid, bovine serum albumin (BSA, stock solution: 4% w/v), hydrogen peroxide, glutaraldehyde (GA) 25% aqueous solution, 3-amino-mercaptopropionic acid (cysteamine powder, CYS), formaldehyde, glucose, dehydrated gold chloride, potassium and sodium phosphate salts were purchased from Sigma-Aldrich. All reagents, buffer and electrolyte supporting solutions, e.g., 0.1 M phosphate buffer (PB), were prepared from deionised water (Synergy 185 apparatus from Millipore^{TM}). All other chemicals and solvents were of analytical grade and used without further purification.

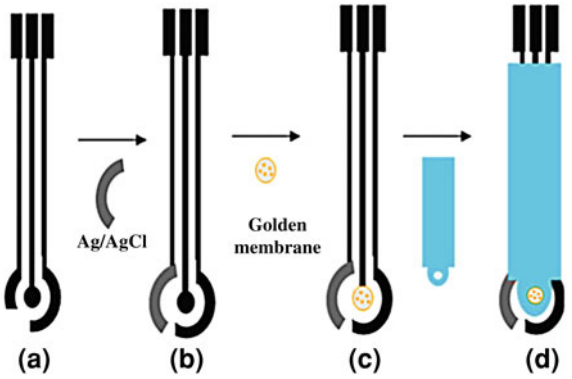

Fig. 18.1 Schematic sequence of NEE/SPS preparation **a** carbon graphite tracks and contact pads by screen printing; **b** Ag/AgCl deposition for reference electrode; **c** deposition on the working of the NEE based membrane; **d** dielectric paste deposition

Template PC membranes were from Anopore™, with density of 6×10^8 pores cm^{-2}, pore diameters of 30, 50 and 200 nm.

Carbon, Silver-Chloride and dielectric pastes for screen printed electrodes were from GWENT Electronics Materials Inc™.

18.2.2 Nanoelectrode Ensembles and Screen Printed Substrate Preparation

Conducting and insulating inks were screen printed on 0.3–0.5 mm thick polyvinyl chloride (PVC) substrates. PC membranes modified with Au nanowires were "glued", using a small drop of carbon paste on the WE, then the upper golden plated surface of the membrane was peeled using Magic Tape™. At last the device was completed by printing the insulator and RE layers as in common screen printing procedure (Fig. 18.1). The active WE area of 2.54 mm^2 is defined by the insulator geometry as elsewhere reported [7].

18.2.3 Instrumentation for NEE/SPS Characterization

Scanning electron microscope (SEM) JEOL JSM-5510 Low Vacuum model was mainly used for the characterization of gold nanowires. The microscope is equipped with an Oxford Instrument EDS 2000 microanalysis detector and software for elementary analysis. No sample coating was performed. Atomic Force Microscopy (AFM) measurements were performed with an SPM Perception (Assing-CNR-ISM).

A high performance liquid chromatograph (Thermo Spectrasystem P4000) was used for the glucose detection in biological fluid. It was equipped with a refractive index detector. The column, a 300 mm × 7.8 mm Rezex ROA-Organic Acid H^+

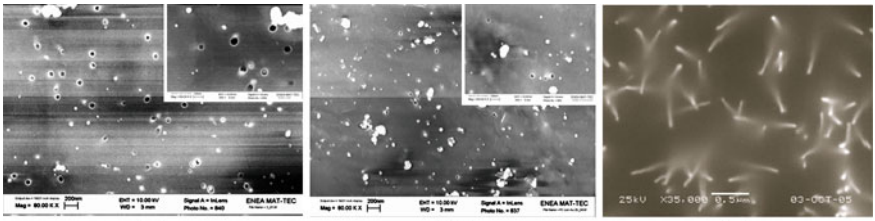

Fig. 18.2 SEM images of Au nanowires deposited into nanoporous polycarbonate membranes with nominal pore size of 30 nm. **a** and **b** images acquired at Energy of 10 kV and magnification of 8×10^4; **c** at Energy of 25 kV and magnification of 3.5×10^4. **a** After 3 h in gold plating bath; **b** after 12 h, **c** after 24 h with formaldehyde as catalyst

(8%) column (Phenomenex) with a 4 × 30 mm security guard cartridge Carbo-H (Phenomenex), was operated at 65°C, using 5 mN H_2SO_4 solution as mobile phase (flow rate of 0.5 ml min^{-1}) [12]. The liquid samples were diluted 1:10 and pretreated with 0.22 μm membrane filter before injection.

For the amperometric detection, a home made flow cell was used provided with a peristaltic pump (Gilson™ Minipuls 3) to propel solution along the injection system, with 115 μL sample loop injection valve (Omnifit™, Cambridge, England). Voltammetric and amperometric measurements, performed, respectively, under batch and flow conditions, were conducted with the Autolab™ potentiostat PGSTAT10.

18.3 Results and Discussion

18.3.1 Morphology of Metallic NEEs and NEE/SPS

Electroless gold deposition into polycarbonate (PC) membranes produces a complete gold coverage and pores filling, as demonstrated by microscopy investigations. By "peeling" only one side of the gold plated membranes, Au nanoelectrodes facing on the surface are obtained. The nano-wires inside the membrane pores offer an open face on one side of the membrane while the other, still covered in gold, provides the electrical contact with the SPE graphite surface. As shown in SEM images (Fig. 18.2) complete pore filling takes place only after a 24 h treatment, in the gold plating bath, using formaldehyde as catalyst.

AFM scans of membranes after peeling (Fig. 18.3) show the nanowires clearly visible on the membrane surface; some appearing slightly out of it or on the same level, while others can be spotted further inside the membrane pores probably due to the mechanical effect of stripping. The resulting process of nanodisks formation on the surface averagely maintains the dimensions of the original pores.

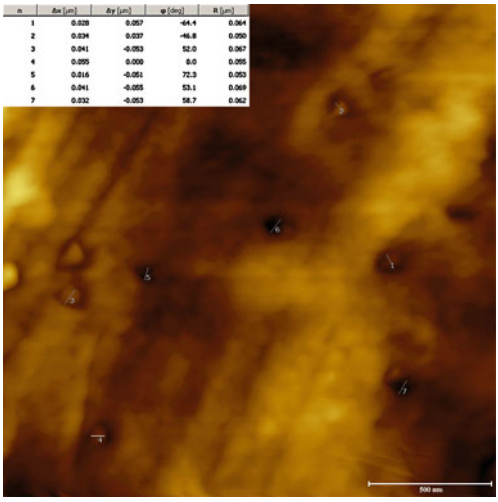

Fig. 18.3 AFM image of Au nanowires (Peeled polycarbonate membrane)

Table 18.1 Glucose concentration during the process of growth in biological medium inoculated with specific bacteria (at time 0, 3 and 6 days)

HPLC method	Medium at T_0	Medium after 3 days	Medium after 6 days
n. replicates	3	3	3
Glucose concentration (mg/L)	533.6	21.6	3.8
precision (RSD %)	4.1	8.0	7.2
Nanobiosensor method	Medium at T_0	Medium after 3 days	Medium after 6 days
n. replicates	4	4	4
Glucose concentration (mg/L)	511.9	20.3	5.7
Precision (RSD %)	4.5	11.2	12.4

18.3.2 Analytical Accuracy for Glucose Detection in Growth Media

A preliminary comparison between the proposed nano-biosensor for glucose detection and a conventional analytical technique with high level of precision and accuracy has been also performed. The glucose was analyzed in growth medium inoculated with bacteria. The substrate was initially added in known amount and the metabolic pathway was followed by measuring the glucose depletion in time (measured in days). Table 18.1 summarizes the results, considering the glucose concentration at the beginning and after 3 and 6 days of growth. Statistical evaluation resulted in no significant differences between the two methods (data not shown).

18.4 Concluding Remarks

Micro and nano gold electrodes on disposable screen printed substrates were assembled using a simple procedure. Nanoelectrode ensemble were synthesized by electroless procedure into template nanoporous membranes, microscopic investigation confirmed the successful deposition of metal in nanostructured membranes and the resulting system is coupled with disposable screen printed electrodes. The same electroless method is going to be extended to produce nickel and platinum nanowires according to similar synthetic routes.

Higher sensitivity of NEEs was observed with respect to macroscopic screen printed probes, due to the lowering of background signal. This work integrates the stability and reproducibility study of the electrochemical response for such nano-sensors with a comparison between nanoelectrode-based biosensors and a chromatographic methodology. No significant differences between the two methods were established.

References

1. Jirage KB, Hulteen JC, Martin CR (1999) Effect of thiol chemisorption on the transport properties of gold nanotubule membranes. Anal Chem 71(21):4913–4918
2. Gamero M, Pariente F, Lorenzo E, Alonso C (2010) Nanostructured rough gold electrodes for the development of lactate oxidase-based biosensors. Biosensors Bioelectronics 25(9): 2038–2044
3. Codognoto L, Winter E, Doretto KM, Monteiro GB, Rath S (2010) Electroanalytical performance of self-assembled monolayer gold electrode for chloramphenicol determination. Microchimica Acta 169(3–4):345–351
4. Menon VP, Martin CR (1995) Fabrication and evaluation of nanoelectrode ensembles. Anal Chem 67(13):1920–1928
5. DeLeo M, Kuhn A, Ugo P (2007) 3D-ensembles of gold nanowires: preparation, characterization and electroanalytical peculiarities. Electroanalysis 19(2–3):227–236
6. Pereira FC, Moretto LM, De Leo M, Boldrin Zanoni MV, Ugo P (2006) Gold nanoelectrode ensembles for direct trace electroanalysis of iodide. Anal Chim Acta 575(1):16–24
7. Vastarella W, Maly J, Ilie M (2009) Integration between template based nanostructured surfaces and biosensors. In: Merkoçi A (ed) Biosensing using Nanomaterials. Wiley, Hoboken, pp 379–419
8. Ugo P, Moretto LM (2007) Metal deposition. In: Zoski CG (ed) Handbook of electrochemistry, Elsevier Science, Amsterdam, Chapter 16, Section 16.2, pp 678–709
9. Brunetti B, Ugo P, Moretto LM, Martin CR (2000) Electrochemistry of phenothiazine and methylviologen biosensor electron transfer mediators at nanoelectrode ensembles. J Electroanal Chem 491(1–2):166–174
10. Moretto LM, Pepe N, Ugo P (2004) Voltammetry of redox analytes at trace concentrations with nanoelectrode ensembles. Talanta 62(5):1055–1060
11. Vastarella W, Della Seta L, Masci A, Maly J, De Leo M, Moretto LM, Pilloton R (2007) Biosensors based on gold nanoelectrode ensembles and screen printed electrodes. Int J Environ Anal Chem 87(10–11):701–714
12. Lee HS, Salerno MB, Rittmann BE (2008) Thermodynamic evaluation on H2 production in glucose fermentation. Environ Sci Technol 42:2401–240

Chapter 19
Synthesis, Characterization, and Ammonia Sensing Properties of Vanadium Pentoxide Nanocrystals

G. Rizzo, A. Bonavita, G. Neri, A. Arena and G. Saitta

Abstract The optical and electrical properties of vanadium pentoxide films simply prepared by direct deposition from stable ethanol suspensions of V_2O_5 nanoparticles, are found to change after exposure to ammonia. Aimed at developing solid state ammonia sensors able to work at room temperature, spectrophotometric investigations and electrical measurements are performed on vanadium pentoxide films deposited on glass, on V_2O_5 films deposited on flexible substrates, having nanosilver electrodes applied on the top, and on *n*-Si/V_2O_5 heterojunctions.

19.1 Introduction

Vanadium pentoxide is a versatile semiconductor, characterized by the property to change its optical and electronic behaviour reversibly, in response to a variety of stimuli including externally applied electric field [1], ultraviolet light irradiation [2], and thermal treatment [3]. In addition V_2O_5 is a promising candidate for gas sensing applications, because of its ability to change its electrical resistance when it is exposed to a variety of gas targets. In common with other transition metal oxides used in resistive sensors, the gas sensing performances of vanadium pentoxide in terms of sensitivity and response/recovery times, are found to

G. Rizzo · A. Bonavita · G. Neri (✉)
Dipartimento di Chimica Industriale e Ingegneria dei Materiali, Università degli Studi di Messina, Salita Sperone 31, 98166, Messina, Italy
e-mail: neri@ingegneria.unime.it

A. Arena · G. Saitta
Dipartimento di Fisica della Materia e Ingegneria Elettronica, Università degli Studi di Messina, Salita Sperone 31, 98166, Messina, Italy

G. Neri et al. (eds.), *Sensors and Microsystems*,
Lecture Notes in Electrical Engineering 91, DOI: 10.1007/978-94-007-1324-6_19,

improve by reducing the crystal size. V_2O_5 processed as nanotubes, nanowires, and nanobelts in order to maximize the surface area, has been used successfully to detect ethanol [4], ammonia [5], and ammines [6]. This paper reports on a simple synthesis to prepare nanostructured vanadium pentoxide having excellent film forming property, and low temperature sensitivity towards ammonia. The material, prepared using as starting reagent ammonium metavanadate (NH_4VO_3), and sintering the reaction product in air at 400°C, is found to consists of highly crystalline V_2O_5 nanoparticles.

19.2 Experimentals

The morphology and microstructural properties of the V_2O_5 nanoparticles are investigated by means of X-ray diffraction (XRD) and transmission electron microscopy (TEM) measurements performed using an Ital Structure APD 2000 diffractometer and a JEOL 2010 EX instrument. Optical measurements were performed using a Perkin–Elmer Lambda 9/19 spectrophotometer and a Nicolet Avatar 360 spectrometer. Electrical characterization of thin V_2O_5 films deposited on *n*-Si wafer and on flexible substrates was performed using a Keithley 2004 sourcemeter, and an Agilent 34970A multimeter. A CMOS sensor (from Sensirion) was used to check the temperature and RH into the measurement chamber. Electrical measurements were performed at constant RH, and under exposure to calibrated NH_3 flux, inserting both the sensor based on V_2O_5 and the reference sensor into an aluminium measurement chamber. The relative humidity level inside the measurement chamber was settled and controlled by mixing steams of dry air and saturated air, using a number of digital mass flow meter controllers connected to dry air and to a bubbler held at constant temperature. NH_3 fluxes were generated by a permeation tube, calibrated to flux 14 ppm ammonia when kept at 50°C. The way V_2O_5 films coated on quartz crystals respond to RH at constant temperature was evaluated using an automated system purchased from BioAge, able to measure the resonance frequency shifts of a coated quartz crystal.

19.3 Results and Discussion

The analysis of XRD patterns (Fig. 19.1a) reveals that the material prepared starting from ammonium metavanadate consists of highly crystalline V_2O_5 nanoparticles, having few tens nanometers average size. High crystalline degree is confirmed by TEM measurements also (Fig. 19.1b).

In addition, TEM investigations reveal that the nanoparticles have a trend to organize aligning along the same preferential direction (Fig. 19.1c).

The film forming attitude shown by the nanoparticles allows compact films, highly adherent to the glass, plastic, and silicon substrates, to be obtained by direct

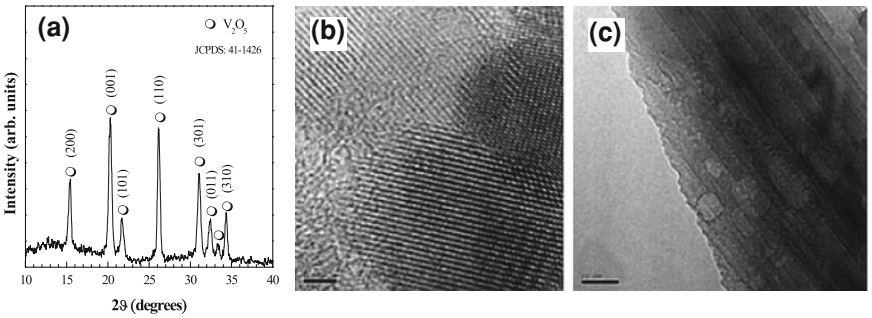

Fig. 19.1 **a** XRD spectrum and **b** TEM image of the V_2O_5 nanoparticles (the scale bar is 2 nm); **c** TEM image of V_2O_5 nanoparticles organized to form an agglomerate evidencing a certain degree of order (the scale bar is 20 nm)

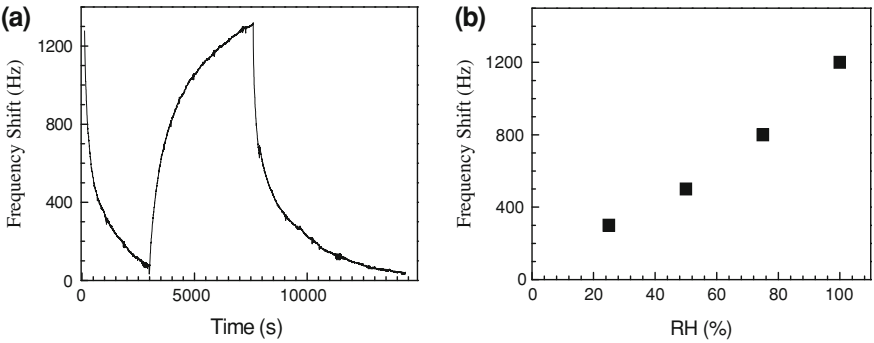

Fig. 19.2 **a** Frequency shift of a QCM coated with vanadium pentoxide, recorded as the RH level inside the measurement chamber changes between 0 and 100%; **b** relationship between the frequency shift and RH

deposition from ethanol nanoparticles suspensions, without the use of any binder, and without the need of any substrate surface treatment.

To investigate on the sensing properties of the nanostructured V_2O_5, thin films have been deposited onto AT-cut quartz crystals (10 MHz) having Al electrodes on the top. The resonance frequency of the coated quartzes changes reversibly as the RH level changes (Fig. 19.2a). The frequency shift is linearly related to the RH level in the range between 0 and 100% RH (Fig. 19.2b).

The absorption spectrum of pale yellow V_2O_5 films deposited on transparent substrates (Fig. 19.3a) is characterized by a band positioned between 350 and 400 nm. The films bleach when exposed in air to concentrated NH_3. Exposure to NH_3 has remarkable effects on the IR spectrum also (Fig. 19.3b).

Figure 19.3 shows that exposure to an elevated concentration of NH_3 at high RH, has remarkable effects in the UV–VIS–IR properties of the nanocrystalline V_2O_5 films under investigation. Such effects are found to be persistent, and likely originate from a reaction that occurs between ammonia and the V_2O_5 nanocrystals,

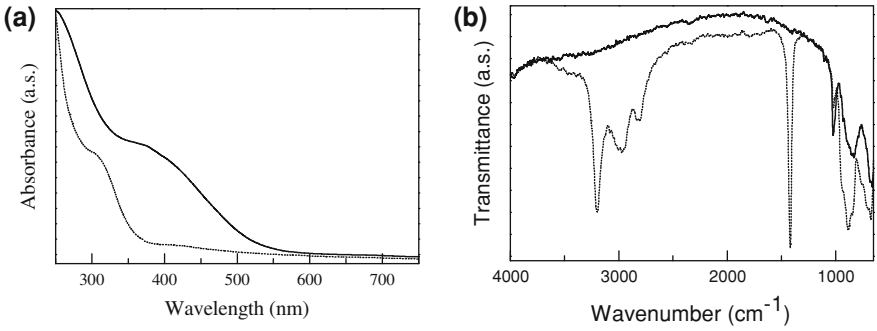

Fig. 19.3 **a** UV–VIS absorption spectrum and **b** FT–IR transmittance spectrum of a V_2O_5 film before (*solid*) and after exposure to highly concentrated ammonia in air, at 28°C, 65% relative humidity

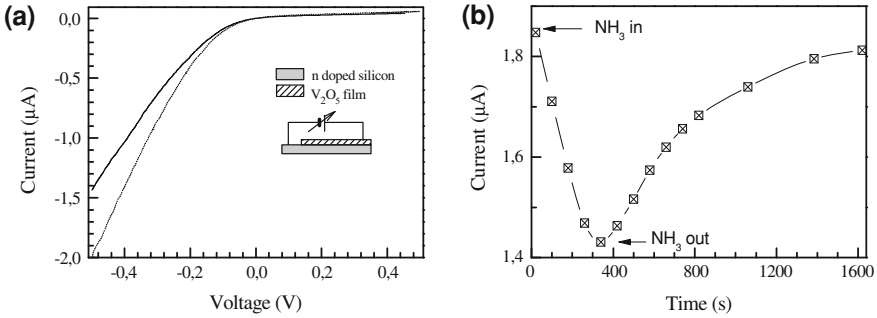

Fig. 19.4 **a** *I/V* plot measured at 28°C on a junction between V_2O_5 and *n*-doped silicon as deposited (*solid*) and after 350 s exposure to 7 ppm dry ammonia; **b** dynamic behaviour of the current through the V_2O_5/*n*-Si measured at $V = -0.5$ V, in response to a 350 s lasting pulse of 7 ppm dry ammonia

yielding ammonium metavanadate as reaction product. NH_4VO_3 converts back to vanadium pentoxide and the optical spectra recover their original shape, by heating the exposed films in air, at about 400°C.

Current–voltage measurements carried out in dry condition on *n*-Si/V_2O_5 heterojunctions show that exposure to calibrated amounts of ammonia in the ppm range results in a decrease of the metal oxide conductivity. This finding is evidenced by comparing the current–voltage plots of a typical *n*-Si/V_2O_5 junction before and after exposure to 7 ppm dry ammonia (Fig. 19.4a). The resistivity changes arising from the interaction between the nanocrystalline V_2O_5 films and NH_3 in dry condition show a partial reversibility, as it is suggested by the evolution of the current measured through the junction at constant voltage, in response to a 350 s lasting pulse of 7 ppm dry ammonia (Fig. 19.4b).

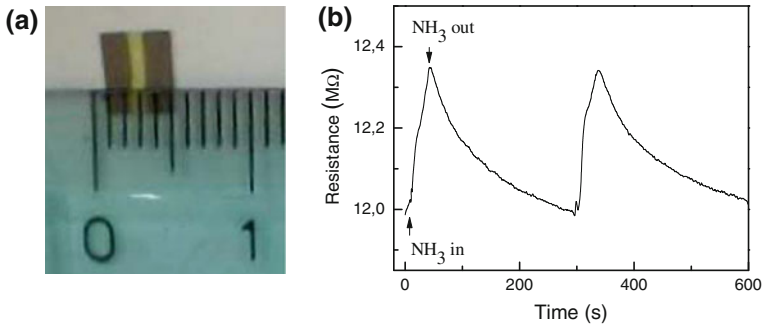

Fig. 19.5 **a** Typical flexible ammonia sensor based on V_2O_5; **b** response of the sensor measured at 28°C, 20% RH, by exposing the sample to a 4 ppm of ammonia

Figure 19.5a shows a typical sensor based on V_2O_5, deposited on a transparency sheet without the need of any post-processing, by direct deposition from stable dispersions of V_2O_5 nanoparticles. Linearly shaped electrodes are applied on the top of the semiconducting film by using standard refillable pens, charged with water dispersions of silver nanoparticles. Figure 19.5b shows the results of electrical measurements performed on the sensor of Fig 19.5a. It can be noticed that the resistance of the device increases with exposure to ammonia.

This latter finding is in disagreement with that commonly reported in literature, according to which V_2O_5 behaves as *n*-type semiconducting oxide, having an electrical conductivity that increases when it is exposed to ammonia [5]. Such a behaviour is commonly ascribed to interaction between the metal oxide and the gas target, resulting in formation of oxygen vacancies, associated to the reduction of vanadium ions from V^{5+} species to V^{4+}. This latter kind of response mechanism is that usually observed at high temperature. The response toward NH_3 observed by us at low temperature, as it is described in Fig. 19.4b, shows a different trend. A possible explanation, may be that the interaction between the oxide films and ammonia is mediated by the presence of thin water layers coating the semiconducting oxide, into which NH_3 dissolves, and dissociates. In such an hypothesis the metal oxide would behave as a pH sensor [7]. It is also noticed that the response of V_2O_5 based sensors is only partially reversible, as a certain uptake of NH_3 is not released during the sensor recovery. This behaviour is ascribable to the irreversible reaction that occurs between vanadium pentoxide nanocrystals and ammonia, resulting in the formation of NH_4VO_3 as reaction product [8].

19.4 Conclusion

Nanocrystalline V_2O_5 films developed by direct deposition from ethanol suspensions are found to have optical and electrical properties that change after exposure to ammonia. In particular while optical changes are ascribable to NH_4VO_3

formation, made reversible only by heating at 400°C, sensitive electrical changes, reversible to a certain extent, are observed at low temperature, in dry conditions, by exposing the V_2O_5 films to few ppm ammonia. These results can be promising in view of applications of the developed material in low temperature ammonia sensing applications.

References

1. Xiong C, Aliev AE, Gnade B, Balkus KJ (2008) Fabrication of silver vanadium oxide and V_2O_5 nanowires for electrochromics. ACSNano 2:293–301
2. Cheremisin A, Putrolaynen V, Velichko A, Pergament A (2009) UV laser modification and selective ion-beam etching of amorphous vanadium pentoxide thin films. Phys Status Solidi A 206:1484–1487
3. Cui N, Teixeira V, Meng LJ, Wang R, Gao JY, Fortunato E (2008) Thermochromic properties of vanadium oxide films prepared by dc reactive magnetron sputtering. Thin Solid Films 516:1484–1488
4. Raj AD, Pazhanivel T, Kumar PS, Mangalaraj D, Nataraj D, Ponpandian DN (2010) Self assembled V_2O_5 nanorods for gas sensors. Curr Appl Phys 10:531–537
5. Shimizu K, Chinzei KI, Nishiyama H, Kakimoto S, Sugaya S, Matsutani W, Satsuma A (2009) Doped-vanadium oxides as sensing materials for high temperature operative selective ammonia gas sensors. Sens Actuators B 141:410–416
6. Raible I, Burghard M, Schlecht U, Yasuda A, Vossmeyer T (2005) V_2O_5 nanofibres: novel gas sensors with extremely high sensitivity and selectivity to amines. Sens Actuators B 106:730–735
7. Helwig A, Müller G, Sberveglieri G, Eickhoff M (2009) On the Low-Temperature Response of Semiconductor Gas Sensors. J of Sens 620720 doi:10.1155/2009/620720
8. Kittaka S, Hamaguchi H, Umezu T, Endoh T, Takenaka T (1997) Interaction of NH_3 with H_2O in the vanadium pentaoxide hydrate interlayer spaces—topotactic crystal-growth of ammonium vanadate film. Langmuir 13:1352–1358

Chapter 20
Synthesis of Silver Nanoparticle Arrays for SERS Based Sensing

C. D'Andrea, F. Neri, P. M. Ossi, N. Santo and S. Trusso

Abstract Recently, noble-metal nanoparticles (NMNPs) were introduced in the sensing discipline, and become one of the most efficient ways to enhance sensors sensitivity. It is known, in fact, that NMNPs possess peculiar optical properties. When NMNPs are illuminated by a laser beam with proper wavelength, the so-called localized surface plasmons, a collective oscillation of conduction electrons on NMNP surface, are excited. The effect is relevant, for example, in Surface Enhanced Raman Spectroscopy, where a significant enhancement of a localized electromagnetic field near NMNPs surface allows to detect species usually undetectable with normal Raman spectroscopy. Here we present a method for the growth of silver NP arrays with controlled morphology by means of the pulsed laser ablation technique performed in presence of a Ar atmosphere. The nanoparticles size and morphology can be tuned, respectively, by the Ar pressure and the laser pulse number. The SERS activity of nanoparticle arrays is investigated by Raman scattering of adsorbed rhodamine 6G (R6G) at different concentrations.

C. D'Andrea · F. Neri
Dipartimento di Fisica della Materia e Ingegneria Elettronica, Università degli Studi di Messina, Viale F. Stagno D'Alcontres 31, 98166, Messina, Italy

P. M. Ossi
Dipartimento di Energia & Centre for NanoEngineered, MAterials and Surfaces NEMAS Politecnico di Milano, Via Ponzio 34-3, 20133, Milan, Italy

N. Santo
Centro Interdipartimentale di Microscopia Avanzata, Università degli Studi di Milano, Via Celoria 26, 20133, Milan, Italy

S. Trusso (✉)
Istituto per i Processi Chimico-Fisici, IPCF-CNR, V.le F. Stagno d'Alcontres 37, 98158 Messina, Italy
e-mail: trusso@me.cnr.it

G. Neri et al. (eds.), *Sensors and Microsystems*,
Lecture Notes in Electrical Engineering 91, DOI: 10.1007/978-94-007-1324-6_20,

20.1 Introduction

Raman spectroscopy is a highly versatile physico-chemical technique that provides information on vibrational modes from chemical species of samples. On the other hand nanostructured materials exhibit properties that are radically different from bulk form [1]. These effects are evident in the interaction of light with matter, such as, for example, in the Raman scattering processes. One of this is the Surface Enhanced Raman Scattering. This effect is characterized by a significant enhancement of a localized electromagnetic field (EM) near noble-metal nanoparticles (NMNPs) surface. The phenomenon of SERS is related to an electromagnetic mechanism, describing the surface electron movement in the nanoparticles and a chemical mechanism caused by charge transfer between the substrate and the analyte molecules [2]. The EM mechanism provides the largest contribution to the enhancement and is linked by the surface plasmon resonance (SPR) of NMNPs. In fact, when NMNPs are illuminated by a laser beam with proper wavelength, the SPR, a collective oscillation of conduction electrons on NMNPs surface, are excited. If the excitation light is resonant with a plasmon, the metal nanoparticles will emit electromagnetic radiation coherent with the exciting field that increases the total field. This is a near-field effect that, typically, is extinguished in less than 20 nm, so, only the analyte molecules near the nanostructure produce appreciable signal. Moreover, the nanostructures not only enhances the incident laser field, but also the Raman scattered field, so it is possible to obtain enhancement factor of 9–10 orders of magnitude. Varying the shape and size of nanostructures is, also, possible to involve different plasmon frequencies and modes.

The enormous enhancement of SERS effect allows to detect species usually undetectable with normal Raman spectroscopy. In the last years, in fact, there is a considerable interest in SERS effect as an ultra sensitive technique of detection of biomolecules such as cancer genes, hemoglobin, glucose and virus [3–5]. The high signal-to-noise ratios permit, also, to obtain in vivo tumor targeting and detection.

In this work we present a method for the growth of silver nanoparticle arrays with controlled morphology by means of the pulsed laser ablation technique performed in presence of argon atmosphere. The nanoparticles size and morphology can be tuned, respectively by the Ar gas pressure and the laser pulses number. The SERS activity of the nanoparticle arrays is investigated by Raman scattering of adsorbed Rhodamine 6G (R6G) at different concentrations.

20.2 Experiment

Silver thin films were grown by means of pulsed laser ablation using a KrF excimer laser ($\lambda = 248$ nm, pulse width 25 ns). The laser pulse is focused onto a pure silver target, positioned inside a vacuum chamber on a rotating holder in

order to avoid craterization phenomena. The substrate holder is positioned in front of the target at a distance of 35 mm. Different substrates were used: c-Si for scanning electron microscopy (SEM), a-C covered copper grids for transmission electron microscopy (TEM) and 7059 Corning glass for Raman and UV–Vis absorption spectroscopy. The other relevant deposition parameters, the laser fluence and the substrate temperature, were kept fixed at 2.0 J cm^{-2} and room temperature (RT), respectively. SEM imaging was carried out using a Zeiss Supra 40 field ion scanning microscope while TEM images were acquired with Zeiss Leo 912AB microscope. In order to test the SERS activity of the samples they were soaked into rhodamine 6G (R6G) aqueous solutions at different concentration for 1 h and then rinsed with deionized water. Four different R6G concentrations were tested in the range between 0.1 mM and 50 nM. Raman characterization was performed using a HR-800 Jobin–Yvon micro-Raman apparatus, using the 632.8 nm line of a He–Ne laser as the exciting source. The laser power incident on the samples surface was kept low, about 100 μW, in order to avoid R6G degradation. Raman spectra were acquired using a 10× microscope objective resulting in a probe area of about 3.2 μm^2, while integration times were varied between 1 s up to 240 s, depending on the signal to noise ratio. UV–Vis spectra were acquired using a Lambda 900 Perkin Elmer spectrophotometer.

20.3 Results and Discussion

In Fig. 20.1 are reported the SEM images of the surface of the samples grown at the Ar pressure of 10, 40 and 70 Pa while the number of laser shots was kept fixed at 15,000. The surfaces are characterized by the presence of silver nanoparticles whose size and shape depend on the adopted Ar pressure. For the samples grown at 10 Pa of Ar, the presence of large NPs ($d > 35$ nm), surrounded by a depletion area with smaller NPs, can be observed. On the other hand, for the samples deposited at 40 and 70 Pa of Ar (Fig. 20.1b, c) the surface is characterized by the presence of nearly spherical NPs with typical dimensions of 10 nm at 40 Pa and 5 nm at 70 Pa.

In previous works [6, 7] we studied the growth mechanism of silver thin films under deposition conditions similar to the ones adopted in this study. In particular our experiments gave evidence for a two step mechanism of film formation: in the first step the presence of the Ar atmosphere induces the aggregation between the silver atoms during the plasma expansion, leading to the formation of NPs; in the second step NPs landing on the substrates and having very low kinetic energies start to aggregate giving rise to larger NPs and finally to a coalesced structure characterized by the presence of an interconnected network of silver island with smooth rounded edges. The dimensions of the NPs, which form in flight, are determined by the Ar pressure [8]. The laser shot number, on the other side, drives the aggregation process on the substrates (at a fixed Ar pressure). By increasing the laser shots number the NP number density on the surface increases and NPs start to

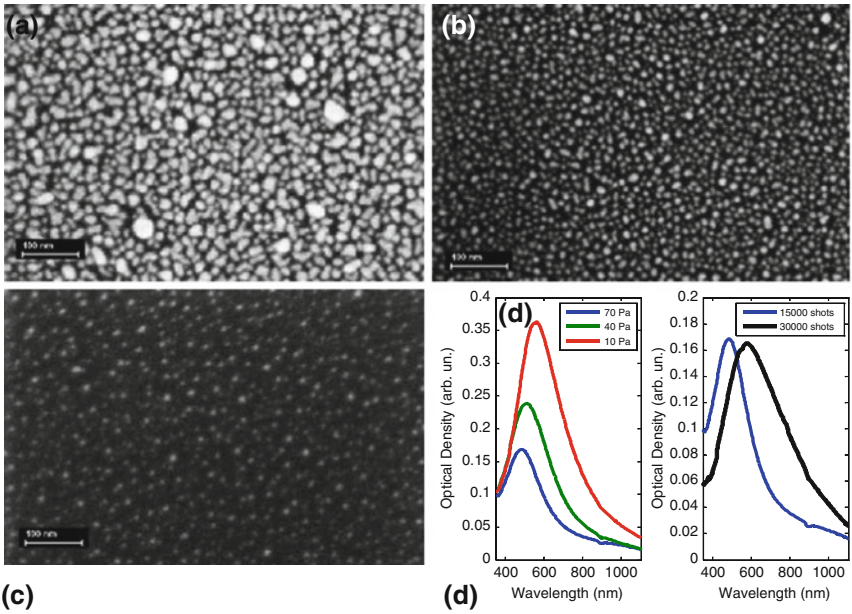

Fig. 20.1 SEM picture of the surface of the samples grown in Ar at **a** 10 Pa, **b** 40 Pa, **c** 70 Pa, using 15,000 laser shots. **d** Absorption spectra of the samples deposited at different Ar pressure and with different laser shots

aggregate. The different observed morphologies lead to different optical properties. Bulk silver shows an absorption peak in the near-UV, due to the coherent oscillations of surface electrons interacting with an external electromagnetic radiation, called surface plasmon resonance (SPR). When typical sizes are reduced to the nanoscale range, the SPR peak shifts to the visible region of the spectrum at about 390 nm. The position and shape of the SPR peak depend on size, shape and mutual aggregation properties of the nanostructures. In Fig. 20.1d are shown the UV–Vis absorption spectra of the samples deposited at different pressures. It can be observed that keeping fixed the number of laser shots at 15,000 and decreasing p_{Ar} from 70 Pa down to 10 Pa, the surface plasmon (SP) position red-shifts from 482 to 558 nm while its width progressively increases from 280 nm to more than 350 nm. A different behavior is observed for the plasmon position of the samples deposited at a fixed Ar pressure of 70 Pa.

The plasmon position red-shifts from 482 to 588 nm when the number of laser shots increases from 15,000 to 30,000. A larger broadening of the absorption band is evident for the sample grown at 30,000 pulses, highlighting that the film, deposited at the highest pulses number, consists of clustered NPs as observed from SEM images. A tuning of the plasmon position is then possible through both the laser pulses number and an appropriate Ar gas pressure. The SERS activity of the deposited film was tested soaking the samples for 1 h in rhodamine 6G (R6G)

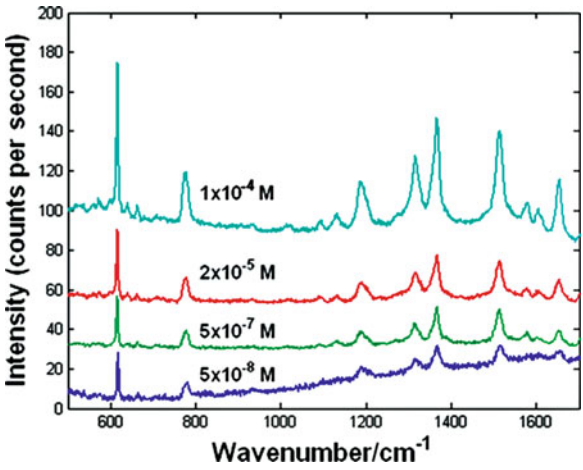

Fig. 20.2 Raman spectra of the sample deposited at 70 Pa of Ar with 30,000 laser shots at different concentration of R6G

diluted aqueous solution with different concentration (1×10^{-4}, 2×10^{-6}, 5×10^{-7} and 5×10^{-8} M), rinsed with deionized water and dried in air.

In Fig. 20.2 are reported the Raman spectra of the sample deposited at 70 Pa of Ar with 30,000 laser shots at different concentration of R6G. The spectra are normalized to their own integration times. R6G dye Raman features can be observed at 615, 777, 1189, 1314, 1366, 1513 and 1,651 cm^{-1} in the spectrum.

20.3.1 SERS Enhancement Factor

The quality of a SERS substrate can be evaluated by an estimate of the Raman enhancement factor (EF), defined as the ratio between the observed SERS intensity per molecule I_{SERS} and the normal Raman intensity per molecule I_R:

$$EF = \frac{I_{SERS}}{I_R}\frac{N_R}{N_{SERS}} \tag{20.1}$$

where N_R and N_{SERS} are the number of molecules which contribute to the normal Raman and the SERS intensities, respectively.

The Raman scattering cross section of R6G is of the order of 10^{-30} cm^{-2} and, since we were unable to detect any Raman signature in the spectra acquired on bare substrates soaked in the highest R6G aqueous solution, we evaluated the EF by comparing the Raman and the fluorescence intensities, according to the method described in [9]. In Fig. 20.3 is reported the Raman spectrum from a glass substrate covered with Ag NPs deposited in presence of 70 Pa of Ar and with 30,000 laser shots, soaked in the 1×10^{-4} M R6G solution, together with the spectrum acquired in the same experimental conditions but recorded on a bare glass substrate. The spectrum recorded from the bare substrate shows only the fluorescence contribution, while the other spectrum is characterized by the R6G features.

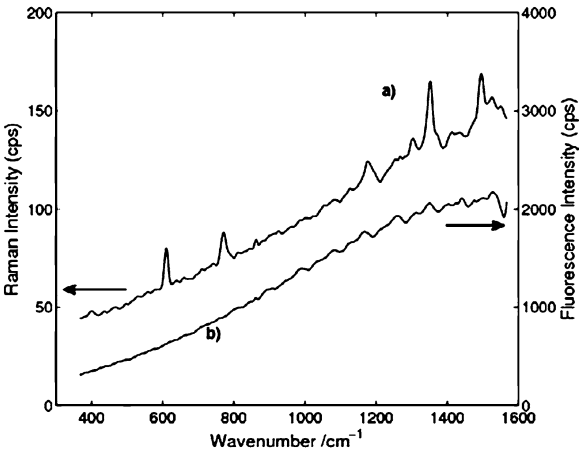

Fig. 20.3 Raman spectra of R6G adorbed (**a**) on a glass substrate covered with silver nanoparticles (70 Pa of Ar, 30,000 shots) and (**b**) on a bare substrate (R6G concentration 1×10^{-4} M)

The difference between the fluorescence intensity recorded in the two spectra is about an order of magnitude and is probably due to fluorescence quenching following the energy transfer from the excited electronic state to the metal surface. Thus, I_R can be now evaluated using the relationship between the Raman intensity and the fluorescence signal. The Raman and the fluorescence cross sections at 514.5 nm, i.e., in resonant condition, are 10^{-25} and 10^{-16} cm^2, respectively, so a factor of about 10^{-9} should be expected from the comparison of the two intensities. From Fig. 20.3 the intensity of the Raman peak at 1,360 cm^{-1} is about 38 cps while the corresponding fluorescence signal is 1,978 cps. Thus the Raman scattering cross section is about two orders of magnitude lower than the fluorescence cross section resulting in an EF of the order of 10^7.

20.4 Conclusions

We prepared, by pulsed laser ablation in presence of Ar gas, SERS active substrates suitable to detect the presence of R6G at concentrations as low as 5×10^{-8} M. Different surface morphologies, SP positions and hence SERS activities were obtained by controlling the laser pulses number and Ar gas pressure, keeping fixed all the other process parameters. The SERS enhancement factor was calculated to be about 10^7.

References

1. Kelly KL, Jensen TA, Lazarides AA, Schatz GC (2002) Modeling metal nanoparticle optical properties. In: Feldheim DL, Foss CA Jr (eds) Metal nanoparticles: synthesis, characterization and applications. Dekker, New York, p 89
2. Banholzer MJ, Millstone JE, Qin L, Mirkin CA (2007) Rationally designed nanostructures for surface-enhanced Raman spectroscopy. Chem Soc Rev 37:885–897

3. Qian XM, Nie SM (2007) Single-molecule and single-nanoparticle SERS: from fundamental mechanisms to biomedical applications. Chem Soc Rev 37:912–920
4. Jarvis RM, Goodacre R (2007) Characterization and identification of bacteria using SERS. Chem Soc Rev 37:931–936
5. Murgida DH, Hildebrandt P (2007) Disentangling interfacial redox processes of proteins by SERR spectroscopy. Chem Soc Rev 37:937–945
6. Fazio E, Neri F, Ossi PM, Santo N, Trusso S (2009) Ag nanocluster synthesis by laser ablation in Ar atmosphere: a plume dynamics analysis. Laser Particle Beams 27:281–290
7. Fazio E, Neri F, Ossi PM, Santo N, Trusso S (2009) Growth process of nanostructured silver films pulsed laser ablated in high-pressure inert gas. Appl Surface Sci 255:9676–9679
8. Bailini A, Ossis PM (2007) Expansion of an ablation plume in a buffer gas and cluster growth. Europhys Lett 79:35002
9. Gupta R, Weimer WA (2003) High enhancement factor gold films for surface enhanced Raman spectroscopy. Chem Phys Lett 374:302–306

Chapter 21
Inkjet Printed Chemical Sensors

F. Villani, I. A. Grimaldi, T. Polichetti, E. Massera, A. De Girolamo Del Mauro and G. Di Francia

Abstract Polymer nanocomposites (PNCs) represent a new class of sensing materials for volatile organic compounds (VOCs) detection. These materials can be simply processed by inkjet printing (IJP) technique, an emerging technology that has assumed a key role in the field of electronics wherever replacing conventional rigid substrates with flexible ones is required. In the present work, we fabricated PNCs chemical sensors inkjet printing a polystyrene (PS)/carbon black (CB) composite based ink on different substrates, flexible and not, such as polyethylene terephthalate (PET), glass and alumina. The sensors responses have been analyzed upon exposure to acetone organic vapors and compared in terms of sensitivity, response time and limit of detection.

21.1 Introduction

Polymer nanocomposites (PNCs) are a new category of materials consisting of an insulating polymer matrix where nanosized inorganic fillers are dispersed in. They combine the simple processability of polymers together with the conductivity and mechanical-stability properties of nanoparticles. The resultant hybrid system is attractive in several research sectors. Chemiresistors based on conductive PNCs are being used in sensing applications thanks to their simple transduction mechanism based on a change of their electric properties when they come into contact with a specific substance; in fact, due to the solvent absorption the polymer volume changes (swelling) [1–3], correspondingly the volumetric fraction of the conductive nanoparticles decreases [4], which reflects as a change of the electrical

F. Villani (✉) · I. A. Grimaldi · T. Polichetti · E. Massera · A. De Girolamo Del Mauro · G. Di Francia
ENEA Research Center, P.le E. Fermi 1, 80055, Portici (Na), Italy
e-mail: fulvia.villani@enea.it

G. Neri et al. (eds.), *Sensors and Microsystems*,
Lecture Notes in Electrical Engineering 91, DOI: 10.1007/978-94-007-1324-6_21,

conductivity. PNCs can be easily processed by techniques such as spin-coating or drop-casting and, recently, also by inkjet printing (IJP) technology, rapidly emerged as an innovative technique for the deposition of a wide variety of materials [5–8]. The advantages of IJP over the aforementioned techniques lie in its patterning capability, the efficient use of material, the reduced waste products and low cost of the process, and its potential for printing at ambient temperature with no contact or vacuum on both non-flexible and flexible substrates. As concerning this last item, the IJP technology has assumed a main role in the field of electronics wherever it is required to replace conventional non-flexible substrates with flexible ones. In the present work, VOCs chemical sensors have been fabricated by printing the PS/CB nanocomposite on different substrates, such as PET, glass, and alumina. The effect of the substrate morphology on the printed film quality and, hence, on the device performances has been investigated.

21.2 Experimental

The employed substrates (5 × 5 mm^2) were PET, glass and alumina. The electrodes have been realized by commercial sputtered ITO for both PET and glass substrates, and by evaporated Au in the case of alumina. The geometry of interdigitated contacts has been always defined patterning ITO or Au by conventional photolithography process. The sensing material is a nanocomposite composed by atactic polystyrene (PS, Sigma–Aldrich) and carbon black (CB, Black Pearls 2000-Cabot Co.). The PS polymer matrix (80 mg) has been dissolved in *n*-Methyl-2-pyrrolidinone (NMP) and the CB conductive filler (20 mg) has been dispersed in the polymeric solution (0.5 wt%) by means of ultrasonic bath. Bigger agglomerates have been removed by filtering the PS/CB suspension through a 0.2-μm filter. The final dispersion has been employed as ink and printed onto 50°C heated electrodes/substrate system. Sequences of overlapping droplets to create a line transverse to the fingers of the interdigitated electrodes have been printed by means of a piezoelectric Drop on Demand print-head (70 μm opening nozzle). The printed material has been investigated by optical micrographs and SEM analysis. The sensor response has been analyzed upon exposure to acetone organic vapors at different concentrations in a test chamber placed in a thermostatic box at controlled temperature and humidity.

21.3 Results and Discussion

Overlapped drops of nanocomposite based ink have been IJ-printed on patterned-ITO/PET and /glass substrates. The optical micrographs of the printed material, reported in Fig. 21.1, highlight the different wettability of the investigated ink/substrate systems. The spreading of the printed droplet depends on both substrate

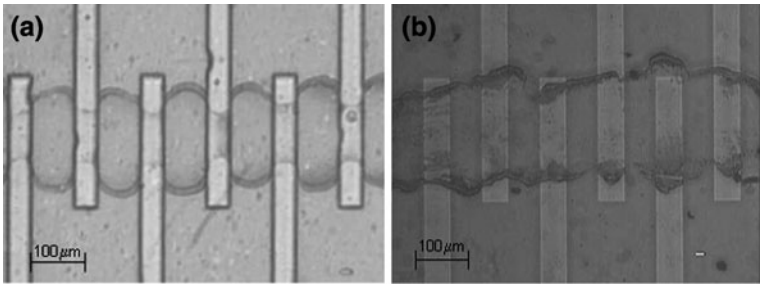

Fig. 21.1 Optical micrographs of the sensing material printed on PET (**a**) and glass (**b**) substrates

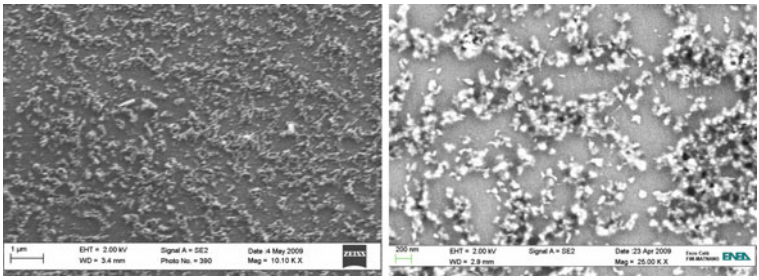

Fig. 21.2 SEM images of PS/CB nanocomposite based ink printed on PET (*left*) and glass (*right*) substrates

surface energies and roughness. In particular, ITO/PET higher roughness (average roughness 8.6 nm) induces a more regular printed pattern as compared to the profile printed onto ITO/glass (average roughness 2.4 nm). SEM images exhibit percolative paths of the conductive filler uniformly distributed on both the substrates (Fig. 21.2). The chemical sensor devices have been fabricated according to three different configurations with mono-, three- and five-overlapped layers with the aim of investigating the thickness effect on the sensor performances. By comparison, the same configurations have been performed on the interdigitated-Au/alumina system, extensively investigated in previous works [7, 8]. The devices electrical responses to acetone vapors are shown in Fig. 21.3a, b and c for PET, glass and alumina substrates, respectively. The parameters that characterize the sensor performances, such as base resistance, sensitivity, lower detection limit (LdL) and time response, are summarized in Tables 21.1, 21.2 and 21.3 for each substrate. For all the substrates, the results indicate that the dynamic responses of the five-layers sensors, the devices with smaller base resistance, are characterized by higher sensitivity and minimum LdL values as compared with the sensors fabricated with a lower layers number. Moreover, the five-layers devices electrical responses do not reach the saturation condition at higher analyte concentration due to the change of the adsorption kinetic of the systems characterized by lower

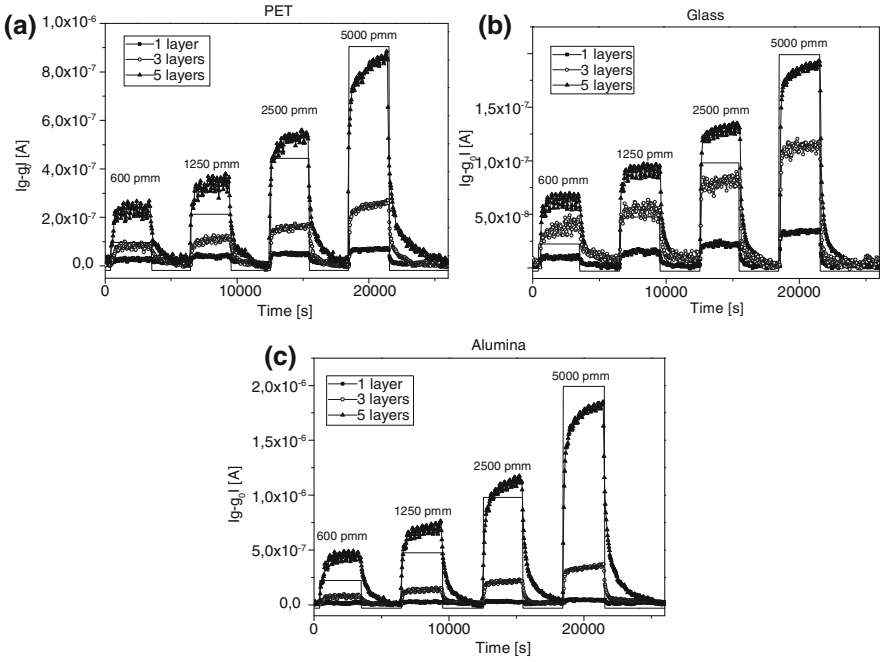

Fig. 21.3 Electrical responses to acetone vapors of one-, three- and five-layers sensors on PET (**a**), glass (**b**) and alumina (**c**)

Table 21.1 Electrical response parameters of the sensors on PET

PET	Resistance (KΩ)	Sensitivity (S/ppm)	Lower detection Limit (LdL) (ppm)	Time response (s)
One layer	230	8.86e-12	800	200
Three layers	70	3.86e-11	300	200
Five layers	17	1.36e-10	100	250

Table 21.2 Electrical responses parameters of the sensors on glass

Glass	Resistance (KΩ)	Sensitivity (S/ppm)	Lower detection Limit (LdL) (ppm)	Time response (s)
one layer	300	5.42e-12	300	100
Three layers	105	1.7e-11	200	100
Five layers	90	2.9e-11	50	100

surface/volume ratio. Finally, it is evident that the response times of the sensors printed on PET are slightly higher than those fabricated on the other substrates. This behaviour can be attributed to the different morphology of the printed material, which is directly correlated to the ink-substrate interaction.

Table 21.3 Electrical responses parameters of the sensors on alumina

Alumina	Resistance (KΩ)	Sensitivity (S/ppm)	Lower detection Limit (LdL) (ppm)	Time response (s)
One layer	200	6.0e-12	2000	100
three layers	40	5.8e-11	86	100
five layers	9	3,05e-10	50	100

21.4 Conclusions

In the present work, we fabricated polymer nanocomposites chemical sensors on different, flexible and not, substrates and investigated how their performances are related to substrate wettability. The sensing material has been deposited by means of ink-jet printing technique in three different configurations, one-, three- and five-layers. The results indicate that the dynamic responses of the five-layers sensors have got the higher sensitivity and minimum LdL values, regardless of substrate. Moreover, the sensors printed onto PET are slower than the other devices probably due to the different morphology of the printed material.

Acknowledgments This work was supported by the TRIPODE project (DM 20160) financed by the Ministero dell'Università e della Ricerca (MUR).

References

1. Chatzandroulis S, Goustouridis D, Raptis I (2005) Characterization of polymer films for use in bimorph chemical sensors. J Phys Conf Series 10:297
2. Goustouridis D, Manoli K, Chatzandroulis S, Sanopoulou M, Raptis I (2005) Characterization of polymer layers for silicon micromachined bilayer chemical sensors using white light interferometr. Sens Actuators B 111:549–554
3. Convertino A, Leo G, Tamborra M, Sciancalepore C, Striccoli M, Curri ML, Agostano A (2007) TiO_2 colloidal nanocrystals functionalization of PMMA: a tailoring of optical properties and chemical adsorption. Sens Actuators B126:138–143
4. Carrillo A, Martin-Dominguez IR, Marquez-Lucero A (2006) Modeling and experimental testing of the effect of solvent absorption on the electric properties of styrene butadiene rubber/carbon black chemical sensors. Sens Actuators B 113:477–486
5. Ballarin B, Fraleoni-Morgera A, Frascaro D, Marazzita S, Piana C, Setti L (2004) Thermal inkjet microdeposition of PEDOT:PSS on ITO-coated glass and characterization of the obtained film. Synth Met 146:201–205
6. Yoshioka Y, Jabbour GE (2006) Desktop inkjet printer as a tool to print conducting polymers. Synth. Met 156:779–783
7. Loffredo F, Burrasca G, Quercia L, Della Sala D (2007) Gas sensor devices obtained by ink-jet printing of polyaniline suspension. Macromol Symp 247:357–363
8. Loffredo F, De Girolamo Del Mauro A, Burrasca G, La Ferrara V, Quercia L, Massera E, Di Francia G, Della Sala D (2009) Ink-jet printing technique in polymer/carbon black sensing device fabrication. Sens Actuators B 143:421–429

Chapter 22
Synthesis, Characterization and Sensing Applications of Nanotubular TiO_2-Based Materials

G. Neri, A. Bonavita, G. Micali, G. Centi, S. Perathoner, R. Passalacqua, Marc-Georg Willinger and N. Pinna

Abstract TiO_2-based nanotubular materials have been synthesized by different methods, i.e. anodic oxidation of Ti foils, hydrothermal process and atomic layer deposition of titania on carbon nanotubes. The effect of the different synthesis methods on the final characteristics of the nanotubular materials obtained have been evaluated by a detailed morphological and microstructural investigation carried out by SEM, TEM and XRD. Films of the synthesized nanotubular TiO_2, deposited on QCM substrates, have shown a promising potential for the monitoring of hydrogen at room temperature.

22.1 Introduction

Nanotubular materials are characterized by extraordinary electrical properties providing prototypical systems to study physics at the nanoscale. They also promise exciting new opportunities and challenges for potential applications in electronic devices, photocatalysis, electrodes for fuel cells and batteries,

G. Neri (✉) · A. Bonavita · G. Micali · G. Centi · S. Perathoner · R. Passalacqua
Dip. Chimica Industriale e Ingegneria dei Materiali, Università di Messina,
Contrada di Dio, S. Agata di Messina, 98166 Messina, Italy
e-mail: neri@ingegneria.unime.it

M.-G. Willinger · N. Pinna
Department of Chemistry, CICECO, University of Aveiro, 3810-193 Aveiro, Portugal

N. Pinna
World Class University (WCU) program of Chemical Convergence for Energy & Environment (C2E2), School of Chemical and Biological Engineering,
College of Engineering, Seoul National University (SNU), Seoul 151-744, Korea

G. Neri et al. (eds.), *Sensors and Microsystems*,
Lecture Notes in Electrical Engineering 91, DOI: 10.1007/978-94-007-1324-6_22,

dye-sensitized solar cells and sensors. Among the nanotubular materials, carbon nanotubes (CNTs) have shown an impressive impulse since their first synthesis in 1991. In recent years, research on nanotube materials have developed into new areas, comprising inorganic and organic/inorganic hybrid nanotubes [1].

Metal oxide-based nanotubes, such as SnO_2, V_2O_5 or TiO_2 are particularly interesting in view of their application in chemical sensors [2]. In this communication we focused our attention on the preparation of TiO_2-based nanotubular materials by different approaches. Specifically, TiO_2 nanotubes have been prepared either by a hydrothermal process and anodic oxidation of Ti foils [3]. Hybrids TiO_2/CNTs nanotubular composites have been also prepared by a novel atomic layer deposition (ALD) process, which allows the coating of CNTs at low temperature, with a precise thickness control at nanometer level, smooth surface, and excellent conformality [4, 5].

The nanostructure of the synthesized TiO_2-based materials was then investigated by SEM, TEM and XRD, with aim to study the effects of the different synthesis conditions on the characteristics of final products. At last, films of the synthesized TiO_2-based nanotubular materials were investigate regarding their hydrogen sensing properties at room temperature.

22.2 Experimental

TiO_2 nanotubes-based materials have been prepared by the following approaches: (1) anodic oxidation of Ti foils; (2) hydrothermal process; (3) coating of CNTs.

Anodic oxidation of Ti foils has been carried out in a stirred electrochemical cell, at room temperature and atmospheric pressure. An Autolab PGSTAT30 potenziostat in a two electrode set-up was used to apply different anodizing voltages: 50 V for times of about 3 h 1/2 in ethylene glycol electrolyte with 0.3 wt% NH_4F and H_2O 2% vol. A platinum electrode served as a cathode.

The synthesis of TiO_2 nanotubes has been performed by a hydrothermal process in a Teflon-lined autoclave at temperatures ranging from 90 to 190°C for 3 days. The starting material, consisting in 0.5 g of tanium dioxide powder, was dispersed in 13 ml, 10 M NaOH aqueous solution pH 6 with deionized water under vacuum. After the synthesis the resulting suspension was washed until and the powders finally dried at 300°C for 20 h in air.

The synthesis of TiO_2/CNTs was done in an ALD reactor working in exposure mode from titanium isopropoxide and acetic acid. Applied Science nanotubes were used as support and treated with concentrated HNO_3 at 100°C for 2 h before deposition. By using carboxylic acids as oxygen source instead of the more traditionally used ones (e.g. water, ozone, oxygen, etc.) titania coating can be grown from the metal alkoxide precursor even at low temperatures.

The morphology and microstructure of the samples were investigated by SEM, TEM and XRD.

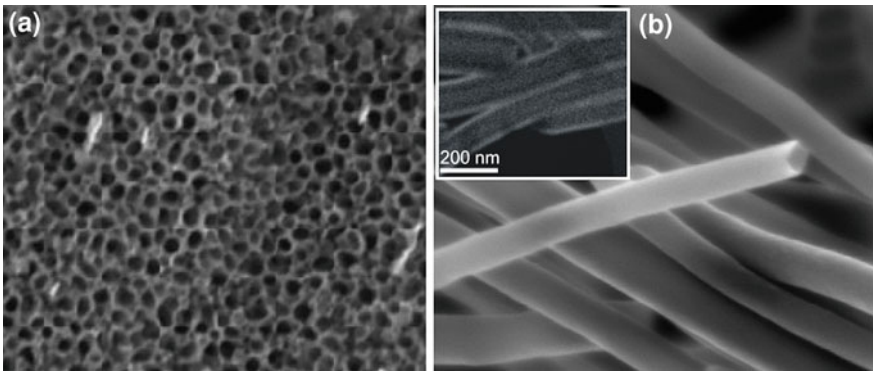

Fig. 22.1 SEM images of nanotubular TiO_2 prepared by: **a** anodic oxidation; **b** atomic layer deposition. Inset shows a TEM image of the same sample

22.3 Results and Discussion

The morphological study carried out by SEM and TEM, has shown the effects of the different synthesis approaches on the final characteristics of the nanotubular materials obtained. The morphology of the prepared TiO_2 nanotubes by anodic oxidation of Ti foils is characterized by an ordered array of vertically aligned 1D nanostructures, as shown in Fig. 22.1a. Hybrids TiO_2/CNTs nanotubular composites prepared by a novel ALD process, are shown in Fig. 22.1b. It can be observed that an homogeneous coating of titania is deposited onto the surface of functionalized carbon nanotubes. TEM clearly prove that the tubes are coated not only on the outer surface but also on the inside (see inset in Fig. 22.1b).

Due to the nanotubular structure with open ends, the synthesized samples show a high surface area (for example, BET give 260 m^2/g for nanotubes prepared by the hydrothermal process at 150°C).

As the morphological and structural features above illustrated can favour the adsorption of gaseous molecules, we decided to investigate the capability of these nanostructures to monitor hydrogen by means of quartz crystal microbalance (QCM) sensors. Hydrogen is largely used in the chemical, petrochemical and semiconductor industry, therefore the development of reliable hydrogen sensors is strongly demanded.

Preliminary hydrogen sensing tests were carried out with a gravimetric QCM sensor, coated with a sensing layer of TiO_2 nanotubes prepared through anodic oxidation of Ti foils, operating at room temperature. As shown in Fig. 22.2, the frequency of the QCM device decreases after a pulse of hydrogen in the nitrogen carrier, due to the mass increase consequently to hydrogen adsorption. The sensor response is fast (around 200 s), suggesting a strong adsorption of the hydrogen on the TiO_2 tubular nanostructure. The recovery time observed is instead longer. Moreover, a partial irreversibility of the desorption process is also noted, likely related to the well known ability of titania to bind strongly hydrogen molecules.

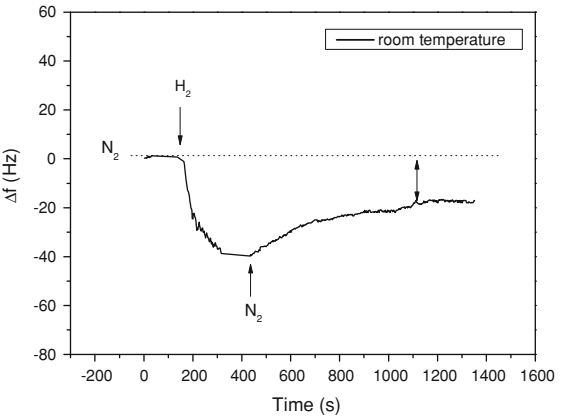

Fig. 22.2 Transient response of a QCM sensor coated with TiO_2 nanotubes prepared through anodic oxidation during a hydrogen pulse

Further experiments are in progress with aim to better understand the phenomena observed.

22.4 Conclusion

Different nanotubular titania structures have been synthesized and widely characterized. Preliminary sensing tests have shown the promising properties of these nanostructures for hydrogen detection at room temperature by means of microgravimetric sensors. Further work is in progress in order to investigate the adsorption mechanism of hydrogen and enhance the performance of the QCM sensor, for example by a suitable metal doping of the TiO_2-based nanotubular structure.

References

1. Liu SM, Gan LM, Liu LH, Zhang WD, Zeng HC (2002) Synthesis of single-crystalline TiO_2 nanotubes. Chem Mater 14:1391–1397
2. Wei M, Konishi Y, Zhou H, Sugihara H, Arakawa H (2005) Formation of nanotubes TiO_2 from layered titanate particles by a soft chemical process. Solid State Commun 133:493–497
3. Centi G, Passalacqua R, Perathoner S, Su DS, Weinberg G, Schlogl R (2007) Oxide thin films based on ordered arrays of 1D nanostructure. A possible approach toward bridging material gap in catalysis. Phys Chem Chem Phys 9:4930–4938
4. Rauwel E, Clavel G, Willinger M-G, Rauwel P, Pinna N (2008) Non-aqueous routes to metal oxide thin films by atomic layer deposition. Angew Chem Int Ed 47:3592–3595
5. Willinger M-G, Neri G, Rauwel E, Bonavita A, Micali G, Pinna N (2008) Vanadium oxide sensing layer grown on carbon nanotubes by a new atomic layer deposition process. Nano Lett 8:4201–4204

Part III
Devices

Chapter 23
Detection of a Tumor Marker in Serum by an Electrochemical Assay Coupled to Magnetic Beads

Q. A. M. Al-Khafaji, S. Tombelli, S. Laschi, G. Marrazza, M. Mascini and N. A. M. Mohammed

Abstract The goal of this work was to design a sandwich assay with electrochemical transduction for the detection of a tumor marker, human epidermal growth factor receptor 2 (HER2), using a simple target capturing step by antibody-functionalised magnetic beads. The HER2 proto-oncogene is amplified and/or overexpressed in approximately 20–25% of invasive breast cancers. The assay is based on a sandwich format in which a primary monoclonal antibody anti-HER2 is coupled to protein A modified magnetic beads. The modified beads are then used to capture the protein from the sample solution and the sandwich assay is performed by adding a secondary monoclonal antibody anti-HER2 labelled with biotin. The enzyme alkaline phosphatase (AP) conjugated with streptavidin and its substrate (α-naphthyl-phosphate) are then used for the electrochemical detection by differential pulse voltammetry (DPV). The conditions for the antibody immobilization and for the protein binding have been first optimised. The performance of the assay in terms of sensitivity, reproducibility and selectivity has been studied in buffer.

Q. A. M. Al-Khafaji · S. Tombelli · S. Laschi · G. Marrazza · M. Mascini (✉)
Dipartimento di Chimica Ugo Schiff, Università degli Studi di Firenze,
Via della Lastruccia 3, 50019, Sesto Fiorentino, Italy
e-mail: marco.mascini@unifi.it

Q. A. M. Al-Khafaji · N. A. M. Mohammed
Al-Nahrain Medical College, Baghdad, Iraq

G. Neri et al. (eds.), *Sensors and Microsystems*,
Lecture Notes in Electrical Engineering 91, DOI: 10.1007/978-94-007-1324-6_23,

23.1 Introduction

HER2 (also known as neu, ErbB-2, ERBB2) stands for "Human Epidermal growth factor Receptor 2" and is a protein giving higher aggressiveness in breast cancers. It is a member of the ErbB protein family, more commonly known as the epidermal growth factor receptor family [1].

The HER2 oncogene is a tyrosine kinase receptor that is over-expressed in approximately 20–30% of high-grade invasive breast carcinomas and has been shown to be a valuable prognostic indicator [2]. HER2 positive tumors can be more aggressive and their status can predict response to targeting therapy such as chemotherapy. Knowing that a cancer is HER2 positive helps a medical team to select the appropriate treatment.

In this paper an electrochemical immunoassay is proposed as a screening device for the detection of HER2. The proposed approach uses disposable screen-printed electrodes as transducers and a simple target capturing step by antibody-functionalised magnetic beads [3].

23.2 Materials and Methods

All the reagents for the buffers and EDTA were from Merck (Milan, Italy). The protein HER2, the monoclonal antibody anti-HER2 and the biotinylated polyclonal antibody anti-HER2 (R&D Systems) were purchased from Space srl (Milan, Italy). Bovine serum albumin (BSA), streptavidin–alkaline phosphatase conjugated, α-naphtyl phosphate, were from Sigma (Milan, Italy). Protein A-coated magnetic beads were purchased from Invitrogen (Milan, Italy).

Electrochemical measurements were performed using a μAutolab type II PGSTAT with a GPES 4.9 software package (Metrohm, Italy). All measurements were carried out at room temperature by using Differential Pulse Voltammetry (DPV) with the following parameters: range potential 0/+600 mV, step potential 7 mV, modulation amplitude 70 mV, standby potential 200 mV, interval time 0.1 s. Carbon-based screen-printed electrochemical sensors were printed in house using a High Performance Multi Purpose Precision Screen Printer DEK 245 (DEK, Weymouth, UK), using different thermoplastic inks.

23.3 Procedure

A sandwich assay for HER2 detection was developed, following the scheme reported in Fig. 23.1.

All the steps were performed at room temperature and the washing and coating phases were carried out under delicate stirring in the sample mixer.

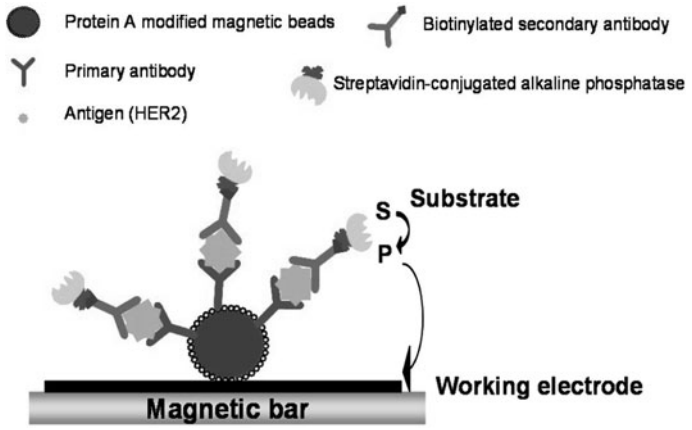

Fig. 23.1 Scheme of the sandwich immunoassay onto screen printed electrochemical sensors

Magnetic beads coated with protein A were completely re-suspended and a suspension of 100 μL of the beads was introduced in a tube containing 400 μL of primary antibody solution. After 30 min of incubation, the tube was positioned on a magnetic block to allow the precipitation of the beads on the bottom of the test tube; the supernatant was then removed and the beads were washed twice with PBS pH 7.4 containing 0.02% Tween 20. The antibody-coated beads could also be prepared in advance and kept at +4°C for several days. 50 μL of suspension containing the primary antibody-coated beads were mixed with 450 μL of solution containing HER2 at different concentrations in 20 mM Tris pH 7.3, 150 mM NaCl. After 30 min or 1 h of incubation time, the beads were magnetically separated to remove the supernatant and then washed twice using Tris buffer. After the binding of HER2, the beads were re-suspended in 500 μL of secondary antibody solution in Tris buffer for 30 min or 1 h and then separated and washed twice using Tris. The beads carrying the affinity complex (primary antibody-analyte-secondary antibody) were re-suspended in 500 μL of streptavidin–alkaline phosphatase conjugated (2.23 U/mL) in Tris buffer for 10 min. After separation and washing, the beads were re-suspended in 50 μL of Tris buffer. For the electrochemical detection, 10 μL of the beads suspension were transferred onto the surface of the working electrode of a screen-printed electrochemical sensor. To better localise the beads, the magnetic block was placed on the bottom of the electrode. Then 60 μL of a solution containing the enzymatic substrate (α-naphtyl phosphate) 1 mg/mL in detection buffer (0.1 M diethanolamine buffer containing 1 mM $MgCl_2$, 100 mM KCl and 0.1% pH 9.6) were deposited on the screen-printed strip. After 5 min, the enzymatic product was determined by DPV.

Table 23.1 Optimization of the secondary antibody concentration

	HER2 0 ng/mL (μA)	HER2 10 ng/mL (μA)	HER2 50 ng/mL (μA)
Secondary Ab 0.5 mg/L	0.15 ± 0.03	0.66 ± 0.13	0.48 ± 0.01
Secondary Ab 1 mg/L	0.49 ± 0.03	0.77 ± 0.01	1.07 ± 0.02

23.4 Results and Discussion

The sandwich assay was optimised with respect to several parameters such as concentration of primary and secondary antibodies, incubation time of antigen and secondary antibody, blocking agent. In Table 23.1 we report the optimization of the concentration of the secondary antibody. The optimization was performed by testing the blank and two concentrations of HER2 (10 and 50 ng/mL) with two different concentrations of secondary antibody (0.5 and 1 mg/L). Better performances both in terms of reproducibility and response linearity were obtained with a 1 mg/L of secondary antibody concentration.

The final conditions for the assay were: 100 mg/L primary antibody, 1 mg/L secondary antibody, 1 h antigen incubation time, 0.5% BSA as blocking agent. The sandwich assay was performed using HER2 standard solutions in the concentration range 2.5–25 ng/mL (Fig. 23.2). The assay was repeated in order to evaluate the reproducibility; at this purpose, three repetitions of each standard solution were carried out. The average coefficient of variation was 7%, calculated as mean of all the concentrations considered. The limit of detection (LOD) of the assay was evaluated as minimum detectable concentration and was calculated by

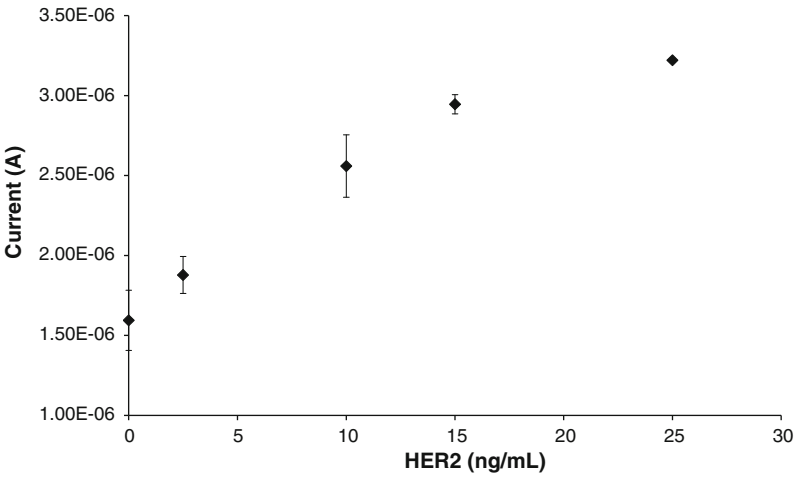

Fig. 23.2 Calibration curve for HER2. The points correspond to the current ± SD calculated for $n = 3$ repetitions

the evaluation of the average response of the blank plus three times the standard deviation; in this case the recorded blank signal was 1.59 ± 0.19 μA, leading to a LOD of 1.7 ng/mL.

Preliminary experiments were conducted on commercial normal human serum diluted 1:5 and spiked with two concentrations of HER2 (15 and 25 ng/mL). The results evidenced the possibility to distinguish between non-spiked serum and serum spiked with HER2 and to distinguish between the two concentrations of HER2 added to serum.

23.5 Conclusions

The different parameters of the assay were optimised and a first calibration was produced in buffer with good sensitivity (1.7 ng/mL) and reproducibility (average CV% = 7%). The reached detection limit is adequate for the analysis of serum samples since 15 ng/mL was defined as the appropriate cut-off between normal and elevated serum HER2 protein levels. Further experiments will be conducted to optimise the measurements in serum and the assay will be then applied to the analysis of serum samples from hospital patients.

References

1. Cussens L et al (1985) Tyrosine kinase receptor with extensive homology to EGF receptor shares chromosomal location with neu oncogene. Science 230:1132–1139
2. Kushlinskii NE, Shirokii VP, Gershtein ES, Yermilova VD, Chemeris GY, Letyagin VP (2007) Soluble fragment of HER2/neu receptor in the serum of patients with breast cancer with different levels of this protein expression in the tumor. Bull Exp Biol Med 143:449–451
3. Centi S, Laschi S, Mascini M (2007) Improvement of analytical performances of a disposable electrochemical immunosensor by using magnetic beads. Talanta 73:394–399

Chapter 24
Smart Multichannel Flow Sensor with Temperature and Pressure Compensation

P. Bruschi, M. Dei, F. Butti and M. Piotto

Abstract A compact sensor for measuring multiple gas flows has been designed and fabricated. The device consists in a single silicon chip where three independent flow sensing structures have been included. The sensing structures are differential micro-calorimeters, equipped with double heaters in order to perform drift-free offset compensation. The chip includes also a versatile electronic interface including a low noise chopper amplifier and an original closed loop heater driver capable of reducing the effects of pressure variations on the flow measurement. The chip has been designed using the BCD6s process of STMicroelectronics. A post-processing step, based on anisotropic etching, is required to complete the smart sensor fabrication.

24.1 Introduction

Microfluidic devices have received considerable interest for their wide field of applications. Wearable systems for autonomous drug delivery, microreactors for chemical synthesis [1] and miniaturized low cost instruments for biological analysis are among the most emerging applications requiring microfluidic devices. Integrated micro flow sensors have been among the first successful examples of Micro-Electro Mechanical Systems (MEMS). Nevertheless, very few commercial products based on integrated flow meters have been proposed so far. This is partly due to limitations still affecting existing devices, such as large intrinsic offset and

P. Bruschi (✉) · M. Dei · F. Butti
Dipartimento di Ingegneria dell'Informazione, via G. Caruso, 16, 56122, Pisa, Italy
e-mail: p.bruschi@iet.unipi.it

M. Piotto
IEIIT – Pisa, CNR, via G. Caruso, 16, 56122, Pisa, Italy

G. Neri et al. (eds.), *Sensors and Microsystems*,
Lecture Notes in Electrical Engineering 91, DOI: 10.1007/978-94-007-1324-6_24,

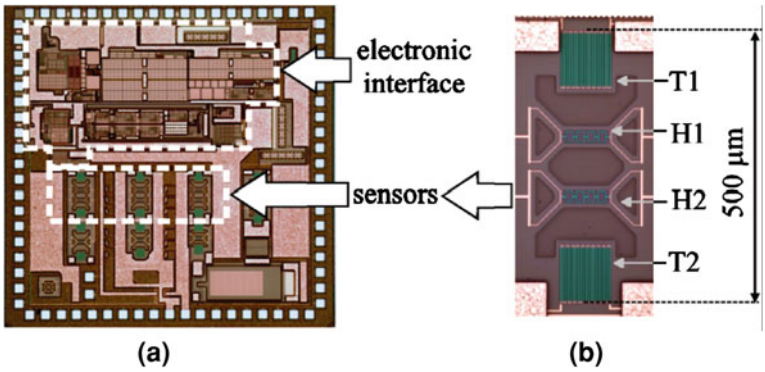

Fig. 24.1 Optical micrograph of the whole chip (**a**) and enlargement of one sensing structure (**b**) with the main elements indicated: H1, H2: heaters; T1, T2: thermopiles

pressure dependence. These aspects limits the potential capability of these sensors of detecting minimal flow rates, which is a critical operation frequently required in microfluidic systems that cannot be accomplished with traditional devices. An interesting example is represented by in the feed lines for ionic and cold gas thrusters, used for controlling the attitude of small artificial satellites [2].

In this work we propose the design and electrical characterization of a smart flow meter consisting of a single $3.8 \times 3.8\ mm^2$ silicon chip including three independent flow sensing structures and an electronic analog interface capable of driving the sensors, reading the signal and correcting the offset and pressure sensitivity of the sensors.

24.2 Device Description

Figure 24.1a shows an optical micrograph of the chip prior to the post-processing step. It is possible to recognize the electronic interface and the three sensing structures that can be connected to the latter through an on-chip four-way analog multiplexer. An optical micrograph of one sensing structure is shown Fig. 24.1b. These devices are composed by two temperature probes (thermopiles T1, T2) symmetrically placed across two heaters (polysilicon resistors H1, H2).

The output signal is the difference between the voltages produced by two thermopiles. The double heater structure allows offset compensation by introducing a proper power unbalance between the heaters [3].

The chip has been designed and fabricated using the Bipolar-CMOS-DMOS process BCD6s of STMicroelectronics. A micromachining step, based on selective anisotropic etching of the bulk silicon, is required to thermally insulate the sensor elements from the substrate. This step is identical to that applied to previous version of the device [4]. The position of the sensors has been chosen to facilitate

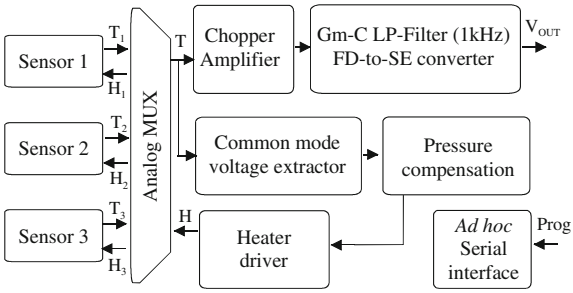

Fig. 24.2 Block diagram of the on-chip integrated interface

the packaging technique described in Ref. [5], successfully applied to the fabrication of two channel flow meters.

A simplified block diagram of the integrated electronic interface is shown in Fig. 24.2. As stated above, the sensors are connected to interface through an analog multiplexer, controlled by two selection bits. Alternatively, the interface can be connected to external pads for characterization or connection to an off-chip sensor. The sensor differential voltage, carrying information on the measured flow, is amplified by a chopper amplifier and filtered by a fully integrated low pass filter with 1 kHz roll-off frequency. The role of the filter is suppressing the amplifier output offset modulated by the clock signal. In addition to the differential voltage, also the thermopile common mode voltage is read, since it has been demonstrated [6] to be a useful indicator of the gas pressure. According to a recently introduced approach [7], the pressure variations can be extracted from the corresponding variations of the common mode voltage and used to modulate the heater power in order to cancel the effect of pressure on the output (differential) voltage.

The heater driver produces two currents feeding the two heaters of the sensing structures. The sum of the two currents is proportional to the input voltage while their difference (power unbalance) is digitally controlled in order to compensate for the sensor structural offset [3].

24.3 Readout Interface Characterization

The interface characterization has been performed on unprocessed chips that have been packaged into standard DIL28 cases and wedge bonded. The experiments have been carried out using a HP4145B parameter analyzer. The power supply voltage was set to 3.3 V and the total current consumption was 4 mA. The 32 bit internal register was programmed using a microcontroller Analog Devices ADuC847 connected to a Personal Computer via serial port. All the tests have been performed connecting the input of the interface to external pins through the analog MUX.

Figure 24.3a shows the response of the differential amplifier for different gain settings ranging from 160 to 1000. The output linearity spans by ±1 V wide

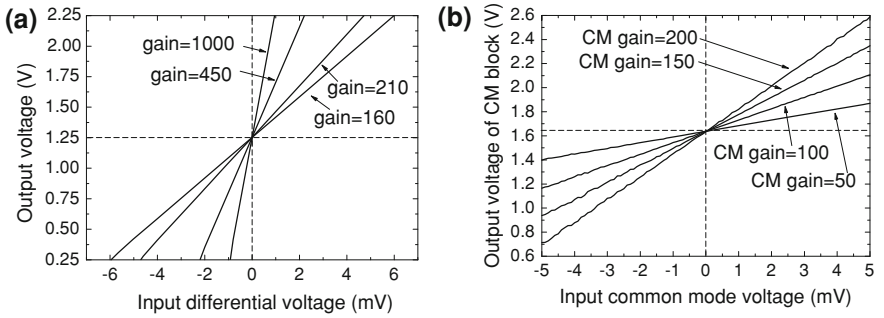

Fig. 24.3 Response of the differential amplifier (**a**) and common mode estimator block (**b**) for various gain settings

around the zero level. The latter has been set to 1.25 V, coinciding with the mid point of the ADuC microcontroller ADCs. The input referred offset voltage of the chopper amplifier was less than 2 μV. The correct operation of the common mode extractor and amplifier is proven by Fig. 24.3b. In this case, the zero level has been fixed to Vdd/2 for optimal interfacing with the pressure compensation block. The possibility of digitally varying the gains improves the adaptability of the interface with respect to a wide range of external sensors.

24.4 Conclusions

A smart sensor, including several flow sensing microstructures and a versatile electronic interface on the same chip, has been designed and fabricated. The interface incorporates several functions that, so far, were implemented only by means of relatively large printed board circuits. These functions were aimed at improving the precision and detection limit of the sensor, through drift free offset compensation and reduction of the sensitivity to pressure. A detailed characterization of the electronic interface has been performed, obtaining a complete agreement with the initial specifications. The devices will be completed by means of post-processing and packaging steps similar to those described in [4].

Acknowledgments The authors would like to thank the R&D group of the STMicroelectronics of Cornaredo (MI, Italy) for fabrication of the chips described in this work.

References

1. Shin WC, Besser RS (2006) A micromachined thin-film gas flowsensor for microchemical reactors. J Micromech Microeng 16:731–741

2. Matticari G, Noci GE, Siciliano P, Colangelo G, Schmidt R (2006) Cold gas micro propulsion prototype for very fine spacecraft attitude/position control. In: Proceedings of AIAA/ASME/SAE/ASEE 42nd joint propulsion conference, Sacramento, USA, pp 5378–5390, July
3. Bruschi P, Dei M, Piotto M (2009) Offset compensation of integrated thermal flow sensors by means of split heater microstructures. In: Proceedings of DTIP 09, Rome, Italy, pp 433–436, April
4. Bruschi P, Piotto M, Bacci N (2009) Postprocessing, readout and packaging methods for integrated gas flow sensors. Microelectron J 40:1300–1307
5. Bruschi P, Dei M, Piotto M (2009) A single chip, double channel thermal flow meter. Microsyst Technol 15:1179–1186
6. Bruschi P, Piotto M, Barillaro G (2006) Effects of gas type on the sensitivity and transition pressure of integrated thermal flow sensors. Sens Actuators A 131:182–187
7. Bruschi P, Dei M, Piotto M (2011) A method to compensate the pressure sensitivity of integrated thermal flow sensors. IEEE Sens J 11:1162–1168

Chapter 25
Field Effect Transistor Sensing Devices Employing Lipid Layers

S. Cotrone, M. D. Angione, M. Magliulo, N. Cioffi, R. Pilolli, G. Palazzo, L. Torsi, A. Mallardi, D. Fine and A. Dodabalapur

Abstract Field-Effect Transistors comprising layers of lipids have been developed and characterized from the electrical point of view. Lipid layers-OTFT are proposed as novel devices for perspective application in the detection of analytes from aqueous samples.

25.1 Introduction

Electronic transduction of bio-recognition events can provide new perspectives for the development of Organic Thin Film Transistor (OTFT) devices. Solid state sensors, such as resistors or transistors, potentially offer the advantage of allowing an "on-line" monitoring of the critical process parameters. OTFTs can be operated as potentially multi-parameter responsive systems, also in a sensing circuits

S. Cotrone · M. D. Angione · M. Magliulo · N. Cioffi (✉) · R. Pilolli · G. Palazzo
L. Torsi
Dipartimento di Chimica, Università degli Studi di Bari, via Orabona 4,
70126 Bari, Italy
e-mail: Cioffi@Chimica.Uniba.It

A. Mallardi
Istituto per i Processi Chimico-Fisici (IPCF), CNR-Bari, Messina, Italy

D. Fine
The Department of NanoMedicine and BioMedical Engineering,
The University of Texas Health Science Center at Houston, Houston, TX, USA

A. Dodabalapur
Department of Electrical and Computer Engineering, Microelectronics Research Center,
The University of Texas at Austin, Austin, TX, USA

G. Neri et al. (eds.), *Sensors and Microsystems*,
Lecture Notes in Electrical Engineering 91, DOI: 10.1007/978-94-007-1324-6_25,

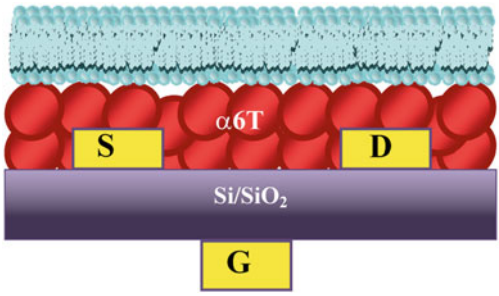

Fig. 25.1 Schematic representation of a lipid layers OTFT

configuration [1]. The smart use of a field-effect device for sensing applications appeared useful also to produce sensors with high repeatability [2]. Exposure of the organic active layer to an analyte leads to charge trapping which prevents the full base line recovery. OTFT sensors exhibited extremely good response repeatability, and their relative sensor response was in the range from 5 to 15%, for 10–100 ppm analyte concentrations, while measurements were carried out at room temperature and in regular laboratory atmosphere [3, 4]. Besides the field-induced response enhancement, also a field-induced sensitivity enhancement has been very recently demonstrated [5]. The OTFT sensitivity can be increased by orders of magnitude and the "turn-on" of the sensitivity occurs in the accumulation mode regime beyond the threshold voltage. This field-induced sensitivity enhancement lead to chiral differential detection, in the vapour phase, at unprecedented low concentrations, i.e. at the low ppm level: three order of magnitude lower than state-of-the-art values [6, 7].

25.2 Device Structure and Electrical Characterization

In the present study, a totally innovative OTFT device has been realized, by fully integrating in the electronic device a lipid layers structure specifically appointed for bio-sensing applications allowing processing in liquid samples.

In particular, a bottom gate, bottom contact OTFT device, whose structure is reported in Fig. 25.1, was fabricated using a SiO_2/n-doped Si substrate. The silicon substrate with a gold pad acts as the gate contact (G) while the silicon dioxide is the gate dielectric. The dielectric surface was covered by a α6T thin-film deposited by thermal evaporation at a low pressure of 5×10^{-7} Torr, with the substrate kept at room temperature. The final thickness of the organic semiconductor film was of 50 nm. To realize the lipid layers, 10 μl of the liposome solution were deposited by drop casting technique, directly over the organic semiconductor active layer. The solution was left to evaporate in nitrogen atmosphere over night.

Previous example of such a device configuration was carried out by X. Zhou and P.L. McEuen at the Cornell University. In this case, a supported lipid bilayer was realized on single-walled carbon nanotubes transistors and the device was used to detect the specific binding of proteins to membrane-embedded targets [8].

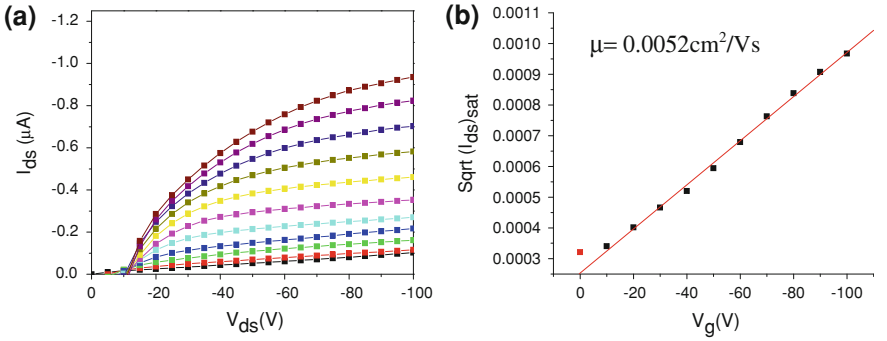

Fig. 25.2 **a** $I_{ds}-V_{ds}$ curves for the lipid layers OTFT; **b** square root of I_{ds} vs. V_g plot of the lipid layers OTFT for the electrical parameter extraction

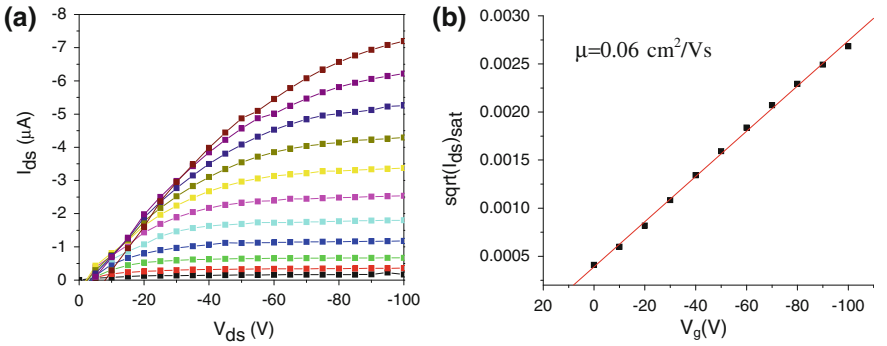

Fig. 25.3 **a** $I_{ds}-V_{ds}$ curves for the α-6T based OTFT; **b** square root of I_{ds} vs. V_g plot of for the α-6T based OTFT for the electrical parameter extraction

In the present study, we focussed on the electrical performances of the transistor and their dependence upon the presence of lipid layers.

In Fig. 25.2a, the source-drain current (I_{ds}) of the lipid layers OTFT is reported as a function of the source-drain bias (V_{ds}) for different gate biases (V_g). The field-effect mobility (μ) is graphically extracted from the relevant square root of I_{ds} vs. V_g plot (Fig. 25.2b) resulting in $\mu = 0.0052$ cm^2/Vs.

In Fig. 25.3, the I_d-V_{ds} characteristics of an OTFT whose active layer consists only in an α6T organic semiconductor is reported. The extracted electrical parameters result in a field effect mobility of 0.06 cm^2/Vs.

The comparison of the electrical performance of these two differently structured OTFT shows a slight decrease of the electrical performances in the case of the lipid layers-OTFT device. This behavior was explained considering that the lipid layers interacting with the organic semiconductor, affect the short-range molecular order of its polycrystalline structure. This can influence the grain boundary

potential barrier height, reflecting directly onto the transistor channel transport. It is important to outline that this is quite a moderate effect that strongly encourages further development of the study and particularly the investigation of sensing applications in aqueous media.

In particular, the immobilization of a protein into lipid layers represents an innovative approach that is going to be soon investigated. This will be also applied to ad hoc modified antibodies although such bio-molecules will be also immobilised directly over the device active surface using more standard approaches. In this respect a properly deposited phospholipid bi-layer, including proteins such as photosynthetic reaction centres and antibodies, will confer specificity. In fact this protein (RC) has been already successfully used as a recognition element in optical biosensor for herbicides detection, achieving detection limits of 0.1 mM [9].

25.3 Conclusions

A totally innovative device, based on an OTFT comprising a properly deposited lipid layer is presented. In order to understand if the lipid layers can affect the electrical performance of the device, a comparison with the electrical performances of a bottom gate-bottom contact α6T based OTFT was performed. Sensing and bio-sensing applications in aqueous media are envisaged, as well.

Acknowledgments The authors acknowledge financial support from the European Project "Electrolyte-Gated Organic Field-Effect Biosensors—BioEGOFET" SEVENTH FRAMEWORK PROGRAMME-THEME ICT-2009.

References

1. Emin D (1975) Phonon-assisted transition rates I. Optical-phonon-assisted hopping in solids. Adv Phys 24:305–348
2. Torsi L, Marinelli F, Angione MD, Dell'Aquila A, Cioffi N, De Giglio E, Sabbatini L (2009) Contact effects in organic thin-film transistor sensors. Org Electron 10:233–239
3. Torsi L, Tanese MC, Cioffi N, Gallazzi MC, Sabbatini L, Zambonin PG, Raos G, Meille SV, Giangregorio MM (2003) Side-chain role in chemically sensing conducting polymer field-effect transistors. J Phys Chem B 107:7589–7594
4. Tanese MC, Fine D, Dodabalapur A, Torsi L (2005) Interface and gate bias dependence responses of sensing organic thin-film transistors. Biosens Bioelectron 21:782–788
5. Torsi L, Farinola GM, Marinelli F, Tanese MC, Hassan Omar O, Valli L, Babudri F, Palmisano F, Zambonin PG, Naso F (2008) Field-effect sensitivity enhanced bilayer chiral sensor. Nat Mater 7:412–417
6. Torsi L, Lovinger AJ, Crone B, Someya T, Dodabalapur A, Katz HE, Gelperin A (2002) Correlation between oligothiophene thin film transistor morphology and vapor responses. J Phys Chem B 106:12563–12568
7. Wang L, Fine D, Dodabalapur A (2004) Nanoscale chemical sensor based on organic thin-film transistors. Appl Phys Lett 85:6386–6388

8. Zhou X, Moran-Mirabal JM, Craighead HG, McEuen PL (2007) Supported lipid bilayer/carbon nanotube hybrids. Nat Nanotechnol 2:185–190
9. Mallardi A, Giustini M, Lopez F, Dezi M, Venturoli G, Palazzo G (2007) Functionality of photosynthetic reaction centers in polyelectrolyte multilayers: toward an herbicide biosensor. J Phys Chem B 111:3304–3314

Chapter 26
The Measure of Atmospheric Electric Field

S. Iarossi, M. Poscolieri, C. Rafanelli, D. Franceschinis, A. Rondini, M. Maggi and A. D'amico

We have developed a prototype of a sensor able to detect and measure electric fields in the atmosphere. The atmosphere is a gaseous envelope gravitationally bound to the Planet. Different atmospheres have very different properties. For instance, the atmosphere of Venus is very thick and cloudy, and is responsible for producing the very high surface temperatures on that planet by virtue of its greenhouse effect. On the other hand, the Martian atmosphere is very sparse. Earth's atmosphere is intermediate between these two extremes. It is distinguished from all other known atmospheres by its very active hydrologic cycle. One need merely examine pictures of Earth from space to appreciate the intricate cloud structures. Water in Earth's atmosphere plays a very important energetic role. Because of its chemical composition, most incoming sunlight passes through Earth's atmosphere and is absorbed at the ground. This heat is transported to the atmosphere through sensible heat and moisture fluxes. Upon condensation, this heat is then released into the atmosphere. The atmosphere may be conceptually divided into several layers, according to its thermal and ionization structure. The region where the temperature decreases because of the upward heat flux is called the troposphere. Above it, there is a layer in which temperature increases upward because of ozone absorption of solar radiation, the stratosphere.

S. Iarossi · M. Poscolieri · C. Rafanelli · A. D'amico
CNR – IDASC,
Via del Fosso del Cavaliere 100, 00133 Rome, Italy

D. Franceschinis · A. Rondini · A. D'amico (✉)
Department of Electronic Engineering, University of Rome Tor Vergata, via del Politecnico, 00133 Rome, Italy
e-mail: damico@eln.uniroma2.it

M. Maggi
INAF, via del Fosso del Cavaliere 100, 00133 Rome, Italy

G. Neri et al. (eds.), *Sensors and Microsystems*,
Lecture Notes in Electrical Engineering 91, DOI: 10.1007/978-94-007-1324-6_26,

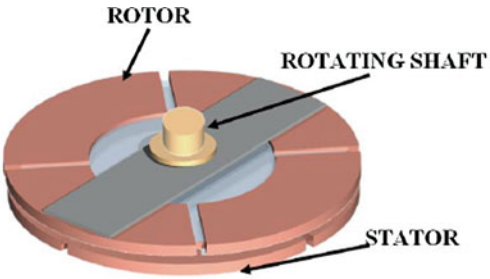

Fig. 26.1 Schematic of the electric field sensor made by a stator and a rotator divided in four sectors. Rotating speed was about 300 rpm

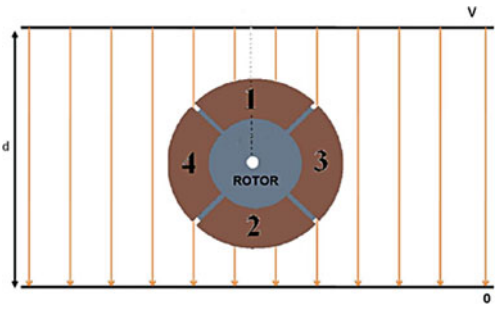

Fig. 26.2 Sensor located inside the calibration chamber

The coupling ionosphere and Earth's body defines a capacitor. To study the electric field between the two plates is a strong challenge, in particular to understand the electrical phenomena and their consequences in atmosphere and at ground.

The atmospheric electric field is a quantitative term denoting the electric field strength of the atmosphere at any specified point in space and time [1]. In areas of fair weather, the atmospheric electric field near the earth's surface typically is about 100 V m^{-1} and is directed vertically in such a sense as to drive positive charges downward to the earth. In areas of fair weather this field decreases in magnitude with increasing altitude, falling, for example, to only about 5 V m^{-1} at an altitude of about 10 km. Near thunderstorms, and under clouds of vertical development, the surface electric field (the electric field measured at the surface of the earth) varies widely in magnitude and direction, usually reversing its direction immediately beneath active thunderstorms. In areas of minimal local disturbance, a characteristic diurnal variation of electric field strength is observed. This variation is characterized by a maximum that occurs (if there are no local sources of pollution) at about 19:00 UTC for all points on the earth and is now believed to be produced by thunderstorms that, for geographic regions, are more numerous for the world as a whole at that universal time than at any other. It is now believed that thunderstorms, by replenishing the negative charge to the earth's surface, provide the supply current to maintain the fair- weather electric field in spite of the continued flow of the air–earth current that tends to neutralize that field. The range of the electric field in fair weather varies considerably with geographical area, from one part of the globe to another [2, 3].

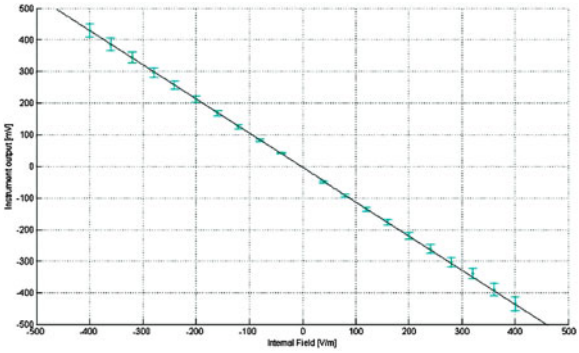

Fig. 26.3 Calibration curve obtained by the calibration chamber

Fig. 26.4 Experimental set up for the preliminary experiments in a partially cloudy day. Changes of the electric field (from 20 to 30 V/m at sunset in a sunny day), up to 800 V/m (during clouds displacement) have been detected

A schematic of our sensor is illustrated in Fig. 26.1 while Fig. 26.2 represents the sensor inside the calibration chamber by which the calibration curve represented in Fig. 26.3 has been derived.

The sensitivity of the sensor has been calculated to be about 1 mV/(V/m). This sensor is based on the possibility to measure the current by the following relationship:

$$i = C\frac{dV}{dt} + V\frac{dC}{dt}$$

where, supposing $V =$ constant, the second term can be neglected. A motor is used to change capacitance and a suitable electronic circuit which includes a lock-in amplifier allows the measurement of the induced charges in the fixed sectors.

The calibration curve has been obtained by setting the sensor inside a parallel copper plate capacitor. A controlled electric field has been generated by the application of a constant DC voltage to the two plates. By changing the applied voltage the curve represented in Fig. 26.3 has been experimentally determined. Figure 26.4 shows the apparatus employed for the so called field test related to different atmospheric conditions. The sensor is here located in the right top end

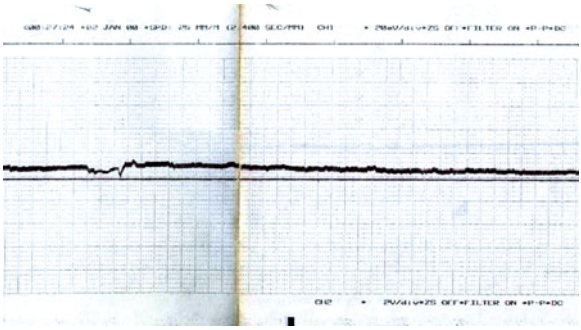

Fig. 26.5 Chart showing the electric field intensity decreasing in the evening

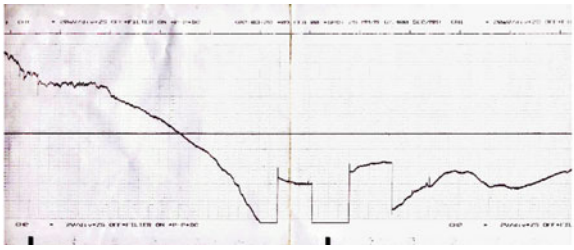

Fig. 26.6 Chart showing the electric field during a storming phenomena

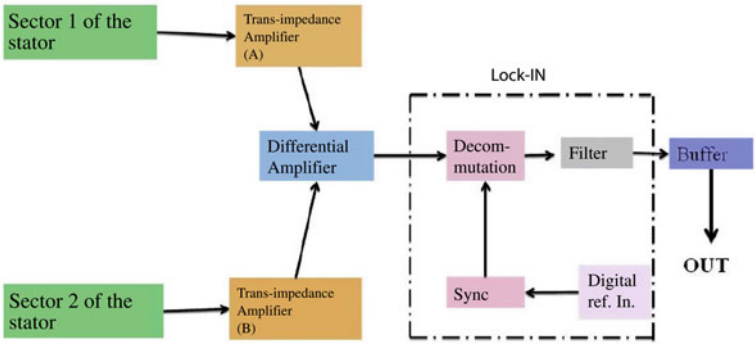

Fig. 26.7 Configuration of a lock-in amplifier employed in the experiment

side of the figure. Figure 26.5 shows part of a time registration of the electric field related to the coming evening.

Figure 26.6 shows the rather strong electric field variation registered during a storming phenomena. It is worth noting the sign change of the electric field probably due to the presence of clouds with opposite charge.

The measurements show a rather interesting reproducibility registered in different days about in the same atmospheric conditions.

Figure 26.7 shows a block scheme employed for this apparatus where it appears the use of a simple lock-in amplifier for weak signals.

Further studies are in progress in order to reduce the dimensions of the basic sensor.

References

1. Hill DA, Kanda M (1999) Electrical field strength. CRC Press LLC, Boca Raton
2. Kanda M (1993) Standard probes for electromagnetic field measurements. IEEE Trans Antennas Propag 41:1349–1364
3. Stratton JA (1941) Electromagnetic theory. McGraw-Hill, New York

Chapter 27
Single Palladium Nanowire: Morphology and its Correlation with Sensing Mechanism

Vera La Ferrara, Brigida Alfano, Tiziana Polichetti, Ettore Massera, Girolamo Di Francia and Giuseppe Fiorentino

Abstract In this work devices based on single palladium nanowire are realized by combining dielectrophoresis and focused ion beam (FIB) and characterized as hydrogen sensor at room temperature. Fixing the geometry of the electrodes, patterned by FIB, several devices are fabricated by varying the frequency of the applied field (DEP), to assess the effect on the shape of nanowire. Different kind of nanowire structures are, then, observed by means of SEM and AFM. The sensing mechanisms in presence of hydrogen are investigated and compared for each, finding that electrical current decreases because of palladium hydride formation.

27.1 Introduction

Grow in place approach is one of the techniques used to fabricate miniaturized devices. It allows to grow, position and align a single nanowire between the contacting electrodes, without any manipulation [1]. Among the *grow in place* techniques, dielectrophoresis (DEP) is receiving an increasing interest. It uses a non-uniform electric field to polarize small particles, suspended in solution, forcing them to move in a well controllable way up to assemble nanowires [2]. The geometry of the electrodes plays a very important part in the realization of

V. La Ferrara (✉) · B. Alfano · T. Polichetti · E. Massera · G. D. Francia
ENEA Research Center, P.le E. Fermi 1, 80055 Portici (NA), Italy
e-mail: vera.laferrara@enea.it

G. Fiorentino
Department of Physics, University "Federico II", Piazzale Tecchio 80, 80125 Naples, Italy

G. Neri et al. (eds.), *Sensors and Microsystems*,
Lecture Notes in Electrical Engineering 91, DOI: 10.1007/978-94-007-1324-6_27,

nanostructured materials through DEP. Focused ion beam (FIB) is the useful tool for patterning microelectrodes creating suitable nucleation points for nanowire growth [3].

In this work, Pd nanowires with different morphologies have been realized, applying an alternating electric field to a palladium electrolyte solution dropped between Pt microelectrodes deposited by FIB. Branched nanowire have been obtained at high electric field frequency while plain nanowire has been assembled at lower frequency. Devices based on single branched and plain nanowires have been electrically characterized in hydrogen environment at RT and their responses have been compared.

27.2 Experimental

A crystalline silicon wafer coated with 100 nm of Si_3N_4 has been used as starting substrate. FIB column, integrated in a FEI Quanta 200 3D dual beam system, has been used for platinum nanoelectrodes patterning. Highly focused gallium ion beam interacts with the platinum organometallic precursor gas. Metal–organic compounds are dissociated and the non volatile part of the compound is deposited onto the sample surface to form electrodes. Using 30 kV as accelerating voltage and 10 pA as emission current for ion beam emission, platinum nanoelectrodes about 8 μm spaced are deposited onto the substrate. The feed solution for DEP processing has been prepared dissolving crystalline Pd(acetate)2 in 10 mM HEPES buffer solution. A function generator and an oscilloscope have been used as the alternating current (AC) source and for monitoring the applied electrical signal, respectively. 2 μl of saturated solution have been deposited by casting onto the substrate, previously washed in isopropyl alcohol, deionised water and dried in a nitrogen flow.

Two series of single Palladium nanowire-based devices have been grown between the electrodes by applying a 10 V_{pp} ($V_{peak\text{-}peak}$) sinusoidal electric field at two different frequency, 300 kHz and 300 Hz. The process stops when the opposite electrodes are short-circuited by the grown nanowire.

The single palladium nanowire-based devices have been tested as hydrogen sensor. The device has been first characterized in direct current (DC) condition at room temperature and in ambient air, showing an ohmic current–voltage (I–V) characteristic between –1 and 1 V, with a typical electrical resistance of about 15–70 kΩ.

A volt-amperometric technique, at constant bias, has been then employed for sensor DC electrical characterization in a controlled gas-flow environment, pre-mixed with dry carrier in the desired percentage by mass flow meters and continuously controlled by means of an on-line Fourier transform infrared spectrometer. All the tested devices have been biased at 5 mV. Total gas flow has been set at 500 sccm.

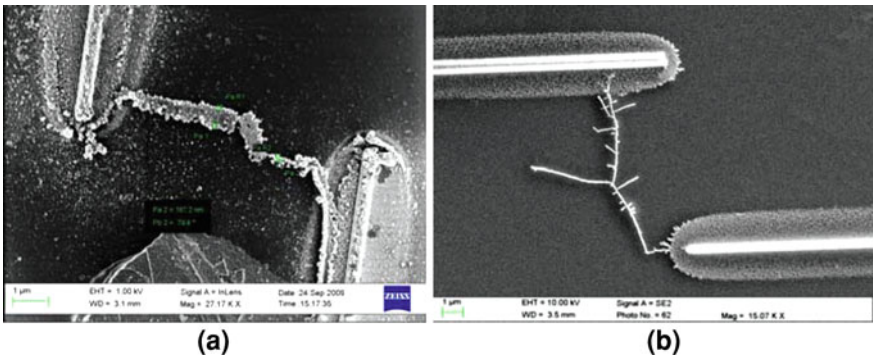

Fig. 27.1 SEM images of Pd nanowires made at 300 Hz (**a**) and at 300 kHz frequency (**b**)

27.3 Results and Discussion

Fixing FIB electrode pattern with 6-μm gap size and no overlapping, two devices have been realized changing the electric field frequency.

In Fig. 27.1a, a SEM image of a device made at 300 Hz frequency is shown (series A). From the movie, recorded during the assembly, a very rapid nanowire formation between the two electrodes has been observed and so the deposition has been stopped after 2 s. The nanowire morphology shows no ramifications, with a thickness varying from 180 to 350 nm. This morphology has been called "plain".

In Fig. 27.1b, it is shown a single Pd nanowire, grown applying a 300 kHz frequency between electrodes (series B). Nanowire is branched with average diameter of about 60 nm.

At low frequencies a thick single palladium nanowire, with no branches, is assembled while at high frequencies a thinner and branched single nanowire is obtained. Under high frequency fields are applied, branched structures may result by Pd ions diffusion towards secondary sites, different from the main nucleating tip, bringing out to the formation of new nucleating points.

Single palladium nanowire morphologies have been analysed using an atomic force microscope (AFM) in tapping mode with the aim to investigate the Pd nanowire morphology obtained at different field frequency.

AFM images (Fig. 27.2) confirm that single nanowires consist of palladium continuous aggregates. As shown in the figures, for both series A and series B the clusters are closely interconnected, settling in overlaid layers, so as to leave no void spaces and creating a continuous structure.

The recorded electrical responses, when devices are under hydrogen gas, are shown in Fig. 27.3. Devices based on single palladium nanowire have been maintained, for 30 min, in a dry air flow for the zero current (baseline) monitoring. Hydrogen concentrations ranging from 0.5 to 4% have been then introduced in the test chamber and the device electrical responses have been recorded.

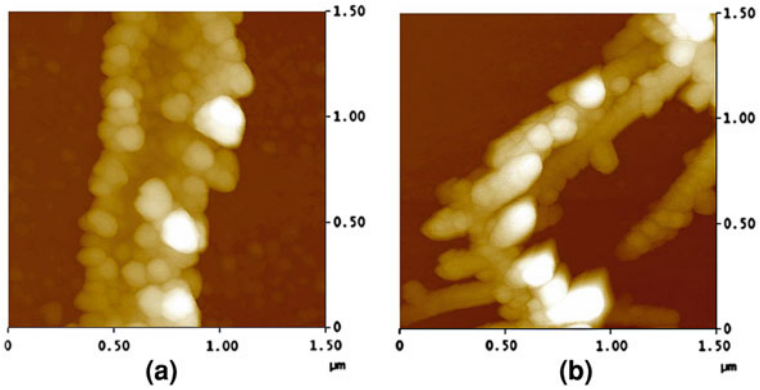

Fig. 27.2 AFM image of palladium nanowire made at 300 Hz, series A (**a**) and 300 kHz, series B (**b**)

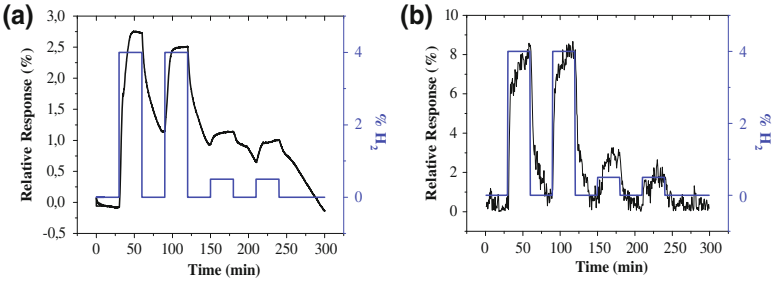

Fig. 27.3 Relative response versus time, recorded at room temperature and at 4 and 0.5% H_2 concentrations in dry air for series A (**a**) and B (**b**). H_2 concentrations are drawn with straight lines

Devices show a current decreasing in presence of hydrogen. Upon exposure to hydrogen, palladium reacts to form the more resistive palladium hydride (PdHx where x is the atomic ratio H/Pd), as a consequence the electric current decreases.

Series B shows a higher relative response as compared with series A, because of the higher Surface/Volume ratio for several ramifications. Series B follows more closely the concentration change and when hydrogen is removed from the test chamber, it shows a lower drift current and greater stability than the series A.

27.4 Conclusions

We have shown how devices based on a single palladium nanowire can be fabricated in well controllable conditions using FIB and DEP combination and how, fixing the electrode geometry, it is possible to change the morphology of nanowires.

Acknowledgment The authors gratefully acknowledge the Ministry of Universities and Research (MIUR) for financial support as part of Public–Private Laboratory TRIPODE (Technologies and Research for the application of polymers in electronics devices).

References

1. Rotkina L, Lin J-F, Bird JP (2003) Nonlinear current-voltage characteristics of Pt nanowires and nanowires transistors fabricated by electron-beam deposition. Appl Phys Lett 83:4426–4429
2. Burke PJ (2004) Nano-dielectrophoresis electronic nanotweezers. In: Nawla HS (ed) Encyclopedia of nanoscience and nanotechnology, vol. 6. American Scientific, Stevenson Ranch, pp 623
3. La Ferrara V, Alfano B, Massera E, Di Francia G (2009) Single palladium nanowire growth in place assisted by dielectrophoresis and focused ion beam. J Nanosci Nanotechnol 9:2931–2936

Chapter 28
Silicon Carbide Schottky Diodes for Alpha Particle Detection

M. Piotto, P. Bruschi, A. Diligenti, R. Ciolini, G. Curzio and A. Di Fulvio

Abstract The fabrication and characterization of SiC Schottky diodes for the detection of alpha particles at room temperature are described. A 5 × 5 matrix of diodes has been fabricated in order to verify the dependence of the device response on randomly distributed wafer defects. A dedicated exposure apparatus has been fabricated to test the detectors. Some preliminary alpha energy spectra obtained with the lowest reverse current diodes are shown.

28.1 Introduction

Silicon carbide (SiC) has been largely investigated for the fabrication of high power, high frequency, high temperature electron devices due to its excellent electronic properties. It is a wide bandgap semiconductor material with high thermal conductivity and high breakdown electric field strength [1]. These properties, connected to a high chemical and radiation resistance, make it suitable for sensor applications in harsh and hostile environments [2]. In the last years, SiC has also been proposed for the fabrication of semiconductor radiation detectors able to work at elevated temperatures in high radiation fields [3, 4].

M. Piotto (✉)
IEIIT – Pisa, CNR, Via G. Caruso 16, 56122 Pisa, Italy
e-mail: massimo.piotto@cnr.it

P. Bruschi · A. Diligenti
Dipartimento di Ingegneria dell'Informazione, Università di Pisa, Via G. Caruso 16, 56122 Pisa, Italy

R. Ciolini · G. Curzio · A. Di Fulvio
Dipartimento di Ingegneria Meccanica, Nucleare e della Produzione, Università di Pisa, Largo L. Lazzarino 2, 56126 Pisa, Italy

G. Neri et al. (eds.), *Sensors and Microsystems*,
Lecture Notes in Electrical Engineering 91, DOI: 10.1007/978-94-007-1324-6_28,

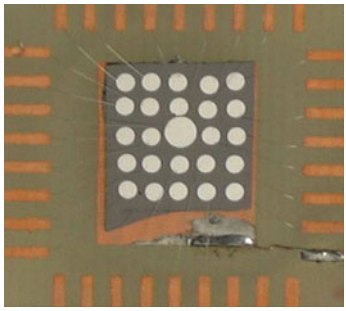

Fig. 28.1 Photograph of the device

In this work we propose the fabrication and characterization of SiC Schottky diodes for the detection of alpha particles at room temperature.

28.2 Device Fabrication and Characterization

Devices were fabricated on a 1 cm × 1 cm sample diced from a 4H-SiC *n* type wafer (SiCrystal AG) with a top low doped *n* type ($N_D = 3 \times 10^{15}$ cm^{-3}), 20 μm thick epilayer, separated from the substrate by a high doped *n* type ($N_D = 1 \times 10^{17}$ cm^{-3}), 2 μm thick buffer layer. In order to verify the dependence of the diode characteristics on the randomly distributed wafer defects, a 5 × 5 matrix of diodes was defined. The ohmic contact, common to all diodes, was deposited by e-beam evaporation on the back side of the die and consists in a double metal thin film (Ti 30 nm/Ni 200 nm). A rapid thermal annealing at 1,000°C for 300 s in nitrogen was performed in order to obtain a good ohmic contact. The 25 Schottky contacts were defined by evaporating a double metal thin film (Ni 100 nm/Al 500 nm) through a stencil mask. After the contact definition, the die was glued to a PCB board by means of silver paste and wedge bonding was used to connect diodes to the board pads.

A photograph of the sample at the end of the fabrication process is shown in Fig. 28.1: all diodes have a diameter of 1.2 mm, except the 3–3 (row–column) diode (2.1 mm).

All devices have been characterized by means of *I–V* measurements at room temperature and the forward *I–V* curves for some diodes are shown in Fig. 28.2a. It can be noted the dispersion of the curves of diodes with the same nominal Schottky contact area. This phenomenon has been found also in the reverse *I–V* curves with a variation of the current density up to five orders of magnitude among diodes placed in different sample areas. Considering that diodes will be reverse biased for radiation detection, the availability of high quality SiC wafers with low density of defects, like micropipes and stacking faults, is mandatory for this type of application.

In Fig. 28.2b the reverse current density of a diode measured at room temperature is shown.

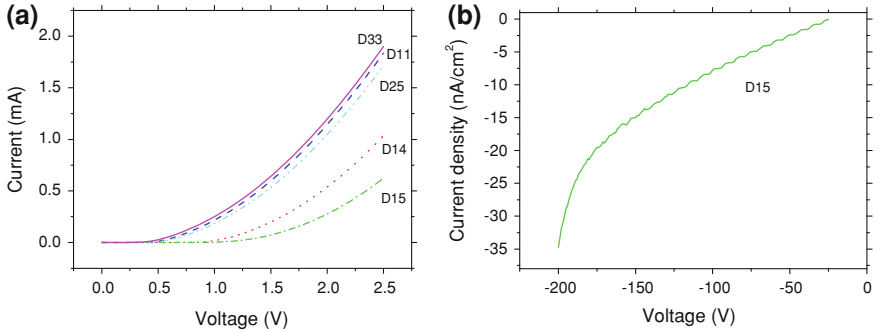

Fig. 28.2 **a** Forward *I–V* curves for some of the tested diodes; **b** reverse current density of a diode measured at room temperature

Table 28.1 Alpha radioactive sources and relative energies and activities

Source	Nuclide	Principal alpha emission energy (MeV)	Activity (kBq)
Source 1	^{239}Pu	5.157	2.22
	^{241}Am	5.486	1.60
	^{244}Cm	5.805	0.95
Source 2	^{239}Pu	5.157	3.70

28.3 Measurement Set-up

In order to test the previously described detector, a dedicated exposure apparatus has been fabricated. It was made up of an aluminum case containing the SiC sample holder which allows to place the detector in front of the ionizing radiation source at an adjustable distance. The case shields the device from electromagnetic external noise and the inner pressure can be reduced by means of a rotary pump. The device output signal was transmitted to the acquisition chain consisting in a charge preamplifier in cascade with a standard Canberra multi channel analyzer (MCA) for signal conditioning and analysis.

28.4 Experimental Results

A multiple alpha (^{239}Pu, ^{241}Am and ^{244}Cm) and a ^{239}Pu radioactive sources were used for the experiments (Table 28.1). The optimum source-to-detector distance which maximizes the alpha energy loss into the diode depletion layer (about 8.5 μm thick at 200 V) was evaluated by the TRIM© code: considering an air gap of 26 mm between the source and the detector, the resulting average alpha range was 8.1 μm with a 2% straggling (Fig. 28.3).

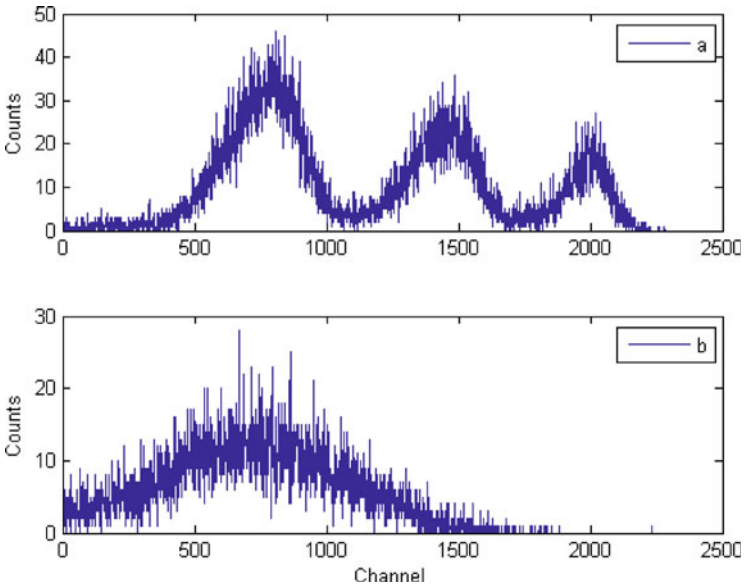

Fig. 28.3 Energy loss per unit length (eV/Å) at a source-to-detector distance of 26 mm

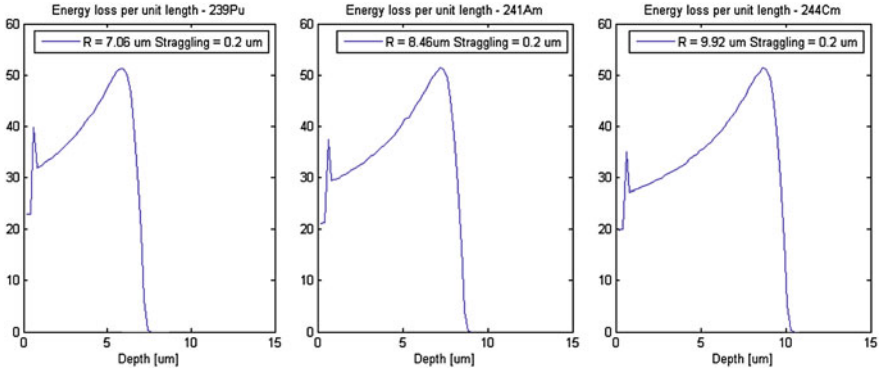

Fig. 28.4 Alpha energy spectra: **a** multiple alpha source (^{239}Pu, ^{241}Am, ^{244}Cm); **b** ^{239}Pu alpha source

Two spectra obtained with a reverse bias voltage of 200 V are shown in Fig. 28.4: (a) multiple alpha source (acquisition time: 14,400 s) and (b) plutonium source (acquisition time: 4,500 s). As it may be noticed, with the same experimental conditions, the single ^{239}Pu peak is coincident with the corresponding plutonium peak from the multiple source.

28.5 Conclusions

The fabrication and characterization of Schottky diodes on a SiC substrate have been described. The Schottky contact consists in a double metal thin film (Ni 100 nm/Al 500 nm) defined by means of evaporation through a stencil mask. The dependence of the diode characteristics on the randomly distributed wafer defects has been confirmed by *I–V* measurements performed on a 5 × 5 matrix of devices. Preliminary detection measurements at room temperature have proven the feasibility of using these devices as alpha particle detectors.

References

1. Saddow SE, Agarwal A (2004) Advances in silicon carbide processing and applications. Artech House, Norwood, Massachusetts, USA
2. Wright NG, Horsfall AB (2007) SiC sensors: a review. J Phys D Appl Phys 40:6345–6354
3. Ruddy FH, Dulloo AR, Seidel JG, Seshadri S, Rowland LB (1998) Development of a silicon carbide radiation detector. IEEE Trans Nucl Sci 45:536–541
4. Nava F, Vanni P, Bruzzi M, Lagomarsino S, Sciortino S, Wagner G, Lanzieri C (2004) Minimum ionizing and alpha particles detectors based on epitaxial semiconductor silicon carbide. IEEE Trans Nucl Sci 51:238–244

Chapter 29
Nano-Devices Based on Spin-Transfer Torque Effects

V. Puliafito and A. Prattella

Abstract The discoveries of giant magneto-resistance and spin-transfer torque effects are milestones in the history of magnetism. During the last two decades, they have fueled a conspicuous research activity in the field of nanotechnology, giving rise even to a new scientific branch, the spintronics, a neologism for spin-based electronics. From the very beginning, in fact, experimental results pointed out several potential applications of spintronic devices, such as magnetic random-access-memories, sensors, nano-oscillators, modulators and receivers working at microwave frequency. An overview of these devices will be here provided, emphasizing their behavior and the applications.

29.1 Introduction

The two scientists Fert and Gruenberg received the 2007 Nobel prize in physics for the discovery of the Giant Magneto-Resistance (GMR) effect in 1988 [1, 2]. Such phenomenon is observed in thin film structures composed of alternating ferromagnetic and non magnetic layers, and it manifests itself as a significant change in the electrical resistance of the structure depending on whether the magnetizations of adjacent ferromagnetic layers are in a parallel or an antiparallel alignment. The overall resistance turns out to be relatively low in the former case and relatively high in the latter one. Eight years after the discovery of GMR effect, in 1996, Slonczewski and Berger predicted that a direct electric current passing through a magnetic material, opportunely thick, becomes spin-polarized along the direction

V. Puliafito (✉) · A. Prattella
Department of Matter Physics and Electronic Engineering,
University of Messina, Salita Sperone 31, 98166 Messina, Italy
e-mail: vpuliafito@unime.it

G. Neri et al. (eds.), *Sensors and Microsystems*,
Lecture Notes in Electrical Engineering 91, DOI: 10.1007/978-94-007-1324-6_29,

of its local magnetization vector. If such a spin-polarized current presents a sufficiently large amplitude and now traverses a second magnetic layer, it can transfer its spin-angular momentum and destabilize the static equilibrium orientation of the magnetization of this latter layer [3, 4]. This phenomenon is known as Spin-Transfer Torque (STT) effect and it can be accounted as the dual of the GMR one, as the GMR effect describes how the electrical configuration is affected by changes of the magnetic state, whereas the STT one describes how the magnetic state is affected by changes of electrical quantities. The discovery that spin-polarized currents can modify a magnetic state opened several perspectives for a new class of nano-scale magnetic devices that specifically take advantage of spin properties instead of, or in addition to, the degree of freedom given by the charge. The corresponding new research area was consequently called spintronics, a short notation for "spin-based electronics".

29.2 Spintronic Devices

From the beginning, GMR and STT effects have been studied in multilayer systems called "spin-valve". A classical spin-valve consists of: a thicker magnetic layer, called fixed or pinned layer (PL), which acts as the spin-polarizer; a thinner magnetic layer, called free layer (FL), which is the one generally subjected to the action of the spin-transfer torque; and a non magnetic spacer, used to avoid exchange coupling between PL and FL. Depending on the electrical conductivity of the intermediate layer, it is possible to build up either "classical" spin-valve (CSV) devices, if the spacer is a metal, or non-classical magnetic tunnel junctions (MTJ), if the spacer is an insulator. Within the class of nano-scale devices, the two most common experimental geometries are the so-called: nano-pillar and nano-contact (or point-contact). The main differences existing between them involve both the lateral sizes and the current density distribution. In fact, nano-contact devices generally present larger lateral dimensions (in the order of tens of microns) with respect to those of nano-pillar (hundreds of nanometers). In addition, the perpendicular-to-plane applied current involves the whole physical (cross-section) area of pillar devices, whereas only a reduced region (the contact area, typically of the radius of 10–80 nm) in nano-contact devices (see Fig. 29.1). The structural differences between these geometries imply not only different technological applications, but also require different approaches in the corresponding numerical investigations [5, 6].

29.3 Applications

Depending on the geometry, on the properties of the layered magnetic structure, on the magnitude and orientation of the external bias field, the STT effect can lead either to the switching of the magnetization direction or to a stable precession of

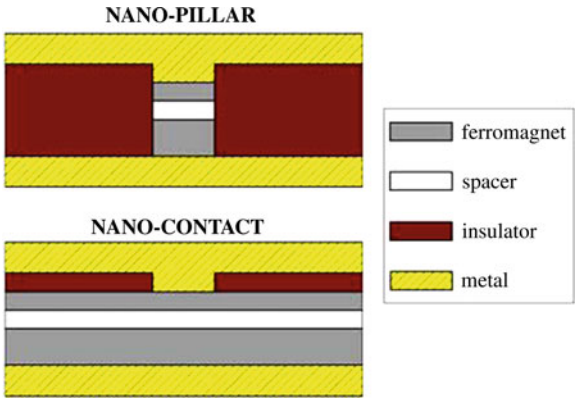

Fig. 29.1 Nano-pillar and nano-contact spin valve geometries

the magnetization of the thinner FL. These particular physical phenomena offer the possibility to design and build up a new class of devices and applications that includes, for example, magnetoresistive random access memory, logic gates, diodes and transistors, nano-oscillators, modulators and receivers.

29.3.1 GMR and TMR Sensors

A classical spin-valve structure can be used as a magnetic field sensitive device, exploiting GMR effect. The presence of an external magnetic field, in fact, can adjust the direction of the magnetization vector in the FL respect to the PL magnetization, increasing or decreasing the output resistance of the device. In the two opposite cases (aligned and not aligned layers), the change in resistance is tipically 10–20%, compared with a maximum sensitivity of a few percent for other types of magnetic sensors. This explains the reason of the term "giant", although it seems incongruous for a nanotechnology device. Tunnel Magneto-Resistance (TMR) is an extension of GMR effect. It takes place when spin-polarized electrons travel perpendicularly to the layers across a thin insulating tunnel barrier (replacing the non ferromagnetic spacer, as in MTJ structures). Since this process is forbidden in classical physics, TMR is a strictly quantum mechanical phenomenon. TMR sensors, for the above-described reasons, get larger magnetoresistance values and a larger sensitivity [7]. The main advantages of GMR and TMR sensors are the sensitivity and the reducing size and power requirement. On the other hand, random high-value fields may represent a problem for the devices.

29.3.2 Magnetic RAM

GMR and TMR devices are used commercially by hard disk drive manufacturers. The read-heads of the modern hard disk drives work, in fact, on the basis of spin-valves and magnetic tunnel junctions. Such structures, besides, can be used as

memory cells, since it is possible to associate two different logic states to the different electric configurations (e.g. bit 0 = low-resistance state, bit 1 = high-resistance state). This is also the basic working principle of magnetic random-access memories, MRAM, one of the most common systems of non-volatile memory. The increasing interest in nano-scale memories, of course, has given rise to plentiful studies on this application of spin-valve structures [8]. In particular, nano-pillar geometries have been analyzed to get the magnetization switching driven by spin-polarized currents, even in the absence of an external magnetic field.

29.3.3 Nano-Oscillators

If the magnetization of the FL undergoes a persistent precession, rather than switching phenomena, the output signal might manifest itself as a periodic variation of the resistance of the device which could be used to build up nano-scale oscillators. Nano-contact geometry becomes particularly suitable to design microwave spin-transfer oscillators with very narrow linewidths because it combines the advantages of having a larger effective volume and a negligible influence of edge roughness and defects. Numerous experimental [9] and numerical [10, 11] analyses have described the nature of such spin-wave modes, showing, for instance, how the output frequency depends on the applied current.

29.3.4 Radio-Frequency Modulators

When a point-contact structure is subjected to the simultaneous action of a direct current and an alternative current, it works as a non linear amplitude and frequency modulator. The direct current fixes the carrier frequency, while the alternative term acts as modulating signal. The output spectra obtained by means of numerical simulations and experiments, in fact, agree with the predictions of the analytical model of analog modulation, in which variations of amplitude and frequency with the modulating input signal are taken into account [12].

29.4 Conclusions

We have described some physical properties of magnetic multilayer structures, GMR, TMR and STT. These structures, in their different and possible geometries, turn out to be very useful in the field of nanotechnology.

References

1. Baibich MN et al (1988) Giant magnetoresistance of (001)Fe/(001)Cr magnetic superlattices. Phys Rev Lett 61(21):2472–2475
2. Binasch G et al (1989) Enhanced magnetoresistance in layered magnetic structures with antiferromagnetic interlayer exchange. Phys Rev B 39(7):4828–4830
3. Slonczewski JC et al (1996) Current-driven excitation of magnetic multilayers. J Magn Magn Mater 159:L1–L7
4. Berger L (1996) Emission of spin waves by a magnetic multilayer traversed by a current. Phys Rev B 54(13):9353–9358
5. Torres L et al (2007) Coupling of spin-transfer torque to microwave magnetic field: a micromagnetic modal analysis. J Appl Phys 101:053914
6. Consolo G et al (2008) Micromagnetic study of the above-threshold generation regime in a spin-torque oscillator based on a magnetic nanocontact magnetized at an arbitrary angle. Phys Rev B 78:014420
7. Finocchio G et al (2007) Micromagnetic modeling of magnetization switching driven by spin-polarized current in magnetic tunnel junctions. J Appl Phys 101:063914
8. Carpentieri M et al (2007) Magnetization dynamics driven by spin-polarized current in nanomagnets. J Magn Magn Mater 316:488–491
9. Rippard WH et al (2004) Direct-current induced dynamics in Co90Fe10/Ni80Fe20 point contacts. Phys Rev Lett 92(2):027201
10. Romeo A et al (2008) A numerical solution of the magnetization reversal modeling in a permalloy thin film using fifth order Runge–Kutta method with adaptive step size control. Physica B 403:464–468
11. Consolo G et al (2007) Magnetization dynamics in nanocontact current controlled oscillators. Phys Rev B 75:214428
12. Consolo G et al (2010) Combined frequency-amplitude non linear modulation: theory and applications. IEEE Trans Magn 46:3629–3634

Chapter 30
Physical and Morphological Characterization of an Innovative System Control for the Accurate Execution of Lung Surgery

L. Fuggiano, R. Caione, F. Casino and R. Rella

Abstract Pulmonary ventilation is an important and indispensable method used in lung surgery. Generally, during the operation it is necessary to exclude one of the two lungs from ventilation. To this purpose the characteristics of the actual bronchial blockers don't let to exclude easily the lung during the surgical maneuvers. The difficulties evidenced during the anesthesia procedures by using a common blocker, have highlighted the need to find a new solution with alternative characteristics, such as to create an exclusion of the lung and at the same time to optimize the position of the blocker throughout the surgical maneuver.

30.1 Introduction

In recent years, commercial blockers have been made available for providing lung isolation. The one-lung ventilation creates differences, even on blood circulation, which undergoes a shunt effect, doubling the volume of blood on the ventilated lung. Any medical prosthesis, if introduced into a bronchus, creates a foreign body that must be managed to avoid the creation of mechanical problems to the patient.

The blocker inserted into the lumen has in the final position a balloon that, once inflated, avoid inflation of the air/oxygen in the lung and at the same time guarantee the residual air contained in the lung to go-out trough the channel inside the blocker [1, 2]. Blockers currently on the market have dimensions that sometime

L. Fuggiano · R. Caione
U.O.C. Anestesia e Rianimazione, Ospedale Civile"V.Fazzi", 73100 Lecce, Italy

F. Casino · R. Rella (✉)
Istituto per la Microelettronica e Microsistemi del CNR–IMM Lecce, via Monteroni, 73100 Lecce, Italy
e-mail: roberto.rella@le.imm.cnr.it

G. Neri et al. (eds.), *Sensors and Microsystems*,
Lecture Notes in Electrical Engineering 91, DOI: 10.1007/978-94-007-1324-6_30,

are not suitable to follow some anatomical variants, preventing its correct position and, consequently, the failure of deflation lung lobes. Sometime, the large footprint of the cuff on the mucosa causes ischemia in surgery and, in very long situation, can be cause even of irreversible damage. The experience demonstrates that, the characteristics of the actual bronchial blockers don't let to exclude easily the lung during the surgical maneuvers. Moreover, in some cases, there are anatomic variations in which the right upper lobar bronchus is located at a few centimeters from the tracheal bifurcation. The difficulties evidenced during the anesthesia procedures by using a common blocker, has highlighted the need of finding a new solution with alternative characteristics, such as to create an exclusion of the lung and at the same time to optimize the position of the blocker throughout the surgical maneuver.

In this paper a new solution has been reported by a suitable redesign of the blocker. This new solution (called fuggiano-blocker) has been designed with a shape similar to a "life jacket" that is very broad in order to occlude the bronchus, and small in order to be used in these anatomic variants. The shape of the cap, checked frequently with the fiberscope, has demonstrated an excellent stability, with no deformation, which allows keeping the blocker in vertical position.

30.2 Experimental Setup

A glass tube of dimensions close to those of a real bronchial channel has been used as a model for the determination of physical parameters involved in the real problem. Obviously the model is not a real situation but we can extract physical parameters such as the pressure inside the balloon and pressure for unit of surface generated to the internal surface of the tube by using image analysis software. A CCD camera give us information about the contact surface between the balloon and the internal surface of the model.

A comparison between the performances of a standard blocker and the novel solution as been performed in term of suitable internal pressure to obtain a correct seal. Analysis of the shape and morphological modification of the balloon as a function of the internal pressure for both cases has been performed. Moreover a control of the seal of the novel device has been performed by using oxygen pressure sensor in order to determine the minimum pressure suitable for a correct seal during the surgery. Finally, Japan's Fuji Company has agreed to produce some prototypes acquiring the CE mark, which allowed us to use this prototype as medical product.

30.3 Results and Discussions

Figure 30.1a, b report the shape of the two analyzed ballon, (a) new and (b) commercial device respectively, inserted in a simulator of lung. As one can see the dimension of the new blocker is smaller respect to the commercial device,

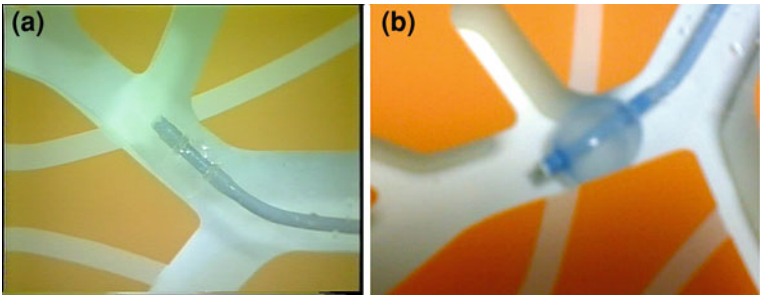

Fig. 30.1 **a** New Fuggiano-blocker, **b** commercial blocker

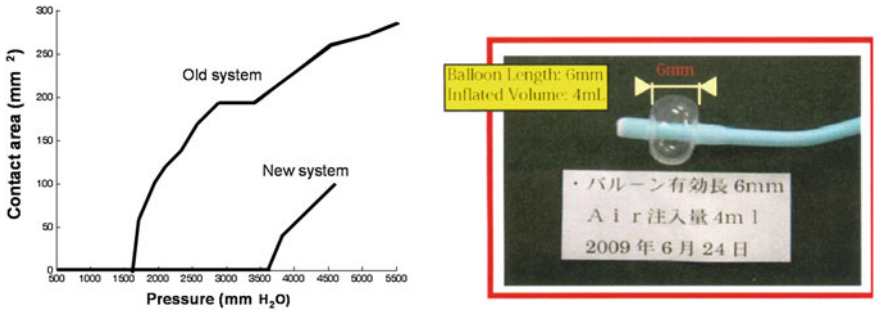

Fig. 30.2 Contact area onto the internal model surface vs inflating pressure

moreover, checked frequently with the fiberscope, has demonstrated an excellent stability, with no deformation. It is able to keep the blocker in vertical position to avoid any changing in the direction of the final point of the tube.

Analysis of the pressure suitable to obtain a good seal in the glass tube model has been evaluated by using specific experimental set-up consisting of two pressure gauges. By a CCD camera, the contact area inside the model tube as a function of the internal pressure has been monitored. Figure 30.2 shows the behavior of the seal cap during the inflation at different pressure for both system, old and new device respectively. Whereas a higher pressure it is need to expand the balloon of the new device until seal condition, a minor contact area it is necessary to guarantee seal in the case of new cap.

Figure 30.3 reports the intensity of the force applied to the internal contact surface of the model as a function of contact area for the new system (black line) and old system (red line) respectively.

The circles evidenced in the Fig. 30.3 put in evidence the optimal seal condition needed to avoid the air flow through the contact region between the two surfaces of interest, the balloon and the model. To do this a suitable control of the seal of the novel device has been performed by an oxygen pressure sensor in order to determine the minimum pressure suitable for a correct seal during the surgery. Notwithstanding an higher inflating pressure in the case of the new device, the seal

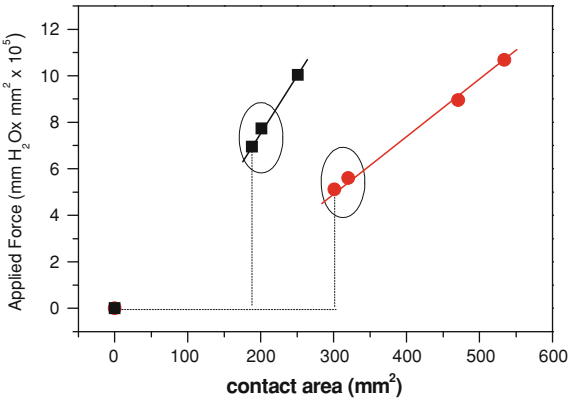

Fig. 30.3 Applied force to the internal contact surface of the model as a function of contact area for the new system (*black line*). The circles indicate the optimum seal condition and old system (*red line*)

is guarantee, when the contact's surface is about 188 mm^2, on the contrary, in the case of the commercial device, this surface must be of about 330 mm^2.

30.4 Conclusions

A novel modified blocker has been developed to be used during the lung-surgery. Comparison between the new system and the commercial one give us interesting results as concerns the reduced invasiveness demonstrated from the new system during the surgery. Moreover a less damage of the mucous membrane of the bronchus has been evidenced. The shape of the blocker provides a supporting surface of the mucosa very least to allow the seal without creating ischemia. Given its its small footprint, also avoids possible desaturation of oxygen, related to compression of arteries in the thickness of the bronchus. The shape of the balloon makes the blocker more stable during all surgical procedures without having to frequently reposition the blocker. The oval shape of the old model displaced the tip, obliterating and preventing air leakage. The fuggiano-blocker keeps the tip at the centre of the bronchus, facilitating the deflation of the lung lobes. Also the material component of the balloon has demonstrated to be suitable for the aim, because it is transparent and allows observation of the bronchus below, bringing together the bronchoscope, thereby ensuring a direct view of the operative field.

References

1. Cohen E (2002) MD-New trends in thoracic anesthesia. ASA Refresher Courses in Anesthesiology 30(1):69–85
2. Allen MS (1996) Video assisted thoracoscopic surgical procedures: the Mayo experience. Mayo Clin Proc 71:351

Chapter 31
Plasmonic and Magneto-Plasmonic Nanostructured Materials for Sensors and Biosensors Application

M. G. Manera, G. S. Masi, G. Montagna, F. Casino, R. Rella, A. Garcia-Martin, G. Armelles, A. Cebollada, J. M. Garcia-Martin, M. U. Gonzalez and E. Ferreiro-Vila

Abstract A new Magneto-Optic Surface Plasmon Resonance (MOSPR) gas sensor is presented. This sensor is based on the combination of the magneto-optic effects of magnetic materials and the Surface Plasmon Resonance in metallic layers. Preliminary results proofed the enhancement in sensitivity of the MOSPR sensor with respect to traditional SPR sensor.

31.1 Introduction

Surface plasmon resonance (SPR) is one of the leading optical methods that provides easy, highly reproducible and sensitive assays for gas an bio-sensing. It relies on the changes in refractive index that occur when a target analyte binds to the metal film or nanoparticles. The sensitivity and limits of detection of SPR sensors can show variations depending on the method used to excite surface plasmons (prism coupling, grating coupling, optical fibers etc.).

Recently, it has been proposed in the literature a novel Magneto-Optic Surface Plasmon Resonance (MOSPR) sensor [1] which performances can be greatly enhanced with respect to traditional SPR sensors (an improvement by a

M. G. Manera · G. S. Masi · G. Montagna · F. Casino · R. Rella (✉)
Istituto per la Microelettronica ed i Microsistemi, via perMonteroni, 73100 Lecce, Italy
e-mail: roberto.rella@le.imm.cnr.it

A. Garcia-Martin · G. Armelles · A. Cebollada · J. M. Garcia-Martin · M. U. Gonzalez · E. Ferreiro-Vila
Insituto de microelectronica de Madrid, Consejo Superior de Investigaciones Cientificas, Isaac Newton, Tres Cantos, Madrid, Spain

G. Neri et al. (eds.), *Sensors and Microsystems*,
Lecture Notes in Electrical Engineering 91, DOI: 10.1007/978-94-007-1324-6_31,

factor of 3 in the limit of detection). The novel device is based on the combination of the magneto-optic (MO) effects of the magnetic materials and the surface plasmon resonance. This combination can be achieved by introducing into the sensing transducer layer a magnetic thin film whose magnetization state change direction alternately during the surface plasmon excitation. By this way, a great enhancement of the magneto-optic effects in the p-polarized light is produced when the resonant condition is satisfied. Such enhancement strongly depends on the refractive index of the dielectric medium, allowing its use for optical gas sensing. Small variations of the refractive index will induce large changes in the MO response, allowing to greatly improve the sensitivity of the MOSPR sensor.

In this work, some preliminary results for both the gas sensing and biosensing schemes are shown. As concerns gas sensing, TiO_2 nanocrystals prepared by chemical route [2] have been deposited in thin film form by spin coating onto the gold surface in contact with the medium to be monitored. Their interaction with Volatile Organic Compounds (VOCs) has been monitored both in a standard SPR and in MOSPR configurations in order to compare their sensing performances. For biosensing applications, the response of the MOSPR device for adsorption of Bovine Serum Albumin (BSA) proteins onto the gold surface and its interaction with its specific antibody has been tested. In both cases a smart enhancement in sensitivity of the MOSPR sensor with respect to the SPR sensor can be evidenced.

31.2 Experimental Setup

The experimental set-up of the MOSPR is very similar to that developed for standard SPR sensors, the only difference is the introduction of a magnetic layer and a magnetic actuator to control the magnetization state of the magnetic layer. In a Kretschmann arrangement, the enhancement of the MO Kerr effects in the reflected light can be achieved through the combination of Co/Au multilayers. If the magnetization is in the plane of the magnetic layer and perpendicular to the propagation plane of the light (transversal configuration), the MO effect produces a relative change of the reflectivity of the p-polarized light.

$$\frac{\Delta R}{R} = \frac{R(+M) - R(-M)}{R(0)}$$

Figure 31.1 shows the MO effects of the p-polarized light in the transversal configurations for a system formed by a Co/Au multilayer in a Kretschmann arrangement in which the incident medium is glass and the outer medium is water. The MO effects are very localized and show a very sharp curve. As a consequence, small variations of the refractive index will induce large changes in the MO response (Fig. 31.2).

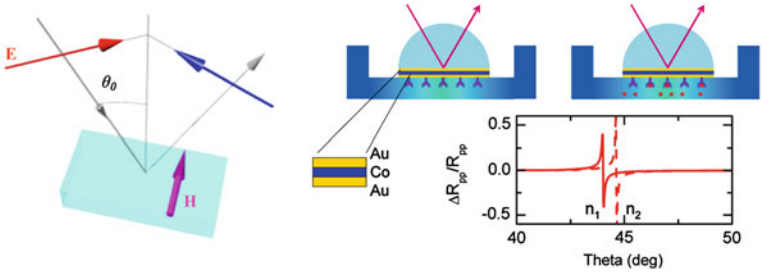

Fig. 31.1 Scheme of the experimental setup for MO-SPR characterization in transversal configuration for gas and biosensing measurements

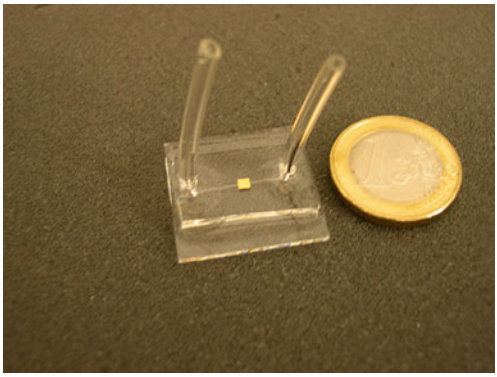

Fig. 31.2 Picture of the sensing chip provided with microfluidics channel for inlet and outlet of analytes

31.3 Preparation of the Sensing and Biosensing *Active Layers*

Au/Co/Au multilayers were deposited by dc magnetron sputtering in an ultra-high-vacuum chamber after a thin layer of Cr adhesion layer onto two different glass slides: BK7 ($n = 1.5$ at $\lambda = 633$ nm) for gas sensing purposes and SF10 ($n = 1.7$ at $\lambda = 633$ nm) for biosensing purposes.

The thickness of the involved multilayers are the following (starting from the glass): 2 nm Cr /25 nmAu/ 6 nm Co/ 15 nm Au. These values have been choosen on the basis of a theoretical simulation of the MO activity of such layers with respect to the sensing application.

In addition, a thin film of TiO_2 nanocrystal were spin coated onto Au/Co/Au multilayers deposited on BK7 glass and used as active layer for gas sensing purposes. Instead, the multilayers deposited onto SF10 glass have been used for biosensing, namely they have been properly functionalized for the further immobilization of BSA proteins.

31.4 Fabrication of Microlfuidics Devices

The inlet and outlet of solutions containing the investigated biomolecules in each step is carried out by microfluidics channels which have been realized on purpose. The fabrication of microfluidics device is based on standard photolithography techniques for master realization.

The SU-8 photoresist is applied n a Silicon wafer with spin-coating process at 500 rpm for 5 s and at 4000 rpm for 40 s, after the master is placed in oven and cured at 65°C for 1 min and at 95°C for 3 min. The exposure to UV radiation is for 80 s followed by another thermal process for 1 min at 65°C and 3 min at 95°C. The hard bake phase is developed at 200°C for 10 min.

The replicas of the inverse pattern is produced using the PDMS of Sylgard; the mixture pre-polymer and current agent is 10:1. The PDMS is cured at 70°C for 1 h or more and peeled off the master, producing the final replica bearing the designed microstructures. Small holes are drilled into the PDMS using a borer to produce inlets and outlets. Finally, PDMS can seal to itself and other flat surfaces reversibly by conformal contact (via van der Waals forces), or irreversibly if both surfaces are Si-based materials and have been oxidized by plasma before contact (a process that forms a covalent O–Si–O bond).

The channel dimensions are 100 μm × 30 μm × 1.5 cm (width, height, length) (Fig. 31.2).

31.5 Results and Discussion

The sensing layer was deposited by spin coating onto the MOSPR substrates (corning glass/Cr/Au/Co/Au); a 35 nm thin layer of TiO_2 nanoparticles prepared by a chemical route was obtained and tested by SPR and MOSPR in controlled atmosphere.

Sensing tests in the presence of mixture of VOCs (ethanol, methanol, isopropanol) sent in the test chamber at different concentration were performed. Preliminary measurements allows obtaining information about the increasing in the sensitivity towards the considered alcohol vapour when a magnetic field is present. Measurements in the presence of different analytes are in progress (Fig. 31.3).

Biosensing tests have been carried out on similar Au/Co/Au multilayers deposited on SF10 glass substrates. First, the investigation was devoted to find the proper conditions of preparation of the multilayers on glass substrates in order to get an high efficiency of immobilization of biomolecules. A morphological characterization of the Au/Co/Au multilayer after the immobilization procedure confirmed the presence of at least one monolayer of proteins onto the Au surface wich results from different features having an higher thickness and less sharp edges.

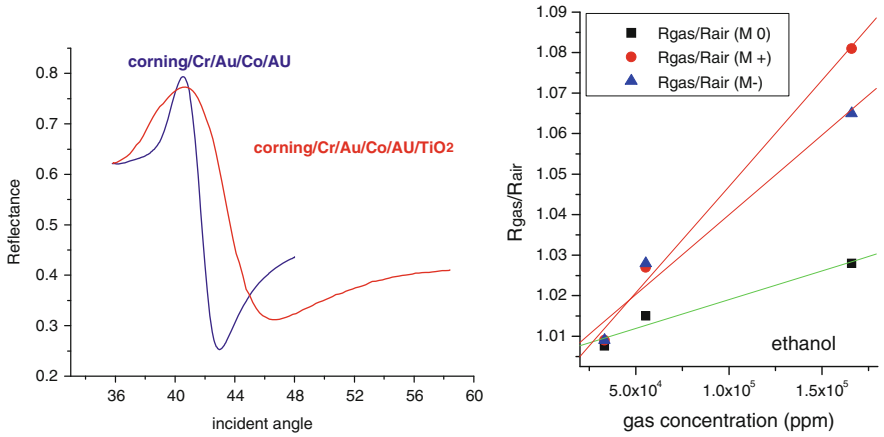

Fig. 31.3 Comparison of SPR curves of the bare Au/Co/Au multilayer on glass and after consideration of TiO2 sensing layer; Sensor calibration comparison relative to ethanol vapours

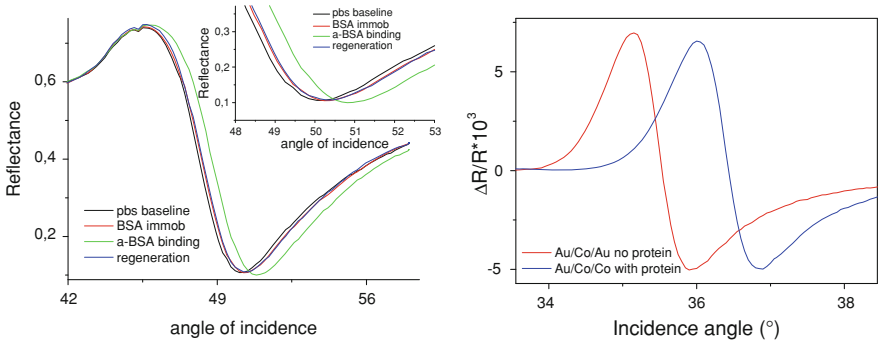

Fig. 31.4 SPR and MOSPR curves comparison relative to each step of the biosensing protocol. The shift in the curve minima upon protein immobilization is apparent

A complete biosensing test has been carried out onto the Au/Co/Au deposited on SF10 glass substrates and each step have been monitored by SPR characterization in liquid conditions.This biosensing tests consisted in the following steps:

- baseline in buffer condition
- immobilization of BSA protein dissolved in the same buffer solution (500 ppm)
- binding between BSA protein and the anti-BSA antibody (300 ppm)
- regeneration step consisting in the separation of anti-BSA antibody from the protein in order to control the ripetibility of the measurement.

Figure 31.4 shows the SPR curves recorded in correspondence of each mentioned step in absence of a magnetic field.

Also in this case, a shift of the minimum of the curve towards higher angles can be noticed, thus confirming the presence of at least a layer of proteins onto the Au surface.

Preliminary measurements of the dynamic interaction BSA protein/anti-BSA performed in liquid phase by SPR equipment give us information about the binding and allows us to compare the results obtained without the application of a magnetic field and after applying a magnetic field in trasversal configuration.

31.6 Conclusions

In this work preliminary results concerning the increase in sensitivity of a MOSPR sensor and biosensor are presented. For gas sensing, a TiO_2 nanocrystal based thin film has been used as active layer, for biosensing the immobilization of BSA protein onto the Au/Co/Au multilayer have been analyzed reporting interesting and promising results that are going to be further investigated.

Acknowledgments This work was supported by Nanomagma Euorpean Project.

References

1. Sepúlveda B, Calle A, Lechuga AM, Armelles G (2006) Highly sensitive detection of biomolecules with the magneto-optic surface plasmon resonance sensor. Opt Lett 31:1085–1087
2. Cozzoli PD, Kornowski A, Weller H (2003) Low-temperature synthesis of soluble and processable organic-capped anatase TiO_2 nanorods. J Am Chem Soc 125:14539–14548

Chapter 32
Nonlinear MEMS Mechanism for Energy Harvesting from Mechanical Vibrations

B. Andò, S. Baglio and C. Trigona

Abstract The aim of this paper is the realization of a novel bistable U-shaped micro-electro-mechanical system to efficiently harvest energy from ambient vibrations. The classical approach is based on vibrating mechanical bodies (linear systems) that allow for collecting energy through the adoption of smart materials, magnetic or electrostatic solutions. The idea pursued in this work is to consider the device vibrations biased by external vibration sources and also a double well dynamic in order to increase the harvest performances. The switching mechanism is based on a U-shaped structure that oscillates around two stable states when the stimulus is large enough to exceed the potential barrier. The device has been designed and realized performing a custom technology (BESOI) based on 15 μm c-Si wafer. Numerical simulations and preliminary measurement campaign validate the nonlinear mechanism showing that the nonlinear system exhibits a behaviour suitable to harvest energy from ambient vibrations.

32.1 Introduction

The trends in technology allow the decrease in both size and power consumption of sensor nodes, wireless sensor networks and more generally battery-powered electronic systems. However, battery supply presents several disadvantages, it increases the space occupied by the supplied system, furthermore it introduces maintenance, replacement costs and, large size and weight compared to integrated technology and microsystems. In order to get over this energy limitation a possible approach is represented by energy recovery techniques. Energy harvesting

B. Andò · S. Baglio · C. Trigona (✉)
Dipartimento di Ingegneria Elettrica Elettronica e dei Sistemi, D.I.E.E.S.,
Università degli studi di Catania, V. le A. Doria 6, 95125 Catania, Italy
e-mail: carlo.trigona@diees.unict.it

G. Neri et al. (eds.), *Sensors and Microsystems*,
Lecture Notes in Electrical Engineering 91, DOI: 10.1007/978-94-007-1324-6_32,

techniques are emerging as environmental friendly energy sources, which form a promising alternative to existing energy resources. In fact many researches are looking into developing reliable solutions that would be able of generating power and performing devices that require no human intervention to replace or recharge batteries. Self-powered integrated systems, autonomous MEMS transducers, batteryless sensor nodes, smart systems and self-contained sensors [1–3], represent a set of devices that adopt the harvested energy to sustain or to supply an electronic device. Energy resources include energy harvesting from passive human power, wind energy, solar power, acoustic and mechanical vibrations. In particular, focusing on the latter source, a wide range of applications and solutions have been performed as vibration-based energy harvesters [4]. The standard approach consists on a linear vibrating body that oscillates around its mechanical resonance frequency. However external vibration sources, such as seismic noise, vehicle motion, thermal noise, noisy environments and equipments present an energy spread over a wide spectrum of frequencies, typically limited in the range of few thousands of Hz [5, 6].

Several ways to optimize the amount of harvested energy have been explored in literature, as regards the conversion and extraction mechanisms oriented to obtain a wider equivalent bandwidth. There are a number of techniques through which the resonance frequency of the device can be tuned realizing a uniform power distribution.

The easiest ways to change frequency of the device would be to alter the mass, length, or thickness of the vibrating structure [7]; however, it would be challenging to alter these parameters while the device is operational. As alternative to the cantilevers array approach, in [6] the authors proposed a resonance frequency tunable energy harvester based on a magnetic force technique.

Here, the idea is to consider a single oscillating device based on a nonlinear behaviour (bistable) to enhance device performances in terms of response to external vibrations. The switching mechanism is based on a structure that oscillates around two stable states as soon as it is excited over the threshold. A response improvement can be demonstrated compared to the classical linear approach. Indeed, a wider spectrum will appear as an effect of the nonlinear term.

32.2 Working Principle: Brief Overview

The approach that will be pursued in this work is based on the exploitation of dynamic properties of nonlinear oscillators, in particular bistable systems [8]. Figure 32.1 shows the nonlinear mechanism implemented. High distance between the two magnets implies a linear behaviour and the parabolic function describes the energy.

Furthermore two equilibrium states x_1 and x_2 will appear when the mass spring damper system is subjected to the effect of the neighbor external magnet; x_0 represents an unstable condition (on the right). The term $2k$ represents the

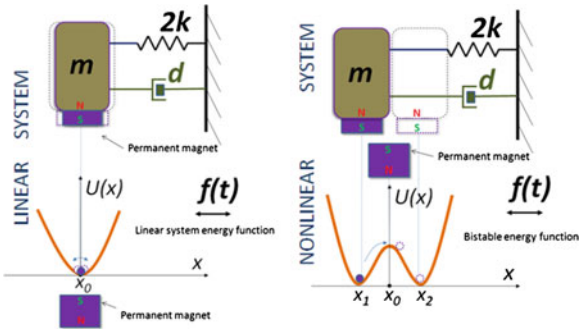

Fig. 32.1 Nonlinear mechanism applied in a MEMS U-shaped device

contribution of the two parallel springs, d is the damper and m the mass at the tip of the cantilever. The dynamical model can be expressed as following:

$$m\ddot{x} + d\dot{x} + \frac{\partial U(x)}{\partial x} = g(t) \tag{32.1}$$

The elastic contribution is included in the potential energy function $U(x)$, that presents a double well shape having a potential barrier correlated with the distance Δ between the two magnets [9–11]: the first one belonging the mass oscillator and the latter frontally disposed.

The time-dependant function $g(t)$ represents the external vibrations source, while the state variable x denotes the displacement of the mechanical nonlinear oscillator.

32.3 The BESOI U-Shaped Device

The micromachined investigated device is a U-shaped cantilever, realized by using a BESOI (Bulk and Etch Silicon on Insulator) process, performed at the CNM of Barcelona. It offers several advantages in terms of robustness, flexibility, adopting a Silicon On Insulator (SOI) wafer based on 15 μm c-Si layer and 450 μm of substrate with 2 μm of buried oxide. In order to release beam and flexible structures a front/bottom deep reactive-ion etching has been performed, as shown in Fig. 32.2. The designed U-shaped cantilever, consists on two parallel cantilever beams having a length of 2,500 μm and width of 700 μm, connected at their tip by an arm of 3,400 μm × 700 μm and having a thickness of 15 μm.

32.3.1 Numerical Simulations and Experimental Results

The dynamical model has been simulated by using a Matlab® routine based on the Euler–Maruyama method. In order to emulate the external vibrations, gaussian white noise having a standard deviation of 20 μN has been used as stochastic

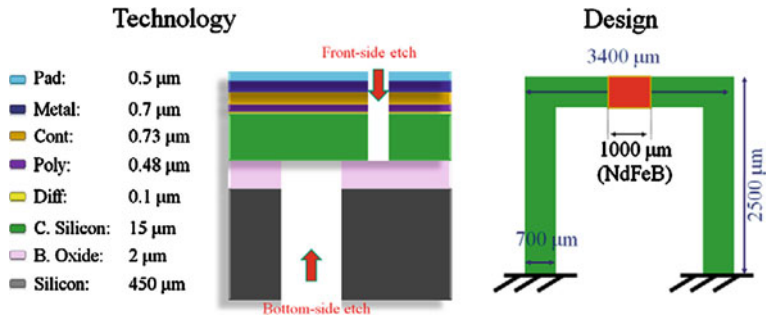

Fig. 32.2 On the *left* the MEMS process adopted and on the *right* the U-shaped oscillator with the permanent magnet (NdFeB) disposed at the tip of the beam

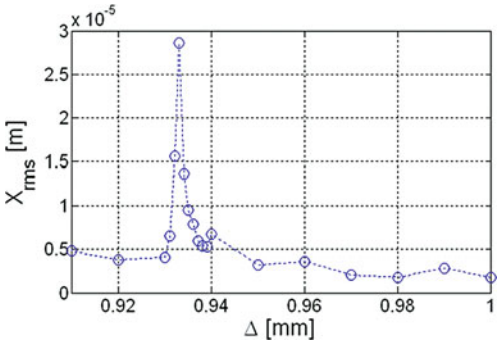

Fig. 32.3 Simulation result: displacement of the U-shaped device (AC component), having an elastic constant (single beam) of 6.35 kg/s^2, damping coefficient of 1e − 5 kg/s and excited by gaussian noise having standard deviation of 20 µN

source. Figure 32.3 shows the displacement of the micromachined device as function of the distance between the two magnets, the DC component has been filtered and a resonance spike has been detected at $\Delta = 0.933$ mm. For smaller values of distance the system becomes highly nonlinear (high barrier of potential), whereas for higher values of Δ, the system tends asymptotically to be linear.

The integrated system has been also realized by using the BESOI technology. The principle has been experimentally validated through an external permanent magnet stack and a translator system, in order to tune the distance between the two magnets, a shaker to stimulate the structure, an active Wheatstone bridge as conditioning circuit of an integrated strain gauge polysilicon-based and having a static resistance of 390 Ω. Finally a LabVIEW^{TM} routine has been performed to filter the bias signal and to drive the shaker. A resonance condition has been experimentally verified that represents the maximum value of the beam displacement and a bistable condition with a low energy barrier. Coherence as respect the simulation results has been detected ($\Delta = 0.94$ mm). Figure 32.4a shows the output signal of the bridge when a distance of 0.94 mm between the two magnets occurs, while Fig. 32.4b shows the output spectrum evaluated through the measure

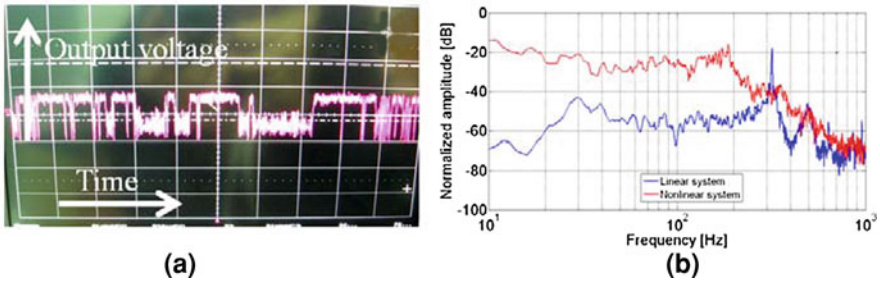

Fig. 32.4 Experimental results: **a** conditioning circuit output, **b** spectrum of the nonlinear/linear oscillator

campaign: a wider spectrum compared to the linear case appears for the nonlinear system, so more energy can be saved adopting a bistable dynamic.

The proposed mechanism validated for a MEMS device, evinces an improvement of the performance with respect to a linear oscillator. The obtained results confirm the nonlinear principle applied to a micromachined transducer, moreover they represent a major advance with respect to the state of the art in the integrated energy harvesting area; in fact the device that has been designed, realized and validated can be highly efficient for scavenging energy from a large range of vibration sources having different nature and therefore different spectral content. As a future trend a PZT material and magnetic stack deposition will be performed.

References

1. Lallart M, Guyomar D, Jayet Y, Petit L, Lefeuvre E, Monnier T, Guy P, Richard C (2008) Synchronized switch harvesting applied to self-powered smart systems: piezoactive microgenerators for autonomous wireless receivers. Sens Actuators A Phys 147:263–272
2. Marzencki M, Ammar Y, Basrour S (2008) Integrated power harvesting system including a MEMS generator and a power management circuit. Sens Actuators A Phys 145–146:363–370
3. Ferrari M, Ferrari V, Guizzetti M, Marioli D (2009) An autonomous battery-less sensor module powered by piezoelectric energy harvesting with RF transmission of multiple measurement signals. Smart Mater Struct 18:1–9
4. Priya S, Inman DJ (2009) Energy harvesting technologies. Springer, New York. ISBN: 978-0-387-76463-4
5. Roundy S, Wright PK, Rabaey J (2003) A study of low level vibrations as a power source for wireless sensor nodes. Comput Commun 26:1131–1144
6. Challa VR, Prasad MG, Shi Y, Fisher FT (2008) A vibration energy harvesting device with bidirectional resonance frequency tunability. Smart Mater Struct 17
7. Ferrari M, Ferrari V, Guizzetti M, Marioli D, Taroni A (2008) Piezoelectric multifrequency energy converter for power harvesting in autonomous Microsystems. Sens Actuators A 142:329–335
8. Strogatz SH (1994) Nonlinear dynamics and chaos. With applications to Physics, Chemistry and Engineering. Addison-Wesley, Cambridge
9. Cottone F, Vocca H, Gammaitoni L (2009) Nonlinear energy harvesting. Phys Rev Lett 102(8)

10. Ferrari M, Ferrari V, Guizzetti M, Andò B, Baglio S, Trigona C (2009) Improved energy harvesting from wideband vibrations by nonlinear piezoelectric converters. In: Proceedings of eurosensors XXIII 2009, Lausanne, Switzerland, September 6–9, pp 1203–1206
11. Andò B, Baglio S, Dumas N, Latorre L, Nouet P, Trigona C (2010) Nonlinear behaviour of a micromachined SOI device for energy harvesting application. In: Proceedings of DTIP 2010, Seville, Spain, May 5–7, pp 263–265

Part IV
Systems

Chapter 33
Liquid-Flow Measurements in Silicon Dioxide Channels with Micron-Sized Dimension

G. Barillaro, A. Diligenti and L. M. Strambini

Abstract Flow measurements on silicon dioxide microchannels featuring inner cross-section as low as 16 μm^2 and aspect-ratio as high as 50 have been performed using liquids with different dynamic viscosities. The microchannels, arranged in a square array with density of 1×10^6 channel/cm^2, are embedded into a silicon substrate and connected to a reservoir grooved on the backside of the substrate. Flow measurements were performed by using an original, purposely designed system. In this work, details on both the measurement systems and the flow properties of such a small channels are reported and discussed.

33.1 Introduction

In last two decades, driven by the development of microfluidic systems for biomedical and optofluidic applications, significant attention has been paid to liquid-flow in microchannels. Although the liquid-flow properties of tubes with inner side (diameter) of tens of microns have been extensively studied [1–4] and reported to obey the Hagen–Poiseuille (H–P) law, only a few studies on circular tubes with inner diameter of a few microns have been reported so far. On the other hand, due to the trend of scaling-down both microfluidic devices and systems, understanding fluid-flow in micron-sized tubes is becoming more and more important.

In this paper flow measurements on silicon dioxide microchannels with length of 200 μm and inner side of 4 μm (square section) are reported, along with a brief

G. Barillaro (✉) · A. Diligenti · L. M. Strambini
Dipartimento di Ingegneria dell'Informazione: Elettronica, Informatica, Telecomunicazioni, Università di Pisa, via G. Caruso 16, 56122, Pisa, Italy
e-mail: g.barillaro@iet.unipi.it

G. Neri et al. (eds.), *Sensors and Microsystems*,
Lecture Notes in Electrical Engineering 91, DOI: 10.1007/978-94-007-1324-6_33,

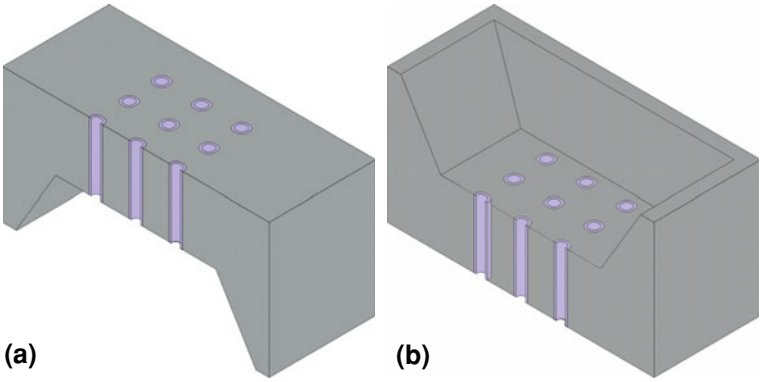

Fig. 33.1 Sketch of the silicon chip used for fluid-flow measurements, consisting of an array of microchannels embedded into a silicon substrate in communication with a reservoir etched on the backside of the chip: **a** *top-view* of the chip; **b** *bottom-view* of the chip

description of the fabrication process. Moreover, the experimental system purposely set up to perform flow measurements is also described.

33.2 Fabrication Process

Figure 33.1 shows a sketch of the silicon chip used for microchannel liquid-flow characterization. The chip consists of an array of high-aspect ratio (up to 50) hollow silicon dioxide channels, with inner side of 4 μm, length of 200 μm, density of 10^6 needles/cm^2, embedded into a silicon substrate and in communication with a reservoir grooved on the backside of the chip.

The fabrication process consists of the following main steps: (1) photo-electrochemical etching (PEC) of a *n*-type silicon substrate ((100) oriented, with resistivity of 3–8 Ω cm and thickness of 550 μm) allowing a deep, ordered macropore array to be etched [5–8]; (2) wet thermal oxidation of the macropores to obtain silicon dioxide micropipes, still closed at their bottom-side; (3) anisotropic silicon wet etching (TMAH) on the backside of the substrate to define a reservoir, and (4) silicon dioxide wet etching (BHF) on the backside of the substrate to open the micropipes bottom-side and obtain hollow microchannels in communication with the reservoir.

Vertical and horizontal uniformity of the channels basically depends on two technological steps: (1) the electrochemical etching step and (2) the thermal oxidation step. If good uniformity was expected for the PEC step, due to the feedback mechanism ruling macropore growth [5–8], the same result was not easily predictable for thermal oxidation of deep macropores. Measurements of the oxide thickness along the pore axis, performed by SEM observation of the cross-section of oxidized samples, confirmed that no appreciable changes in the oxide thickness occur along the macropore axis, at least for depths up to 200 μm.

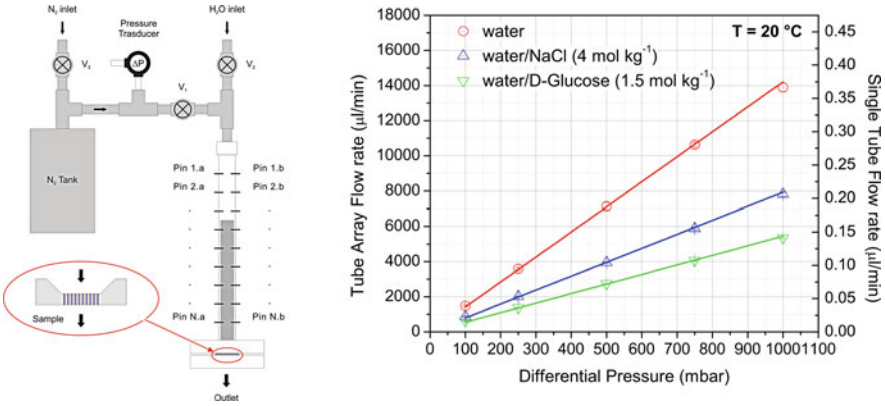

Fig. 33.2 (*left*) Experimental setup used for liquid-flow measurements. (*right*) Flow rate versus pressure drop for an array of 38,000 silicon-dioxide tubes with square section for three different solutions

33.3 Experimental Set-Up and Flow Measurements

The experimental setup used for liquid-flow measurements is sketched in Fig. 33.2. The silicon chip (inset in Fig. 33.2 left), containing the microchannel array with geometrical characteristics as here above described, was put at the end of a graduated pipe, which was filled with the liquid under investigation. A number of couples of electrodes placed at regular distance (2 cm) along the pipe were used to monitor the liquid level by resistance value measurements. A constant differential pressure drop $P_D = P_{in} - P_{out}$ (P_{out} being the reference atmospheric pressure) was maintained between the top of the liquid column and the chip outlet during the whole experiment, thanks to a reservoir with a volume (4,300 cm^3) much larger than the pipe (about 10 cm^3). A maximum relative pressure variation $\Delta P_D/P_D$ of about 2×10^{-3} was measured during experiments.

Liquid-flow measurements as a function of the pressure drop were performed with deionized water (DI H_2O) and, NaCl (4 mol kg^{-1}), D-glucose (1.5 mol kg^{-1}) acqueous solutions, which have dynamic viscosities of 1.0, 1.5, 2.24 mPa s, respectively [9]. The viscosity of the three test solutions was measured by means of a standard viscosimeter and resulted in good agreement with literature values [9]. Liquid-flow measurements were carried out using differential pressures P_D in the range 100−1,000 mbar.

In order to avoid partial or full obstruction of the channel array during measurements, the solutions were filtered with 0.22 μm filters before their introduction in the graduated pipe. Moreover, in order to verify possible channel obstruction, before and after each measurement cycle (with a given liquid in the whole P_D range) a control measurement was performed at $P_D = 500$ mbar using DI H_2O. Control measurements confirmed that the same number of channels in the array was actually active during flow measurements with the three tested solutions.

Experimental results on the three tested solutions are resumed in Fig. 33.2, which shows the liquid-flow rate F versus the differential pressure P_D, both for the whole microchannel array (left scale) and the single tube (right scale). Measurement results highlight a linear relationship between F and P_D for each microtube, according to the Hagen–Poiseuille law:

$$F = \frac{A}{L}\frac{2D_h^2}{C_{fr}\mu}P_D \tag{33.1}$$

where A is the cross-section area, L is the channel length, D_h is the hydraulic diameter, $C_{fr} = 57$ is the friction coefficient for square section, and μ is the dynamic viscosity, even if the channel section is only a few (less than 16) μm^2. The number of active channels is about 38,000, as obtained both by SEM observations and by best-fitting of experimental data using the Hagen–Poiseuille law.

33.4 Conclusions

In this work the liquid-flow properties of high aspect-ratio microchannels have been experimentally investigated using three test solutions with different dynamic viscosities. Flow measurements, to our knowledge performed for the first time on channels with cross-section of a few square microns, highlighted that: (i) the Hagen–Poiseuille law still holds for tubes with such a reduced cross-section area; (ii) an array of 38,000 channels with cross-section of about 16 μm^2 allows solutions of sanitary interest to be delivered at rate comparable with that of commonly used macroscopic hypodermic needles. The latter result is very important for drug delivery application, as the microchannel fabrication process reported in this work can be easily modified for the formation of an array of pain-free microneedles to be inserted in the outermost layer of the skin for transdermal drug delivery.

Acknowledgments This work was supported by Fondazione Cassa di Risparmio di Pisa, Pisa, Italy in the frame of the Project "Microsistema integrato per l'iniezione sottocutanea controllata di piccole quantità di medicinali" ("Integrated microsystem for the controlled delivery of small drug quantities").

References

1. Jiang XN, Zhou ZY, Huang XY, Liu CY (1997) Laminar flow through microchannels used for microscale cooling systems. In: Proceedings of the electronic packaging technology conference, EPTC, pp 119–122
2. Mala GhM, Li D (1999) Flow characteristics of water in microtubes. Int J Heat Fluid Flow 20:142–148
3. Park H, Pak JJ, Son SY, Lim G, Song I (2003) Fabrication of a microchannel integrated with inner sensors and the analysis of its laminar flow characteristics. Sens Actuators A 103: 317–329

4. Steinke ME, Kandlikar SG (2006) Single-phase liquid friction factors in microchannels. Int J Thermal Sci 45:1073–1083
5. Lehmann V (1993) The physics of macropore formation in low doped n-type silicon. J Electrochem Soc 140:2836–2843
6. Lehmann V, Gruning U (1997) The limits of macropore array fabrication. Thin Solid Films 297:13–17
7. Barillaro G, Nannini A, Piotto M (2002) Electrochemical etching in HF solution for silicon micromachining. Sens Actuators A 102:195–201
8. Barillaro G, Bruschi P, Diligenti A, Nannini A (2005) Fabrication of regular silicon microstructures by photo-electrochemical etching of silicon. Phys Stat Sol (c) 2:3198–3202
9. Comesaa JF, Otero JJ, Garcia E, Correa A (2003) Densities and viscosities of ternary systems of water + glucose + sodium chloride at several temperatures. J Chem Eng Data 48:362–366

Chapter 34
Fiber Optic Broadband Ultrasonic Probe for Virtual Biopsy: Technological Solutions

E. Biagi, S. Cerbai, L. Masotti, L. Belsito, A. Roncaglia, G. Masetti and N. Speciale

Abstract An ultrasonic probe was developed by using, in conjunction, opto-acoustic and acousto-optic devices based on fiber optic technology. A Micro-Opto-Mechanical-System (MOMS) approach is proposed to realize the broadband ultrasonic probe on micromachined silicon frames suited to be mounted on the tip of optical fibers.

34.1 Introduction

Our group proposed the design and realization of an ultrasonic source based on opto-acoustic effect in 1996, with a metal layer over the fiber optic tip as absorbing target [1]. In 2001 we improved, of about two orders of magnitude, the opto-acoustic conversion by replacing the metal absorbing target with a graphite one [2]. The transmitting element, depicted in Fig. 34.1a, is constituted by a fiber optic on whose tip an absorbing layer is deposed; Thermo-elastic Ultrasound Generation (TUG) takes place when the laser pulse hits this absorbing thin layer and the induced thermal expansion generates a mechanical shock wave.

The receiving element is constituted by an extrinsic fiber hydrophone, based on a Fabry–Perot interferometer, as depicted in Fig. 34.1b. A continuous wave laser

E. Biagi (✉) · S. Cerbai · L. Masotti
Electronics and Telecommunications Department, University of Florence, Florence, Italy
e-mail: elena.biagi@unifi.it

L. Belsito · A. Roncaglia
Microelectronics and Microsystems Institute, CNR, Bologna, Italy

G. Masetti · N. Speciale
Electronics, Informatics and Systems Department, University of Bologna, Bologna, Italy

G. Neri et al. (eds.), *Sensors and Microsystems*,
Lecture Notes in Electrical Engineering 91, DOI: 10.1007/978-94-007-1324-6_34,

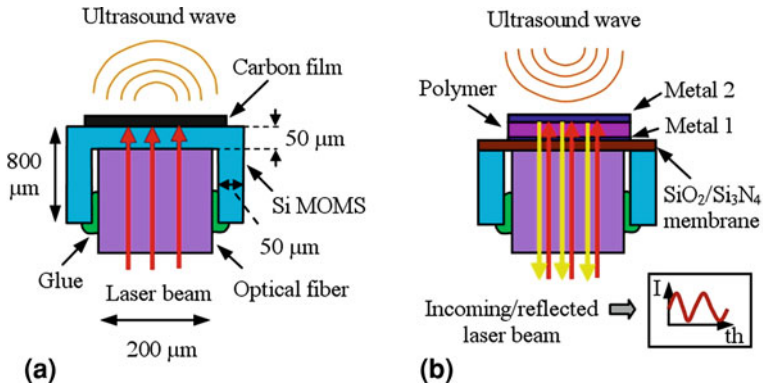

Fig. 34.1 MOMS opto-acoustic transmitter (**a**) and receiver (**b**) mounted on an optical fiber

beam is launched inside a fiber. The device works as follows: a pressure wave, impinging over the interferometer, modulates its thickness. This change in thickness produces a modification in the interferometer reflectance, defined as the ratio between the reflected and incident light power, and thus induces a change in the light intensity detected by a photodiode. For the proposed probe, completely based on a fiber optic technology, a strong miniaturization can be obtained, making it suitable for intravascular, endoluminal and percutaneous applications. In 2006 the first ultrasonic images obtained with a fully fiber optic ultrasonic probe were presented [4].

34.2 Technological Solutions and Measurements

In both devices, micromachined silicon MOMS (Micro Opto Mechanical Systems) are used to permit the housing of the optical fiber close to the optical layers used for ultrasound emission and detection. For the transmitting element a carbon film with high optical absorption is deposited and patterned on the MOMS upper surface.

For the receiver, a planar Fabry–Perot interferometer is realized on a dielectric membrane (SiO_2/Si_3N_4) obtained, on the silicon substrate, by backside etching. The interferometer is constituted by a polymer spacer with a low elastic modulus, so that its thickness can be modulated by an incoming ultrasound wave. For the carbon layers, photoresist carbonization on silicon has been investigated as a fabrication technique, using OIR 908-35 positive photoresist from Fujifilm. The technological process, reported in Fig. 34.2a, has been adopted to realize some prototype samples. Starting from 500 μm thick <100> oriented silicon substrates, a thermal oxidation step has been carried out at 1,000°C in wet environment, yielding a roughly 500 nm thick silicon oxide layer on both sides of the wafer (step 2). This layer has been used as a mask for the subsequent silicon micromachining (step 4), after backside patterning and etching with Buffered

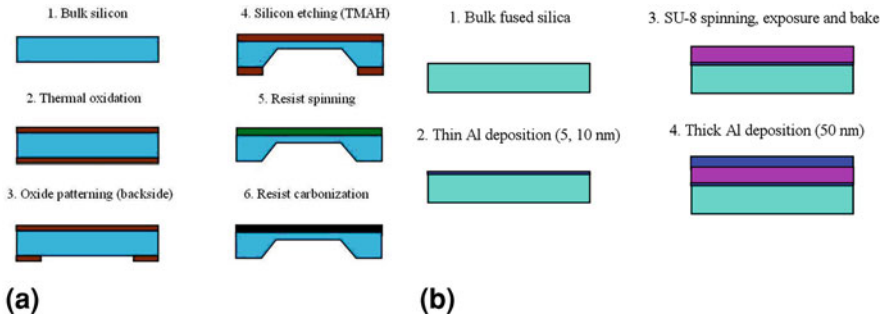

Fig. 34.2 Technological process used to realize carbon layers (**a**) and planar Fabry–Perot interferometers (**b**) on fused silica substrates

Oxide Etch (BOE, step 3). In this way, square silicon membranes with thickness around 200 μm and area of 1×1 mm^2 have been obtained on the wafer. After removing the SiO_2 mask, OIR 908-35 photoresist has been spinned on the wafer front side at 3,000 rpm, yielding a roughly 4 μm thick film. The resist layer has been subsequently carbonized by means of an annealing step performed at 750°C in argon atmosphere for 30 min. With the same procedure, carbon layers have also been realized on double-side polished wafers for the optical measurements. It has been observed that the carbon layer obtained after carbonization is roughly 1 μm thick, as a result of volume shrinking of the starting resist layer. For the detector, negative resist SU-8 has been chosen to fabricate the polymer spacer. For the preliminary tests, planar Fabry–Perot interferometers with different thicknesses of the spacer and of the thinnest metal film have been realized on fused silica substrates (pure SiO_2) according to the process flow of Fig. 34.2b. Fused silica has been chosen to mimic the optical properties of the SiO_2/Si_3N_4 membrane that is expected to be adopted in the detectors. Aluminum has been deposited by evaporation to realize both the thin and the thick metal layers of the interferometers. The thickest layer was 50 nm thick, while two thicknesses have been tested for the thinnest one (5 and 10 nm). SU-8 has been deposited by spinning, in 5 and 10 μm thick layers, obtained by varying the spinning speed. The resist layers were exposed to UV light and hard baked at 200°C for 5 min on a hotplate before depositing the last Al layer (50 nm).

The carbon layers on silicon and the Fabry–Perot interferometers on fused silica have been subjected to optical and acoustic characterizations. The optical transmittance of carbon layers obtained on double-side polished 500 μm thick silicon substrates has been measured with a Nicolet 5700 Fourier Transform Infrared (FTIR) spectrometer and compared with the one of a plain silicon wafer (Fig. 34.3a). The measurement shows an evident decrease of the silicon wafer transmittance in the near IR range due to the presence of the heavily absorbing carbon film.

The reflectance of the Fabry–Perot interferometers realized on fused silica has been also measured both in the optical and IR range. In Fig. 34.3b, the results of

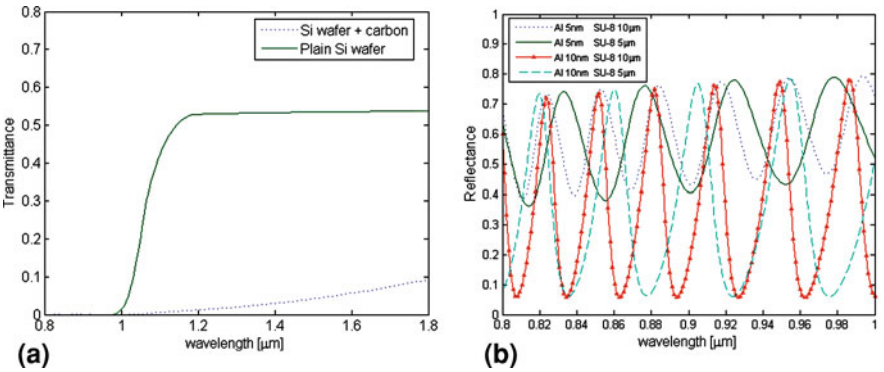

Fig. 34.3 **a** NIR transmittance of a carbon layer on a double-side polished silicon wafer compared with the one of a plain silicon wafer. **b** NIR reflectance of planar interferometers realized with different thicknesses of the SU-8 spacer and of the thin Al layer

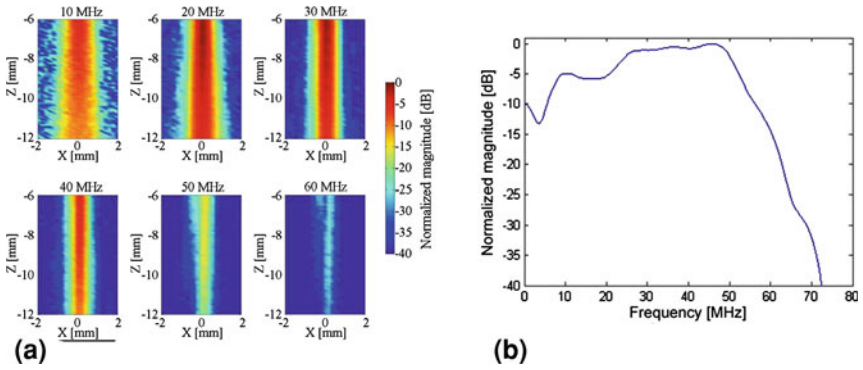

Fig. 34.4 **a** Magnitude of acoustic field longitudinal section, filtered at six different frequencies. **b** Spectral response of the MOMS fiber optic probe

the optical characterizations performed in the visible and NIR range on interferometers with different thickness features are summarized.

A longitudinal section of the acoustic field, generated by the opto-acoustic transmitter, was acquired by employing a PVDF membrane hydrophone (Marconi 699/1/00002/200). In Fig. 34.4a, the magnitude of the acoustic field filtered at six different frequencies is reported for 6–12 mm distance from the transducer. The colormap represents the same magnitude level for the all six pictures. The decrease in magnitude observed for high frequencies range is partially due to the hydrophone frequency response (60 MHz cut-off).

The global response of the MOMS fiber optic probe has been obtained by facing the transmitter and receiver elements with each other and acquiring the ultrasonic signal. In Fig. 34.4b the spectral response of the probe is reported.

34.3 Conclusions

Preliminary results are presented on the opto-acoustic emission properties of carbon films (thickness around 1 μm) and about the optical and acoustic behaviour of planar Fabry–Perot interferometers composed by thin metal layers and SU-8 negative photoresist on fused silica substrates.

The high frequencies and large bandwidth in conjunction with the extreme miniaturization derived from the MOMS technology could open a way towards "virtual biopsy", intended as the possibility for studying and characterizing the nature and health conditions of living tissues "in situ".

References

1. Biagi E, Fontani S, Francini F, Masotti L, Pieraccini M (1996) Photoacoustic generation all-fiber optic transducers. In: Ultrasonic symposium 1996 proceedings, vol 2, pp 921–924
2. Biagi E, Margheri F, Menichelli D (2001) Efficient laser-ultrasound generation by using heavily absorbing films as targets. IEEE Trans Ultrason Ferroelect Freq Control 48(6):1669–1680
3. Masotti L, Biagi E, Margheri F, Menichelli D (2003) Opto-acoustic generator of ultrasound waves from laser energy supplied via optical fiber. U.S. Patent 6 519 376, February
4. Biagi E, Acquafresca A, Cerbai S, Gambacciani P, Masotti L (2006) Fully fiber optic ultrasonic probes for virtual biopsy. In: Ultrasonic symposium 2006 Proceedings, pp 556–559

Chapter 35
Design, Fabrication and Characterization of a New Hybrid Resonator for Biosensing Applications

C. Ciminelli, C. M. Campanella and M. N. Armenise

Abstract A novel optical biosensor realized in SOI technology has been proposed. A preliminary study involving common configurations such as ring- and disk-resonator has been carried out in order to design and then to test the new resonator, which we call hybrid resonator because it shows ring resonator shape and an optical behavior (in terms of Q factor) similar to the one of a disk-resonator. A detection limit of 5×10^{-3} RIU has been demonstrated for the detection of glucose inside an aqueous solution.

35.1 Introduction

In the last decade, the increasing demand for high-sensitive and low-cost biosensors devoted to an easier monitoring of the most common human diseases gave the scientific community the input to study new sensing techniques.

This is the reason because integrated optical devices based on microresonant cavities, already widely investigated to realize devices such as lasers, switches and add-drop filters, have been introduced in literature as new bio-sensing platforms.

The advantages in using optical devices for sensing activity are their immunity to electromagnetic interference, together with their capability to perform both remote sensing and multisensing onto a single chip.

Different platforms for optical sensing have been proposed: interferometers based-, optical waveguides based-, photonic crystal based- and ring resonator based biosensor [1]. Peculiarities of microresonant biosensors are the small dimensions,

C. Ciminelli (✉) · C. M. Campanella · M. N. Armenise
Optoelectronics Laboratory, Politecnico di Bari, Via E.Orabona n. 4, 70125 Bari, Italy
e-mail: c.ciminelli@poliba.it

G. Neri et al. (eds.), *Sensors and Microsystems*,
Lecture Notes in Electrical Engineering 91, DOI: 10.1007/978-94-007-1324-6_35,

the high sensitivity, the high capability of integration onto a chip and the good suitability for mass-production.

The high sensitivity of microsphere and microtoroid configurations is due to the excitation of whispering gallery modes, but the fabrication process is complicated and expensive and it is affected by bad reproducibility [2].

For these reasons, optical characteristics of microring resonator and microdisk resonator configurations are been investigated both theoretically and experimentally.

35.2 Resonant Cavity-Based Biosensor

As above mentioned, different biosensor configurations based on resonant cavities are available in literature. As for their performance, they should show high sensitivity, low detection limit, good reliability and reproducibility, fast response. Low cost, simple fabrication process and robustness are also highly desirable.

The two main parameters taken into account in the biosensor design are the sensitivity and the detection limit. Detection limit is the minimum amount of analyte able to induce a detectable change in the resonator optical properties. Sensitivity is generally defined as the ratio between the change in the optical properties of the resonator and the change in the analyte properties. The analytical definition of sensitivity is related to the sensing mechanism and the transducing methods adopted.

35.2.1 Transducing Methods

In contrast to the widely employed fluorescence based detection, where either target molecules or biorecognition molecules are labeled through fluorescent tags, the sensing mechanism assumed in this work (label free detection) does not modify molecules inside the analyte and does not require the presence of a biorecognition molecules layer. The transducing method employed is based on refractive index change induced by the presence of an analyte.

35.3 Biosensor Design

Optical characteristics of two standard SOI (Silicon on Insulator) microresonators, a ring- and a disk-resonator (Fig. 35.1), coupled to two separate bus waveguides have been investigated both theoretically and experimentally.

Waveguides physical dimensions (width = 500 nm, thickness = 220 nm) have been determined in order to excite a TE_0 mode when a source light having

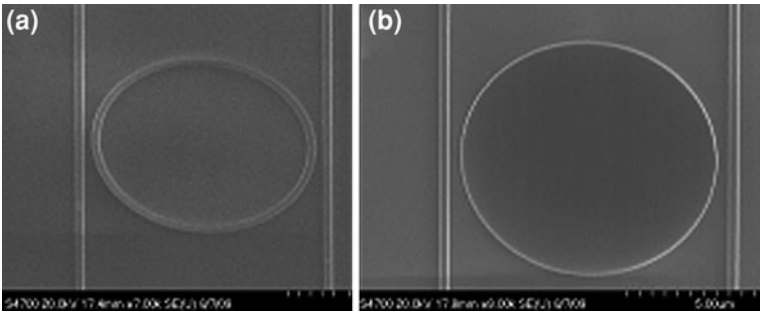

Fig. 35.1 SEM picture of **a** microring resonator, **b** microdisk resonator

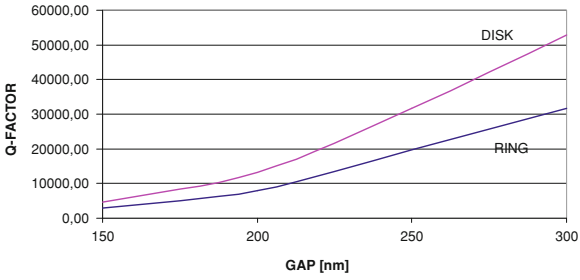

Fig. 35.2 Comparison between the Q-factor of the ring and disk resonator

wavelength in the range 1.52–1.59 μm is applied. Effective index calculated for the TE_0 mode is 2.6. The radius of both microdisk and microring resonator has been fixed to 5 μm, while the gap between the microcavity and the waveguides was varied from 100 to 500 nm in order to achieve the biggest possible value of the Q-factor (parameter strictly related to the detection limit) [3, 4]. The optical properties of both microresonators have been investigated via a 2D Finite Differences Time Domain (FDTD) method by setting the frequency resolution to 10 pm. When the gap increases, the Q-factor increases too and the coupled power decreases. A Q-factor of 3×10^4 has been calculated for the microring, while 5×10^4 is the microdisk Q-factor with a gap of 300 nm for both the resonators. The free spectral range FSR is 30 nm for both the configurations.

After this preliminary study, the inner area of the ring resonator has been supposed to be filled with different glucose concentrations. A shift $\Delta\lambda_{res} = 120$ nm of the fundamental mode resonant wavelength has been observed for a change in glucose refractive index $\Delta n = 5 \times 10^{-2}$ RIU and sensitivity has been calculated as the ratio $\Delta\lambda_{res}/\Delta n$.

The next step was the investigation of the optical behaviour of a new resonator shape, named "hybrid resonator". It has a geometry similar to that of a ring resonator and a quality factor Q of the same order of a microdisk resonator (bigger than the microring one, for fixed radius R, gap g and waveguides width w, Fig. 35.2).

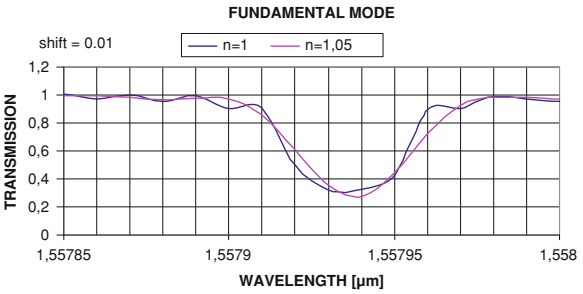

Fig. 35.3 Fundamental mode resonance shift, $\Delta R = 1$ µm

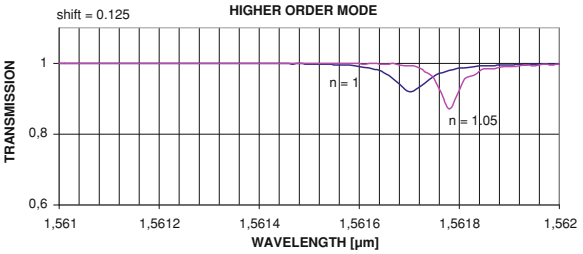

Fig. 35.4 Higher order mode resonance shift, $\Delta R = 1$ µm

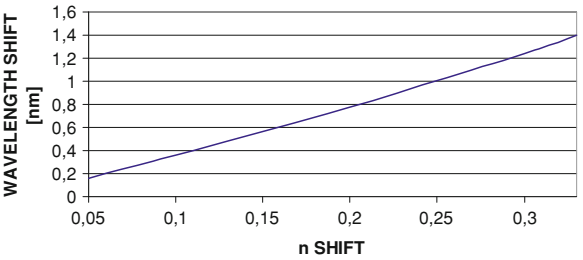

Fig. 35.5 Relationship between the resonance shift and the refractive index change of different glucose solutions

To study the new resonator configuration, the ring width (defined as the difference ΔR between the outer radius and the inner radius) has been changed until the optical properties of the "hybrid structure" became similar to the ones of the disk resonator. For a g of 300 nm, a w of 500 nm and a resonator outer radius of 5 µm, several configurations have been investigated. The limit value beyond which the hybrid resonator Q-factor is comparable to the disk Q-factor has been found to be $\Delta R = 2$ µm. If $\Delta R \geq 1$ µm, the wavelength shift does not affect the fundamental mode, but only higher order modes, so it is not useful for sensing (Figs. 35.3 and 35.4).

A good value of detection limit $D = 5 \times 10^{-3}$ RIU has been found for $\Delta R = 750$ nm. If different concentrations of glucose dissolved in water are investigated, a linear relation between the resonance shift and the refractive index change is derived (Fig. 35.5).

Both ring and disk microresonators have then been fabricated (Fig. 35.1), through e-beam lithography and dry etching ICP techniques.

35.4 Conclusions

Preliminary results encourage a deeper investigation of the new resonator configuration, which appears to be well suitable for homogeneous sensing applications, as above demonstrated.

References

1. Yalçın A, Popat KC, Aldridge JC, Desai TA, Hryniewicz J, Chbouki N, Little BE, King O, Van V, Chu S, Gill D, Anthes-Washburn M, Goldberg B (2006) Optical sensing of biomolecules using microring resonators. IEEE J Sel Top Quantum Electron 12:148–155
2. Fan X, White IM, Shopova SI, Zhu H, Suter JD, Sun Y (2008) Sensitive optical biosensors for unlabeled targets: a review. Anal Chim Acta 620:8–26
3. Lee HS, O BH, Lee SG, Lee EH (2008) Design of a silicon optical micro-ring resonator sensor of improved sensitivity and selectivity. In: Optoelectronic integrated circuits X. Proceedings of the SPIE, vol 6897, pp 68970 W-13
4. Campanella CM (2009) Design and fabrication of an optical cavity resonator based biosensor. Laurea thesis in Control Systems Engineering, Politecnico di Bari

Chapter 36
Comparison Between Integrated Transmitter Typologies for Monolithic Wireless Smart Sensors

Letizia Fragomeni, Fabio Zito and Francesco G. Della Corte

Abstract Two different integrated transmitter topologies, each exploiting an on-chip loop antenna and implementing an on–off key (OOK) modulation, have been implemented using a standard 0.35 μm CMOS process. The implemented transmitters use two different directly modulated oscillator topologies, namely a 2.5 GHz complementary cross-coupled LC oscillator and a 1 GHz current-starved ring oscillator, whose outputs are employed respectively to feed their own loop antenna. The cross-coupled LC transmitter and the ring oscillator topology consume, respectively, 22 and 4.4 mW from 3.3 V supply voltage. The average power consumption can be decreased to few tens of microwatt by duty-cycling the transmitters and by increasing the data rate of the packet to be transmitted up to 2 Mbit/s for the cross-coupled LC typology and 1 Mbit/s for the ring oscillator transmitter. The employed integrated small loop antenna radiate sufficient power for few meters communication range.

36.1 Introduction

Smart sensors are rapidly growing in importance in the last years because of the necessity of monitoring several kinds of physical parameters in all applications where electro-mechanical systems must interact with their environment [1]. Furthermore, providing the sensors with a wireless communication channel to transmit the detected information allows to set up networks of wireless nodes, each

L. Fragomeni (✉) · F. Zito · F. G. Della Corte
DIMET – Department of Information Science, Mathematics,
Electronics and Transportations, "Mediterranea" University of Reggio Calabria,
Via Graziella, Loc. Feo di Vito, 89122 Reggio Calabria, Italy
e-mail: letizia.fragomeni@unirc.it

G. Neri et al. (eds.), *Sensors and Microsystems*,
Lecture Notes in Electrical Engineering 91, DOI: 10.1007/978-94-007-1324-6_36,

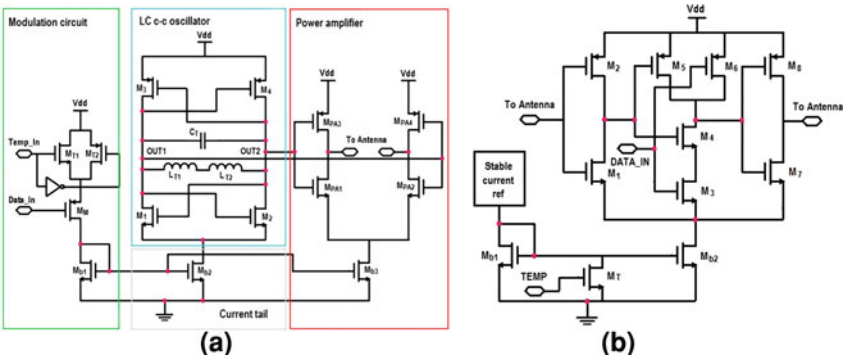

Fig. 36.1 Circuit schematic of the implemented transmitters: **a** LC c–c oscillator based transmitter; **b** ring oscillator based topology

having sensing, computational and communication capabilities. In this context, a fully embedded wireless system for short range applications can be realised exploiting an integrated loop antenna [2, 3].

In this paper the comparison between two different transmitter topologies made with a standard CMOS process, each exploiting an integrated loop antenna and implementing an on–off key (OOK) modulation, are discussed. The circuits can be seen as the RF sections of monolithic smart RFID based sensory systems.

36.2 Transmitter Architectures

A time-varying envelope modulation scheme, such as on–off keying (OOK), can be preferred with respect to a frequency modulation structure for the implementation of low-power transmitters [4]. In this case, in fact, the modulator architecture is usually simple to be implemented and allows to reduce the power consumption.

In this paper, two directly on–off keying (OOK) modulated oscillator based transmitters are proposed. The circuit schematics of the implemented architectures are shown in Fig. 36.1.

The first transmitter topology uses a complementary cross-coupled LC oscillator [5] implemented with standard transistors provided by the four-metal layer AMS CMOS 0.35 μm technology. The resonating circuit employs two 2.6 nH square spiral inductors fabricated in the top layer metallization and a polysilicon capacitor appropriately sized for getting 2.5 GHz oscillation frequency. The transistors pairs, together with the current tail source, have been sized for obtaining the needed negative transconductance for sustaining oscillations and to properly bias the coupled differential buffer, that is connected at the oscillator outputs, at the switching point. The buffer is used to feed the integrated 6.6 mm length loop antenna. A start-up circuit allows for enabling the transmitter and for implementing the OOK modulation.

Table 36.1 Parameters of the implemented integrated antenna

Parameter	Loop 1 (@ 2.5 GHz)	Loop 2 (@ 1 GHz)
Area (μm^2)	1620 × 1620	1520 × 1088
Trace width (μm)	20	20
Feeding gap (μm)	139	70
G (dB)	−35	−52

The second transmitter is based on a three-stage single-ended current-starved ring oscillator biased by mean of a current sink with high stability over supply voltage fluctuations that alleviates the oscillation frequency variations due to bias current fluctuations [6]. The integrated 5.1 mm length loop antenna is connected between the first inverter stage and the last one to create both the feedback path and the wireless communication channel. The OOK modulation is implemented by exploiting a two inputs NAND gate, one of those is provided with the modulating signal.

A single turn small loop antenna topology has been chosen to be implemented directly on chip mainly because it can surround the whole chip and, consequently, maximize its area. In particular, two separate radiating elements have been implemented. Table 36.1 contains the geometrical parameters of the radiating structures and their theoretical gain, calculated as reported in [7].

36.3 Experimental Results

The implemented transmitters have been characterized using a logarithm periodic dipole antenna connected to a R&S FSV signal and spectrum analyzer acting as receiver. The experimental measurements show a carrier frequency of the complementary cross-coupled LC oscillator based transmitter of about 2.57 GHz with a phase noise of −87 dBc/Hz at 1 MHz offset. The ring oscillator based typology has a carrier frequency of about 1 GHz with a phase noise of −71 dBc/Hz at 1 MHz offset. The carrier frequencies of the implemented transmitters are shown in Fig. 36.2.

The cross-coupled LC transmitter and the ring oscillator topology consume, respectively, 22 and 4.4 mW from 3.3 V supply voltage. The average power consumption can be decreased to few tens of microwatt by turning on the transmitters only for a packet transmission in a second and by increasing the data rate of the data to 2 Mbit/s for the cross-coupled LC topology and 1 Mbit/s for the ring oscillator transmitter.

The loop antennas radiate a power of about −58 dBm at 10 cm that allows to enable a few meters communication range.

Finally, the capabilities of the discussed circuits to transmit an OOK modulated packet of data have been tested using an 8-bit digital code. Figure 36.3 shows the received signal, demodulated using the AM demodulation mode of the R&S FSV spectrum and signal analyzer.

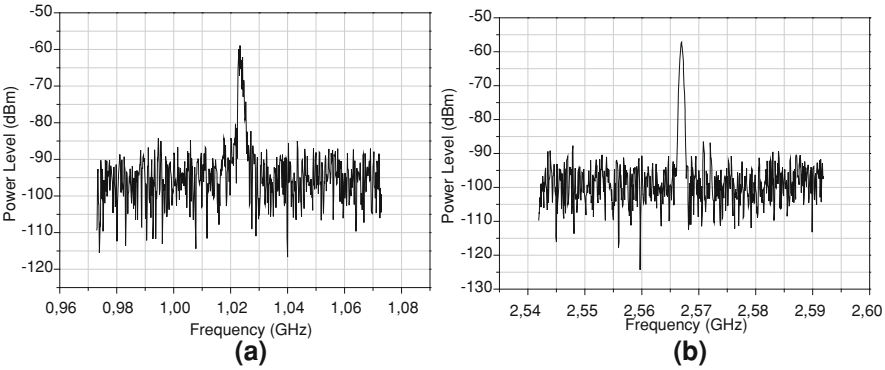

Fig. 36.2 Carrier frequencies of the implemented transmitters **a** RO based typology; **b** c–c LC oscillator based topology

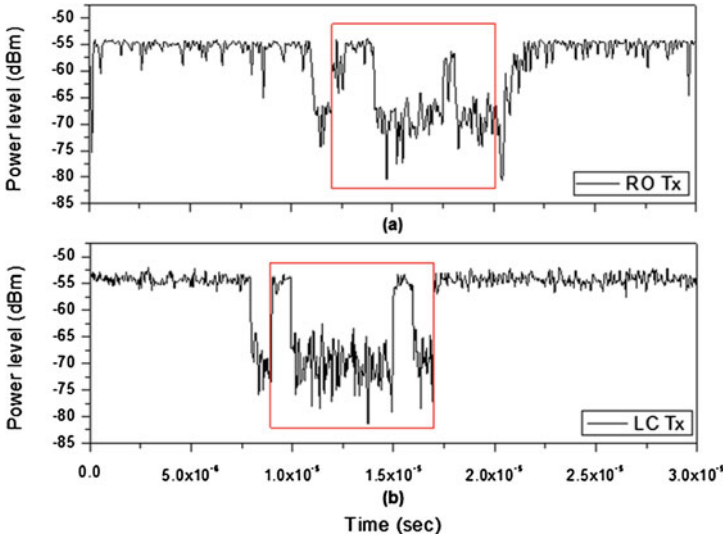

Fig. 36.3 Demodulated 625 kbit/s signal: **a** transmitted using the RO based topology (11000100); **b** transmitted using the c–c LC oscillator based topology (10000010)

36.4 Conclusions

Two fully integrated OOK transmitter topologies, made with a standard 3.3 V CMOS 0.35 μm process, have been presented. The systems are provided with an RF communication channel realized by mean of two single turn small loop antennas, implemented using the top metal layer of the CMOS technology. The radiated power is sufficient for a few meters communication range, thus the transmitters represent an effective solution for the realization of monolithic wireless systems, such as smart sensors.

References

1. Zhang Y et al (2004) Progress of smart sensor and smart sensor networks. In: Proceedings of the 5th world congress on intelligent control and automation, June
2. Aquilino F et al (2009) CMOS fully-integrated wireless temperature sensors with on-chip antenna. In: IEEE proceedings of the 39th European microwave conference
3. Della Corte FG et al (2009) A microchip integrated temperature sensor with RF communication channel and on-chip antenna. Procedia Chem 1(1):473–476
4. Shuguang H et al (2006) A 8.0-mW 1-Mbps ASK transmitter for wireless capsule endoscope applications. In: IEEE radio frequency integrated circuits (RFIC) symposium
5. Jia L et al (2004) 93–104-GHz-band cross-coupled complementary oscillator with low phase-noise performance. IEEE Trans Microw Theory Tech 52(4):1273–1278
6. Zhao X et al (2004) A wide tuning range voltage-controlled ring oscillator dedicated to ultrasound transmitter. In: The 16th international conference on microelectronics
7. Balanis CA (1997) 'Loop antennas' in "antenna theory: analysis and design", 2nd edn. Wiley, New York

Chapter 37
Digital Processing of Intracranial Pressure Signal Acquired by Means of a Strain Gauge Sensor

A. Calisto, A. Bramanti, M. Galeano and S. Serrano

Abstract The aim of this work is to exploit an automatic system to make it easier, more quickly and costless the evaluation of Intracranial pressure (ICP) signal in cerebral pathology affected patients. The authors have developed a tool able to filter, analyze and extract features from ICP signal or recording. For the conducted study we have used the ICP MicroSensor, a catheter with a micro miniature silicon strain gauge type sensor mounted at one end and an electrical connector at the other end. We studied 16 continuous pressure recordings of different patients who underwent an infusion test. The digital signal processing (DSP) performed consists in: signal filtering, peaks identification, location of single pressure waves and extraction of features from each single wave. The outflow of the elaboration is composed by the 14 parameters trends which allows an easy analysis of intracranial pressure. It can be intended as a valid, consistent, reliable and easy-computing tool that might be used by the medical team in all those cases that involve brain damages or diseases.

37.1 Introduction

The cranial compartment is incompressible, and its internal pressure is determined by the sum of contributes due to three compartments: haematic, parenchymal and liquoral. It is difficult to define an ordinary intracranial pressure (ICP) value, i.e. it depends on patient's age, position and clinical condition. An average value for a sane adult patient in horizontal position is in the range 7–15 mmHg [1].

A. Calisto (✉) · A. Bramanti · M. Galeano · S. Serrano
Department of Matter Physics and Electronic Engineering, University of Messina, via Stagno D'Alcontres, 31, Messina, Italy
e-mail: acalisto@unime.it

G. Neri et al. (eds.), *Sensors and Microsystems*,
Lecture Notes in Electrical Engineering 91, DOI: 10.1007/978-94-007-1324-6_37,

ICP monitoring is considered the most useful clinical technique in the management of patients with intracranial disease. If the cerebral vessels are not reactive, an increase in cerebral perfusion pressure may result in several grave forms of pathology [2]. Since the 1980s continuous intracranial pressure monitoring has become more widely used, due to the development of new types of sensors.

ICP values analysis is strictly related to the investigating pathology, i.e. in case of suspect hydrocephalus a 15 mmHg value is to be deemed as an excessive one; whereas in case of suspect cerebral damage, the intensive care starts round about at 25 mmHg. Only in the last few years the scientific community has turned attention to the different components included in the ICP signal. Limiting the survey to the mean ICP value or to a fixed time windows could result in a heavy fault.

The aim of this work is to exploit an automatic system to make it easier, more quickly and costless the evaluation of ICP signal in cerebral pathology affected patients. The authors have developed a tool able to filter, analyze and extract features from ICP signal or recording.

37.2 ICP Measurement and the Used Sensor

For ICP monitoring, a small pressure transducer is inserted through the skull into the brain or ventricles to measure the cerebrospinal fluid (CSF) pressure. Pressure monitoring, either by the lumbar catheter or the intracranial method, requires admission to a hospital. It can detect an abnormal pattern of pressure waves as well as low or high pressure.

For the conducted study we have used the ICP MicroSensor which is a new miniature strain gauge device manufactured by Codman (Johnson and Johnson). It is slimmer and more flexible than fiber-optic sensors (e.g. Camino). These last ones are subject to fracture of the transducer at the neck of the fixation screw, while the MicroSensor is less likely to suffer from such breakage and is small enough to be inserted into the spinal column for lumbar monitoring.

The Codman MicroSensor ICP Transducer is a catheter with a micro miniature silicon strain gauge type sensor mounted at one end and an electrical connector at the other end. It is designed for use with Codman interface control monitor (ICP express). Moreover it may be interfaced to a wide variety of patient monitoring system for ICP waveform display and for consolidation of ICP data with other vital signs information [3].

The output signal of the transducer is the unbalanced output voltage of a resistive bridge sensor.

37.3 Infusion Test and Signal Acquisition

We studied 16 patients (X males and Y females, age range 24–78). All data analyzed come from continuous CSF pressure recordings of different patients who underwent an infusion test to investigate the altered dynamics of CSF. The test is

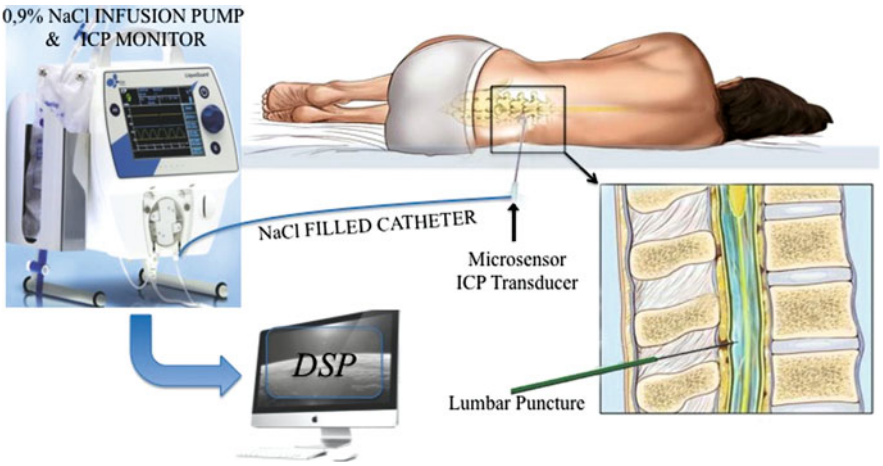

Fig. 37.1 It is shown the ICP monitoring diagram adopted to perform the infusion test, the most commonly performed test for evaluating NPH related features recording

performed to investigate the dynamic ICP trend under forced and modified condition. It requires the simultaneous infusion of artificial spinal fluid and measurement of CSF pressure and it is generally performed through a lumbar puncture by 1 or 2 needles inserted into the lumbar subarachnoid space (see Fig. 37.1). The infusion test is performed through the scheme shown in Fig. 37.1: the infusion pomp instills a 0.9% NaCl solution at settable constant rate (set at 1.5 ml/min) by means of a stiff saline-filled specific catheter which has mounted on it a pressure transducer.

The test starts with calibration phase, fundamental to offset the atmospheric pressure. Then a couple of minutes is needed to determine the baseline ICP (ICP_B), i.e. the medium value of ICP in not altered dynamic condition, after that the pump is switched on and it stays on until the ICP reaches a steady state medium value called Plateau ICP (ICP_P) in fully agreement with safety condition for the patient. When this step is reached, the infusion is stopped but the recording is still going on to allow a further investigation on the dynamic of the reabsorbition phase.

37.4 Signal Processing

The digital signal processing (DSP) performed consists in: signal filtering, peaks identification, location of single pressure waves and extraction of features from each single wave (see Fig. 37.2). Noise and artifacts (i.e. unwanted patient's movement, speeches and coughing during the recording) are pruned by means of signal filtering. Filtering is performed through a FIR equiripple low-pass filter, implemented with a suitable cut-off frequency.

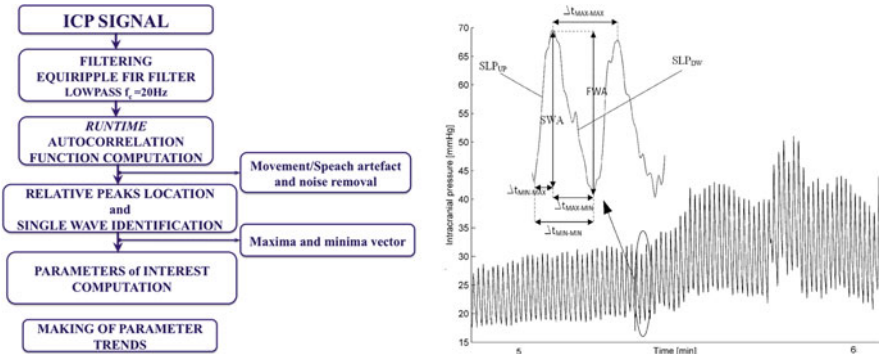

Fig. 37.2 (sx) Algorithm's flowchart—(dx) Example of ICP signal and parameters computed on it

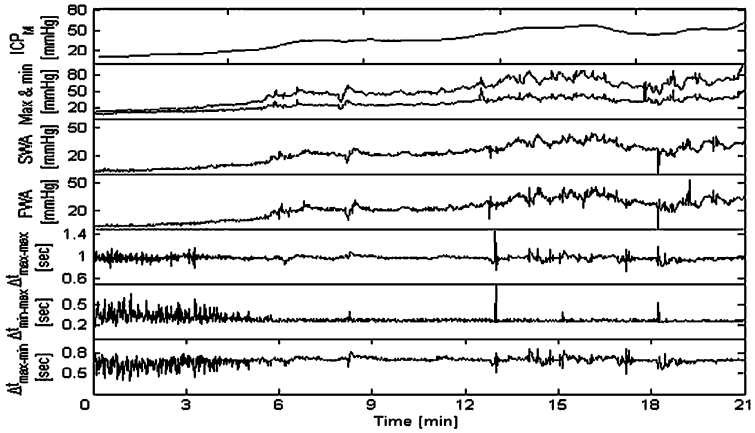

Fig. 37.3 Example of some trends

Peaks and other features revelation is estimated through the use of an algorithm for high-precision signal period identification and single-waveform location [4]. The algorithm computes the running autocorrelation function on the acquired and filtered buffered signal to obtain the updated fundamental period of the signal. Additional error correction control is performed to cut off those maxima or minima values out of expected range. Once the fundamental period is knew, the algorithm process the samples to recognize the boundary of each single-wave (which composes the pressure signal) in the acquired signal. In the next step the algorithm performs the identification of relative maxima and minima of each single-wave and the successive calculation of the parameters of interest as indicated in Fig. 37.2.

37.5 Results

The outflow of the elaboration is composed by the 14 parameters trends: maxima, minima, ICP_M, Δ_{ICP}, $\Delta t_{MIN–MAX}$, $\Delta t_{MAX–MIN}$, $\Delta t_{MAX–MAX}$, $\Delta t_{MIN–MIN}$, SWA, FWA, SLP_{UP}, SLP_{DW}, R_{OUT} and RAP (Fig. 37.3).

37.6 Conclusions

We have addressed a study to allow a deep investigation in ICP signals. The authors' algorithm developed allows an easy analysis of intracranial pressure. It can be intended as a valid, consistent, reliable and easy-computing tool that might be used by the medical team in all those cases that involve brain damages or diseases.

References

1. Albeck MJ, Borgesen SE, Gjerris F et al (1991) Intracranial pressure and cerebrospinal fluid outflow conductance in healthy subjects. J Neurosurg 74:597–600
2. Czosnyka M, Pickard JD (2004) Monitoring and interpretation of intracranial pressure. J Neurol Neurosurg Psychiatr 75:813–821
3. Codman MicroSensor Skull Bolt Kit (2003)
4. Calisto A, Bramanti A, Galeano M, Angileri F, Campobello G, Serrano S, Azzerboni B (2009) A preliminary study for investigating idiopatic normal pressure hydrocephalus by means of statistical parameters classification of intracranial pressure recordings. In: 31st annual international IEEE EMBS conference of the IEEE engineering in medicine and biology society

Chapter 38
Fabrication of Planar Sub-Micron Schottky Diodes for Terahertz Imaging Applications

Francesco Gatta, Roberto Casini, Arnaldo D'amico, Michele Ortolani, Ennio Giovine, Donatella Dominijanni and Vittorio Foglietti

Abstract Imaging sensors employing sub-millimeter waves and terahertz radiation (frequencies from 100 to 3000 GHz) are needed for security applications requiring stand-off, non-destructive sensing, due to its much larger penetration depth into dielectric materials.

38.1 Introduction

Imaging sensors employing radiation at frequencies beyond the visible range are crucial in security applications, as threats may come from concealed objects which cannot be detected by visual inspection. Microwave devices using radiofrequency (RF) up to several tens of GHz are currently employed for security sensing (e.g. in RF metal detectors and in body scanners), but they can hardly detect the shape of the concealed object, as the resolution of microwave imaging is limited by diffraction, and they cannot provide substance-specific contrast due to the lack of spectral signatures in the microwave range. Therefore, there is a considerable effort to bring concepts and devices from both the microwave and the infrared range towards the terahertz range, which sits in between them, with the aim of performing standoff imaging of concealed objects [1].

F. Gatta · R. Casini · A. D'amico
Dipartimento di Ingegneria Elettronica, Università degli studi di Roma "Tor Vergata", Via del Politecnico 1, 00133 Rome, Italy

M. Ortolani (✉) · E. Giovine · D. Dominijanni · V. Foglietti
Istituto di Fotonica e Nanotecnologie, Consiglio Nazionale delle Ricerche, Via Cineto Romano 42, 00156 Rome, Italy
e-mail: michele.ortolani@ifn.cnr.it

G. Neri et al. (eds.), *Sensors and Microsystems*, Lecture Notes in Electrical Engineering 91, DOI: 10.1007/978-94-007-1324-6_38,

In this paper, we present a process for the fabrication of Schottky diodes which can operate in the terahertz range. The diode is based on a Ti/*n*-GaAs junction with very low junction capacitance. For operation as terahertz sensor, the signal is fed to the diode through an on-chip terahertz antenna, and the diode can be used either as video detector, hence providing, after a low-pass filter, a dc output proportional to the intensity of the radiation power [2], or as mixer, with a local oscillator beam quasi-optically coupled to the same antenna [3]. Indeed, commercial Schottky diodes are currently employed as RF sensors up to 100 GHz, but their fabrication process has to be strongly modified to make them sensitive to terahertz radiation, as we will show in this paper. Furthermore, our process is fully planar, in order to fabricate monolithic matrixes of radiation detectors which could then be used to acquire real-time terahertz images in a focal plane array configuration, similar to infrared vision devices or digital cameras.

38.2 Device Design

The main parameter which limits the operation frequency of the Schottky diode is the junction capacitance, which is proportional to the junction area. We will show below that sub-micron junctions are needed for terahertz operation, which can be fabricated by high-resolution electron-beam lithography, instead of conventional optical lithography. Parasitic capacitances between the contact pads should be minimized by physically decoupling the contact pads, leaving metal microbridges for connection between them. A third parameter which limits the cutoff frequency is the series resistance, which can be reduced by using high-electron mobility Gallium Arsenide (GaAs) epitaxial layers as the semiconductor material, instead of Silicon. The target device is a fully planar monolithic Schottky diode working at terahertz frequencies which can be fabricated in arrays on a semiconductor wafer for imaging applications.

A measure of the quality of a radiation detector is its noise equivalent power (NEP). The noise power of a real Schottky diode is hard to predict, as it is the sum of several contributions (recombination current, Johnson noise, 1/f noise) which in turn depend on the signal read-out frequency. Therefore, we only performed calculations of the voltage responsivity β_V with a simplified diode model [4], which includes its series resistance *Rs*, its junction resistance *Rj*, and its junction capacitance *Cj*. The latter two quantities were derived from the junction dimensions by geometrical calculations.

The plot shown in Fig. 38.1 summarizes the results of the calculations, and clearly shows that sub-micrometric areas are necessary to reach terahertz frequencies. Junction with these dimensions cannot be produced with conventional optical lithography. This is the reason why we had to implement in the present Schottky diode fabrication process the “T-gate” technology based on electron beam lithography used for high electron mobility transistors.

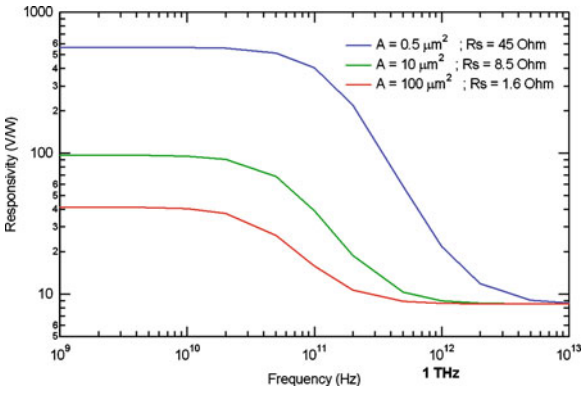

Fig. 38.1 Calculated responsivity of a Schottky diode detector as a function of diode parameters

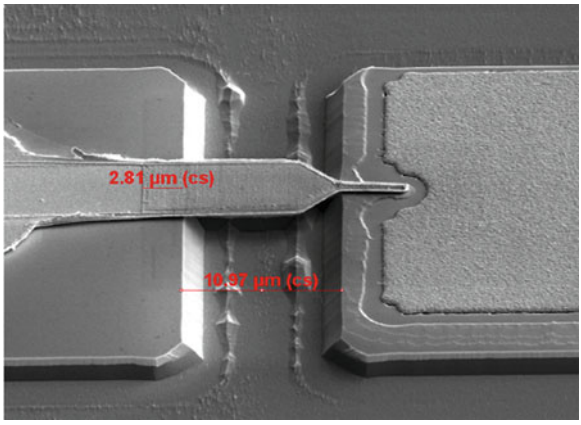

Fig. 38.2 SEM image of a terahertz Schottky diode fabricated at IFN-CNR

38.3 Diode Fabrication

Monolithic arrays of Schottky diodes are fabricated on a GaAs wafer with a layer structure on top. On the GaAs semi-insulating substrate, a 1-micron thick n^+-doped ($n_D = 5 \times 10^{18}$ cm^{-3}) and a 0.1-micron thick n-doped ($n_D = 1 \times 10^{18}$ cm^{-3}) GaAs layers have been sequentially grown by Molecular Beam Epitaxy. The device layout is based on two rectangular mesas of 30 × 150 microns separated by a 10-micron gap, which actually form a dipolar antenna tuned at 220 GHz. A Ge/Au/Ni metallization followed by annealing at 405°C on the n^+-doped layer is used for the ohmic contact to the cathode (semiconductor side of the junction). An evaporated Ti/Au bilayer on the n-doped GaAs forms the anode (metal side of the junction) with the following special layout obtained by electron-beam lithography on a trilayer resist structure: a large contact pad on the first mesa, a micrometric air-bridge between the mesas and a sub-micron finger with a "T-gate" profile displaying a 1 micron wide "head" and a footprint of 200 nm (see Fig. 38.2). The "T-gate" profile allows a small Schottky junction area, however not affecting too

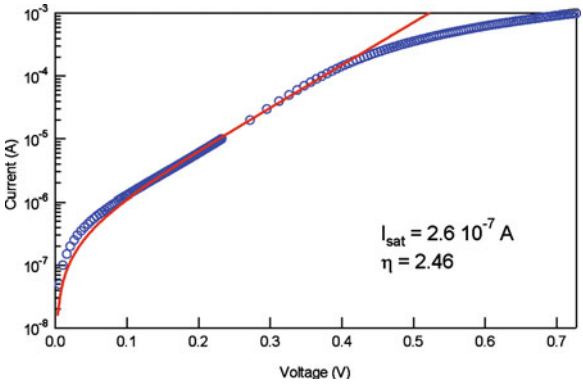

Fig. 38.3 DC *I–V* characteristics of a typical diode displaying pure exponential behaviour (*continuous line*) over two decades in current

much the contribution to the series resistance and inductance due to the anode metal finger. After the two metallization steps, a wet mesa-etching step is performed to isolate the anode and cathode contact pads. Also, at the mesa etching step the air-bridge is formed, and this eliminates the parasitic capacitance associated with the anode contact pad.

38.4 *I–V* Characterization

After device fabrication, selected diodes were wire-bonded and mounted in a package for dc characterization. The forward-bias *I–V* characteristics of the diode are shown in Fig. 38.3. To fit the data we used the classical Schottky model:

$$I(V) = I_{\text{sat}}(\exp(q(V - IRs)/\eta k_B T) - 1)$$

where I_{sat} is the saturation current, η is the ideality factor, Rs is the series resistance and q is the electron charge. The continuous line is a fit to the classical Schottky model with saturation current and ideality factor values reported in the plot. The deviation from the fit above 10^{-4} A is to be attributed to the voltage dependence of $\eta\tau$ and therefore data above $V = 0.4$ V are disregarded in the fit. A series resistance $R_s = 150 \pm 50\ \Omega$ is extracted from the fit (the uncertainty being related to assumptions on the ideality of the junction [5]). The junction capacitance C_j is estimated from geometrical calculations to be 5×10^{-15} F, with a resulting cutoff frequency $f_c = 1/2\pi R_s C_j = 210 \pm 60$ GHz. Efforts are ongoing to improve the junction ideality by surface treatment prior to anode metal deposition and to decrease R_s by Ohmic contact optimization.

38.5 Conclusions

In this work we presented the design, fabrication and dc characterization of Schottky diodes with cutoff frequency in the terahertz range. The devices were

designed to operate as direct detectors of terahertz radiation and fabricated in monolithic arrays for imaging applications.

References

1. Tonouchi M (2007) Cutting edge terahertz technology. Nat Photon 97:1
2. Chahal P, Morris F, Frazier G (2005) Zero bias resonant tunnel Schottky contact diode for wide-band direct detection. IEEE Electron Dev Lett 26:894
3. Siegel P, Smith R, Gaidis M, Martin S (1999) 2.5 THz. GaAs monolithic membrane-diode mixer. IEEE Trans Microw Theo Tech 47:596
4. Anand Y, Moroney W (1971) Microwave mixer and detector diodes. Proc IEEE 59:1182
5. Aubry V, Meyer F (1994) Schottky diodes with high series resistance: limitations of forward $I \pm V$ methods. J Appl Phys 76:7973

Chapter 39
Power Management Systems for Photovoltaic Energy Harvesters

M. Ferri, D. Pinna, M. Grassi, E. Dallago and P. Malcovati

Abstract In this chapter we present two different solutions of integrated photovoltaic energy harvesting, realized for discrete and continuous time working systems. The first solution is realized in a standard 0.35 μm CMOS technology: it collects light energy from the environment, by means of 2 mm^2 on-chip integrated micro-solar cells, and accumulates it in an external capacitor. While the capacitor is charging, the load is disconnected. When the energy in the external capacitor is enough to operate the load for a predefined time-slot, the load is connected to the capacitor by a power management circuit. The second solution is realized in 0.35 μm SOI CMOS technology. The energy harvesting elements consist of 35 trench-insulated *p–n* junctions, while the sensing system consists of a bandgap reference circuit, including an integrated high precision temperature sensor, and a high voltage low drop-out voltage regulator.

M. Ferri · D. Pinna · M. Grassi (✉) · E. Dallago · P. Malcovati
Department of Electrical Engineering, University of Pavia,
Via Ferrata 1, 27100 Pavia, Italy
e-mail: marco.grassi@unipv.it

M. Ferri
e-mail: massimo.ferri@unipv.it

D. Pinna
e-mail: daria.pinna@unipv.it

E. Dallago
e-mail: enrico.dallago@unipv.it

P. Malcovati
e-mail: piero.malcovati@unipv.it

G. Neri et al. (eds.), *Sensors and Microsystems*,
Lecture Notes in Electrical Engineering 91, DOI: 10.1007/978-94-007-1324-6_39,

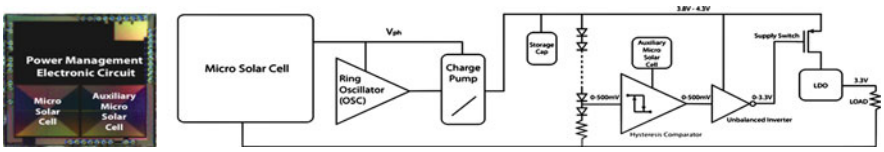

Fig. 39.1 Microphotograph and block diagram of the energy harvester in 0.35 μm CMOS technology for discrete-time working microsystems

39.1 Introduction

Integrated systems are constantly improving in terms of functionalities and computational capabilities [1, 2]. On the other hand, the battery energy density is not improving with the same speed and battery life is becoming in many cases a real bottleneck, especially for portable applications [3, 4]. Energy harvesting systems are becoming the new challenge in both commercial and research communities as alternative, or additional, power source. In many cases, in fact, the final application operates in environment with many energy sources, such as light, vibrations or thermal gradients. In this case energy harvesting represents an optimum option to increase the performance of the device, reducing its volume and weight. Light can be considered the most copious energy source in most environments, thus making the photovoltaic energy harvesting the largest contribute to the power supplying process. When the electronic circuits required for the power management system has to be implemented on the same chip of the photovoltaic energy harvesting elements, the choice of the fabrication technology of the microsystem is subordinated to the final application, leading to a trade-off between costs and feasibility.

39.1.1 Power Management Systems

We present two different solutions of integrated photovoltaic energy harvesting, realized for discrete and continuous time working systems. The first solution is realized in a cheap standard 0.35 μm CMOS technology, while the second in 0.35 μm SOI CMOS technology. Figure 39.1 shows the microphotograph and the block diagram of the chip implementing the first solution, where a generic resistive load has been considered. The block diagram of the proposed system is shown in Fig. 39.1. A first solar cell provides the power supply to an oscillator and to eight parallel Dickson charge pumps. In order to simplify the schematic, we reported only one charge pump. The storage capacitor C_S is external, thus allowing us to choose the capacitance value, according to the operating time-slot required by each application. The voltage across capacitor C_S is monitored by an hysteresis comparator followed by a level shifter. When the charge stored on C_S is sufficient to reach a given voltage, in the considered design equal to 4.3 V, the comparator provides a signal that, by means of the level shifter, turns on the *p*-MOS switch,

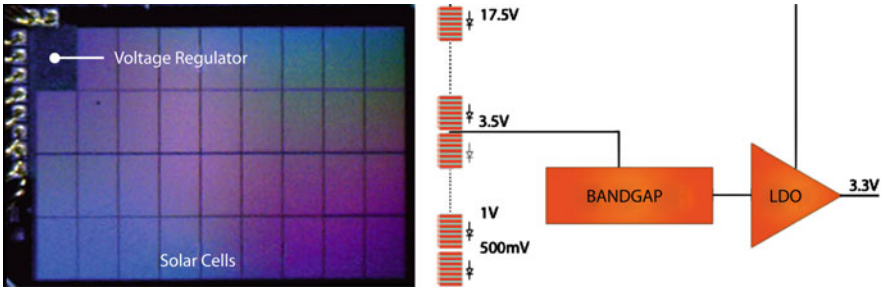

Fig. 39.2 Microphotograph and block diagram of the energy harvester in 0.35 μm CMOS SOI technology for continuous-time working microsystems

which connects the LDO to the supply voltage (i.e. the storage capacitor), thus supplying the load. When the external capacitor discharges, and the voltage decreases below 3.8 V, the load is disconnected, and, hence, switched off.

The main drawback of this solution, and of all those where insulation is guaranteed by the reverse biasing of the substrate connected junctions, is the impossibility to create series of solar cells on the same silicon wafer. The common presence of the substrate, in fact, introduces photoelectric phenomena also for the parasitic junctions. For this reason the circuit presented in Fig. 39.1 elevates with a charge pump the photogenerated voltage of a single solar cell and charges an external capacitor, in order to supply with 3.3 V, through a linear voltage regulator (LDO), the load for a given time-slot, in asynchronous discrete-time regime. The time-slots dedicated to energy accumulation and system operation are established automatically by the system. In fact, it is possible, by choosing the value of the external capacitor, to trade the amount of power available for the load with the time required to accumulate it, thus allowing to supply the load for the required time-slot with the necessary current and duty-cycle. Figure 39.2 shows instead the micro-photograph and the block diagram of the photovoltaic energy harvester realized in 0.35 μm CMOS SOI technology for continuous-time working microsystems. This solution consists of the series of 35 trench-insulated *p–n* junction, a bandgap device and an high voltage LDO circuit. This regulator allows to provide a fixed 3.3 V, also in low environment illumination conditions, as the large number of micro photo-structure chain elements allows each cell to decrease its voltage of almost 20%, when the power curve changes for illumination variations, or due to a larger load power request than typical. Moreover, the series connection of photovoltaic cells allows us to obtain directly all the reference voltages required for the entire system.

The CMOS SOI technology used in this solution together with the configuration realized, allow us to create series structures and to provide a voltage higher than 3.3 V, eliminating the parasitic diode between each single cell and the chip substrate. In particular, since the open circuit voltage V_{oc} for each illuminated cell is almost 530 mV, the entire chain can provide up to 17.5 V. On the other hand, this fabrication technology is more expensive than the standard CMOS.

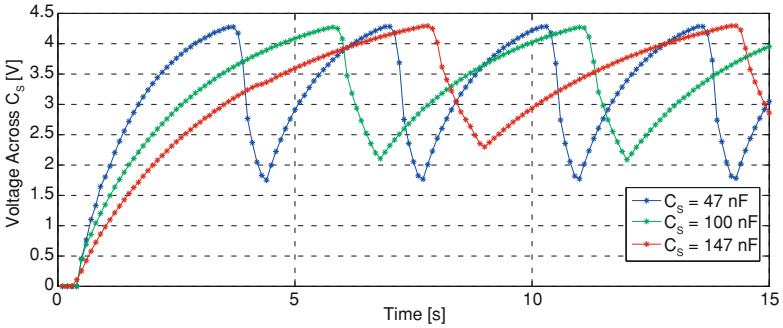

Fig. 39.3 Measurement of the voltage across the storage capacitor with different values of C_S (47, 100 and 147 nF)

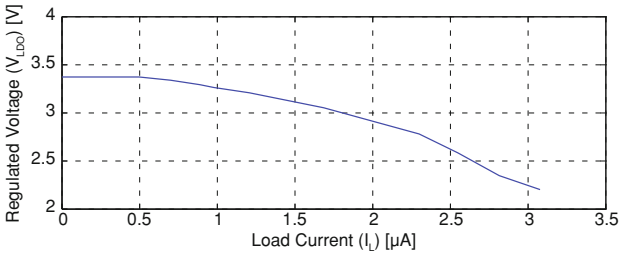

Fig. 39.4 SOI harvester power curve

39.2 Measurement Results

In this paper we proposed two different energy harvesting systems. Figure 39.3 shows a measured working cycle of the standard CMOS solution. In detail, it shows the measured voltage across the storage capacitor, acquired over a time-slot of 15 s, obtained for different values of C_S (47, 100 and 147 nF).

The system is illuminated with a light source, delivering about 300 W/m^2 and the load is a 10 MΩ resistor (1 μW power at 3.3 V). The maximum value of the voltage is adjustable by changing the value of the threshold voltage of the hysteresis comparator. The upper limit of the achievable voltage is a trade-off between the charge-pump transfer rate, the leakage current of the external capacitor, and the current that flows in the other electronic blocks. Figure 39.4 shows the power curve referred to the SOI photovoltaic energy harvester.

The system delivers a regulated output voltage of 3.3 V for load currents up to 500 nA with 600 W/m^2 of the incident light power (3.3 μA are consumed by the LDO circuit). Both solutions have been realized as integrated circuits and completely characterized with laboratory measurements.

39.3 Conclusions

In this paper we presented integrated photovoltaic energy harvesting circuits, realized for discrete and continuous time working systems. The first circuit, realized with a 0.35 μm CMOS technology, accumulates energy in an external capacitor and delivers it to the load when the voltage across the capacitor is sufficiently high. The choice of the value of the capacitance determines the operating time-slot of the load. The second circuit is realized in 0.35 μm SOI CMOS technology and consists of a bandgap reference circuit and of an high voltage LDO circuit. The realized chips have been extensively simulated and measured, showing a good agreement between simulated and experimental results. Presently, we are designing an integrated solution in order to obtain a completely autonomous wireless sensor node.

References

1. Andre W, Martel S (2007) Preliminary design of an autonomous microrobot propelled by magnetotactic bacteria. In: Proceedings of IEEE ASME international conference on advanced intelligent mechatronics, Sept 2007, pp 1–6
2. Ho HL, Steigerwalt MD, Walsh BL, Doney TL, Wildrick D, McFarland PA, Benedict J, Bard KA, Pendleton D, Lee JD, Maurer SL, Corrow B, Sadana DK (2001) A 0.13 μm high-performance SOI logic technology with embedded DRAM for system-on-a-chip application. In: IEEE international electron devices meeting (IEDM), Technical Digest, Dec 2001, pp 22.3.1–22.3.4
3. Gao J, Yu L (2007) Use of battery ohmic testing to improve network reliability and decrease battery maintenance cost. In: Proceedings of international telecommunications energy conference (INTELEC). Oct 2007, pp 194–202
4. Dondi D, Brunelli D, Benini L, Pavan P, Bertacchini A, Larcher L (2007) Photovoltaic cell modeling for solar energy powered sensor networks. In: international workshop on advances in sensors and interface(IWAS), June 2007, pp 1–6

Chapter 40
A Low Noise 32-Channel CMOS Read-Out Circuit for X-ray Silicon Drift Chamber Detectors

L. Picolli, M. Grassi, M. Ferri and P. Malcovati

Abstract In this paper we present a 32-channel integrated front-end circuit for low-energy (0.5–100 keV) X-ray detection with a multi-anode silicon drift detector. The front-end circuit includes 32 read-out pixel cells (RPC), each consisting of a low noise preamplifier, a second-order RC-CR pulse shaper, a peak stretcher, an amplitude and a peak discriminator, as well as a reset and pile-up rejection circuit. Most of the parameters of the front-end circuit are programmable through a digital configuration register, supporting daisy-chain connection. At room temperature the equivalent noise charge of the RPC is 18.3 e^- and its linearity error is lower than 5% over the complete input range. The front-end circuit has been designed in a 0.35-μm CMOS technology with main 3.3-V power supply. A single RPC occupies an area of 200 × 380 μm^2 and consumes 0.4 mW.

40.1 Introduction

Semiconductor devices for X-ray imaging and spectroscopy gained significant importance in the last decade and their exploitation is still growing, since they are the key elements in many medical and scientific applications [1, 2]. Pixel detectors

L. Picolli · M. Grassi (✉) · M. Ferri · P. Malcovati
Department of Electrical Engineering, University of Pavia, Via Ferrata 1, 27100 Pavia, Italy
e-mail: marco.grassi@unipv.it

L. Picolli
e-mail: luca.picolli@unipv.it

M. Ferri
e-mail: Massimo.ferri@unipv.it

P. Malcovati
e-mail: piero.malcovati@unipv.it

G. Neri et al. (eds.), *Sensors and Microsystems*,
Lecture Notes in Electrical Engineering 91, DOI: 10.1007/978-94-007-1324-6_40,

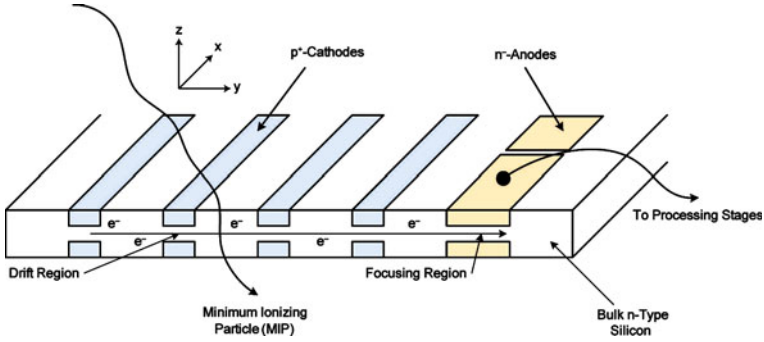

Fig. 40.1 Simplified structure of a typical silicon drift detector

and, in particular, silicon drift chambers play an important role in this field, because of their affordable manufacturing technology, high energy resolution, and nevertheless, low noise performance. The simplified structure of a silicon drift detector is shown in Fig. 40.1. This device consists of a pattern of cathodes (p^+ implants) on both sides of the silicon chip and a set of anodes (n^+ implants) at the edge of the chip, connected to the readout electronics [1].

Drift detectors have demonstrated excellent energy resolution because of their very small read-out anode geometry (hence capacitance), which allows the minimization of the contribution of the electronic noise of the preamplifier on the overall performance of the detection system. The charge carriers produced in the detector by the incident radiation, thanks to the transversal electric field, drift toward the anodes, where they are collected. The position of the anode collecting the charge provides the *x* coordinate of the incident radiation position, while from the drift time it is possible to determine the *y* coordinate. Therefore, with drift detectors it is possible to reconstruct the spatial position of the incident radiation on the plane (*x* and *y* coordinates), using a linear array of front-end circuits to read-out the information, instead of a matrix as in conventional pixel detectors. The output signal of a drift detector is a charge pulse, as in conventional pixel detectors, but with opposite polarity, which must be amplified and shaped, in order to extract the useful information.

40.2 Front-End Circuit Description

The block diagram of the proposed integrated front-end circuit is shown in Fig. 40.2. It consists of 32 RPCs, a digital logic block for system programmability and trigger management, two digital-to-analog converters (DACs) for generating programmable reference voltages (for calibration purpose), and an analog output buffer. The block diagram of the RPC is instead shown in Fig. 40.3. The circuit is based on the same architecture presented in [3], but, as mentioned, it has been

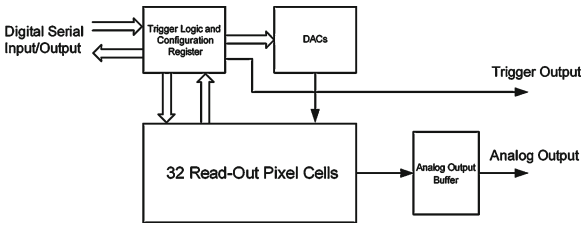

Fig. 40.2 Simplified block diagram of the proposed integrated front-end circuit

modified for handling electrons instead of holes as input signal and its functionality has been optimized for reading out silicon drift detectors with the required input signal range (0.5–100 keV, corresponding to 60–27,000 e^-). The RPC is divided into two main parts: an analog section, which includes a low-noise preamplifier, a pulse shaper, and peak stretcher, as well as a mixed-signal section, which includes an amplitude discriminator, a peak discriminator, and the digital logic required for reset and pile-up rejection [4]. The input low noise preamplifier is based on a folded cascode architecture with also an additional dedicated supply (2.0-V), to avoid interference from main 3.3-V rail. When disabled, the preamplifier sinks the detector current, thanks to the low input impedance by design, and ensures proper biasing of the anode of the detector, without providing any output signal. The output of the preamplifier is connected to the second order RC-CR pulse shaper. The shaping time can be digitally selected among eight different values, ranging from 0.7 to 5.5 μs, by means of two sets of switches controlled by a 3-bit digital word, stored in the configuration register. The two shaping stages are coupled by a gain compensation circuit, whose function is to maintain the gain constant for different shaping times. The output stage of the shaper also sets the desired baseline voltage (V_{bl}) by means of a feedback loop.

The peak stretcher is based on a differential input stage with an unidirectional current source, which charges the hold capacitor. When the pulse shaper output is below the threshold of the amplitude discriminator, the circuit behaves as a unity gain voltage buffer. When the amplitude discriminator is triggered by an input signal over threshold, the circuit follows instead the input signal up to its peak and then holds it, since the hold capacitor has no path for discharging. When the input signal reaches its peak, the peak stretcher also generates a trigger signal which connects its input node to a fixed voltage, lower than V_{bl}, in order to avoid variations of the held voltage due to noise peaks. The reset of the peak stretcher is performed by discharging the hold capacitor with a constant current source. An analog multiplexer, controlled by the digital bit Signal Selector, stored in the configuration register, allows the connection of either the pulse shaper output or the peak stretcher output to the analog output buffer, for testing purposes. The analog output buffer has been designed for low noise and low input capacitance, in order to avoid the degradation of the settling performance of the previous stage. The amplitude and peak discriminators generate two different digital trigger signals. In particular, the amplitude discriminator output signal rises when the pulse shaper output signal crosses a programmable threshold and it is used to arm

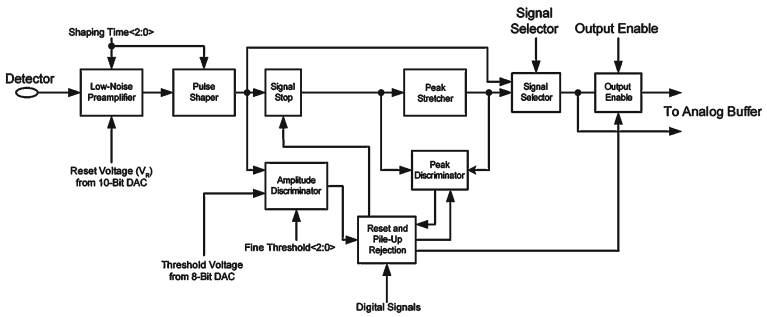

Fig. 40.3 Detailed architecture of a single RPC

the peak stretcher. The amplitude discriminator features global and local threshold level settings: the global threshold value is generated by an on-chip 8-bit resistive DAC controlled by a digital word stored in the configuration register and it is common for all the RPCs in the array, while the local or fine threshold value is set, separately for each RPC, by three bits stored in the configuration register. The global threshold tuning range is 60–1,400 e^- while the fine threshold tuning step is 50 e^-. The configuration register allows us to calibrate the front-end circuit parameters. It consists of a shift register, which receives as input a serial bitstream, and a configuration memory, which holds the configuration parameters of the circuit. Default values are provided after reset for typical operation.

40.3 Simulation Results

The proposed front-end circuit for low-energy X-rays detection has been designed in a 0.35-μm CMOS technology with 3.3- and 2.0-V power supply. The circuit has been simulated at transistor level, including post-layout capacitive and resistive parasitic extraction. Table 40.1 summarizes the achieved performance, while Fig. 40.4 represents the layout of the RPC. The power consumption per channel is 0.4 mW, while the input referred equivalent noise charge is 18.3 e^-_{rms}. The simulated distortion of the channel is lower than 5%.

40.4 Conclusions

In this paper we presented a 32-channel integrated front-end circuit for low-energy X-ray detection, designed for a multi-anode silicon drift detector. The chip has been designed in a 0.35-μm CMOS technology with a main 3.3-V power supply

Table 40.1 Simulated performance summary

Technology	CMOS 0.35 μm, 2-Poly, 4-Metal
Supply voltage	3.3 V, 2.0 V
Power consumption	0.4 mW per channel
Input signal range	500 eV–100 keV (60 e^-–27,000 e^-)
Equivalent noise charge	18.3 e^- rms
Full scale linearity	5%
Shaping time	0.7–5.5 μs
Output voltage swing	1.1 V

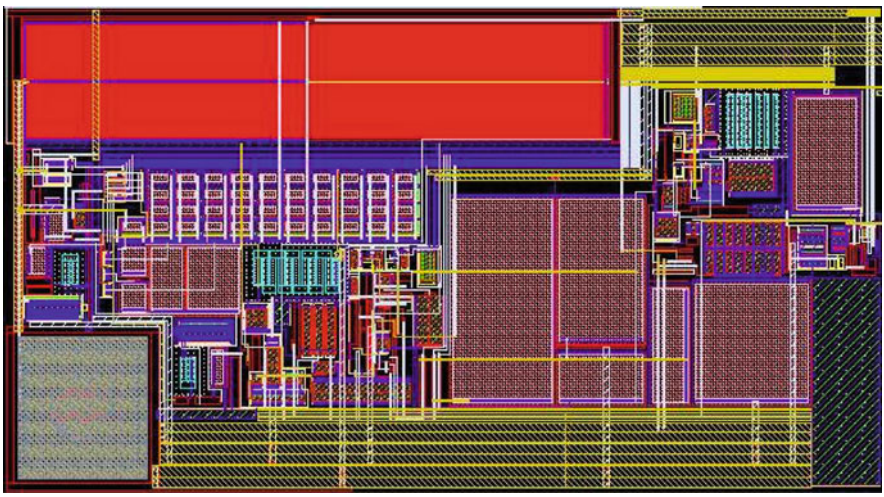

Fig. 40.4 Layout of the RPC

and consumes 0.4 mW per channel. The area of a single channel is 200 × 380 μm^2. A dedicated memory is provided for calibration purpose.

References

1. Labanti C et al (1999) ICARUS ASIC: a 16 channel photodiode read-out system. IEEE Trans Nucl Sci 46(3):144–149
2. Debertin K, Helmer RG (1988) Gamma and X-ray spectrometry with semiconductor detectors. North-Holland, Amsterdam
3. Caccia S et al (2008) A mixed-signal spectroscopic-grade and highfunctionality CMOS readout cell for semiconductor X-gamma ray pixel detectors. IEEE Trans Nucl Sci 55(5):2721–2726
4. Bastia P et al (2006) An integrated reset/pulse pile-up rejection circuit for pixel readout ASICs. IEEE Trans Nucl Sci 53(1):414–417

Chapter 41
Complexity Management in Manufacturing Microsystems: Remarks on Artificial and Natural Systems Comparison

U. Mastromatteo

Abstract In order to improve the efficiency in manufacturing complex Microsystems, a comparison between artificial and natural systems "growing" mechanisms and architecture have been investigated. As an example we have compared the process to fabricate a microelectronic chip with a size of ¼ of square centimeter and the biological process needed to make a similar size biological cell: a wheat grain. Just estimating the energy needed to make the two systems, we see that the energy balance differs of about three orders of magnitude. In fact, to make the silicon microchip of that size with a medium complexity, the energy used is more than 1 kWh, while a wheat grain energy need is less than 1 Wh. If we consider, following a common thinking, that the artificial processes are conceived as an emulation of the natural processes, this strong difference in the energy balance appears a quite strange surprise. Moreover, it is worth taking into account that the complexity of a biological eukaryotic cell is much higher than the microchip one. The understanding of mechanisms the biologic world uses to achieve its extraordinary efficiency, is very important to design cheaper artificial manufacturing processes to make systems more and more complex when the minimum dimensions the process is able to control inside the system goes in the range of nanometers.

41.1 Introduction

Among artificial systems that human intelligence can design and manufacture, the most difficult ones to make are microchips. This is due to the need to arrange very complex architectural geometries in a scale size level of tens of nanometers.

U. Mastromatteo (✉)
STMicroelectronics, Via Tolomeo 1, 20010 Cornaredo, Italy
e-mail: ubaldo.mastromatteo@st.com

G. Neri et al. (eds.), *Sensors and Microsystems*,
Lecture Notes in Electrical Engineering 91, DOI: 10.1007/978-94-007-1324-6_41,

In synthesis, the work to be done to make microchips consists in structuring very thin layers on top of silicon mono crystalline substrate (the electrical properties used in integrated circuits require very pure silicon substrates and a perfect crystalline structure). The arrangement of each layer defines the characteristics of adjacent portions having a certain minimum size. The minimum size determines the maximum number of configurations obtainable for a single layer. The total number of stacked layers may be greater than thirty and the total process is conceived in a way to maintain certain "independence" (not only in statistical sense) in the single layer manufacturing. The final configuration looks like a memory with a defined content of "bits". According to Landauer's principle, a decrease in entropy of "k ln(2^n)" is produced, corresponding to the equivalent entropy increase due to the erasure of "2^n" memory accessible states [1]. The quantity of work to be done to make that configuration will depend from the quantity of matter used (the mass or the number of moles). So, structures with the same number of possible configurations will require different amounts of work (extracted from a suitable energy source). In fact, a different amount of energy is necessary in arranging tiny tiles in a mosaic, or bricks for a house, even if the possible configurations are the same.

41.1.1 Work Needed to Lower the Entropy in a Complex System

The entropy variation for a selected geometrical configuration, still referring to what happens in a layer used in integrated circuit manufacturing processes as shown in the "Fig. 41.1", is given by the entropy variation ΔS in the material layer induced by the "geometries" creation process. Just due to a selected configuration we have: $Sc = k\ln(1/w)$ (Landauer) [1] where Sc is the configuration entropy and "w" the number of possible configurations ($w = 2^n$).

However, fixing a specific configuration in an ergodic process requires to go through all the possible configurations via a logarithmic exclusion (this fact explains the very low efficiency in the manufacturing complex systems like integrated circuits), hence, if the configurations number is "w", to have the value of the work (L) needed to obtain that configuration at a given temperature (T), we need to multiply the entropy variation (the absolute value) by "ln(w)", then the required work will be:

$$L = T\Delta S\ln(w) \tag{41.1}$$

And because

$$1/w = e^{Sc/k} \tag{41.2}$$

Then

$$L = T\Delta S\ln\left(e^{-Sc/k}\right) \tag{41.3}$$

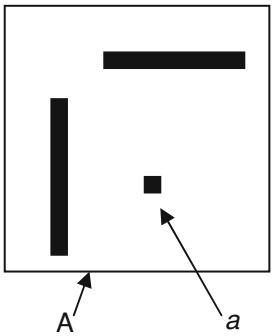

Fig. 41.1 In a given area "A" there are $w = 2^n$ ways to arranging minimum size geometries of area "a", where "n" is the A/a ratio. All the configurations are statistically equivalent. To any chosen configuration, for a given value of "w" corresponds a negative configurational entropy $Sc = -k\ln(w)$

Remembering that

$$-Sc/k = (A/a)\ln(2) \tag{41.4}$$

Substituting the (41.4) in the (41.3) we have:

$$L = T\Delta S(A/a)\ln(2) \tag{41.5}$$

Of course, ΔS accounts the contribution to the work (L) due to the "mass" of the "bit" (material of the minimum size formed layer). As a consequence of the above considerations, it is clear that the work needed to create complexity is usually huge. This is also the reason why microchips have to be very small [2]. Applying the formula (41.5) to a real device with "A" = 1/4 cm^2, "a" = 4 μ^2 and including 20 stacked layer 1 μ thick, we get for "L" a value of about .3 kWh. In practice, considering other processes inefficiencies, the work to spend is more than 1 kWh.

41.1.2 Micro Chip and Living Cell Comparison

The work needed to make the silicon chip, as explained above and shown in Fig. 41.1, strongly depends from the A/a ratio and from the number of layers stacked to build the complete device able to perform correctly the designed function. In the case of a living cell, in spite of the complexity is considerably higher than that of a microchip, the growing process of the living organism, a wheat ear as an example, does not need to make the extra work of eliminating all the alternative configurations to what is determined by the instructions "written" into the genetic code of the specific organism; this happens because the living system is intrinsically non ergodic. Then, if we go to quantify the work (L_{liv}) necessary to make only the order and functionality of the living organism, in the formula (41.5) used for the microchip, we need to eliminate the "A/a ln(2)" term, unavoidable consequence of the ergodicity of artificial systems. So, the needed work, considering that ΔS is negative, would only be:

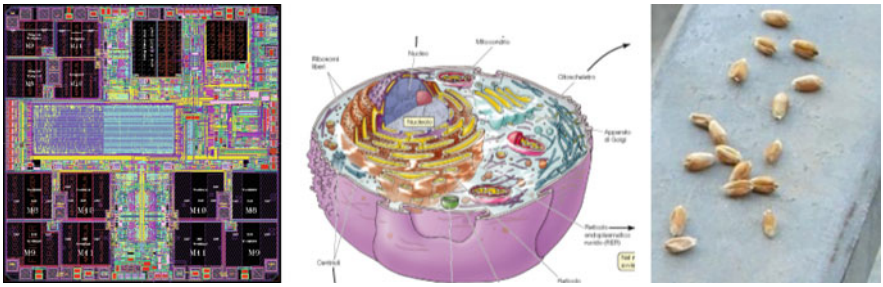

Fig. 41.2 On the *left* a top view of a silicon chip, on the *right* wheat grains and in the *center* an enlarged sketch of an eukaryotic cell

$$L_{liv} = -T\Delta S \tag{41.6}$$

where the spent work to produce negative entropy variation is only due to the chemical reactions making ordered biopolymers starting from small molecules; while the "effective" negative entropy variation (ΔS_{eff}), due to the very high ordered structure of the living organism is proportional to the "virtual" work required to set an equivalent order of a non living aggregate of matter and energy, and so, in analogy with the complexity creation for artificial systems, reintroducing the dimensions ratio, the form of a general expression formula for the entropy variation is:

$$\Delta S_{eff} = -L/T = \Delta S(A/a)\ln(x) \ll 0 \tag{41.7}$$

As already mentioned "a" for a living organism is in the range of nanometers, while "A" is in the range of millimeters; "x" is an average of the number of possible states for built macromolecules, 4 in the case of DNA and 20 (amino acids) in the case of proteins [3]. What stated above is confirmed observing that in spite of such huge difference in complexity, the work needed by growing living organisms is much less than what needed in manufacturing complex artificial systems of similar dimensions. The implication of this observed facts go well behind the limits of the short description we are doing here [3] (Fig. 41.2).

41.2 Conclusions

Trying to summarize what has been described so far, we can remind the main statements we consider may lead to very relevant conclusions. The first one concerns the analogy between what happens during the manufacturing of high technology complex systems, acquired in many years of experience in the field, and the entropy decrease in growing living systems, both due to a "programmed" space structuring and matter distribution: any system submitted to such kind of processes lowers its own entropy.

A second one concerns the ergodicity of the artificial systems manufacturing processes. This characteristic derives from the need to select the designed configuration among all the possible ones passing through a logarithmic selection of them (as an example we may consider the need to purify all the materials used in Integrate Circuits manufacturing to avoid any impurity on the silicon surface that might affect the proper designed configuration: this preprocessing of all the materials implies a drastic efficiency decreasing as the system complexity increases). A last one regards the living systems, in which the ergodicity process doesn't occur at all (as we experience for the plants, which do not need any purification of the air, water and soil), and so they can demonstrate a very high efficiency in making all the choices they need for the self organization: even the photosynthesis process is submitted and managed by the information contained in the system itself, just like it would happen if a group of Maxwell's demons would be inside operating very precise tasks using energy coming from the outside environment [4].

In conclusion, as for hypothesis from eminent scientists, it seems that a physical law just valid for the living systems and not belonging to the group of physical laws valid for non living systems may exist. This clearly copes hardly with the problem of physical non reducibility of living systems.

References

1. Bennet CH (1995) Diavoletti, Macchine e il secondo principio. Le Scienze – quaderni 85:8–14
2. Mastromatteo U, Pasquinelli P, Giorgetti A (2007) Thermodynamics, information and complexity, in artificial and living systems. Int J Ecodynamics 2(1):39–47
3. Borghi C (1978) Saggi sul problema religioso. Citta' Armoniosa: Reggio Emilia, pp 25–41
4. Tiezzi E (2006) Verso una fisica evolutiva, Donzelli Editore: Roma, pp 53–69, 151–160

Chapter 42
Enhanced Mass Sensitivity of Carbon Nanotube Multilayer Measured by QCM-Based Gas Sensors

M. Penza, P. Aversa, R. Rossi, M. Alvisi, G. Cassano, D. Suriano and E. Serra

Abstract A Quartz Crystal Microbalance (QCM) gas sensor coated with carbon nanotubes (CNTs) layered films as chemically interactive nanomaterial is described. A QCM resonator integrated on AT-cut quartz substrate has been functionally characterized as oscillator at the resonant frequency of 10 MHz. The CNTs have been grown by chemical vapor deposition (CVD) system onto alumina substrates, coated with 2.5 nm thick Fe catalyst, at a temperature of 750°C in H_2/C_2H_2 gaseous ambient as active materials for gas sensors. CNTs multilayers, with and without buffer layer of cadmium arachidate (CdA), have been prepared by the Langmuir–Blodgett (LB) technique to coat at the double-side the QCM sensors for organic vapor detection, at room temperature. It was demonstrated that the highest mass sensitivity has been achieved for CNTs multilayer onto CdA buffer material due to the greatest gas adsorbed mass. The sensing properties of the CNTs-sensors at enhanced mass sensitivity have been investigated for three different vapors of ethylacetate, acetone and m-xylene in the range of gas concentration from 10 to 800 ppm. The CNTs-based QCM-sensors exhibit high sensitivity (e.g., 5.55 Hz/ppm to m-xylene of the CNTs-multilayer) at room temperature, fast response, linearity, reversibility, repeatability, low drift of the baseline frequency, potential sub-ppm range detection limit.

M. Penza (✉) · P. Aversa · R. Rossi · M. Alvisi · G. Cassano · D. Suriano
Brindisi Technical Unit for Technologies of Materials, ENEA, PO Box 51, Postal Office Br4, 72100 Brindisi, Italy
e-mail: michele.penza@enea.it

E. Serra
Casaccia Technical Unit for Technologies of Materials, ENEA, Via Anguillarese 301, 00060, Rome, Italy

G. Neri et al. (eds.), *Sensors and Microsystems*,
Lecture Notes in Electrical Engineering 91, DOI: 10.1007/978-94-007-1324-6_42,

42.1 Introduction

Quartz Crystal Microbalances (QCMs) have been widely used as high-performance transducers and promising sensor platforms for chemical detection of targeted analytes in air [1] and/or water [2] phase. The QCM sensors are very interesting for practical applications owing to their high sensitivity and ease of measurement. QCM measurements rely on the Sauerbrey equation, which relates the change in the resonant frequency of a quartz crystal (Δf) to the change in mass due to gas adsorption on the crystal (Δm):

$$\Delta f = \frac{2f_o^2}{A\sqrt{\rho_q \mu_q}} \Delta m$$

where f_o is the resonant frequency of the unloaded crystal, A is the active area of the crystal between the two electrodes, ρ_q is the density of the quartz (2.648 g/cm^3), and μ_q is the shear modulus of quartz (2.947×10^{11} g/(cm s^2)). The frequency shift of a QCM sensor is strongly depending on squared frequency, typically ranging from 5 to 30 MHz, and surface density ($\Delta m/A$) of the sensitive film. In fact, the mass sensitivity of a QCM resonating at 10 MHz is typically in the range of 0.1–1.0 Hz/(ng/cm^2), which is very high to detect very-low concentrations of gases up to sub-ppm level. Therefore, QCM sensitivity can be improved by mass amplification using very adsorbent materials which increase the adsorbed mass. In this context, nanomaterials with high surface area and high chemical reactivity are very useful for fabricating high-sensitivity chemical sensors with room-temperature operations for low power consumption.

Gas sensors based on carbon nanotubes (CNTs) have been studied both in the form of nanocomposites [3–7] and networked films [8, 9] for high-sensitive VOCs detection SAW and QCM applications, at room temperature. Here, CNTs multi-layered films have been prepared by Langmuir–Blodgett (LB) technique onto double-side AT-cut quartz 10 MHz QCM equipped by Al electrodes. A buffer layer of Cadmium Arachidate (CdA) has been used to promote the adhesion of the CNTs multilayer onto QCM surface. The detection of volatile organic compounds (VOCs) of ethylacetate, acetone and m-xylene at enhanced mass sensitivity by QCM-sensors coated with CNTs-multilayers has been investigated by achieving linearity in the response and low limit of detection of a few ppm for a given targeted analyte.

42.2 Experimental Details

CNTs films were grown by CVD technology. The CNTs films were deposited onto large-size cost-effective alumina (40 mm width × 40 mm length × 0.6 mm thickness), coated with growth-catalyst of iron (Fe) nanoclusters with a nominal thickness of 2.5 nm and sputtered at 10^{-2} Torr. The Fe-catalysed alumina

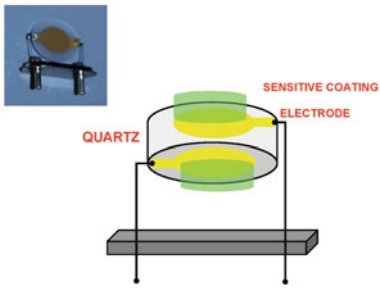

Fig. 42.1 Scheme of the QCM-sensor measured and image of a typical QCM

substrates were heated to 750°C by a rate of 10°C/min in H_2 atmosphere upon flow of 100 sccm at a total pressure of 1.5 Torr. In the gas-plasma, the flow rate ratio between C_2H_2 and H_2 was kept constant at 20/80 sccm, respectively. The CNTs deposition was performed at a constant pressure and temperature of 5 Torr and 750°C, respectively for 30 min by depositing a vertically-aligned CNTs film with thickness of 10–12 μm.

After CNTs growth, the nanomaterial was mechanically removed from substrate to prepare a solution as precursors for the LB film deposition. A dispersion of the CNTs in a DMF solvent has been prepared to promote their de-bundling before LB film deposition. In addition, a buffer layer of cadmium arachidate (CdA) has been used to promote the adhesion of the CNTs multilayer onto QCM surface.

The scheme of the QCM sensor is shown in Fig. 42.1. A piezoelectric sensor based on unloaded AT-cut quartz oscillating at a frequency of 10 MHz has been used as transducer equipped by Al electrodes with an active area of 12.56 mm^2.

Three different QCM-sensors have been fabricated by depositing LB layered films as depicted in the Fig. 42.2. The process parameters for LB film deposition are reported elsewhere [3–6, 8]. The QCM sensors investigated are so-described:

Sensor type-A—10 MHz AT-cut quartz QCM coated by a LB film of CdA with a thickness of 10 layers onto double-side of the quartz.

Sensor type-B—10 MHz AT-cut quartz QCM coated by a LB film of CNTs with a thickness of 10 layers onto double-side of the quartz.

Sensor type-C—10 MHz AT-cut quartz QCM coated by a LB multilayered film of CNTs with a thickness of 10 layers onto the buffer layer of CdA with a thickness of 10 layers onto double-side of the quartz.

The so-fabricated QCM sensors have been located in a test cell (1500 ml volume) for gas exposure measurements. The cell case is able to host up to twelve piezoelectric sensors. Dry air was used as reference gas and diluting gas to air-conditioning the sensors. The gas flow rate was controlled by mass flowmeters. The total flow rate per exposure was kept constant at 1500 ml/min. The gas sensing experiments have been performed by measuring the resonant frequency of the three QCM sensors upon controlled ambient of individual volatile organic compounds (VOCs) of ethylacetate, acetone and m-xylene in the range of 160–495, 265–800, and 16–50 ppm, respectively, at sensor temperature of 20°C.

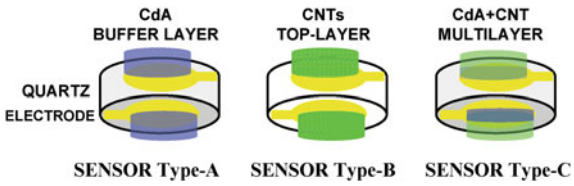

Fig. 42.2 Three different types of investigated QCM-sensors coated at double-side by **a** CdA buffer layer; **b** CNTs top-layer film and **c** CNT multilayer onto CdA buffer layer

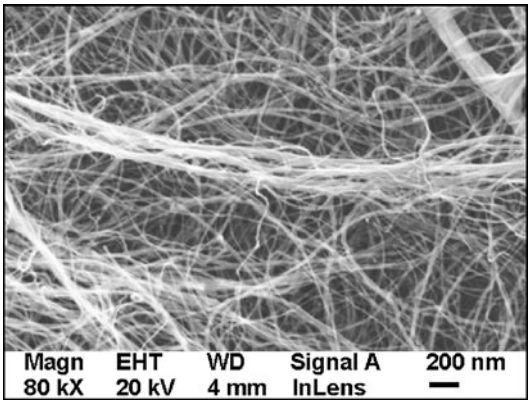

Fig. 42.3 FE-SEM image of CNTs treated with DMF and prepared on Si substrate

The frequency output of the QCM-sensors has been measured by a frequency counter (Agilent, 53132A) with a multiplexed read-out by a switch unit (Agilent, 34970A) driving two 50 Ω, 4 × 1 rf multiplexers (Agilent, 34905A). A J-type thermocouple was used to control the temperature in the sensor cell and its voltage output was measured by a multimeter (Agilent, 34401A). Data were collected and stored for further analysis in a PC interfaced with a GPIB card in the VEE-software ambient (Agilent).

42.3 Results and Discussion

The morphology and structure of the CNTs multilayer, treated with DMF solvent, has been characterized by FE-SEM, as reported in Fig. 42.3. A substrate of silicon has been used to deposit DMF-treated CNTs layers for electron microscopy observations. A dense network of bundles of multiple tubes consisting of multi-walled carbon nanostructures appears with a maximum length of 5 μm and single-tube diameter varying in the range of 5–35 nm.

Figure 42.4 shows the typical time responses in terms of frequency shift for three QCM sensors based on LB films of CdA buffer layer, CNTs top-layer, and multilayer of CNTs films onto buffer CdA, exposed towards 5 min six pulses of

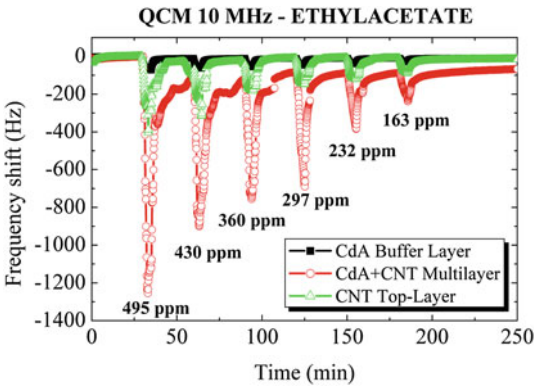

Fig. 42.4 Room-temperature time response towards 5 min six pulses of ethylacetate for three QCM sensors coated by CdA buffer layer, or CNT layer, or CdA + CNT multilayer

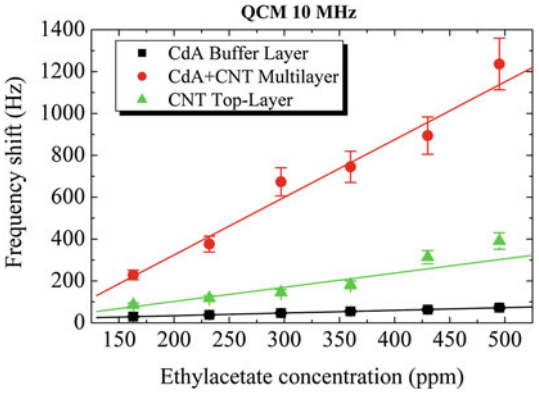

Fig. 42.5 Calibration curves of the three 10 MHz QCM-sensors to ethylacetate, at room temperature

ethylacetate, at room-temperature. The resonant frequency of all CNTs-sensors decreases upon a single exposure of the ethylacetate caused by the mass loading of the molecules adsorption. All three QCM-sensors demonstrate reversibility of the response upon switching of the target analyte concentration into dry air. In addition, a total recovery of the baseline frequency for all QCM-sensors has been measured. The highest mass sensitivity has been achieved for multilayer CdA + CNTs due to the greatest gas adsorbed mass. A linearity in the calibration curves for all QCM-sensors was measured, as reported in Fig. 42.5.

The gas sensitivity, expressed by the slope of the linear curves, has been plotted towards three tested different analytes (ethylacetate, acetone, m-xylene) for all three studied coatings, as reported in Fig. 42.6. These results demonstrate that multilayer CdA + CNTs exhibits the maximum sensitivity measured for three VOCs under test due to its highest capability of gas adsorption. A decreasing sensitivity towards aromatics (m-xylene), esters (ethylacetate) and ketones (acetone) has been detected for any considered sensitive coating.

The gas adsorption can be considered as the contribution of the main sensing mechanism of mass loading, as measured by the linearity in the gas response in terms of frequency shift as a function of gas concentration.

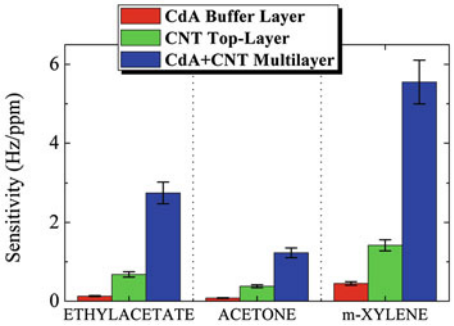

Fig. 42.6 Room-temperature pattern sensitivities of the three 10 MHz QCM-sensors coated by CdA buffer layer, or CNT layer, or CdA + CNT multilayer towards three different VOCs of ethylacetate, acetone and m-xylene. The range of the tested gas concentration of ethylacetate, acetone and m-xylene is 163–495, 265–800, and 16–50 ppm, respectively

42.4 Conclusions

CNTs-multilayer for 10 MHz QCM sensors have been prepared by Langmuir–Blodgett technique for enhanced mass sensitivity to detect VOCs of ethylacetate, acetone, and m-xylene up to ppm level of concentration, at room temperature. Chemical sub-ppm level of the VOCs is potentially measurable by tested QCM-sensors. The sensing properties have been investigated comparing the gas response of the buffered and un-buffered CNT multilayers to maximize sensitivity of the CNT sensors. The results demonstrate that the CdA-buffered CNTs-multilayer exhibits the highest gas sensitivity towards tested VOCs of ethylacetate, acetone and m-xylene, at room temperature. This is caused by the mass loading of the adsorbed gas molecules.

The CNTs-multilayers based QCM-sensors show high sensitivity, linearity, fast response, potential sub-ppm detection level, good reproducibility and reversibility. The studied QCM sensors with enhanced gas sensitivity and broader selectivity based on CNTs-multilayers are useful for chemical detection at room temperature and low power consumption and for applications in environmental air-emission monitoring.

References

1. Ballantine DS, White RM, Martin SJ, Ricco AJ, Zellers ET, Frye GC, Wohltjen H (1997) Acoustic wave sensors. Academic Press, San Diego
2. Rabe J, Buttgenbach S, Schroder J, Hauptmann P (2003) Monolithic miniaturized quartz microbalance array and its application to chemical sensor systems for liquids. IEEE Sens J 3(4):361–368
3. Penza M, Tagliente MA, Aversa P, Cassano G, Capodieci L (2006) Single-walled carbon nanotubes nanocomposite microacoustic organic vapor sensors. Mater Sci Eng C 26:1165–1170

4. Penza M, Tagliente MA, Aversa P, Cassano G (2005) Organic vapor detection using carbon nanotube composites microacoustic sensors. Chem Phys Lett 409:349–354
5. Penza M, Tagliente MA, Aversa P, Re M, Cassano G (2007) The effect of purification of single-walled carbon nanotube bundles on the alcohol sensitivity of nanocomposite Langmuir-Blodgett films for SAW sensing applications. Nanotechnology 18:185502
6. Penza M, Aversa P, Cassano G, Wlodarski W, Kalantar-zadeh K (2007) Layered SAW gas sensor with single-walled carbon nanotube based nanocomposite coating. Sensor Actuat B 127:168–178
7. Chen H-W, Wu R-J, Chan K-H, Sun Y-L, Su P-G (2005) The application of CNT/nafion composite material humidity sensing measurement. Sensor Actuat B 104:80–84
8. Consales M, Campopiano S, Cutolo A, Penza M, Aversa P, Cassano G, Giordano M, Cusano A (2006) Sensing properties of buffered and not buffered carbon nanotubes by fiber optic and acoustic sensors. Meas Sci Technol 17:1220–1228
9. Su P-G, Tsai J-F (2009) Low-humidity sensing properties of carbon nanotubes measured by a quartz crystal microbalance. Sensor Actuat B 135:506–511

Chapter 43
2D Anemometer Based on Multichannel Single Chip Flow Sensor

M. Piotto, P. Bruschi, F. Butti and G. Pennelli

Abstract A compact 2D wind sensor made up of an integrated, single chip, double channel flow sensor and a PMMA cylinder is proposed. The flow sensor is a standard micro calorimeter designed with a commercial CMOS process and thermally insulated from the substrate by means of a post-processing technique. The cylinder has two orthogonal active sections with an original channel configuration that connects the outer surface of the cylinder surface to the flow sensor. The optimization of the channel configuration allows to obtain a cosine dependence of the measured flow on the wind direction.

43.1 Introduction

Wind sensors are widely employed for meteorological monitoring and forecast, instrumental navigation assistance and airport danger condition detection. Recently, the increased awareness for the quality of life in urban and industrial areas has favored the development of compact units for monitoring the concentration of dangerous pollutants. In these devices, an anemometer capable of detecting both the direction and velocity of the local air circulation plays a crucial role. Unfortunately, the anemometer has been only marginally involved in the continuous scaling down of the sensors that led to the production of very compact acquisition units. The reason is that most commercial anemometers are still based

M. Piotto (✉)
IEIIT—Pisa, CNR, Via G. Caruso, 16, 56122 Pisa, Italy
e-mail: massimo.piotto@cnr.it

P. Bruschi · F. Butti · G. Pennelli
Dipartimento di Ingegneria dell'Informazione, Via G. Caruso, 16, 56122 Pisa, Italy

G. Neri et al. (eds.), *Sensors and Microsystems*,
Lecture Notes in Electrical Engineering 91, DOI: 10.1007/978-94-007-1324-6_43,

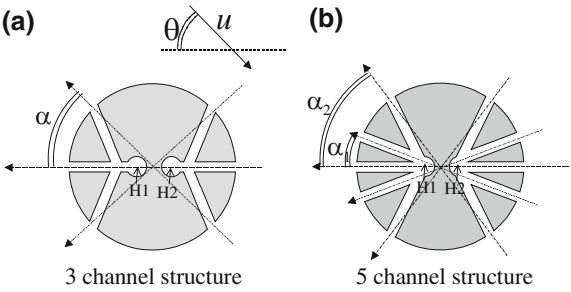

Fig. 43.1 **a** Cross sections of the cylinder active area in the case of the previous three channel structure and **b** the proposed five channel improvement

on the traditional "cup and vane" model. Alternative solutions, represented by ultrasonic [1] and macroscopic thermal anemometers [2], are either too expensive or too power hungry for application in low cost, battery powered sensor units. On the opposite side, MEMS (Micro Electro-Mechanical Systems) anemometers can be effectively miniaturized and use acceptable power levels but are too fragile to be directly exposed to the wind.

Recently, we have proposed an original approach [3, 4] that makes use of microchannels to probe the pressure distribution around a cylinder exposed to the air stream. Figure 43.1a shows the previously proposed three channel structure [3, 4], where the channels communicate with the cylinder lateral surface at points placed along three different diameters. It has been demonstrated that, with a proper choice of angle α, it is possible to produce a pressure difference (across H1, H2) depending only, in a non linear monotonic fashion, on the wind velocity component along a reference axis of the channel structure. Using two structures identical to that of Fig. 43.1a, rotated by 90°, and measuring the corresponding pressure differences is possible to derive the wind direction and intensity. In the device proposed in Ref. [3] the pressure differences are transformed into flow rates, which are measured with two distinct MEMS flow sensors. The MEMS structures operate inside channels that protect them against direct exposure to the wind.

In this work we propose an improvement of the previously proposed device consisting in: (i) use of a five channel structure to improve precision and (ii) use of a single chip, double channel flow sensor to improve miniaturization.

43.2 Device Design

The proposed five channel structure is depicted in Fig. 43.1b. Cubic spline approximations of pressure distribution data collected in Ref. [5] have been used to estimate the pressure difference dependence on the wind incidence angle and optimize angle α_1 and α_2 to obtain a sinusoidal relationship. Sweeping the angles α_i from 0 to 90° by a step of 1°, we found the optimum values $\alpha_1 = 21°$ and $\alpha_2 = 53°$.

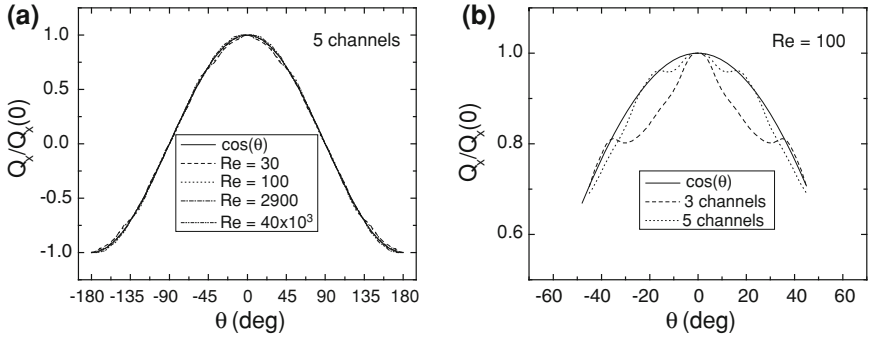

Fig. 43.2 **a** Calculated flow rate Q_x as a function of the wind direction θ for different Reynolds numbers; **b** comparison between three and five channel structures for Re = 100 and low θ values

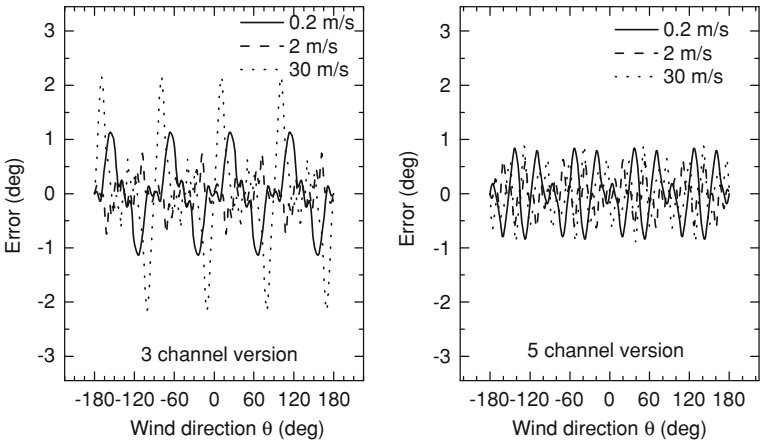

Fig. 43.3 Comparison between the simulated angular error obtainable with the three and five channel structures

The calculated flow rate Q_x between H1 and H2, normalized to the value at $\theta = 0^\circ$, for different Reynolds numbers is shown in Fig. 43.2a. It can be noted that the approximation of the ideal function $\cos(\theta)$ is good in the whole velocity range. The greater deviation from the ideal curve has been found for low values of wind direction θ, as visible in the enlarged view shown in Fig. 43.2b where the behavior obtained with a three channel structure is also reported for comparison. It can be noted that the five channel structure led to a better approximation of the ideal cosine function.

The angular precision of an anemometer based on the five channel structure has been compared to that of the previous three channel structure over a wide velocity range and the results are shown in Fig. 43.3. Note that, with the new five channel structure, the angular error is less than $\pm$ 1° over the whole velocity range.

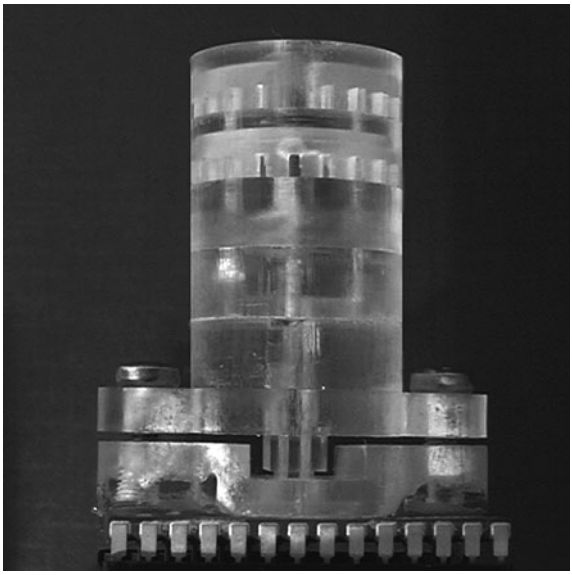

Fig. 43.4 Photograph of the assembled device

43.3 Prototype Fabrication

As far as the prototype fabrication is concerned, we have exploited a recently introduced low cost packaging technology [6] applied to a chip including several thermal gas velocity micro detectors.

The chips were designed and fabricated using the BCD6 process of STMicroelectronics and subsequently post-processed to produce the required thermal insulation between the sensing structures and the substrate.

A cylinder including the two active sections has been fabricated by piling up different Poly Methyl Methacrilate (PMMA) disks where the required channel layout has been milled using a computer controlled precision milling machine. The air flows derived by the pressure differences produced across points H1–H2 of the two orthogonal structures are conveyed to the single chip flow sensor by means of PMMA elements fabricated using the same milling machine.

The overall dimensions of the resulting prototype, shown in Fig. 43.4, are only $5 \times 4 \times 2$ cm.

43.4 Conclusions

The design and fabrication of a compact 2D wind sensor have been described. A micromachined, single chip, double channel flow sensor is connected to the outer surface of a PMMA cylinder by means of two orthogonal active sections. Each section has a five channel structure whose geometry has been optimized in

such a way that the measured flow is proportional to the cosine of the wind direction. The calculated angular error is less than $\pm 1^{\circ}$ for velocities up to 30 m/s. Preliminary experimental tests confirm the calculated device response.

Acknowledgment The authors wish to thank the STMicroelectronics of Cornaredo (Italy) for fabricating the chips.

References

1. Han D, Kim S, Park S (2008) Two-dimensional ultrasonic anemometer using the directivity angle of an ultrasonic sensor. Microelectron J 39:1195–1199
2. Ruser H (2005) Smart robust wind sensor using a simple optimization procedure. In: Proceedings IEEE Sensors 2005, pp 672–675
3. Bruschi P, Dei M, Piotto M (2009) A low-power 2-D wind sensor based on integrated flow meters. IEEE Sensor J 9:1688–1696
4. Piotto M, Dei M, Pennelli G, Bruschi P (2009) A miniaturized 2D solid state anemometer based on thermal flow sensors.In: Proceedings of Eurosensors XXIII, Procedia Chemistry, vol 1, Sept 2009, pp 1463–1466
5. Zdravkovich MM (1997) Flow around circular cylinders: a comprehensive guide through flow phenomena, experiments, applications, mathematical models and computer simulation. Oxford University Press, Oxford, U.K, pp 1–109
6. Bruschi P, Dei M, Piotto M (2009) A single chip, double channel thermal flow meter. Microsyst Technol 15:1179–1186

Chapter 44
Electro-Optical Modulating Multistack Device Based on the CMOS-Compatible Technology of Amorphous Silicon

Sandro Rao, Francesco G. Della Corte and Caterina Summonte

Abstract We report results on a field-effect induced light modulation at $\lambda = 1.55$ μm in a high-index-contrast waveguide based on a multisilicon-on-insulator (MSOI) platform. The device is realized with the hydrogenated amorphous silicon (α-Si:H) technology and it is suitable for monolithic integration in a CMOS integrated circuit. The device exploits the free carrier optical absorption electrically induced in the multistack core waveguide.

44.1 Introduction

In recent years, hydrogenated amorphous silicon (α-Si:H), grown by Plasma Enhanced Chemical Vapour Deposition (PECVD), has gained considerable attention due to its unique characteristic of transparency at the infrared wavelengths, refractive index tunability [1], and good technological compatibility with all microelectronic processes. As a consequence, several α-Si:H based optoelectronic devices, such light emitting diodes, photodetectors and optical modulators [1] have been successfully fabricated.

S. Rao (✉) · F. G. Della Corte
Department of Information Science, Mathematics, Electronics and Transportations (DIMET) "Mediterranea" University, Via Graziella Loc. Feo di Vito, 89131 Reggio Calabria, Italy
e-mail: sandro.rao@unirc.it

C. Summonte
Consiglio Nazionale delle Ricerche—Unit of Bologna, Institute for Microelectronics and Microsystems, Via Gobetti 101, 40129 Bologna, Italy

G. Neri et al. (eds.), *Sensors and Microsystems*,
Lecture Notes in Electrical Engineering 91, DOI: 10.1007/978-94-007-1324-6_44,

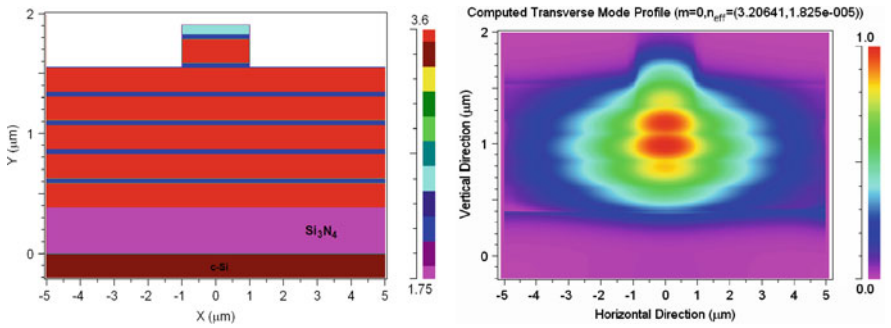

Fig. 44.1 (*left*) Schematic cross sections of the realised waveguide and corresponding refractive index colour bar. The crystalline silicon substrate is 300 μm-thick. (*right*) Fundamental TE mode in the *x*–*y* plane

Thermo-optical and all-optical effects have been exploited in α-Si:H to demonstrate modulation or switching action in planar devices for integrated photonics [1, 2]. Electro-optical effects, in contrast, have been rarely considered in this material due to the weak incidence of electric field on the refractive index [3], on one side, and the difficulty of reaching a significant carrier injection across p–n junctions in amorphous semiconductors, on the other side.

44.2 Design and Fabrication

Figure 44.1 (left) illustrates the schematic cross section considered in this work. The waveguide consists of the stack of six bi-layers each composed of a 0.2 μm-thick α-Si:H layer and a 40 nm-thick α-SiCN layer, deposited on a <100> heavily doped silicon substrate. The substrate and the stack are separated by a 0.39 μm-thick Si_3N_4 low refractive index cladding layer ensuring a strong vertical optical confinement. An 80 nm-thick transparent conductive Indium Tin Oxide (ITO) thin film forms the top contact, while the bottom contact is the Si substrate itself.

Simulation results [4] demonstrated that the designed waveguide supports only one mode for TE polarization once a 2 μm wide rib is defined by photolithographic patterning and wet etching in 5% HCl solution. The etch depth is 0.35 μm. Due to the geometry of the waveguide, the TM mode exhibits high losses and low modulation efficiency, therefore only the TE-like polarization will be considered hereafter. Figure 44.1 (right) shows the fundamental TE_0 mode, well confined under rib region, characterized by propagation losses of 1.47 cm^{-1} at $\lambda = 1.55$ μm in agreement with experimental results.

In the present device the thin α-SiCN highly insulating layers [5] break the conduction among the α-Si:H films so that the device electrically behaves as the series of capacitors. The application of a biasing voltage between the ITO layer and the c-Si substrate determines an accumulation of electrons and holes at the

opposite ends of each internal α-SiCN dielectric layer. The presence of more α-SiCN regions between the α-Si:H layers allows a distribution of the excess free carriers across the device section contributing to create a highly-effective absorption variation [6, 7].

The refractive index and absorption coefficient change in silicon, due to injection or depletion of free carrier at $\lambda = 1.55$ μm, can be derived to a first order approximation from the classical Drude model also for amorphous silicon semiconductor [8].

The device was modelled both for its static and dynamic behaviour using ATLAS, the device simulation package from Silvaco [9]. We obtained a carrier concentration change, close to the α-Si:H/α-SiCN interface, of $\sim 10^{18}$ cm^{-3} when a bias of 20 V is applied across the six bi-layer device.

Mixed electrical-optical simulations were run in order to model the modulation effect for the realized device. We calculated, at several bias points, the accumulated carrier profiles and the corresponding free carrier induced optical absorption variations.

The calculated new absorption profile was fed into the optical simulator, which returned a theoretical modulation in good agreement with the measured one.

44.3 Experimental Results and Discussion

The modulation measurements were performed avoiding every ambiguity in the polarisation state of an optical signal entering or exiting the chip under test. Hence a free-space experimental setup was developed. A broadband polarising cube beamsplitter and a half-wave plate were placed in the beam path allowing for the linear polarisation state of the input beam to be converted from TE to TM or vice versa. The 15 mW laser beam was focused onto the input facet of the waveguide and the modulated light emerging from the chip was collected and collimated by an objective and detected by an InGaAs photodiode.

The waveguide propagation losses were first measured by the cut-back technique. To improve the accuracy of this method, the device was cut from the substrate by cleavage several times. We obtained samples with lengths in the range 0.7 to 1.1 cm. Sample facets did not receive polishing treatment. From these samples we calculated a loss coefficient of 2.26 ± 0.04 cm^{-1}, mainly due to the fundamental absorption/scattering phenomena in the α-Si:H layers and to the thin Si_3N_4 cladding which does not completely prevent the optical field tail from extending into the lossy substrate. The overall insertion losses of the device are above 11 dB, with the main contribution due to the coupling losses, a drawback of the high refractive index of silicon used as the core material.

Subsequently, a set of three samples ($L = 0.7$, 1 and 1.1 cm) were used to characterize the modulation effect by applying square voltage pulses to the electrodes.

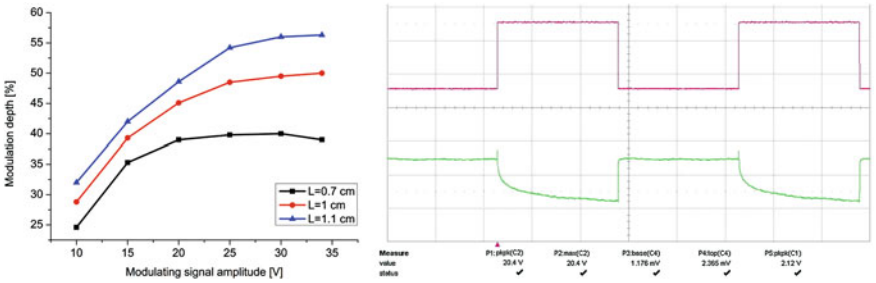

Fig. 44.2 (*left*) Dependence of *M%* on the modulating signal amplitude for three different lengths (six bi-layers, 1.2 μm overall core thickness). (*right*) Applied voltage (*top trace*) and output light power (*bottom trace*) for the six bi-layers, 1.1 cm long, waveguide. The modulating signal has Vmin = 0 V, Vmax = 20 V, duty-cycle = 50%. The time base is 20 ms/div

Figure 44.2 (left) reports the dependence of *M%* on the modulating signal amplitude at low frequency and a duty cycle of 50% for the three different lengths. A maximum modulation depth up to 55% is obtained for the 1.1 cm long sample.

44.4 Conclusion

A multi-stack structure, based on the CMOS-compatible technology of amorphous silicon, has been explored for enhancing electro-optical modulation effects in integrated, waveguide embedded, photonic devices.

The waveguiding structure deposited by PECVD on a c-Si substrate, were realized and characterized. It showed propagation losses lower than 2.3 cm^{-1} at the wavelength of 1.55 μm. The application of an external electric field across the structure produces carrier accumulation at the intermediate semiconductor/insulator interfaces, which is in turn responsible of an enhanced optical absorption. We measured a $\Delta\alpha_{eff}$ of 0.75 cm^{-1} when an electric field of 0.39 MV/cm is applied across each α-SiCN dielectric thin film.

Acknowledgments IMM-CNR (Naples, Italy) for optical simulations, G.T. Reed and W. Headley (University of Surrey, Guildford, UK) for helps in some experiments and for stimulating discussions.

References

1. Cocorullo G, Della Corte FG, De Rosa R, Rendina I, Rubino A, Terzini E (1998) Amorphous silicon-based guided-wave passive and active devices for silicon integrated optoelectronics. IEEE J Sel Top Quantum Electron 4:997–1002

2. Della Corte FG, Gagliardi M, Nigro MA, Summonte C (2006) In-guide pump and probe characterization of photoinduced absorption in hydrogenated amorphous silicon thin films. J Appl Phys 100:033104
3. Zelikson M, Weiser K, Chack A, Kanicki J (1996) Direct determination of the quadratic electro-optic coefficient in an α-Si:H based waveguide. J Non Cryst Sol 198–200:107–110
4. RSoft Photonics CAD Layout User Guide, Rsoft Design Group, Inc. Physical Layer Division, 200 Executive Blvd. Ossining, NY 10562
5. Lavareda G, Nunes de Carvalho C, Fortunato E, Amaral A, Ramos AR (2004) Properties of α-Si:H TFTs using silicon carbonitride as dielectric. J Non Cryst Sol 338–340:797–801
6. Della Corte FG, Rao S, Nigro MA, Suriano F, Summonte C (2008) Electro-optically induced absorption in α-Si:H/α-SiCN waveguiding multistacks. Optics Express 16:7540–7550
7. Rao S, Della Corte FG, Summonte C (2010) Electro-optically induced absorption in *a*-Si:H/*a*-SiCN waveguiding multistacks. J Eur Optical Soc Rapid Publ 5:10002
8. Fauchet PM, Hulin D, Vanderhaghen R, Mourchid A, Nighan WL Jr (1992) The properties of free carriers in amorphous silicon. J Non Cryst Sol 141:76–87
9. ATLAS device simulation software user's manual, SILVACO Int., Santa Clara, CA (2005)

Chapter 45
Improved SQUID Sensors for Biomagnetic Imaging

Antonio Vettoliere, C. Granata, S. Rombetto and M. Russo

Abstract Improved niobium-based SQUID sensors in a magnetometer and a gradiometer configuration are presented. The SQUID magnetometer has an integrated square superconducting sensing coil with an area of 9 mm^2, much smaller than a typical SQUID magnetometers keeping a comparable magnetic field sensitivity but a higher spatial resolution. At $T = 4.2$ K, an intrinsic magnetic field noise spectral density of 5.8 fT/$\sqrt{}$Hz, has been measured in the flux locked loop configuration. The SQUID planar gradiometer with a long baseline (50 mm) has a pickup antenna consisting of a series of two integrated rectangular coils inductively coupled to the SQUID in a double washer configuration. At $T = 4.2$ K a magnetic flux noise spectral density of 3 $\mu\Phi_0/\sqrt{}$Hz has been measured. The spectral density of the magnetic field noise referred to one sensing coil, is 3.0 fT/$\sqrt{}$Hz resulting in a gradient spectral noise of 0.6 fT/cm $\cdot$ $\sqrt{}$Hz.

45.1 Miniaturized SQUID Magnetometer

Magnetometers based on the superconducting quantum interference device (SQUID) are very sensitive low-frequency magnetic field sensors and are widely used in several applications which require a high magnetic field sensitivity [1]. One of the most interest is in biomagnetic imaging. Since the magnetic flux noise increase with the SQUID inductance, to increase sensitivity an integrated superconducting flux transformer is used. To ensure the necessary magnetic field

A. Vettoliere (✉) · C. Granata · S. Rombetto · M. Russo
Istituto di Cibernetica "E. Caianiello" del CNR,
via Campi Flegrei, 34 - 80078, Pozzuoli (NA), Italy
e-mail: a.vettoliere@cib.na.cnr.it

G. Neri et al. (eds.), *Sensors and Microsystems*,
Lecture Notes in Electrical Engineering 91, DOI: 10.1007/978-94-007-1324-6_45,

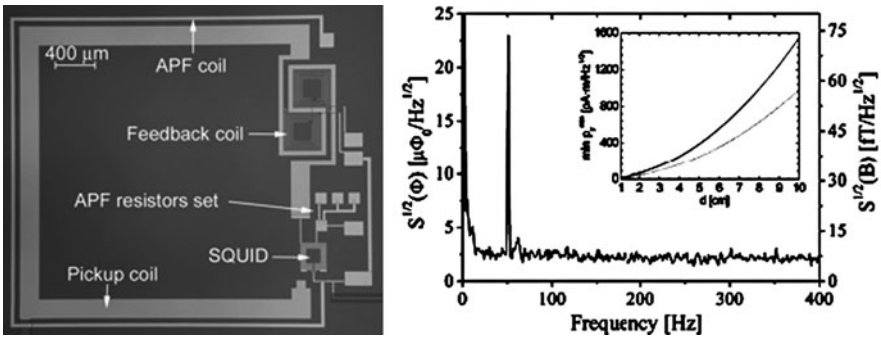

Fig. 45.1 Picture of a fully integrated SQUID magnetometer (*left figure*). Magnetic flux noise spectral density, measured, at $T = 4.2$ K, in FLL configuration (*right figure*). The inset shows the minimum dipole detectable by the sensors as a function of the relative distance

sensitivity for biomagnetic applications the devices have typically an area no less than 60 mm^2 [1], limiting the number of sensors that can be allocated in biomagnetic systems.

Here, a high sensitive miniaturized dc SQUID magnetometer based on niobium technology is reported. It is a fully integrated device having an area less than 10 mm^2 which includes a superconducting flux transformer consisting of a square pickup coil with a side length and width of 3 mm and 0.2 mm respectively; in series with a 8-turn input coil, which is coupled to the SQUID loop in a washer configuration; it also includes an additional positive feedback (APF) circuit and a bipolar feedback coil for low cross-talk operations. Apart from a better spatial resolution, a small pick-up coil minimizes its antenna gain reducing the effects of radio frequency interference. In order to improve the coupling properties between the SQUID and the input circuitry, a SQUID with a large inductance (250 pH) has been used. The consequent sensitivity degradation, due to non-optimal noise conditions, has been avoided by inserting of a damping resistor across the SQUID loop [2]. Such design allows to obtain a suitable flux-to-field conversion efficiency (B_Φ) and a high flux gain G_Φ, that is the ratio between the magnetic flux treading the SQUID loop (Φ_S) and that one applied to the pick-up coil (Φ_p). The integrated APF circuit reduces the equivalent preamplifier flux noise with respect to the SQUID one in the case of direct-coupling readout scheme. It makes the voltage to magnetic flux characteristic ($V-\Phi$) asymmetric, so, if the SQUID is biased on the steeper side, an effective increase of the SQUID responsivity ($V_\Phi = \partial V/\partial\Phi$) is achieved [3]. The bipolar design of the feedback coil consisting of two multiturn coil allows to reduce cross-talk between neighboring sensors [4]. The sample fabrication process, capable to routinely produce high quality window-type junctions, has been well described elsewhere [4]. A picture of the device is shown in Fig. 45.1. The SQUID sensors have been characterized at $T = 4.2$ K in a high shielded environment. A $B_\Phi = 3.2$ nT/Φ_0 has been measured by applying an external magnetic field by means of calibrated Helmholtz coils. By using a low noise read-out electronics based on Flux Locked Loop (FLL) with a direct

coupling scheme, an intrinsic flux noise spectral density as low as 2.2 $\mu\Phi_0/\sqrt{\text{Hz}}$ in the white region, corresponding to 7.0 fT/$\sqrt{\text{Hz}}$, has been measured (Fig. 45.1). The intrinsic noise obtained by subtracting the amplifier contribution is 5.8 fT/$\sqrt{\text{Hz}}$ [5]. The minimum value of current dipole detectable by this magnetometer and a typical one, having a 9 mm pickup coil side length and a suitable sensitivity for biomagnetic applications, have been computed and compared showing that the differences are appreciable only for deeper source (inset of Fig. 45.1) [6].

45.2 Planar SQUID Gradiometer

Since background noise signals exceed those of the biomagnetic sources by many orders of magnitude, both high shielded room and sophisticated noise cancellation techniques must be employed. In spite of this, hardware or electronic gradiometers are typically used to increase signal–noise ratio [7].

Here, a fully integrated first order planar SQUID gradiometer is presented. It has a high intrinsic balance thanks to the precision of the photolithographic techniques used in the fabrication process [8]. Moreover, the inductances of pickup and input coils are well matched ensuring a good signal coupling with the SQUID. Furthermore, the unreliable superconducting soldering are avoided. The pickup antenna consists of a series of two rectangular coils (12×10 mm^2) having a distance between their center (baseline) of 50 mm, guaranteeing a suitable sensitivity also to the deep biomagnetic sources. The pickup coil, with a total inductance $L_p = 90$ nH, is connected in series with an input coil consisting of a series of two coils (16 turns each), magnetically coupled to SQUID loop having a parallel double washer configuration. The inductances of the input coil and the SQUID are respectively $L_i = 90$ nH and $L_S = 109$ pH and the relative mutual inductance is $M_i = 3.4$ nH. The device includes an integrated feedback coil for Flux Locked Loop operation (FLL), consisting of two multiturn coils (10 turns each) in a bipolar design allowing to reduce crosstalk between neighboring sensors [4]. The high intrinsic voltage-to-flux conversion factor V_Φ (responsivity), obtained increasing a critical current, reduces the flux noise contribution of the preamplifier to a tolerable value. To prevent a noise performance degradation, a thin film resistor across the SQUID inductance has been inserted [2]. It also eliminates possible washer resonances and guarantees smooth $V-\Phi$ characteristics. The fabrication process is well described in Ref. [3]. In Fig. 45.2, a picture of the device and its particulars is shown. The read-out electronic for the measurements of both $V-\Phi$ characteristics and noise performances is integrated on a very-low-noise miniaturized detection circuit having radio frequency filters on the electrical connections to room temperature. In such a configuration the SQUID is directly coupled to a preamplifier, which contributes to the overall magnetic flux noise by adding the term $S_{V,\text{amp}}^{1/2}/V_\Phi$ where $S_{V,\text{amp}}^{1/2}$ is the spectral density of the amplifier voltage noise (0.5 nV/$\sqrt{\text{Hz}}$ at 10 Hz). The SQUID sensors have been characterized at liquid helium temperature, exhibiting a critical current of 33 μA.

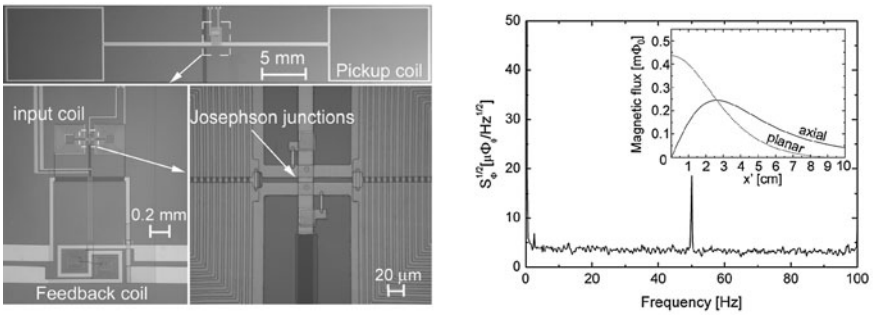

Fig. 45.2 Picture of a fully integrated planar gradiometer showing the particulars of feedback and input coils and of the Josephson junctions (*left figure*). In the right figure the magnetic flux noise spectral density measured at T = 4.2 K in FLL configuration is shown. The inset shows the net magnetic fluxes of the gradiometers in both planar and axial configuration as function of the off-axis dipole position x'

A maximum V_Φ value of 500 μV/Φ_0 can be evaluated from the $V-\Phi$ characteristics that has a voltage swing of 65 μV. The magnetic field sensitivity B_Φ referred to the single pick-up coil is about 1 nT/Φ_0. The magnetic flux noise spectral density of the sensor, measured in flux looked loop without any high magnetic permeability shields was 3 $\mu\Phi_0/\sqrt{\text{Hz}}$, corresponding to a magnetic field noise referred to the single pick-up coil of 3 fT/$\sqrt{\text{Hz}}$. Being a baseline length $d = 50$ mm, the resulting spectral density of the field gradient noise is 0.6 fT/(cm · $\sqrt{\text{Hz}}$) [9].

In order to verify the device effectiveness for biomagnetic imaging, the magnetic responses of this planar sensor, in a vertical arrangement, to a current dipole has been computed. The results has been compared with those relative to a first order axial gradiometer having the same baseline, pick-up coil's size, and the same SQUID design parameters.

Following the same procedure reported in Ref. [6], the net device flux, for planar and axial configuration, is obtained by taking the difference of the magnetic fluxes treading the bottom coil and the top one ($\Phi_N^P = \Phi_B^P - \Phi_T^P$). The output magnetic flux of the sensors, given by $\Phi_S = G_\Phi \cdot \Phi_N^P$, where $G_\Phi = M_i/\left(L_p + L_i\right)$ is the flux gain [6], are reported in Fig. 45.2.

For a small range of off-axis distance x' around the peaks, the magnetic strengths of the planar gradiometer are appreciably greater than the axial ones; For longer x' distance, the magnetic strengths of the planar device falls faster than the axial one; however, in multichannel systems, the dipole sources having a x' distance greater than 2–4 cm can be effectively investigated by the neighboring sensors. The curves have been computed using for both sensors a current dipole strength ($p_y = 10$ nA·m), a flux gain $G_\Phi = 0.02$ and a distance between the current dipole and sensor of 4 cm [9].

45.3 Conclusions

A miniaturized dc SQUID magnetometer and a long baseline planar SQUID gradiometer, based on niobium technology, have been presented. The effectiveness of these device designs has been confirmed by both the experimental results and numerical simulations of the output magnetic flux. On the basis of such results, the sensors are suitable for high sensitivity applications such as the systems for biomagnetic imaging

Moreover, the miniaturized magnetometer is very useful when a large sensor density is required while the planar gradiometer can be employed in multichannel system working in a soft shielded environment.

References

1. Clarke J, Braginski AI (2004) Applications of SQUID and SQUID system. In: Clarke J, Braginski, AI (eds), Weinheim The SQUID Handbook, vol 2. Wiley, New York
2. Enpuku K, Muta T, Yoshida K, Ire F (1985). Noise characteristics of a dc SQUID with a resistively shunted inductance. J Appl Phys 58:1916
3. Drung D (1996). Advanced SQUID read-out electronics. In: Weinstock H (ed) SQUID sensors: fundamentals, fabrication and application, series E, vol. 329, Kluwer Academic, Dordrecht, p 63
4. Granata C, Vettoliere A, Russo M (2006). Improved superconducting quantum interference device magnetometer for low cross talk operation. Appl Phys Lett 88:212506
5. Granata C, Vettoliere A, Russo M (2007) Miniaturized superconducting quantum interference magnetometers for high sensitivity applications. Appl Phys Lett 91:122509
6. Granata C, Vettoliere A, Rombetto S, Nappi C, Russo M (2008) Performance of compact integrated magnetometer for biomagnetic imaging. J Appl Phys 104:073905
7. Vrba J, Robinson SE (2002). SQUID sensor array configurations for magnetoencephalography applications. Supercond Sci Technol 15:R51
8. Stolz R, Fritzsch L, Meyer H-G (1999). LTS SQUID sensor with a new configuration. Supercond Sci Technol 12:806
9. Granata C, Vettoliere A, Lisitskiy M, Nappi C, Russo M (2009) Long baseline planar superconducting gradiometer for biomagnetic imaging. Appl Phys Lett 95:042502

Chapter 46
A Millimetre Size Wireless Temperature Sensor with Digital Conversion and Embedded 2.5 GHz Transmitter and Antenna

F. Zito, L. Fragomeni and F. G. Della Corte

Abstract The on-chip antenna concept is the actual trend in integrated wireless sensor systems because it is a practical solution to compact, small size and low cost devices for short range wireless applications, like RFID tags and biomedical sensor data transmitters and other related applications. Due to the typical small chip dimension, only high frequency bands can use these antennas in optimum, i.e., resonating, conditions. Although the chip dimension do not allow resonant radiating elements, nevertheless this does not seem to be a limit for the specific application in contactless sensing, where a short distance wireless link is sufficient. In this paper an improvement of a wireless temperature sensor with on-chip antenna is presented. This solution, realized in 0.35 μm CMOS technology, exploits a proportional to absolute temperature (PTAT) voltage scheme, where the difference between two base-emitter voltages under different bias current densities is constantly measured. The availability of bipolar transistors in CMOS technology allows to exploit their properties in temperature sensor applications. The signal is transmitted by a small loop antenna structure which is realized by aluminium deposition on the top surface of the chip.

F. Zito (✉) · L. Fragomeni · F. G. Della Corte
DIMET, "Mediterranea" University of Reggio Calabria, Via Graziella, Loc. Feo di Vito, 89060 Reggio Calabria, Italy
e-mail: fabio.zito@unirc.it

L. Fragomeni
e-mail: letizia.fragomeni@unirc.it

F. G. Della Corte
e-mail: francesco.dellacorte@unirc.it

G. Neri et al. (eds.), *Sensors and Microsystems*,
Lecture Notes in Electrical Engineering 91, DOI: 10.1007/978-94-007-1324-6_46,

46.1 Introduction

The feasibility of wireless sensor devices has been fully demonstrated recently [1, 2] with a wide use of different interfaces and transmission standards and various antenna topologies. The link with the RFID technology can be a practical and low-cost solution to associate radio frequency identification with the measure of the temperature of product, animal or people with dynamic variable data acquisition from on-board sensors.

This study originates from a previous work, which deals with a wireless sensor with on-chip antenna for short range biomedical applications. A single-loop antenna is used in that case [3] and the device proves the possibility of realizing an on-chip antenna. When the RFID is combined with sensory systems, its application area can be extended to environmental monitoring such as temperature, humidity and pressure sensing. The new temperature sensor exploits the proportional to absolute temperature (PTAT) voltage, which is the difference between two base emitter voltages under different bias current densities. The availability of bipolar transistors, in CMOS technology, allows us to exploit their properties in temperature sensor applications. The sensitivity, signal level and linearity of the sensor interface were specially conditioned in order to simplify further Analog-to-Digital conversion (ADC). The idea is to convert the analog signal, i.e., PTAT voltage, to a N-bits digital signal, where each bit can modulate a Radio Frequency (RF) carrier generated, for example, by a ring oscillator, using the On–Off Keying (OOK) modulation.

46.2 The Temperature Sensing Principle

Many implementations of temperature sensors have been reported, relying on the well-known temperature dependency of bipolar devices. Considering CMOS technology, lateral as well as vertical substrate PNP transistors can be applied. The vertical substrate transistors have the better performance with respect to non-idealities of the characteristics $I_C(V_{BE}, T)$.

The PTAT temperature sensor uses the phenomenon that difference between voltages of two bipolar elements, which have different areas and conduct the same current (i.e., different current densities), is proportional to absolute temperature (PTAT). The base-emitter voltage of bipolar transistors or, more generally, the forward voltage of pn-junction diode exhibits a negative temperature coefficient ($\partial V_{BE}/\partial T \approx -1.5$ mV/°C). As well-know, if two different bipolar transistors (i.e., PNP substrate transistors for CMOS technology) operate at unequal current densities, then the difference between their base-emitter voltages is directly proportional to absolute temperature.

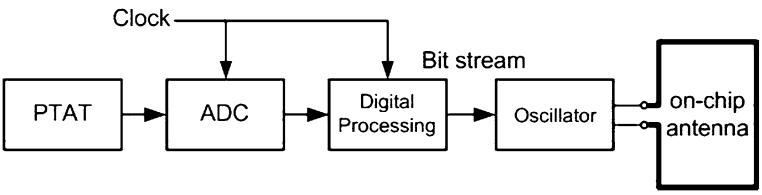

Fig. 46.1 Block diagram of the "RFID" temperature sensor

46.3 Chip Design

The electronic design of the RFID sensor has been carefully tuned to get a linear dependence of voltage versus temperature for a wide temperature range (room temperature to 100°C). This voltage, converted to a digital signal, is an output bit stream that can be used to drive a RF-oscillator, as shown in Fig. 46.1. The RFID temperature sensor comprises four major blocks: a proportional-to-absolute temperature (PTAT) voltage generator, an analog-to-digital converter (ADC) with a maximum resolution of 8-bits, a digital processing circuit and a RF transmitter.

Simulations regarding the radiating element has been conducted in Ansoft HFSS at a frequency of 2.4 GHz, for its tuning and for obtaining its characteristic values (to be used in Cadence). The stack-up refers to a 0.35 μm CMOS standard technology and consists of a 300 μm thick Si substrate ($\rho = 19\ \Omega{\cdot}cm$) and an Al metal layer on top. A 4 μm oxide layer ($\rho = 10^{10}\ \Omega{\cdot}cm$) between the metal layer and the lossy Si substrate acts as insulation. The typical dimensions of the metal cross-section are $20 \times 1\ \mu m^2$. Chip dimensions are about $2.5 \times 2.5\ mm^2$. The antenna structure is examined, investigating the effects in its behavior induced by varying the geometric and technological parameters. Inductive and radiation characteristics are calculated. Two sources of losses should be considered: losses due to the metal conductivity (these losses are in fact neglected) and losses in substrate volume. A lossy substrate decreases the radiation efficiency, which depends on the conductivity of the substrate material.

46.4 Results

Eddy currents are induced in the substrate as the effect of the current flowing in the antenna. Induced current causes poor values of the radiation efficiency. Comparing the simulations on air and on the substrate, the value of R_d remains substantially unaltered (about 0.16 Ω) but, more important, an increase in R_{loss} value is observed (it varies from 6.15 to 10.25 Ω with the introduction of the substrate). This implies an input impedance value $Z_{in} = 11 + j103$, with a radiation

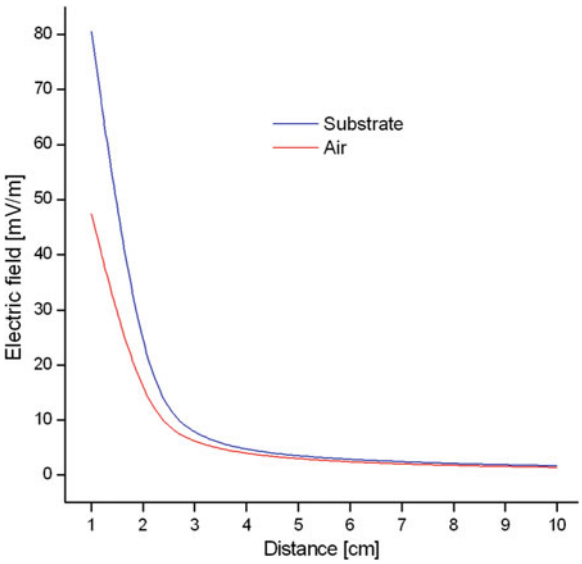

Fig. 46.2 Electric field versus distance on air and on substrate for the loop antenna

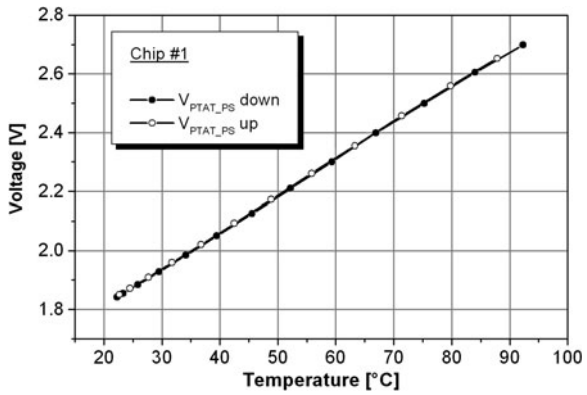

Fig. 46.3 Measured PTAT voltages versus temperature

efficiency value of 1.5% and a −41 dB gain in presence of the substrate. The electric field shows an inverse behaviour at a short distance, as can be observed in Fig. 46.2, where the fields on air and in presence of the substrate are reported.

The device showed a linear voltage versus temperature dependence for a wide temperature range: from room temperature to 100°C, applying both positive and negative temperature ramps (called up and down in Fig. 46.3). The voltage $V_{\text{PTAT-PS}}$, shows a linear dependence on the temperature changes, with temperature sensitivities equal to $\Delta V_{\text{PTAT-PS}}/\Delta T = 10.62$ mV/°C. After the temperature to voltage transduction, it is necessary to digitalize this signal with an ADC. We choose to implement an 8-bit ADC and thus the analog input voltage will be converted on 256 quantization levels. If we consider the interval between 20 and

100°C, we have a range of about 80°C. This means that the analog signal $V_{PTAT\text{-}PS}$, has a swing of 810 mV, with a resolution of about 3 mV, which translates into an error of 0.3°C.

The bias voltage for the device is 3.3 V with a low DC current consumption of about 70 μA for the PTAT sensor in continue operation mode. About the analog-to-digital conversion and digital processing, the dynamic power consumption does not represent a considerable value in terms of dissipated power because the temperature is periodically acquired with a very long time interval, for example at 1 Hz or less.

46.5 Conclusions

A fully integrated wireless temperature sensor, exploiting on-chip antenna for short range applications, has been presented. The sensor provides a voltage versus temperature sensitivity of 10.62 mV/°C, at 3.3 V bias voltage, for the PTAT sensing element. The sensor has been implemented in 0.35 μm CMOS technology. In consequence of its dimensions, antennas are far from resonance conditions and therefore their gain and radiation diagrams, although well far from being optimal, are still enough for enabling a short range RF communication channel.

References

1. Kenneth KO et al (2005) On-chip antennas in silicon ICs and their application. IEEE Trans On Electron Devices 52(7):1312–1323
2. Kenneth KO et al (2005) The feasibility of on-chip interconnection using antennas, IEEE Int Conf Comput Aided Des, San Jose, CA, pp 976–981
3. Aquilino F, Merenda M, Zito F, Della Corte FG (2008) 2.4 GHz fully integrated wireless temperature sensor with on-chip antenna. In: Proceedings of the XIII AISEM conference on sensors and microsystems

Part V
Applications

Chapter 47
High Sensitivity Mach–Zehnder Interferometer for Sub-Nanoliter Liquid Sensing

G. Testa, L. Zeni, Yujian Huang, P. M. Sarro and R. Bernini

Abstract In this paper we present a new configuration of an integrated optofluidic Mach–Zehnder interferometer based on liquid core ARROW waveguide that permits to obtain high sensitivity for liquid sensing. The proposed devices have been realized and optically characterized. The experimental results are in good agreement with the theoretical ones.

47.1 Introduction

Integrated Mach–Zehnder (MZ) interferometers are very powerful optical sensor device, able to detect low refractive index changes with very high accuracy.

Due to the well-known sensing capabilities, these devices are widely applied in chemical and biochemical applications, where the sensing is performed on sample dispersed in liquid. In the last few years new configurations, capable to enhance the optical sensitivity of these devices, have been proposed [1, 2]. One possible approach to improve the sensitivity is to employ liquid core waveguides. In comparison to conventional MZI, liquid core MZI offers the advantage to have an improved sensitivity due to the direct optical coupling of the light with the liquid sample. Such a new optofluidic configuration has recently attracted much attention and some examples of liquid interferometers have been reported [2, 3].

G. Testa · R. Bernini (✉)
IREA-CNR, Via Diocleziano 320, 80124 Naples, Italy
e-mail: bernini.r@irea.cnr.it

L. Zeni
DII Seconda Università di Napoli, Via Roma 29, 81031 Aversa, Italy

Y. Huang · P. M. Sarro
ECTM-DIMES, TUDelft. NL, 2600, GB, Delft, The Netherlands

G. Neri et al. (eds.), *Sensors and Microsystems*,
Lecture Notes in Electrical Engineering 91, DOI: 10.1007/978-94-007-1324-6_47,

The use of liquid core waveguide permits to maximize the partial sensitivity of the interferometer, defined as the rate of change of the effective refractive index of the guided mode as the liquids index varies. In this case, since the mode field is almost completely confined into the liquid core of the waveguide, the coupling between sample and light is very strong, leading to a partial sensitivity that can approach to one. Recently our group have proposed an optofluidic Mach–Zehnder interferometer based on liquid core ARROW waveguide [3]. However, the asymmetric geometry induces a low visibility of the interferometer with a strong degradation of the device's performances, which became even more evident by increasing the sensing length.

Here we demonstrate that with an accurate design of the device geometry, it is possible a great improvement of interferometer's visibility also for highly asymmetric Mach–Zehnder configurations, improving in this way the overall sensitivity of the device [4].

47.2 Operating Principle

The proposed interferometer has been realized with liquid ARROW waveguides. ARROW waveguides are able to confine the light into the liquid core by high reflectivity Fabry–Perot mirror composing the waveguide claddings. By choosing the appropriate cladding materials, we have designed the waveguide to perform low loss propagation at $\lambda = 635$ nm with a core refractive index of $n_c = 1.33$.

The fabricated ARROW has been realized in silicon [5]. The waveguide channels shaping the interferometer have been etched on the bottom silicon wafer by mask lithography. The high index contrast cladding layers thicknesses have been chosen in order to minimize the propagation loss [5]. The first cladding is composed by a titanium dioxide layer $(n_1 = 2.49)$ with a thickness of $d_1 = 75.4$ nm deposited by atomic layer deposition. The second cladding is silicon dioxide layer $(n_2 = 1.46)$ and it has been deposited by LPCVD $(d_2 = 262\,\text{nm})$. The liquid into the core was infiltrated by capillary effect (methanol, $n_c = 1.32$).

The visibility of a MZI is strictly related to the polarization and the intensity balancing between the beams emerging from the two arms of the interferometer. The filtering properties of the ARROW in terms of polarization permit to get the interfering beams with the same polarization (TE) independently to input polarization [3]. Hence, to achieve a good visibility factor we modified the shape of the arms in order to balance, as well as possible, the intensity of the interfering beams. A schematic layout of the proposed device is showed in Fig. 47.1.

The device is composed by an input straight waveguide, followed by a taper waveguide ending into a T-branch that splits equally the input power into the two arms of the interferometer. The final width of the taper has been set to 20 μm in order to get the fundamental guided mode substantially widened for matching the width of the input port of the T-branch. Moreover, by numerical simulations, we have found that a length of the taper of 500 μm permits us to realize a slowly

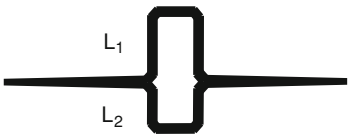

Fig. 47.1 Schematic layout of the MZI

varying tapered waveguide so as to avoid the propagation of higher-order modes and to maximize the power coupling of the fundamental input mode with the fundamental mode of the output waveguide. Each 90°-bent waveguides composing the two arms of the MZI consists of cut-type bends. After propagating in the two arms (L_1, L_2), the emerging beams accumulate a phase difference given by

$$\Delta\varphi = \frac{2\pi}{\lambda} n_{eff}(L_1 - L_2) \tag{47.1}$$

where n_{eff} is the effective index of the fundamental propagating mode and λ is the working wavelength. Since liquid waveguides compose the device, a length difference $\Delta L = L_1 - L_2$ between the two arms is required to achieve a phase delay between beams at the output. The transmitted intensity from the device is given by

$$I \propto 1 + V\cos(\Delta\varphi), \tag{47.2}$$

where the phase difference $\Delta\varphi$ is given by Eq. 47.1, $V = (\mathrm{I_{max}} - \mathrm{I_{min}})/(\mathrm{I_{max}} + \mathrm{I_{min}})$ is the visibility of the interferometer. In the proposed layout, the intensity unbalance between interfering beams is only due to the different length of the straight waveguides of the arms that causes different propagation loss.

47.3 Experimental Results

We have fabricated and optically characterized two unbalanced MZ configurations ($\mathrm{MZ_1}$ and $\mathrm{MZ_2}$) with different sensing length ΔL by varying the separation between arms. In the $\mathrm{MZ_1}$ configuration the sensing length is $\Delta L_1 = 100\,\mu\mathrm{m}$, while for $\mathrm{MZ_2}$ it is $\Delta L_2 = 200\,\mu\mathrm{m}$. The total length of the devices is 2.5 mm and the required volume is about160 pl.

In Fig. 47.2 is shown a scanning electron microscope image of the MZI.

The free-spectral range (FSR) of the interferometer, defined as the spectral distance between two adjacent maxima (minima) in the interference pattern, have been theoretically estimated, resulting in $\mathrm{FSR_1} = 3$ nm and $\mathrm{FSR_2} = 1.52$ nm for $\mathrm{MZ_1}$ and $\mathrm{MZ_2}$, respectively. In Fig. 47.3 the normalized transmitted spectrum from $\mathrm{MZ_1}$ (a) and $\mathrm{MZ_2}$ (b) are shown. From the measured spectra we have evaluated a FSR at around $\lambda = 640$ nm of $\mathrm{FSR_1} = 2.80$ nm and of $\mathrm{FSR_2} = 1.48$ nm; in good agreement with the theoretical ones.

The visibility of the fringes measured from the transmitted interferometric pattern is $V_1 = 0.990$ for $\mathrm{MZ_1}$ and $V_2 = 0.977$ for $\mathrm{MZ_2}$. By taken into account the attenuation losses of the fabricated liquid ARROWs [5], a visibility of about

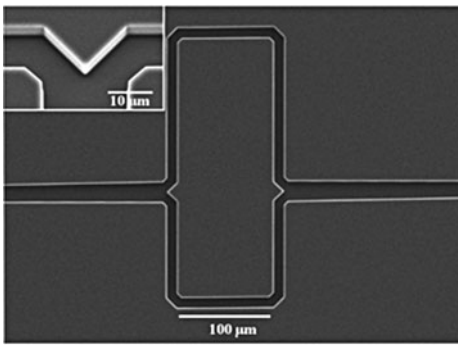

Fig. 47.2 SEM picture of the fabricated device. Inset, detail of the T-branch

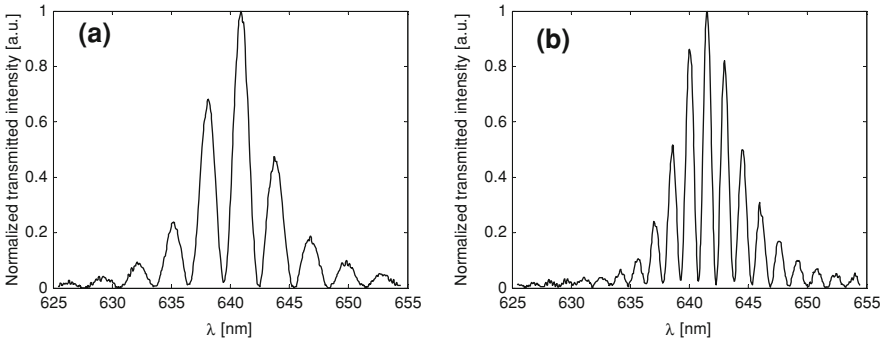

Fig. 47.3 Measured transmitted spectra from MZ_1 (**a**) and MZ_2 (**b**), FSR1 $\Delta\lambda \sim 3$ nm, FSR_2 $\Delta\lambda \sim 1.52$ nm

99.9% is theoretically calculated for both MZ_1 and MZ_2. These values agree well with the measured ones. This MZ interferometer can be applied as high sensitivity optical sensor. If the liquid core refractive index changes, a variation of the optical output power can be detected at fixed wavelength; the estimated sensitivity is 10^{-6} RIU, around $\lambda = 640$ nm and at $n_c = 1.33$ for MZ_2.

Acknowledgments The authors thank the IC Process Group of DIMES for help in device fabrication.

References

1. Densmore A, Xu DX, Janz S, Waldron P, Mischki T, Lopinski G, Delâge A, Lapointe J, Cheben P, Lamontagne B, Schmid JH (2008) Spiral-path high-sensitivity silicon photonic wire molecular sensor with temperature-independent response. Opt Lett 33:596–598
2. Dumais P, Callender CL, Noad JP, Ledderhof CJ (2008) Integrated optical sensor using a liquid-core waveguide in a Mach–Zehnder interferometer. Opt Express 16:18164–18172
3. Bernini R, Testa G, Zeni L, Sarro PM (2008) Integrated optofluidic Mach–Zehnder interferometer based on liquid core waveguides. Appl Phys Lett 93:011106–011109

4. Testa G, Huang Y, Zeni L, Sarro PM, Bernini R (2010) High-visibility optofluidic Mach–Zehnder interferometer. Opt Lett 35:1584–1586
5. Testa G, Huang Y, Zeni L, Sarro PM, Bernini R (2010) Liquid core ARROW waveguides by atomic layer deposition. IEEE Photon Technol Lett 22:616–618

Chapter 48
One-Dimensional Polyaniline Nanotubes for Enhanced Chemical and Biochemical Sensing

Francesca Berti, Giovanna Marrazza, Marco Mascini, Silvia Todros, Camilla Baratto, Matteo Ferroni, Guido Faglia, Dhana Lakshmi, Iva Chianella, Michael J. Whitcombe, Sergey Piletsky and Anthony P. F. Turner

Abstract In this work we explored a simple, cheap and fast route to grow polyaniline (PANI) nanotubes arranged in an ordered structure directly on an electrode surface by electrochemical polymerisation. The deposited nanostructures were electrochemically and morphologically characterised and then used as a functional substrate for biochemical sensing by combining the intrinsic advantages of nanostructures as optimal transducers and the well known benefits of molecularly imprinted polymers (MIPs) as receptors. The hybrid nanostructured-MIP sensor was applied to the molecular recognition of catechol. Moreover, a gas sensing application was also investigated by exploiting resistance variation of the polymer in presence of different gases (CO, NO_2, NH_3 and ethanol).

48.1 Introduction

Among nanomaterials, conductive polymers nanostructures offer ease of preparation by chemical or electrochemical methods, sensitivity towards a wide range of analytes, great signal amplification due to their electrical conductivity and fast electron transfer rate [1].

F. Berti (✉) · G. Marrazza · M. Mascini
Department of Chemistry, University of Florence, Via della Lastruccia 3, 50019 Sesto Fiorentino, Italy
e-mail: francesca.berti@unifi.it

S. Todros · C. Baratto · M. Ferroni · G. Faglia
Department of Chemistry and Physics, CNR—IDASC SENSOR Laboratory, University of Brescia, Via Valotti 9, 25133 Brescia, Italy

D. Lakshmi · I. Chianella · M. J. Whitcombe · S. Piletsky · A. P. F. Turner
Cranfield Health, Cranfield University, Cranfield, Bedfordshire, MK43 0AL, UK

G. Neri et al. (eds.), *Sensors and Microsystems*,
Lecture Notes in Electrical Engineering 91, DOI: 10.1007/978-94-007-1324-6_48,

In this work, we grew polyaniline (PANI) nanostructures directly in an ordered arrangement on an electrode surface by electrochemical polymerisation, using alumina nanoporous membranes as template. Molecularly imprinted polymers (MIPs) were then grafted on PANI nanowires, developing a nanostructured hybrid device for biosensing of catechol. MIPs are synthetic polymers with artificial recognition cavities [2].

A novel hybrid material, N-phenylethylene diamine (NPEDMA) [3] was used as monomer, combining two orthogonal polymerisable functionalities, an aniline group and a methacrylamide. In this way, the polymerisation of NPEDMA resulted in a conductive system of nanowires which allowed direct electrical connection between the electrode and the MIP. The MIP, a Tyrosinase-mimicking polymer imprinted with catechol [4], was photochemically grafted over the polyaniline nanotube via iniferter activation of the methacrylamide groups. Thus, hybrid catalytic material electrodes were prepared and the ability to detect catechol was evaluated.

Moreover, these structures were connected directly to two electrical contacts for applications in chemical gas sensing by exploiting the variation in resistance of the polymer in the presence of different gases (i.e., CO, NO_2, NH_3 and ethanol), responsible of changing the doping level of the polymer [5].

48.2 Experimental

48.2.1 Template Synthesis of PANI Nanostructures

The aniline monomer (NPEDMA) was electropolymerised by cycling an Au sputtered membrane (Whatman Anopore, $Ø = 0.02$ μm) between −0.4 and +1.0 V (vs. Ag/AgCl, scan rate 50 mV s^{-1}, 10 cycles) in a solution of NPEDMA (2.4 mmol L^{-1} in methanol) in 50 mmol L^{-1} $HClO_4$.

All electrochemical experiments were performed with an AUTOLAB PGSTAT 10 digital potentiostat/galvanostat with a GPES 4.8 software package (Eco Chemie). All the potentials were referred to the Ag/AgCl reference electrode. All the experiments were carried out at room temperature (25°C).

48.2.2 Catechol Detection

A layer of MIP was photochemically grafted over the polyaniline nanowires, following the procedure developed by Lakshmi et al. [6].

Cathecol was detected by cyclic voltammetry. Firstly 1 mL of $CuCl_2$ 5 mmol L^{-1} was added on the sensor for 5 min. After washing with PBS, fresh solutions of catechol (in PBS, pH 7.4), were added to the electrochemical cell containing the

Cu-loaded hybrid electrode. The CV was recorded applying the following parameters: start potential −0.5 V, first vertex potential 0.9 V, second vertex potential 0.5 V, step potential 0.01 V, scan rate 0.05 V s^{-1}.

48.2.3 Gas Sensing

Gas sensing measurements have been carried out in a temperature-stabilised sealed chamber at 20°C in constant humidity conditions (relative humidity RH = 50% at 20°C). Sensor signal has been measured by volt-amperometric method. A constant bias of 1 V has been applied to the sensing layer while measuring through the current by means of a picoammeter.

Each measure consists in a time interval of gas exposure of 60 min followed by a recovery interval of 90 min, to allow sensors recovery of their baseline value.

48.3 Results and Discussion

48.3.1 PANI Nanostructures for Biochemical Sensing

To our knowledge, this is the first MIP-sensor realised using a nanostructured conductive polymer-based platform for electrochemical transduction and could represent a novel strategy for overcoming a recurrent problem of MIP based electrochemical sensors: the lack of a direct path for conduction from the active sites to the electrode. The MIP we employed was a well characterised Tyrosinase-mimicking polymer, imprinted with catechol [4]. The electrochemical behaviour of the nanostructured sensor in the presence of catechol was investigated by comparing CV scans before and after MIP grafting.

Figure 48.1a shows CV scans of a 100 μmol L^{-1} solution of catechol in PBS buffer recorded using an Au-sputtered alumina membrane before electropolymerisation (red line), the same membrane after PANI nanostructures were grown (green line), and the MIP-grafted sensor (black line). Oxidation and reduction peaks are visible at 0.1 and −0.1 V, respectively, only with the MIP-grafted sensor, thus demonstrating that recognition and catalytic oxidation of catechol occur only in the presence of MIP and NPEDMA polymeric nanowires, which facilitate electron exchange between the biorecognition site and the electrode. Moreover, the response of the sensor when varying the concentration of catechol was tested. Voltammograms reported in Fig. 48.1b shows that redox peaks intesities grow when increasing the concentration, thus demonstrating the reliability of the sensor for catechol monitoring.

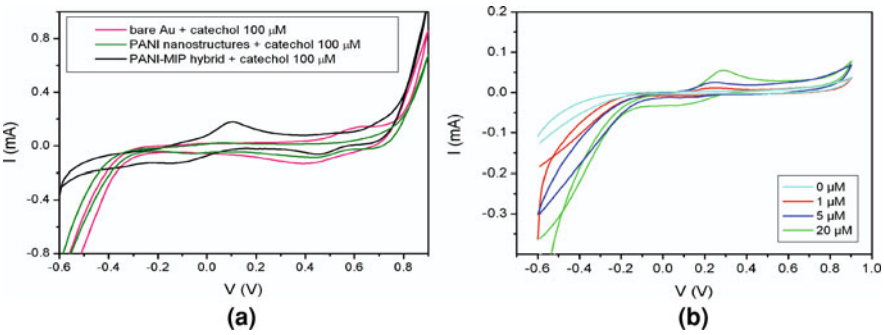

Fig. 48.1 CV signals of catechol, obtained using different sensors (**a**), and testing different concentrations with a MIP-grafted sensor (**b**)

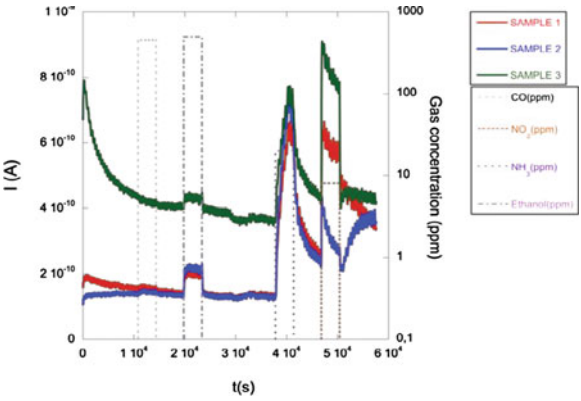

Fig. 48.2 Current variation of PANI nanotubes exposed to CO, NO_2, NH_3 and ethanol

48.3.2 PANI Nanotubes for Gas Sensing

PANI has been widely used for gas sensing applications, exploiting both its chemical and physical interaction with gases. Chemical reactions induce changes in the doping level of the polymer, followed by a modification of physical properties [7]. The response of three similar samples of PANI nanotubes to CO, NO_2, NH_3 and ethanol is shown in Fig. 48.2. Results evidence that the sensor is sensitive to such compounds, mainly to NO_2 and NH_3. Further studies are now in progress.

48.4 Conclusions

In this work, we designed an innovative biochemical sensor based on polyaniline (PANI) nanotubes arranged in an ordered structure directly on an electrode surface by electrochemical polymerisation. These nanotubes were grafted with MIPs and

applied to the molecular recognition of catechol. Moreover, resistance variation of the polymer in presence of different gases (CO, NO_2, NH_3 and ethanol) was exploited to develop a gas sensor.

References

1. Yoon H, Jang J (2009) Conducting-polymer nanomaterials for high-performance sensor applications: issues and challenges. Adv Funct Mater 19:1567–1576
2. Mosbach K (1994) Molecular Imprinting. Trends Biochem Sci 19:9–14
3. Lakshmi D, Whitcombe MJ, Davis F, Chianella I, Piletska EV, Guerreiro A, Subrahmanyam S, Brito PS, Fowler SA, Piletsky SA (2009) Chimeric polymers formed from a monomer capable of free radical, oxidative and electrochemical polymerisation. Chem Commun 2759–2761
4. Piletsky SA, Nicholls IA, Rozhko MI, Sergeyeva TA, Piletska EV, El'Skaya AV, Karube IO (2005) Molecularly imprinted polymers–tyrosinase mimics. Ukr Biokhim Zh 77:63–67
5. Virji S, Huang J, Kaner RB, Weiller BH (2004) Polyaniline nanofiber gas sensors: examination of response mechanism. Nano Lett 4:491–496
6. Lakshmi D, Bossi A, Whitcombe MJ, Davis F, Chianella I, Fowler SA, Subrahmanyam S, Piletska EV, Piletsky SA (2009) Electrochemical sensor for catechol and dopamine based on a catalytic molecularly imprinted polymer-conducting polymer hybrid recognition element. Anal Chem 81:9576–9584
7. Lange U, Roznyatovskaya NV, Mirsky VM (2008) Conducting polymers in chemical sensors and arrays. Anal Chim Acta 614:1

Chapter 49
Odorant Binding Proteins as Sensing Layers for Novel Gas Biosensors: An Impedance Spectroscopy Characterization

S. Capone, C. De Pascali, L. Francioso, P. Siciliano, K. C. Persaud and A. M. Pisanelli

Abstract In this work, an ab-initio study of the electrical response to odorants of a self-assembled monolayer of a pig OBP immobilized onto a miniaturized Si-substrate equipped with gold interdigitated electrodes (IDE), was started. Electrical Impedance Spectroscopy (EIS) was used as electrical characterization technique and a dedicated experimental set-up was arranged in order to carry out EIS measurements in controlled environment. The EIS data was fitted by using a fitting software based on Levenberg–Marquardt (LEVM) algorithm to determine the equivalent circuit of the system.

49.1 Introduction

In animal olfactory systems, odour sensing is fulfilled in a primary step by Odorant Binding Proteins (OBPs) and Olfactory Receptors Proteins (ORPs). OBPs are abundant small soluble extracellular proteins secreted in the nasal mucus of many animal species and in the sensillar lymph of chemosensory sensilla of insects. Vertebrate OBPs belong to the lipocalin superfamily. The members of this superfamily have poor sequence similarity but all of them show a conserved folding pattern, that is an 8-stranded β-barrel flanked by an α-helix at the C-terminal end of the protein chain. The β-barrel defines a central apolar cavity, called calyx, whose

S. Capone (✉) · C. De pascali · L. Francioso · P. Siciliano
Institute for Microelectronics and Microsystems, CNR-IMM,
via Monteroni, 7310 Lecce, Italy
e-mail: simona.capone@le.imm.cnr.it

K. C. Persaud · A. M. Pisanelli
School of Chemical Engineering and Analytical Science (SCEAS),
University of Manchester, Manchester, UK

G. Neri et al. (eds.), *Sensors and Microsystems*,
Lecture Notes in Electrical Engineering 91, DOI: 10.1007/978-94-007-1324-6_49,

role is to bind and transport hydrophobic molecules [1]. The exact role of OBPs in vertebrates is not yet well defined, but in insects the role is very clear. The OBPs bind molecules that are transported to the receptors. Here, a OBP releases in a reversible way the bound odorant molecule to the Olfactory Receptors Proteins (ORPs), that are heptahelical membrane proteins coupling via G-proteins on to intracellular transduction cascades. Extensive research in the last two decades have extended the range of OBPs' putative function to a wider range of different functions, however, their precise physiological role still remains elusive [2, 3].

Great expectations in gas sensing rise from a novel biomimetic approach that throws out the innovative idea to use native as well as engineered non-natural biological molecules, as OBPs or ORPs, as possible active elements in gas sensors of new generation. A major driving force to study OBPs and ORPs is the idea that such biological elements are optimized for specific olfactory tasks by evolution and natural selection. The main natural feature of such proteins, that make them attractive for biomimetic sensing platforms, is that the binding of the odorant molecule may induce a small conformational change of the protein. Indeed, the β-barrel of an OBP encloses a quite stable ligand-binding site composed of both an internal cavity and an external loop scaffold. It is the diversity of cavity and scaffold that gives rise to a variety of different binding modes each capable of accomodating ligands of different size, shape and chemical character. Such binding events might, by itself, cause a change in the electrical properties of the protein. The possible connections between binding events and electrical properties changes might build the novel detection principle of biohybrid sensors of new generation. In this context, the electrical characterization of OBPs and ORPs in controlled environment is of extreme importance both from a fundamental and applied point of view.

Recent electrochemical impedance studies of specific ORPs stimulation by odorants in solution performed in conventional electrochemical cell with a three electrodes system have been reported [4–6].

In this work, for the first time, we transfer a self-assembled monolayer of a porcine Odorant Binding protein (pOBP) onto a miniaturized Si-substrate equipped with gold interdigitated electrodes (IDE) and we characterized it by Electrical Impedance Spectroscopy (EIS) in air both in absence and in presence of odorant molecules (as methanol), in order to measure an expected odorant-dependant signal change. EIS is a powerful method for the analysis of the complex electrical impedance of a system, and it is particularly suited to the detection of binding events on the transducer surface [7].

49.2 Experimental and Methods

49.2.1 Biomaterials and Chemicals

Porcine odorant binding protein (pOBP) is a monomer of 157 amino acid residues, purified in abundance from pig nasal mucosa [10]. Recombinant Pig Odorant Binding Protein (modified in the 2 position with a Cysteine Residue, so that the

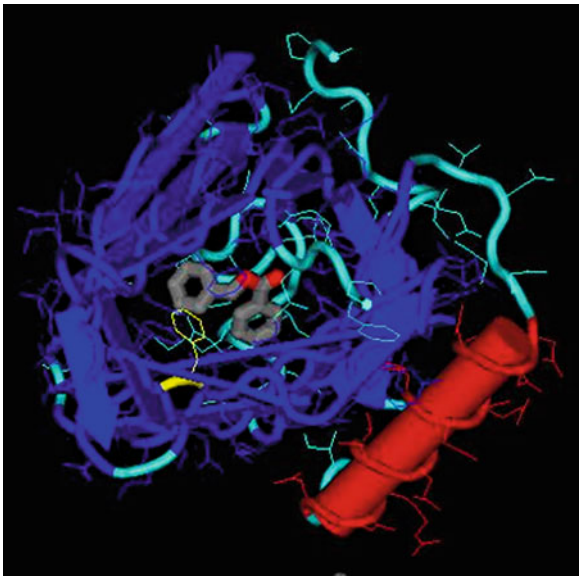

Fig. 49.1 Structure of the Porcine OBP (courtesy Dr. P. Pelosi, Un. of Pisa)

protein could be directly immobilised on a gold electrode surface, courtesy Paolo Pelosi, University of Pisa) present in pig saliva and belonging to the protein subclass of chemical communication was considered in this work. Its typical structure is shown in Fig. 49.1. The Pig OBP was suspended in a working 10 mM phosphate buffer solution pH 7.4.

49.2.2 Preparation of Au IDE Trasduction Platform and Pig OBP Immobilization

Miniaturized silicon substrates (1.5 × 1.5 mm sized) equipped with gold interdigitated electrodes were prepared using standard photolithography technologies. Starting from a 3″ Si wafer with a 500 nm-thick SiO_2 layer, a 20 nm-thick titanium layer and a 200 nm-thick gold top layer were deposited by evaporation under vacuum. Eleven pairs of fingers spaced 10 μm were prepared in a central area of 440 × 440 μm. The single die was cut and bonded onto a standard TO-39 socket for electronic components.

A 1 μl aliquot of Pig OBP was placed on a Si substrate functionalized by Au IDEs, previously cleaned with acetone and isopropilic alcohol, washed in distilled water and dried in nitrogen. After drying the Pig OBP in air, an self-assembly of the protein formed. Due to the cysteine substitution of the Pig OBP easy immobilization onto the Au microelectrodes is achieved Fig. 49.2.

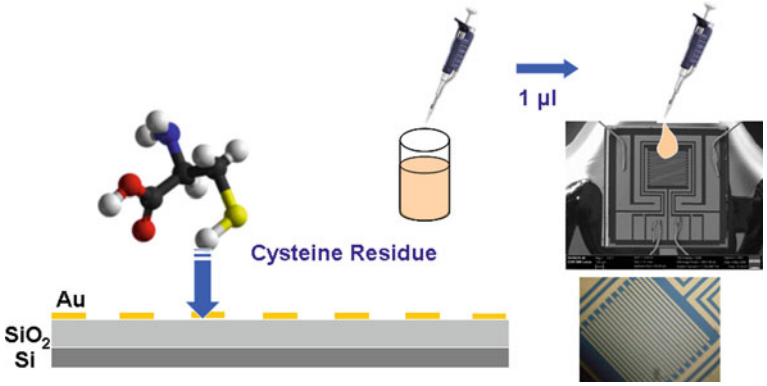

Fig. 49. 2 Deposition and immobilization of OBP onto IDE transducer

49.2.3 Electrical Impedance Spectroscopy Set-up

After immobilization of the Pig OBP layer onto Au IDE transduction microplatform, the sample bonded onto TO-39 socket was introduced into a suitable brass test chamber for Electrical Impedance Spectroscopy (EIS) measurements. An LCR-meter (mod. HP 4284A) was used for the experiments carried out in a frequency range of 20–1 MHz with a sinusoidal voltage input at a polarization potential of 0 V with a frequency modulation of 20 mV. The sample was connected to LCR-meter in 4-terminals configuration (HiPotential-LowPotential, HiCurrent-LowCurrent) by 1 m long BNC cables. The EIS test chamber was connected to a gas-mixing bench in order to evaluate the AC characterization of the Pig OBP in air in controlled conditions (gas flow, relative humidity, odorant concentration in air). The system allows to get different concentrations of gas and/or volatiles by suitable dilution of the related analyte flow in reference air flow. A scheme of the Electrical Impedance Spectroscopy set-up for Pig OBP electrical characterization is reported in Fig. 49.3.

49.3 Results-EIS Analysis

Impedance measurements on biological system are of fundamental importance to understand charge transport as well as charge exchange, surface phenomena and binding events, and diffusion processes. Impedance measurements are made by applying a small alternating voltage V of known angular frequency ω (=2πf, f frequency) and small amplitude V_0 to a system and measuring the amplitude I_0 and phase shift ϕ of the concomitant electrical current that develops across it. Impedance is usually represented by a phasor, i.e. a vector Z of magnitude $Z_0 = |Z|$

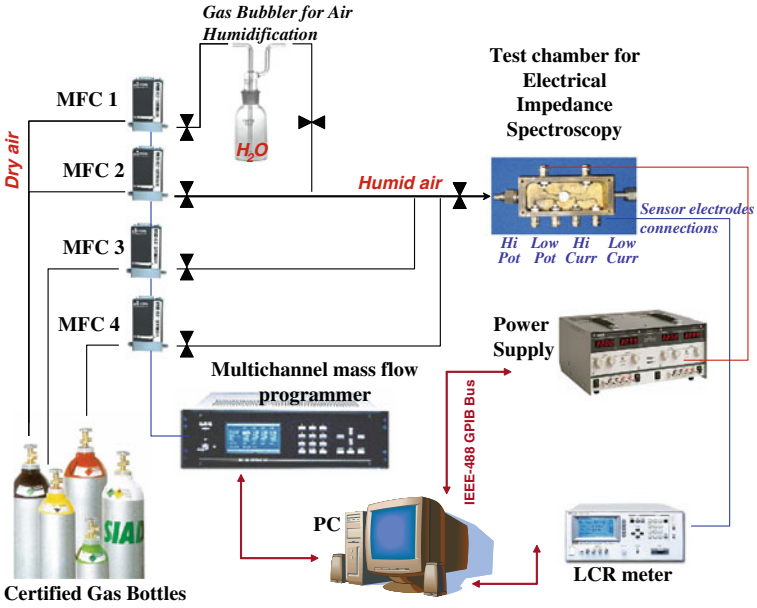

Fig. 49.3 Electrical Impedance Spectroscopy set-up for Pig OBP electrical characterization

and phase ϕ = arg|Z|. In cartesian coordinates, impedance becomes a complex number:

$$\begin{aligned} Z(\omega) &= Z_0 \cdot \exp(j\omega) \\ &= Z_0 \cdot (\cos\phi + j\sin\phi) \\ &= R + jX \end{aligned} \tag{49.1}$$

The Real (ReZ) and Imaginary (ImZ) parts of Z describe the resistance (R) and reactance (X) respectively and can be represented by an appropriate electrical circuit in series. Therefore, the results of an impedance measurement can be illustrated in two different ways: using a Bode plot which plots log|Z| and Φ as a function of log(f), or using a Nyquist plot which plots (-ImZ) versus ReZ.

The analysis of a impedance spectra is often complicated and ardous, since it consists in building an equivalent circuit model of the measured system and in determining the parameter values of all the elements of the equivalent circuit, by non-linear fitting of EIS data.

In this work different samples of the considered Pig OBP were immobilized onto the Au interdigitated microlectrodes and analysed by EIS. After first drying in ambient air, each Pig OBP sample was put into the test chamber under a constant flow of humid air and the impedance spectra acquired stepwise in discrete intervals in order to study the evolution of the system up to a steady state indispensable to measure the EIS spectrum.

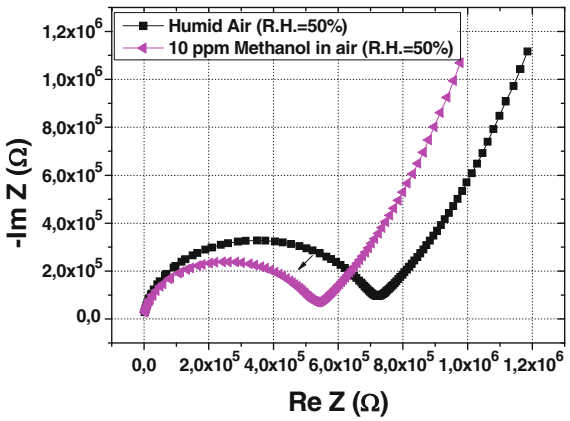

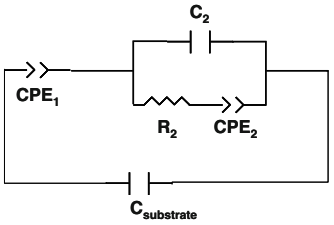

		Air RH=50%	10 ppm Methanol in air R.H.=50%
$C_{substrate}$		9.60 pF	7.36 pF
CPE_1	Y_0	$0.11 10^{-5}$ F(rad/s)$^{1-\alpha}$	$0.13 10^{-5}$ F(rad/s)$^{1-\alpha}$
	α	0.01	0.03
C_2		9.04 nF	0.64 nF
R_2		1.02 MΩ	0.10 MΩ
CPE_2	Y_0	$0.71 10^{-8}$ F(rad/s)$^{1-\alpha}$	$0.25 10^{-7}$ F(rad/s)$^{1-\alpha}$
	α	0.80	0.70

Fig. 49.4 Nyquist plots for a Pig OBP under exposure in humid air at RH = 50% and under 10 ppm ethanol in humid air at RH = 50%; equivalent circuit and table with fitted circuital parameters

In the following we report the results related to a Pig OBP sample for which a steady state in humid air at RH = 50% was achieved. We exposed the sample to methanol in low concentration (10 ppm in humid air RH = 50%) by measuring the impedance curves both in reference humid air (RH = 50%) and in presence of methanol vapours (Fig. 49.4). As can be observed the impedimetric curve under exposure to methanol is smaller as compared to the impedimetric curve in humid air. This effect can be attributed to occurred binding events between the Pig OBP sample and the analytes molecules, that cause probable conformational changes and/or molecular rearrangement of the proteins. Experiments tests and data analysis are in course in order to explain such gas sensing phenomena.

The experimental impedance spectra were best fitted with the equivalent circuit shown in Fig. 49.4 by making use of a Complex NonLinear Least Squares (CNLS) method based on a Levenberg–Marquardt (LEVM) algorithm [8] In particular, a LEVM software developed by Macdonald [9] was used for fitting.

Both the structure as well as the elements of the equivalent circuit are correlated to different physichemical properties of the biological system under investigation. Once a good fit with the combination of a representative circuital model and suitable starting fitting parameter values is achieved, the next step is to explain the

obtained fit results in terms of the real components of the system and the phenomena associated with the biological element. Such studies are in progress.

49.4 Conclusions

An ab initio study of electrical impedance spectroscopy (EIS) of a Pig Odorant Binding Protein exposed to air and target odorant species was started. Only a few studies regarding EIS on Odorant Binding Proteins (OBPs) and Odorant Receptors Proteins (ORPs) are reported in the literature and these study the protein only in solution. This study is, hence, particularly interesting since: (a) it is a fundamental study of the electrical properties of Odorant Binding Proteins outside their living ambient, useful to understand the preservation of their functionality, (b) it is an explorative study to estimate the feasibility of a novel chemosensor based on a OBP or ORP.

Moreover, a equivalent circuit model was developed and a very good fit for the impedance spectra were obtained. However, a lot of efforts have to be devoted both to the definition of a experimental measurement procedure and to understand the sensing mechanisms by which the odorant molecule interacts with the OBP layer by using the circuit model obtained by EIS characterization.

Acknowledgment We are grateful to GOSPEL (FP6-IST 507610) for financing this initial study, and to Prof. Paolo Pelosi, University of Pisa for the Pig Odorant Binding Proteins.

References

1. Flower DR, North ACT, Sansom CE (2000) The lipocalin protein family: structural and sequence overview. Biochim Biophys Acta 1482:9–24
2. Breer H (2003) Olfactory receptors: molecular basis for recognition and discrimination of odors. Anal Bioanal Chem 377:427–433
3. Pelosi P (2001) The role of perireceptor events in vertebrate olfaction. Cell Mol Life Sci 58:503–509
4. Hou Y, Jaffrezic-Renault N, Martelet C, Tlili C, Zhang A, Pernollet J-C, Briand L, Gomila G, Errachid A, Samitier J, Salvagnac L, Torbiro B, Temple-Boyer P (2005) Study of Langmuir and Langmuir-Blodgett films of odorant-binding protein/amphiphile for odorant biosensors. Langmuir 21(5):4058–4065
5. Hou Y, Jaffrezic-Renault N, Martelet C, Zhang A, Minic-Vidic J, Gorojankina T, Persuy M-A, Pajot-Augy E, Salesse R, Akimov V, Reggiani L, Pennetta C, Alfinito E, Ruiz O, Gomila G, Samitier J, Errachid A (2007) A novel detection strategy for odorant molecules based on controlled bioengineering of rat olfactory receptor I7. Biosens Bioelectron 22:1550–1555
6. Benilova IV, Minic Vidic J, Pajot-Augy E, Soldatkin AP, Martelet C, Jaffrezic-Renault N (2008) Electrochemical study of human olfactory receptor OR 17–40 stimulation by odorants in solution. Mater Sci Eng C 28:633–639
7. Lisdat F, Schäfer D (2008) The use of electrochemical impedance spectroscopy for biosensing. Anal Bioanal Chem 391:1555–1567

8. Marquardt DW (1963) An algorithm for least-squares estimation of nonlinear parameters. SIAM J Appl Math 11:431
9. Macdonald JR (1963) CNLS (Complex nonlinear least squares): immittance, inversion, and simulation fitting programs—LEVM Manual. SIAM J Appl Math 11:431 (Version 8.08, Issue data: February, 2007D.W. Marquardt.)
10. Vincent F, Spinelli S, Ramoni R, Grolli S, Pelosi P, Cambillaud C, Tegoni M (2000) Complexes of porcine odorant binding protein with odorant molecules belonging to different chemical classes. J Mol Biol 300:127–139

Chapter 50
Fluorescence Detection of Hydrocarbons in Harbour Water

A. Catini, F. Dini, D. Polese, S. Petrocco, M. De Luca, C. Di Natale, A. D'amico and R. Paolesse

Abstract In harbor water, the hydrocarbons pollution identification represents an important issue. Hydrocarbon presence derives from oil spills, for instance in bilge water, or it may come from industrial discharge. A prompt identification of oil presence is crucial for living beings and for the maintenance of a healthy marine environment. Both crude oil and fuels contain different fluorophores that under ultraviolet radiation exhibit a strong fluorescence which varies in intensity and hue. Fluorescence results mainly from the emission of aromatic hydrocarbons. Indeed, fluorescence spectroscopy is a widely used technique for characterization of oil samples.

50.1 Introduction

In this work we propose a system for a direct detection of oil in harbor water with a fluorescence-based identification of aromatic hydrocarbons. It consists of an ultra violet (UV) lamp used as a light source and a computer camera that acts as

A. Catini (✉) · F. Dini · D. Polese · S. Petrocco · C. Di Natale · A. D'amico
Department of Electronic Engineering, University of Rome Tor Vergata,
Via del Politecnico 1, 00133, Rome, Italy
e-mail: CATINI@ING.UNIROMA2.IT

M. De Luca
CNR - Institute od Acoustic "O.M. Corbino", Via fosso del cavaliere, 100,
00133, Rome, Italy

R. Paolesse
Department of Chemical Science and Technology, University of Rome Tor Vergata,
Via della Ricerca Scientifica 1, 00133, Rome, Italy

G. Neri et al. (eds.), *Sensors and Microsystems*,
Lecture Notes in Electrical Engineering 91, DOI: 10.1007/978-94-007-1324-6_50,

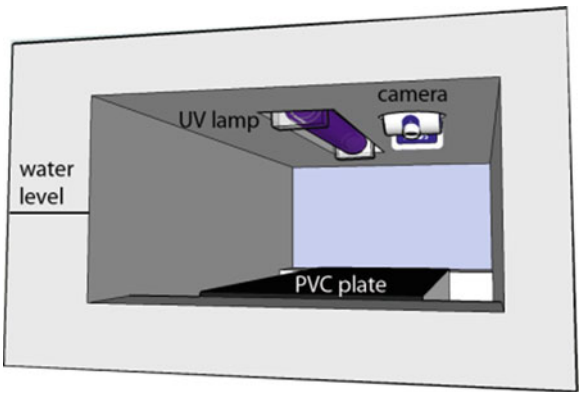

Fig. 50.1 Sketch of the experimental arrangement. A floating platform holds the UV lamp and the camera that images a black slab of PVC to provide an uniform background

detector. Computer camera was already employed in spectroscopic [1] and fluorescence [2] applications.

The optical transduction setup for oil detection is hold within a floating buoy. The camera frames a scene that is bordered on a black slab of PVC that provides a uniform background for the image (Fig. 50.1).

A PVC cage surrounds the system, protects the measurement area from interfering solids such as algae, plastic bags, or rubbish, and helps stabilizing the system against the wave motion.

The UV lamp peak occurs at 365 nm, with a spread between 300 and 400 nm. Such a range makes the light source separated from the responses of camera filters. The camera offers the chance to image and analyze a relatively large area, and to evaluate the fluorescence in individual pixels. The whole setup is connected to a computer in order to simultaneously acquire and process captured images and sensor data. To remove influences from external light conditions, a reference image is taken right before the lamp is switched on. The scene framed under UV illumination is then subtracted to the reference image so that all fluorescence contributions may be identified.

50.2 Experimental Results

The mixture of aromatic hydrocarbons contained in fuels that can be found in harbour water, such as diesel oil and gasoline, emits a luminescent radiation that is well detectable with the experimental apparatus composed of the UV lamp and the web camera. The two mixtures are found to emit in partially separated spectral regions (Fig. 50.2).

In water, droplets of oil are formed at water surface, which are detected by their fluorescence emissions. An estimation of pollution level may be given by oil extension within the image framed and by the evaluation of the thickness of the oil

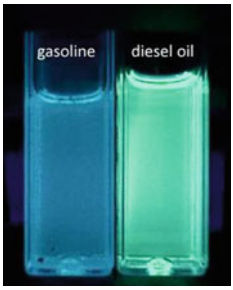

Fig. 50.2 Samples of diesel oil and gasoline as imaged by the camera under the UV illumination

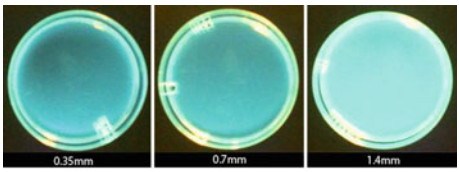

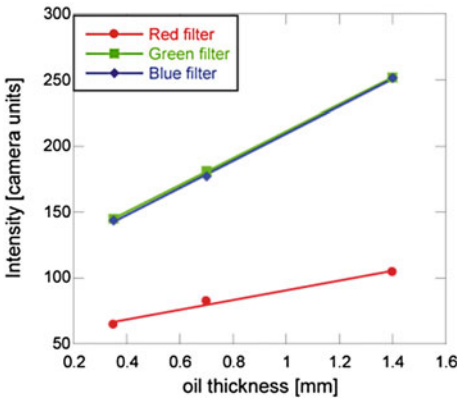

Fig. 50.3 Relationship between oil thickness and emission intensity in the three camera filters

Fig. 50.4 Floating buoy installed in Neptune (Rome) harbour

layer above the water surface. Oil thickness estimation is possible through the measure of the fluorescence intensity. A regression curve that correlates oil depth and the intensity of emission was evaluated, and a linear relationship between emission and diesel oil height is found for the three camera filters (Fig. 50.3).

One of the main feature related to the designed apparatus is the capability of keeping the sea water level inside the test chamber almost unperturbed even if the surrounding sea water presents highly disturbing wave fluctuations. The mechanical and fluidodynamic design (Fig. 50.4) allows acceptable measurements to be done even in 50 cm peak to peak waves.

50.3 Conclusions

Preliminary experiments performed at indoor laboratory level have shown the satisfactory operation of the bidimensional detector and the possibility to use this sensing platform for on-site continuous monitoring of sea water pollution in harbours. The recognition of the hydrocarbons presence will be done remotely through a wireless system in a local network configuration. Indeed, at least three of these new apparatus will be installed with the aim of controlling three different locations of the harbour and verify the reliability of the network configuration.

Acknowledgments This work has been supported by Port Authority of Nettuno (Rome) and CRESM (Centro Radiolelettrico Sperimentale Guglielmo Marconi) within the SEASPORT project.

References

1. Filippini D, Alimelli A, Di Natale C, Paolesse R, D'Amico A, Lundström I (2006) Angew Chem 118:3884–3887
2. Filippini D, Gatto E, Malik M, Di Natale C, Paolesse R, D'Amico A, Lundstrom I (2008) Polychromatic fingerprinting of excitation emission matrices. Chem Eur J 14:6057–6060

Chapter 51
A Research Study and Development of a Hydrogen Sensor for Fuel Cells

A. Bonavita, G. Micali, G. Neri, N. Donato, M. Latino and S. Licoccia

Abstract The design and development of a new sensor prototype for hydrogen concentration detection in the fuel cells stream is reported. The sensor's operation principle is based on the effects induced to high thermal conductivity of hydrogen, monitored by means of a PID (proportional-integral-derivative) control. The sensor is also implemented with a semiconducting layer which provides an additional output response. The sensor shows good linearity in the 0–100% range and it is suited to detect hydrogen in the stream of fuel cells with fast response.

51.1 Introduction

In the near future hydrogen will gain greater importance as a clean fuel in fuel cells for automotive, maritime and space system power applications. Inexpensive hydrogen sensors are then crucial for the future hydrogen economy. Hydrogen sensors may be used in a fuel cell to monitor possible hydrogen leak and hydrogen concentration in the fuel stream [1, 2]. Hydrogen concentration may be used as an indicator of the fuel cell performance and operating efficiency. For example, an excessive amount of hydrogen in the fuel stream exhausted from the fuel cell may

A. Bonavita · G. Micali · G. Neri
Departmant of Industrial Chemistry and Materials Engineering, University of Messina, Messina, Italy

N. Donato (✉)
Departmant of Matter Physics and Electronics Engineering, University of Messina, Messina, Italy
e-mail: ndonato@unime.it

M. Latino · S. Licoccia
Departmant of Chemical Science and Technologies, University of Rome Tor Vergata, Rome, Italy

G. Neri et al. (eds.), *Sensors and Microsystems*,
Lecture Notes in Electrical Engineering 91, DOI: 10.1007/978-94-007-1324-6_51,

indicate poor operating efficiency. Hydrogen which is not consumed in the stack may be recycled to the main hydrogen stream. However, an undesirable amount of nitrogen is often present in the unused hydrogen exiting the fuel cell. Before reintroducing the unused hydrogen into the main hydrogen supply, a portion of the hydrogen/nitrogen mixture is exhausted into the atmosphere. Instead of simply periodically purging the anode exhaust stream, the anode exhaust could be purged as a result of a measured hydrogen concentration falling below a threshold value.

The main requirements for a hydrogen concentration sensor for fuel cells are: hydrogen detection in an inert atmosphere (nitrogen) up to 100% H_2 without saturation effects, fast response, and insensitivity to humidity and CO concentrations. To accomplish these stringent requirements, the design and development of a sensor prototype for hydrogen detection was undertaken. The operation principle of the sensor was based on the peculiar thermal properties of hydrogen that allow to distinguish it from other gases present in the environment, due to its highest cooling effect. In an up-dated configuration, the sensor was implemented with an additional semiconducting layer with the aim of providing an additional output response.

51.2 Experimental

The prototype of hydrogen gas sensor under study consists of a planar Pt heater deposited by high vacuum sputtering on a ceramic substrate. Pt contacts are 250 μm wide and the gap between the contacts is 150 μm wide. Thickness of the Pt contacts is about 5 μm and the measured resistance at 25°C is around 3 Ω. The planar Pt heater is able to maintain constant the temperature within 0.1°C at operating temperature in the range 50–500°C. On the backside of the sensor, a TiO_2-based semiconducting layer was deposited on Pt interdigitated contacts.

The devices are powered by a DC power supply (Agilent E3632A) and controlled by a software interface ad hoc realized on IEEE 488 protocol.

51.3 Results and Discussion

In a previous report, we discussed on the possibility of using transient thermal effects during gas detection for monitoring hydrogen in H_2/N_2 mixtures [3]. This was accomplished by developing a simple device, consisting in a platinum heater on a ceramic substrate, under a home-made PID control.

The sensor detection mechanism relies on the transient variation of temperature under different hydrogen concentrations. Indeed, as hydrogen posses the highest thermal conductivity of all known gases, 0.172 W/m K at 20°C, one order of magnitude higher than value for nitrogen (0.0234 W/m K) at the same temperature, a gas stream containing H_2 has a higher capability to cool the sensor surface

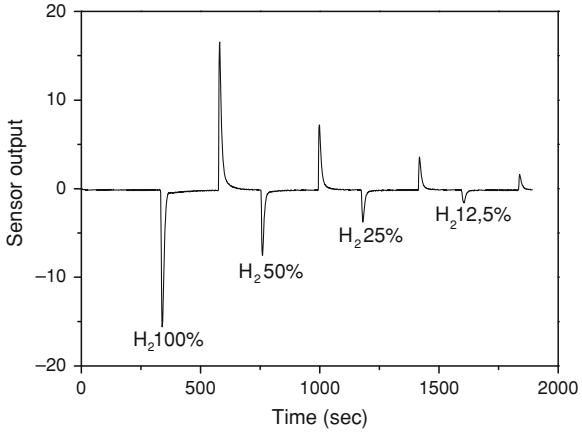

Fig. 51.1 Sensor output to different concentrations of H_2 in N_2. Working temperature = 150°C

than pure N_2. The transient thermal effect associated can be easily monitored through the PID control, by means of the variation of power (sensor response) supplied to the heater (Fig. 51.1).

As the H_2 concentration in the mixture varies there is a variation in temperature which results in a change of the Pt heater resistance. The developed sensor was sensitive to H_2 gas over a wide range of concentration: the lowest concentration tested being $\sim$2% H_2 in nitrogen. No saturation of the signal was observed up to 100% H_2 flow. In the continuous operation mode with varying H_2 concentration, a clear and sharp response was recorded with no memory effects during ramping up and down cycles of H_2 concentration in nitrogen mixture, and with no humidity interference [3].

The above sensor was further implemented with a semiconducting layer with the aim to provide an additional response channel and allow to investigate the hydrogen sensing mechanism. A thick TiO_2-based semiconducting film was then deposited on the interdigitated platinum contact on the backside of the ceramic substrate, so that the variation of the semiconducting film resistance could be monitored in real time. Figure 51.2a reports the resistance of the semiconducting film in air in the range of temperature investigated.

Figure 51.2b shows the simultaneous measurements of the TiO_2-based film resistance and power supplied to the heater of the same device, during successive H_2 pulses of different concentration in nitrogen. The resistance of the semiconducting film increases as a result of the presence of hydrogen in the mixture, while the power supplied to the heater decreases when the sensor is exposed to H_2, and increases in pure N_2.

In inert atmosphere, the interaction between the TiO_2 sensing layer and hydrogen occurs via chemisorption of the dissociated hydrogen on the metal oxide surface. As TiO_2 is a n-type semiconducting metal oxide, a decrease of resistance should be observed [4]. The increase of resistance after hydrogen addition, along with the sharp response, suggests instead that the resistance variations originate from the cooling effect of hydrogen in agreement with a report by Fawcett et al. on

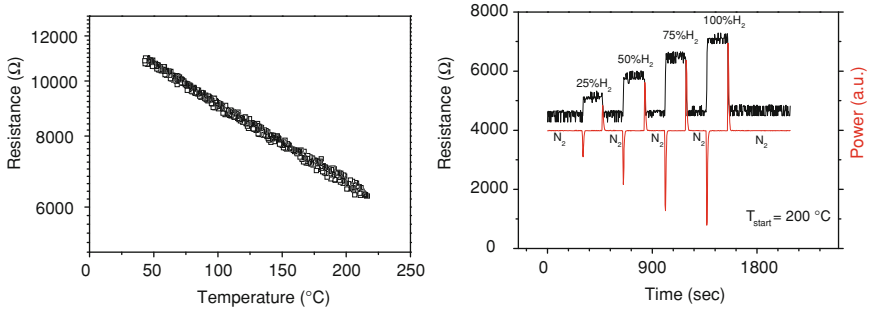

Fig. 51.2 **a** Resistance versus temperature in air of the TiO_2-based semiconducting film; **b** Simultaneous measurement of the TiO_2-based film resistance and power supplied to the heater during successive H_2 pulses

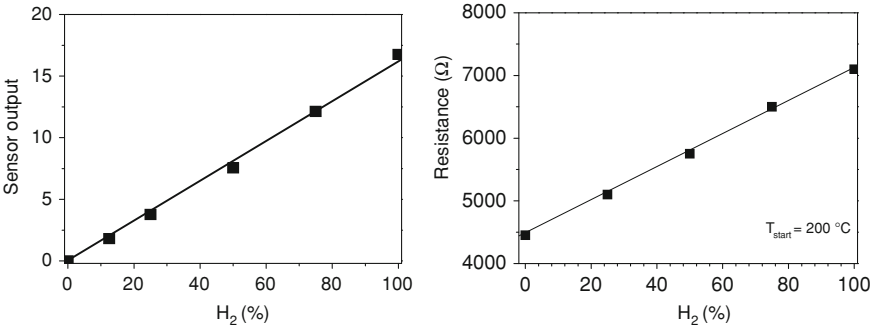

Fig. 51.3 **a** Sensor output versus different concentrations of hydrogen in N_2. Working temperature = 150°C; **b** Resistance of the TiO_2-based semiconducting film versus the hydrogen concentration in N_2

a SiC-based resistive sensor. On the basis of the increase of resistance observed during hydrogen pulses and the associated temperature variations, they provide evidence that the hydrogen sensing mechanism on the SiC sensor is most likely driven by thermal effects [5].

It can be noted that both the output response and resistance of the TiO_2-based semiconducting film (Fig. 51.3a–b), show a linear relationships with H_2 concentration in the H_2/N_2 mixture.

51.4 Conclusion

The design and development of a new sensor prototype for hydrogen detection has been reported. The sensor developed shows good linearity in the 0–100% H_2 concentration range. The sensor capability to detect high hydrogen concentration

with sufficient sensitivity and fast response, makes this device well suited for applications in fuel cells.

References

1. Arndt M, Simon I (2001) Hydrogen sensor for application in fuel cell vehicles. In: Proceeding of Sensor 2001, Nürnberg, 8–10 May 2001, pp 541–545
2. Aroutiounian V (2007) Metal oxide hydrogen, oxygen and carbon monoxide sensors for hydrogen setups and cells. Int J Hydrogen Energy 32:1145–1158
3. Neri G, Bonavita A, Micali G, Donato N, Development of a self-calibrating hydrogen leak sensor, 7th IEEE Conference on Sensors, Lecce, June 2008
4. Varghese OK, Gong D, Paulose M, Ong KG, Grimes CA (2003) Hydrogen sensing using titania nanotubes. Sensor Actuat B 93:338–344
5. Fawcett TJ, Wolana JT, Spetz AL, Reyes M, Saddow SE (2006) Thermal detection mechanism of SiC based hydrogen resistive gas sensors. Appl Phys Lett 89:182102

Chapter 52
A New Potentiometric Urea Biosensor Based on Urease Immobilized in Electrosyntesised Poly (*O*-Phenylenediamine)

Daniela Chirizzi and Cosimino Malitesta

Abstract A potentiometric urea biosensor based on urease (Ur) electrochemical immobilisation by poly(*o*-phenylenediamine) (PPD) is proposed. Polymer films have been grown by cyclic voltammetry on a glassy carbon (GC) electrode, using an unconventional "upside-down" (UD) geometry. GC/Ur-PPD electrodes exhibit a rapid (5–10 s) and sensitive response to urea concentration and lifetime of at least 5 weeks. Work is in progress to optimise the sensor and study its behaviour in the presence of possible interferences.

52.1 Introduction

The urea determination is of great interest in different fields as pharmaceutical industry, food industry, environmental protection, production of fertilizers, but the most important applications are in biomedical and clinic analysis. Urea is a waste product resulting from the proteins division and main nitrogen component of urine. It is produced in the liver and is eliminated by kidneys. Normal values range is from 10 to 30 g in urine collected in a 24 h sampling. Out range values suggest different conditions such as: renal insufficiency, diet rich in protein, poisoning phosphorus, hyperpyrexia, hyperthyroidism, leukemia, burns, diarrheal diseases, diabetes mellitus, fasting, dehydration, liver disease, pregnancy, chronic renal

D. Chirizzi (✉) · C. Malitesta
Dipartimento di Scienza dei Materiali, Università del Salento, Laboratorio di Chimica Analitica, via Monteroni, 73100 Lecce, Italy
e-mail: daniela.chirizzi@unisalento.it

G. Neri et al. (eds.), *Sensors and Microsystems*,
Lecture Notes in Electrical Engineering 91, DOI: 10.1007/978-94-007-1324-6_52,

failure, hypothyroidism and vomiting. Therefore, it is common to detect urea in serum or urine samples [1].

Urease has been utilized as the biological sensing material for the fabrication of many types of urea sensors, like thermal [2], amperometric [3], conductometric [4], piezoelectric [5] and potentiometric [6], the last one being the most extensively used. Enzymatic potentiometric determination of urea has been preferred due to easy sensor fabrication, effectiveness and simplicity [7]. In urea biosensors, the immobilized urease enzyme (Ur) hydrolyses urea and releases ammonia and carbon dioxide which produces a pH change.

Several potentiometric urea biosensors based on detecting pH change, ammonia gas, or ammonium ions generated by enzymatic reactions have been proposed. The enzyme can be immobilized at electrode surface in enzymatic biosensor by several techniques. Electrochemical immobilisation has been proposed since several years as an effective way because it produces on electrodes biosensors in single step on electrode of any shape or size. In particular poly(*o*-phenylenediamine) (PPD) results a very efficient material because conjugates enzyme entrapping capacity to interfering rejection [8].

In this work we propose to apply PPD as an entrapping membrane and a pH-sensitive film. In additional an unconventional "upside-down" cell configuration is employed to increase enzyme loading.

52.2 Experimental

Urease (from *Canavalia ensiformis—Jack bean*; 97,000 units/g) and urea, were obtained from Sigma. KCl (Sigma), *o*-Phenylenediammine (1,2-diaminobenzene) (*o*–PD) ca. 99% was obtained from Aldrich. Ultrapure water (Millipore Milli-Q, 18.2 $M\Omega cm^{-1}$) was used. stock urea solutions ware freshly prepared. Urea standards were prepared by serial dilution of the stock solution. All electrochemical experiments were carried out by using a CH-instruments Model 620A electrochemical analyzer controlled by computer. Cyclic voltammetry was performed using an unconventional "upside-down" (UD) geometry for the three-electrode cell with a GC disk (surface area, 0.1256 cm^2) as working electrode, and two Pt wires as counter and quasi reference respectively. Potentiometric experiments were carried out using GC/Ur-PPD electrode (or GC/PPD one) as working electrode and a saturated calomel electrode (SCE) as reference in stirred potassium chloride solution 0.1 M. All the measurements were taken at 30°C. pH-meter (HI 223 Hanna instrument) was used for pH measurement. GC/PPD-Urease electrode was electrochemically prepared with 100 unit of Urease (Ur) in a fresh solution containing 5 mmol/L of *o*-phenylenediamine (OPD) by cyclic voltammetry in the range −0.1 to 1.0 V (scan rate 0.1 V/s, 15 cycles) versus Pt (QRE) on a glassy carbon (GC) electrode, using an unconventional "upside-down" (UD) geometry for the three-electrode cell. The enzyme electrode was washed after preparation and stored in KCl 0.1 M at +4°C when not in use.

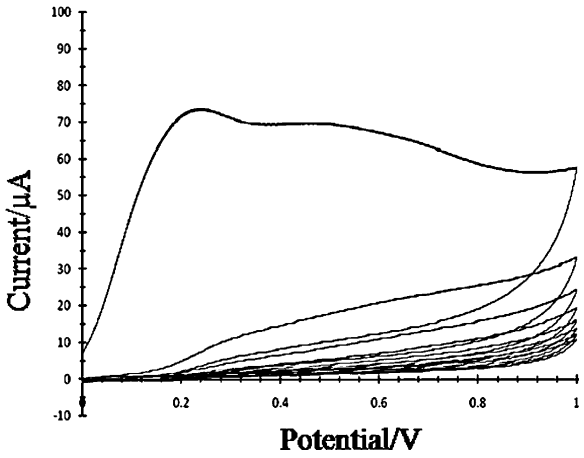

Fig. 52.1 Electrochemical preparation of urease biosensor

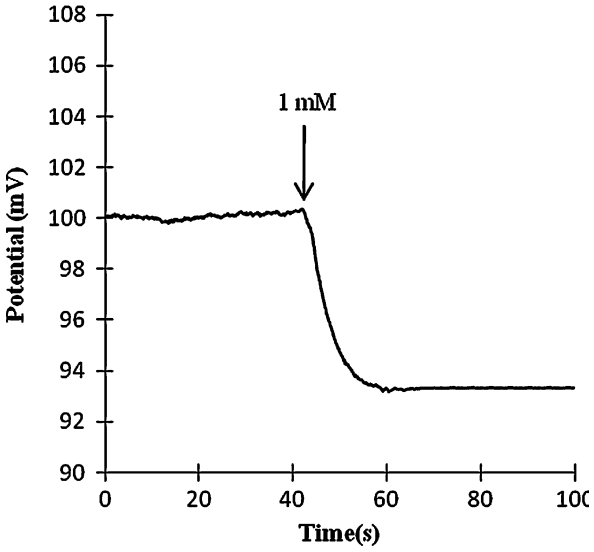

Fig. 52.2 Potentiometric responses of a GC/PPD-urease to urea 1 mM in KCl 0.1 M under stirring

52.3 Results and Discussion

CV recorded during sensor preparation is showed in Fig. 52.1. Voltammetric curve are in agreement with PPD growth reported in literature [8].

Figure 52.2 shows a typical potentiometric response of a GC/Ur-PPD electrode to urea 1 mM in KCl 0.1 M under stirring. It can be seen that sensor exhibits a rapid and sensitive response. Figure 52.3 shows the variation of response following increase in urea concentration of GC/Ur-PPD and GC/PPD. A clear difference between them is evident. The measurements was performed in triplicate on three different electrodes.

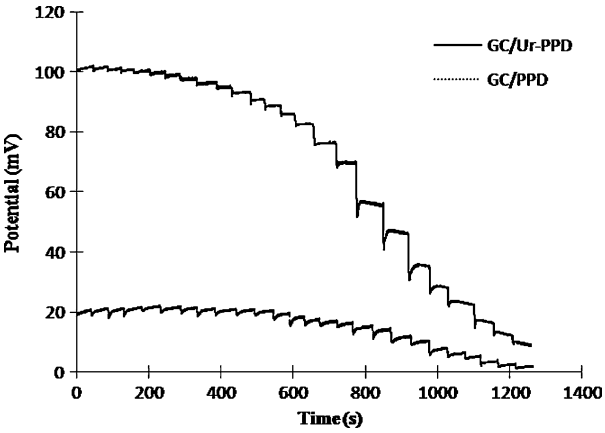

Fig. 52.3 Potentiometric response of urease biosensor on GC/Ur-PPD (*solid curve*) and on GC/PPD (*dot curve*) to successive injections of urea in KCl 0.1 M for response to urea

52.4 Conclusions

A novel urease biosensor was successfully prepared by enzyme entrapping urease in PPD electrosynthesised. The resulting potentiometric sensor for urea showed short response times (5–10 s), response over 0.1–100 mM concentration range and a lifetime of at least 5 weeks.

Work is in progress to optimise the sensor and study its behaviour in the presence of possible interferences.

References

1. Taylor EH (1989) In: Winefordner JD (ed) Chemical Analysis, vol 106. John Wiley & Sons, New York
2. Xie B, Danielsson B (1996) An integrated thermal biosensor array for multianalyte determination demonstrated with glucose, urea and penicillin. Anal Lett 29:1921–1932
3. Rajesh, Bisht V, Takashima W, Kaneto K (2005) An amperometric urea biosensor based on covalent immobilization of urease onto an electrochemically prepared copolymer poly(*N*-3-aminopropyl pyrrole-co-pyrrole) film. Biomat 26:3683–3690
4. Castillo-Ortega MM, Rodriguez DE, Encinas JC, Plascencia M, Mendez-Velarde FA, Olayo R (2005) Conductometric uric acid and urea biosensor prepared from electroconductive polyaniline—poly(*n*-butyl methacrylate) composites. Sens Actuators B 85:19–25
5. Konck R, Lenarczuk T, Radomska A, Glab S (2001) Optical biosensors based on Prussian blue films. Anal 126:1080–1085
6. Komaba S, Seyama M, Momma T, Osaka T (1992) Potentiometric biosensor for urea based on electropolymerized electroinactive polypyrrole. Electrochim Acta 42:383–388
7. Correia DPA, Magalhaes JMCS, Machado AASC (2005) Array of potentiometric sensors for simultaneous analysis of urea and potassium. Talanta 67:773–782
8. Malitesta C, Palmisano F, Torsi L, Zambonin PG (1990) Glucose fast-response amperometric sensor based on glucose oxidase immobilized in an electropolymerized poly(*o*-phenylenediamine) film. Anal Chem 62:2735–2740

Chapter 53
Electrochemical and Spectroscopic Characterization of Glucose Oxidase Immobilized in Polyvinyl Alcohol and Applications in Glucose Detection

D. Chirizzi, M. R. Guascito, C. Malitesta and E. Mazzotta

Abstarct A simple and novel amperometric biosensor for glucose detection is proposed. It is based on the immobilization of glucose oxidase in a poly(vinyl alcol) matrix drop casted on a platinum electrode surface (Pt/GOx-PVA). The composite material GOx-PVA has been characterized by UV-vis spectroscopy to verify the preservation of enzyme structural integrity and of the enzymatic activity in PVA membrane. X-ray Photoelectron Spectroscopy (XPS) characterization revealed a homogeneous film deposited on Pt whose structure is preserved under operative conditions. Glucose was determined in the absence of a mediator used to transfer electrons between the electrode and the enzyme. Amperometric characterization has been performed at −400 mV by using pulsed amperometric detection (PAD). Under the selected optimal conditions, the biosensor showed wide dynamic range (0.1–37 mM) yielding a low limit of detection (10 μM). Biosensor performance was satisfactory also in terms of repeatability, reproducibility and anti-interference ability.

53.1 Introduction

Enzyme-based biosensors for glucose detection continue to attract nowadays much interest due to the clinical importance of glucose and thus to the necessity of developing new rapid and easy procedures for its monitoring, especially in analysis in vivo [1]. In this contest, amperometric enzyme electrodes based on

D. Chirizzi (✉) · M. R. Guascito · C. Malitesta · E. Mazzotta
Dipartimento di Scienza dei Materiali, Università del Salento, via Monteroni, 73100 Lecce, Italy
e-mail: daniela.chirizzi@unisalento.it

G. Neri et al. (eds.), *Sensors and Microsystems*,
Lecture Notes in Electrical Engineering 91, DOI: 10.1007/978-94-007-1324-6_53,

glucose oxidase (GOx) have played a leading role in the move to simple easy-to-use blood sugar testing [2]. Most methods of glucose detection are based on the use of enzymatic biosensors in which an electrons transfer mediator is applied to shuttle the electrons between the redox centers of the enzyme and the electrode [3]. On the contrary, in mediators free enzyme biosensors the electron is transferred directly GOx to the electrode via the active site of the enzyme [4]. In this way, it is possible to work at low operating potential, close to that of the redox potential of the enzyme, thus leading to a very high selectivity as the interference of other electroactive species is drastically reduced.

In our work, a novel mediator-free glucose biosensor is proposed. It is fabricated by a simple immobilization procedure of GOx into a biocompatible polymer, poly(vinyl alcohol) (PVA), deposited on a Pt electrode (Pt/GOx-PVA). The choice of PVA relies in its recognized properties as an ideal enzyme immobilization material mimicking the enzyme's natural environment and able to stabilize enzymatic activity [5]. The very low operating potential (−400 mV versus SCE) as well as the successful glucose detection in the absence of oxygen evidence the mediator-less electron transport occurring [2]. The composite material GOx-PVA has been characterized by UV-vis spectroscopy to verify the preservation of enzyme structural integrity and of the enzymatic activity in PVA membrane. Moreover, XPS characterization revealed a homogeneous film deposited on Pt substrate whose structure is not altered under operative conditions.

53.2 Experimental

GOx (type VII from *Aspergillus niger*; 179,000 units/g), β-D-glucose and all other chemicals were obtained from Sigma. All reagents were analytical grade. 1 M stock glucose solutions (prepared every 2 weeks in a phosphate buffer solution (PBS) pH 7.0, $I = 0.2$) were allowed to mutarotate at room temperature overnight before use.

All electrochemical experiments were performed on a PalmSens electrochemical workstation (PalmSens instruments BV, The Netherlands) using a conventional three-electrode cell with a Pt disk (surface area, 0.0314 cm^2), a Pt wire and a saturated calomel electrode (SCE) as working, counter and reference electrodes, respectively. All electrochemical experiments were carried out in PBS (pH 7.0, $I = 0.2$). The buffer was purged with high-purity nitrogen prior to each electrochemical measurement and a nitrogen environment was kept over solution during experiments to prevent the solution from oxygen.

Modified electrodes were prepared by drop casting depositing on the electrode surface a drop of modifier solution, prepared as follows. Firstly, 3 mg of GOx (500 units/mL) were dissolved in 1 mL aqueous solution of 10% PVA in ultrasonic bath for 5 min. Afterwards 2 μL of GOx-PVA solution were deposited by casting on the Pt surface and left to evaporate for 45 min at room temperature. The same protocol was followed to prepare XPS samples onto Pt foils (area 3 cm^2).

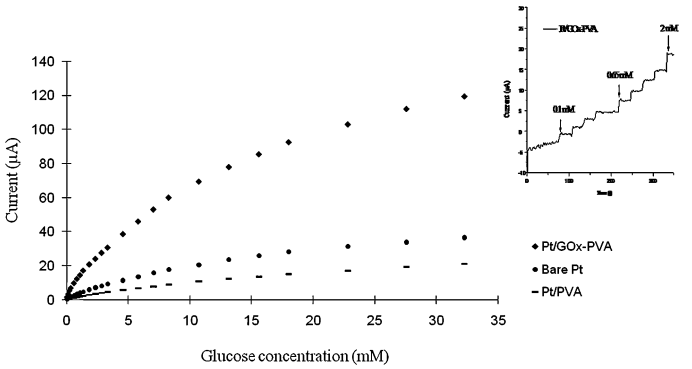

Fig. 53.1 Calibration curves on Pt/GOx-PVA, bare Pt and Pt/PVA (glucose 0.1–37 mM). Inset: amperometric response of Pt/GOx-PVA to glucose 0.1–2 mM in stirred and nitrogen saturated PBS (pH 7.0, $I = 0.2$). Applied potential: −630 mV for 0.2 s, +600 mV for 0.2 s and −400 mV for 0.4 s

XPS analysis was carried out by using a Leybold LHS10 spectrometer equipped with an unmonochromatized AlKα source (operating at 10 kV and 17 mA) and a SPECS multi-channel detector. For UV-vis experiments 200 μL of GOx-PVA mixture was deposited on a quartz slide and left evaporate for 1 h at room temperature. UV-vis spectra were recorded using a Varian Cary 50 UV-vis spectrophotometer in the wavelength range from 300 to 700 nm.

53.3 Results and Discussion

Glucose detection has been performed amperometrically at −400 mV by using pulsed amperometric detection (PAD). Figure 53.1 reports calibration curves on Pt/GOx-PVA, bare Pt and Pt/PVA (glucose 0.1–37 mM). In the inset Pt/GOx-PVA amperometric response to glucose 0.1–2 mM is shown. In this range a linear relationship was observed ($R^2 = 0.9913$) with a sensitivity of 9.66 $\mu A mM^{-1}$. A linear relationship between the reciprocal of current response (1/I) and the reciprocal of glucose concentration (1/C) was obtained in the concentration range 2.0–37 mM ($R^2 = 0.9944$). Biosensor performance was satisfactory in terms of limit detection (10 μM), repeatability (relative standard deviation (RSD) of 5.6%) and reproducibility (RSD of 5.7%), tested in triplicate on the same film and on three different films, respectively. Moreover, response stability revealed to be another interesting feature of the developed system as it was almost completely recovered 87% after 35 days in air at room temperature.

Moreover, biosensor selectivity was verified. Amperometric response revealed in fact to be specific to glucose without significant interference from other sugars as fructose (Fru) and sorbitol (Sor) or from electroactive species as ascorbic acid (AA) and uric acid (UA) coexisting with glucose in biological fluids (Fig. 53.2).

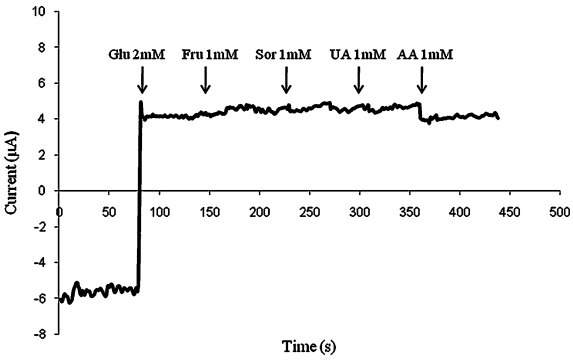

Fig. 53.2 Amperometric response to Glu 2, Fru 1, Sor 1, UA 1 and AA 1 mM in stirred and nitrogen saturated PBS (pH 7.0, $I = 0.2$). Applied potential: −630 mV for 0.2 s, +600 mV for 0.2 s and −400 mV for 0.4 s

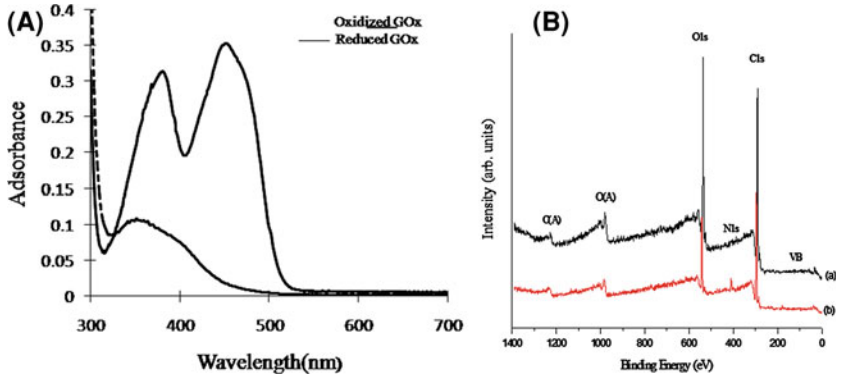

Fig. 53.3 **A** Uv-vis pectra of GOx in PVA film in the oxidized (*solid line*) and reduced state (*dotted line*) after the addition of glucose 10 mM. **B** Wide XPS spectra of Pt/GOx-PVA after its preparation (a) and after amperometric measurements in PAD mode with glucose 10 mM (b)

As a verification of enzyme integrity when it is embedded PVA, UV-vis spectra of GOx in PVA film were acquired. Results collected in Fig. 53.3A show GOx spectra in PVA matrix in the oxidized form (solid line) and its transformation in the reduced state (dotted line) after the addition of glucose 10 mM, according to literature data [6].

XPS analysis on Pt/GOx-PVA film was performed soon after its preparation (Fig. 53.3B(a)) and after being subjected to PAD measurements (Fig. 53.3B(b)) in the presence of glucose 10 mM. The absence of Pt4f signal evidenced a homogeneous deposition on Pt substrate that is preserved after the use of film in glucose detection. The film showed in fact high stability under operative conditions, as shown by the comparison between XPS spectrum of freshly prepared film (a) and of film exposed to glucose (b).

53.4 Conclusions

A new mediator free glucose biosensor based on the immobilization of GOx in PVA matrix on Pt electrode was proposed. The structural integrity of enzyme was confirmed by UV-vis and film homogeneity was verified by XPS analysis. Electrochemical investigations of the system by PAD in the presence of glucose revealed a wide dynamic range with a low limit of detection. Moreover the biosensor performance was satisfactory also in terms of repeatability, reproducibility and selectivity.

References

1. O'Neill RD, Lowry JP, Rocchitta G, McMahon CP, Serra PA (2008) Designing sensitive and selective polymer/enzyme composite biosensors for brain monitoring in vivo. Tr Anal Chem 27:78–88
2. Wang J (2008) Electrochemical glucose biosensors. Chem Rev 108:814–825
3. Heller A, Feldman B (2008) Electrochemical glucose sensors and their applications in diabetes management. Chem Rev 108:2482–2505
4. Zhang W, Li J (2004) Third-generation biosensors based on the direct electron transfer of proteins. Anal Sci 20:603–609
5. Wong F-L, Adbdul-Aziz A (2008) Comparative study of poly(vinyl alcohol)-based support materials for the immobilization of glucose oxidase. J Chem Technol Biot 83:41–46
6. Massey V (2000) The chemical and biological versatility of riboflavin. Biochem Soc Trans 28:283–296

Chapter 54
Innovative Integrated-Optic Resonator for Angular Rate Sensing: Design and Experimental Characterization

Caterina Ciminelli, Francesco Dell'Olio, Carlo E. Campanella and Mario N. Armenise

Abstract In this paper we report on the design, fabrication and characterization of an integrated-optic spiral resonator for angular rate sensing applications. The spiral resonator design has been optimized through a parametric analysis and a minimum angular velocity of about 10°/h, suitable for aerospace applications, has been theoretically predicted. The resonator has been fabricated in silica-on-silicon technology and characterized. Experimental results are in good agreement with the theoretical predictions.

54.1 Passive Resonator Angular Velocity Sensor

During the last decades optoelectronic technologies have enabled the development of very sensitive gyroscopes based on Sagnac effect [1, 2].

Integrated-optics for angular rate sensing may solve some open issues in gyro technology such as the need of both weight and size reduction, cost lowering, power consumption decrease, thermal effects limitation, and reliability increase. Photonic technologies could allow the integration of a gyroscope on a single chip and this can be surely pointed out as a very interesting research target especially in the framework of micro- and nano-satellites development.

In passive integrated optical angular rate sensors, an optical cavity is excited by two beams counter-propagating in clockwise (CW) and counter-clockwise (CCW) direction. When the gyro rotates, the resonance frequencies of the cavity relevant

C. Ciminelli (✉) · F. Dell'Olio · C. E. Campanella · M. N. Armenise
Optoelectronics Laboratory, Politecnico di Bari, Via E. Orabona 4,
70125 Bari, Italy
e-mail: c.ciminelli@poliba.it

G. Neri et al. (eds.), *Sensors and Microsystems*,
Lecture Notes in Electrical Engineering 91, DOI: 10.1007/978-94-007-1324-6_54,

to the two propagation directions are not equal. The difference between them is proportional to the angular rate and increases by enlarging the optical path. Passive integrated optical gyros typically employ a low-loss large-radius ring resonator having a high quality factor as sensing element. Silica-on-silicon technology allows to fabricate very low-loss (<0.1 dB/cm) optical waveguides operating at 1.55 μm. Propagation loss of these waveguides depends also on index contrast Δ between the guiding and the cladding layer and values around 0.01–0.03 dB/cm has been achieved for $\Delta < 1\%$. Bending loss exponentially decreases with curvature radius, so a curvature radius larger than a few millimetres is required to achieve negligible bending loss.

54.2 Integrated-Optic Spiral Resonator

The innovative integrated optical resonator, here proposed, consists of a waveguide in a spiral closed loop. This geometry has been chosen with the aim of increasing the optical path length. The spiral resonator is coupled to two straight bus waveguides, as it is shown in Fig. 54.1, in order to allow the propagation of two counterpropagating beams. When light is coupled to the spiral loop through the input waveguide, it builds up in intensity over multiple round-trips due to constructive interference. Only some wavelengths resonate within the spiral loop.

The spiral geometry proposed in [3] allows to enhance the quality factor and Sagnac effect if compared to the ring geometry because a longer optical path can be realized in the same area. On the other hand, silica-on-silicon technology allows to reduce propagation loss so further improving much more the quality factor.

Through port and drop port are, respectively, the output taken on the same input waveguide and the output on the adjacent waveguide. Each coupler can be modelled as a transfer matrix derived by the coupled mode theory [4].

The spectral response of the cavity has been obtained by using the transfer matrix method, neglecting the coupling effect due to the interaction of the two counter-propagating modes because they are supposed to be not simultaneously launched in [5, 6].

54.3 Detection Limit Optimization of the Spiral Resonator Based Sensor

The minimum detectable angular velocity ($\delta\Omega$) of a passive ring resonator gyro is limited by the shot noise at the photodetector included in the read-out system and is expressed as [3]:

$$\delta\Omega = \frac{2\pi}{L}\frac{1}{\sqrt{\eta P}}\frac{\sqrt{hc^3 B}}{\sqrt{2\lambda}}\frac{1}{Q\sqrt{\rho}}$$

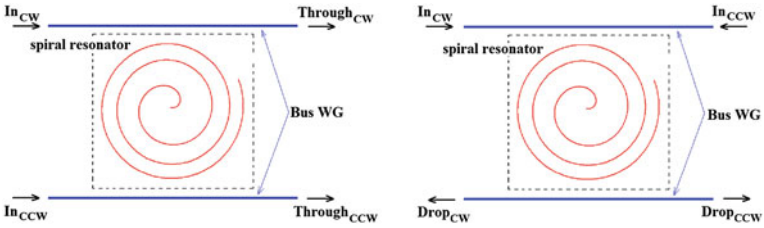

Fig. 54.1 Through (*left*) and drop (*right*) port configuration of the spiral resonator

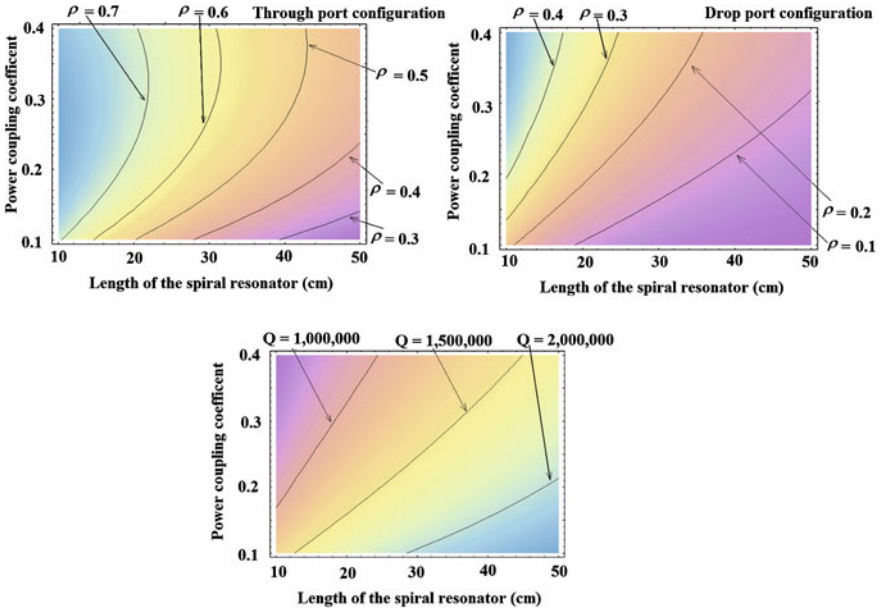

Fig. 54.2 Resonance depth as function of power coupling coefficient and spiral length for through port (*top left*) and drop port (*top right*). *Q*-factor (*bottom*) as function of power coupling coefficient and spiral length

where λ is the operating wavelength, c is the light velocity in the vacuum, h is Planck's constant, P is the optical power at the input of the photodetector, B is the sensor bandwidth, η is the photodetector quantum efficiency, L is the spiral perimeter, Q is the resonator quality factor and ρ is the resonance depth. To reduce $\delta\Omega$, Q needs to be increased as well as the resonance depth.

Both resonance depth and the quality factor variations as a function of the spiral resonator length (ranging from 10 to 50 cm) and of the power coupling coefficient between the resonator and the bus waveguides (in the range 10–40%) have been

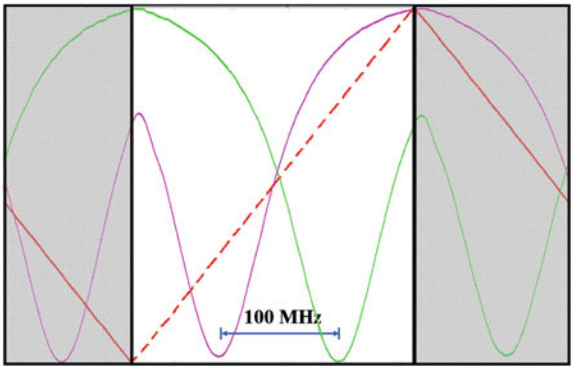

Fig. 54.3 Through port spectral response of the spiral silica resonator for the two propagation directions (*green* and *purple*) when the sawtooth signal (*red*) is applied to the laser module

investigated. The results of this parametric analysis are reported in Fig. 54.2. Propagation loss of the silica-on-silicon waveguide (=0.1 dB/cm) and guiding structure effective index (=1.457) have been kept constant.

To reduce the detection limit, a good trade-off between quality factor and resonance depth has to be assured for each possible configuration (drop port and through port).

By assuming a spiral length longer than 30 cm, quality factors higher than 10^6 are achievable although the resonance depth cannot be optimized at the same time. Since the *Q*-factor stronger influences the sensitivity, the spiral has been designed to optimized it. A resolution in the range 10–100°/h can be obtained. By reducing propagation loss until 0.01 dB/cm, the resolution can be lowered in the range 1–10°/h. As an example, assuming drop port configuration, for a resonator length of 38.4 cm the sensitivity is 28.5°/h when propagation loss is 0.1 dB/cm and the coupling strength is 20%. By assuming the same length, sensitivity becomes 14.8°/h when propagation loss is 0.05 dB/cm and the coupling strength is 10% and 3.0°/h for propagation loss of 0.01 dB/cm and coupling strength of 2%.

54.4 Experimental Characterization of the Spiral Resonator

The spiral resonator has been fabricated at CIP (Centre for Integrated Photonics, Ipswich, UK) by using silica buried waveguides with a core size of 6×6 μm^2 and an index contrast of 0.75% at $\lambda = 1.55$ μm [3]. Figure 54.3 shows the experimental results obtained for a 42 cm long spiral having through port configuration, with a coupling coefficient of 40%.

The spectral response has been measured by using a thermally tuneable fiber laser having a linewidth <1 kHz, an acousto-optic frequency shifter driven by a signal generator, a variable optical attenuator, a 50/50 fiber splitter, a polarization controller, two photodetectors, an oscilloscope and a signal generator. A sawtooth signal having a frequency of 0.2 kHz has been applied to the laser module for frequency modulation. The frequency of the two optical signals exciting the cavity

varies accordingly to the saw-tooth waveform and the two frequencies exhibit a fixed difference of 100 MHz due to the presence of the acousto-optic frequency shifter.

From the measured spectrum a quality factor Q equal to 1.55×10^6 has been calculated. This result, better than the simulated Q value ($=1.4 \times 10^6$) is due to the lower propagation losses of the fabricated waveguides estimated to be about 0.08 dB/cm. Thus, a sensitivity value of about 10°/h has been demonstrated.

References

1. Ciminelli C, Dell'Olio F, Campanella CE, Armenise MN (2010) Photonic technologies for angular rate sensing. Adv Optics Photonics 2:370–404
2. Ciminelli C, Campanella CE, Dell' Olio F, Passaro VMN, Armenise MN (2009) A novel passive ring resonator gyroscope. DGaO/SIOF Joint Meeting, Brescia, 2–5 June 2009
3. Integrated-Optics Laser Gyro Technology (IOLG), ESA/ESTEC—MI CONTRACT n. 16782/02/NL/PA
4. Yariv A (2000) Universal relations for coupling of optical power between micro-resonators and dielectric waveguides. Electron Lett 36:321–322
5. Ciminelli C, Campanella CE, Armenise MN (2009) Optimized design of integrated optical angular velocity sensors based on a passive ring resonator. J Lightwave Tech 27:2658–2666
6. Armenise MN, Campanella CE, Ciminelli C (2009) Theoretical investigation of two beams optical ring resonators for new generation photonic sensors. International conference on transparent networks, Ponta Delgada, Azores, 28 June–2 July (invited paper)

Chapter 55
Electrochemical DNA Sensors for the Detection of Benzo[a]pyrene Toxicity

Michele Del Carlo, Manuel Sergi, Marialisa Giuliani, Dario Compagnone and Attila Kiss

Abstract In the present study we report the use of gold screen printed electrodes for the detection of the oxidized form of Benzo[a]pyrene via DNA based sensing. Benzo[a]pyrene-r-7,t-8-dihydrodiol-t-9,10-epoxide (DE–BaP) was the target molecule. Our approach consisted in the design of an electrochemical biosensor able to generate a response upon the formation of a stable adduct between DNA and DE–BaP. Such a device should be, in principle, able to predict the formation of an adduct between an immobilized DNA strand and the toxic molecule.

55.1 Introduction

The toxic effect of polycyclic aromatic hydrocarbons (PAHs) occurs via their activation to more reactive species, usually oxidized species, via metabolic pathways [1]. Benzo[a]pyrene has been classified by IARC as highly toxic among the PAHs. Toxicity is exerted by the formation of benzo[a]pyrene-r-7,t-8-dihydrodiol-t-9,10-epoxide (DE–BaP) that is able to form adducts with the guanine base of DNA causing mutagenesis and cancer. In this work we have used a DNA sensor to detect the adduct formation taking advantage of the inhibition caused on the hybridization reaction.

The probe was designed according to literature information on target sequences for PAHs. For example an oncosuppressor gene (p-53) situated in the 17p13.1 chromosome is frequently mutated in different human cancers, after exposition to

M. Del Carlo · M. Sergi · M. Giuliani · D. Compagnone (✉)
Dipartimento di Scienze degli Alimenti, Università degli Studi di Teramo,
Via Lerici 1, 64023 Teramo, Italy
e-mail: dcompagnone@unite.it

A. Kiss
Egerfood Regional Research Centre, Eszterhàzy Kàroly University, Eger, Hungary

G. Neri et al. (eds.), *Sensors and Microsystems*,
Lecture Notes in Electrical Engineering 91, DOI: 10.1007/978-94-007-1324-6_55,

cancerogenic substances including PAHs [2]. In the lung cancer several G → T transversions are present, in most cases clustered in "hot spot" codons (for ex. 157-158-248-249-273-282) in the 5 and 8 exons, were the most conserved domains of the gene are located. Therefore, we have chosen the target triplets GTC(157), CGG(248), AGG(249) and CGT(273), spaced by unreactive triplets, in order to have a 24-bases probe.

The DNA probes have been immobilized using the reactivity of the thiol groups towards gold surfaces, obtaining the orientation of the DNA strand, and the detection has been obtained using a biotinilated probe in conjunction with a avidin–alkaline phosphatase conjugate.

55.2 Materials and Instruments

BaP–DE solution (Benzo[a])pyrene-7,8-dihydrodiol-9,10-epoxide(±)(anti) from National Cancer Institute—Midwest Research Institute, Mo., USA) have been freshly prepared in acetate buffer 0.2 M (AB) (Sodium Acetate Sigma-Aldrich s.r.l, Milan, Italy) 10% Methanol, pH 4.7 or in Tris-HCl buffer 50 mM, pH 7.4.

Stock solution of thiolated DNA probes (from Sigma), have been prepared in 10 mM Tris-1 mM EDTA pH 8 and stored freezed. Dilutions were carried out daily in 0.5 M phosphate buffer, pH 8.5 (PB) before use. Stock solution of biotinilated complementary DNA probe have been prepared in 10 mM Tris-1 mM EDTA pH 8 and diluted daily in Sodium Citrate buffer (SSC2X) containing NaCl 0.3 mol/L and $C_6H_5Na_3O_7$ 0.03 mol/L, pH 7.4 before use. The sequence of the bases used for the oligos are reported in Table 55.1.

Avidin–alkaline phosphatase conjugate (from Sigma-Aldrich s.r.l, Milan, Italy) has been freshly prepared in DEA–BSA buffer (Diethanolammine 0.1 mol/L, $MgCl_2$ 1 mmol/L, KCl 0.01 mol/L 1% BSA, 0.1%Tween 20 (Sigma-Aldrich s.r.l, Milan, Italy).

After immobilization of the DNA probes the electrodes have been blocked with 1 mmol/L 6-Mercapto-1-Exanol (MHC) (Sigma-Aldrich s.r.l, Milan, Italy).

1 mg/mL 1-Naphthylphosphate solution (Sigma-Aldrich s.r.l, Milan, Italy) has been prepared in DEA buffer every day.

Gold Screen Printed electrodes were from Ecobioservices and Research (Florence).

All the measurements have been performed with a AUTOLAB potentiostat PGSTAT12, electrochemical analysis system (Eco Chemie, Utrecht, The Netherlands).

55.3 DNA Immobilization Procedure and Control

Six microliters of 1 μmol/L thiolated DNA probe have been deposited onto the surface of the gold working electrodes (WE) and left for 16 h at room temperature.

Table 55.1 DNA oligo sequences for this method

Oligos	Sequence
Thiolated Probe DNA	5′[ThiC6] TTTGTCCAACGGAGGTCTCGTATA 3′
Biotinilated Compl. DNA	3′AAACAGGTTGCCTCCAGAGCATAT[biot]5′

The electrodes have been then washed with SSC2X, and the free surface of the WE has been blocked with 6 μL of 1 mmol/L MHC for 1 h at room temperature.

After washing with AB, the immobilization of the probe has been evaluated through potentiometric stripping electrochemical analysis using these parameters: Current 20 μA; Time of measure: 60 s; Final Potential: 1.2 V. The signal due to the oxidation of the residues of guanine and adenine bases of the DNA probes was related to the immobilized probe.

In order to evaluate the best concentration of biotinilated complementary DNA sequences, 6 μL of biotinilated DNA (10–5–1–0.1 μM) have been deposited onto the same surface and then incubated for 20 min at room temperature, to evaluate the maximum of hybridization signal. The electrodes have been then rinsed with DEA buffer and incubated with 6 μL of 5 μM Avidin–Alkaline phosphatase, for 20 min at room temperature. After a further wash, the surface of the electrodes has been covered with a drop of 100 μL of 1 mg/mL 1-naphthylphosphate for 20 min at room temperature. The enzyme avidin–alkaline phosphatase catalyzes the hydrolysis of 1-naphthylphosphate to naphthol, that is oxidized at +0.2 V versus pseudo-Ag/AgCl reference electrode. The voltammetric signal taken was the height of the peak current generated from the oxidation of the 1-naphthol, and is dependent on the amount of hybridized biotinilated DNA. Differential pulse voltammetry has been used with the following parameters: *Conditioning potential:* 0.04 V *for* 10 s; *modulation time*: 0.05 s; *Interval time*: 0.15 s; *Amplitude:* 70 mV; *Potential scan from* +0.05 V *to* +0.6 V.

55.4 Determination of DE–BaP–DNA Adduct

The effect of increasing concentration of DE–BaP on the selected DNA target sequence has been studied by incubation (10 min) onto the surface of the working electrode prepared as described in the previous paragraph. When the formation of the DNA-DE–BaP adduct occurs a displacement of the hybridization reaction is expected. A typical calibration curve obtained using 0.1 μg/mL of the DNA probe is reported in Fig. 55.1. The calibration showed a typical hook effect at low concentrations of DE–BaP that requires further investigation. Nevertheless a clear correlation exists between sub-micromolar DE–BaP concentration and the inhibition of the hybridization reaction of the DNA probe selected. Better results were obtained when the incubation between the toxic and the DNA was carried out on the immobilised DNA rather than with the complementary strand. Inter-electrode relative standard deviation was of the order of 15–20%, that is typical of these screening assays.

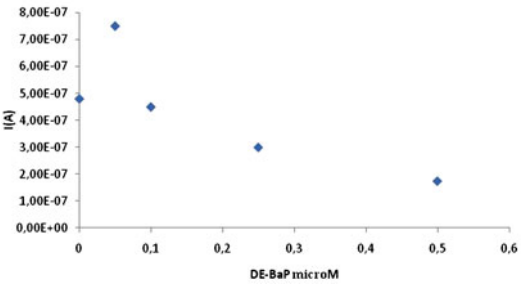

Fig. 55.1 Typical calibration curve obtained using DE–BAP and 0.1 μg/mL of DNA sequence on the electrode

55.5 Conclusions

A DNA sensor for the detection of the metabolic oxidized toxic form of benzo[a]pyrene has been realized using a selected target sequence of DNA. Inhibition of the hybridization reaction allowed to detect the toxic compounds at submicromolar level. The sensor appears promising for the screening of potentially toxic compounds forming stable adducts with DNA.

Acknowledgments With the Contribution of Ministero degli Affari Esteri, Direzione Generale per la Promozione e la Cooperazione Culturale.

References

1. Shemer H, Linden KG (2007) Aqueous photodegradation and toxicity of the polycyclic aromatic hydrocarbons fluorene, dibenzofuran, and dibenzothiofene. Wat Res 41:853–886
2. Xue W, Warshawsky D (2005) Metabolic activation of polycyclic and heterocyclic aromatic hydrocarbons and DNA damage: A review. Toxicol Appl Pharmacol 206:73–93

Chapter 56
Electrochemical Sensing Approach for the Selective Determination of Hg^{2+}

M. Del Carlo, A. Ricci, C. Lo Sterzo and D. Compagnone

Abstract In this work, a glassy carbon electrode was modified with a methionine functionalized conjugated molecule, realizing a novel Hg^{2+} electrochemical sensor. The overall assay scheme included an accumulation step, the electrochemical measurement and a regeneration step. All these aspects have been optimized including accumulation time, cleaning procedure and stability of the sensing layer.

56.1 Introduction

Fully conjugated organic materials might display unique opto-electronic performances due to the extended electronic delocalization spanning along the unsaturated backbone. The insertion of properly designed chemo- or bio-receptors into the conjugation path, or their appending as side functionalities to the main backbone, is becoming a current strategy for the realization of advanced chemo and biosensing devices [1, 2]. Recently, we reported [3] the sensing properties of DMM (N,N′-[2,5-bis(phenylethynyl)terephthaloyl](S,S)di-methionine methyl ester) (Fig. 56.1), an assembling characterized by the linkage of two aminoacidic (methionine) moieties to a poly(arylene ethynylene) (PAE) platform [4].

Photophysical studies [3] have shown the ability of DMM to selectively detect Hg^{2+} ions in CH_3CN solution, by a complete luminescence quenching.

M. Del Carlo · A. Ricci (✉) · C. Lo Sterzo · D. Compagnone
Dipartimento di Scienze degli Alimenti, Facoltà di Agraria, Università degli Studi di Teramo, Via Carlo R. Lerici 1, 64023 Mosciano Sant'Angelo, Teramo, Italy
e-mail: aricci@unite.it

M. Del Carlo · C. Lo Sterzo
Istituto CNR di Metodologie Chimiche (IMC-CNR), Sezione Meccanismi di Reazione, Dipartimento di Chimica, Università La Sapienza, P.le Aldo Moro 5, 00185 Rome, Italy

G. Neri et al. (eds.), *Sensors and Microsystems*,
Lecture Notes in Electrical Engineering 91, DOI: 10.1007/978-94-007-1324-6_56,

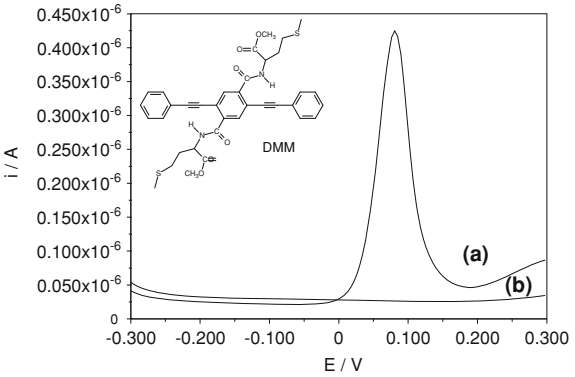

Fig. 56.1 Differential pulse voltammograms recorded **a** after a 30 min accumulation step in 0.5 ppm Hg^{2+} solution in 10^{-4} perchloric acid, and **b** after the cleaning step performed by stirring in 0.01 M nitric acid for 10 min. *Inside* chemical structure of DMM

The severe health and environmental concerns regarding bioaccumulation of mercury [5] are urging more sensitive, selective and easily accessible detection of this heavy metal. In order to exploit the potential of DMM toward higher sensing performances, we investigated the detection of Hg^{2+} ions using a DMM modified glassy carbon electrode [6, 7].

56.2 Experimental

56.2.1 Reagents and Chemicals

DMM [3] was dissolved in acetonitrile (1.2 mg/ml).

Mercury(II) nitrate, potassium thiocyanate, methanol, perchloric acid, acetonitrile, nitric acid were obtained from Sigma, Italy.

Ultrapure water was obtained with PURELAB pro 20 apparatus (USF).

A mercury(II) nitrate stock solution was prepared by dissolving the salt in 10^{-4} M perchloric acid, was filtered and then standardized (58 ppm Hg^{2+}) by spectrophotometric determination of nitrate ion. Working solutions were daily prepared by diluting the stock solution with 10^{-4} M perchloric acid.

56.2.2 Apparatus

Electrochemical experiments were carried out using a PGSTAT12 potentiostat (AUTOLAB, Eco Chemie, The Netherlands) with GPES 4.7 software.

A conventional three-electrode system, consisting of a chemically modified glassy carbon electrode as working electrode, a platinum-wire counter electrode, and an Ag/AgCl reference electrode, was assembled. Measurement were carried out at room temperature using potassium thiocyanate as supporting electrolyte [8].

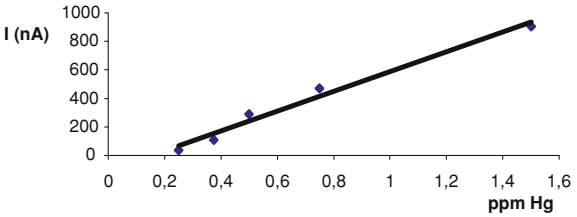

Fig. 56.2 Peak currents vs Hg^{2+} concentration

56.2.3 Working Electrode Preparation

The mirror-like surface of a glassy carbon rod (3 mm diameter) was carefully polished on a wet soft cloth using Al_2O_3 powder (0.3 μm), washed with water and rinsed with methanol. Then, five subsequent deposition steps consisting in (a) casting of 3 μl of 1.8 mM DMM in acetonitrile, (b) solvent evaporation in air for 15 min, and (c) heating in the oven at 100°C for 5 min, were performed.

56.3 Results and Discussion

56.3.1 Mercury Detection by DMM Modified Glassy Carbon Electrode

Mercury determination experiments were carried out following a three steps procedure: accumulation step/voltammetric measurement/regeneration step.

The DMM modified working electrode was first allowed to capture Hg^{2+} ions by immersion in the stirred 10^{-4} M perchloric acid solution of Hg^{2+} to be tested for 30 min. The study of dependence of the peak current vs. accumulation time (0.5 ppm Hg^{2+}) showed a linear dependence between 10 and 60 min, while saturation was occurring for longer exposition times.

After removal from the testing solution, and rinsing with water, the electrode was placed in an electrochemical cell containing the supporting electrolyte solution. Performing a voltage scan from −0.3 to +0.3 V the reduction of the complexed Hg^{2+} to Hg^0 was first caused, then, as evidenced in Fig. 56.1a, an evident oxidation peak was observed due to $Hg^0 \rightarrow Hg^{2+}$ reaction.

After the measurement, the regeneration step was performed by immersion of the electrode in a stirred 0.01 M nitric acid solution for 10 min. Figure 56.1b accounts the absence of any residual Hg^{2+} ions on the cleaned electrode, that was ready for the next determination.

The stability of the modified working electrode was checked by repeating the accumulation/measurement/cleaning cycles (Hg^{2+} 1 ppm). No more than five measures can be performed with one electrode, as a loss of sensitivity is appearing. This limitation might be attributable to the weak interaction between electrode

surface and DMM film, with consequent loss of sensing material from electrode surface, and resulting decrease of sensitivity.

56.3.2 Dependence of the Voltammetric Response on Hg^{2+} Concentration

Calibration curve between 0.2 and 1.5 ppm Hg^{2+} range showed a good linear behavior (Fig. 56.2), with variations over four measurements on the same sample below 5% in the entire calibration range.

56.4 Conclusions

The novel Hg^{2+} electrochemical sensor made of a glassy carbon electrode modified with a methionine functionalized conjugated molecule (DMM) demonstrated to be able to detect Hg^{2+} ions in aqueous solutions, with a linear voltammetric response over the concentration range 200–1500 ppb.

The drawback represented by the limited number of measurement cycles that can be done with a single electrode, could be overcome either by the use of disposable screen printed electrodes, or by the covalent binding of DMM to the properly activated electrode surface.

Moreover, in order to confirm the high selectivity toward Hg^{2+} showed by DMM in the photophysical studies [3], before testing real samples (drinking water, fish extracts, etc.), we will investigate eventual interference by other metal ions, electroactive or not, also in excess respect to Hg^{2+}.

Acknowledgments This work has been supported by MIUR through PRIN 2007 project "Optoactive molecular systems, conjugated polymers, and nanoparticles for the development of new chemical sensors".

References

1. Malhotra BD, Chaubey A, Singh SP (2006) Prospects of conducting polymers in biosensors. Anal Chim Acta 578:59–74
2. Thomas SW, Joly GD, Swager TM (2007) Chemical sensors based on amplifying conjugated polymers. Chem Rev 107:1339–1386
3. Compagnone D, Ricci A, Del Carlo M, Chiarini M, Pepe A, Lo Sterzo C (2010) New poly(aryleneethynylene)s as optical active platforms in biosensing. Selective fluorescent detection of Hg(II) obtained by the use of aminoacidic groups anchored on conjugated backbones. Microchim Acta 170:313-319
4. Goldratt, E. M. (1991). *Haystack Syndrome*. Great Barrington, MA: North River Press.
5. Wang QR, Kim D, Dionysiou DD, Sorial GA, Timberlake D (2004) Sources and remediation for mercury contamination in aquatic systems—a literature review. Environ Pollut 31:323–336

6. Wu D, Zhang QZ, Chu X, Wang H, Shen G, Yu R (2010) Ultrasensitive electrochemical sensor for mercury(II) based on target-induced structure-switching DNA. Biosens Bioelectron 25:1025–1031
7. Stojko NY, Brainina KZ, Faller C, Henze G (1998) Stripping voltammetric determination of mercury at modified solid electrodes. I. Development of the modified electrodes. Anal Chim Acta 371:145–153
8. Sousa MFB, Bertazzoli R (1996) Preconcentration and voltammetric determination of mercury(II) at a chemically modified glassy carbon electrode. Anal Chem 68:1258–1261

Chapter 57
An Amperometric Sensor for the Selective Determination of Ortho-Diphenols in Olive Oil

Michele Del Carlo, Alessia Pepe, Flavio Della Pelle, Marcello Mascini, Dario Compagnone, Aziz Amine, Azedin Kadi, Nora Amraoui Bendriss and Giuseppe Christian Fusella

Abstract An electrochemical flow injection analysis method for the selective determination of ortho-diphenols have been developed and optimized. The method is based on the use of sodium molybdate as an electrochemical mediator. The selectivity of the measurement has been evaluated with respect to different ortho-diphenols and phenols that are usually found in extra-virgin olive oil. After FIA optimization the protocol has been applied to the detection of olive oil samples and results were compared with a reference method.

57.1 Introduction

The evaluation of the quality of extra-virgin olive oil (EVOO) is based on some classical analysis, such as the titration of the free acidity, the determination of the peroxide value and some spectrophotometric index (K232, K270 and ΔK). Oxidative stability is a central parameter in the estimation of EVOO quality, as it gives a reliable evaluation of the susceptibility to oxidative degeneration, which is the main cause of its adulteration. The shelf life of olive oil is strictly related to rancidity development, which could depend on the autoxidation of fatty acids. This phenomenon takes place in the presence of oxygen, generating some unstable

M. Del Carlo · A. Pepe · F. Della Pelle · M. Mascini · D. Compagnone (✉) · G. C. Fusella
Dipartimento di Scienze degli Alimenti, Facoltà di Agraria, Università degli Studi di Teramo, Via Carlo R. Lerici 1, 64023 Mosciano Sant'Angelo (Teramo), Italy
e-mail: dcompagnone@unite.it

A. Amine · A. Kadi · N. Amraoui Bendriss
Faculté des Sciences et Techniques, Laboratoire Analyses Chimiques et Biocapteurs Université, HassanII B.P. 146, 20800 Mohammedia, Morocco

G. Neri et al. (eds.), *Sensors and Microsystems*, Lecture Notes in Electrical Engineering 91, DOI: 10.1007/978-94-007-1324-6_57,

compounds that can modify the sensory and nutritional characteristics of the oil, thus leading to product spoilage. Although unavoidable, the oxidation process can be delayed by endogenous antioxidant that enhance the oxidative stability by preventing the propagation of lipid peroxidation or removing free radicals. Antioxidants are reported as molecules which, when present at low concentrations compared to those of an oxidable substrate, significantly delay or prevent oxidation of that substrate [1]. In EVOOs, different classes of compounds having antioxidant activity are present, namely polyphenols (both simple and aglycons) tocopherols, carotenoids, and chlorophylls. Among polyphenols, ortho-diphenols, are recognized as the most important in relation to their antioxidant activity. It has been demonstrated that o-dipehnols posses most of the antioxidant activity of olive oil, moreover, recently other pharmacological effects have been described for some quantitatively relevant o-diphenols of olive oil [2]. In addition, oleoeuropein, a quantitatively important ortho-diphenol, is involved in the formation of the EVOO taste. Ortho-diphenols can be quantitatively determined either by HPLC or, as a class, via a spectrophotometric method. Both these methods require an extraction step that, in the case of HPLC can be a liquid liquid extraction (LLE), and in the case of the spectrophotometric step is solid phase extraction (SPE).

The aim of our research is to develop an electrochemical method for the selective determination of ortho-diphenols that, at the end, might be operated in untreated EVOO samples. The method is based on the use of an electrochemical mediator based on Mo^{6+}. In the selective reaction with ortho-diphenols it is reduced to Mo^{4+} that is the re-oxidised to the graphite electrode at when a positive potential is applied.

57.2 Experimental

57.2.1 Reagents and Chemicals

Sodium molybdate, ortho-diphenol and phenol standards, HCl, were obtained from Sigma, Italy. Ultrapure water was obtained with PURELAB pro 20 apparatus (USF). The mediator was freshly prepared daily to avoid oxidation phenomena.

57.2.2 Apparatus

Voltammetric experiments were carried out using a PGSTAT12 potentiostat (AUTOLAB Eco Chemie Netherlands) with GPES 4.7 software.

Amperometric measurement were carried out both with a Palmsens potentiostat and with an AMEL, model 559. The Flow injection system consisted of a peristaltic pump (Gilson, France) and low pressure injection valve (Rheodyne, USA) a home made flow cell. The electrochemical cell consisted in a screen printed carbon

based electrode which was assembled into the flow cell. Measurement were carried out in flow injection mode using HCl 0.01 M as a carrier, with or without the electrochemical mediator, sodium molybdate. All measurements were performed at room temperature.

57.2.3 Modified Electrode Preparation

Modified screen printed electrode have been prepared using sodium molybdate as electrochemical modifier. The mediator was dissolved in HCl, mixed with Nafion and deposited by casting on the surface of the working electrode. Evaporation was carried out at controlled 80°C temperature for 1 h. The electrode were then rinsed with water and evaluated by cyclic voltammetry or used in the FIA apparatus.

57.2.4 Electrochemical Determination of Ortho-Diphenols

The selective determination of ortho-diphenols was carried out using a modified carrier containing the electrochemical mediator in solution. Twenty microliter of standard/sample solution were injected into the carrier stream and the current recorded. The applied potential was optimized by hydrodynamic voltammetry.

57.3 Results and Discussion

57.3.1 Voltammetric Study of Mediated Ortho-Diphenols Oxidation

The aim of our application was to obtain a selective electrochemical method for the detection of ortho-diphenols in presence of other phenolic compound. Therefore the first evaluation was aimed to demonstrate this selectivity.

In Fig. 57.1 the cyclic voltammogram obtained for catechol with respect to non ortho-diphenols compounds is reported. It is evident that a strong catalytic activity is present when ortho-diphenols are exposed to the electrochemical mediator.

Via hydrodynamic voltammetry, data not shown, the optimal potential for the determination of ortho-diphenols was chosen, it was +300 mV versus Ag/AgCl. Using this potential and using the mediator in solution we obtained a calibration curve for a model ortho-diphenol, catechol, in the interval 0.2–2.5 ppm, Fig. 57.2.

A single electrode could be used up to 20 repetition of the calibration without any response decrease.

A noteworthy selectivity with respect to the direct electrochemical oxidation of catechol was observed at this potential with a signal ratio $i_{catechol(m)}/i_{catechol} = 15, 0,$

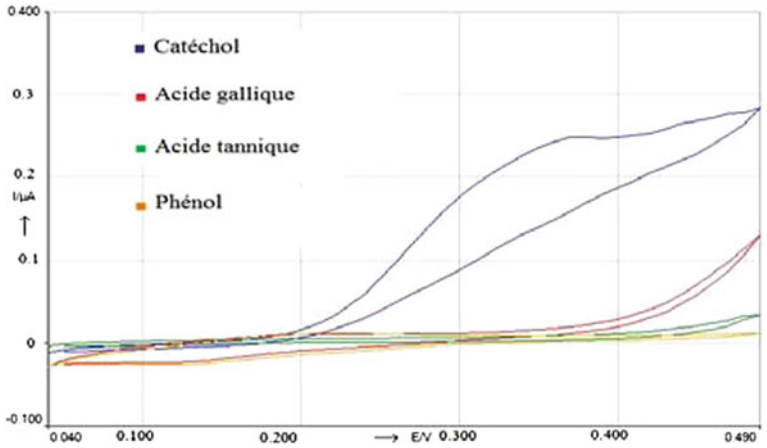

Fig. 57.1 Voltammetric study showing the selective response of Mo^{6+} to ortho-diphenols. In this case the mediator was placed in solution

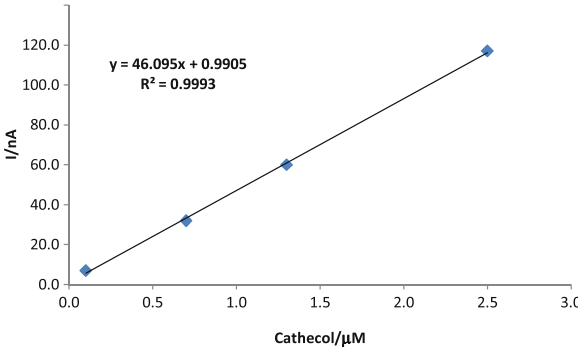

Fig. 57.2 Catechol calibration curve in the concentration interval 0.2–2.5 ppm

where $i_{catechol(m)}$ is the slope of the calibration curve in presence of Mo^{6+} and $i_{catechol}$ is the slope without Mo^{6+}. After this step, the direct immobilization of Mo^{6+} was done in order to modify the electrode and surface and to obtain a chemically modified electrode selective for ortho-diphenols. The electrode was modified by a mixed physical absorbtion and chemical entrapment approach on the surface of a graphite electrode. The modified electrode showed a significant increase of the anodic current when catechol or hydroxytyrosol were used as a substrate. Though a poor stability of the sensor limited its application in sample analysis; in fact up to 35 consecutive determination could be performed with a signal loss of 40%. Therefore sample analysis was performed using the mediator in solution.

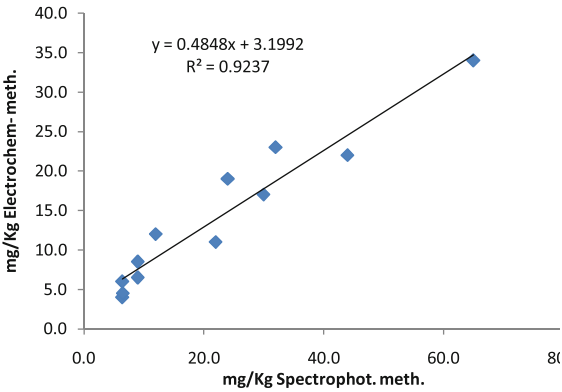

Fig. 57.3 Comparison of the electrochemical method versus spectrophotometric one

57.3.2 Sample Analysis

Twelve olive oil sample were used to compare the performance of the electrochemical method with the spectrophotometric one. Phenolic were extracted by SPE extraction using a diol bonded cartridge according. The methanolic extract was used for both the determination. In Fig. 57.3 the data correlation is reported. A good correlation coefficient was appreciated, whereas an underestimation when measuring with the proposed electrochemical method was also observed. This could be due to the selectivity of the electrochemical method with respect to the spectrophotometric one. In fact the latter requires 15 min of sample incubation that may lead to a response by non ortho-diphenols. On the contrary, in the proposed FIA electrochemical method a fast and kinetic reaction is measured resulting in an increased selectivity.

Acknowledgments The European Project PEOPLE, MARIE CURIE ACTIONS International Research Staff Exchange Scheme no. 230815 is acknowledge.

References

1. Del Carlo M, Saccheti G, Di Mattia C, Compagnone D, Mastrocola D, Liberatore L, Cichelli A (2004) Contribution of the phenolic fraction to the antioxidant activity and oxidative stability of olive oil. J Agric Food Chem 52:4072–4079
2. Kiritsakis AK (1990) Olive oil. AOCS Press, Champaign

Chapter 58
Thick-Film Inclinometer Based on Free Convective Motion of an Heating Air Mass

Damiano Crescini and Marco Romani

Abstract Using thick-film technology on a ceramic substrate, a new tilt senor based on the heat transfer principle has been developed. The sensor is fabricated from ceramic materials and thick-film technology that results in an accuracy of about 2% full scale output, repeatability of about 0.2°C and thermal stability <0.2%/°C over a ±50° range. The TFT tilt sensor is capable of resolving less 0.1°. Finally, the sensor is inexpensive enough to be, in the near future, competitive with other types of commercial tilt transducer.

58.1 Introduction

Thick-film technology (TFT) was introduced about 30 years ago as a means of producing *hybrid* circuits. Such circuits comprise semiconductor devices, monolithic ICs and other discrete devices in addition to the thick-films themselves. A key factor distinguishing a thick-film circuit is the method of film deposition, namely screen-printing, which is possibly one of the oldest forms of graphic art reproduction. Thick-film hybrid circuits are generally regarded as being compact, robust and relatively inexpensive and have found application in areas such as televisions, calculators, telephones, automotive electronics and missile guidance systems to name but a few. Thick-film sensors are a relatively new application of the technology, with a majority of the published working appearing in the past decade [1–4]. It should be noted; however, that the technology is also widely used

D. Crescini (✉) · M. Romani
Dipartimento di Elettronica per l'Automazione, Università degli Studi di Brescia,
Via Branze 38, 25123 Brescia, Italy
e-mail: damiano.crescini@ing.unibs.it

G. Neri et al. (eds.), *Sensors and Microsystems*,
Lecture Notes in Electrical Engineering 91, DOI: 10.1007/978-94-007-1324-6_58,

for the fabrication of chemical and gas sensors and many commercial devices exist. The integrability of the technology also allows combination with other enabling technologies, such as silicon, to provide powerful and economically viable solid-state sensors. This paper describes a thick-film tilt sensor utilizing all of the above aspects.

58.2 The Operating Principle and the Fabrication Method in Thick-Film Technology

The principle of operation of the TFT devices is based on heat transfer by natural convection.

The devices measure internal changes in heat transfer caused by the inclination using the force of gravity as an input. The devices are functionally equivalent to traditional proof-mass accelerometers.

The proof mass in the new thick-film sensor is a gas. The gaseous proof-mass provides great advantages over the use of the traditional solid proof mass. The device does not display striction and particle contamination problems associated with competitive devices and provides a high shock survival leading to significantly lower failure rates and lower loss due to handling during assembly. The arrangement necessary for measuring the inclination effects on heat transfer is described next.

A double structure heat source, centred in the ceramic substrate is suspended across a cavity. Equally spaced temperature sensors are located equidistantly on all two sides of the heat source. Under zero inclination, a temperature gradient is symmetrical about the heat source, so that the temperature is the same at all two temperature sensors, causing them to output the same voltage (reference Fig. 58.1a). Inclination in the sensing direction will disturb the temperature profile, due to free convection heat transfer, causing it to be asymmetrical (reference Fig. 58.1b). The temperature, and hence voltage output of the two temperature sensors will then be different. The differential voltage at the temperature sensor outputs is directly proportional to the inclination.

The TFT tilt sensor is most sensitive to changes in position, or tilt, when the sensitive axis is perpendicular to the force of gravity, or parallel to the Earth's surface. Similarly, when the sensitive axis is parallel to the force of gravity (perpendicular to the Earth's surface), it is least sensitive to changes in tilt. The fabrication method involves the standard thick-film procedures on 96% alumina substrate. The planar resistor adopted for the heating processes is based on a Pt/Au ink. In order to achieve adequate electrical characteristics, a firing process has been adopted at a peak temperature of about 950°C. The temperature sensor is based on an nickel conductor (with a nominal resistance of about 200 Ω). The nickel film (20 μm thick) has a high positive temperature coefficient of resistance ($\cong$5,000 ppm/°C) and it is suitable candidate for commercial temperature-sensing

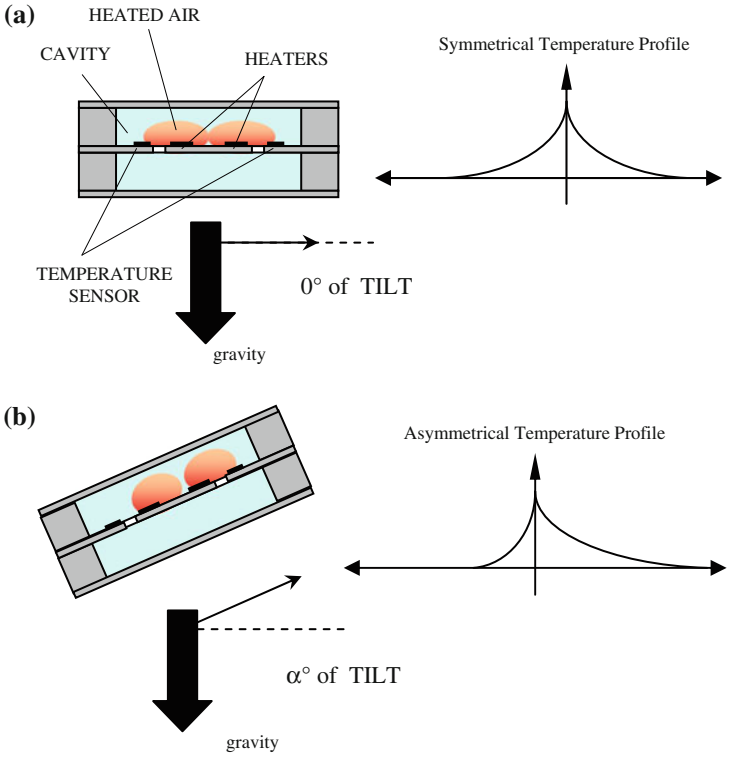

Fig. 58.1 Vertical cross-section showing the sensing sequence: **a** 0° TILT angle, **b** αα° TILT angle

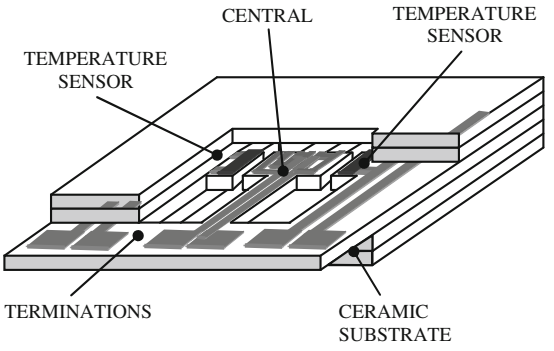

Fig. 58.2 Schematic drawing of the tilt sensor in thick-film technology

applications. The nickel conductor is termined onto a conductive film based on Pt/Au ink. The aim is to give a solderable connection. In Fig. 58.2 a schematic drawing of the sensor prototype is presented. The central heater is suspended on a cavity by means of a bridge structure. The temperature sensors are located

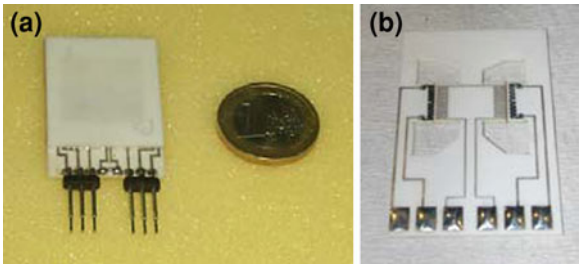

Fig. 58.3 **a** Photograph of the sensor prototype in TFT, **b** Al_2O_3 substrate

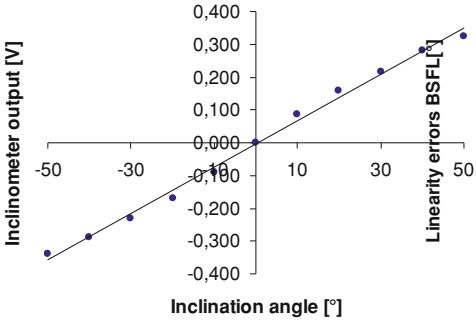

Fig. 58.4 Inclinometer output versus inclination angle

equidistantly on two sides of the heat source. Figure 58.3 shows a photograph of the TFT prototype of the inclinometer sensor. In Fig. 58.3a the central heater and the RTD detectors are clearly distinguishable. In Fig. 58.3b sensing element is presented onto Al_2O_3 alumina substrate.

58.3 Experimental Results

Preliminary tests on the first prototypes show a sensitivity of about 8 mV/° from +50° to 0. Figure 58.4 illustrates, in the case of a constant room temperature, the inclinometer output at different inclination angles. Figure 58.5 illustrates the percentage deviation of the experimental data from the regression line. A maximum error of about 3° can be found in the case of ±50° full scale output. Differently, a lower nonlinearity errors near 0.3° can be obtained adopting a 20° maximum range. The repeatability has been evaluated and a value <0.2° has been observed. Thermal tests from 0 to 50°C show a zero shift of about 0.2%/°C. The supply current is less than 20 mA while the settling time is 1,500 ms at 20°C. Note that the voltage output change for a small inclination angle is relatively small (9 mV for 1°arc), so careful consideration to noise must be applied in the TFT inclinometer design. A noise filter that limits the bandwidth to 1 Hz will display a

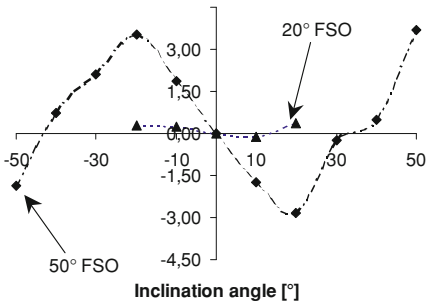

Fig. 58.5 Linearity errors

noise level in the order of 0.1 mVrms. With such an accelerometer the inclination output noise would be less than 0.1°arc rms.

58.4 Conclusion

Using TFT on a ceramic substrate, a new tilt senor based on the heat transfer principle has been developed. The sensor is fabricated from ceramic materials and TFT that results in an accuracy of about 2% full scale output, repeatability of about 0.2° and thermal stability <0.2%/°C over a ±50° range. The TFT tilt sensor is capable of resolving less 0.1°. Finally, the sensor is inexpensive enough to be, in the near future, competitive with other types of commercial tilt transducer.

References

1. Prudenziati nad M, Morten B (1992) The state of the art in thick-film sensors. Microelectron J 23:133–141
2. Brignell JE, White NM, Cranny AWJ (1988) Sensor applications of thick-film technology. IEE Proc Part-I 135(4):77–84
3. Crescini D, Marioli D, Sardini E, Taroni A (2001) Large bandwith and thermal compensated piezoelectric thick-film accelerometer transducer. Sensor Transducer A 87:131–138
4. Crescini D, Marioli D, Ferrari V, Taroni A (1995) Vibration and vibrating sensor in thick-film technology. Mach Vib 4:161–167

Chapter 59
Development of an E-Nose Solution for Landfill and Industrial Areas Emission Monitoring: Selection of an Ad-Hoc Sensor Array

Saverio De Vito, Ettore Massera, Girolamo Di Francia, Carmine Ambrosino, Paola Di Palma and Vincenzo Magliulo

Abstract This contribution focus on the selection of sensor array for the use in olfactive nuisance detection and analysis inlandfill and industrial area chemical emissions monitoring. Electrochemical and polymer based sensors are tested for the use in electronic nose instrumentation for the selected application. Two sites, a landfill and an industrial sites are used as testing locations. Results support the feasibility of usage of a subset of the investigated sensors in such scenarios.

59.1 Introduction

Olfactive nuisance caused by industrial or waste management plants, has recently become an issue of increasing concern. Actually, dynamics of urbanization make more and more probable for this special sites to be located very close or inside urban areas.

Even if released chemicals are not toxic or harmful, olfactive nuisance is a known source of multiple unpleasant effects on human beings ranging from reduced working efficiency to headaches. However, currently there is a recognized lack of instrumental assessment capability for olfactive nuisance. In facts, the characteristics of chemical signals propagation in outdoor and the discontinuous nature of emissions and perception call for the development of a portable sensing device capable of continuous unmanned operations for several hours or days. Real

S. De Vito (✉) · E. Massera · G. Di Francia
ENEA UTTP-MDB C.R. Portici, P.le E. Fermi 1, 80055 Portici, NA, Italy
e-mail: saverio.devito@enea.it

C. Ambrosino · P. Di Palma · V. Magliulo
ENEA/CNR-ISAFOM, via Patacca 85, 80056 Ercolano, Naples, Italy

G. Neri et al. (eds.), *Sensors and Microsystems*,
Lecture Notes in Electrical Engineering 91, DOI: 10.1007/978-94-007-1324-6_59,

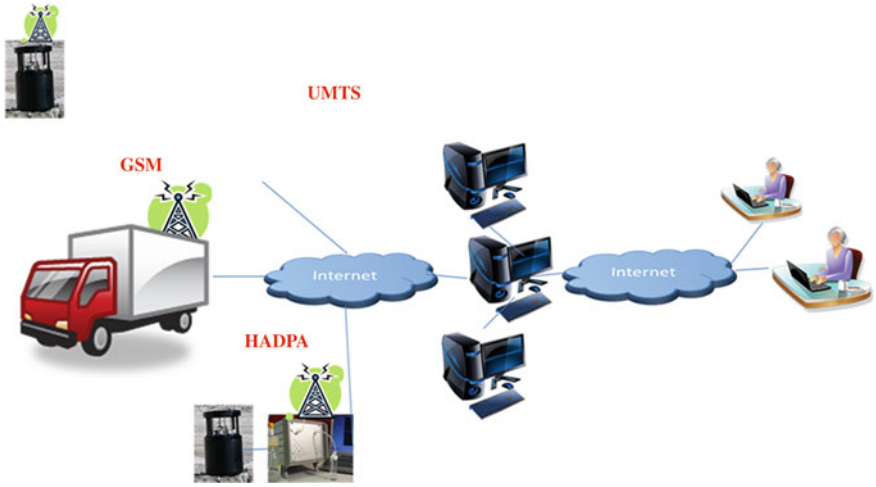

Fig. 59.1 Architectural design of data acquisition, transmission and processing in project SIMMA. Mobile truck mounted conventional analyzers and solid state multisensory devices are integrated in a value added chain for chemical environmental monitoring

emission monitoring will also require networking capability for allowing distributed sensing. Electronic nose technology is now considered the primary candidate for the development of a viable solution and some recent work has explored the usage of a general purpose MOX based e-nose in real setup with very encouraging results [1]. Actually, e-nose fingerprinting capabilities could be exploited not only for nuisance detection but also for source declaration (i.e. identification of the actual nuisance source) from complex plants where different source of emissions are present. However, the research for a customized ad-hoc multisensor device is still open and many solutions are currently under investigation.

ENEA, [2] the Italian agency for new technologies, energy and sustainable economic development, is recently involved in the investigation of artificial olfaction technologies for the development of a network of monitoring devices for real time continuous assessment of waste management plant emissions in Campania region in the framework of the SIMMA Project. The SIMMA project foresee the integration of conventional and innovative solid state multisensory platforms in a self contained hardware and software architecture aiming to empower SMEs to offer distributed chemical monitoring services to public administration entities (see Fig. 59.1).

59.2 Experimental and Results

In this work, we present the preliminary results of a measurement campaign aimed to test on field detection capabilities of an array of electrochemical and polymer based solid state sensors. In our first campaign we selected as measurement site a

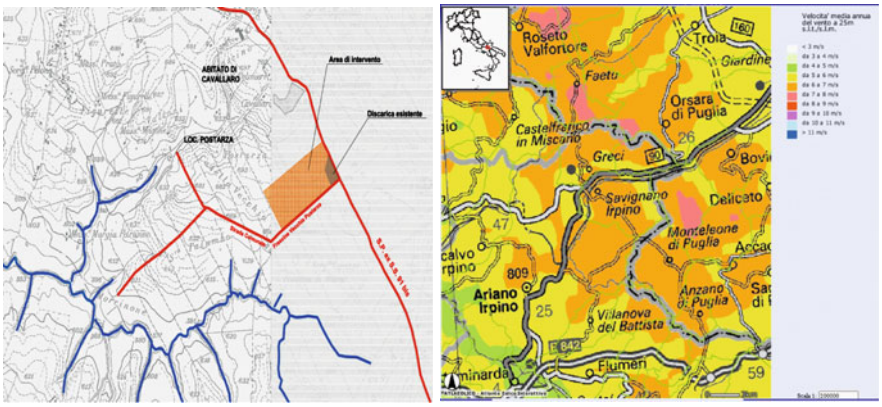

Fig. 59.2 Topographic (**a**) and wind (**b**) maps of the Savignano Irpino Landfill (Loc. Postarza (BN), Italy) where preliminary measurements have been carried out

landfill recently set up for servicing stabilized organic municipal waste fraction (see Fig. 59.2). This class of landfills are source of limited olfactive nuisance with respect to general purpose landfills. The landfill is also characterized by the presence of a biogas and percolating fluids capture installation.

The ENEA NASECANE e-nose (see [3]) has been equipped with a set of seven commercial electrochemical sensors by Alphasense inc., targeting inorganic analytes emissions.

Measurements took place on May, 2009 and sensor responses was recorded for 10 h in multiple sites on the landfill perimeter, wind velocities and directions have also been recorded. Although very preliminary, results seems to support the hypothesis that the EC sensors equipped e-nose are capable to detect inorganic gas emissions from the landfill. In particular, significant variation of the H_2S and CO targeted sensors have been recorded (see Fig. 59.3) with respect to their baseline captured in the control sites (ACQ1, ACQ2 in Fig. 59.3).

A site measurement survey has also been conducted in an Industrial Area that is located in the Caserta province in the north Campania. It hosts several companies industrial sites with core business ranging from chemical to food industry. It is also located near the perimeter of a stabilized municipal waste temporary deposit. As such, multiple potential olfactive nuisance sources are concentrated in a limited area and thus represent a suitable test site for mobile or distributed chemical pollution or olfactive nuisance monitoring architectures. The complete measurement campaign will be conducted jointly by the project partners with the use of two electronic nose systems, a fully equipped mobile air pollution analyzer (Polyproject s.r.l.) and complete meteo stations capable to fully characterize the measurement site microclimatic characteristics (CNR-ISAFOM).The campaign is aimed to locate potential measurement sites,

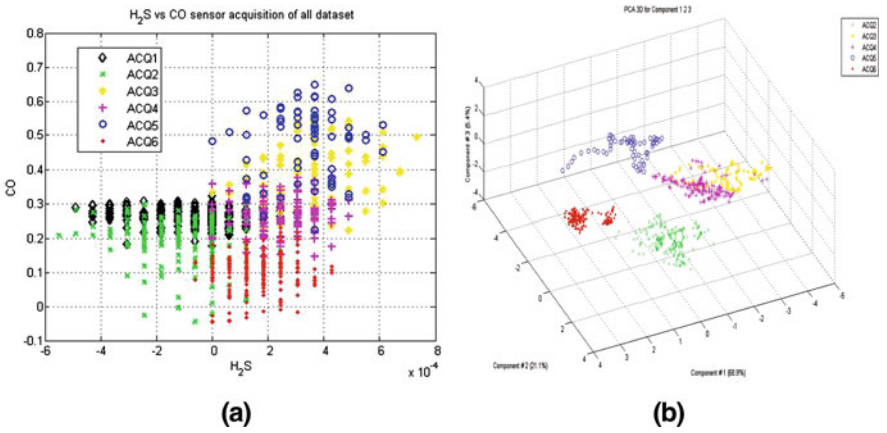

Fig. 59.3 H_2S versus CO sensors scatter plot shows significant variation of respective response while recording at active landfill site (ACQ3, 4, 5) with respect to control sites (ACQ1, 2) (**a**). Site fingerprinting by means of principal component analysis (**b**)

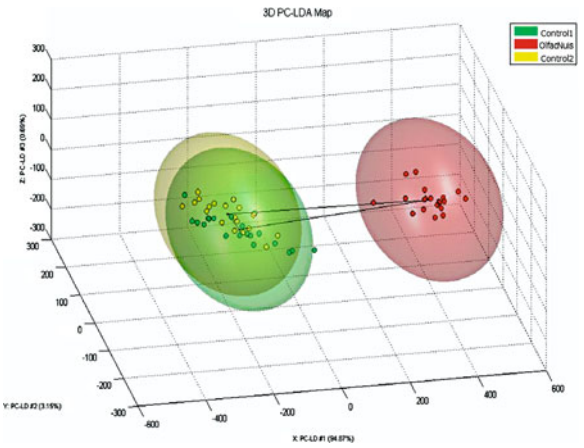

Fig. 59.4 LDA plot for the industrial site survey. A distinct response pattern has been recorded for an area affected by frequent presence of olfactive nuisance with respect to control sites

potential sources and test odour detection and fingerprinting capabilities of the instrumentation under analysis. ENEA is testing the capability of a commercial array of six commercial and non-selective conductive polymer for detecting and discriminating olfactive nuisance sources. During the site survey, the electronic nose response at three locations, one of which was interested by sensible olfactive nuisance were captured analyzed for a total number of 120 acquisitions. Olfactive patterns were analyzed by means of LDA technique and a significant difference in the pattern was measured for the olfactive nuisance affected location with respect to the control locations Fig. 59.4.

59.3 Conclusions

Although very preliminary in a scientific view, the obtained results support the feasibility of usage of a subset of the tested sensors for applications in the selected scenarios.

References

1. Sironi S et al (2007) Development of a system for the continuous monitoring of odours from a composting plant: focus on training, data processing and results validation methods. Sens Actuator B Chem 124:336–346
2. Capelli L et al (2008) Electronic noses for the continuous monitoring of odours from a wastewater treatment plant at specific receptors: focus on training methods. Sens Actuator B Chem 131:53–62
3. De Vito S et al (2007) Analysis of volcanic gases by means of electronic noses. Sens Actuator B Chem 127:36–41

Chapter 60
Artificial Immune Systems: A Novel Approach to Electronic Nose Patterns Classification

Saverio De Vito, Girolamo Di Francia, E. Martinelli, R. Di Fuccio, C. Di Natale and A. D' Amico

Abstract This decade have seen the development of a novel pattern recognition paradigm, named Artificial Immune Systems, based on peculiar features expressed by mammalian immune systems. Apart from some controversy, typical of a newly developed paradigm, AISs semmes to express interesting features that could be exploited also in the field of artificial olfaction. In facts, AO practitioners have been exploring the neural metaphors since years now but have never explored the potentiality of the immune metaphor. In this paper, we experiment the use of AIRS, an AIS based classifier, comparing its performance with the well established FFNN classifier in a typical AO setting. Results are quite interesting highlighting the possibility to introduce AIS in artificial olfaction exploiting their novel features, particularly as regards as drift impact reduction and internal knowledge representation readability.

60.1 Introduction

Artificial olfaction data analysis is an active field of research gaining the attention of many pattern recognition practitioners. Several classical or ad-hoc approaches have been explored or developed for the use in signal processing (drift reduction), explorative data analysis, qualitative olfaction tasks as well as quantitative gas concentration estimation tasks. Most applications rely on the

S. De Vito (✉) · G. Di Francia
ENEA—UTTP-NANO—C.R. Portici, P.le E. Fermi 1, 80055 Portici, NA, Italy
e-mail: saverio.devito@enea.it

E. Martinelli · R. Di Fuccio · C. Di Natale · A. D' Amico
Department of Electronic Engineering, University of Rome "Tor Vergata", Via del Politecnico 1, 00133 Rome, Italy

G. Neri et al. (eds.), *Sensors and Microsystems*,
Lecture Notes in Electrical Engineering 91, DOI: 10.1007/978-94-007-1324-6_60,

use of statistical sub-symbolic approaches ranging from simple use of linear techniques (e.g. PCA, LDA, etc.) to the use of different neural networks based architectures including SVMs [1, 2].

In the last ten years a novel biomimetic approach named Artificial Immune Systems (AIS), based on mammalian immune system analogy, is being explored in different application fields both as a data clustering and pattern recognition architecture [3]. In fact, advancements in immune systems theory have explained their peculiar and rather interesting features like self/non-self recognition, i.e. the capability of identifying the presence of hostile intruders, and memory effects, i.e. the capability of retaining a memory image of the past hostile encounters exploiting it for setting up a fast and efficient immune response to future infections. Actually, these features are recognized as the base of many machine learning paradigms and, in facts, AIS are mainly based on the exploitation of these features in order to build a biomimetic approach for instance-based pattern recognition expressing tuning capabilities for the plasticity/stability trade-off.

Mammalian immune systems theory is primarily based on the concept of an innate immune response embedded in an immune memory cells set. This set evolves in time as immune cells come in touch with different potentially pathogenic intruders, gaining and retaining a "knowledge" of the intrusion that will be useful for setting up a faster, massive response for future encounters. This recognition/evolution/memory framework is characterized by the antibody/antigen binding relationship: basically different B class lymphocytes cells carry different molecular receptors (i.e. the antibody) that bind with peculiar molecular loci on foreign pathogenic materials actually recognizing it by molecular complementarities. These binding events trigger the multiplication of the recognizing B cell (clonal expansion); after the infection, part of these mature cells (clonal selection) are retained in the body building up the immune system "memory" capability.

Here, we explore the possibility to use of AIS for artificial olfaction data analysis while introducing it to the AO community. One of the most recently developed supervised AIS algorithm is Artificial Immune Recognition System (AIRS) based on an idea originally developed by Watkins and Timmis in 2002 [4]. In the AIRS approach, a preliminary memory cells set characterized by their antibodies is generated starting from randomly chosen antigens (training) samples; actually, antibody and antigens are encoded as vectors whose dimensions are equal to data feature space dimensions. Memory cells are then tagged with a particular dataset class so to become one possible representative sample for this particular class. Affinity (computed as vector Euclidean distance) is a key idea for AIRS. Dataset items (antigens) are at this point, presented to the memory set; among all memory cells tagged with the presented antigen class, those showing a low affinity value with it are selected to be cloned. The number of generated clones is controlled with relative affinity. Afterwise, clones undergo a maturation process introducing random mutations. Candidate memory cells showing smaller antigen affinity are selected to be cloned again while the remaining set is discarded. Several cloning/pruning cycles, including a competition for limited resource

Table 60.1 Performance comparison between AIRS and BPNN classifiers at different training/test set partition percentage

Training set percentage	Best AIRS result	Best NN result
10	65.29 (3.77)	69.50 (7.95)
25	78.52 (3.32)	86.29 (3.75)
35	81.74 (2.79)	88.86 (3.27)
50	84.05 (2.57)	91.01 (2.41)
75	87.42 (3.59)	92.93 (2.75)
90	88.99 (5.45)	94.02 (6.03)

For AIRS, 50 different parameter setup have been explored with a total of $50 \times 30 \times 6 = 9000$ training runs. Average correct classification percentages of best performing classifier setup together with computed standard deviations are reported

phase, are carried out until a stop condition, controlled by a user parameter, is reached. The process encompass all training set samples.

At the very end of the process, a compact memory set embedding the immune system knowledge about the training set classes has been developed. A KNN algorithm is then applied to reach the classification of unseen samples.

60.2 Experimental

In this work, we compare the results obtained by a properly trained AIRSv2 algorithm with a classic BPNN approach on a publicly available dataset (Coffee blends, PCA based dataset [5]) at different training/test set partition percentage. The dataset is characterized by 5 MOX sensors steady state readout of the pico-nose response to coffee samples belonging to 7 different blends. Best results are pursued by exploring AIRS, as well as BPNN, parameter space with a brute force approach, i.e. for each partition percentage, a multidimensional matrix of possible parametric setup is explored for obtaining best performance for the two classifier.

For each point in the selected parameter space, 30 training runs have been performed with different random choice of training and test samples and classification performance on test set have been averaged in order to tackle statistical performance variability of the overall model. At each partition, AIRS and NN classification best results have been computed by using WEKA framework (see [6]) and compared while differences have been checked for statistical significance at 95% confidence level.

60.3 Results and Conclusions

Results reported in Table 60.1 show that the generalization performance obtained with the artificial immune system approach are quite comparable with those of one of the best performing statistical classifier used in artificial olfaction community.

NN approach retain a slight advantage as regards as classification results but a deeper analysis of the same results shows how this difference cannot be deemed as significant from the statistical point of view. Here, it is worth to note that generally AIS approaches have been investigated and tuned only for a few years with respect to the well established neural framework and hence are expected to improve their performance figures.

As regards as an architectural comparison, it seems that artificial immune systems are characterized by a significantly higher number of parameters with respect to the NN paradigm. In truth, for the AIRS classifier, a stability analysis reveals that selected best parameters values are almost constant among the different training/test splits analyzed in this work. Furthermore overall performance seems to be strongly related only to the values of a limited (2–3) number of parameters. In particular, stimulation value and affinity threshold scalar, that basically control the number of iteration of cloning/selection cycles and candidate inclusion in the memory cells set, respectively, retain the greatest influence on final classification performances.

We believe that AIS carry significant novelty features both for the preliminary data analysis point of view (clustering, data compression, class related characteristic pattern identification etc.) and from classification point of view. Furthermore they express improved output readability with respect to classical statistical pattern recognition approaches (e.g. neural networks) while having the potential to efficiently represent an evolving knowledge about sensor response that could be potentially exploited for drift effects mitigation.

Acknowledgments Authors wish to thanks Dr. M. Pardo, INFN Sensor Lab, Brescia, Italy for having made publicly available the dataset we have used in this work.

References

1. Hierlemann A, Gutierrez-Osuna R (2008) Higher-order chemical sensing. Chem Rev 108:563–613
2. De Vito S et al (2007) Gas concentration estimation in ternary mixtures with room temperature operating sensors using tapped delay architectures. Sens Actuators B Chem 124:309–316
3. de Castro LN, Timmis J (2002) Artificial immune systems: a new computational intelligence approach. Springer, London
4. Watkins A et al (2004) Artificial immune recognition system (AIRS): an immune-inspired supervised learning algorithm. Genet Prog Evolvable Mach 5(3):291–317
5. Pardo M, Sberveglieri G (2002) Coffee analysis with an electronic nose. IEEE Trans Instrum Meas 51:1334–1339
6. Mark H et al (2009) The WEKA data mining software: an update. SIGKDD Explor 11(1): 10–18

Chapter 61
Innovative Sensor Techniques for Aircraft Maintenance Applications

Giulio Liotti, Roberto De Pompeis, Girolamo Di Francia, Saverio De Vito, Palumbo Pasquale, Vincenzo Della Corte and Giuseppe Del Core

Abstract Aircraft Maintenance Organizations are facing the needs for a significant technology innovation phase due to emerging novel standards and security needs. These are fostered by political and environmental situation characterized by strong commitments for security and "green aircraft" operations. Novel sensing technologies are at the core of this revolution being primary player both in the novel aircraft concept development and for the development of the associated novel maintenance standards. Authors are involved in these efforts by teaming up for the proposition of research initiative that will lead to the development of innovative operative supports and knowledge in the field of aircraft maintenance. In this contribution, key technologies and their state of the art are briefly identified together with their possible application. The technology oriented initiatives proposed by the authors companies are also introduced.

Novel, emerging technologies in the field of optoelectronics, miniaturized multisensors devices and composites are more and more influencing the design and development of the new generation aircrafts. Actually, the strong commitment concerning energy and environmental issues is included in the overall effort aimed to research the potentiality for a broaden application of innovative sensor techniques. A new attention for the potential applications of innovative sensors as dealt in this paper, so far not yet commercially available, is also arising from the

G. Liotti · R. De Pompeis
ATITECH, Palazzo ATITECH, Aeroporto di Capodichino, 80144 Naples, NA, Italy

G. Di Francia · S. De Vito (✉)
ENEA UTTP-MDB C.R. Portici, P.le E. Fermi, 1, 80055 Portici, NA, Italy
e-mail: saverio.devito@enea.it

P. Pasquale · V. Della Corte · G. Del Core
University of Naples "Parthenope", Flight Security Section, CDN Isola C4, 80143 Naples, NA, Italy

G. Neri et al. (eds.), *Sensors and Microsystems*,
Lecture Notes in Electrical Engineering 91, DOI: 10.1007/978-94-007-1324-6_61,

continuous improvements of safety requirements, during flights, and through relevant new aircraft health monitoring systems. In this contribution, we focus on those sensor techniques being in the fastest growing segments of the analytical and sensing instrumentation that can also be used on a broad set of application. In particular, it looks out to hyperspectral technologies and to miniaturized solid state sensor techniques considered as an initial scientific buffer to extend opportunities in the field of aircraft maintenance.

Aircraft maintenance organizations is expected to face this cross-cutting technology still in its development stage in the next future when, for instance, systems for structural health monitoring will be in operation or new standards for engine emissions and health management restrictions will come out. Distributed monitoring of cabin air quality or contamination detection (from many sources including terrorist attacks) by means of miniaturized sensors, is another example of such new requirements. A medium term consequence for the Maintenance and Repair Organization (MRO) should be a possible modification campaign of aging aircrafts to the same extent the digitalization of the flight instrumentation did in the past or the relevant implications connected with new requirements on composite repair procedures.

Extending this scenario, the worldwide aircraft greening initiatives are jumping to the operation phase and moves the research forward the design and certification phases in areas where also the aim of this research policy exert its state of being active.

This contribution present state of art of the above related issues mainly focusing on two types of sensor technologies: (1) miniaturized solid state sensors and (2) Fourier spectrometer imaging and on the data analysis by means of pattern recognition technologies. Finally the ATIMA—Campus project, mainly devoted to the investigations of the above techniques, will be presented.

Distributed solid state sensing research is primarily driven by the amazing evolution of wireless radio communications and embedded computing platforms that is leading to the wireless sensor networks revolution [1]. Application example ranges from environmental monitoring to structural health monitoring [2, 3] and may have a relevant impact on aircraft health monitoring systems giving birth to a new generation of on-line tools for aircraft lifetime health management. Distributed air quality sensing [4], on the other hand, is still in its infancy due to the peculiarity of chemical signal propagation ad solid state chemical sensing state of the art, but it can be recognized as a unique solution to the cabin air quality monitoring issue [5]. Solid state chemical sensing could also be exploited for fuel or hydraulic fluids spills detection during maintenance or routine security checks. This could have a significant impact on the labor hours needed to perform the aircraft maintenance duties. Just as an example, the possibility to classify, in real time and in situ fashion, the primary chemical in contaminations will help to determine the aircraft systems in which contamination has its source, speeding up the labor-intensive inspection task. Contamination detection will be more and more important for the risk associated in adhesive bonding of composites that will become soon a standard for structural maintenance operations. Adhesive bonds of fuel, skydrol or simply water contaminated composites will result in weak bonds

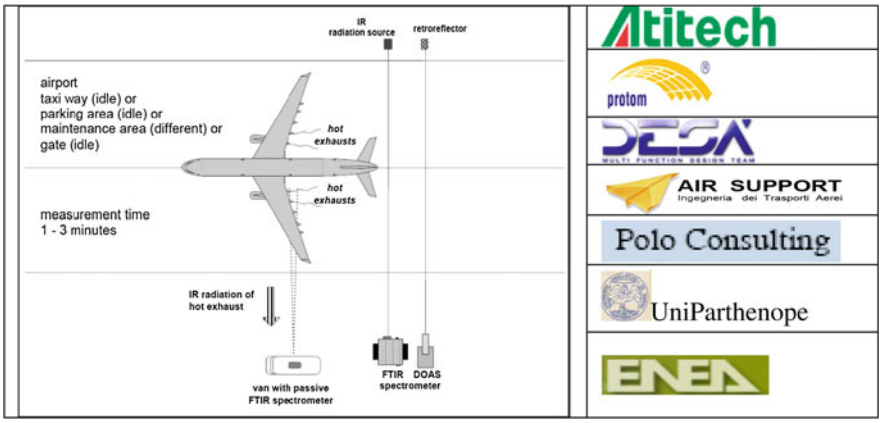

Fig. 61.1 A proposed setup design for aircraft emission measurement based on hyperspectral technologies (combined IR-FTIR-DOAS technique)

with potential security risks. In this scenario, we think that electronic nose based solutions and the associated pattern recognition techniques, could play a significant role in the development of portable instrumentation capable to produce rapid assessment of the possible cause of contamination by identifying and quantifying the contaminant mixture.

Aircraft engines are sources of a complex mix of harming pollutants like NOx, SO_2, O_3, HA, PM, etc. New guidelines to take into account the effects caused by PM10 and PM2.5 are still under evaluation. ICAO will issue standards on precursors of volatile particles from HC as a long term target, and also expects new technology and reliable measurement development.

The measure and the analysis of fine and ultrafine particulates present in exhaust gases has important implications for:

a. the certification of engines for commercial use (Smoke Number);
b. the analysis of combustion efficiency and the evaluation of aging.

The techniques of sampling of aerosols and methods for the analysis in situ of particulate form exhausts can be provided by the adaptation of techniques already developed and used for the analysis of atmospheric sampling (gravimetric techniques and optical detection). In situ detection can be complemented by laboratory IR and Raman spectrometric analysis and optical and electronic microscopy.

In this framework, ATIMA is a three years research and development program sponsored by Atitech aimed to develop tools and techniques for characterizing engine air bleed, venting and exhaust gaseous emissions directed to the aircraft engines health management purposes. It aims at gaining or consolidating information helpful for the engine health management by means of a new technology and to strengthen its contribute to the environmental protection Fig. 61.1.

The collaborative CAMPUS initiative, (financed by Campania regional institutions) by Atitech with the contribution of DESA' Engineering, PROTOM,

Air Support, and Polo Consulting fosters a better integration of the existing local engineering competence, clearly oriented to pursuit scientific knowledge once adapted to the evolving needs and business opportunities in the aeronautical field. In a longer term vision it is expected to enforce the competitiveness of the MRO by providing high value services to the operators, including local airports authorities, and allowing the local partners' entities to participate as producers of the custom ready system for possible routine applications.

The cooperation work programme is structured in three main steps: the first is devoted to the development of a the cited new sensors technologies relying on the contribution of the two research centers ENEA and PARTHENOPE University, the second in designing a prototype system for a mobile customer ready work-station and the third one with "in situ" development testing.

References

1. Lewis FL (2004) Wireless sensor networks. In: Cook DJ, Das SK (ed) Smart environments: technologies, protocols, and applications. John Wiley, New York
2. Lynch JP, Loh KJ (2006) A summary review of wireless sensors and sensor networks for structural health monitoring. Shock Vib Digest 38:91–128
3. Spencer BF, Ruiz-Sandoval ME, Kurata N (2004) Smart sensing technology: opportunities and challenges. J Struct Control Health Monitor 11:349–368
4. De Vito S et al (2008) TinyNose: developing a wireless e-nose platform for distributed air quality monitoring applications. Proceedings of IEEE Sensors Conference 2008, pp 701–704
5. Dechow E (2006) Air quality in airplane cabins and similar enclosed spaces. Springer, Berlin

Chapter 62
Stand-Alone System for Inflammation Analysis

A. Giannetti, C. Trono, F. Senesi, F. Baldini, L. Bolzoni and G. Porro

Abstract In the present paper a novel optical system for the monitoring and measurement of different analytes in Point of Care Testing (POCT) is presented. It is based on an optical biochip constituted by a two-piece polymethylmetacrylate (PMMA) chip, with 13 microchannels through which the analysed sample flows. The sensing layer, where the immunochemical reaction takes place, is located on the bottom side of the upper piece of the PMMA chip. All the electronic, opto-electronic and fluidics component are embedded in a portable instrument that is totally controlled by software. Preliminary tests on C-reactive protein (CRP) and procalcitonin (PCT) immunoassay are reported.

62.1 Introduction

The monitoring and measurement of different analytes is extremely important for physicians to define the etiology of sepsis in Point of Care Testing (POCT). The basis of POCT devices is the need of physicians to have a fast and reliable response near the site of patient care, in order to formulate the right diagnosis or to decide the correct therapy, avoiding to deliver the samples to the central laboratories and to wait for the results of the analysis [1]. In the recent years, the diagnosis in reasonably short times of severe inflammation or sepsis in intensive care has become a strong requirement of physicians. Following an acute-phase

A. Giannetti (✉) · C. Trono · F. Senesi · F. Baldini
Istituto di Fisica Applicata "Nello Carrara" IFAC-CNR, Via Madonna del Piano 10, 50019 Sesto Fiorentino, FI, Italy
e-mail: a.giannetti@ifac.cnr.it

L. Bolzoni · G. Porro
Datamed s.r.l., Via Papa Giovanni XXIII 45, 20090 Rodano, MI, Italy

G. Neri et al. (eds.), *Sensors and Microsystems*,
Lecture Notes in Electrical Engineering 91, DOI: 10.1007/978-94-007-1324-6_62,

stimulus, the circulating concentration of human CRP rises from normal levels of about 1–10 mg L^{-1} up to 20–40 mg L^{-1} for a viral infection or even up to about 500 mg L^{-1} in case of a bacterial infection, also for periods 24–48 h long [2]. Circulating levels of PCT in microbial infections and in various forms of severe systemic inflammation increase several fold, with the increase often correlated with the severity of the condition and mortality [3]. The circulating concentration of human PCT in healthy patients is less than 0.1 μg L^{-1}, but, in the presence of infection, these values can raise up to 100 μg L^{-1}.

In the present paper a novel optical platform for the implementation of fluorescence-based multiple immunoassays is described. Preliminary tests on C-reactive protein (CRP) and procalcitonin (PCT) immunoassay are reported, showing the potentiality of the method.

62.2 Methodology

The heart of the platform is an optical biochip constituted by a two-piece polymethylmetacrylate (PMMA) chip, with 13-microchannels through which the analyzed sample flows (Fig. 62.1a). It is constituted by a transparent cover that allows the light excitation and the fluorescence collection and by a black bottom that strongly reduces the background due the scattered light, coming directly from the optical source.

The cross section of each micro channel is a rectangle 600 μm wide and 50 μm high (Fig. 62.1b). The chip was produced by injection molding by the German company MicroFluidic ChipShop GmbH, on the basis of the IFAC and Datamed design. The sensing layer, where the immunochemical reaction takes place, is located on the bottom side of the upper piece of the PMMA chip. The excitation source is a laser diode emitting at 635 nm (it depends on the emission band of the antibody label, in this case DY647). A laser line ($\sim$10 mm) is generated by means of a cylindrical lens and excites the sensing layer of a channel in all its length. The emitted fluorescence, which comes from the sensing layer, where the specific biologic interaction takes place, is mainly coupled to the PMMA cover of the chip. This occurs thanks to the fluorescence anisotropy, which is exhibited whenever the fluorophore is located at a distance of a medium interface comparable to the emission wavelength. When this condition is satisfied, the fluorescence is mainly directed towards the denser medium with well-defined preferential directions, characterised by angles larger than the total reflection angle of the medium interface. Therefore, great many of the fluorescence emitted by the sensing layer, located at the interface between the rarer liquid medium and the denser PMMA medium, is guided inside the top transparent part of the chip thanks to total internal reflection. The fluorescent signal is laterally collected by a single plastic optical fibre and coupled to a cooled Hamamatsu photodiode. A high-pass filter cuts out the 650 nm light coming from the source and scattered by the PMMA chip. The particular shape of the top of the chip, with suitable air gaps (Fig. 62.1), allows a

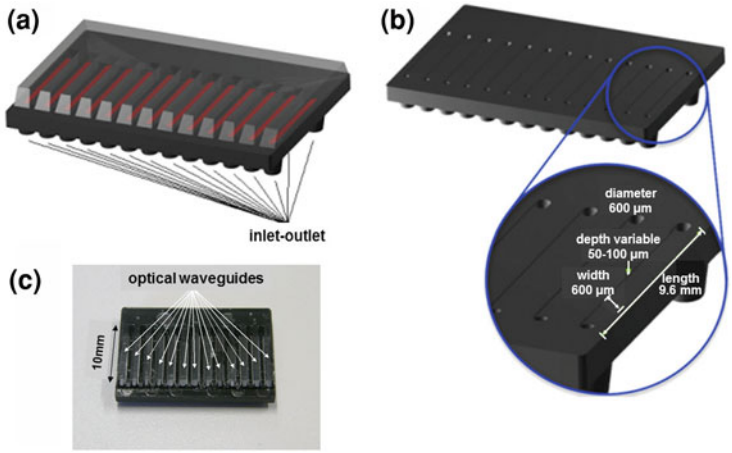

Fig. 62.1 **a** Image of the assembled PMMA chip; **b** bottom part of the chip with the flow channels and the inlet- outlet holes; **c** photo of the biochip

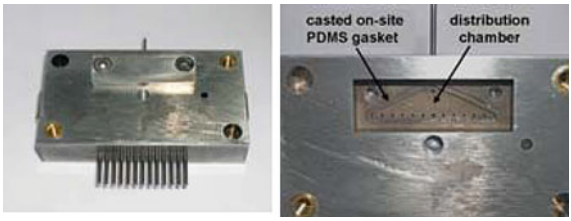

Fig. 62.2 Manifold 1–13 (*left*) and details of the embedded fluidics (*right*)

physical separation of the fluorescent signal coming from the different channels, so that each channel is optically separated from the others. The end-face of the cover is polished at 60° to facilitate the alignment with the collecting fibre and to optimize the light coupling. A motorised translation stage allows the serial automatic scanning of the 13 different microchannels. The optical fibre which interrogates the different channels is moved together with the laser diode, whereas the PMMA chip is motionless. A syringe pump drives the fluids to the chip through a microfluidic manifold and allows to pump the sample under test through the different microchannels. A channel valve allows to select different driving, mixing and delivering configurations. A manifold (one inlet and 13 outlets) allows pumping the sample through the different microchannels at the same time (Fig. 62.2). All the system is embedded into a portable instrument and it is totally controlled by software. The sensing layer is constituted by the capture antibody (clones C5 and PROC1 3G3 for CRP and PCT, respectively) covalently immobilised on the upper surface of the microchannel. Both detection antibodies (clones C7 and PROC4 6C6 for CRP and PCT, respectively) were labelled with the fluorophore DY647 (absorption and emission peaks at 635 and 675 nm, respectively). The conditions for the sandwich assay were: (i) 10-min incubation for the

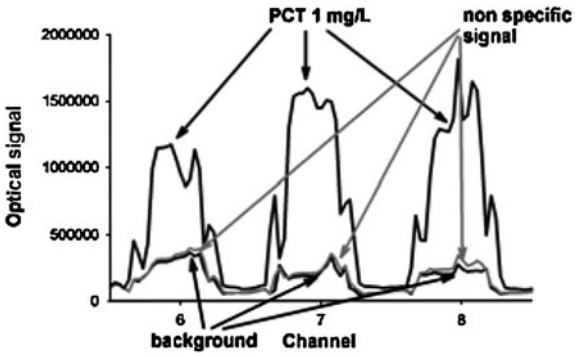

Fig. 62.3 The PCT (1 mg L^{-1}) sandwich assay performed on channels 6, 7 and 8. The response of the sensing layer to non specific interaction is also shown

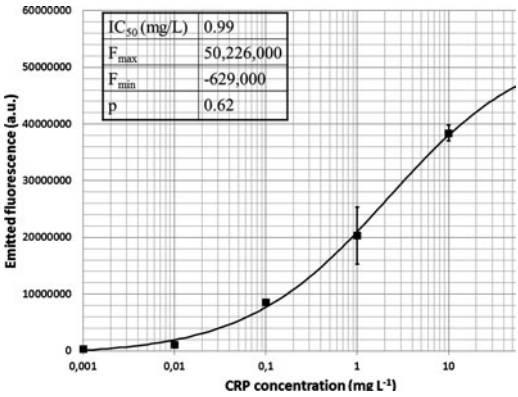

Fig. 62.4 Calibration curve for CRP

antigen, (ii) 3-min washing step, (iii) 10-min incubation of the labeled target antibody, (iv) 3-min washing step. All these steps were performed at a flow rate of 50 μL min^{-1}.

62.3 Results

The performances of the PMMA chip was already investigated with the implementation of the CRP [4] and PCT assay [5] on a single channel, using a spectrum analyzer as detecting system. In this work the capability of the device was tested using the amplified photodetector. The intra-channel reproducibility was studied carrying out the same PCT assay on three different channels. Figure 62.3 shows the achieved result with a concentration of PCT equal to 1 mg L^{-1}. The standard deviation on the three different channels is of the order of 10%, which is comparable with the standard deviation found in biochip based on spotted sensing sites. Figure 62.3 shows for the three channels also the response in the case of non specific interaction between the PCT target antibody (10 mg L^{-1}) and the sensing layer, without any previous pumping of the PCT protein.

Figure 62.4 shows the calibration curve for different concentrations of CRP (from 1 μg L^{-1} up to 100 mg L^{-1}). The fitting with the logistic function

$$y = F_{\max} + \frac{F_{\min} - F_{\max}}{1 + (x/x_0)^p}$$

is also shown where $F_{\max}$ and $F_{\min}$ are the asymptotes of the sigmoidal curve, x_0 is the value of the concentration for which the fluorescence signal is equal to the 50% of the dynamic range and p is a coefficient related to the slope of the curve for $x = x_0$. The standard deviation shown in the figure is evaluated on three replicas performed on three different channels.

62.4 Conclusions

A novel optical system for the interrogation of a 13 microchannel-based biochip was manufactured and characterized. Preliminary results achieved with CRP and PCT immunoassay are very promising.

Acknowledgments This research study was supported by the European Community within the framework of the five-year EU funded project under IST priority, CARE-MAN (HealthCARE by Biosensor Measurements and Networking).

References

1. Annane D, Aegerter P, Jars-Guincestre MP, Guidetand B (2003) Current epidemiology of septic shock. Am J Respir Crit Care Med 168:165–172
2. Ridker PM, Buring JE, Cook NR, Rifai NR (2003) C-reactive protein, the metabolic syndrome, and risk of incident cardiovascular events: an 8-year follow-up of 14, 719 initially healthy American women. Circulation 107:391–397
3. Weglohner W, Struck J, Fischer-Schulz C, Morgenthaler NG, Otto A, Bohuon C, Bergmann A (2001) Isolation and characterization of serum procalcitonin from patients with sepsis. Peptides 22:2099–2103
4. Baldini F, Carloni A, Giannetti A, Porro G, Trono C (2009) An optical PMMA biochip based on fluorescence anisotropy: application to C-reactive protein assay. Sens Actuators B 139:64–68
5. Baldini F, Bolzoni L, Giannetti A, Kess M, Krämer PM, Kremmer E, Porro G, Senesi F, Trono C (2009) A new procalcitonin optical immunosensor for POCT applications. Anal Bioanal Chem 393:1183–1190

Chapter 63
Luminescent Porous Silicon Nanoparticles as Drug Carrier

Vera La Ferrara, Girolamo Di Francia and Giuseppe Fiorentino

Abstract In this work, the applicability of luminescent porous silicon (PS) nanoparticles as ascorbic acid (AA) carrier has been studied. PS nanoparticles have been realized reducing in multi-sized particles porous silicon free-standing film placed in deionized water by sonication and filtering through 0.45 μm membrane. The PS nanoparticles are water-soluble and highly fluorescent. PS nanoparticles are loaded by AA, monitoring the fluorescence spectra by a spectrofluorimeter. Before assessing the loading of AA into PS nanoparticles dispersed in water, the emission stability of PS solution has been acquired. Once stabilized the signal and loaded the AA, the presence and the real absorption of AA onto PS nanoparticles has been evaluated from emission quenching of the silicon nanoparticles.

63.1 Introduction

In recent years, nanomaterials are investigated as potential carriers of drugs. They must have properties of biocompatibility, biodegradability and ability to change their structure depending on the loaded drug. A material with such characteristics is porous silicon (PS). It is one of the most promising system for drug delivery applications. Using hydrofluoric acid-based solutions, nanometer size pores with a high aspect ratio can be realized in silicon wafers. The resultant material is still pure

V. La Ferrara (✉) · G. Di Francia
ENEA Research Center, P.le E. Fermi, 1, 80055 Portici, NA, Italy
e-mail: vera.laferrara@enea.it

G. Fiorentino
Department of Physics, University "Federico II", Monte Sant'Angelo, 80125 Naples, Italy

G. Neri et al. (eds.), *Sensors and Microsystems*,
Lecture Notes in Electrical Engineering 91, DOI: 10.1007/978-94-007-1324-6_63,

silicon, but it shows a strong photoluminescence in the visible region with a large surface area. The nanostructured silicon crystal-lattice scaffold of PS is, then, an ideal matrix for high capacity and efficient drug loading and release. More recently, porous silicon nanoparticles have been used for in vivo monitoring, exploiting their photoluminescence property, loaded with therapeutics and engineered to degrade into benign components that clear renally within specific timescales [1].

In pharmaceutical field, preparations based on vitamins receiving an increasing interest. Ascorbic acid, in particular, also known as vitamin C, naturally occurs in several vegetables and fruit, and it is also present in several biological tissues and multivitamin preparations. Furthermore AA is a medication for liver disease, allergic reactions and atherosclerosis and also helps promote healthy cell development, calcium absorption and normal tissue growth. Because of its importance, development of materials for pharmaceutical preparations has received much attention. Photoluminescent nanoparticles can be a interesting candidate for this application for their unique property originating from quantum size effect [2].

In this work, luminescent nanoparticles (NPs) of porous silicon have been realized and used as potential drug carriers, loading ascorbic acid (AA). Nanoparticles have been obtained by reducing a freestanding film of PS in multi-sized particles by sonication. After a filtration step, optical characterizations of PS nanoparticles suspended in aqueous solution have been acquired by means of a spectrofluorimeter. Porous silicon nanoparticles are water-soluble, stable and have an emission band at about 670 nm. Fluorescence time-signal of NPs solution has been monitored for evaluating the signal change after the addition of vitamin C into the solution. A quenching effect on the emission of porous silicon nanoparticles has been found, suggesting an absorption of ascorbic acid in NPs solution.

63.2 Experimental

Porous silicon nanoparticles have been obtained reducing in size a free-standing film of porous silicon. It is realized by electrochemical etching of p-type monocrystalline silicon, orientation <100> with a resistivity 0.0007–0.0013 ohm cm. The electrochemical anodization has been performed in the usual cell arrangement [3], using a constant current density of 200 mA/cm^2 for 150 s in a 3:1 (v/v) electrolyte of 48% aqueous HF/ethanol. A freestanding film of the porous silicon has been then removed from the crystalline silicon substrate by application of a 4 mA/cm^2 current for 250 s in a solution of 3.3% (by volume) 48% aqueous HF in ethanol. The freestanding hydrogen-terminated porous silicon film was placed in deionized (DI) water and fractured into multi-sized particles by sonication overnight. The particles were then filtered through a 0.45 μm filtration membrane (Millipore). The nanoparticles were further incubated in DI water for about 2 weeks to activate their luminescence in the near-infrared range. All measurements were conducted with a SPEX Fluorolog-3 spectrofluorimeter, with a xenon lamp (450 W) as the excitation light source and a R 928 photomultiplier

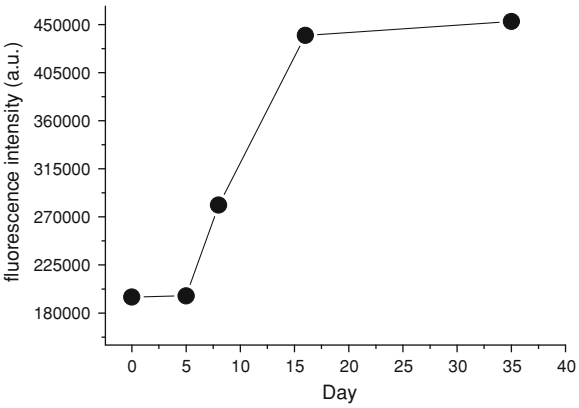

Fig. 63.1 Fluorescence maximum intensity of PS nanoparticles recorded for 35 days

tube powered by 950 V (Hamamatsu Co.) as detector. The excitation wavelength, for all the measurements, has been fixed at 300 nm.

L-Ascorbic acid reagent powders (Aldrich) has been used to study drug loading into porous silicon nanoparticles water solution. AA has been dissolved in distilled water; the solution (0.012 M) has been dropped into nanoparticles dispersion at room temperature and fluorescence change has been monitored.

63.3 Results and Discussion

The fluorescence of the nanoparticles in aqueous solution has been monitored to check the stability of signal. For nearly one month, fluorescence spectra of solution have been acquired, finding an emission band at 670 nm, that becomes stable after 15 days storage in DI water. In Fig. 63.1 the maximum intensity at 670 nm has been plotted during the monitoring time. After the stabilization, 0.012 M ascorbic acid has been added into the nanoparticle dispersion.

In Fig. 63.2 the acquired fluorescence measurements have been plotted and compared for porous silicon nanoparticles, ascorbic acid and PS nanoparticles added with AA solution.

The graph contains two emission peaks corresponding to the water Raman at 370 nm and to 2-nd order transmission through the emission monochromator at 600 nm. Furthermore, the typical band of ascorbic acid at 470 nm and the emission band at 670 nm characteristic of porous silicon are shown.

The comparison between the curves suggests that the presence of ascorbic acid in solution induces a decrease of emission of porous silicon at 670 nm. This indicates the interaction of the organic compound with nanoparticles.

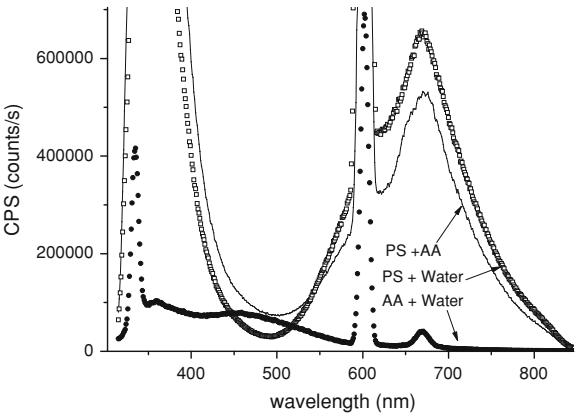

Fig. 63.2 Fluorescence spectra of PS nanoparticles (PS + water), ascorbic acid (AA + water) and PS nanoparticles added with AA (PS + AA)

63.4 Conclusions

Luminescent porous silicon nanoparticles have been realized, starting from free-standing porous silicon film, by sonication and filtering at 0.45 μm. The emission stability of PS solution has been monitored before loading AA. PS nanoparticles are loaded by AA in water, monitoring the fluorescence spectra by a spectrofluorimeter. The presence and the real absorption of AA onto PS nanoparticles has been evaluated from the quenching of porous silicon nanoparticles photoluminescence.

Acknowledgment The authors gratefully acknowledge the Ministry of Universities and Research (MIUR) for financial support as part of Public-Private Laboratory TRIPODE (Technologies and Research for the application of polymers in electronics devices).

References

1. Park J-H, Gu L, von Maltzahn G, Ruoslahti E, Bhatia SN, Sailor MJ (2009) Biodegradable luminescent porous silicon nanoparticles for in vivo applications. Nat Mat 8:331–336
2. Parka HW, Alama SM, Leea SH, Karima MM, Wabaidura SM, Kangb M, Choi JH (2009) Optical ascorbic acid sensor based on fluorescence quenching of Ag nanoparticles. Luminescence 24:367–371
3. Halimaoui A (1997) Porous silicon formation by anodisation. In: Cahnam L (ed) Properties of porous silicon, pp 12–22, ISBN 0852969325

Chapter 64
Range Imaging for Fall Detection and Posture Analysis in Ambient Assisted Living Applications

A. Leone, G. Diraco and P. Siciliano

Abstract The chapter presents an automated monitoring system for the detection of dangerous events of elderly people (such as falls) in AAL applications. In order to provide a self-contained technology solution not requiring neither the environment rearrangement, nor the presence of specialized staff, nor a priori information about elderly characteristics/habitude, the focus is placed on the classification of human postures and the detection of related adverse events. The people is detected through a non-wearable device (a TOF camera), overcoming the limitations of the wearable approaches (accelerometers, gyroscopes, etc.) for human monitoring (the devices are prone to be incorrectly worn or forgotten). The system shows high performances in terms of efficiency and reliability on a large real dataset of falls acquired in different conditions. The posture recognition is carried out by using a topological approach on the 3D points cloud. Experimental results validate the soundness of the posture recognition scheme.

64.1 Introduction

The problem of falls in the elderly has become a health care priority in all industrialized countries due to the related high social and economic costs [1]. Since fall detection is an ill-defined process, it is an interesting scientific problem. Many solutions have been proposed and developed in detection and prevention of falls and recently some methodological and technological classification studies attempt to bring clarity in this plethora [2, 3]. This chapter presents a self-calibrated active vision system (Fig. 64.1) based on the commercial MESA

A. Leone (✉) · G. Diraco · P. Siciliano
Istituto per la Microelettronica ed i Microsistemi, Consiglio Nazionale Delle Ricerche, Via Monteroni, Presso Campus Universitario, Palazzina A3, 73100 Lecce, Italy
e-mail: alessandro.leone@le.imm.cnr.it

G. Neri et al. (eds.), *Sensors and Microsystems*,
Lecture Notes in Electrical Engineering 91, DOI: 10.1007/978-94-007-1324-6_64,

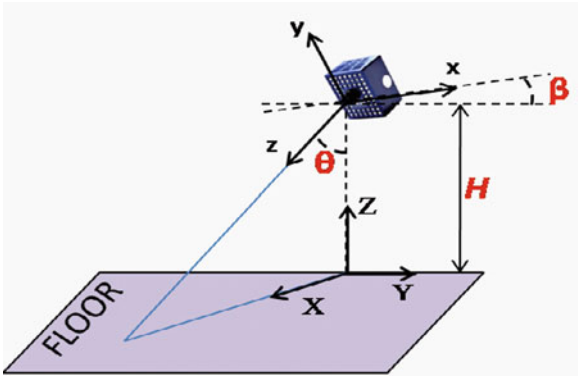

Fig. 64.1 Active vision system setup

SR3000 camera [4] for the real-time detection of dangerous fall events and the recognition of four main human postures in AAL applications.

64.2 Methodology and Experimental Results

The abnormal behaviors recognition is realized according to a tree-level features hierarchy for the characterization of the body position, moving speed and posture dynamics frame-by-frame.

64.2.1 First Feature Level for Critical Events Detection

At the first feature level the body is considered as a whole by extracting 3D position of its centre-of-mass; dangerous events such as falls can be detected by evaluating the height of the centre-of-mass from the floor plane during the time. The external calibration is necessary for the estimation of the camera position and orientation with respect to a world coordinate system (Fig. 64.1); the calibration parameters are estimated by using a coordinate system changing from the camera coordinate system (O_c, x, y, z) to the world coordinate system (O_w, X, Y, Z). The detection of the external calibration parameters (θ, β, H) is accomplished by searching the calibration plane (i.e. the floor plane). The calibration plane is detected by a three-steps strategy: (1) planes detection through a RANSAC [5] approach; (2) planes filtering; (3) external parameters estimation. For segmentation purpose, a Mixture of Gaussians (MoGs) [6] background modeling and a Bayesian segmentation are used (Fig. 64.2). Once the 3D center-of-mass has been computed, the ConDensation [7] tracking strategy allows to link people silhouettes in different time instants.

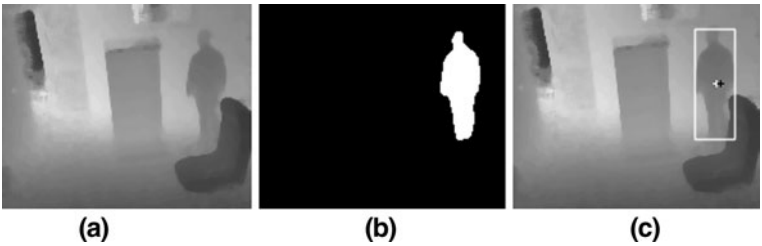

Fig. 64.2 The segmentation (**b**) is accurate on raw depth map (**a**). In white the measured 3D centroid (*cross*) and the bounding box of the blob (*rectangle*) (**c**)

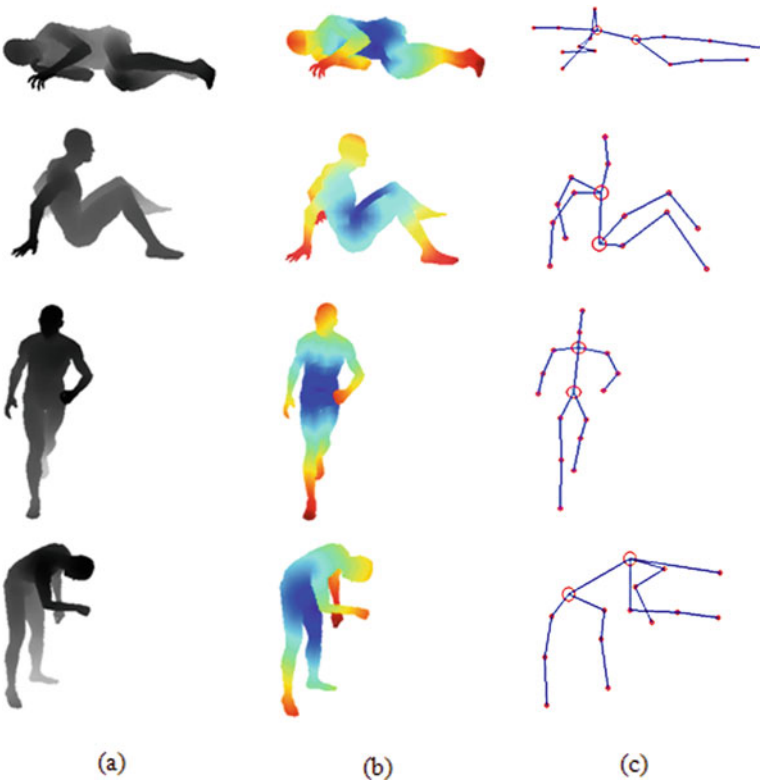

Fig. 64.3 Depth map, Geodesic distance map and skeleton are presented in the columns (**a**), (**b**) and (**c**), respectively. The principal nodes in the skeleton are shown with the bigger *red circles*

64.2.2 Second Feature Level for Critical Events Detection

The second feature level adds posture information allowing to recognize activities more precisely. The body posture is classified on the basis of four main postures (standing, lying, bending and sitting, see Fig. 64.3a). The new feature is the body

Table 64.1 Fall detection efficiency and reliability

Threshold for centroid height (m)	Efficiency (%)	Reliability (%)
0.3	51.1	99.2
0.4	80.0	97.3
0.5	81.3	89.3

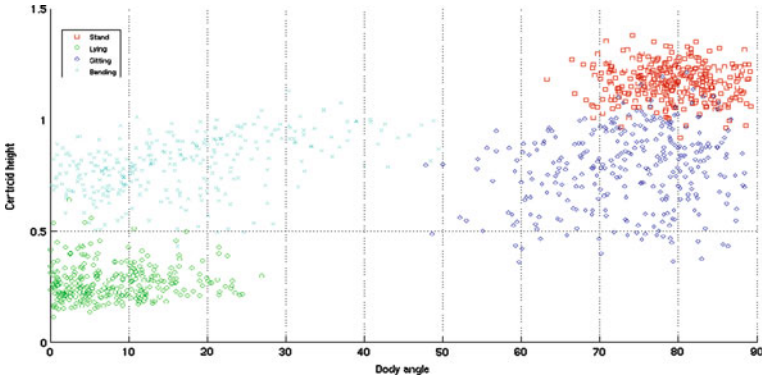

Fig. 64.4 A 2D space is used for the posture discrimination: the torso orientation is reported on the *x-axis* and the centroid distance is reported on *y-axis*. The four clusters are qualitatively well separated

torso orientation: its joined usage with the body centre-of-mass position allows to discriminate the postures. The orientation of the body torso is obtained by extracting the 3D skeleton of the segmented people, according to a Discrete Reeb Graph (DRG) [8]. The prototypal system for posture discrimination has been validated by using synthetic range data in order to have a ground-truth.

64.2.3 Third Feature Level for Critical Events Detection

At the third feature level, the potential of the range sensor is fully exploited by estimating the position of main body parts (head, arms, trunk and legs) and their movements. The use of an unsupervised learning strategy allows the system to detect the occurrence of abnormal situations for a particular elder by discriminating usual and unusual behaviors during the execution of the activities of daily living. The system performance has been evaluated at the first feature level by using a wide dataset of simulated falls acquired in a home-like environment and in quasi-real conditions. The detection of dangerous events (falls) shows high performance in terms of efficiency and reliability (Table 64.1). The employment of the second and third feature levels is yet at the early stage; however the preliminary study carried out by using synthetic data validates the soundness of the proposed posture classification approach (Fig. 64.4).

64.3 Conclusions

This chapter presents an automated method for fall detection in 3D range image that combines information about the 3D position of the centroid of the people with the detection of inactivity. Well-known techniques for background modeling, people segmentation and tracking have been used and the obtained performances demonstrate the goodness of the proposed method in real-time. A novel approach for posture recognition is proposed exploiting the usefulness of topological information for posture discrimination. A preliminary study based on four main postures and synthetic range data allows to validate the approach.

Acknowledgments The presented work has been developed within the Netcarity consortium, funded by the European Commission.

References

1. Elliott S et al (2009) Living alone and fall risk factors in community-dwelling middle age and older adults. J Comm Health 34:301–310
2. Noury N et al (2007) Fall detection—principles and methods. In: Proceedings of the 29th annual international conference of the IEEE EMBS, Lyon, France, pp 1663–1666, 23–26 August 2007
3. Yu X (2008) Approaches and principles of fall detection for elderly and patient. In: Proceedings of the 10th IEEE HealthCom 2008, Singapore, pp 42–47, 7–9 July 2008
4. http://www.mesa-imaging.ch
5. Fischler MA, Bolles RC (1981) Random sample consensus: a paradigm for model fitting with applications to image analysis and automated cartography. Comm ACM 24(6):381–395
6. Lee DS (2005) Effective gaussian mixture learning for video background subtraction. IEEE PAMI 27(5):827–832
7. Isard M, Blake A (1998) Condensation—conditional density propagation for visual tracking. Int J Comput Vis 29(1):5–28
8. Xiao Y, Siebert P, Werghi N (2003) A discrete Reeb graph approach for the segmentation of human body scans. In: Proceedings of the 4th IEEE international conference on 3-D digital imaging and modeling, Banff, Canada, p 378

Chapter 65
Multiple Minima Hypersurfaces Procedures for Biomimetic Ligands Screening

M. Mascini, M. Del Carlo, D. Compagnone, G. Perez, L. A. Montero-Cabrera, S. Gonzalez and H. Yamanaka

Abstract In this work the interaction of the pesticide carbaryl with two groups of biomimetic ligands, peptides and MIPs was screened by multiple minima hypersurfaces (MMH) procedures, through the AM1 semiempirical method. Data related to the properties of the molecular association of the complex biomimetic ligand-pesticide were obtained and compared with another molecular modeling algorithm named Leapfrog, as included in the Sybyl software package, and experimental results from the literature, remarking good correlation between them. All important MMH program parameters (cells number, box size, conformers) were studied and optimized with the aim of getting the minimum computation time without losing the correlation with experimental data. The data demonstrated that MMH approach can be used as a fast biomimetic ligand screening tool for MIPs. In the case of peptides the computation time was not comparable with the molecular dynamics methods conventionally used for this approach.

65.1 Introduction

In the past decade, development of biomimetic ligands such as molecular imprinted polymers (MIPs), aptamers, or peptides has enabled rapid advances as

M. Mascini (✉) · M. Del Carlo · D. Compagnone
Department of Food Science, University of Teramo, 64023 Teramo, Italy
e-mail: mmascini@unite.it

G. Perez · L. A. Montero-Cabrera · S. Gonzalez
Laboratory of Computational and Theoretical Chemistry, Faculty of Chemistry, University of Havana, 10400 Havana, Cuba

H. Yamanaka
Departamento de Quımica Analıtica, Instituto de Quımica, Universidade Estadual Paulista, Caixa Postal 355, 14800-900 Araraquara, SP, Brazil

G. Neri et al. (eds.), *Sensors and Microsystems*,
Lecture Notes in Electrical Engineering 91, DOI: 10.1007/978-94-007-1324-6_65,

alternative candidates to antibodies in the development of affinity-based analytical procedures [1–3]. The use of molecular modelling software potentially offers a great help for the rational design of biomimetic systems with high selectivity and affinity. The strength and type of interactions existing between ligands and target determine the recognition properties of the complex. In principle, the ligands giving the highest binding score are the best candidates for the molecular recognition system preparation [4].

In this paper, we explored the feasibility of a procedure of molecular modeling known as multiple minima hypersurfaces (MMH) through the AM1 semiempirical method, for carbaryl determination by using molecularly imprinted polymer materials and peptides for analyte recognition [5–7]. The combination of semi-empirical quantum chemical procedures for calculating the interaction energies corresponding to local minima of molecular associations together with a statistical thermodynamics approach for calculating a true average of energy association (including entropic contributions) serve for both, the evaluation of effective macroscopic association energies and the possible reduction by average of absolute errors intrinsic to the parametrized Hamiltonian. An appropriate model for comparing experimental and theoretical results are presented by relating some of our results with theoretical and experimental data reported in others works.

65.2 Experimental

All computational procedures were performed by using windows XP platform on an Intel Core 2 Duo CPU 2.1 GHz. Peptides, monomers for MIPs and pesticides were designed and firstly minimized using the software Hyperchem 8.0. All molecules were initially optimized by using molecular mechanic's Amber force field, with the "Steepest Descents" algorithm converging at 0.02 kJ $\times$ mol^{-1} in 32767 as maximum of cycles. After, using Openeye scientific software applications (www.openeye.com) all molecules were compacted in a single file and fast minimized by SZYBKI module. To take into account the flexibility of molecules, conformers were generated for each one by means of the OMEGA module the systematic high-throughput conformers generator by Openeye.

Then the molecules were analyzed using MMH using two kind of minimization keywords: the former "am1 ef mmok t = 3d xyz" for minimizing every single molecule by the semi-empirical method before calculating the complex interaction, and the latter "am1 ef mmok t = 3d geo-ok int" used for minimizing every single cell of the complex ligand-target.

Different MMH parameters were modified, such as the number initial random structure cells from 25 to 100, box sizes from 4 to 10 Å. The temperature was kept at 298 K, the convergence energy at 0.001 kJ $\times$ mol^{-1} and the Tanimoto index at 0.85 for comparing the resulting optimized cluster structures and discarding those being redundant.

Table 65.1 MMH thermodynamic properties, binding scores from Leapfrog and experimental affinity retention of the interactions of carbaryl with peptides (experimental data from Ref. [3]) and monomers used for MIP (experimental data from Ref. [4])

	MMH thermodynamic properties			Leapfrog® binding score (kJ/mol)	Experimental affinity retention (%)
	E-Eo (kJ/mol)	S (j/K × mol)	(A-Eo) (kJ/mol)		
Peptides					
A	−216.0	10.7	−219.2	−94.4	88.6 ± 3.6
B	−68.4	11.2	−72.6	−85.7	51.1 ± 2.1
C	−47.1	17.1	−52.2	DS	59.2 ± 2.4
Monomers					
Allylamine	−36.2	13.6	−40.3	−48.1	ND
AMPSA	−29.7	14.5	−34.1	−32.8	100 ± 1
Acrylamide	−29.3	13.0	−33.1	−29.9	100 ± 1

ND no determined. *DS* discarded by leapfrog. The MMH results were obtained using 4 Å as ½ size box and 100 cells (randomized configurations)

Once the run is completed a file with all summarized statistical results together with the molecule files containing the docked structures were generated. Computation times, thermodynamic properties, association energies (E^{assoc}, kJ/mol), entropies (S, J/mol × K) and association-free energies (A-Eo, kJ/mol) were taken as the main results to study the binding of the complex ligand-target.

The chosen peptides were the following: (A) [N] His-Glu-Pro-Ser [C]; (B) [N] His-Gly-Ser-Ala [C]; (C) [N] Glu-Pro-Ser-Ala [C], as used in a previous work [3], the monomers were acrylamide, 2-acrylamido-2-methyl-1-propanesulfonic acid (AMPSA) and allylamine as used in the work of Sanchez-Barragan et al. [4].

65.3 Results and Discussion

In Table 65.1 are shown the results related to the interaction of the pesticide carbaryl with peptides and MIPs by using MMH procedures. The MMH thermodynamic properties of the molecular association of the complex biomimetic ligand-pesticide were compared with the binding score from another molecular modeling algorithm named Leapfrog, from Sybyl software package, and experimental data from the available literature [3, 4].

From MMH thermodynamic properties, the association-free energies (A-Eo, kJ/mol) gave an idea of the binding energy of the complex. In the case of peptides this energy was very well correlated with the experimental data even better than the Leapfrog algorithm. In the case of monomers the association-free energies were very close to the Leapfrog binding score.

The average time for minimizing one cell was 2 s for monomers and 120 s for peptides, respectively. In order to get the minimum computation time for MMH runs the number of the randomized configurations was decreased from 100 to 25

but even if the association-free energy did not change significantly, following the relative populations of the states parameter (n/N) the set of cells that could represent the most significant contributions decreased drastically form 5 to 1. Also the dimension of the ½ size box was changed from 10 to 4 Å remarking an increase of the association-free energy. A length less than 4 Å caused a steric hindrance of the complex resulting in significant configuration failures.

To overcome the strong limitation of considering molecules as rigid, the openeye software OMEGA generated ten representative possible shapes for each molecule. The peptide and monomer conformer database was screened against the pesticide conformers database. The conformers average of energy had a variation of less than 10% for all cases demonstrating that the MMH run can be done using just one representative conformer for peptides, monomers or pesticide, and saving computation time.

65.4 Conclusions

An experience with the AM1 semiempirical minimization method for biomimetic ligand-pesticide complexes by considering the statistical treatment of their multiple minima hypersurfaces was shown. The data demonstrated that MMH coupled with AM1 semiempirical approach can be used as a fast biomimetic ligand screening tool for MIPs, although the computation time was not comparable with the conventional molecular dynamics methods used for this approach in the case of peptides. Additional work is under progress to change the minimization method within MMH to reduce computation time in molecular systems like peptides.

Acknowledgments This work was supported by the 7th Framework Programme Marie Curie Actions People IRSES N°230849 Biomimic.

References

1. Navani NK, Li Y (2006) Nucleic acid aptamers and enzymes as sensors. Curr Opin Chem Biol 10:272–281
2. Tombelli S, Minunni M, Mascini M (2005) Analytical applications of aptamers. Biosens Bioelectron 20:2424–2434
3. Mascini M, Sergi M, Monti D, Del Carlo M, Compagnone D (2008) Oligopeptides as mimic of acetylcholinesterase: from the rational design to the application in solid-phase extraction for pesticides. Anal Chem 80(23):9150–9156
4. Sanchez-Barragan I, Karim K, Costa-Fernandez JM, Piletsky SA, Sanz-Medel A (2007) A molecularly imprinted polymer for carbaryl determination in water. Sens Actuators B 123:798–804
5. Montero LA, Esteva AM, Molina J, Zapardiel A, Hernandez L, Marquez H, Acosta A (1998) A theoretical approach to analytical properties of 2,4-diamino-5-phenylthiazole in water solution. Tautomerism and dependence on pH. J Am Chem Soc 120(46):12023–12033

6. Montero LA, Molina J, Fabian J (2000) Multiple minima hypersurfaces of water clusters for calculations of association energy. Int J Quantum Chem 79:8–16
7. Codorniu-Hernandez E et al (2005) Essential amino acids interacting with flavonoids: a theoretical approach. Int J Quantum Chem 103:82–104

Chapter 66
Electrochemically Synthesized Molecularly Imprinted Polymers for Sensing Applications

Elisabetta Mazzotta and Cosimino Malitesta

Abstract A novel imprinting scheme, combining for the first time electropolymerization with metal-ion coordination, has been proposed. A MIP for a pesticide (4-(2,4-dichlorophenoxy)butyric acid (2,4-DB)) has been prepared from a Co-porphyrin (Co(III)tetrakis(o-aminophenyl) porphyrin (CoTAPP)) as functional monomer. Such an approach aims to combine advantages of electropolymerization with ones related to the use of metal complexes in imprinting procedures. After verification of template entrapment and subsequent removal by XPS spectroscopy, the imprinting effect was verified by comparing electrochemical responses of MIP and not-imprinted polymer (NIP) tested by Cyclic Voltammetry (CV). MIP revealed an enhanced electrocatalytic activity towards 2,4-DB reduction as well as a good selectivity against both pesticides and structurally related compounds.

66.1 Introduction

Considerable scientific research is devoted to the development of tailor-made receptors capable of recognizing and binding the molecular target with high selectivity. Molecularly Imprinted Polymers (MIPs) have peculiar recognition properties due to imprinted cavities formed during polymerization process whose size, shape and three-dimensional arrangement of binding sites are determined by the structure of the template molecule [1]. A molecular memory is thus introduced into the polymer that is able to recognize the template and to selectively interact with it [1]. MIP-based sensors attract increasing attention on account of their specificity,

E. Mazzotta (✉) · C. Malitesta
Laboratorio di Chimica Analitica, Dipartimento di Scienza dei Materiali, Università del Salento, via Monteroni, 73100 Lecce, Italy
e-mail: elisabetta.mazzotta@unisalento.it

G. Neri et al. (eds.), *Sensors and Microsystems*, Lecture Notes in Electrical Engineering 91, DOI: 10.1007/978-94-007-1324-6_66,

stability, robustness and low cost [2]. Among different strategies proposed for MIP integration with the transducer, MIP electropolymerization has emerged as an effective way of synthesizing and anchoring MIP to the transducer surface [3]. It allows polymeric films to be easily grown adherent to substrate with a controlled thickness. During the last decade, several electrosynthesized MIPs have been proposed as recognition element, particularly in electrochemical sensors (see e.g. [4, 5]). Nevertheless, only recently this approach has been extended to the preparation of metal complexes MIPs [6] although metal coordination has emerged as a promising opportunity in imprinting field [7] due to the related advantages (no influence of solvent environment, rapid rebinding kinetics, possible electrocatalytic activity).

The present work describes the assembly of a voltammetric sensor for 2,4-DB based on the electropolymerization of a metal complex based MIP. Template removal from imprinted cavities was verified by XPS analysis. MIP electrode showed an enhanced electrocatalytic activity in comparison to Not Imprinted Polymer (NIP) as well as a good ability to reject some potential interfering compounds as commonly used pesticides or substances structurally similar to template.

66.2 Experimental

4-(2,4-dichlorophenoxy)butyric acid (2,4-DB), 4-(2,4-dichlorophenoxy) propionic acid (2,4-DP), dichloroacetic acid (DAA), phenoxyacetic acid (POAA), 4-chlorophenylacetic acid (PAA), 4-chlorocatechol, 2-chlorophenol and tetrabutylammonium hexafluorophosphate ($TBAF_6P$) were of analytical grade and were used as received from Sigma–Aldrich, as all other chemicals employed. Co(III)tetrakis(o-aminophenyl) porphyrin (CoTAPP) was from Frontier Scientific (UK). Acetonitrile (ACN) and methanol (MeOH) were of HPLC quality. CoTAPP and 2,4-DB solutions were in $TBAF_6P$ 0.1 M/ACN.

Electrochemical experiments were carried out with a computer-controlled potentiostat CHI 620A (CH Instruments) interfaced with a conventional three-electrode cell. A Pt disk (surface area 0.0314 cm^2), a Pt wire and an Ag/Ag^+ 0.1 M in ACN were used as working, counter and reference electrode, respectively. For XPS characterization film was deposited on a Pt foil (exposed area 0.8 cm^2). XPS measurements were performed with a Leybold LHS10 spectrometer upgraded with a PHOIBOS 100/MCD5 analyser–detector system (Specs) and equipped with a twin-anode (MgKα/AlKα) non-monochromatic source (operated at 200 W *ca.*). The binding energy (BE) spectrometer scale was calibrated by assigning BE $Cu2p_{3/2} = 923.6$ eV, BE $Au4f_{7/2} = 84.0$ eV. Charging correction was performed by use of adventitious carbon calibrant (BE C1s = 284.8 eV).

MIP and NIP were electrosynthesized as previously described [6]. MIP was then washed 24 h in MeOH under stirring. XPS spectra of pristine and washed MIPs were acquired.

MIP electrocatalytic properties were studied by CV between −0.1 and −1.7 V (scan rate 100 mV/s) in the presence of 2,4-DB (200 μM−1 mM) in $TBAF_6P$

0.1 M/ACN. MIP selectivity was evaluated by testing its response to some interferences (2,4-DP, DAA, PAA, POAA, 4-chlorocatechol and 2-chlorophenol) at a concentration of 200 μM. In all electrochemical experiments a nitrogen flow was left over the solution.

66.3 Results and Discussion

66.3.1 Evaluation of Template Removal After Washing by XPS Analysis

The signal of Cl2p has been used as a marker for the presence of 2,4-DB in MIP imprinted cavities before and after washing treatments. Figure 66.1 reports the comparison between Cl2p detailed spectra in MIP before (Fig. 66.1a) and after (Fig. 66.1b) washing. It is evident that almost the total amount of chlorinated compound was removed from imprinted matrix after washing treatment. Cl/N ratio equal to zero was evaluated in washed MIP being equal to 0.058 in pristine film.

As shown in Fig. 66.1, pristine MIP exhibited the presence of two distinct Cl species that could be related to the existence of two different populations of binding sites. One could be due to coordination with Co centers and another one could be based on hydrogen bonds with free amino groups of the electrosynthesized polymers [8]. Finally, it was observed that such washing procedure did not determine any Co removal, contrarily to other tested washings in ACN (results not shown). A similar value of N/Co ratio is in fact evaluated in pristine and washed MIPs equal to 8.6 and 8.7, respectively.

66.3.2 Electrochemical Detection of 2,4-DB by Imprinted Electrode

Imprinting effect was verified by exposing MIP to increasing 2,4-DB concentration. A typical MIP-based sensor CV response to 2,4-DB 400 μM is reported in Fig. 66.2a (solid curve). MIP clearly exhibited a catalytic effect in the reduction of the analyte that determined an increase of Co(II)/Co(I) peak current at about −1.4 V. NIP based electrode (Fig. 66.2a, dashed curve) showed evidently a much lower response. 2,4-DB electroactivity on bare Pt was also analyzed under the same experimental conditions and no significant response was observed.

Figure 66.2b reports a comparison between calibration curves at MIP- and NIP-modified electrodes. It is evident that sensitivity was significantly enhanced by MIP-modified electrode. Also an appreciable improvement of response reproducibility was observed on MIP sensor with an average relative standard deviation of only 12%, much better than that on NIP sensor equal to 34%.

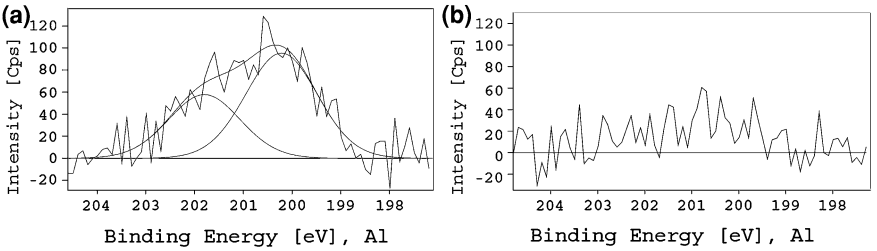

Fig. 66.1 XP spectra of Cl2p region for pristine MIP (**a**) and washed MIP (**b**)

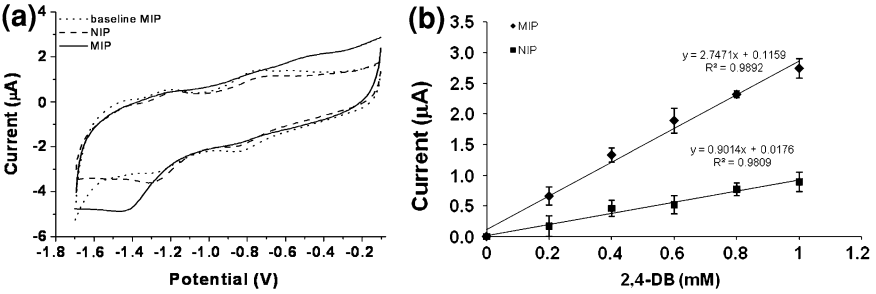

Fig. 66.2 **a** CV responses to 2,4-DB 400 μM by MIP (*solid curve*) and NIP (*dashed curve*) in $TBAF_6P$ 0.1 M/ACN (scan rate: 100 mV/s). Dotted curve represents CV recorded at MIP electrode in the absence of 2,4-DB. **b** 2,4-DB calibration plots at MIP- and NIP-modified electrodes. Current values refer to the mean of triplicate measurements on freshly prepared films

Table 66.1 Results of interference study. I.R. represents Interference Ratio calculated as the ratio between MIP response to 2,4-DB 200 μM and to each interference 200 μM

Interference	I.R.
2,4-DP	1.8
DAA	1.8
PAA	2.3
POAA	2.9
4-chlorocathecol	5.3
2-chlorophenol	∞

Results of MIP selectivity are shown in Table 66.1. Interference Ratio (I.R.) for each tested molecule was calculated as the ratio between MIP response to 2,4-DB and to each interference both at a concentration of 200 μM.

It is particularly interesting to observe that MIP-based sensor exhibited a very good selectivity against 4-chlorocatechol and it does not show any response to 2-chlorophenol.

66.4 Conclusions

In the present paper the development of a novel Co-porphyrin based MIP was presented. XPS characterization provided the evidence of template—a toxic organohalide, 2,4-DB—entrapment in MIP matrix as well as the successful removal of the template from the imprinted cavities. The developed MIP was successfully applied to the electrocatalytic detection of the template by CV. Also results of selectivity test were satisfactory, particularly MIP ability to reject chlorophenols, confirming a remarkable imprinting effect for the polymeric matrix.

References

1. Ye L, Haupt K (2004) Molecularly imprinted polymers as antibody and receptor mimics for assays, sensors and drug discovery. Anal Bioanal Chem 378:1887–1897
2. Holthoff EL, Bright FV (2007) Molecularly templated materials in chemical sensing. Anal Chim Acta 594:147–161
3. Malitesta C, Losito I, Zambonin PG (1999) Molecularly imprinted electrosynthesized polymers: new materials for biomimetic sensors. Anal Chem 71:1366–1370
4. Blanco-Lopez MC, Gutierrez-Fernandez S, Lobo-Castanon MJ, Miranda-Ordieres AJ, Tunon-Blanco P (2004) Electrochemical sensing with electrodes modified with molecularly imprinted polymer films. Anal Bioanal Chem 378:1922–1928
5. Ozcan L, Sahin Y (2007) Determination of paracetamol based on electropolymerized-molecularly imprinted polypyrrole modified pencil graphite electrode. Sensor Actuat B 127:362–369
6. Mazzotta E, Malitesta C (2008) Preliminary study on electrosynthesis of a Co-porphyrin based molecularly imprinted polymer for the selective detection of the herbicide 2,4-dichlorophenoxy carboxylic acid. Sensor Lett 6:618–622
7. Dhal PK (2001) Metal-ion coordination in designing molecularly imprinted polymeric receptors. In: Sellergren B (ed) Man-made mimics of antibodies and their applications in analytical chemistry, molecularly imprinted polymers. Elsevier Science, Amsterdam, pp 185–201
8. Gómez-Caballero A, Ugarte A, Sánchez-Ortega A, Unceta N, Goicolea MA, Barrio RJ (2010) Molecularly imprinted poly[tetra(o-aminophenyl)porphyrin] as a stable and selective coating for the development of voltammetric sensors. J Electroanal Chem 638:246–253

Chapter 67
Wireless Energy Consumption Monitor

Massimo Merenda, Demetrio Artuso and Francesco G. Della Corte

Abstract In this work, a wireless energy consumption monitor made up of a current transformer with its analog interface and an 8-bit microcontroller that acquire sensor's data is presented. The whole system is wireless connected to a PC through a Bluetooth module for the sending of the data that are managed and collected by the host software developed in LabVIEW, a multiplatform graphical programming environment. A digital programmable potentiometer have been used to allow the system's electronic to dynamically tune the sensitivity of the measurement by means of the firmware implemented in the μC that let to obtain both result accuracy and a fast convergence of the algorithm. The entire design address the need of the reduction of the electronic system's energy consumption with the utilization of advanced low power technique both hardware and software.

67.1 Introduction

Electricity monitors help user to be aware of the amount of electricity they are using and wasting, allowing them to predict the amount of their bill and to optimize energy consumption in a world that is requiring even more attention to energy waste.

The link with the Bluetooth technology allows every user with an entry-level PC to collect and manage dynamic power consumption data from on-board sensors.

M. Merenda (✉) · D. Artuso · F. G. Della Corte
Dipartimento di Informatica, Matematica, Elettronica e Trasporti (DIMET),
Università degli Studi "Mediterranea"di Reggio Calabria,
Via Graziella Loc. Feo di Vito, 89060 Reggio Calabria, Italy
e-mail: massimo.merenda@unirc.it

G. Neri et al. (eds.), *Sensors and Microsystems*,
Lecture Notes in Electrical Engineering 91, DOI: 10.1007/978-94-007-1324-6_67,

The digital potentiometer allows to change dynamically the level of signal which is obtained from the current transducer. Specifically, it allows to amplify or to reduce the level of signal with the aim of adapting this one to the input scale of the ADC inside the microcontroller and also to tune the sensitivity of the measurement. All the operations are governed from an 8-bit general purpose Microchip microcontroller.

67.2 Experimental

Wireless energy monitors have two parts. A sensor which simply clips around the outside of one of the wires at the point of measurement and a battery operated transmitter unit which sends the information picked up by the sensor by means a Bluetooth module. The time in which there is no wireless link with an host PC for the data download, the historical data are safely stored in an on-board EEPROM up to 2 months. The operations of the Software of the Host PC as connection with the transmitter unit and the data download are fully automated at the start of the application.

Current transformers (CT) are simple and inexpensive devices for measuring current waveforms that provide electrical isolation from the rest of the circuit.

AC CTs are based on the magnetic coupling principle, consisting of a toroidal ferromagnetic core, on which a copper wire of n turns is wound [1]. The secondary winding is terminated with a sense resistor or burden resistance R. The principle of operation of AC CT is based on the combination of both Ampere's and Faraday's laws [2] (Fig. 67.1).

Current waveforms that are observed by the CTs can be non-sinusoidal waveforms. Also for this reason, the measurement are carried out obtaining the Root Mean Square (RMS) value of the current that flow into the R resistor, that is indeed in relationship with the primary current value as specified in the datasheet of the device, depending of the number of windings and the characteristics of the ferromagnetic toroidal core. The true RMS value is obtained by sampling 100 current values, spaced 2.5 ms each other.

The burden resistance value has influence on the sensitivity of the system. A digital programmable potentiometer that allows the system's electronic to select dynamically the optimum resistance value for the single measurement has been used as burden resistance in our work, allowing the tuning of the sensitivity in a selectable numbers of iterations. This choice is a trade-off between result accuracy and a fast convergence of the algorithm.

Data that are managed and collected by the host software developed in LabVIEW, that is a graphical programming environment used by millions of engineers and scientists to develop sophisticated measurement, test, and control systems. The developed LabVIEW software, shown in Fig. 67.2, is multiplatform and allows the user to monitor real time power consumption, historical and average data and to add, name, and select the appropriate tariff for up to 5 sensor

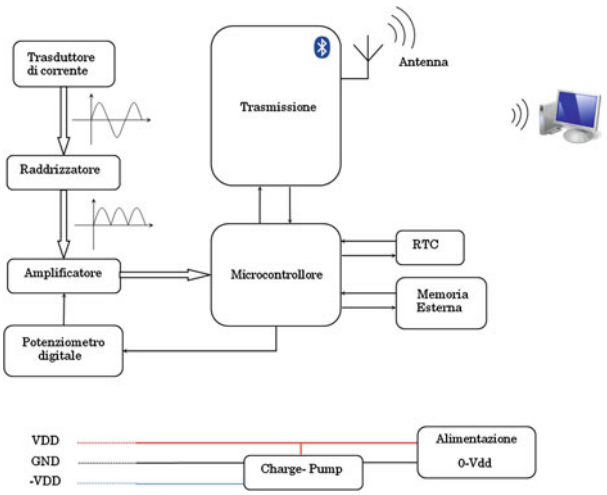

Fig. 67.1 Block diagram of the system

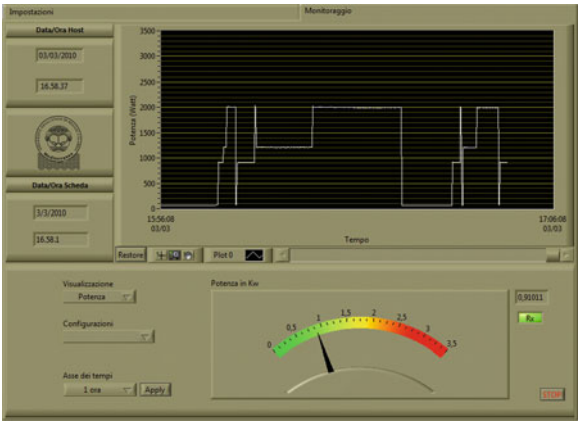

Fig. 67.2 Software—front panel

units that can be monitored and charted in the screen. LabVIEW software also allows the user to calibrate remote sensors and to check battery charge status.

67.3 Results

Valuable results both as performance and power consumption have been obtained. The following table summarizes the specifications of the realized device (Table 67.1).

Table 67.1 Specifications

Parameters	Min	Typ	Max	Unit
Input voltage range	3.5		6	V
Memory			1024	kbyte
Range of transmission		100	250	m
Resolution		2.3		W
Measurement range	0.01		50	A
Data transmission interval		5	9	sec
Current consumption	1.5	2.3	4.62	mA
Current consumption in download phase	17		23	mA
Battery lifetime (2000 mAh)	18	30	40	days

Fig. 67.3 Realized device

In order to measure the power consumption of the device, several tests have been carried out using LabVIEW software and a digital multimeter, showing an average consumption of 2.3 mA at 3.3 V.

In Fig. 67.3 the realized device is showed into a IDG-B enclosure designed to mount onto a DIN-rail (EN50022) with a snap-in clip.

67.4 Conclusions

A Wireless Energy Consumption Monitor with current transformer connected to a PC through a Bluetooth module has been realized. Results show that an application specific algorithm allows the tuning of the sensitivity in a selectable numbers of iterations. The used set-up allows to measure AC current from 0.01 to 50 A, with a current resolution of 10 mA in the whole range of measurement. The error in I_{RMS}, estimated by comparison with a calibrated amperometer, is ± 10 mA.

References

1. Kondrath N, Kazimierczuk MK (2009) Bandwidth of current transformers. IEEE Trans Instrum Meas 58(6):2008–2016
2. Paul R (2005) Electromagnetics for engineers with applications. Wiley, New York, pp 186–188

Chapter 68
Remotely Powered Smart RFID Tag for Food Chain Monitoring

Massimo Merenda, Francesco G. Della Corte and Marcello Lolli

Abstract The pervasiveness of RFID technology in novel application fields, such as agriculture and food chain integrated management, is related to the addition of sensor and computational capabilities to the systems, and as a consequence, their powering become a challenge. Passively powered devices, such as inductively coupled passive HF RFID systems, utilize an external electromagnetic field to operate without an internal power source. This paper presents a battery-less RFID sensor useful to create a safer and more manageable food supply chain of perishable comestibles.

68.1 Introduction

The system is an improvement of a previous one [1], and includes a temperature sensor with its interface circuit, a microcontroller for the acquisition of data and for managing the TX and RX functions emulating a 13.56-MHz RFID transponder. The surplus of power required for the additional components needs a rethinking of the basic power supply system of an HF RFID passive tag. For this reason, a DC/DC buck converter is a part of a RF energy scavenging circuit used for gathering from an external RFID reader the energy required for powering the whole Smart Tag.

M. Merenda (✉) · F. G. Della Corte
Dipartimento di Informatica, Matematica, Elettronica e Trasporti (DIMET),
Università degli Studi "Mediterranea" di Reggio Calabria,
Via Graziella Loc. Feo di Vito, 89060 Reggio Calabria, Italy
e-mail: massimo.merenda@unirc.it

M. Lolli
Smart Res Spa, Via Dei Marmorari, 84, 41057 Spilamberto (MO), Italy

G. Neri et al. (eds.), *Sensors and Microsystems*,
Lecture Notes in Electrical Engineering 91, DOI: 10.1007/978-94-007-1324-6_68,

68.2 Experimental

The system's operation can be summarized as follow. When the RFID reader beams the RF field, an external LC resonator induces an AC voltage that generates DC voltage through a full-wave rectifier. A DC/DC buck converter then uses the generated DC voltage to create a stable supply voltage for the circuits. When the chip enters the RF field's vicinity, the digital controller restart from the initial state. To communicate with a reader via the RF link, the chip uses the load modulation in a back-scattering manner to send data back. It uses a demodulator to detect an encoded command signal sent from a reader.

The RFID energy harvesting is generally achieved with a fine tuning of the resonance of the tag antenna coil and of the voltage regulator. The input of the latter is the output voltage induced on the antenna from the RFID reader (Fig. 68.1).

For the purpose of the actual work, the antenna was outlined with copper wire using a patented INLAY-LESS technique from Smartres S.p.A. on flexible adhesive substrate realized in different sizes for matching different working situations (Fig. 68.2).

An high efficiency step-down DC/DC buck converter has been designed, using a Linear LTC3632 IC that draws only 12 μA typical DC supply current at no load while maintaining output voltage regulation.

The converter has a wide 4.5–50 V input range and internal overvoltage monitor capable of protecting the part through 60 V surges and can supply up to 20 mA load current and features a programmable peak current limit that provides a simple method for optimizing efficiency in lower current applications.

Additionally, it includes a precise run threshold and soft-start feature to guarantee that the power system start-up is well-controlled in any environment (Fig. 68.3).

68.3 Results

DC/DC buck converter test results showed an efficiency greater than 85% regardless the input voltage value, ensuring at the same time an improvement in the functioning distance of about 1 m for the system, with output voltage as low as 1.8 V in order to supply power to an Extreme Low Power microcontroller. The following table summarizes the functioning distances at various load resistance of the DC/DC buck converter at a fixed output voltage of 3.3 V (Table 68.1).

From the sensor point of view, the resolution of the system could be 0.01°C, corresponding to 5 mV across the NTC. However, the used NTC shows a 0.1°C resolution in the 10–40°C temperature range, fixing the total system resolution to this value.

In Fig. 68.4 the realized device is showed. The spiral integrated antenna can be seen. The flexible PCB area is 50×50 mm^2.

Fig. 68.1 The smart RFID tag used to monitor wine temperature

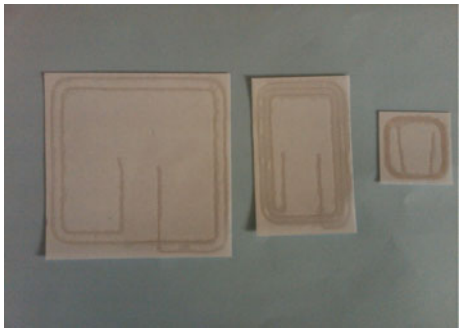

Fig. 68.2 Prototype antenna on flexible adhesive substrate

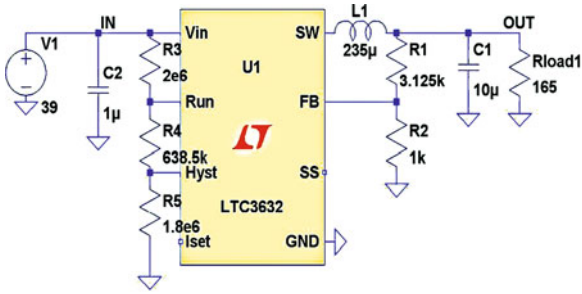

Fig. 68.3 Schematics of DC/DC buck converter

68.4 Conclusions

A smart RFID tag with a temperature sensor has been presented. Data is transmitted by means of an 8-bit microcontroller that emulates an RFID emitter module, tuning or detuning an LC resonant circuit to obtain modulation. The receiver channel in the reader detects the amplitude modulated signal and reconstructs the modulation data.

Table 68.1 Functioning distances at various load resistance

Load resistance R_L	Distance (cm)
82 Ω	6
100 Ω	10
330 Ω	15
670 Ω	16
1 kΩ	17
4 kΩ	20
6.7 kΩ	23
10 kΩ	24
38.5 kΩ	24.5

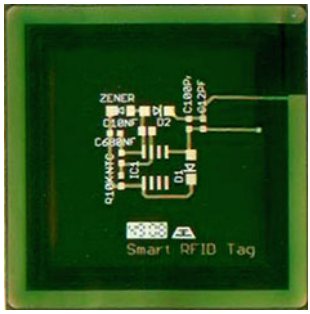

Fig. 68.4 The realized smart RFID sensor

The design of a DC/DC buck converter that allows to obtain a fixed output voltage sufficient to supply power to the microcontroller and to the sensors has been developed.

Results showed an efficiency greater than 85% regardless the input voltage value, ensuring the functioning with output voltage as low as 1.8 V in order to supply power to an Extreme Low Power microcontroller.

The whole smart RFID tag was then realized for test purpose on a 5 × 5 cm PCB on Kapton flexible substrate and tested.

An alternative solution for remotely power the chip was also designed for test purpose as a part of an VLSI Integrated Circuit (IC) in 0.35 μ CMOS, using an improvement of the Dickson [2] multiplier circuit with multiple stages topology.

References

1. Merenda M, Della Corte FG (2008) 13.56 MHz smart RFID tag with on-board microcontroller and temperature sensor. In: Proceedings of the XIII AISEM conference on sensors and microsystems
2. Dickson JF (1976) On-chip high-voltage generation in MNOS integrated circuits using an improved voltage multiplier technique. IEEE J Solid State Circuits SSC-11:374–378

Chapter 69
Characterization of Nanoparticles in Seawater for Toxicity Assessment Towards Aquatic Organisms

M. L. Miglietta, G. Rametta, G. Di Francia, S. Manzo, A. Rocco, R. Carotenuto, F. De Luca Picione and S. Buono

Abstract The fate and the behaviour of nanoparticles in seawater, which is the ultimate sink for any release of nanoparticles, is a very important issue for the assessment of their environmental impact. Despite this concern, only few studies regarding the ecotoxic effect of NPs upon marine organisms were conducted. In this work the dispersion behaviour of NPs in a seawater matrix has been investigated and their physicochemical properties characterized. The ecotoxicological impact towards marine organisms of several nanoparticles has been also examined.

69.1 Introduction

Nanomaterials are nowadays commonly employed in a huge number of industrial sectors ranging from personal care products to organic electronics, from sensor devices to drug delivery systems.

The recent advances in nanotechnology and the corresponding increase in the use of nanomaterials and nanoparticles (NPs) in almost every sector of the society have resulted in uncertainties regarding their environmental impact.

Coastal systems are likely to be the ultimate sink for any nanomaterial and nanoparticle, deliberately or purposely discharged into the environment. The fate and the behaviour of NPs in seawater strongly depend on different physicochemical characteristics that could affect aggregations and colloid chemistry.

M. L. Miglietta (✉) · G. Rametta · G. Di Francia · S. Manzo · A. Rocco · R. Carotenuto · F. De Luca Picione · S. Buono
ENEA Centro Ricerche Portici, Piazzale E. Fermi 1, 80055, Portici, NA, Italy
e-mail: mara.miglietta@enea.it

G. Neri et al. (eds.), *Sensors and Microsystems*,
Lecture Notes in Electrical Engineering 91, DOI: 10.1007/978-94-007-1324-6_69,

NP aggregates could be an ecotoxicological risk both for pelagic and, after deposition in sediment, for benthic species. Despite this concern, only few studies regarding the ecotoxic effect of NPs upon marine organisms were conducted [1–3].

The aim of this work is to evaluate the dispersion behaviour of NPs in a seawater matrix and to characterize their physicochemical properties in marine environment. Furthermore, the ecotoxicological effects of four different NPs (ZnO, SiO_2 Carbon black, SWCNT) towards marine organisms with different biological complexity have been investigated [4–7]: the sea urchin *Paracentrotus lividus* (embryotoxicity test), the crustacean *Artemia salina* (acute toxicity test) and three species of marine microalgae (*Dunaliella tertiolecta*, *Isocrisys galbana*, *Tetraselmis suecica*; 96 h growth inhibition test).

69.2 Nanoparticles Characterization

Four different NPs have been tested: zinc oxide (<100 nm, surface area 15–25 m^2/g, Sigma-Aldrich), single-walled carbon nanotubes (>50%, 1.1 nm × 0.5–100 μm, BET surface area 400 m^2/g, Sigma-Aldrich), silicon dioxide (99.5%, 5–15 nm (TEM), 590–690 m^2/g (TEM), Sigma-Aldrich), carbon black (Black (12 nm) Pearls® 2000, CABOT Corporation).

NPs have been dispersed in 500 ml of standard seawater by bath-sonication for 30 min. Half of each NP suspension has been centrifuged at 12,000 rpm for 10 min; both centrifuged and not centrifuged samples have been analysed.

Hydrodynamic diameter of nanoparticles in solution have been determined by Dynamic Light Scattering technique (DLS) with a Malvern HPPS-ET Standard System operating with a backscatter detection at 173° and with an He–Ne gas laser as light source ($\lambda = 632.8$ nm). Samples have been measured at a temperature of 25°C. The reported results for particle mean size and size distribution have been averaged from more than five measurements.

The analysis of the raw correlation data and of the size distribution highlights a remarkable difference between centrifuged and not centrifuged samples for all the selected NPs. In particular, centrifuged samples are always more dilute and with smaller particle mean size (Table 69.1).

Table 69.1 Hydrodynamic radius of NPs in standard seawater

Particles	Concentration (mg l^{-1})	Size range (nm)	
		Centrifuged	Not centrifuged
ZnO	133	–	1860–2500
SWCNTs	66	650–780	800–1800
SiO_2	200	400–460	950–1840
CB	66	–	1130–1560

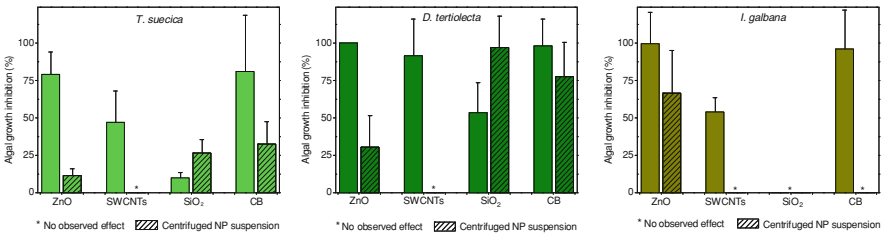

Fig. 69.1 Mean percent algal growth inhibition upon 96 h exposure to seawater dispersions of ZnO, SWCNTs, SiO_2 and CB nanoparticles. *Error bars* are also shown

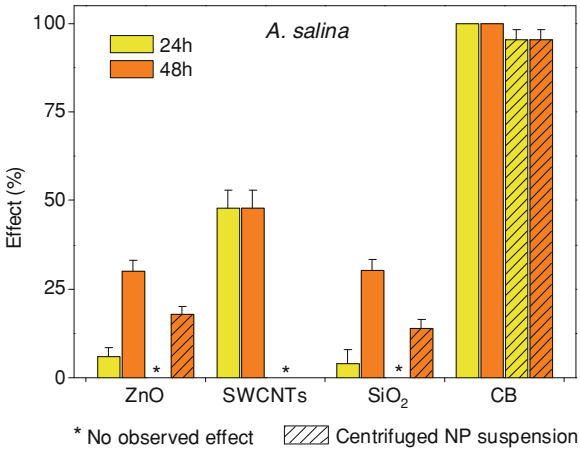

Fig. 69.2 Mean percent effect on *A. salina* exposed to NPs samples. *Error bars* are also shown

69.2.1 Ecotoxicological Effects

The growth inhibition effects of algal species (*T. suecica*, *D. tertiolecta*, *I. galbana*) upon exposure to the selected NPs are summarized in Fig. 69.1. The algae get quite similar responses to the NPs except for the SiO_2 which showed a low effect on the growth inhibition of *T. suecica* and even no effect on *I. galbana*. The most sensitive organism, *D. tertiolecta*, underwent a very toxic effect owing to NPs exposure, including SiO_2.

Overall, it can be noticed that centrifugation lower the toxic effect. This is most likely to be ascribed to an appreciable decrease of the concentration of suspended particles in the seawater samples, confirmed by the halved mean count rate in the light scattering measurements, rather than to the different mean size of the particles and size distribution. The effect of particles stripping through the centrifugation step is particularly evident in the case of SWCNTs which showed a moderate to high toxic effect when not centrifuged samples are used and that exhibited no effect at all, towards all the tested organisms, when the seawater sample supplied to the algae were centrifuged. This result strongly suggests that the absence of any

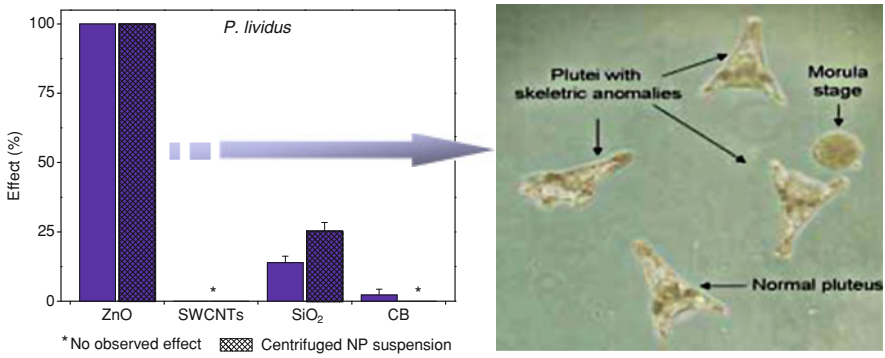

Fig. 69.3 Mean percent effect on sea urchin embryos. *Error bars* are also shown

toxic effect could be related to the very low concentration of carbon nanotubes in the centrifuged seawater suspension.

Crustaceans have shown the highest sensitivity to carbon based nanoparticles. In fact, tests with *A. salina* showed a fair mean percent effect after 48 h for ZnO and SiO_2 NPs in the not centrifuged suspensions, whereas exposure to CB and SWCNTs suspensions caused 50% and >95% respectively, of mortality of the *A. salina* organisms already after 24 h. As can be seen in Fig. 69.2, the toxic effect of CB NPs is so marked that the response is equivalent with both samples, centrifuged and not centrifuged.

Echinoids revealed as the most sensitive organisms to ZnO NPs (see Fig. 69.3). The SiO_2 showed only a moderate toxic effect. On the other hand, SWCNTs and CB did not show any toxic effects towards sea urchin embryos.

69.3 Conclusions

The selected marine organisms have shown different sensitivity to the different nanoparticles tested. Toxicity assays on microalgae show a noticeable growth inhibition upon exposure to the selected NPs, with an higher sensitivity to not centrifuged NPs suspensions. This make believe that the higher concentration of suspended particles in the water fed to the soil is the main parameter affecting the toxic action. *D. tertiolecta* revealed as the most sensitive alga. Crustaceans have shown the highest sensitivity to carbon based nanoparticles with responses equivalent to both samples, centrifuged and not centrifuged. Finally, the growth of *P. lividus* embryos is strongly affected by ZnO.

It is worth noting that SWCNTs centrifuged samples did not exert toxic effect towards any of the tested organisms likely because of the severe stripping of nanotubes from the solution induced by centrifugation.

References

1. Shtykova L, Fant C, Handa P, Larsson A, Berntsson K, Blanck H, Simonsson R, Nydén M, Ingelsten Härelind H (2009) Adsorption of antifouling booster biocides on metal oxide nanoparticles: effect of different metal oxides and solvents. Prog Org Coat 64:20–26
2. Blickley TM, McClellan-Green P (2008) Toxicity of aqueous fullerene in adult and larval *Fundulus Heteroclitus*. Environ Toxicol Chem 27:1964–1971
3. Koehler A, Marx U, Broeg K, Bahns S, Bressling J (2008) Effects of nanoparticles in *Mytilus edulis* gills and hepatopancreas—a new threat to marine life? Mar Environ Res 66:12–14
4. Pagano G, Cipollaro M, Corsale G, Esposito A, Ragucci E, Giordano GG, Trieff NM (1986) The sea urchin: bioassay for the assessment of damage from environmental contaminants. In: Cairns J (ed) Community toxicity testing. ASTM STP920. American Society for Testing and Materials, Philadelphia, pp 66–92
5. USEPA (1995) Short-term methods for estimating the chronic toxicity of effluents and receiving waters to West Coast marine and estuarine organisms. EPA 600R95136, pp 324–366
6. IRSA-CNR (1997) Saggio di tossicità acuta con *Artemia sp*. Metodo per la determinazione di effetti tossici acuti con Artemia sp. Metodi Analitici. Saggi di tossicità: Artemia, Biologia Ambientale n. 1/1997
7. IRSA-CNR (1978) Metodologia di saggio algale per lo studio della contaminazione delle acque marine. Quaderni dell'Istituto di Ricerca sulle Acque n. 39-IT ISNN 0390-6329

Chapter 70
Diffuse-Light Absorption Spectroscopy in the VIS and NIR Spectral Ranges for Adulteration Assessment of Extra Virgin Olive Oils

Anna G. Mignani, Leonardo Ciaccheri, Heidi Ottevaere, Hugo Thienpont, Lanfranco Conte, Milena Marega, Angelo Cichelli, Cristina Attilio and Antonio Cimato

Abstract A fiber optic setup for diffuse-light absorption spectroscopy in the wide 400–1700 nm spectral range is experimented for detecting and quantifying the adulteration of extra virgin olive oil caused by lower-grade olive oils. Absorption measurements provide spectral fingerprints of authentic and adulterated oils. A multivariate processing of spectroscopic data is applied for discriminating the type of adulterant and for predicting its fraction.

70.1 The Authentic Extra Virgin Olive Oil and its Adulterants

Optical spectroscopy has been frequently proposed for detecting and quantifying extra virgin olive oil (EVOO) adulteration. It allows rapid and non-destructive analysis and requires minimum sample preparation. Infrared, mid-infrared, and fluorescence

A. G. Mignani · L. Ciaccheri (✉)
CNR-IFAC, Sesto Fiorentino, FI, Italy
e-mail: l.ciaccheri@ifac.cnr.it

A. G. Mignani
e-mail: a.g.mignani@ifac.cnr.it

H. Ottevaere · H. Thienpont
Brussels Photonics Team of the Vrije Universiteit Brussel, Brussels, Belgium

L. Conte · M. Marega
Dipartimento di Scienze degli Alimenti, Università degli Studi di Udine, Udine, Italy

A. Cichelli
Dipartimento di Scienze, Università G. D'Annunzio, Pescara, Italy

C. Attilio · A. Cimato
CNR-IVALSA, Sesto Fiorentino, FI, Italy

G. Neri et al. (eds.), *Sensors and Microsystems*,
Lecture Notes in Electrical Engineering 91, DOI: 10.1007/978-94-007-1324-6_70,

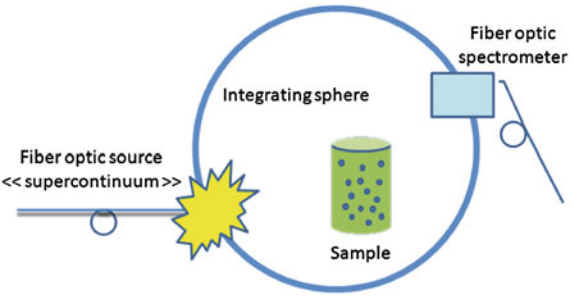

Fig. 70.1 Setup for diffuse-light absorption spectroscopy—the scheme

spectroscopic techniques have been proposed, as well as absorption spectroscopy in the ultraviolet and visible (VIS), or near-infrared (NIR) spectral ranges. These techniques are usually combined with chemometric methods for spectroscopic data processing, which are capable of providing an excellent EVOO authentication [1–5]. However, none of the optical techniques experimented so far takes into account the intrinsic turbidity of the oil, which can considerably impair optical measurements because of the unavoidable scattering effects produced by suspended particles.

This paper shows the potential of absorption spectroscopy in the wide 400–1700 nm spectral range for EVOO authentication. The spectral fingerprints of authentic EVOOs and of the same oils adulterated by addition of lower-grade olive oils are measured by means of a fiber optic setup for diffuse-light absorption spectroscopy, which provides intrinsically scattering-insensitive measurements. Then, a customized multivariate processing of spectroscopic data is applied for a straightforward detection of adulterant type and for prediction of adulterant fraction.

70.2 Diffuse-Light Absorption Spectroscopy

Diffuse-light absorption spectroscopy makes use of an integrating cavity that contains the sample under test [6, 7]. If an integrating sphere is used, the source and the detector can be butt-coupled anywhere onto the sphere. Almost all the light shining on the sphere surface is diffusely reflected, and by inserting an absorbing sample in the cavity, a reduction of the radiance in the sphere occurs. The detected light power is independent of non-absorbing objects within the sample such as suspended scattering particles. This technique has been recently proposed for effective gas analyses [8, 9].

A scheme of the setup used for the experiment here reported is given in Fig. 70.1. A fully optical fiber-based setup was used which was made of commercially-available components [10]. The Fianium-SC400 fiber optic *supercontinuum* source was used for illumination: it emits 4 Watts throughout the entire 415–1800 nm spectral range. The Instrument System-Spectro 320 fiber optic spectrometer was used as detector, and scanned the wide 400-1700 nm spectral range with a resolution of 1.37 nm. The Labsphere LMS100 cavity was used as a diffusing sphere, the ports of which were equipped by means of fiber optic connectors for coupling to both the

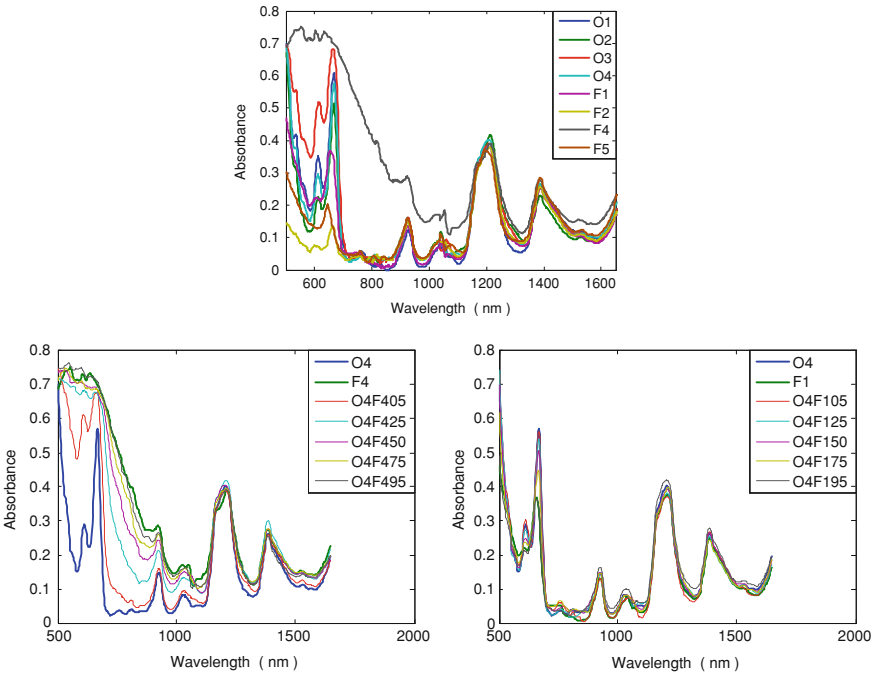

Fig. 70.2 Diffuse-light absorption spectra of the entire collection of authentic EVOOs and adulterants (*top*), and two examples of highly different or very similar spectral signatures of mixtures (*bottom*)

source and the detector. The oil sample under test was contained in a glass vial having a volume of 32 cm^3. This setup was previously used for lubricant oil analysis—it allowed for a successful spectral fingerprinting of the oil and for predicting functional parameters and wear indicators [11].

70.3 The Collection of Analyzed Olive Oils

Four authentic EVOOs were collected in Tuscany, a centrally located Italian region where EVOO is one of the most important and popular agricultural products. They were identified by means of the O1, O2, O3, and O4 codes. The lower-grade olive oils selected as adulterants were: olive-pomace oil (code F1), refined olive oil (code F2), deodorized olive oil (code F4), and refined olive–pomace oil (code F5).

Four series of EVOO-adulterant mixtures were prepared by spiking each authentic EVOO with 5, 25, 50, 75, and 95% w/w of adulterant. They were used for calibration procedures. Also, replica mixtures of EVOOs with 25, 50, and 75% w/w of adulterants were prepared for validation purposes. The entire collection of

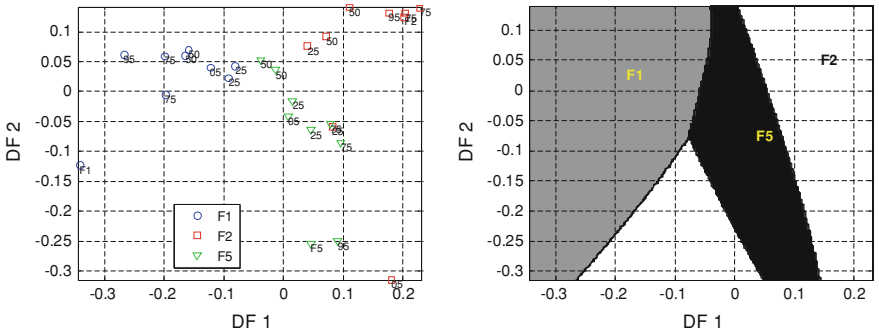

Fig. 70.3 *Left* DF map for discriminating F1, F2, and F5 adulterants in O1 EVOO. *Right* the domains

measured oils consisted of 136 samples, 88 for calibration and 48 for validation, respectively.

Figure 70.2-top shows the measured diffuse-light absorption spectra of all authentic EVOOs and adulterants. Their mixtures shows intermediate spectra: as an example, Fig. 70.2-bottom shows the same EVOO adulterated by means of two adulterants, deodorized olive oil and olive-pomace oil, respectively, providing highly different (O4F4 mix) or very similar (O4F1 mix) spectra.

70.4 Discrimination of Adulterant Oil and Prediction of its Fraction

Before any further processing, the spectra were smoothed by means of Savitsky-Golay algorithm, employing a 2nd degree polynomial and a smoothing window of 15 points (30 nm). Then, two different processing methods were used for discrimination of adulterant type and for prediction of adulterant fraction [12].

Detection of adulteration with F4 is straightforward, because this oil has a peculiar absorption band between 700 and 900 nm, in which all other oils of the dataset, both authentic EVOOs and adulterants, have negligible absorbance.

Discriminating between F1, F2 and F5 is, however, much more difficult, because they exhibit quite similar spectra. For this scope we employed the multivariate analysis called *Linear Discriminant Analysis* (LDA). LDA projects the data points onto particular "axes" in the space spanned by the spectroscopic variables, called *discrimianating functions* (DFs). The criterion driving LDA in the axes choice is to maximize the separation between different clusters of points. This was made separately for each authentic EVOO. Before applying LDA, the *Principal Component Analysis* (PCA) was used, for data dimensionality reduction and noise removal. The discriminant analysis was set up as a three-class problem, relative to F1, F2, and F5 adulteration. The results of this processing showed the

Table 70.1 Summary of parameters for predicting the fraction of adulterant

EVOO-adulterant mix	# PF	RMSEC	RMSEP	R^2
O1F1	1	0.09	0.05	0.947
O1F2	1	0.06	0.07	0.975
O1F4	2	0.07	0.05	0.971
O1F5	1	0.07	0.13	0.964
O2F1	2	0.03	0.06	0.996
O2F2	1	0.01	0.06	0.933
O2F4	2	0.07	0.06	0.969
O2F5	2	0.02	0.08	0.997
O3F1	2	0.02	0.05	0.996
O3F2	2	0.02	0.02	0.997
O3F4	2	0.05	0.04	0.985
O3F5	1	0.10	0.10	0.932
O4F1	1	0.10	0.03	0.926
O4F2	1	0.07	0.07	0.966
O4F4	2	0.07	0.06	0.968
O4F5	2	0.04	0.08	0.990

following percentages of wrongly classified samples: 7.4% for O1, 3.7% for O2, 56% for O3, and 7.4% for O4.

While the accuracy of adulterant type discrimination was acceptable for O1, O2, and O4, it was rather poor for O3. This is probably due to the fact that the O3 absorbance is much higher than adulterant absorbance in the whole VIS band, meaning that, in any case, the main effect of adulteration was a general lowering of VIS absorption. On the contrary, the action of adulteration on O1, O2 and O4 spectra was more selective, because their spectra were closer to those of the adulterants, except in specific absorption bands that were different for each substance.

Since LDA generates N-1 DFs for an N number of classes to be discriminated, we obtained a bi-dimensional representation of dataset. As an example, Fig. 70.3-left shows the DF map for discriminating the F1, F2, and F5 adulterants in O1 EVOO, while Fig. 70.3-right shows the domains belonging to the three classes. Similar maps were obtained for the other EVOOs.

The prediction of the adulterant fraction in each OxFy mixture was made by using a multivariate analysis method called *Partial Least Squares* regression (PLS). PLS looks for a limited number of PLS "factors" (PF) which are linear combinations of the original predictors. These new variables are mutually orthogonal (thus uncorrelated) and have the maximum possible covariance with the target variable, among all possible combinations of the original predictors. The estimation of the optimal number of PF needed to fit the data is a critical issue of PLS. The optimal number of PF was assessed by testing each PLS model on the validation set and minimizing the RMSEP (Root Mean Square Error of Prediction). Two other parameters were evaluated in order to assess the goodness of the fit: the RMSEC (Root Mean Square Error of Calibration) and the determination

coefficient (R^2). RMSEC is, like RMSEP, an estimation of the "expected" prediction error, but is evaluated on the calibration set. R^2 is the squared correlation coefficients between predicted and true values for the calibration set; thus the fit is as better as this value is closer to 1.

Table 70.1 summarizes the values of these parameters for each EVOO-adulterant mixture, together with the chosen number of PF (# PF). Indeed, the values of R^2 are very good. The best prediction is obtained for O3 EVOO adulterated by means of refined olive oil (F2), showing $R^2 = 0.997$ and RMSEP = 0.02. The worse prediction is obtained for O2 EVOO adulterated again by means of refined olive oil (F2), showing $R^2 = 0.933$ and RMSEP = 0.06.

70.5 Perspectives

Diffuse-light absorption spectroscopy performed in the 400–1700 nm spectral range, combined with a multivariate processing of spectroscopic data, have demonstrated the capability of revealing the type of adulterant, among diverse lower-grade olive oils which are frequently used for commercial frauds of authentic EVOOs. Then, the fraction of adulterant has been successfully predicted. Being scattering-independent, this technique can be used for EVOO analysis during the entire product shelf-life. The obtained results are encouraging, especially because of the chemical similarities of authentic EVOOs and adulterants. To the best of our knowledge, we have demonstrated for the first time that optical spectroscopy can be successfully used to quantify the fraction of deodorized olive oil in authentic EVOO. This is an innovative result, especially in view of the growing use of deodorized olive oil as adulterant.

Acknowledgments The EC Networks of Excellence "NEMO" and "P4L", and the CNR Short-Term Mobility Programme are acknowledged for partial financial support.

References

1. Lerma-Garcìa MJ, Ramis-Ramos G, Herrero-Martìnez JM, Simò-Alfonso EF (2010) Authentication of extra virgin olive oils by fourier-transform infrared spectroscopy. Food Chem 118:78–83
2. Gurdeniz G, Ozen B (2009) Detection of adulteration of extra-virgin olive oil by chemometric analysis of mid-infrared spectral data. Food Chem 116:519–525
3. Poulli KI, Mousdis GA, Georgiou CA (2007) Rapid synchronous fluorescence method for virgin olive oil adulteration assessment. Food Chem 105:369–375
4. Christy AA, Kasemsumran S, Du Y, Ozaki Y (2004) The detection and quantification of adulteration in olive oil by near-infrared spectroscopy and chemometrics. Anal Sci 20:935–940
5. Torrecilla JS, Rojo E, Dominguez JC, Rodrìguez F (2010) A novel method to quantify the adulteration of extra virgin olive oil with low-grade olive oils by UV-vis. J Agric Food Chem 58:1679–1684

6. Elterman P (1970) Integrating cavity spectroscopy. Appl Opt 9:2140–2142
7. Fry ES, Kattawar GW, Pope RM (1992) Integrating cavity absorption meter. Appl Opt 31:2055–2065
8. Hawe E, Fitzpatrick C, Chambers P, Dooly G, Lewis E (2008) Hazardous gas detection using an integrating sphere as a multipass gas absorption cell. Sens Act A 141:414–421
9. Hodgkinson J, Masiyano D, Tatam RP (2009) Using integrating spheres as absorption cells: path-length distribution and application of Beer's law. Appl Opt 48:5748–5758
10. Source: http://www.fianium.com/, Detector: http://www.instrumentsystems.com/, Integrating sphere: http://www.labsphere.com/
11. Mignani AG, Ottevaere H, Ciaccheri L, Thienpont H, Cacciari I, Parriaux O, Johnson M (2009) Innovative spectroscopy of liquids: a fiber optic supercontinuum source and an integrating cavity for scattering-free absorption measurements. In: Proceedings of 20th International Conference on optical Fibre Sensors, vol. Proceedings of SPIE 7503, pp 750377-1/4
12. Naes T, Isaksson T, Fearn T, Davies T (2007) A user-friendly guide to multivariate calibration and classification. NIR Publications, Chichester

Chapter 71
Bridge Monitoring by Distributed Strain Measurement Using a Time-Domain Brillouin Sensing System

R. Bernini, L. Amato, A. Minardo and L. Zeni

Abstract We report the results of a load test performed on a road-bridge. In particular, the tests were performed by a portable prototype based on stimulated Brillouin scattering (SBS) in optical fibers. The optical fiber sensor, previously attached along the steel beam, was able to provide the strain profile along the structure, with a spatial resolution of 3 m and a strain accuracy of ± 20 $\mu\varepsilon$. A comparison with finite-elements-method simulations, as well as with data collected by vibrating wire strain gauges, permitted to confirm the validity of the SBS-based approach in monitoring the deformation of large structures.

71.1 Introduction

The safety assessment of ordinary structures is usually based on the experimental testing of displacements or strains under the design loads, by taking into consideration measures related to a selected discrete number of points. For many engineering works of strategic significance like bridges, pipes, rising buildings, dams and tunnels, safety should be continuously assessed during their complete lifetime. The experimental reading of strains over the entire structure has become

R. Bernini (✉)
Istituto per il Rilevamento Elettromagnetico dell'Ambiente,
Consiglio Nazionale delle Ricerche, Via Diocleziano 328, 80124 Naples, Italy
e-mail: bernini.r@irea.cnr.it

L. Amato
Tecno In S.p.A., -II Trav. Strettoia S. Anna alle. Paludi 11, 80142 Naples, Italy

A. Minardo · L. Zeni
Dipartimento di Ingegneria per l'Informazione, Seconda Università di Napoli,
Via Roma, 29, 81031 Aversa, Italy

G. Neri et al. (eds.), *Sensors and Microsystems*,
Lecture Notes in Electrical Engineering 91, DOI: 10.1007/978-94-007-1324-6_71,

possible today thanks to distributed optical fiber sensors based on stimulated Brillouin scattering (SBS) [1–3]. The experimental procedure consists of durable devices set on the structure at an early stage of the building process. Distributed optical fiber sensors furnish a continuous profile of the measured value of strain. Because optical fiber length reaches tens of kilometers, they can set up for the monitoring and safety assessment of large structures.

In this work, we report the result of a load test performed on a road-bridge. In particular, the tests were performed by an SBS-based portable sensor prototype, operating in the time-domain. In brief, a pulsed laser light and a frequency-shifted continuous-wave (CW) laser light are launched simultaneously at the two opposite ends of an optical fiber. By measuring the intensity of the CW light emerging from the fiber at various frequency shifts, the Brillouin frequency shift profile along the fiber is retrieved. As the Brillouin frequency shift is linearly dependent on strain (with a coefficient of about 500 MHz/%), the instrument provides a measure of strain at each location of the fiber, with a spatial resolution determined by the duration of the optical pulses employed for the measurements (we set a 3 m-spatial resolution in our tests).

71.2 Experimental and Numerical Results

The fiber employed for the measurements was a PVC-coated, single-mode, standard telecom optical fiber. The fiber was bonded along the lower flange of a 44-m-long, double-T steel beam, by use of a cianoacrilate adhesive. Strain measurements were performed while loading the bridge with an increasing weight by use of gravel-loaded trucks.

During the loading test, data were also collected by other instruments. In particular, two vibrating wire strain gauges were previously spot-welded to the surface of the steel beam, so as to provide the strain at the quarter and the middle section of the loaded beam. Moreover, a laser telemeter was employed in order to measure the deflection of the beam at the middle section.

In Fig. 71.1, we report the results of the optical fiber measurements, for different load conditions. In particular, the solid lines refer to the bridge loaded by two, four, and five gravel trucks, respectively. Each truck had a weight of approximately 47 tons. The same figure also reports the results of a finite- element-method (FEM)-based numerical analysis (circles). Numerical data were obtained by modeling each gravel truck as three concentrated loads applied in correspondence of the three truck axles. From Fig. 71.1, it can be seen that a good agreement exists between the experimental and numerical data. The standard deviation was always less than 20 με, corresponding to the nominal accuracy of the instrument. Moreover, the maximum strain provided by the optical fiber sensor (≈350 με), is in good agreement with the value provided by the strain gauge placed at the middle beam section (≈330 με). Another interesting feature is that the optical fiber sensor

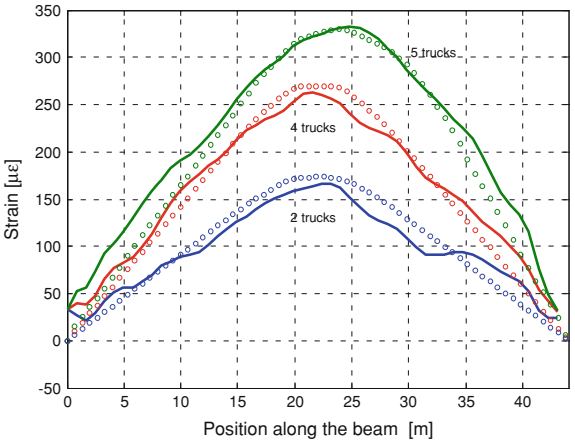

Fig. 71.1 Distributed strain measurement along the 44 m-beam, as measured for different load conditions (*solid lines*). The *open circles* indicate the results of FEM simulations

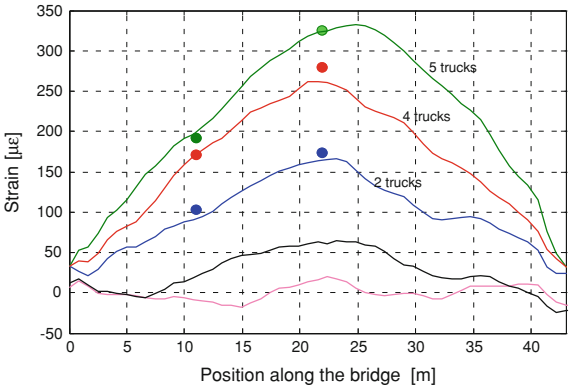

Fig. 71.2 Distributed strain measurement along the 44 m-beam, as measured for different load conditions (*solid lines*). The *closed circles* indicate the results from strain gauges

was able to reveal the right-shift of the center of gravity (CG), when loading the beam with five tucks.

Actually, the fifth truck was not disposed symmetrically with respect to the middle of the bridge; rather it was closer to the right side. As a consequence, the section at which maximum strain occurs is shifted to the right in the final load test.

In Fig. 71.2 we compare the measurements provided by the optical fiber sensor, with the data obtained by the strain gauges (circles). It can be seen that there is a good agreement with the optical fiber measurements. In the same figure, the black curve represents the strain profile measured by the SBS-based sensor a few minutes after the unloading of the bridge, revealing a residual strain of about 60 με in the middle section.

On the other hand, the same measurement performed about one month later (magenta curve), shows no residual deformation.

A possible explanation of the residual stress measured immediately after the unloading of the bridge, can be found by keeping in mind that the sensing fiber was

protected by an outer PVC jacket with a diameter of 900 μm. While this jacket is essential to give mechanical strength to the fiber, it may induce some "jacket effects". The latter appear as a gradual increase or decrease of the measured strain, when the structure is subjected to a fixed load or when it is unloaded [4]. These effects can be attributed to creep deformation and stress relaxation of the jacket, and can be observed within a time interval as long as several hours.

71.3 Conclusions

The results reported in this work demonstrate the potentiality of SBS-based sensors in the field of structural heath monitoring. The use of distributed sensors permits to obtain the strain at each location of the investigated structure, rather than only at few selected points. Actually, in case of damage, the strain gauge may fail to reveal the defect if it is not located in proximity of the damaged region. Another advantage of the proposed approach is that, after installation, the same optical fiber can be re-used several times. Hence, a periodic acquisition of the strain profile is possible, permitting to monitor the health of the investigated structure during its whole life-time.

References

1. Bao X, DeMerchant M, Brown A, Bremner T (2001) Tensile and compressive strain measurement in the lab and field with the distributed Brillouin scattering sensor. J Lightw Technol 19:1698–1704
2. Bernini R, Minardo A, Zeni L (2007) Vectorial dislocation monitoring of pipelines by use of Brillouin-based fiber-optics sensors. Smart Mater Struct 17:015006
3. Muraiama H, Kageyama K, Naruse H, Shimado A (2004) Distributed strain sensing from damaged composite materials based on shape variation of the Brillouin spectrum. J Intel Mater Syst Struct 15:1539–1543
4. Ding Y, Shi B, Bao X, Gao Y (2006) Jacket effect on strain measurement accuracy for distributed strain sensors based on Brillouin scattering. Optica Applicata 36:57–76

Chapter 72
Assessment of Fuel Cell's Endplate Out of Plane Deformation Using Digital Image Correlation

R. Montanini, G. Squadrito and G. Giacoppo

Abstract The achievement of proper electrochemical performance in proton exchange membrane fuel cells depends on a number of factors, among which the difficulty in obtaining a uniform pressure distribution over the whole fuel cell active area. For a given stacking design, contact pressure levels are usually controlled by selecting an appropriate external clamping pressure on the endplates. Hence, the actual out-of-plane deformation of the endplates is believed to play a critical role. The goal of this study is to investigate this aspect by using an optical full-field measurement technique based on stereoscopic digital images correlation. The preliminary results reported in this paper, obtained by testing a PEMFC with 13 mm thick Cu endplates, shows that the endplates bend noticeably under loading, leading to an uneven distribution of the out-of-plane deformation field.

72.1 Introduction

Proton exchange membrane fuel cell (PEMFC) is an electrochemical device that converts the chemical energy stored in hydrogen and oxygen into electricity, without generating pollutants. A conventional PEMFC (Fig. 72.1) basically consists of two composite graphite plates with multiple serpentine flow fields and a membrane electrode assembly (MEA) inserted between them. Highly conductive

R. Montanini (✉)
Dipartimento di Chimica Industriale e Ingegneria dei Materiali, Università degli Studi di Messina, Viale F. Stagno D'Alcontres 31, 98166, Messina, Italy
e-mail: rmontanini@ingegneria.unime.it

G. Squadrito · G. Giacoppo
Istituto di Tecnologie Avanzate per l'Energia "Nicola Giordano", Salita Santa Lucia Sopra Contesse 5, 98126, Messina, Italy

G. Neri et al. (eds.), *Sensors and Microsystems*,
Lecture Notes in Electrical Engineering 91, DOI: 10.1007/978-94-007-1324-6_72,

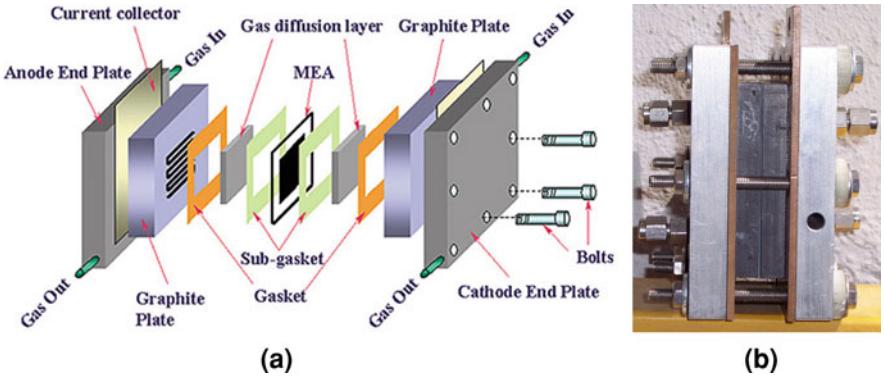

Fig. 72.1 **a** Sketch showing the individual components of a conventional PEMFC; **b** assembling

collectors are used to drive the dc current, whereas rigid endplates are employed as part of the clamping system to provide compressive force in order to bundle the single fuel cells together to form a stack. Different requirements have to be addressed in the design of the fuel cells endplates, since they must also accomplish functions such as ensuring good electrical contact between multiple layers and good sealing at various interfaces, providing passages for the reactants, products and cooling agents to enter and leave the fuel cell. Although the current design of fuel cell endplates can provide the above listed functions in a somewhat satisfactory manner, there is still some lack of knowledge about the relationship existing between the externally applied clamping torque and the pressure distribution within the fuel cell [1–3]. To achieve good electrochemical performance, it is believed that, for a given stacking design, there exists an optimal level of the pressure distribution acting on the MEA. Ideally, the optimum value has to be achieved throughout the fuel cell active area, but, in practice, because of the design of conventional endplates, it can only be achieved in a small portion of the electrode area, as already reported by the authors in a previous study [4], in which matrix-based piezoresistive thin-film sensor interposed between the membrane electrode assembly and the graphite plate of a PEMFC were used to investigate the actual correlation between the pressure distribution and the clamping torque.

On the ground of these findings, the present study is aimed to assess, by means of digital image correlation, the out of plane deformation of the endplates, which it is thought to play an important role in determining the actual pressure distribution within the fuel cell.

72.2 Digital Image Correlation

Digital image correlation (DIC) is an optical full-field measurement technique based on the comparison between digital images of the specimen surface recorded in the un-deformed (or reference) and deformed states respectively [5].

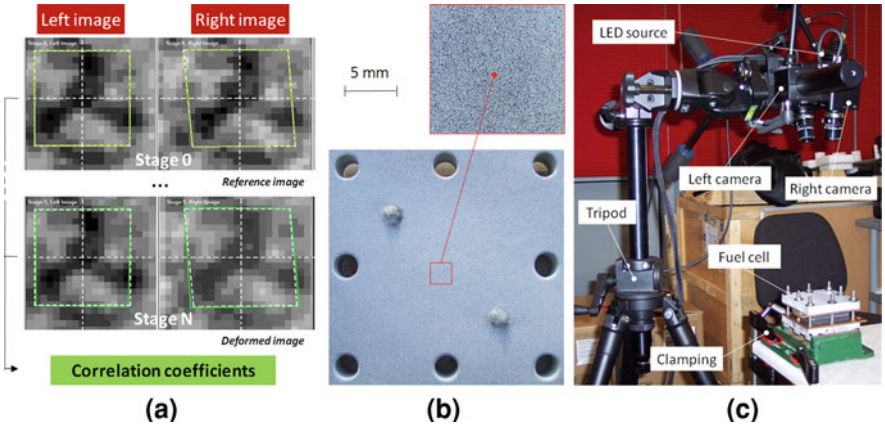

Fig. 72.2 **a** Measuring principle of DIC 3D; **b** random gray intensity distribution; **c** lab setup

The approach relies on random speckle patterns (Fig. 72.2b) sprayed onto the specimen surface which deforms together with the object as a carrier of deformation information. If two image acquisition systems are used simultaneously (stereoscopic setup), all the three components of the displacement vector can be determined by tracking the motion of each image point in the field of view.

The DIC measuring principle can be illustrated synthetically as follows. As shown in Fig. 72.2a, a subset of $(2M + 1) \times (2M + 1)$ pixels centred at point (x_0,y_0) from the reference image is first chosen and used to determine its corresponding location in the deformed image. A sum-square difference (SSD) correlation is then carried out to evaluate the similarity between the reference subset and the target subset. The matching procedure is carried out numerically through searching the peak position of the distribution of correlation coefficients. Once the maximum correlation coefficient is detected, the target subset in the two images can be determined, allowing the three displacement components to be calculated. The use of a complex stereo setup (which was compulsory in order to measure the out-of-plane displacement component of the fuel cell endplate) required a preliminary calibration to determine the cameras configuration (distance and orientation) as well as the image characteristics of the lenses (e.g. focus, lens distortions). The measuring volume was calibrated using a ceramic calibration panel with coded reference markers and scale bars, determining the 3D coordinates of the reference points in the 2D camera image. For the position of the reference points, this results in a reference point deviation (intersection error) which was typically less than 0.1 pixels. Figure 72.2c shows the actual experimental setup used to make the tests.

The uncertianty of the out-of-plane displacement DIC measurements was estimated to be ± 1.2 μm; it has been assessed through dedicated calibration tests carried out using a high accuracy laser triangulation sensor as reference.

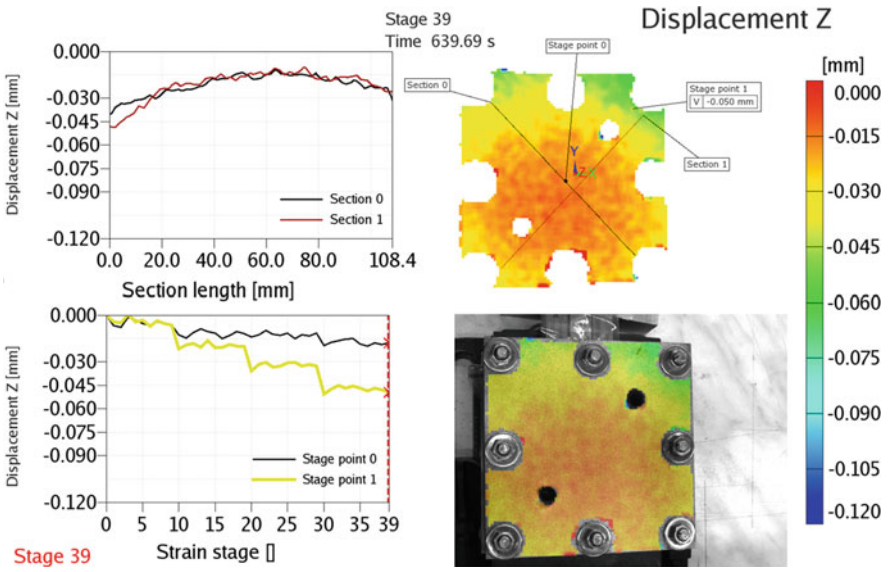

Fig. 72.3 False colour out-of-plane displacement map at 10 Nm (*bottom right*), time history plots at stage points 0 and 1 (*bottom left*), spatial distribution of the displacement field on the fuel cell endplate along diagonal sections (*top left*), reference points and section lines (*top right*)

72.3 Results

The PEMFC (Fig. 72.1b) used for the experimental tests has a multiple serpentine flow field with two 13 mm thick copper endplates clamped together by means of 8 × M6 steel bolts. The active area (i.e., area of the membane electrode assembly) is about 25 cm^2, while the endplates have a square shape of about 7 cm width. The random gray intensity distribution was created using opaque black piant deposited over a matt white uniform layer (Fig. 72.2b). Experimental tests were carried out by varying the external clamping pressure step by step. This was obtained by using a calibrated torque wrench with torque values of 7, 8, 9 and 10 Nm. At each step, after waiting for about 30 s, the torque value on each bolt was checked to account for possible gasket or porous membrane electrode relaxations. The eight bolts were clenched using always the same sequence. Measurements were taken waiting 180 s after each step increase or decrease. For each step, 10 digital images were recorded. Figure 72.3 reports the main results. A noticeably uneven distribution of the out-of-plane deformation was observed, due to the increasing bending of the endplate as the clamping pressure is raised. More specifically, the innermost area (which is in contact with the bottom graphite plate containing the MEA) remains relatively unloaded, while highest displacements (0.050 mm) occurs at the borders, due to the compression force transmitted by the bolts.

72.4 Conclusions

To achieve good performance in a PEMFC, it is believed that a uniform pressure distribution should be attained onto the membrane electrode assembly. This study showed that conventional fuel cell Cu endplates, as normally used in reference laboratory cells, are not likely to allow an even compression of the membrane electrode assembly and this might have a significant effect on PEMFC electrochemical performance.

References

1. Chang WR, Hwang JJ, Weng FB, Chan SH (2007) Effect of clamping pressure on the performance of a PEM fuel cell. J Power Sources 166:149–154
2. Wang X, Song Y, Zhang B (2008) Experimental study of clamping pressure distribution in PEM fuel cells. J Power Sources 179:305–309
3. Lee SJ, Hsu CD, Huang CH (2005) Analyses of the fuel cell stack assembly pressure. J Power Sources 145:353–361
4. Montanini R, Squadrito G, Giacoppo G (2009) Experimental evaluation of the clamping pressure distribution in a PEM fuel cell using matrix-based piezoresistive thin-film sensors. In: Proceedings of XIX IMEKO World Congress, Lisbon (P), 6–11 September 2009
5. Pan B, Qian K, Xie H, Asundi A (2009) Two-dimensional digital image correlation for in-plane displacement and strain measurement: a review. Meas Sci Technol 20:1–17

Chapter 73
A Piezoelectric Quartz Crystal Sensor Applied for Thrombin-Binding Aptamers

Ilaria Lamberti, Jan Rakitka, Tibor Hianik and Lucia Mosiello

Abstract The temperature-dependent UV spectroscopy and thickness shear mode acoustic method were applied to study of thermodynamics and binding properties of DNA aptamers sensitive to thrombin depending on the substitution of bases in G-quadruplex. The substitution of thymidines by adenines in TT and TGT loops of G-quadruplex resulted in destabilization of aptamers and in decrease of sensitivity to human thrombin.

73.1 Introduction

The DNA/RNA aptamers are single stranded in vitro selected oligonucleotides (typically 30–60 bases) that in certain conditions (ionic strength, pH) form in a solution three-dimensional structure with specific binding site to low or macromolecular ligands [1, 2]. The affinity of aptamers is similar or even higher than those of antibodies. However, the aptamers are more stable than antibodies and do not induce immune response. They can be chemically modified by various compounds, which increase their stability and allowing immobilisation at a surface. Increased interest in study of aptamers is connected with their high potential in cancer therapy, for the treatment of age related macular degeneration and for

I. Lamberti · J. Rakitka · T. Hianik (✉)
Department of Nuclear Physics and Biophysics, Comenius University, Mlynska dolina F1, 84248 Bratislava, Slovakia
e-mail: tibor.hianik@fmph.uniba.sk

I. Lamberti · L. Mosiello
ENEA, Italian National Agency for New Technologies, Energy and the Environment, Via Anguillarese 301, 00060 Rome, Italy

G. Neri et al. (eds.), *Sensors and Microsystems*,
Lecture Notes in Electrical Engineering 91, DOI: 10.1007/978-94-007-1324-6_73,

targeted drug delivery [2, 3]. The common binding motif of some aptamers including those of thrombin is guanine quadruplex (G-quadruplex) [4]. It is formed by guanine bases stabilized by Hoogsten hydrogen bonds [5]. The resulted planar G-quartets can be connected by intermediate sequences that form loops. The loops play key role in the aptamers stability and in their binding to the ligands. Among DNA aptamers those sensitive to fibrinogen binding site of thrombin is one of most studied [4]. According to NMR data [6], the eight guanine residues form G-tetrads that are connected at one end by two TT loops and at the other end by one TGT loop. This aptamer has been originally developed as inhibitor of coagulation effect of thrombin. However, later it has been used also for development various thrombin biosensors [7]. Among biosensors, those based on surface acoustic method are rather promising due to their sensitivity to surface modification. Recently it has been shown, that substitution of nucleotides in TT loop by U and substitution of G in TGT loops by A, C or T increased the stability of G-quadruplex [8]. We have studied how the substitution of thymidines by adenines in TT and TGT loops of G-quadruplex responsible for thrombin binding affects the thermodynamics and binding properties of the aptamers.

73.2 Materials and Methods

The HPLC purified DNA aptamers were purchased from Thermo Fisher Scientific (Ulm, Germany): TT: 5' GGT TGG TGT GGT TGG T_{15} 3'; AT: 5' GGT TGG TGT GG**A** TGG T_{15} 3'; AA: 5'GGT TGG TGT GG**A** **A**GG T_{15} 3'; AGA: 5' GGT TGG **A**G**A** GGT TGG T_{15} 3'. All aptamers were extended by 15-mer thymidine chains modified at 3' end by biotin, which was necessary for biosensor preparation. The TT is conventional aptamer sensitive to fibrinogen binding site at thrombin. Other aptamers: AT, AA and AGA differ from TT aptamer by substitution of thymidines by adenines in the position marked by underlined bold. The thermodynamic properties of aptamers have been studied by UV absorption spectroscopy. The melting temperature at wavelength 297 nm has been determined using thermoelectrically controlled UV–VIS spetrometer Shimadzu 1700 (Japan) with a scan rate 0.5°C/min. The melting of aptamers at this wavelength is characterized by larger hypochromic effect in comparison with hyperchromic effect at 260 nm [8]. The melting temperature T_m and Van Hoff enthalpy changes, ΔH_{VH}, have been determined by fitting the normalized plot of absorbance versus temperature using Eq. (73.1).

$$A = \frac{A_F + A_U e^{(\Delta H_{vH}/R)*(1/T-1/T_m)}}{1 + e^{(\Delta H_{vH}/R)*(1/T-1/T_m)}} \tag{73.1}$$

where A, A_F and A_U are total, folded and unfolded aptamer normalized absorbance, respectively. R is gas constant and T is absolute temperature. The binding of human thrombin (Sigma–Aldrich, USA) to the aptamers was analyzed by

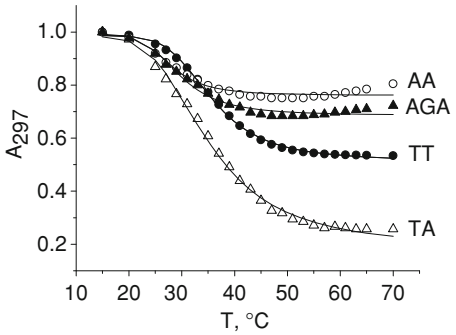

Fig. 73.1 Normalized plot of absorbance at wavelength 297 nm versus temperature for all aptamers studied. The full lines are fits according to Eq. (73.1)

Table 73.1 The thermodynamics parameters of aptamers studied: T_m—melting temperature, ΔH_{VH}—Van Hoff enthalpy changes, $\Delta G^0_{(20)}$—changes of standard Gibbs energy at 20°C, ΔS—entropy change ($\Delta G^0_T = \Delta H_{cal}\ (1-T/T_m) = \Delta H_{VH}\ (1-T/T_m) = \Delta H_{VH} - T\Delta S$, where ΔH_{cal} is calorimetric enthalpy. $\Delta H_{cal}/\Delta H_{VH} = 1$ for two-state transition [8]). Results are mean ± S.D. (n = 3)

Aptamer	T_m (°C)	ΔH_{VH} (kcal/mol)	$\Delta G^o_{(20)}$(kcal/mol)	$T\Delta S$ (kcal/mol)
TT	35.3 ± 0.5	−40.4 ± 0.4	−2.00 ± 0.02	−38.40 ± 0.40
TA	34.2 ± 0.4	−31.6 ± 0.6	−1.46 ± 0.03	−30.14 ± 0.60
AA	26.8 ± 1.0	−45.6 ± 5.9	−1.03 ± 0.13	−44.57 ± 5.90
AGA	29.6 ± 0.8	−40.5 ± 2.8	−1.28 ± 0.09	−39.22 ± 2.80

thickness shear mode (TSM) acoustic method. The aptamers have been immobilised at clean gold surface of TSM transducer (fundamental frequency 8 MHz) by neutravidin-biotin technology [9]. The TSM method is based on determination of series resonant frequency, f_S, and motional resistance, R_m, from impedance spectra of quartz transducer. f_S and R_m reflect energy storage and dissipation, respectively [9, 10]. Thermodynamic and binding experiments were performed in following buffer: 140 mM NaCl + 5 mM KCl + 1 mM $CaCl_2$ + 1 mM $MgCl_2$ + 20 mM Tris–HCl (pH 7.4). TSM experiments were performed at T = 20°C.

73.3 Results and Discussion

The plot of absorbance versus temperature for all aptamers studied is presented in Fig. 73.1. It is seen that the absorbance has sigmoid shape typical for two-state transition. The fit of experimental results using Eq. 73.1 allowing determination of thermodynamics properties of aptamers (Table 73.1). It is seen from Table 73.1, that substitution of nucleotides resulted in decrease of T_m and in less favorable Gibbs energy changes in comparison with TT aptamers. Most remarkable instability took place for AA aptamers. The favorable changes in enthalpy are in this

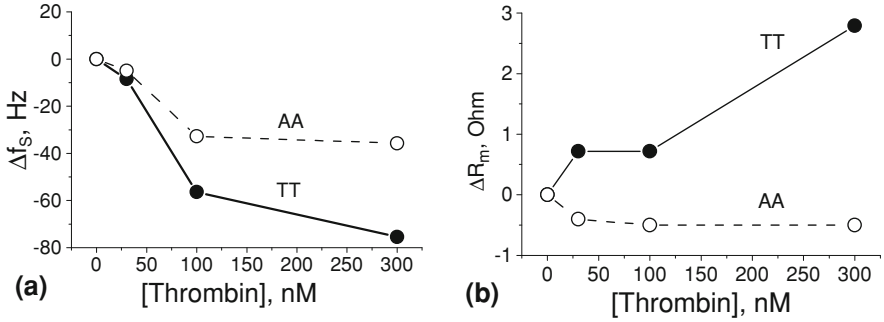

Fig. 73.2 Representative plots of Δf_S (**a**), and ΔR_m (**b**), as a function of thrombin concentration of TSM sensor with immobilised TT or AA aptamers. S.D. did not surpass 15%

case compensated by entropy contribution. The changes in entropy can be due to uptake of ions or water into the G-quadruplex [8]. The lower values of T_m in comparison with those reported in [8] are due to less KCl concentration used, presence of NaCl and due to thymidine spacer.

The interaction of thrombin with aptamers immobilised at TSM transducer correlates with thermodynamic properties of aptamers. Most remarkable differences in the acoustic parameters following addition of thrombin were observed for TT and AA aptamers. The resonant frequency for both aptamers decreased with increasing thrombin concentration. However, for TT aptamers these changes were substantially larger, which suggest higher sensitivity to the thrombin. Substantial differences were observed in changes of motional resistance for these aptamers. While for TT aptamers the motional resistance increased with increasing the thrombin concentration, opposite changes in R_m took place for AA aptamers (Fig. 73.2). This suggests different conformation/surface properties of the thrombin-aptamer complexes for these aptamers and as a result changes in coupling of the surface and liquid-higher coupling for TT (increase in R_m), decoupling for AA (decrease in R_m) [10]. AGA and AT have revealed comparable sensitivity with those of AA in respect of frequency changes, but R_m slightly increased for these aptamers.

73.4 Conclusions

We showed that substitution thymidines by adenines in the thrombin-binding site of G-quadruplex substantially affect both thermodynamic and binding properties of the DNA aptamers immobilised on TSM transducer.

Acknowledgments We thank to Slovak National Scholarship Program and to Agency for Promotion Research and Development (project APVV-0362-07) for financial support.

References

1. Ellington AD, Szostak JW (1990) Selection in vitro of an RNA enzyme that specifically cleaves single-stranded DNA. Nature 344:467–469
2. Jayasena SD (1999) Aptamers: an emerging class of molecules that rival antibodies in diagnostics. Clin Chem 45:1628–1650
3. Vorhies JS, Nemunaitis JJ (2007) Nucleic acid aptamers for targeting of shRNA-based cancer therapeutics. Biol: Targets Ther 4:367–376
4. Bock LC, Griffin LC, Latham JA, Vermaas EH, Toole JJ (1992) Selection of single-stranded DNA molecules that bind and inhibit human thrombin. Nature 355:564–567
5. Hardin CC, Perry AG, White K (2001) Thermodynamic and kinetic characterization of the dissociation and assembly of quadruplex nucleic acids. Biopolymers 56:147–194
6. Schultze P, Macaya RF, Feigon J (1994) Three-dimensional solution structure of the thrombin-binding DNA aptamer d(GGTTGGTGTGGTTGG). J Mol Biol 235:1532–1547
7. Hianik T, Wang J (2009) Electrochemical aptasensors—recent achievements and perspectives. Electroanalysis 21:1223–1235
8. Ohsen CM, Lee H-T, Marky LA. Unfolding thermodynamics of intramolecular G-quadruplex: base sequence contribution of the loops. J Phys Chem B 113: 2587–2595
9. Hianik T, Grman I, Karpisova I (2009) The effect of DNA aptamer configuration on the sensitivity of detection thrombin at surface by acoustic method. Chem Commun pp 6303–6305
10. Ellis JS, Thompson M (2004) Acoustic coupling at multiple interfaces and the liquid phase response of the thickness shear-mode acoustic wave sensor. Chem Commun pp 1310–1311

Chapter 74
Application of Epoxy/Carbon Nanotube Composites as Microwave Absorber at Frequencies up to 25 GHz

R. Di Giacomo, H. C. Neitzert, L. Vertuccio, A. Sorrentino and S. Sabbatino

Abstract A new type of Epoxy/CNT composite has been fabricated based on bisphenol A-epoxy resin, loaded with 0.5wt% of commercial multiwall carbon nanotubes. Exploiting the resulting high conductivity of this composite material, we tested the possibility to use it as absorber of electromagnetic waves at microwave frequencies up to 25 GHz. For this purpose the sample, to be tested, was placed as substrate of a microstrip transmission line. Measurements of the scattering parameters, done with a vectorial network analyzer, have been used in order to obtain the power absorption (PA) spectra. Special attention was paid to the optimization of the microstrip geometry. A comparison of the PA spectrum with the absorption spectra of commercial cavity absorbers showed encouraging results, regarding the microwave absorption capability of the new nanocomposite material.

R. Di Giacomo · H. C. Neitzert (✉)
Dipartimento di Ingegneria Elettronica e Ingegneria dell'Informazione (DIEII), Università degli Studi di Salerno, Via Ponte Don Melillo 1, 84084 Fisciano, SA, Italy
e-mail: neitzert@unisa.it

L. Vertuccio · A. Sorrentino
Dipartimento di Chimica Alimentare (DICA), Università degli Studi di Salerno, Via Ponte Don Melillo 1, 84084 Fisciano, SA, Italy

S. Sabbatino
AVAGO Technologies, Torino, TO, Italy

Present Address:
S. Sabbatino
Avio S.p.A., Via 1°Maggio 99, 10040 Rivalta, TO, Italy

G. Neri et al. (eds.), *Sensors and Microsystems*,
Lecture Notes in Electrical Engineering 91, DOI: 10.1007/978-94-007-1324-6_74,

74.1 Introduction

Carbon nanotubes addition to polymer [1] or epoxy material [2] is improving the mechanical properties and also strongly enhancing the thermal and electrical conductivities of the organic material. The good conductivity of this nanocomposites makes this type of materials attractive for the realization of electrical heaters [3] and sensors [4] and for applications regarding electromagnetic shielding [5–7].

74.2 Composite Preparation

Epoxy/CNT composite have been fabricated as follows: A diglycidyl ether of bisphenol A-epoxy resin (DGEBA) has been mixed together with ultrasonically dispersed multiwall carbon nanotubes (MWCNTs) and subsequently hardened with 4,4'diamine-dibenzyl-sulfone (DDS) hardener and cured in a two-step process first at 130°C and subsequently at 180°C. Because the percolation threshold of these kind of nanocomposites is rather low, CNT concentrations below 0.5wt% are sufficient to create a stable conducting nanotube network. More detail regarding the sample preparation can be found in [8].

74.3 Measurement Procedure for the Determination of the Microwave Power Absorption

The Power Absorption (PA) has been determined in the frequency range between 130 MHz and 25 GHz, using measurements in microstrip geometry with a Vectorial Network Analyzer (VNA) of the scatter parameters S_{11} and S_{21}. The material, to be characterized, was the substrate of the microstrip, on which by gold evaporation a small top metal strip has been deposited. The geometry and a photo of the connectorized sample are shown in Fig. 74.1. More details regarding the used measurement procedure and the parameter determination can be found in [5].

As we call SE the shielding effectiveness, R the first reflection term, A the absorbtion term and M the multiple reflection inside the material thickness term we have:

$$SE_{dB} = R_{dB} + A_{dB} + M_{dB} \tag{74.1}$$

The microstrip geometry was determined according to the fact, that if the first reflection term R_{dB} derived from S_{11} is smaller than 12 dB, this will ensure that we can use the S_{21} scattering parameter as the PA $= 20 \log_{10}| e^{\gamma L} |$, where L is the length in meter of the microstrip and γ the propagation constant in the material. As shown in Fig. 74.2 we use an experimental successive approximation way to find

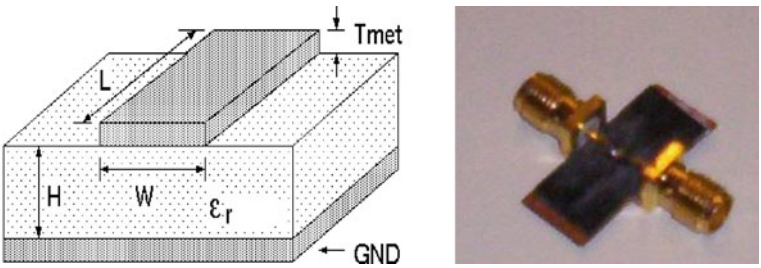

Fig. 74.1 Microstrip geometry and photo of an connectorized sample

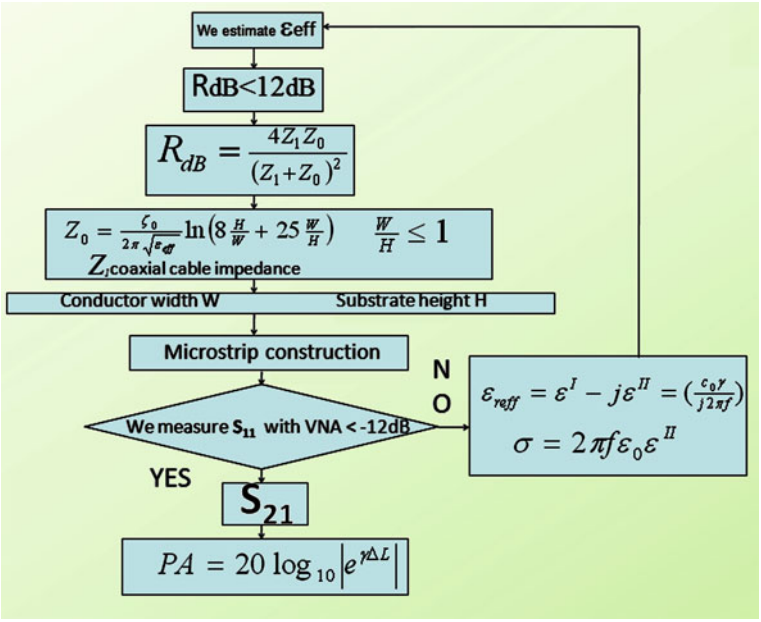

Fig. 74.2 Flowchart of the procedure for the determination of the power absorption in an optimized microstrip geometry

the optimal microstrip geometry, measuring and adjusting step by step the various geometrical parameters until R_{dB} is reduced below the desired value. For this purpose, we derive γ from the S_{21} measurement values even when S_{11} is greater than 12 dB. In this case, however, γ is overestimated and consequently also the values of ε_{eff} and R_{dB} so that we need to adjust the geometrical parameters. The procedure is repeated until R_{dB} has a value below 12 dB. Now the power absorption can be directly determined by the S_{21} value.

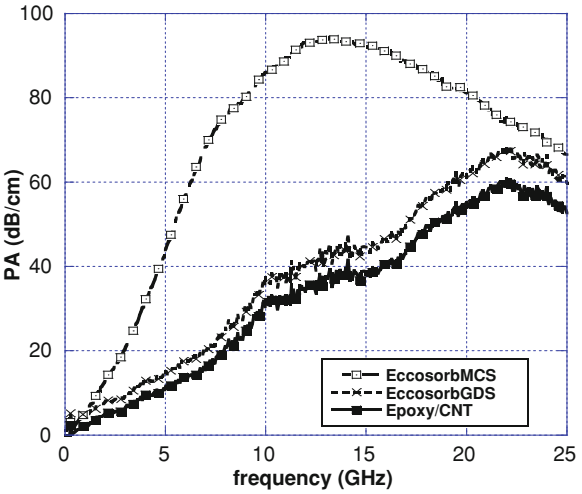

Fig. 74.3 Microwave power absorption spectrum of an Epoxy/CNT composite in comparison with the spectra of two different commercial cavity resonance absorbers

74.4 Measurement Results

The microwave power absorption spectrum of the nanocomposite is shown in Fig. 74.3 in comparison to the spectra of two different commercial cavity resonance absorbers. These latter absorbers are thin, flexible, magnetically loaded, high-loss silicone rubber based films and electrically non-conductive. It can be seen, that the Epoxy/CNT composite material has approximately the same microwave power absorption capability as the ECCOSORB®MCS commercial absorber, specified from the manufacturer to be used in a wavelength range between 6 GHz and 35 GHz, but inferior properties, when compared to the ECCOSORB®GDS commercial absorber (specified for a wavelength range between 0.8 GHz and 18 GHz).

74.5 Conclusions

Epoxy/CNT has been tested as absorber material at microwave frequencies and compared to two different commercial cavity resonance absorber materials. The first results, obtained without any optimization of the nanocomposite regarding this specific application, are encouraging to further investigate the possibility to use the new low-cost composite material for electromagnetic shielding applications.

References

1. Xie XL, Mai Y-W, Zhou X-P (2005) Mat Sci Eng R 49:89
2. Kim JT, Kim HC, Kim SK, Kathi J, Rhee K-Y (2009) J Composite Mater 43:2533

3. Neitzert HC, Sorrentino A, Vertuccio L, Vittoria V (2009) Proceedings of the 17th international conference on composites or nano engineering (ICCE/17), Honolulu, to be published
4. Neitzert HC, Sorrentino A, Vertuccio L, Vittoria V (2009) Proceedings of the AISEM 2009, sensors and microsystems. Lect Notes Electr Eng 54:241
5. Saib A, Bednarz L, Daussin R, Bailly C, Lou X, Thomassin JM, Pagnoulle C, Detrembleur C, Jerome R, Huynen I (2006) Carbon nanotube composites for broadband microwave absorbing materials. IEEE Trans Microwave Theory Tech 54:2745
6. Liu Z, Bai G, Huang Y, Ma Y, Du F, Li F, Guo T, Chen Y (2007) Carbon 45:821
7. Deng L, Han M (2007) Appl Phys Lett 91:023119–1
8. Guadagno L, Naddeo C, Vittoria V, Sorrentino A, Vertuccio L, Raimondo M, Tucci V, De Vivo B, Lamberti P, Iannuzzo G, Calvi E, Russo S (2010) Cure behavior and physical properties of epoxy resin—filled with multiwalled carbon nanotubes. J Nanosci Nanotechnol 10:2686

Chapter 75
An Infrared Thermal Measuring System for Automotive Applications and Reliability Improvement

S. Panarello, S. Patane', A. Testa, S. De Caro, R. Letor, S. Russo and D. Patti

Abstract In the last years the global energy economy hangs in the balance, pushing up the research interest in novel and renewable energy sources and in innovative engines able to improve performances saving the efficiency. This frame requires the development of power electronics subsystems and the continuous increase of working temperatures; hence reliability has become the most critical requirement for any new device design. The temporal evolution of temperature distribution on the surface of a power electronic device undergoing an exerted stress plays a fundamental role in studying and improving reliability. A suitable scanning measuring system has been realized in order to allow the analysis of fast transient states and the localization of "hot-spots" which could be a cause of a premature failure and unreliability of the devices.

75.1 Introduction

The reduction in scale of integrated circuit technology, the continuous increasing of the power density and the operative temperatures of the devices, give rise to challenging problems in the design of the electronic circuits and their packages.

S. Panarello (✉) · S. Patane'
Dip. di Fisica della Materia e Ingegneria Elettronica, University of Messina, Messina, Italy
e-mail: spanarello@unime.it

A. Testa · S. De Caro
Dip. di Chimica Industriale ed Ingegneria dei Materiali, University of Messina, Messina, Italy

R. Letor · S. Russo · D. Patti
STMicroelectronic, Catania, Italy

G. Neri et al. (eds.), *Sensors and Microsystems*,
Lecture Notes in Electrical Engineering 91, DOI: 10.1007/978-94-007-1324-6_75,

All the devices which are employed in "mission-critical" tasks must show high longevity and reliability to ensure a very small number of parts per million of dead devices, ensuring the correct operation of the entire system as long as possible. The "mission critical" power devices are used in severe environments where a failed or bad working part could be the cause of irreparable damage. The temperature is surely a critical parameter for power dissipating devices, due to its influence on the working parameters and life time. For example when they undergo a strong stress some key characteristics, such as their resistivity, show a noticeable shift from the typical values.

The distribution of the temperature on a power electronic device can show transients also in the microseconds scale with variations of more than 90–100 K. This fast temperature gradient cannot be sensed by a conventional infrared camera which usually has a few milliseconds response time.

A new approach to the measurement of the temperature consists in a scanning procedure which reconstructs the thermal map rastering the sample surface and collecting the intensity of the electromagnetic radiation emitted point by point while the device undergoes power cycling. A simple software procedure is able to give the thermal map at a precise time after the power firing, or to show the thermal evolution during the stress. This result requires a precise synchronization between the current cycling and the sampling of the signal coming out from the thermal sensor. Hence the instrument allows the users to analyze fast transient states and to indicate "hot-spots" which could be a cause of a premature failure and unreliability of the devices in which they are present.

75.2 The Measuring Instrument

The measuring instrument consists of the following components:

- An XY mechanical displacement system.
- A wide optical bandwidth reflective objective.
- An infrared optical detector optimized for working in the 6–12 microns range.
- Two acquisition boards (PCI-6014, PCI-5102, National Instruments) to control and synchronize the instrument movement, and to collect the data. The PCI 6014 board gives also the trigger pulse to the power supply of the device under test (DUT).

75.2.1 The Reflective Objective

Measuring the thermal radiation requires special care in the objective performances either in terms of optical bandwidth, lateral resolution, numerical aperture and throughput. A device able to fulfill all the requirements is not easy to find, the

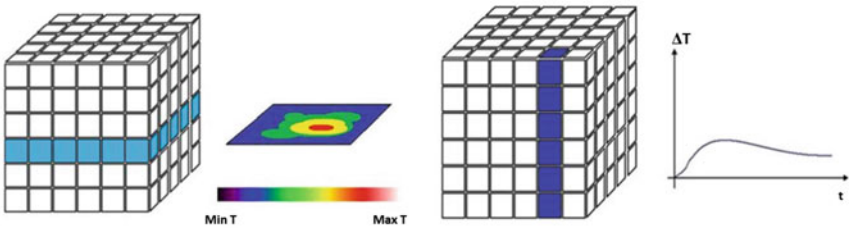

Fig. 75.1 Organization of the thermal maps and the time arrays in the data matrix

best choice we found consists of a reflective objective designed in a reversed Cassegrain configuration. The mirrors are aluminum coated, therefore a bandwidth ranging from the Ultraviolet to the far Infrared is guaranteed (namely from 200 nm to about 20 μm). The objective has a magnification of 36X, a numerical aperture of 0.52, it is infinity corrected, and due to its special configuration it has zero chromatic aberration.

75.2.2 The Infrared Detector

The detector that has been used consists of a thermoelectrically cooled photovoltaic sensor (PVMI-2TE-10.6, Vigo System). It has a sensitive area of 1 mm^2 and a response time better of 3 ns. The device working temperature is controlled by a thermoelectric cooler and an electronic feedback-loop. The temperature control is a crucial point to assure the detector efficiency, the PVMI-2TE-10.6 working temperature is set to −40°C while the thermoelectric cooler requires a room temperature below to 24°C to properly work. During the measurement phase, the room temperature near the sample and, consequently, near to detector could increase. In order to deal with this problem, an external liquid-cooling system has been realized to assure the heat be quickly moved away both from the sample holder and from the sensor.

75.3 Working Principle

The instrument carries out a spatial scanning of the samples surface, based on a cyclic repetition of displacements and acquisitions. The devices under test are repetitively submitted to the same electrical transient and, as a consequence, to the same thermal transient for each scanned point. Hence, point by point the light collected by the objective is transformed in an electrical signal and then simultaneously sampled by the two acquisition boards. The PCI-6014 board collects the

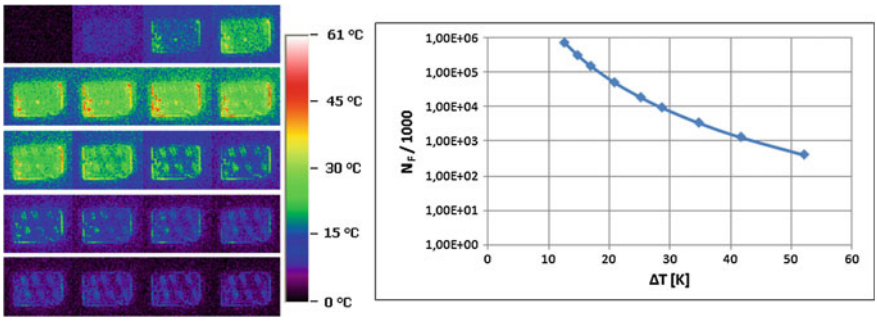

Fig. 75.2 Sequence of reconstructed maps from the analysis of the thermal stress for a given mission (*left*). Characterization curve performed with different exerted stress (*right*)

signal during the entire current cycle at a sampling rate of 200 KS with a 16 bit resolution. The PCI-5102 board, is dedicated to very high speed acquisitions (20 MS/s) of reduced temporal windows that can be freely selected by the user inside the entire temporal cycle. For each point that is analyzed, a vector, containing the digital data that describes the thermal behavior, is stored in the personal computer memory. The collected data are therefore organized in a three dimensional matrix with two spatial dimensions and a third temporal one (see Fig. 75.1).

75.4 Reliability Model and Lifetime Estimation

Evaluation of device failure probability has been performed by studying a suitable number of devices, forcing them to undergo the thermal cycle related to a given mission [1]. Devices have been tested with different peak currents in order to correlate the number of cycles to fail to the temperature variation. The obtained results are shown in Fig. 75.2.

The reliability model that best describes the experimental results is a simplified Coffin-Manson law. Such a law well predicts the failure due to cracks and material fatigue or deformation caused by cycles of stress or changes in temperature.

The reliability model considered is given by the following expression:

$$N_F = \alpha \Delta T^{-m} \tag{75.1}$$

where N_F is the number of cycles to 10 ppm (pieces per million) failures, ΔT is the thermal gradient during a cycle and a and m are two parameters to be experimentally found.

Starting from the experimental results and using the simplified Coffin–Manson model, the device degradation in terms of number of cycles as function of ΔT can be predicted, according to the diagram of Fig. 75.2.

75.5 Conclusions

The described measuring instrument intends to be a versatile tool to obtain the high speed maps of the radiation emitted from the surface of an active component. Its main feature, hardly attainable with other kinds of instruments, consists of the very high speed of sample rate and equivalent frame-rate.

Thanks to the "open" setup, the size of the scanned areas, the spatial resolution and the speed of acquisition can be easily changed. With the simple substitution of the objective, the optical magnification can also be changed and the ultimate limit to the lateral resolution is imposed by the diffraction limit, which is related to the wavelength of the analyzed radiation.

All the performed thermal measurements have been useful for the design improvement, quality and reliability control of power electronic devices in the automotive field and beyond. From an industrial point of view, the thermal analysis has been performed above all on new generation devices.

The performed measurements have allowed the improvement of the layout of several tested devices in order to perform a better dissipation of the temperature and the valuation of their reliability, correlating the thermal stress to the number of thermoelectric cycles that can be supported without failure.

Reference

1. Testa A, De Caro S, Panarello S, Patanè S, Letor R, Russo S, Poma S, Patti D (2008) Stress analysis and lifetime estimation on power MOSFETs for automotive ABS systems. In: 39th IEEE power electronics specialists conference (PESC 2008), pp 1169–1175, June 2008

Chapter 76
Fast Multi-Channel Driver for High-Voltage Micromirrors Switches

Andrea Simonetti, Stefano De Luca and Alessandro Trifiletti

Abstract The most popular micromirrors switches, work with a sinusoidal low-frequency carrier obtained by a simple generator with a rough shift-level circuitry. Aiming to the problem for the pulsed rectangulars carrier signals, more and more used in the digital and scanning bonded silicon mirrors, the analog amplifiers arranged to operate in a saturation region, decrease the sharpness of leading and trailing edges of a rectangular pulse envelope (i.e. audio amplifiers). This approach makes unusable a set of features of these actuators. The well-known systems, based on high-voltage logic ports, capable of resulting an output carrier that having the shape substantially a square waveform, require large current and are very expensive. In the proposed architecture, it is possible to reduce both the excessive and unnecessary spectral components resulting from the rapid rise and fall time of the rectangular envelope as also relax the current requirements with a dedicated circuitry arrangement that modifies the output source in a trapezoidal envelope. A new scheme for decreasing power requirements using a source degenerated logic port is introduced. This method, addresses these issues by tracking the output current with a very simple approach that doesn't require an additional consumption as most solutions do.

A. Simonetti (✉) · A. Trifiletti
Department of Electronic Engineering, University of Rome "La Sapienza",
00184 Rome, Italy
e-mail: simonetti@die.uniroma1.it, simonetti@evodevo.it

A. Trifiletti
e-mail: trifiletti@die.uniroma1.it

A. Simonetti · S. De Luca
EvoDevo Labs, 00040 Pomezia, Italy
e-mail: s.deluca@evodevo.it

G. Neri et al. (eds.), *Sensors and Microsystems*,
Lecture Notes in Electrical Engineering 91, DOI: 10.1007/978-94-007-1324-6_76,

76.1 Introduction

Scanning and digital micro-mirrors are some of the most important elements of the MOEMS (Micro-Opto-Electro-Mechanical Systems) devices. Particularly, the micro-machined based switches are an attractive solution for the all-optical networks (i.e. telecommunications) such as the optical switches [1, 2, 3], the phase-modulation-induced switching [4] and frequency down-conversion [5]. The MOEMS switches require a square-wave excitation with a depth of modulation that may be more than one hundred volts at a frequency of repetition that is closely related to the particular device, similarly to effective tilting angle. Nonetheless, the current state-of-the-art technology demonstrates the lack of economic tools to drive the array of these actuators or the multi-axis micro-mirrors. It should be noted that the power density is also an appreciable figure-of-merit in the market context, so higher frequencies thus higher loads and higher voltages capability, requires everything else to get smaller and there is thus a greater emphasis to very advanced designs built with manufacturing processes such as surface-mount techniques. Therefore, in this work we propose a low-priced, multi-channel digital handheld drive with an advanced feedback loop that allows fast slopes with a very large voltage and high frequency span. Experimental waveforms for the proposed interface are also given to demonstrate its validity.

76.2 Basic Principle

Starting on the output side and assuming a capacitive load, the proposed interface is based on a high-voltage CMOS (Complementary Metal-Oxide Semiconductor) logic port capable of a zero-return condition, where the active devices must have a low channel charge accomplished with a high voltage and high current capability. As described in Ref. [6], the power consumption of a logic port has an optimal trade-off when the input and the output rise and fall times are equalized. The energy of the switching losses doesn't depend on the buffer design but essentially from the load, the frequency and the output swing, and are hard to reduce. Instead, the short-circuit losses are strongly related to design of the buffer [7–10].

Figure 76.1b shows a MOS pairs commonly used as a digital port. Since these devices are selected for the maximum dynamic load, when the circuit is not charged at full design condition, short-circuit losses increase. A possible solution in order to keep a high efficient circuitry is the gate signal manipulation that appreciably decreases gate-losses and modulates the output rise and fall-time. Nevertheless, by introducing a source-degeneration scheme based on an inductive feedback, the network around the source track the load changes and allows a proportional gate modulation that replicates same trapezoidal shape obtained with more sophisticated techniques. A little overshoot in the shape edges appears with large inductance values (about a thousand times the parasitic of the MOS and the

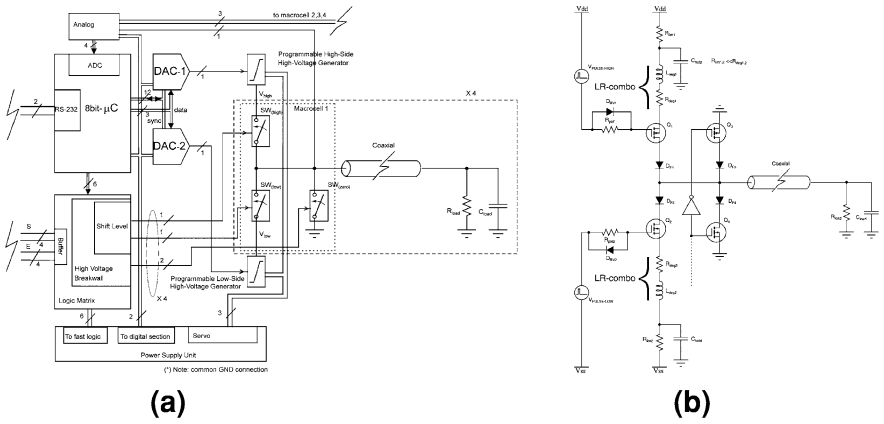

Fig. 76.1 **a** The conceptual scheme of digital driver especially designed for long wire connections (i.e. coaxial cable). **b** A detail of the source degeneration technique

circuit), but under these conditions a reduction up to one quarter of the switching losses is reached. The resistor in the LR-combo can be adjusted to satisfy both the overall stability and the transient response.

76.3 Interface Description

Preliminarily, a simple wired-based logic circuit makes this system less cost effective and faster than the PAL (Programmable Array Logic) or the FPGA (Field Programmable Gate Array) conventional solutions. The shift-level block is performed with a fast opto-couplers system that allows a high isolation among the logic and the power sections. In order to deal with high-frequency inputs, this block is connected as a bootstrapping circuitry to reduce signal distortion by keeping a constant gate-to-source voltage of the output coupled MOS. Synchronization for the complementary ground referenced MOS switches (zero return totem-pole), is obtained by processing the gate signals of the floating switches that are properly shifted also with an opto-couplers devices, with an external input signal. The logic flow, delays the starting of the zero return state after the end of the main logic state, such as the return at the normal operation is delayed at the end of the zero return condition. Since the controller is based on a completely static asynchronous state-machine, the output analog level (positive voltage, negative voltage, ground connection), can be maintained for an indefinite time. Now, considering that the zero-return overcomes the standard input signals (similarly to an enabling function), it is possible to obtain a sophisticated modulation of the micro-mirrors switches. The grounded low-impedance also prevents the breakdown voltage on the capacitive loads, which is induced by the parasitic currents.

76.4 Experimental Results

Figure 76.2 shows the proposed interface built on a printed circuit board using customized magnetic components and optimized layout. The output amplitude is digitally selectable, independently for each level, from 1 to 250 $V_{p\text{-}p}$ with four channels simultaneously loaded at 400 pF and 22 KOhm up to 1 MHz input

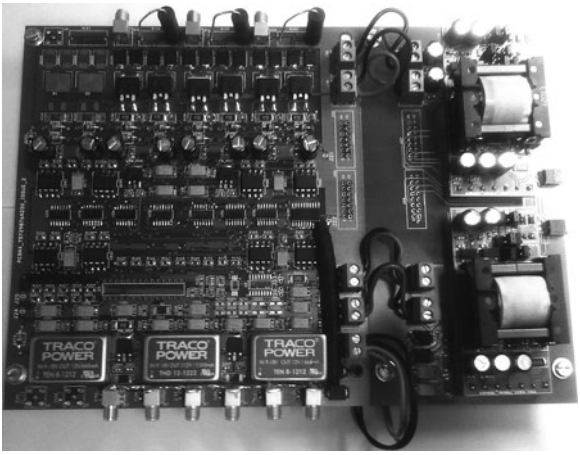

Fig. 76.2 The proposed drive in the four channel version. The digital inputs are 3.3 V and 5 V compatible. This device is powered by an unregulated power-supply from 11 to 18 V with a typical power consumption of 12 W at full load. Optional microprocessor and serial port are also provided to support a pc-based instrument

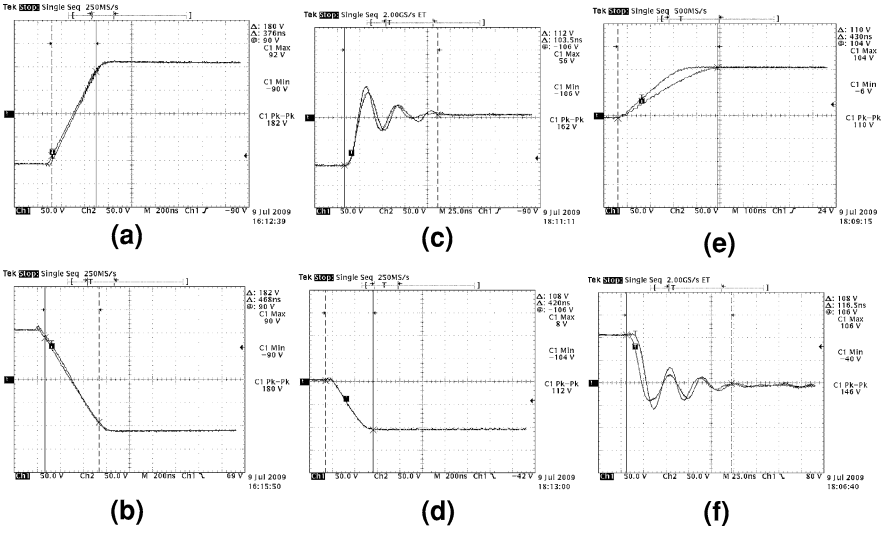

Fig. 76.3 The output waveforms with two channels simultaneously activated. Particular of the output with the enable input set to low and the main input set from low to high (**a**) and high to low (**b**). Particular of the output with the enable input set from low (disabled) to high (**c**, **f**) and high to low (**d**, **e**) with the main input set to low (**c**, **d**) and high (**e**, **f**) respectively. Only in the **c** and **f** results a little overshoot smaller than 20nS. In the other cases, the settling-time is negligible

frequency. The minimum slew rate is 450 V/μS in the normal operation and 1000 V/μS for the zero-return. The experimental waveforms with a 5 V, 50 kHz square-wave input are shown in Fig. 76.3a, b respectively. The zero-return has been characterized by applying the same previous excitation to its port with the main input alternately forced between low and high logic levels, as shown in Fig. 76.3c, d and in Fig. 76.3e, f respectively.

Acknowledgments Research sponsored by the EvoDevo company, I-00040 Pomezia, Italy.

References

1. Kim, Park N, Kim YK (2002) Reflective type variable optical attenuator using off-axis misalignment. In: IEEE/LEOS international conference on optical MEMS (2002), pp 55–56
2. Yang MS, Noh YO, Won YH, Hwang WY (2001) Very low crosstalk 1 × 2 digital optical switch integrated with variable optical attenuators. Electron Lett 37:587–588
3. Giles CR, Aksyuk V, Barber B, Ruel R, Stulz L, Bishop D (1999) A silicon MEMS optical switch attenuator and its use in lightwave subsystems. IEEE JQE 5:18–25
4. Guerra DN, Imboden M, Mohanty P (2008) Electrostatically actuated silicon-based nanomechanical switch at room temperature. Appl Phys Lett 93:033515
5. Chan HB, Stambaugh C (2006) Fluctuation-enhanced frequency mixing in a nonlinear micromechanical oscillator. Phys Rev B 73:224301
6. Veendrick HJM (1984) Short-circuit dissipation of static CMOS circuitry and its impact on the design of buffer circuits. IEEE JSSC SC-19:468–473
7. Changsik Y (2000) A CMOS buffer without short-circuit power consumption. IEEE Trans Circ Syst II 47(9):935–937
8. Garverick SL, Nagy ML, Kane MJ (2003) Bipolar pulse width modulation driver for MEMS electrostatic actuator arrays. In: Proceedings of IEEE CIC conference, pp 481–484, 21–24 September 2003
9. Saul PH, Brunson KM, Bunyan RJT (2003) Versatile high voltage level shift and driver for MEMS applications. Electron Lett 39(2):185–186
10. Yuan M, Xiqun Z, Newcomb RW (2005) Cost effective high voltage driver for large channel count optical MEMS switch applications. Proc IEEE ISCAS 6:5397–5400

Chapter 77
Cross Selectivity Immunoaffinity and Applications for Lactoferrin Immunosensor

M. Tomassetti, E. Martini and L. Campanella

Abstract After recent research carried out by our team aimed at developing new immunosensors for lactoferrin, in the present note are reported the results of research carried out to determine the constant of affinity between Lactoferrin and the corresponding antibody (human anti-lactoferrin). In addition, a detailed investigation was made of immunosensor selectivity and the cross selectivity of the immunosensor developed towards the principal proteins present in milk which are considered as possible interference in Lactoferrin determination in milk and its derivatives, or in saliva.

77.1 Introduction

Lactoferrin, a glycoprotein of transferrin family, appears to exert immunomodulatory activity. However, it is also a protective protein that plays an important role in the transfer of passive immunity from the mother to the neonate as it is contained in her milk. The increasing commercial interest in exploiting the therapeutic value of lactoferrin has stimulated interest in developing reliable assays for its determination at the endogenous level in mother's milk, or in dairy milk products for unweaned babies, but also in saliva and tears. Our team recently developed different kinds of lactoferrin immunosensors. Initially, competition immunosensors were developed using different transducers and two different measurement geometries [1, 2]. More recently a new direct measurement method was developed which allows considerable reduction in analysis time [3].

M. Tomassetti (✉) · E. Martini · L. Campanella
Department of Chemistry, University of Rome "La Sapienza", P. le Aldo Moro 5, 00185 Rome, Italy
e-mail: mauro.tomassetti@uniroma1.it

G. Neri et al. (eds.), *Sensors and Microsystems*,
Lecture Notes in Electrical Engineering 91, DOI: 10.1007/978-94-007-1324-6_77,

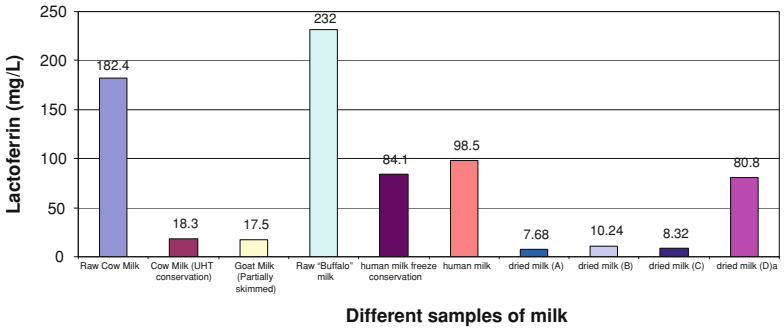

Fig. 77.1 Different lactoferrin content found in several samples of fresh, frozen, or dried milks. **a** Product to which lactoferrin was also added by producer

77.2 Result

First, new immunosensors for the analysis of lactoferrin protein in human or bovine milk and dairy products were fabricated and optimized. To this end, three different transducers [1] were tested, while peroxidase was used as marker in all cases. In previous research, the more sensitive immunosensor, i.e. the one using H_2O_2 electrode as transducer, was applied to Lactoferrin determination in several human and animal milk samples (Fig. 77.1).

The study has now been extended to the ability of the antibody used to produce the immunocomplex with the test analyte. As the immunoaffinity characteristic of the antigen for the immunoreagent is of the utmost importance in any immunological method, a rough estimation of the K_{aff} of the test antigen (i.e. lactoferrin) was obtained at the midpoint of the Langmuir curve, where $K_{aff} = 1/IC_{50}$. In our case IC_{50} was calculated as the concentration of analyte that binds 50% of the antibody to the sensor surface. The K_{aff} value was found to be of the order of 10^6 M^{-1}, in all cases, i.e. using different geometries, different transducers and different measurement methods (see Fig. 77.2).

In addition the selectivity features were studied with reference to other possible interfering milk or serum proteins. This study was performed in two ways. First immunosensor response was compared with the same fixed concentration of lactoferrin or other protein i.e. casein, human and bovine lactoglobulin, lactalbumin, IgG and IgA (Table 77.1).

Then, the cross-selectivity values for each one of these proteins were experimentally determined and compared toward human Lactoferrin (Table 77.2).

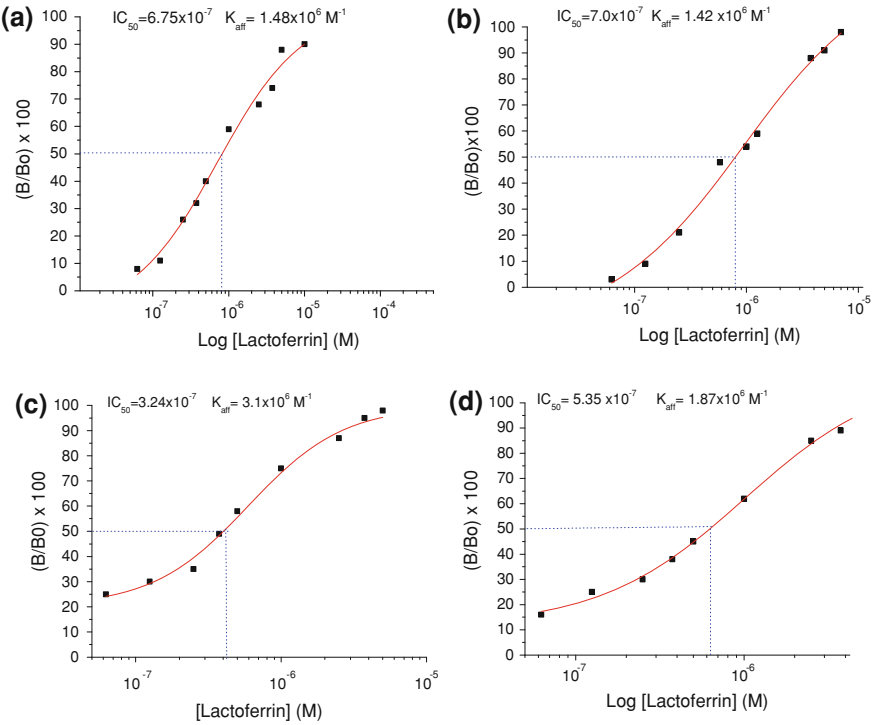

Fig. 77.2 K_{aff} calculation: using H_2O_2 electrode as transducer in (**a**) first competition procedure and in (**b**) second competition procedure; using Iodide as transducer in (**c**) first competition procedure and in (**d**) second competition procedure

Table 77.1 Selectivity features with reference to several common proteins contained in milk and in saliva; data obtained using the 1° competition method an H_2O_2 electrode as transducer. All proteins were measured at the same concentration, i.e. $\approx 5.0 \times 10^6\ M^{-1}$

Protein	Response to lactoferrin checked as 100% $n = 5$, RSD% ≤ 5
Human lactoferrin	100.0
Casein	36.0
Lactoglobulin	42.3
Bovine lactalbumin	39.4
Human lactalbumin	40.5
IgA	13.9
IgG	15.5

Table 77.2 Percent cross selectivity values for several common proteins contained in milk and saliva toward lactoferrin, using our immunosensor

Protein	Percent cross selectivity values for lactoferrin immunosensor. $n = 5$; RSD% ≤ 5
Human lactoferrin	100.0
Casein	11.3
Lactoglobulin	30.4
Bovine lactalbumin	23.3
Human lactalbumin	25.2
IgA	4.4
IgG	3.5

77.3 Discussion

On the basis of the results obtained using either different transducers, or the competition or direct method, respectively, or the different operating procedures, the K_{aff} value was consistently found to be of the order of 10^6 M^{-1}. As far as selectivity is concerned, it clearly emerges how its determination using the first method, the results of which are summarized in Table 77.1, in this case is characterized by much higher interference values than those obtained using the classical cross-selectivity method shown in Table 77.2; although the first method was much faster, it seems to produce results that are much less accurate than the second.

77.4 Conclusions

In conclusion, the K_{aff} value obtained is more or less in line with the scanty data reported in the literature. This value is also sufficiently high for a good immunological method to be developed.

As far as selectivity is concerned, the cross-selectivity values indicate that the only protein likely to cause some degree of interference is lactoglobulin.

Acknowledgments Research funded by "La Sapienza" University of Rome, "Ateneo and University Projects".

References

1. Campanella L, Martini E, Tomassetti M (2008) New immunosensor for lactoferrin determination in human milk and several pharmaceutical dairy milk products recommended for the unweaned diet. J Pharm Biomed Anal 48:278–287

2. Campanella L, Martini E, Pintore M, Tomassetti M (2009) Determination of lactoferrin and immunoglobulin G in animal milks by new immunosensors. Sensors 9:2202–2221
3. Campanella L, Martini E, Tomassetti M (2009) Further development of lactoferrin immunosensor. In: Abstract book of 13th international meeting RDPA, Milan, Italy, p 77, 9–12 Sept 2009

Chapter 78
OPEEs to Investigate the Isothermal Rancidification Process in Olive Oils

Mauro Tomassetti, Luigi Campanella and Stefano Vecchio

Abstract Continuation of our team's study of olive oil rancidification carried out in recent years using ad hoc biosensors. While in the preceding research the thermo-oxidative decomposition of extra-virgin olive oil (EVOO) at high temperatures was investigated, in the present work the aim was instead to make a more in-depth study of the principal processes that occur when an oil sample is artificially rancidified isothermally at 98°C in a air stream, using the classical American official method (AOM method, official method). The principal processes taking place were essentially monitored using three different organic phase enzyme electrodes (OPEEs) as well as by two other ancillary non biosensor methods. Furthermore, the present research was not limited to the study of EVOO. The kinetic investigation using biosensor methods was extended to include olive oil (OO) and olive oil residue (OOR).

78.1 Introduction

Research on olive oil continued in several stages over the past few years [1, 2]. Previous papers described the thermooxidative decomposition of extra-virgin olive oil (EVOO) at high temperatures and were aimed at determining the time span over which the product can be used effectively and safely for cooking and frying [1, 2].

M. Tomassetti (✉) · L. Campanella
Dipartimento di Chimica, Università di Roma "La Sapienza", P.le A. Moro 5, 00185 Rome, Italy
e-mail: mauro.tomassetti@uniroma1.it

S. Vecchio
Dipartimento di Ingegneria Chimica Materiali Ambiente, Università di Roma "La Sapienza", Via del Castro Laurenziano 7, 00161, Rome, Italy

G. Neri et al. (eds.), *Sensors and Microsystems*,
Lecture Notes in Electrical Engineering 91, DOI: 10.1007/978-94-007-1324-6_78,

The aim of the present research was instead to study in greater depth the kinetics of several of the principal processes, which are probably interdependent and occur when an oil sample is artificially rancidified isothermally at 98°C in an air stream, using the classical American official method (AOM method, official method) of the American oil chemistry society (AOCS) [3]. Essentially, the principal processes taking place during EVOO thermooxidation were monitored using three different organic phase enzyme electrodes (OPEEs), as described in a previous paper [2]. Once again the biosensors operating in organic solvents proved extremely useful and suitable for performing measures in hydrophobic matrixes like oils, which are practically insoluble in water. Oils are, however, extremely soluble in non polar solvents, such as hexane and decane, which make it much easier and simpler to carry out accurate and precise analyses of hydrophobic matrixes such as oily solutions.

78.2 Methods

The OPEEs used in the present research are numbered (4), (5) and (6) in Table 78.1, in which the principal OPEEs developed recently by our research group are displayed.

Clearly, the processes taking place during thermooxidative decomposition, although distinct, are interdependent. For the sake of completeness two other ancillary, non biosensor, methods were also used, namely peroxide number [1] and antioxidant capacity measurement [2]. Lastly, the apparatus used to study isothermal olive oil sample rancidification at 98°C in an oxidizing atmosphere, i.e. a constant air stream of 140 mL min^{-1}, is shown in previous papers [1, 2].

78.3 Results

In a previous kinetic investigation performed at different temperatures and using model-fitting [2] on the thermo-oxidative decomposition of the polyphenols contained in EVOO and on the accompanying decrease in EVOO antioxidant capacity, a very "robust" activation energy (E_a) value, 38 kJ/mol, was found [1, 2]. Using the model-fitting kinetic method, applied to both the thermo-oxidative decomposition of polyphenols at several selected temperatures and the parallel decrease in the antioxidant capacity of EVOO, it was also possible to select four possible algorithms, identified as D1, D2, F1, F2, which fit the above-mentioned EVOO thermo-oxidative processes more satisfactorily (Table 78.2).

Also three other processes occurring during thermooxidation of EVOO were experimentally tested (the *peroxide number* (PN), the *hydroperoxide* (HP) and the *b*/*a* value [3], related to *free-radical* formation (FR)). Although quite distinct from the first two, the latter processes are, of course, related to them. Judging from the high degree of uniformity of the *k* values obtained (Table 78.3) in the operating

Table 78.1 Main OPEEs recently developed by the present authors

	OPEEs (organic phase enzyme electrode) recently developed by the present authors	
(1)	Phospholipase D + choline oxidase OPEE	For lecithin determination in hydrophobic foodstuffs and in hydrophobic pharmaceutical preparations
(2)	Butyrylcholinesterase + choline oxidase OPEE	Inhibition OPEE for several pesticide analyses (organophosphates and carbamates)
(3)	Catalase OPEE	For hydroperoxide analysis in oils, in pharmaceutical and cosmetic products
		For water trace determination in organic solvents
(4)	Tyrosinase OPEE	For total polyphenol determination in olive oils
		For total polyphenol determination in oil mill wastes
		For water trace determination in organic solvents
		For triazinic and benzotriazinic pesticides determination in real matrices after organic solvent extraction
(5)	Bienzymatic substrate competition (peroxidase + tyrosinase) OPEE	For hydroperoxide determination in edible oils
(6)	Superoxide dismutase OPEE	For the antioxidant capacity determination in hydrophobic matrices (foods or drugs)
		For free radical determination in edible oils
(7)	Alcohol oxidase OPEE	For ethanol determination in leadless fuels
(8)	Monoenzymatic substrate	For ethanol determination in biofuels
	Competition (catalase) OPEE	For ethanol determination in leadless fuels
(9)	Immobilized cells (Pseudomonas pudida) OPCE	For benzene determination in fuels

Table 78.2 Best model function selected (D1, D2, F1, F2)

The integral function $g(\alpha) = \int_0^{\alpha} d\alpha/f(\alpha)$	
D1: $g(\alpha) = \alpha^2 = k \cdot t$	D2: $g(\alpha) = (1-\alpha)\cdot\ln(1-\alpha) + \alpha = k \cdot t$
F1: $g(\alpha) = -\ln(1-\alpha) = k \cdot t$	F2: $g(\alpha) = 1/(1-\alpha)-1 = k \cdot t$

conditions described, the algorithm D1 appears to provide the most reliable results. The value of k thus obtained was always found to be of the order of 10^{-4} min^{-1}.

Also for olive oil (OO) and olive oil residue (OOR) in the thermo-oxidative process, again performed at 98°C using the AOM method, it was found that the values obtained were more homogeneous when algorithm D1 was used (see Table 78.4). Moreover, the kinetic constants obtained were comparable to those found for EVOO (Table 78.3). Lastly, to obtain the thermo-oxidation process reaction order, that is, to complete the kinetic model, the values of two experimental curves monitored during the oil degradation process using the AOM model (namely the trends of degradation of total polyphenols TDTP and the peroxide number PN, were processed using classical kinetic methods, expressing the reaction rate as a function of the variation in these values. Considering a priori the reaction respectively as zero order, first order or second order, a linear relationship is obtained as the solution of the relative differential equation.

Table 78.3 Kinetic rate constants of extra-virgin olive oils (EVOO) degradation occurring at 98°C as determined using the isothermal model-fitting method and D1 model function according to the trends of thermal degradation of total polyphenols (TDTP), the total antioxidant capacity value (TACV), the peroxide number (PN), the hydroperoxide (HP) and the b/a value related to the free-radical formation (FR)

Model function	$10^{-4} \cdot k$ (min^{-1}) (RSD $\leq$ 5%)				
	TDTP	TACV	PN	HP	FR
D1	2.1	2.5	1.3	1.8	18

Table 78.4 Comparison of kinetic constant rates of degradation occurring at 98°C in extra-virgin olive oil (EVOO), olive oil (OO) and olive oil residue (OOR) as determined using the isothermal model-fitting method and D1 model function according to the trends of degradation of total polyphenols (TDTP) and the peroxide number (PN)

Model functions	$10^{-4} \cdot k$ (min^{-1}) (RSD $\leq$ 5%)					
	TDTP			PN		
	EVOO	OO	OOR	EVOO	OO	OOR
D1	2.1	4.3	5.1	1.3	3.1	3.8

Table 78.5 Comparison of kinetic constant rates of degradation occurring at 98°C in extra-virgin olive oil (EVOO), olive oils (OO) and olive oil residue (OOR) as determined using the trends of the thermal degradation of the total polyphenol concentration (TDTP) and the peroxide number (PN) according to the traditional kinetic method, and considering a first-order process

Reaction order (n)	$10^{-4} \cdot k$ (min^{-1}) (RSD $\leq$ 4%)					
	TDTP			PN		
	EVOO	OO	OOR	EVOO	OO	OOR
1	2.5	4.8	8.0	3.7	8.8	13.5

On the grounds of the best R^2 values observed for the linear relationship thus determined, it seems legitimate to infer that the reaction order of the thermo-oxidative process is of the first order. The k values calculated using the first-order model for the two experimental curves considered are reported in Table 78.5.

Even in this case, the k values found were of the order of 10^{-4} min^{-1}. However, as expected, these values increased in the following order:

$$OOR > OO > EVOO$$

78.4 Conclusion

The kinetic model was thus found to be adequately consolidated. In obtaining this result the contribution made by OPEEs once again proved decisive. This confirms the usefulness and importance of these biosensors.

References

1. Campanella L, Nuccilli A, Tomassetti M, Vecchio S (2008) Biosensor analysis for the kinetic study of polyphenol deterioration during the forced thermal oxidation of extra-virgin olive oil. Talanta 74:1287–1298
2. Amati L, Campanella L, Dragone R, Nuccilli A, Tomassetti M, Vecchio S (2008) New investigation of the isothermal oxidation of extra virgin olive oil: determination of free radicals, total polyphenols, total antioxidant capacity, and kinetic data. J Agric Food Chem 56:8287–8295
3. AOCS, Methods Cd 12–57 (1964) In: Official and tentative methods of the American oil chemist's society, 3rd edn. vol 1. AOCS, Champaign, pp 1–4

Chapter 79
Ultrasensitive Detection of Non-amplified Genomic DNA

Laura Maria Zanoli, Roberta D'Agata, Giuseppe Spoto, Roberto Corradini, Rosangela Marchelli, Cristina Ferretti and Marcello Gatti

Abstract The combined use of peptide nucleic acid probes and ultrasensitive nanoparticle-enhanced SPRI detection is shown to allow the ultra-sensitive detection of non-amplified genomic DNA.

79.1 Introduction

The most widely used method for detecting DNA requires both the polymerase chain reaction (PCR) amplification of the DNA target as well as its labeling with fluorophores [1]. Both the mentioned procedures imply additional steps in sample pre-treatment, are time consuming and require expensive reagents. So a major challenge in DNA detection is represented by the development of label-free rapid and multiplexed methods that do not require the PCR amplification of the genetic samples. Label-free and real time analyses can be carried out with high-throughput and low sample consumption by coupling microfluidic devices with the surface

L. M. Zanoli
Scuola Superiore di Catania, c/o Dipartimento di Scienze Chimiche, Università di Catania, Catania, Italy

R. D'Agata · G. Spoto (✉)
Dipartimento di Scienze Chimiche, Università di Catania, Viale Andrea Doria 6, 95125, Catania, Italy
e-mail: gspoto@unict.it

R. Corradini · R. Marchelli
Dipartimento di Chimica Organica ed Industriale, Università di Parma, Viale G.P. Usberti 17/a, 43100, Parma, Italy

C. Ferretti · M. Gatti
Neotron S.p.a., Stradello Aggazzotti 104, S. Maria di Mugnano, 41010, Modena, Italy

G. Neri et al. (eds.), *Sensors and Microsystems*,
Lecture Notes in Electrical Engineering 91, DOI: 10.1007/978-94-007-1324-6_79,

plasmon resonance imaging (SPRI) biosensing [2] and the peptide nucleic acid (PNA) improved selectivity and sensitivity in targeting complementary DNA sequences [3]. However, the use of SPRI for genomic assays is limited by the reduced sensitivity in the detection of nucleic acids hybridization reactions. Thus, a number of different strategies aimed at amplifying the SPRI response have been recently investigated. Among them, the amplification obtained by using colloidal gold nanoparticles (AuNPs) has been in particularly effective [4].

Herein, we describe the results obtained by using peptide nucleic acid (PNA) probes for the ultrasensitive nanoparticle-enhanced SPRI detection of non-amplified genomic DNA samples carrying different amounts of genetically modified (GM) sequences (Roundup Ready soybean, RR) for which certified reference materials with different GM mass fractions (<0.03% GM-free, 0.10 ± 0.05, 0.50 ± 0.10, 2.00 ± 0.26 and 5.00 ± 0.53%) are available.

79.2 PCR-Free Detection Scheme

A sandwich hybridization strategy was used for the ultrasensitive detection of non-amplified genomic DNA (Fig. 79.1).

The experiments were carried out according to procedures elsewhere reported [5] by using a 15-mer PNA sequence specifically designed to identify roundup ready (RR) genetically modified soybean (Fig. 79.1) [6].

The PNA probe immobilization was obtained by injecting the probe solution into microchannels in contact with a gold surface modified with the dithiobis(succinimidyl propionate) linker; two 2-(2-aminoethoxy)ethoxyacetic acid (LL) linkers were present at the N-terminus of the PNA probe (Fig. 79.1) in order to increase accessibility of the target DNA.

Solutions for the SPRI detection were prepared by diluting the DNA samples with PBS buffer to a total concentration of both GM and GM-free genomic samples of 10 pg μL^{-1}; a solution of genomic DNA from calf thymus (DNA-CF, 10 pg μL^{-1}) was used as the negative control. Before SPRI analysis, genomic DNAs were fragmented by sonication (2 min) and by vortexing (1 min). The double-stranded DNA containing samples were heated (95°C, 5 min) in order to denaturate the DNA strands, and rapidly cooled on ice thus preventing strands re-association. In order to minimize any interaction or crosslink between the single strands, the DNA solutions were introduced into the SPRI microfluidic apparatus as soon as possible (about 1 min) after the above described treatments. The direct hybridization of GM DNA (samples 0.1, 0.5, 2 and 5%), GM-free DNA (sample <0.03%) and DNA-CF to the surface-immobilized PNA did not generate SPRI responses useful for samples discrimination (data not shown). Thus this direct detection scheme failed to detect target DNA at such low concentrations.

AuNPs conjugated to a 13-mer oligonucleotide sequence (Fig. 79.1) complementary to a tract of the DNA target not involved in the hybridization with the PNA probe were used in order to enhance the SPRI response. After capture of the target DNA by the PNA probe, the conjugated AuNps were fluxed into the

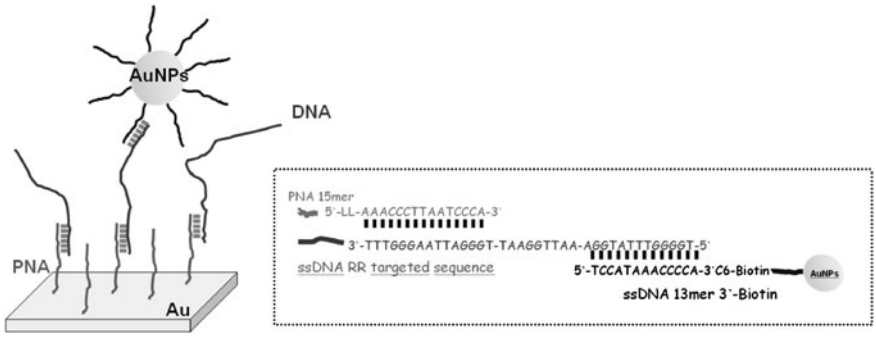

Fig. 79.1 The adopted sandwich hybridization strategy

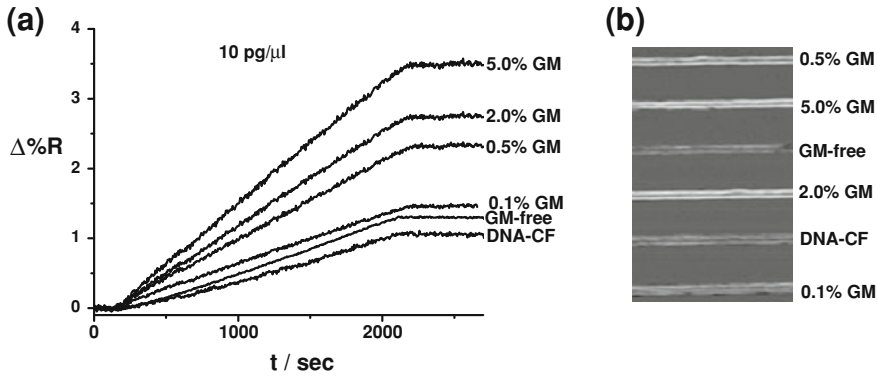

Fig. 79.2 Time-dependent SPRI curves obtained after the adsorption of DNA 13-mer-AuNps on GM DNA, GM-free and DNA-CF (**a**); SPR difference image (**b**)

channels (Fig. 79.1) in order to enhance detectability. The SPRI responses after the adsorption of DNA 13-mer-AuNps on GM DNA, GM-free and DNA-CF are shown in Fig. 79.2a where the change in percent reflectivity (Δ%R) over time is reported. Replicated experiments (Fig. 79.3) allowed to conclude that the Δ%R caused by the nanoparticle-enhanced SPRI detection allows to significantly distinguish between GM-free and 0.5%, 0.5 and 2%, 2 and 5% GM samples. No discrimination was achieved between 0.1% and GM-free, when using 10 pg μL^{-1} DNA solutions. These results allow to estimate that the described method can selectively identify the GM target sequence down to a 70 zM concentration (calculated for the 0.5% GM DNA. Estimated DNA molecular weight 7.3×10^{11}) in solutions containing a total of GM and of GM-free genomic DNA at a 14 aM concentration. Comparison of the results with those obtained with real-time PCR showed that the present technology is accurate and allows to use much lower concentrations of the DNA in the samples.

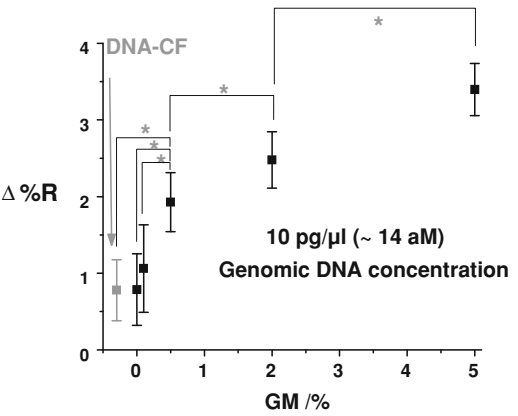

Fig. 79.3 Mean Δ%R values obtained from replicated independent experiments. Error bars represent the 95% confidence interval (*CI*) of the mean. *p-value < 0.05

79.3 Conclusions

These results show that the combined use of nanoparticle-enhanced SPRI and PNA probes provides a new tool for the rapid, specific and ultra-sensitive detection of genomic DNA. The detected DNA sample concentrations are compatible with a PCR-free detection approach since a 70 zM (7.0×10^{-20} M) sensitivity in targeting non-amplified genomic DNA, in solutions containing a total of GM and of GM-free genomic DNA at a 14 aM concentration (10 pg μL^{-1}) was achieved.

Acknowledgments We acknowledge support from MIUR (PRIN 2007 n 2007F9TWKE, FIRB RBRN07BMCT). Dr. M. Bigi and Dr. F. Totsingan are thanked for their assistance.

References

1. Shi L, Perkins RG, Fang H, Tong W (2008) Reproducible and reliable microarray results through quality control: good laboratory proficiency and appropriate data analysis practices are essential. Curr Opin Biotechnol 19:10–18
2. Grasso G, D'Agata R, Zanoli L, Spoto G (2009) Microfluidic networks for surface plasmon resonance imaging real-time kinetics experiments. Microchem J 93:82–86
3. Zanoli L, D'Agata R, Spoto G (2008) Surface plasmon-based optical detection of DNA by peptide nucleic acids. Minerva Biotecnologica 20:165–174
4. D'Agata R, Corradini R, Grasso G, Marchelli R, Spoto G (2008) Ultrasensitive detection of DNA by PNA and nanoparticle-enhanced surface plasmon resonance imaging. ChemBioChem 9:2067–2070
5. D'Agata R, Grasso G, Spoto G (2008) Real-time binding kinetics monitored with surface plasmon resonance imaging in a diffusion-free environment. Open Spectrosc J 1:1–9
6. Germini A, Rossi S, Zanetti A, Corradini R, Corrado F, Marchelli R (2005) Development of a peptide nucleic acid array platform for the detection of genetically modified organisms in food. J Agric Food Chem 53:3958–3962

Chapter 80
Cytotoxicity of Multiwalled Carbon Nanotube Buckypaper in Human Lymphocytes

O. Zeni, A. Sannino, S. Romeo, M. R. Scarfì, L. Coderoni, F. Micciulla, I. Sacco and S. Bellucci

Abstract An in vitro study to assess toxicological properties of buckypaper made from multiwalled carbon nanotubes is presented. Human peripheral blood lymphocytes have been chosen as cell model, and cytotoxicity has been investigated as it is a crucial factor in understanding the mechanisms of action of nanomaterials on cells and tissues. Buckypaper treatment has resulted in a reduction of cell growth of phytoemaglutinin stimulated human lymphocytes. In view of the potentially widespread use of this nanomaterial in pharmacological and biological applications, for which injection into human body is foreseen, we believe the results of the present study can contribute to the knowledge of the human health risk related to the use of buckypaper.

80.1 Introduction

In recent years great advances have been made in developing new nanomaterials for industrial and biomedical applications. Therefore, the corresponding novel field of nanotoxicology has become increasingly attractive for multidisciplinary

O. Zeni (✉) · A. Sannino · S. Romeo · M. R. Scarfì
CNR-IREA, Via Diocleziano, 328, 80124 Naples, Italy
e-mail: zeni.o@irea.cnr.it

A. Sannino
Department of Pharmaceutical Science, University of Salerno,
via Ponte don Melillo, 84084 Fisciano, Salerno, Italy

S. Romeo
Department of Information Engineering, Second University of Naples,
via Roma 29, 81031 Aversa, Italy

L. Coderoni · F. Micciulla · I. Sacco · S. Bellucci
INFN-Frascati National Laboratories, Via E. Fermi, 40,
00044 Frascati, Rome, Italy

G. Neri et al. (eds.), *Sensors and Microsystems*,
Lecture Notes in Electrical Engineering 91, DOI: 10.1007/978-94-007-1324-6_80,

research groups and has acquired public visibility, in order to match expectations of a sharp increase in both occupational and public exposure to nanomaterials. Among the new nanomaterials, carbon-based nanostructures are largely studied especially in the medical field as diagnostic and therapeutic tools due to their unique properties (high tensile strengths, ultra-light weight, thermal and chemical stability, metallic and semi-conductive electronic properties). Despite that, there is a paucity of information on their toxicological properties to assess potential human health risk, even if it is somewhat possible that carbon nanofibers, mostly single walled and multi walled carbon nanotubes, alter the function of human cells resulting in loss of cell viability [1]. Buckypaper (BP) is a carbon nanotubes-based nanomaterial, for which the main usages envisaged include electrochemical electrodes, filters, scaffolds, cell culturing, composites, with possible pharmacological and prosthetic applications. To our knowledge, just one study has been devoted to investigate cytotoxicity of BP [2]. The aim of this study was to extend the investigation on the intrinsic cytotoxicity of multiwalled carbon nanotube BP in human peripheral blood lymphocytes that participate in the recognition of foreign material in the blood.

80.2 Methods

80.2.1 Buckypaper

BP was obtained from NanoLab Inc (Newton, MA 02458 USA). It is a free-standing carbon nanotube paper made from 95% purity multiwall carbon nanotubes. Carbon nanotubes are suspended in a fluid and then filtered onto a membrane support. After drying, the paper is removed from the support, leaving a free-standing paper (http://www.nano-lab.com/buckypaper.html).

80.2.2 Biological Procedure

Human peripheral blood lymphocytes (HPBL) were obtained with informed consent from anonymized buffy coats of 2 healthy donors. They were isolated through lymphoprep density gradient centrifugation, in accordance with the manufacturer's instructions. Lymphocyte cultures were established by seeding 5×10^5/ml cells in 3 ml complete medium (RPMI 1640 supplemented with 15% foetal bovine serum; 1% L-glutamine and 1% Penicillin/Streptomycin), and phytoemagglutinin (PHA, 1%) was added as mitogen to stimulate T-lymphocytes to enter the cell cycle [3]. Cultures were maintained at 37°C and 5% CO_2. All the reagents employed for the experiments were of analytical grade.

BP fragments (<1 mg weight) were sterilized by autoclavation, and added at the start of cell cultures. Treatments with ethanol (5% final concentration for 2 h)

were also included as positive control. For each donor/treatment duplicate cultures were established.

For each culture, three different aliquots were collected following 24, 48, 72 and 96 h of growth, and three cytotoxicity assays with different mechanisms/endpoints to assess cell growth and viability were performed: trypan blue dye exclusion (TBDE) method, the Resazurin and Neutral Red assays.

The TBDE method is based on the principle that trypan blue dye enters only dead cells via damaged cell membrane. Just prior to counting, cells were treated with 0.4% (w/v) trypan blue, and the number of viable cells was determined by using a Burker hemocytometer under light microscope. Cell viability was calculated as a fraction of viable cells of the total cells expressed as percentage.

The Resazurin system measures the metabolic activity of living cells [4]. Resazurin (blue and non-fluorescent) is reduced to resorufin (pink and highly fluorescent) by oxidoreductases in mitochondria, thus, measurement of resorufin fluorescence is an indicator of mitochondrial function [5]. Therefore, a direct correlation exists between the reduction of resazurin in the growth medium and the metabolic activity of living cells. Cells were incubated at 37°C with 10 mg/ml resazurin until the appearance of detectable colour change. The production of resorufin was analysed in supernatants with a fluorometer (Perkin-Elmer, LS50B, Perkin Elmer Instruments, Norwalk, CT) at an excitation wavelength of 530 nm and an emission wavelength of 590 nm. To quantify resorufin production, a standard curve of fluorescent product was assessed. The results were expressed as μg of resorufin produced/ml/min.

The Neutral Red is a cationic dye which passes through cell membrane and accumulates inside lysosomes in a process requiring cellular energy. Chemical or physical treatments damaging lysosomal membranes or interfering with the normal energy requiring endocytosis process will decrease the ability of cells to take up neutral red [6]. The Neutral Red assay was carried out as follows: cells were treated with 0.066% (v/v final concentration) Neutral Red for 3 h, washed in PBS and lysed in 200 μl of cold lysis buffer (50 mM Tris/HCl, pH 7.4, 150 mM NaCl, 5 mM DTT, 1% Triton X-100) containing 1% acetic acid and 50% absolute ethanol. The absorbance of lysed cells was measured spectrophotometrically at 540 nm.

80.3 Results and Discussion

The results obtained indicate that BP treatment inhibited cell growth of HPBL. As a matter of fact, a strong reduction in cell number has been recorded in BP treated cultures with respect to control ones (CTRL) after 48 h of growth. Such a reduction appeared more evident after 72 and 96 h of growth as shown in Fig. 80.1a where cell counting by TBDE assay is presented. This result has been confirmed by applying Resazurin (Fig. 80.2) and Neutral Red (Fig. 80.3) assays, even if both assays showed a reduction at 96 h respect to 72 h of growth due to

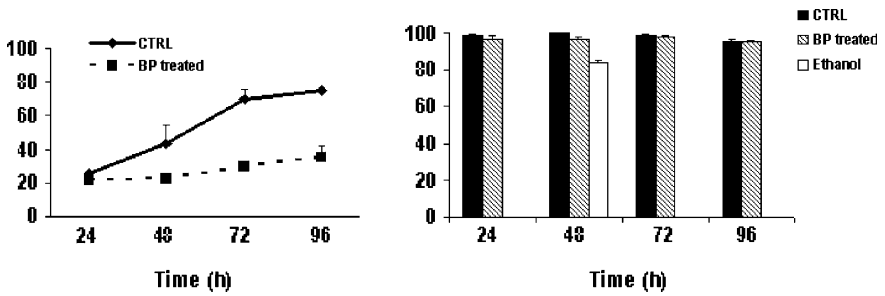

Fig. 80.1 Cell counting (**a**) and viability (**b**) of PHA stimulated HPBL assessed by TBDE assay. Each data point represents the mean ± SD of 2 healthy donors

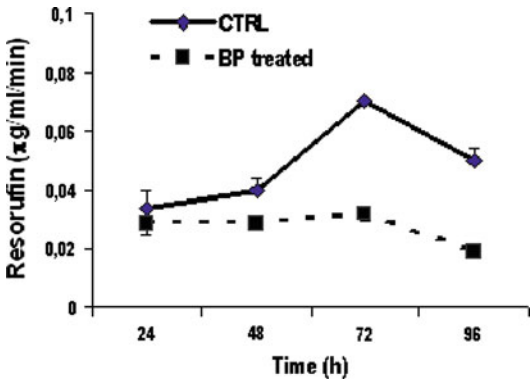

Fig. 80.2 Growth curve of PHA stimulated HPBL assessed by measuring metabolic activity by means of resazurin assay. Mean ± SD of 2 healthy donors

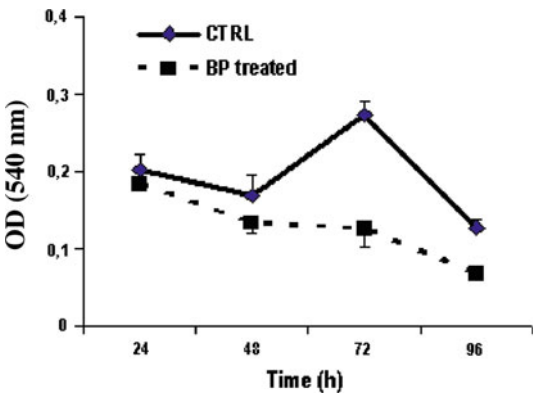

Fig. 80.3 Growth curve of PHA stimulated HPBL assessed by measuring membrane integrity by means of neutral red assay. Mean ± SD of 2 healthy donors

culture medium consumption that compromises energy requiring activities. The observed reduction could be ascribed to a cell growth arrest, as suggested by the absence of cell death in BP-treated cells respect to control ones for all the harvesting times considered (TBDE assay), shown in Fig. 80.1b. On the contrary,

following ethanol treatment (5% for 2 h) about 20% cell death was induced. In a previous work Bellucci and co-workers found that in vitro treatments with the same BP employed in this study, induced decreased proliferation of several human cancer cell lines growing both attached at the bottom of the culture well and floating, while no effects were detected when normal cells, growing attached, were treated [2]. The results here presented on healthy human lymphocytes, growing floating, suggest that the growth feature could also have a role in eliciting the cytotoxic effect of BP.

Taking into account the relevance of cytotoxicity in pathological processes such as carcinogenesis and inflammation, the present investigation deserves further study in order to understand the mechanisms of action of such nanomaterial. Moreover, the possibility of cytotoxicity to arise from carbon nanotubes released into the cell medium must be assessed [7, 8]. Work is in progress aiming to validate the observed effect on a larger number of donors, and to determine the possible involvement of apoptosis and cell cycle dysfunction in the observed effect.

References

1. Genaidy A, Tolaymat T, Sequeira R et al (2009) Health effects of exposure to carbon nanofibers: systematic review, critical appraisal, meta analysis and research to practice perspectives. Sci Total Environ 407:3686–3701
2. Bellucci S, Chiaretti M, Cucina A et al (2009) Multiwalled carbon nanotube buckypaper: toxicology and biological effects in vitro and in vivo. Nanomedicine (Lond) 4:531–540
3. Boyum A (1968) Isolation of leukocytes from human blood. Further observations. Methylcellulose, dextran and ficoll as erythrocyte aggregation agents. Scand J Clin Lab Invest 97:31–50
4. O'Brien J, Wilson I, Orton T et al (2000) Investigation of the Alamar blue (resazurin) fluorescent dye for the assessment of mammalian cell cytotoxicity. Eur J Biochem 267:5421–5426
5. Zhang HX, Du GH, Zhang JT (2004) Assay of mitochondrial functions by resazurin in vitro. Acta Pharmacol Sin 25:385–389
6. Fautz R, Husein B, Hechenberger C (1991) Application of the neutral red assay (NR assay) to monolayer cultures of primary hepatocytes: rapid colorimetric viability determination for the 17 unscheduled DNA synthesis test (UDS). Mutat Res 253:173–179
7. Chiaretti M, Mazzanti G, Bosco S et al (2008) Carbon nanotubes toxicology and effects on metabolism and immunological modification in vitro and in vivo. J Phys Condens Matter 20:474203–474207
8. Zeni O, Palumbo R, Bernini R et al (2008) Cytotoxicity investigation on cultured human blood cells treated with single wall carbon nanotubes. Sensors 8:488–499